NASA-CR-192104

PART 2, VOLUME II

(NASA-CR-192104) THE JOINT NASA/GEOSAT TEST CASE PROJECT, PART 2, VOLUME 2 Final Report (JPL) 393 p

N93-72311

Unclas

Z9/43 0152657

The Joint NASA/Geosat Test Case Project

Final Report

Michael J. Abrams
James E. Conel
Harold R. Lang
Jet Propulsion Laboratory
California Institute of Technology
Pasadena, California

Editor
Helen N. Paley
Jet Propulsion Laboratory

October 1984

AAPG BOOKSTORE
P.O. Box 979
Tulsa, OK 74101, USA

The research described in this publication was carried out jointly by the Jet Propulsion Laboratory, California Institute of Technology, under a contract with the National Aeronautics and Space Administration, and by The Geosat Committee, Inc., and its members.

Reference herein to any specific commercial product, process, or service by trade name, trademark, manufacturer, or otherwise, does not constitute or imply its endorsement by the United States Government, The Geosat Committee, Inc., and its members, or the Jet Propulsion Laboratory, California Institute of Technology.

Published by
The American Association of Petroleum Geologists
Tulsa, Oklahoma 74101, USA

Copyright © 1985 by
The American Association of Petroleum Geologists
All Rights Reserved
ISBN: 0-89181-654-2
Library of Congress Cataloging in Publication Data

Abrams, Michael J.
The Joint NASA/Geosat Test Case Project.

Sponsored by NASA, Jet Propulsion Laboratory, and Geosat
October 1984
Includes bibliographies
1. Joint NASA/Geosat Test Case Project. 2. Geology—Remote sensing. 3. Petroleum—Geology—Remote sensing. 4. Mines and mineral resources—Remote sensing. I. Conel, James E. II. Lang, Harold R. III. Paley, Helen N. IV. United States. National Aeronautics and Space Administration. V. Jet Propulsion Laboratory (U.S.) VI. Geosat Committee. VII. Title.
QE33.2.R4A27 1985 622'.1 85-1381

Preface

This volume of the *Joint NASA/Geosat Test Case Project Final Report* contains the results from the petroleum studies and the Technical Appendix. Part 2, Volume I, contains the results from the porphyry copper and uranium studies as well as the Project Description and Sensor Assessment Report. A key to the bandpasses of the multispectral scanners used in this study is included in the Map Envelope, Part 3. Part 1 is a summary of the entire Joint NASA/Geosat Test Case Project.

PRECEDING PAGE BLANK NOT FILMED

Contents

Selected Acronyms and Abbreviations A-1

10. Petroleum Commodity Report 10-i
11. Patrick Draw, Wyoming, Petroleum Test Site Report 11-i
12. Lost River, West Virginia, Petroleum Test Site Report 12-i
13. Coyanosa, Texas, Petroleum Test Site Report 13-i
14. Technical Appendix 14-i

PRECEDING PAGE BLANK NOT FILMED

INTENTIONALLY BLANK

Selected Acronyms and Abbreviations

AAPG	American Association of Petroleum Geologists
ACSM	American Congress on Surveying and Mapping
AEC	Atomic Energy Commission
AIME	American Institute of Mining Engineers
ANAMAX	Mining company owned by AMAX and Anaconda mining companies
ASARCO	American Smelting and Refining Company
ASP	American Society of Photogrammetry
ATI	Apparent thermal inertia
BCF	Billion cubic feet
BLM	Bureau of Land Management
BMD	Biomedical Computer Program Series; a set of statistical computer programs developed by the University of California at Los Angeles
CCT	Computer-compatible magnetic tapes
CIR	Color infrared
CRC	Color ratio composite
CSD	Cross-strike discontinuity
CT	Canonical transformation
DEC	Digital Equipment Corporation
DN	Digital number
DOE	Department of Energy
ERIM	Environmental Research Institute of Michigan
EROS	Earth Resources Observation Systems
FLD	Fraunhofer Line Discriminator
FOV	Field of view
Geosat	The Geosat Committee, Inc.
GSA	Geological Society of America
HCMM	Heat Capacity Mapping Mission
HH	Parallel polarized; horizontally transmitted and horizontally received radar signal
HP	High-pass; a contrast enhancing filter
HSI	Hue, saturation, and intensity
HV	Cross polarized; horizontally transmitted and vertically received radar signal

IEEE	Institute of Electrical and Electronics Engineering
IFOV	Instantaneous field of view
IGARSS	International Geoscience and Remote Sensing Symposium
IPL	JPL's Image Processing Laboratory
IR	Infrared
JPL	Jet Propulsion Laboratory
JSC	Johnson Space Center
LP	Low-pass; a contrast subduing filter
MCF	Thousand cubic feet
MFMR	The aircraft Multifrequency Microwave Radiometer
M^2S	The aircraft Modular Multispectral Scanner
MSS	Multispectral Scanner; a system on Landsat satellites
NASA	National Aeronautics and Space Administration
NS-001	The aircraft Thematic Mapper Simulator
NURE	National Uranium Resource Evaluation
PC	Principal component
PCA	Principal components analysis
PDB	Pee Dee belemnite
PFRS	Portable Field Reflectance Spectrometer
pixel	Picture element
PMIS	The aircraft Passive Microwave Imaging System
RME	Rocky Mountain Energy
SAR	Synthetic Aperture Radar
SCS	Soil Conservation Service
SEG	Society of Exploration Geophysicists
SLAR	Side-looking airborne (aircraft) radar
SLR	Side-looking radar
SMIRR	Shuttle Multispectral Infrared Radiometer
SMOW	Standard mean ocean water
SPIE	Society of Photo-Optical Instrumentation Engineers
SPOT	Système Probatoire d'Observation de la Terre; a French multispectral satellite terrestrial remote sensing system
TC	True color
TI	Thermal inertia
TIR	Thermal infrared
TM	Thematic Mapper; a multispectral scanner system on Landsat 4
USDA	United States Department of Agriculture
USGS	United States Geological Survey
VH	Cross polarized; vertically transmitted and horizontally received radar signal
VNIR	Visible and near infrared
XRD	X-ray diffraction

Figure Credits

The following figures were reprinted with permission of the copyright holders: Figure 10-8 by permission of the Geological Survey of Canada, Ottawa; Figures 11-2 and 11-3 by permission of the Rocky Mountain Association of Geologists, Denver; Figure 11-19 by permission of the Macmillan Publishing Co., Inc., New York; Figure 12-1 by permission of the West Virginia Geological and Economic Survey, Morgantown; Figure 12-61 by permission of Chapman and Hall Publishers, London; Figure 13-11 by permission of the West Texas Geological Society, Midland; Figure 13-13 by permission of the Oil & Gas Journal, Tulsa; and Figures 14-5 and 14-6 by permission of the Air Pollution Control Association, Pittsburgh.

Section 10

Petroleum Commodity Report

Authors/Editors

Harold R. Lang
Jet Propulsion Laboratory

Paul H. Nadeau
The Geosat Committee, Inc.
San Francisco, California

Contributors

Matt D. Matthews
Gulf Science and Technology Co.
Pittsburgh, Pennsylvania

Harry E. Stewart
Sunmark Exploration
Dallas, Texas

Floyd F. Sabins, Jr.
Chevron Oil Field Research Company
La Habra, California

Section 10

Petroleum Commodity Report

Contents

I. Introduction 10-1

II. Characteristics of Commercial Oil and Gas Accumulations 10-1

III. Conventional Oil and Gas Exploration Methods 10-5

IV. Remote Sensing in Oil and Gas Exploration 10-9

V. Background and Site Selection 10-10

A. Background 10-10

B. Site Selection 10-10

VI. Comparative Results 10-12

A. Introduction 10-12

B. Physical Basis of Geologic Remote Sensing 10-13

C. General Comparison of Sensors 10-14

D. Processing 10-16

E. Information Extraction 10-16

1. Structural geology 10-17
2. Soil/stratigraphic mapping 10-18
3. Geobotany 10-18

VII. Exploration Model Development 10-19

VIII. Conclusions and Recommendations 10-22

References 10-25

Bibliography 10-27

Figures

10-1. Map of the United States showing the major oil- and gas-producing provinces and the locations and names of the three petroleum test sites studied 10-2

10-2. Map of the world showing major sedimentary basins 10-3

10-3. Map of the United States showing the major sedimentary basins and the locations of the three petroleum test sites 10-4

PRECEDING PAGE BLANK NOT FILMED

10-4. Age distribution of hydrocarbon reserves contained in giant fields as of 1973 10-5
10-5. Common trap types in schematic cross section 10-6
10-6. Histograms illustrating oil volumes contained by different types of known giant field traps as of 1980 10-7
10-7. Relationship of world and U.S. crude oil production and reserves to selected significant developments in exploration technology 10-8
10-8. Block diagram illustrating components at the Earth's surface that can potentially contribute to remote sensing data 10-13
10-9. Generalized absorption spectrum of the atmosphere showing names of spectral regions of interest for geologic remote sensing 10-14
10-10. Diagrammatic illustrations of the empirical remote sensing exploration model developed in the Patrick Draw, Wyoming, test site study 10-20
10-11. Diagrammatic illustrations of the empirical remote sensing exploration model developed in the Lost River, West Virginia, test site study 10-21

Tables

10-1. Characteristics of the three petroleum test sites 10-11
10-2. Site characterization information acquired for test site investigation 10-12

Section 10

Petroleum Commodity Report

I. Introduction

This section summarizes some basic concepts of petroleum geology and highlights the characteristics, methods of study, and results obtained at the three petroleum test sites (Figure 10-1). Additionally, selected papers that cover in greater detail the concepts introduced here are included in the References and Bibliography at the end of this section. Information in this section provides the perspective necessary to understand details of individual test site reports (Sections 11, 12, and 13) in terms of the overall project goal—to evaluate the utility of state-of-the-art remote sensing technology for geologic mapping and oil and gas exploration.

II. Characteristics of Commercial Oil and Gas Accumulations

Commercial oil and gas accumulations are mixtures of gaseous and liquid hydrocarbon compounds that occur primarily in sedimentary rocks. The compounds form from organic material preserved in sediments that have been buried to sufficient depth to thermally evolve mobile fluids. These fluids then migrate into porous and permeable subsurface zones (reservoirs) within geological features (traps) from which they can be commercially extracted by wells.

Known global and U.S. sedimentary basins containing commercial hydrocarbon accumulations are shown in Figures 10-2 and 10-3, respectively. These basins occur in the interior of continents, on continental margins, and on offshore continental shelves. For comparative purposes, U.S.-proven hydrocarbon reserves for onshore and offshore basins are estimated to be 26.8 billion barrels[1] of oil/159.7 trillion cubic feet of gas and 3 billion barrels of oil/39.3 trillion cubic feet of gas, respectively (Department of Energy, 1980). Generally, sedimentary rocks in interior continental basins are older than those of the continental margin. The degree of structural deformation of both marginal and interior basins can vary from minor (characterized by essentially flat-lying strata) to severe (characterized by faulted, steeply dipping, and overturned strata), depending on their specific geological setting and history. Although hydrocarbon accumulations are widely distributed, more than 85 percent of the world's total hydrocarbon production is obtained from fewer than 5 percent of the individual fields (McCulloh, 1973).

Sediments that contain suitably preserved organic material for the generation of mobile hydrocarbons are known as source rocks. Source rocks are usually dark gray to black in color and are composed of fine-grained material. They are deposited in marine, river, deltaic, and lake environments. Because organic material is commonly destroyed by oxidation within a few centimeters of the sediment–water interface (Sweeney and Kaplan, 1980), the organic material must be isolated (by rapid burial) from oxidizing environments and organisms so that it can be preserved in the potential source rock.

Immobile sedimentary organic material, which is the precursor of mobile hydrocarbons, is called kerogen. Kerogen forms from algal material preserved in lake sediments, from planktonic material preserved in marine sediments, or from herbaceous or woody material preserved in terrestrial sediments (Tissot and Welte, 1978). The type of kerogen present largely determines the type of mobile hydrocarbon product generated. When kerogen-bearing sediments encounter sufficient temperatures, often related to their depth of burial, the generation of mobile hydrocarbon compounds occurs. Because the thermal gradient

[1] 1 barrel (bbl) = 42 U.S. gallons and is the standard U.S. unit of measure for liquid petroleum.

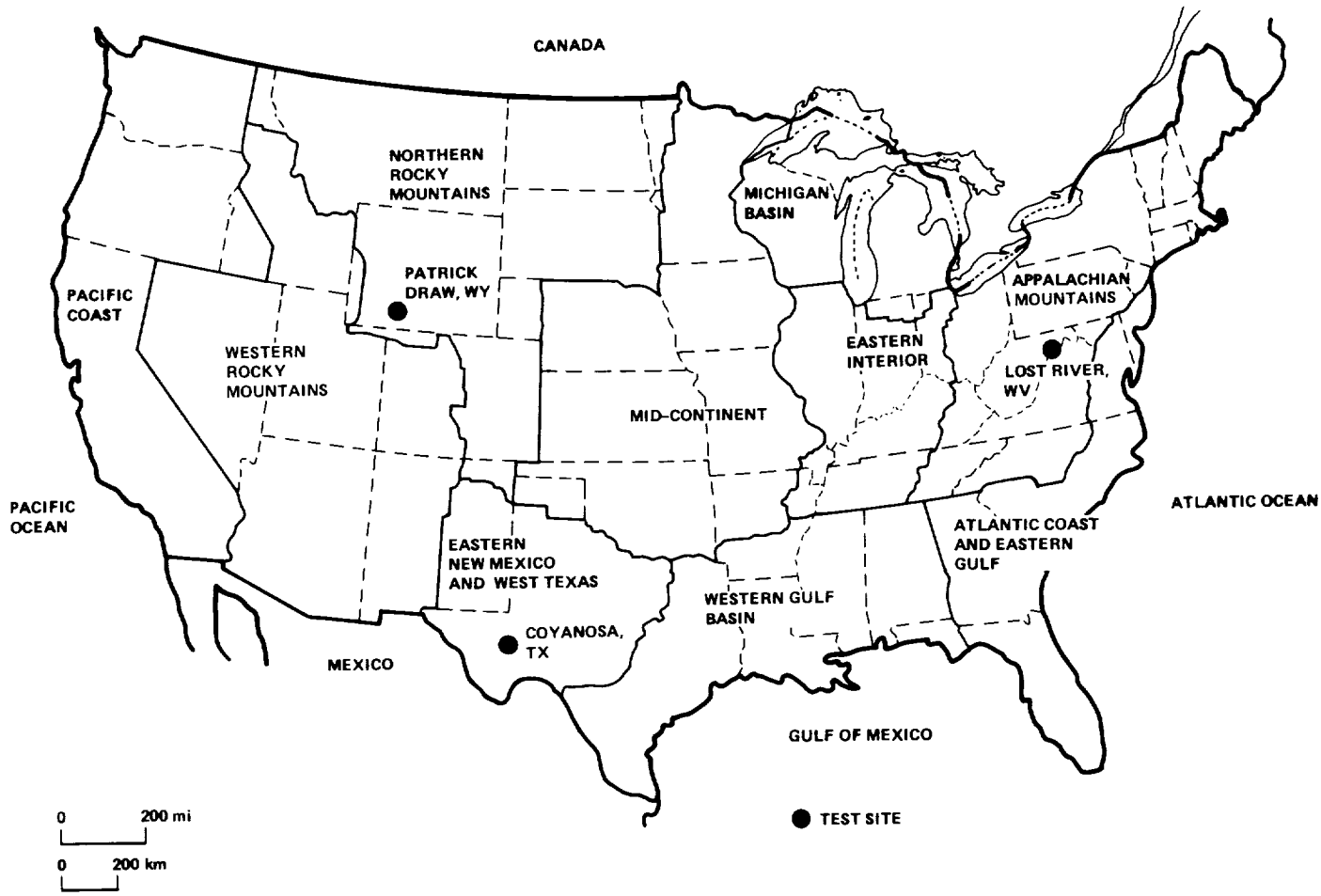

Figure 10-1. Map of the United States showing the major oil- and gas-producing provinces (Cram, 1971, Figure 1, p. 2) and the locations and names of the three petroleum test sites studied

(change in temperature with depth) differs from basin to basin and over geologic time, the depth of hydrocarbon generation is variable but averages about 2 to 3 km (6000 to 10,000 ft). Because oil is often generated at a lower temperature than gas, the depth of generation of hydrocarbons within a basin is a function of the type and quantity of kerogen present and the thermal gradient. The geologic history of a basin must be assessed, therefore, to determine if and when hydrocarbons were generated.

Hydrocarbon production with respect to the age of the reservoir for commercial U.S. and world accumulations is shown in Figure 10-4. The discrepancy between the two is mainly due to the huge Mesozoic accumulations of the Middle East. Nonetheless, these data suggest that there were periods in the Earth's history and certain regions that were more favorable than others for the generation and accumulation of hydrocarbons.

Once hydrocarbons are generated, the complex and imperfectly understood process of migration occurs. The transport of mobile hydrocarbons within narrow pores of the fine-grained source rock and en route to the reservoir rock is called primary migration. Movement of the hydrocarbons through the larger pores within the more permeable reservoir rocks is called secondary migration. Pores in the subsurface are generally filled with water trapped during sediment burial or squeezed from underlying sediments by compaction. Because gas and oil have a higher buoyancy than water, hydrocarbons are generally found in the high areas of the reservoir rocks, i.e., at the upper end of tilted strata or at the tops of fold structures. The normal reservoir fluid sequence from the highest part of a reservoir to the lowest is gas, oil, and water.

Hydrocarbons are commercially produced from reservoirs that are subsurface zones characterized by intercon-

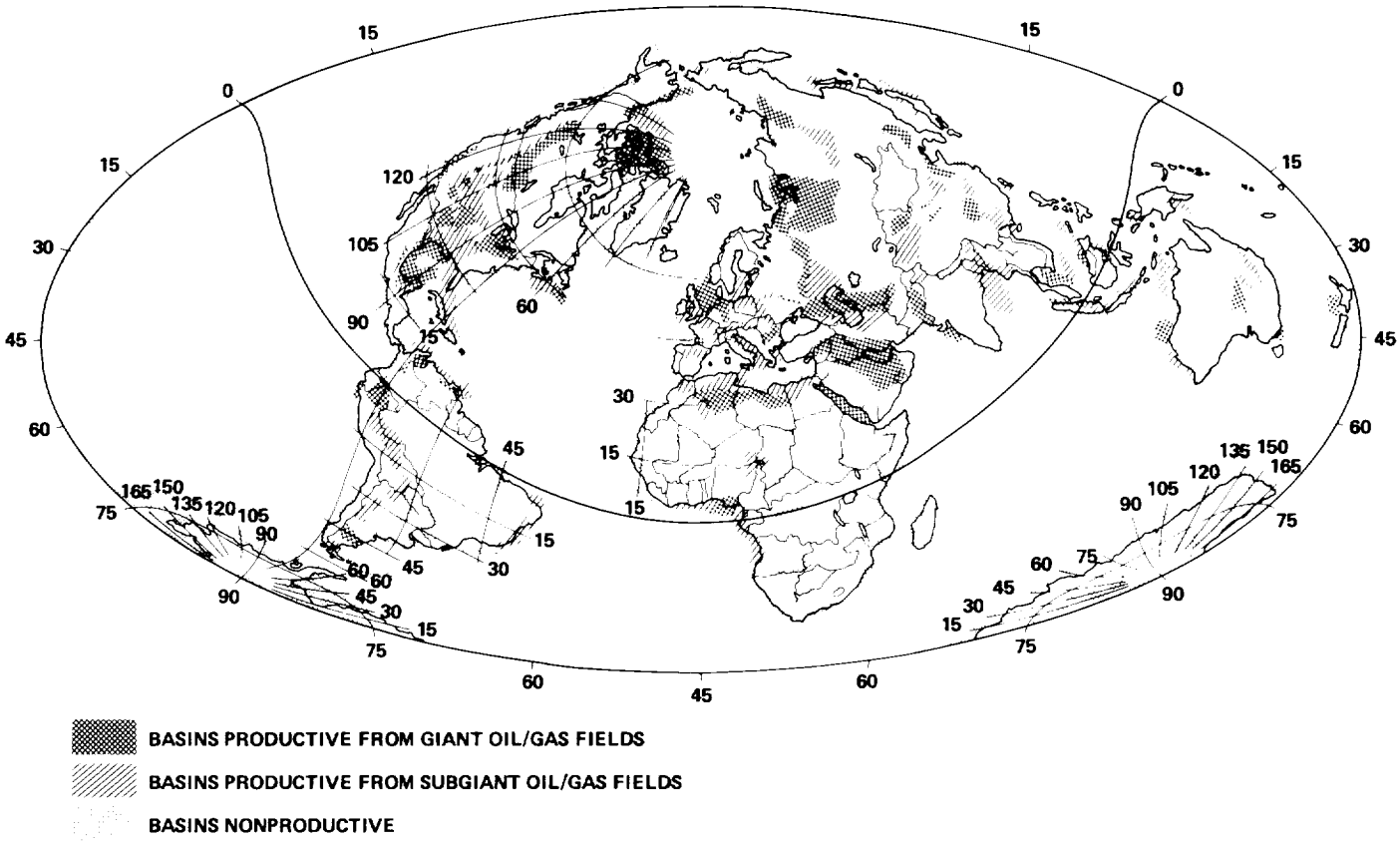

Figure 10-2. Map of the world showing major sedimentary basins. Basins are rated according to production history and exploration potential as of 1981 (basin data after St. John, 1981, Plate 1; Nordic projection after The Times, 1980, Plate 8).

nected pores which result in permeability. Porosities[2] of typical reservoirs range from 5 to 30 percent. Permeabilities of typical reservoirs range from 1 to 1000 millidarcies (md).[3] Porosity is a measure of total pore space, and permeability is a measure of the degree of pore interconnection. Commercial reservoirs occur in both clastic (sandstone and shale) and carbonate (limestone and dolomite) sedimentary rocks. The porosity of carbonate reservoirs is usually less than that of sandstone reservoirs; the permeability, however, can be higher. More than 60 percent of all commercial oil occurrences are in sandstones, 30 percent are in carbonates, and 10 percent are in fractured shales. Minor reservoirs have been discovered in igneous and metamorphic rocks.

Porosity in reservoirs is classified as either primary or secondary. Intergranular pore diameters may typically range from 0.05 to 0.25 mm. This intergranular porosity, related to the size, size variability, and packing of sedimentary particles, is created at the time of deposition and is known as primary porosity. During burial, chemical changes referred to as diagenesis occur in sedimentary rocks. Diagenesis usually destroys primary porosity by filling intergranular pores with mineral compounds. By chemically removing mineral compounds, some diagenetic processes can also create secondary porosity and permeability, particularly in carbonates and carbonate-cemented sandstones. Another form of secondary porosity is caused by structural deformation, which can create fractures and increase the pore volume and permeability of the reservoir rock. In fact, hydrocarbon well completion techniques commonly include chemical and/or mechanical methods to artificially create this type of secondary porosity and permeability.

Once located by drilling, surface production of hydrocarbon accumulations can be facilitated by the presence of

[2]$\text{Porosity} = \frac{\text{pore volume}}{\text{bulk volume}} \times 100$

[3]1 md, the standard unit of measurement for permeability, is 0.001 Darcy; 1 Darcy is that permeability which will allow 1 ml of a fluid of 1-centipoise viscosity (water at 20° C) to move 1 cm under a pressure gradient of 1 atmosphere through a cross-sectional area of 1 cm^2 in 1 s.

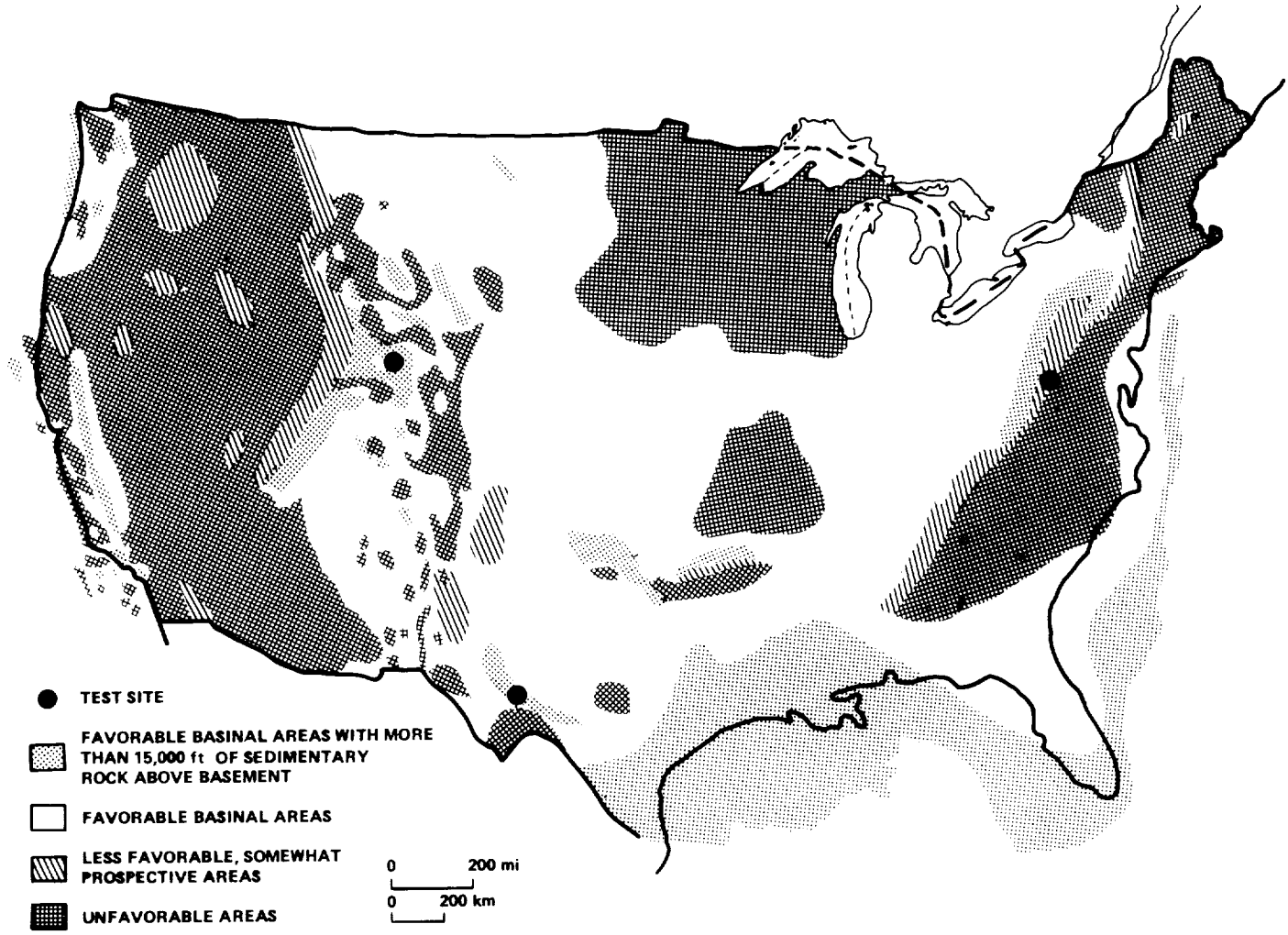

Figure 10-3. Map of the United States showing the major sedimentary basins and the locations of the three petroleum test sites. Basins are rated according to production history and exploration potential as of 1971 (Cram, 1971, Figure 2, p. 6).

hydrostatic pressure (water drive) or by the presence of high-pressure gas (gas expansion drive). Hydrocarbon accumulations that do not possess sufficient pressure to flow naturally through a well bore to the surface are either pumped to the surface or displaced to the surface by the injection of water or a variety of gases. The commercial producibility of subsurface hydrocarbons is determined by the size of the accumulation, its depth, the porosity and permeability of the reservoir rocks, the pressure of the reservoir fluids, and the composition of the fluids produced.

Reservoir depths can vary from near-surface to over 6 km (20,000 ft). The average reservoir depth, however, is about 1.2 km (4000 ft). The maximum potentially productive depth is controlled by factors including the diagenetic and mechanical destruction of porosity which can occur at depths greater than 6 km (20,000 ft), physiochemical limits on the generation and stability of hydrocarbons, and economic/technologic limitations on drilling/production depths.

Geological features that enclose reservoirs are called traps. Traps are overlain and sealed by relatively impermeable rocks that define the size of the hydrocarbon accumulation. A trap can have several reservoirs within it containing oil and/or gas and water. Traps are classified as structural or stratigraphic (Figure 10-5). The most important structural traps are anticlinal (Figure 10-5a, b, c, g) and can be large features up to several tens of kilometers in length. Other structural traps include fault-bounded features (Figure 10-5d, e, f) and those associated with salt domes (Figure 10-5h).

Stratigraphic traps form as a result of spatial variations in sedimentation and/or erosion. They are more difficult to

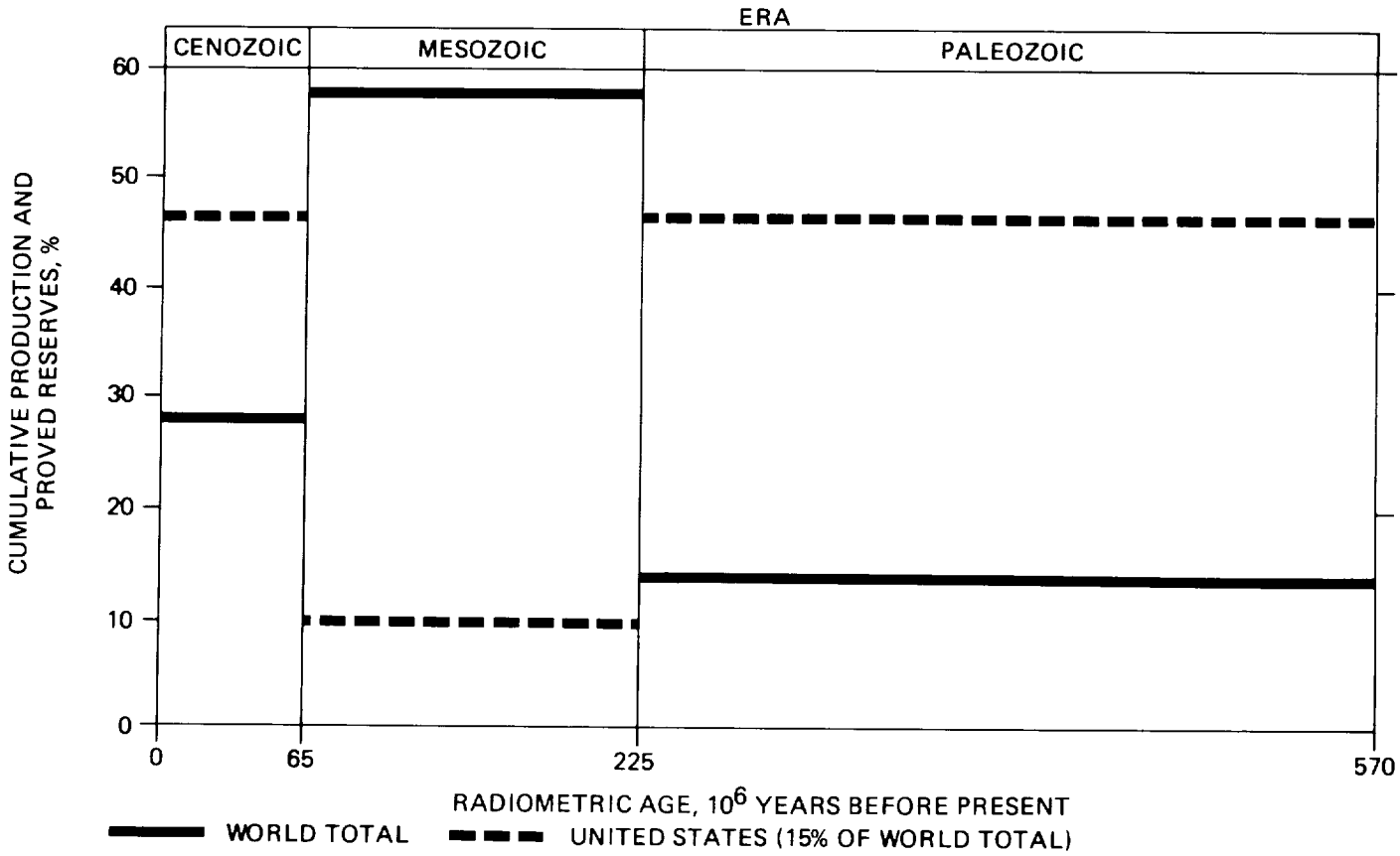

Figure 10-4. Age distribution of hydrocarbon reserves contained in giant fields as of 1973 (McCulloh, 1973, Figure 58)

detect and delineate than structural traps. Examples of stratigraphic traps include marine barrier bar sandstones, fluvial and deltaic channel sandstones, and carbonate reefs (Figure 10-5i, j, k). All of these are porous and permeable strata encased in impermeable shales. Erosional surfaces (unconformities) may truncate porous and permeable zones which can be covered and sealed by subsequently deposited sediments, thus forming a trap (Figure 10-5*l*). Deposits of evaporitic minerals such as salt and gypsum may also act as effective seals over porous rocks.

Other traps that have both stratigraphic and structural elements are called combination traps. Traps can also form in response to hydrodynamic flow through reservoir rocks. Figure 10-6 illustrates oil volumes contained by different types of traps.

Regardless of the nature of traps, it must be emphasized that their existence is temporary in terms of geologic time. Traps are dynamic systems. Recent research has demonstrated that some classically accepted characteristics of oil and gas traps may not be completely valid; for example, Roberts (1980) has argued that all traps must leak to some degree. The timing and duration of trap development with respect to hydrocarbon generation and migration as well as to changes in the chemical and physical environment are critical in creating commercial accumulations.

III. Conventional Oil and Gas Exploration Methods

Petroleum exploration today is a synergistic process involving the integration of data acquired by many technologies. Rarely is a commercial oil or gas discovery attributable to a single exploration tool. The introduction of new exploration tools has never resulted in a significant jump in the rate of discovery as expressed by cumulative production plus proved reserves. The history of petroleum exploration technology and the rate of discovery, illustrated in Figure 10-7, clearly document this observation. Additionally, there is a long lag time between the introduction of a new technology and its benefits in terms of proven reserves. The increase in reserves with time, however, is largely a measure of the historical improvement of the exploration process by using new data acquired from new tools.

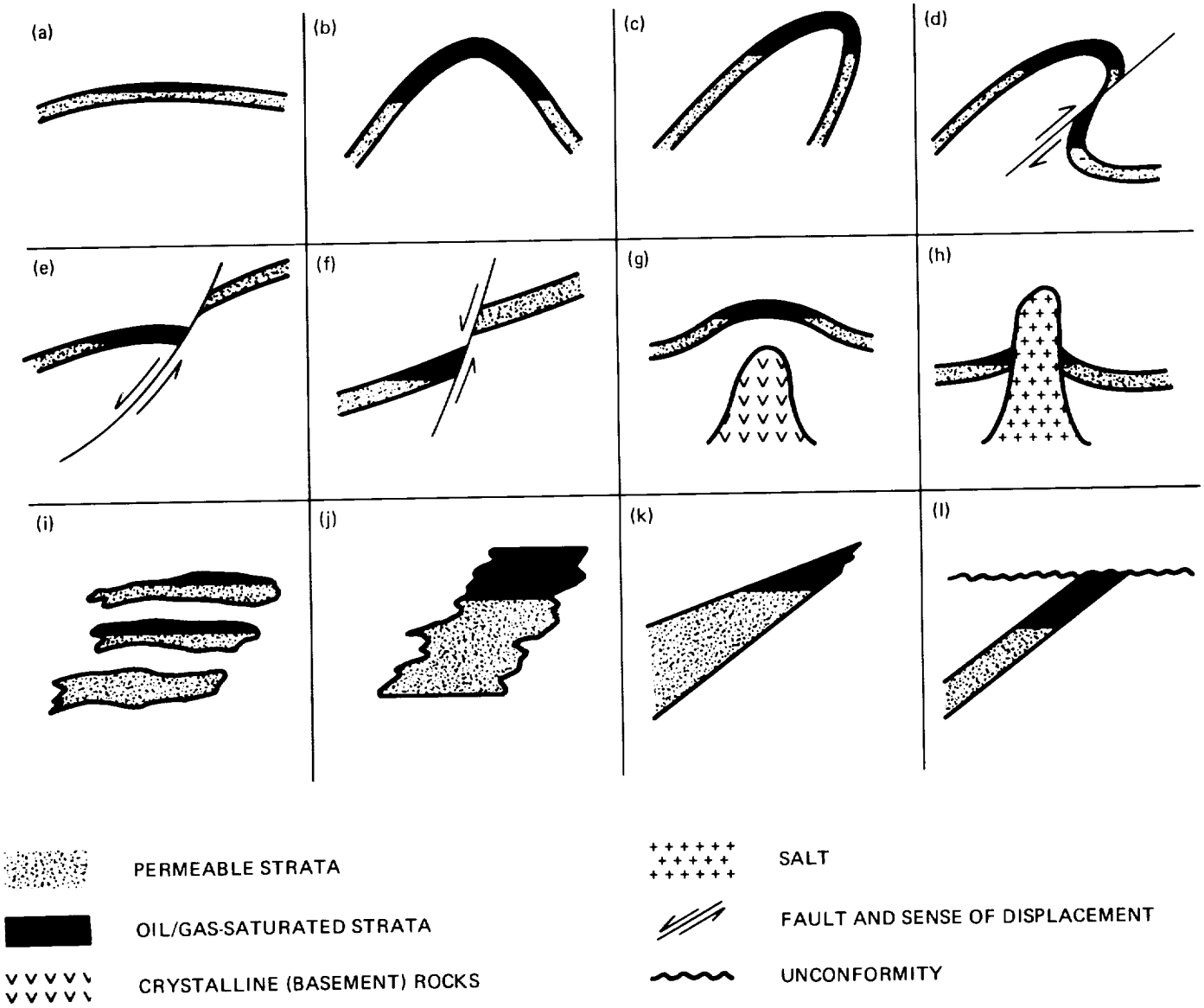

Figure 10-5. Common trap types in schematic cross section. Elements (a) through (h) are usually classified as structural (d, e, and f are fault traps); (i) through (l) as stratigraphic.

Hydrocarbon accumulations were first exploited by mining or by collecting fluids from natural surface and near-surface seeps. Early wells were dug or drilled near surface seeps, and most of the important oil-producing regions of the world were first identified by the presence of surface oil and gas seeps (Link, 1952). Shortly after the first U.S. oil well was completed in 1859, it was suggested that petroleum accumulations occur in anticlines (White, 1885). With this observation, the principle of surface geological mapping was developed to determine the possible presence of anticlinal traps in the subsurface based on their surface expression.

Geological and seep mapping were the primary means of exploration until 1920 when subsurface geology was first extensively employed in exploration. From the analysis of subsurface rock samples obtained by drilling, the ability to directly map subsurface structures, not evident at the surface, was developed. Core samples made it possible to identify stratigraphic controls on the location of zones of favorable porosity and permeability in potential reservoir rocks.

In the 1930s, subsurface exploration technology was improved by the introduction of mechanical, electrical, and

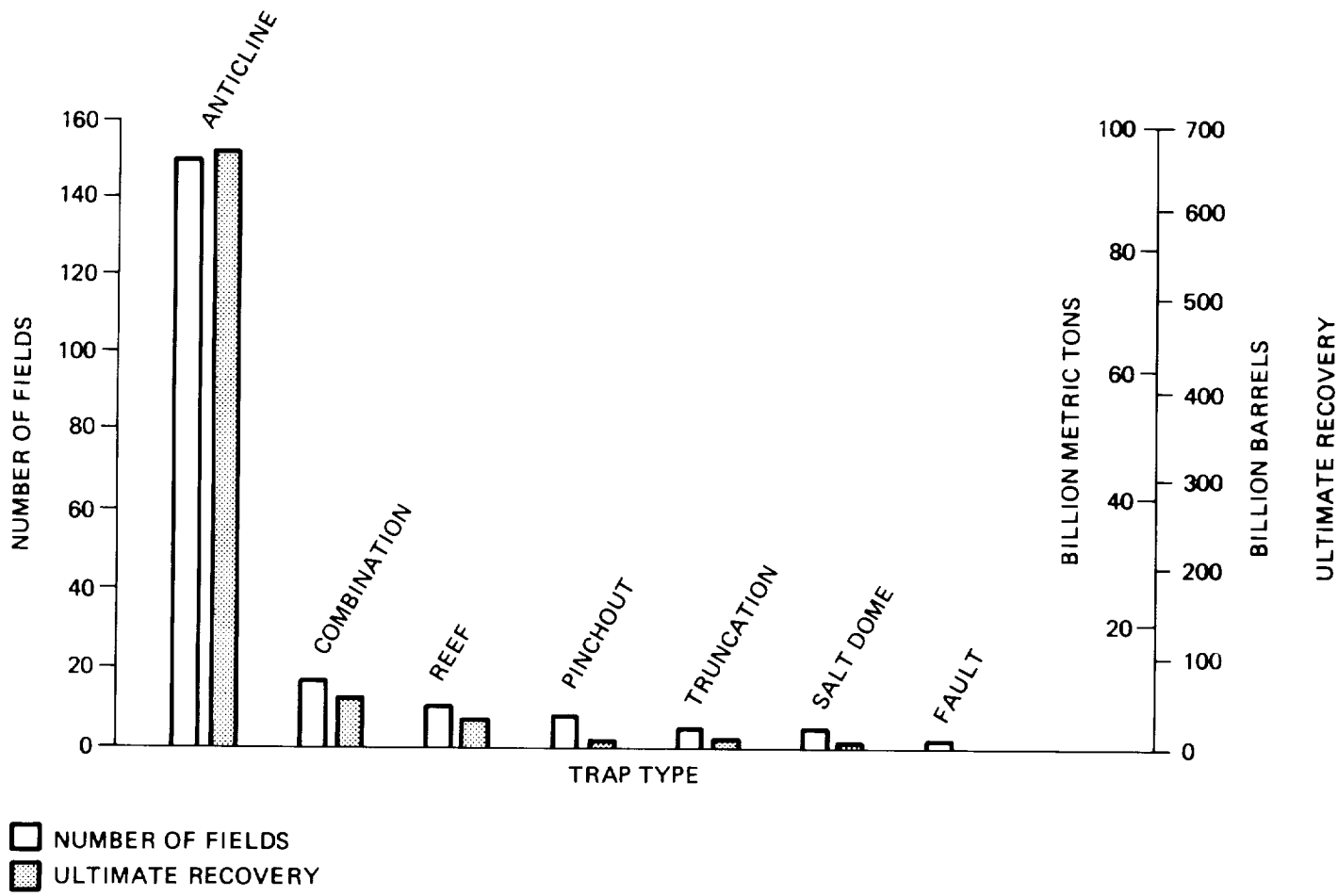

Figure 10-6. Histograms illustrating oil volumes contained by different types of known giant field traps as of 1980. The forms of anticlinial traps are depicted in Figure 10-5(a), (b), (c), (g); reef traps, Figure 10-5(j); pinchout traps, Figure 10-5(k); truncation traps, Figure 10-5(l); salt dome traps, Figure 10-5(h); and fault traps, Figure 10-5(d), (e), (f). (From Roberts, 1980, Figure 3, p. 221.)

other methods of geophysical well logging. Instruments lowered into the bore hole on a wire line measured physical properties of the rocks penetrated, including lithology, porosity, permeability, and degree of gas, oil, and water saturation. Well logging advanced to a high degree of sophistication and is still a major exploration tool today.

Geophysical exploration methods were introduced in the 1930s and 1940s. These included gravity, magnetics, and elementary seismic refraction and reflection. Gravity and magnetic methods were useful in determining gross configuration of crystalline rocks (basement) beneath potentially economic sedimentary strata as well as in identifying major structural discontinuities such as subsurface faults. Detailed gravity surveys were also capable of delineating subtle subsurface structures not obvious at the surface. The advent of the analog and digital computer increased the level of analytical sophistication for all exploration methods. The greatest impact of the computer, however, was on the acquisition and processing of seismic reflection data. Seismic techniques developed in the 1950s and 1960s became the major exploration method used by industry in both onshore and offshore environments. By delineating the interfaces between rocks with different sonic velocities, seismic reflection methods had the ability to determine both subsurface structure and stratigraphy. In some cases, particularly in the Gulf Coast region of the United States, the interface between gas-saturated and water-saturated zones could also be detected with seismic data. Reflection seismology is the dominant exploration tool used by industry today.

Geochemistry has found several applications in hydrocarbon exploration. Presently, conventional geochemical techniques are used to analyze the organic matter in sedimentary rocks, to identify potential source rocks, and to determine their states of thermal maturity with respect to hydrocarbon generation (Tissot and Welte, 1978). These

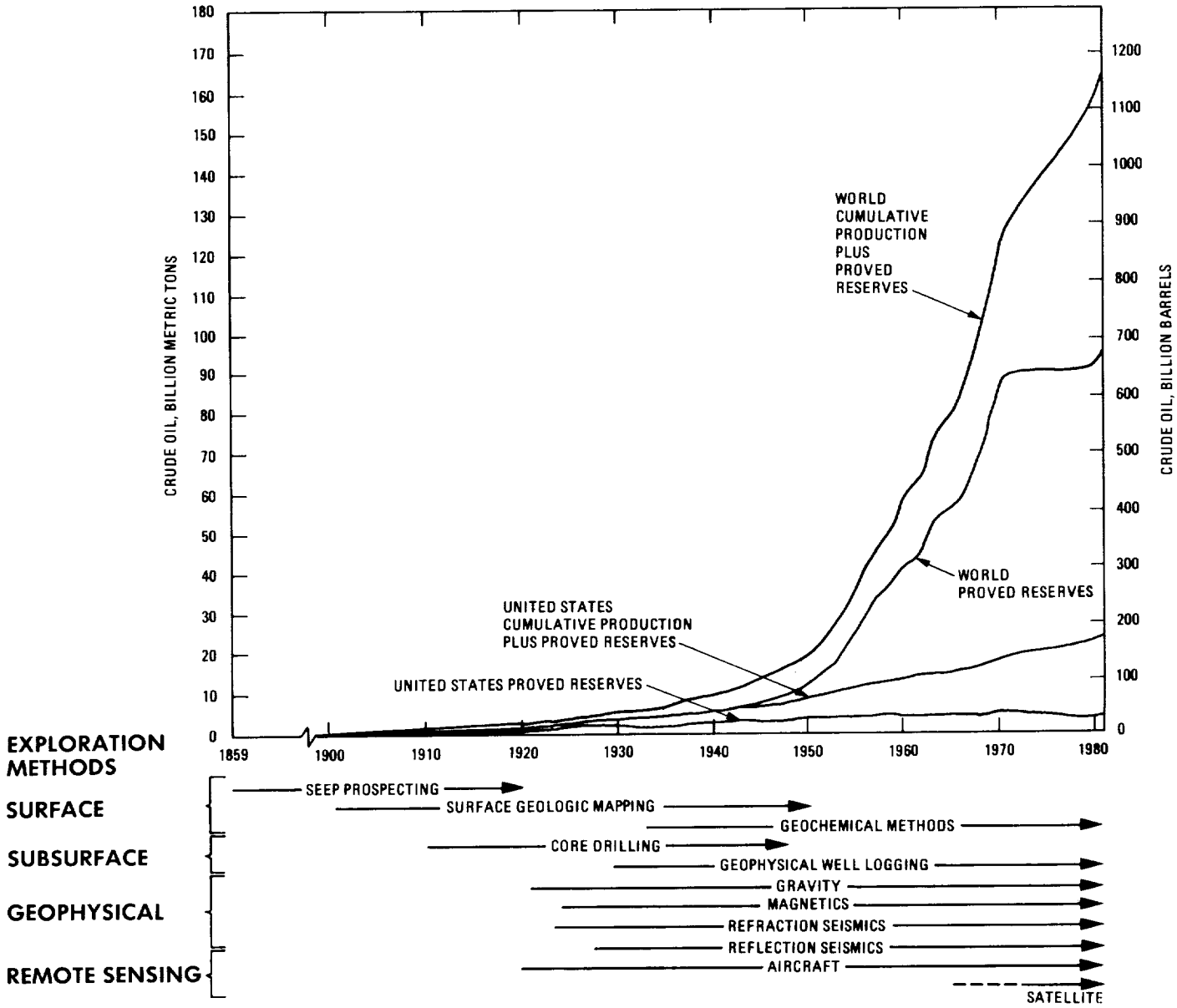

Figure 10-7. Relationship of world and U.S. crude oil production and reserves to selected significant developments in exploration technology. Production/reserve curves to 1971 are from McCulloh (1973, Figure 61, p. 492), data for 1971 through 1981 are from Auldridge (1979) and Enright (1981).

analyses, when combined with analyses of crude oil samples, can be used to identify the source rocks that are responsible for specific petroleum occurrences. This information can then be integrated into basin evolution studies used in exploration programs.

Less conventional geochemical prospecting methods began development as an exploration tool in the late 1930s. Various types of soil hydrocarbon analyses have been used to detect subsurface accumulations, based on the concept of the dominantly vertical migration of light hydrocarbons from leaking subsurface traps. Soil gas surveys produced inconsistent results and are still controversial, as summarized by Hunt (1979). Encouraging geochemical results have also been obtained by the analysis of hydrocarbon gases dissolved in well waters and offshore marine waters. Other less conventional geochemical methods include soil analyses of helium gas (Roberts et al., 1977), carbonate mineralogy (Donovan, 1974; Rosaire, 1940), carbonate isotopes (Donovan et al., 1974), trace element concentrations (Don-

ovan and Dalziel, 1977), soil and rock bleaching (Ferguson, 1975), and radiometric analyses. Additionally, there are unpublished industry reports of increased pore carbonate and changes in clay mineralogy in rocks overlying reservoirs. These methods are all based on the assumption that hydrocarbons and/or associated compounds migrate from leaking subsurface traps, which result in a detectable geochemical expression in soils at the surface.

Geobotanical methods, closely related to the less conventional geochemical exploration techniques, have found limited application in oil and gas exploration since the 1930s. Variations in both the distribution and vigor of plants are, in part, a response to changes in the soil environment. Geobotanical techniques have been used in hydrocarbon exploration, primarily in the Soviet Union, with variable success. To detect the effects of leaking subsurface hydrocarbon deposits, geobotanists map vegetation cover including plant distribution, presence of indicator plants, or morphological changes in plants induced by excesses or deficiencies in available soil nutrients (Brooks, 1972). Geobotanical effects of hydrocarbons leaking into soils above gas pipelines and landfills have been documented by Davis (1977) and Flower et al. (1981). Geobotanists seek vegetation "anomalies" and, for this reason, must first assess "normal" plant variability (Siegel, 1974, p. 121–151). Because of the necessity of establishing baseline plant variability, geobotany is multidisciplinary in scope and involves such diverse disciplines as biochemistry, biogeochemistry, biogeography, plant anatomy, plant physiology, botany, chemistry, geochemistry, geology, forestry, soil science, and statistics (Brooks, 1972).

IV. Remote Sensing in Oil and Gas Exploration

Remote sensing data most widely used in hydrocarbon exploration are aerial photography, airborne radar, and Landsat Multispectral Scanner (MSS) satellite data.

Aerial photography was developed as an exploration tool in the 1930s. Black-and-white, normal-color, and infrared-color aerial photographs for structural and stratigraphic mapping have the advantages of high spatial resolution and stereoscopic viewing with vertical exaggeration. Disadvantages include the unavailability of aerial photography for many areas, weather and logistical problems of acquisition, and limited areal coverage of individual photographs.

Since the 1950s, side-looking radar images have been acquired from aircraft. An advantage of this active imaging system is that radar provides its own source of radiation, making all-weather and day or night operation possible. Spatial resolution of 10 to 40 m is typically obtained. An important advantage of radar is the controllable illumination geometry. Radar images can enhance subtle topographic features that may be the surface expression of subsurface geologic structures.

As part of a regional exploration program, Wing and Mueller (1975) used Ka-band (0.86-cm wavelength) real aperture radar images to map structural features in the Mamika–Eilandan Basin of Indonesia. In the Haysi gas field region of Virginia and Kentucky, fracture patterns were interpreted from X-band (3-cm wavelength) synthetic aperture radar images (Goetz and Rowan, 1981). Development gas wells drilled on the basis of this information were more productive than the wells drilled without this information, supporting a relationship between surface fractures and fractures in the reservoir at depth. In Indonesia, Froidevaux (1980) demonstrated the value of aircraft radar images for mapping structural patterns that were used to estimate hydrocarbon potential.

The Seasat satellite, which operated from June to October 1978, acquired L-band (23.5-cm wavelength) synthetic aperture radar data covering much of North America and portions of Western Europe. Structural information has been obtained from Seasat images (Elachi, 1980). This digital data set is comparable in scale to Landsat data and can provide textural information that correlates with rock and soil surface roughness and topography. Seasat radar data have been merged with Landsat multispectral data to produce a significantly improved soil and rock classification accuracy (Stewart et al., 1980). The major disadvantage of Seasat radar data is the lack of worldwide and regional coverage.

Since their availability in the early 1970s, images produced from Landsat satellite multispectral data have been used extensively in hydrocarbon exploration (Halbouty, 1976, 1980; Johnston and Janza, 1977). Miller (1975) recognized major linear features (lineaments) on Landsat MSS images that appeared to form the boundaries of a sedimentary basin and defined new stratigraphic relationships in eastern Kenya. Later, geophysical and subsurface data confirmed the Landsat MSS interpretations. Experience has shown that digitally processed Landsat MSS images can be interpreted to add details to the existing reconnaissance maps and can provide a cartographic base for subsequent use in exploration and development programs. These and other examples of the use of Landsat MSS data in exploration are discussed by Sabins (1978). Mapping iron-oxide anomalies with Landsat MSS data may also have applications in hydrocarbon exploration because of the reduction associated with leaking hydrocarbons (Vincent, 1977).

Landsat MSS information is especially valuable when used in the early reconnaissance phase of exploration, particularly by revealing regional features such as basins, arches, and major fault/joint systems. Landsat MSS images have the advantages of worldwide, seasonal, and large areal coverage, digital computer compatibility for image processing and enhancement, and relatively low data cost. Disadvantages include low spatial resolution, coarse spectral resolution, lack of stereo capability, and inability to acquire data through cloud cover.

V. Background and Site Selection

A. Background

Areas of commercial oil and gas production offered several attractive characteristics as prospective test sites for evaluating the geological utility of state-of-the-art remote sensing techniques. Oil and gas are produced from sedimentary basins in most of the geologic and climatic provinces of the United States. Consequently, numerous candidate petroleum test sites representing diverse geology, terrain, and vegetation were available for study. Most producing oil and gas accumulations have been well characterized geologically during the course of discovery and development. Thus, adequate background data existed for evaluating information derived from remote sensing data. Industry information, however, concentrated on the subsurface near the reservoirs. Comparatively little surface and near-surface information was generally available. Although the genesis of commercial hydrocarbon accumulations was fairly well understood and remote sensing techniques had been applied to exploration problems, no generally accepted remote sensing exploration model existed. Thus, research at sites of known oil and gas production provided the opportunity to develop new exploration models based on remote sensing measurements. Geosat members were actively involved in oil and gas exploration and development. As a result, industry expertise and participation were assured.

B. Site Selection

The Petroleum Test Site Selection Committee met in 1977 to select three test sites for the Project. The criteria for site selection were:

(1) The sites must be representative of typical commercial oil and gas accumulations. This implied that sites characterized by different trapping mechanisms, different production characteristics, different geologic settings, and different surface characteristics should be selected.

(2) Cultural disturbance must be minimal. This was considered to be a minor problem for typical oil- and gas-producing areas where drilling pads, lease roads, and production facilities typically represent a small part of the total surface area.

(3) Access must be assured for fieldwork in the test site area. Preferably the site would be owned/operated by a Geosat member company to avoid problems of public disclosure or land acquisition if new target areas of exploration interest were identified during the study.

(4) Adequate background information must be available. This implied the existence and availability of surface and subsurface geological and geophysical maps and reports. Soil maps should also exist for the site. The probability of obtaining reservoir information would be greatly increased if a Geosat member company owned/operated the test site.

On the basis of these criteria, three sites were selected: Patrick Draw, Wyoming; Lost River, West Virginia; and Coyanosa, Texas (Figure 10-1).

As summarized in Table 10-1, the characteristics of these three sites clearly satisfy site selection criterion 1. The Patrick Draw test site encompasses the Patrick Draw oil field, a Cretaceous stratigraphic trap with a sandstone reservoir having primary porosity. It is representative of many similar Cretaceous oil and gas fields of the Western Interior of North America. The Lost River test site encompasses the Lost River gas field, a Paleozoic anticlinal trap with a sandstone reservoir having secondary porosity. It is representative of many similar gas fields of the Appalachian fold belt of North America. The Coyanosa test site encompasses several oil and gas fields. Paleozoic sandstone and carbonate reservoirs having both primary and secondary porosity occur in a wide variety of traps. This test site is representative of many of the prolific Paleozoic oil- and gas-producing regions of the mid-continent of North America.

The vegetation cover present at the three petroleum test sites posed a realistic and challenging problem for extracting geologic information from remote sensing data. Vegetation cover at Patrick Draw and Coyanosa is sparse and is representative of the brush–grasslands typical of semiarid regions. Lost River was selected specifically because of its near total vegetation cover, representative of the forestlands typical of temperate regions.

Cultural disturbance was minimal at the three sites (criterion 2), ranging from approximately 10 percent at Patrick

Table 10-1. Characteristics of the three petroleum test sites

Parameters	Test Site		
	Patrick Draw, Wyoming	Lost River, West Virginia	Coyanosa, Texas
Latitude, N/Longitude, W	41′30°/108′30°	39′00°/78′50°	31′18°/103′12°
Test site area, km^2	350	200	1400
Productive area, km^2	70	20	500
Production			
Gas	0	1.3×10^{10} ft^3[c]	1.2×10^{14} ft^3[b]
Oil	1.2×10^8 bbl[a]	0	2.1×10^7 bbl[b]
Reservoir			
Age	Cretaceous	Devonian	Paleozoic
Depth, m (ft)	1600 (5000)	2300 (7000)	1100 (3400)–7000 (21,000)
Rock type	Sandstone	Sandstone	Carbonate and sandstone
Porosity type	Primary	Secondary	Primary and secondary
Trapping mechanism	Stratigraphic	Anticlinal	Stratigraphic and structural
Geologic setting	Interior basin	Fold belt	Interior basin
Climate	Semiarid	Temperate	Semiarid
Vegetation type	Sage grassland	Deciduous forest	Sonoran Mesquite
(% Cover)	(40)	(99)	(40)

[a]Estimated ultimate recovery.
[b]Cumulative to 1979.
[c]Ultimate recovery.

Draw and Lost River to approximately 30 percent at Coyanosa (most of which is an agricultural area on the eastern edge of the site). Access to the three sites was assured (criterion 3): blanket access was obtained for Patrick Draw from Champlin and for Lost River from Columbia Gas; section-by-section access permits were assured for Coyanosa by Exxon and Gulf.

Adequate background information for site characterization and image evaluation (criterion 4) was either already available or acquired as part of the test site studies (Table 10-2). The type of site characterization data acquired during the investigation was diverse, and the level of analysis and interpretation was variable. This diversity is an indication of the high level of interest and participation generated by the Project. Approximately 60 individuals, most with geological backgrounds and others with expertise in disciplines ranging from geophysics to plant anatomy, contributed to the test site studies. These individuals represented over 40 exploration companies, government agencies, and universities. The selection of the types of site characterization data acquired was determined by the *interests* of *independent* participants and by the *information requirements* defined by image interpretations.

A variety of maps, digital terrain data, cross sections, and other geological data (Table 10-2) was obtained for each test site. This information and field observations served as the baseline for evaluating the quality of information extracted from the remote sensing data.

Topographic maps were of critical importance for image interpretation at the three test sites. When combined with topographic data, images acquired a third dimension. With this added geometric control, refined surface structural interpretations and inferences regarding subsurface structure were possible.

Soil maps were useful for understanding the physical meaning of units identified on images. To a large extent, the soil scientist's view of soil units (characterized by composition, texture, genesis, slope, and associated vegetation) approximates a sensor's view of the Earth's surface (Figure 10-8).

Field and laboratory spectral surveys were conducted to evaluate differences between a human observer's view of the Earth's surface (restricted to visible wavelengths, Figure 10-9) and a sensor's view (which can extend beyond the visible, Figure 10-9). Spectral information was used to determine the physical meaning of image units and to identify optimal image displays of sensor data. Additionally, the laboratory and field spectral data were used as standards for evaluating the spectral fidelity of sensor data.

Vegetation and soil geochemical surveys were conducted at all test sites to establish background variability and to identify any changes in surface materials that might be caused by the migration of hydrocarbons from subsurface traps. These data were considered in image interpretation at all test sites.

Table 10-2. Site characterization information acquired for test site investigation

Type of Information	Test Site		
	Patrick Draw, Wyoming	Lost River, West Virginia	Coyanosa, Texas
Topographic maps	C	C	C
Regional (1:250,000)	C	C	C
Test site (1:48,000)	C	C	N/A
Digital terrain data (1 x 2 ft)			
Geological maps	C	C	C
Regional (1:200,000–500,000)	C	C	C
Test site (1:48,000)	C	C	C
Oil/gas field data: discovery, production, and reservoir characteristics			
Subsurface structure maps	C	C	C,P
Well data	N/A	P	N/A
Seismic reflection	C	C,P	C
Cross sections	C	C	C
Soil maps (1:48,000)	T	T	T,P
Field/laboratory spectral surveys	T	T	T
Field vegetation survey			
Soil geochemical surveys	T	T	T
X-ray diffraction mineralogy			
Elemental geochemistry	N/A	T	N/A
Leachate	T	N/A	T
Bulk	T	N/A	T
Carbon isotope	T	N/A	T
Oxygen isotope	T	N/A	N/A
Hydrocarbon gas	T	N/A	N/A
Helium gas	T	N/A	N/A
pH	N/A	T	N/A
Bacteria	C	N/A	C,P
Previous remote sensing studies			

C – Public information, including maps, reports, papers, theses, and compilations of such information.
T – Study conducted during the test site investigation.
P – Proprietary data made available for the test site investigation.
N/A – Not available/not acquired.

VI. Comparative Results

A. Introduction

Remote sensing techniques are essentially restricted to observations of the Earth's surface. Some methods, such as passive and active microwave and thermal inertia measurements, may penetrate the near surface (Elachi, 1980; Kahle et al., 1981). Remotely sensed measurements, therefore, respond directly only to surface materials: vegetation, soil, and exposed bedrock (modified by atmospheric, topographic, and cultural effects) (Figure 10-8).

Oil and gas reservoirs are restricted to the subsurface. They exist well beyond the depth of penetration of any existing remote sensing techniques. To use remote sensing data for oil and gas exploration, a model must be employed to relate remotely sensed observations to oil and gas in the subsurface; for example, widely accepted exploration models based on the surface expression of porphyry copper and uranium deposits are used today by the mineral exploration industry (Sections 3 and 7). These models are directly applicable to the use of remotely sensed data for exploration, primarily because mineral commodities are usually mined, at least in the early development phase, at the surface. Since the 1920s, geophysical and subsurface methods have largely replaced surface observation in oil and gas exploration (Figure 10-7). The near total reliance of the oil and gas industry on geophysical data is made apparent by noting that, by 1974, the typical petroleum company spent over 90 percent of its exploration budget for geophysical surveys and less than 10 percent for related exploration research, a small part of which included surface observations (Siegel, 1974, p. 230). The petroleum test site investigation therefore required a step backward in exploration thinking. The conceptual model, or perhaps more accurately the strategy employed in the processing, analysis, interpretation, and evaluation of remote sensing data, was

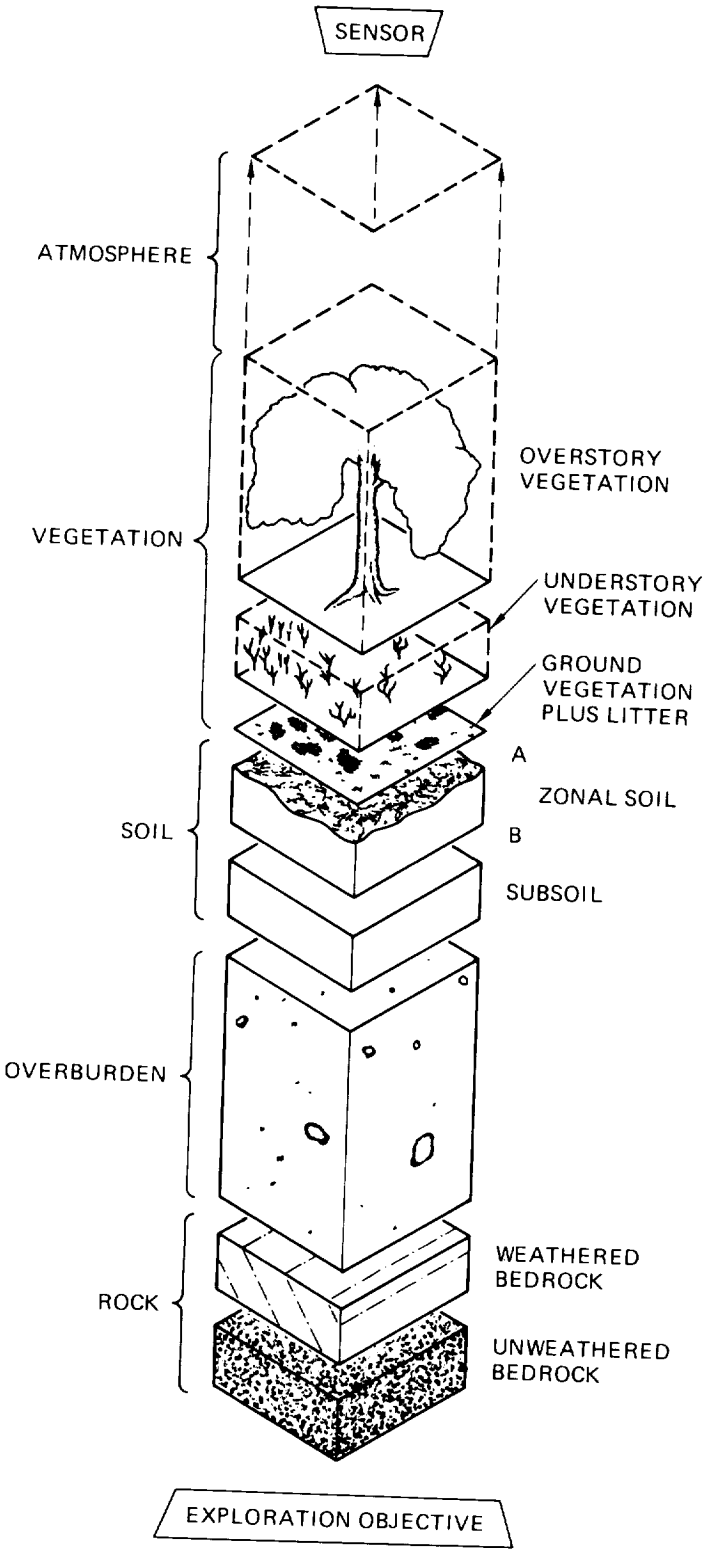

Figure 10-8. Block diagram illustrating components at the Earth's surface that can potentially contribute to remote sensing data (from Brooks, 1972, Figure 1-1)

based on two of the earliest approaches used in petroleum exploration (Figure 10-7):

(1) Seepage prospecting

(2) Surface geologic mapping

Remote sensing data were studied to determine their utility for delineating surface lithologic and structural features which might serve as clues to the presence of subsurface geological conditions that favor the formation and accumulation of oil and gas. Surface indications of leaking hydrocarbons were also sought.

B. Physical Basis of Geologic Remote Sensing

Two approaches are used for extracting geologic information from remotely sensed data. The spectral approach uses knowledge about the spectral properties of materials to extract compositional information from remotely sensed data. This approach is used principally in the analysis of multispectral data. The photogeologic/photogeomorphic approach uses knowledge about the weathering and erosional characteristics of earth materials and their topographic expression to imply the presence of geological structures at the Earth's surface and to project observed structural relationships into the subsurface. Information contained in an image produced from almost any type of remote sensing data can be useful for photogeologic/photogeomorphic analysis.

Laboratory spectral data have been used to establish the physical basis for the remote determination of the composition of earth materials. Laboratory and field data enable spectral theory to be related to remotely observed spectral features of pure and mixed surface materials including minerals, rocks, soils, and plants. This understanding of remotely sensed spectral data has led to sensor designs and image processing techniques that supply information required for the solution of a wide variety of geologic mapping and oil and gas exploration problems.

The wavelengths of interest for geologic remote sensing extend from approximately 0.4 μm to over 50 cm. The absorption spectrum of the atmosphere in this region may be divided into segments: ultraviolet, visible and near infrared, short wavelength infrared, mid-infrared, and microwave (Figure 10-9). Major atmospheric absorption bands near 0.3, 0.9, 1.4, 1.9, 2.7, 4.2, 6.0, 9.5, and 15 to 900 μm render these wavelengths unsuitable for geologic remote sensing. The physical basis for using available spectral intervals for determining the composition of earth materials is presented by Goetz and Rowan (1981). Some important characteristics of these spectral intervals are briefly discussed below.

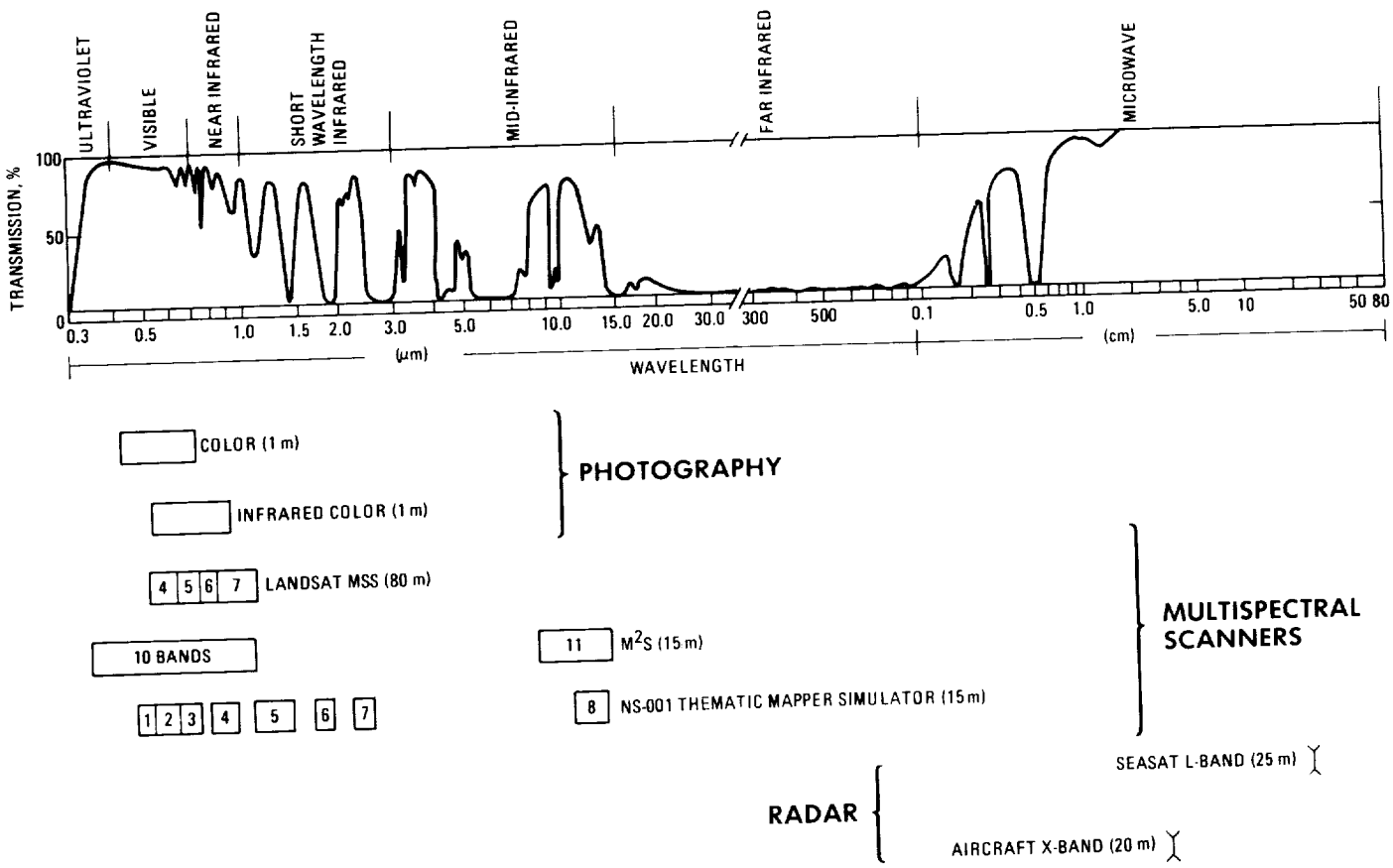

Figure 10-9. Generalized absorption spectrum of the atmosphere showing names of spectral regions of interest for geologic remote sensing (Goetz and Rowan, 1981, Figure 1). Remote sensing systems, their ground resolution, and spectral regions sampled at all three petroleum test sites are also shown.

Spectral reflectance data acquired between 0.5 and 1.1 μm (visible and near infrared) may be used to determine the presence or absence of iron-oxide-bearing minerals (limonite, goethite, and hematite) in soils or rocks and the presence or absence of vegetation. The presence of Fe^{+3}-bearing minerals may be inferred from measurements of the absorption band which affects the 0.4- to 0.6-μm interval. The Fe^{+2} to Fe^{+3} electronic transition may be inferred by its absorption band, which lies between 0.8 and 1.0 μm. The presence of vegetation is inferred from chlorophyll absorption bands located at 0.45 and 0.65 μm.

Spectral reflectance data acquired between 1.0 and 2.5 μm (short wavelength infrared) may be used to determine the presence or absence of hydrous minerals (such as clays, micas, and some oxides and sulfates) and carbonate minerals (calcite and dolomite) in soils and rocks and also to determine the state and vigor of vegetation. Important absorption bands occurring in this wavelength region are associated with hydroxyl ions (near 2.2 μm, 2.3 μm, and the short wavelength wing of a 2.77-μm absorption band which extends to 2.0 μm). A strong carbonate absorption band occurs near 2.35 μm. A broad absorption band which is attributed to leaf water content in vegetation affects the entire 1.5- to 2.5-μm interval. The depth of this absorption band can be related to plant vigor.

Spectral emission data acquired between 8 and 14 μm (mid-infrared, sometimes referred to as thermal IR) can be used to determine relative quartz content of soils and rocks. Information regarding soil and rock thermal inertia, soil moisture content, and vegetation vigor can also be obtained from mid-infrared spectral data.

C. General Comparison of Sensors

Figure 10-9 illustrates selected characteristics of the seven sensors used at all three petroleum test sites. The passive microwave imaging system (PMIS), multifrequency microwave radiometer (MFMR), and Fraunhofer Line Discrim-

inator (FLD) were only used at selected test sites and are not shown. The following general comparison of the sensors shown in Figure 10-9 is based on petroleum test site results. The technical characteristics of all sensors used in the test case program are described in more detail in the Technical Appendix, Section 14.

Sensors used at all three petroleum test sites acquired data which varied in both spatial (ground) resolution and wavelengths sampled. Spatial resolution, or instantaneous field of view (IFOV), ranged from approximately 1 m for color and false-color infrared aerial photography, to approximately 25 m for Seasat radar data, and to 80 m for Landsat MSS data. Intermediate resolution data of approximately 15 m were obtained by the airborne Modular Multispectral Scanner (M^2S), the NS-001 Thematic Mapper Simulator multispectral scanner, and the X-band radar system. The high spatial resolution of the aerial photography made it useful for delineating small features such as individual rock outcrops, trees, and cultural elements. Approximately 1:12,000 23- by 23-cm (9- by 9-in.) prints of the photographic data provided the best base for determining field locations in areas of low relief such as Patrick Draw and Coyanosa. Geological analysis based upon aerial photography was complicated by the limited coverage of individual photographs, which were approximately 8 by 8 km (5 by 5 mi) in size. The coarser resolution and large areal coverage of individual Landsat MSS and Seasat scenes at scales of 1:200,000 to 1:500,000 made these data most useful for regional geomorphic interpretations. This synoptic perspective helped place the individual test sites in a regional structural/stratigraphic context. The intermediate spatial resolution of M^2S, NS-001, and X-band radar data supplied information suitable for 1:48,000 scale interpretive maps covering the entire area of each test site.

As illustrated in Figure 10-9, most geologically useful wavelengths were sampled in the test case program (ranging from 0.33 μm for the first band of the M^2S multispectral scanner to 23.5 cm for Seasat L-band radar). Color and false-color infrared photography, Landsat MSS, the first ten bands of the M^2S, and the first four bands of the NS-001 provided spectral information in the visible and near infrared that was useful for mapping iron oxides and vegetation at all of the test sites. Short wavelength infrared data were acquired only by bands 5, 6, and 7 of the NS-001. These bands provided information about the distribution of hydrous and carbonate minerals at Coyanosa and Patrick Draw and information regarding areal variations in vegetation type and/or vigor at all three test sites. Data from the short wavelength infrared NS-001 bands, which measure variations in leaf water content, were especially useful at Lost River for mapping 10 vegetation classes throughout the test site.

Band 11 of the M^2S and band 8 of the NS-001 acquired daytime mid-infrared data at all of the test sites. Images produced from these data were most useful at Lost River where NS-001 band 8 data were used for structural interpretations. Day–night M^2S band 11 data were used to produce thermal inertia images (see Kahle et al., 1981, for a discussion of this type of image) for Patrick Draw and Coyanosa. These images did not provide any new information.

The active microwave data provided by Seasat L-band and aircraft X-band radar were useful for geomorphic analysis at Lost River, but provided little new information at Patrick Draw and Coyanosa. The extreme geometric distortion (layover) problem precluded direct transfer of Lost River Seasat image interpretations onto a topographic base, thereby limiting the value of these data. In all cases, radar data provided less information than equivalent resolution multispectral data. The chief benefit of the radar systems—providing topographic information in areas of cloud cover—was never realized at the test sites because topographic data were available and weather conditions made acquisition of multispectral data possible.

Photographic and radar data were obtained in analog (film) format, while multispectral data were obtained in digital (magnetic tape) format. Data in digital format were entered into the computer for processing, comparison, and merging with other digital data sets. Radar data were digitized prior to computer analysis. The digitization process was time consuming and resulted in some degradation of original data quality. No attempt was made to digitize photographic data.

Seasat L-band and Landsat MSS data were acquired from satellite platforms at altitudes of 800 and 915 km, respectively. All other data were acquired from aircraft flown at altitudes ranging from 5 km (photographic and multispectral scanner data) to 18 km (aircraft X-band radar data). The effects of platform/altitude variations were apparent in the analysis of remote sensing data. Satellite platforms are more stable than aircraft. Aircraft-acquired multispectral data, therefore, required significant geometric rectification for registration to a cartographic base. This procedure is both computer and personnel intensive. For this reason, such a geometric rectification was only accomplished for one NS-001 data set for Patrick Draw.

The aircraft multispectral instruments scan (sweep) a field of view of 100° during data acquisition (aircraft nadir

± 50°). The Landsat MSS sensor only scans 12°. Because of their higher scan angle and lower altitude, aircraft-acquired multispectral data were more affected by atmospheric and solar illumination variations than were satellite-acquired data. At all petroleum sites, these effects resulted in a scan direction gradient (a progressive change in brightness from one side of the image to the other) in the aircraft spectral data. This artifact had to be removed from the image data prior to spectral interpretation. Gradient removal procedures used for the test site study were both computer and personnel time intensive, but yielded satisfactory results at Patrick Draw and Lost River. In the case of Coyanosa NS-001 data, several attempts at gradient removal yielded unsatisfactory results. Patrick Draw and Lost River multispectral data were acquired along flight lines that were essentially parallel (approximately north–south) to the solar illumination direction (solar azimuth). The fact that Coyanosa data were acquired along flight lines transverse (approximately east–west) to the solar azimuth apparently exacerbated the gradient problem.

Landsat MSS data were obtained at 64 gray levels, while aircraft multispectral data were acquired at 256 gray levels. This theoretical four-fold-improved-precision of NS-001 data compared to MSS data was never practically used in analyses during the test case study. The spectral characteristics of surface materials occurring in the three test sites were determined by over 500 field and laboratory spectral measurements. These data were used to calculate equivalent NS-001 band reflectance values and to identify any absorption bands of interest. The maximum range in reflectance determined for any NS-001 band was 74 percent for band 6 (Figure 10-9) at Patrick Draw. The minimum depth of any identified absorption feature of interest was approximately 1 percent. Based on these test site specific observations, 74 gray levels would probably have been sufficient for the spectral characterization of the test sites with scanner data. Although narrower and more numerous than MSS bands, the eight NS-001 bands were still too broad to take practical advantage of the four-fold increase in precision (256 versus 64 gray levels).

The petroleum test case results demonstrate that the NS-001 and Landsat MSS multispectral scanners supplied the most useful information for geologic mapping and oil and gas exploration. The recognition of the superior information content of NS-001 data early in the test site studies resulted in subsequent emphasis on these data in processing, analysis, and interpretation. Additionally, because the NS-001 scanner was designed to simulate data acquired by the next generation of Landsat sensors – the Landsat 4 Thematic Mapper (TM) – test site participants were interested in these data. Participants saw the opportunity to preview Landsat 4 TM data. For these reasons image processing, information extraction, and model development emphasized NS-001 multispectral data.

D. Processing

Digital image processing, a major field of research involving mathematics, statistics, and computer technology, is used to manipulate and combine large sets of multispectral and other data to produce images amenable to interpretation. (For additional information, refer to Goetz and Rowan, 1981, and Reeves, 1975.) Some of the more important image processing methods applied during the petroleum test site investigation are briefly introduced here. Specific image processing programs used in the test case program are documented in the Technical Appendix, Section 14. Examples from the petroleum test site studies of image processing methods used to solve specific exploration problems are provided in Paragraph E.

Digital image processing methods used in the petroleum test site investigations include stretching to enhance image contrast, spatial filtering to enhance ("high pass") or diminish ("low pass") image tonal/textural boundaries, and band ratioing to enhance the image expression of spectral absorption features or to facilitate the display of many variables on a single image (data compression). Statistical image transformations, such as principal components analysis, were performed to simultaneously analyze the variability of data from many bands. Supervised classification procedures, such as discriminant analysis, were used to produce thematic image maps showing the distribution of rock units (geology), soil units (pedology), or plants (botany).

E. Information Extraction

The purpose of acquiring, processing, and interpreting remote sensing data during the petroleum site investigations was to evaluate the usefulness of remote sensing data in areas containing known deposits of oil and gas. A trained analyst, with an understanding of the physical basis of remote sensing data acquisition, processing, and interpretation supported by image processing facilities, can extract information from raw remote sensing data. A geologist, trained in remote sensing and with a knowledge of the regional geology, geomorphology, and soil and vegetation types can then produce images (maps) designed to display information required to solve a specific exploration problem and provide legends for the thematic image maps. For the petroleum test site studies, the required maps (images) should display surface clues to the existence of the known subsurface hydrocarbon accumulations.

Because of differences in test site size, setting, and participants, analytical methods were not uniform for all test sites. Readers who compare the specific results obtained at one test site to those obtained at another should keep this aspect of the investigation in mind. For example, the Coyanosa test site was seven times larger than Lost River and four times larger than Patrick Draw (Table 10-1). The Patrick Draw study had over 30 participants, while Lost River and Coyanosa studies together had fewer than 20 participants. By far, the highest participation density was at Patrick Draw and the lowest was at Coyanosa.

The results obtained at a test site were determined by whether a specific approach was selected for use at that site. Vegetation density mapping procedures used at Patrick Draw and lineament density analysis procedures used at Lost River, although equally applicable, were not used at Coyanosa. Soil gas surveys, which successfully demonstrated hydrocarbon microseepage at Patrick Draw, were not used at Lost River or Coyanosa. Vegetation community mapping procedures used at Lost River were never attempted at Patrick Draw or Coyanosa. The temporal effect of variability in sparse vegetation on multispectral data was evaluated at Coyanosa, but was not attempted at Patrick Draw. An analysis of spectral changes resulting from bedrock-induced changes in overlying residual soil and vegetation conducted at Patrick Draw was not attempted at either Coyanosa or Lost River.

Because of these differences, the three petroleum test site reports should be viewed as a package. Together they illustrate the type of information and approaches to information extraction available for geologic remote sensing in petroleum exploration. Examples of specific approaches to information extraction and significant results are summarized according to the type of new and useful information obtained: structural geology, soil/stratigraphic mapping, and geobotany.

1. Structural geology. The chief structural application of remote sensing data at the three test sites was to delineate surface structures. The location of a potential subsurface structural target can be inferred from its surface expression. This application of remote sensing data in the reconnaissance phase of oil and gas exploration has been well established (Halbouty, 1976, 1980). Additionally, surface structural information obtained from remote sensing data was used to economize field sampling for soil geochemical surveys conducted at Patrick Draw. Specific results of the structural analysis of remote sensing data verified their utility for delineating both previously mapped and unmapped surface structures and demonstrated some novel analytical approaches.

Subtle folds were mapped on the east margin of the Rocky Mountains at Patrick Draw, Wyoming. Images produced from topographically registered NS-001 data were interpreted at 1:48,000 scale to detect any subtle structures in the test site area. Individual thin sandstone beds were traced throughout the area. With the aid of elevation data, these bedding plane traces were used to determine dip and strike throughout the test site. This information revealed several previously unmapped folds. Examination of stereo aerial photographs and observations in the field confirmed the existence of these subtle structures which have limbs that dip only 1° to 3° and are therefore difficult to identify with limited field dip and strike measurements alone. The available well log data for the Patrick Draw oil field do not confirm the existence of these minor flexures in the subsurface. Although oil field productive limits are best defined by stratigraphic variations, these results nevertheless demonstrate the utility of remote sensing methods for mapping subtle folds.

Areal variations in fracture density were mapped in the Appalachian fold belt at Lost River, West Virginia. Linear discontinuities in the tone or texture of remotely sensed images, referred to as lineaments, may represent the surface expression of subsurface faults and joints (fractures) (Hodgson, 1974). A lineament study was conducted at Lost River to evaluate operator and image bias in lineament interpretation and to develop efficient methods of lineament analysis for locating potential fractured reservoir targets. Analysis of 1:500,000 Landsat MSS image interpretations prepared by independent interpreters demonstrated that subjectivity in recognizing individual lineaments may be obviated by mapping areal variations in lineament density (number of lineaments/unit area). Such maps show the Lost River gas field located beneath an area of high-surface lineament density. Lineament density maps at 1:48,000, derived from NS-001 data processed to enhance specific lineament trends, yielded lineament density isopleths which mimic subsurface structural contours on the reservoir of the Lost River gas field.

Deep-seated subsurface structural discontinuities were mapped according to their surface geomorphic expression in the Permian Basin at Coyanosa, Texas. Photogeomorphic interpretation of 1:500,000 scale Landsat MSS images and 1:48,000 NS-001 images revealed spatial correlations between subtle anomalous drainages and subsurface structures. Many anomalously straight drainages coincide with major faults identified in the subsurface; several anomalously arcuate drainages coincide with domes and horst blocks identified in the subsurface. These features were not previously shown in published geologic maps of the area, apparently because of difficulty in field map-

ping due to the extremely low topographic relief and paucity of bedrock exposures which characterize the Permian Basin.

These examples demonstrate the utility of available remote sensing methods for detecting the subtle surface expression of potential subsurface traps. At all three test sites, new structural information was obtained from the analysis of remotely sensed data. Small-scale 1:500,000 satellite image interpretations can be used in regional analysis to target subareas for detailed evaluation using 1:48,000 aircraft data. The potential of these smaller exploration targets can then be evaluated with conventional field geological, geochemical, and geophysical surveys, improving their efficiency and effectiveness. Furthermore, information regarding bedrock fracture geometry determined from lineament density analysis should be valuable in siting development wells and planning reservoir stimulation operations.

2. Soil/stratigraphic mapping. The chief soil/stratigraphic mapping application of remote sensing data in the test case investigation was the use of multispectral data to delineate surface geomorphic and spectral units that could be related to bedrock stratigraphy. Image interpretations at the three test sites demonstrate the capability of mapping established bedrock units and defining new lithostratigraphic units with the aid of multispectral data. Changes in bedrock lithology are expressed by remotely detectable changes in soil mineralogy, vegetation density and composition, and topography. Image analysis results from Patrick Draw provide an example of the type of stratigraphic information obtainable from multispectral data.

Strata in the Patrick Draw test site are poorly exposed. Rare exposures seen in the field are a monotonous sequence of drab-colored shales, mudstones, and sandstones which are laterally discontinuous. For these reasons, field mapping bedrock units in the area is difficult. Early interpretations of NS-001 Thematic Mapper Simulator images revealed what appeared to be an unmapped stratigraphic unit that could be traced through the entire test site. Evaluations of published soil maps, laboratory and field spectral and mineralogical analyses, and observations in a trench traversing the unit confirmed the lithostratigraphic validity of the unit and demonstrated that its image expression was the result of the following characteristics:

(1) The unit is less resistant and generally finer grained than adjacent units. It is gypsiferous, includes the thickest and highest stratigraphic occurrence of coal, and is characterized by calcite-cemented sandstones.

(2) Residual soils above the unit are grass-bearing, gypsiferous clay loams, while soils over adjacent units are sage-bearing sandy loams.

(3) Reflectance in all NS-001 bands is higher for the unit than for adjacent strata. NS-001 band-ratio values for the unit indicate absorption features attributable to kaolinite, montmorillonite, jarosite, and gypsum.

These and other test site results demonstrate the value of multispectral data for detailed stratigraphic analysis. Multispectral measurements are sensitive to subtle vegetation and mineralogical changes not otherwise readily discernible. With the aid of ancillary field and laboratory spectral data and mineralogical analysis of residual soils, image spectral units can be related to bedrock stratigraphy.

3. Geobotany. The chief geobotanical applications of remote sensing in the test case investigation were the use of multispectral data to facilitate the vegetation mapping process, to evaluate the effects of vegetation in sensor data, and to identify areas of anomalous vegetation attributable to hydrocarbon seepage. Significant results obtained in the three petroleum test site studies are described below:

(1) Interior sage–grassland community mapping was performed at Patrick Draw, Wyoming. NS-001 data were used as variables in a supervised classification computer analysis to produce an accurate map of percent vegetation cover in a 350-km^2 area. The first seven NS-001 bands were used as variables for the classification. This procedure proved to be both time and cost effective and resulted in a map of vegetation density that could not have been produced using conventional field botanical methods. The resulting vegetation density map and field observations revealed normal variability in plant density and verified the existence of an area of abnormally low vegetation cover which had been first recognized in earlier NS-001 images. The area of abnormally low vegetation cover is characterized by stunted sage and a lack of associated grass cover, which surface geochemical data indicate may be a response to hydrocarbon seepage from the gas cap of the Patrick Draw reservoir.

(2) Deciduous forest community mapping was performed at Lost River, West Virginia. NS-001 data were used as variables in discriminant function/supervised classification computer analyses to produce accurate maps of 10 vegetation communities in a 200-km^2 area. Five NS-001 bands and band ratios were found most useful for mapping vegetation communities: 6, 2/5, 4/5, 5, and 2/6. This procedure

proved to be a time- and cost-effective means of mapping vegetation, which would have been impossible using conventional field botanical mapping methods. The resulting vegetation map of the test site revealed normal variability of plant distribution and delineated two areas of abnormal maple concentration. The abnormal maple concentrations may be a response to hydrocarbon seepage from the reservoir of the Lost River gas field.

(3) Sonoran mesquite–desert community mapping, with spatial and temporal variability, was performed at Coyanosa, Texas. Analysis of multitemporal Landsat MSS color-infrared composite images revealed spatial variations in vegetative cover and vigor correlated to annual, seasonal, and local variability in precipitation in a 1400-km^2 area.

These examples demonstrate the potential utility of available multispectral remote sensing systems for detecting subtle vegetation changes associated with hydrocarbons leaking from subsurface oil and gas accumulations. Additionally, the potential geobotanical utility of multispectral sensor systems with greater spectral resolution than systems presently available has been demonstrated (Collins et al., 1981). Collins and his coworkers showed that subtle changes in plant spectra due to geochemical stress can be identified with a high-resolution, experimental airborne spectrometer. The geobotanical utility of multispectral remote sensing data should therefore find broad application in oil and gas exploration and also in other fields of geological research, renewable resource management, environmental monitoring, and atmospheric science research.

VII. Exploration Model Development

Much of the site characterization and image analysis effort in the three petroleum test site investigations was aimed at the development of exploration models that use remote sensing methods to "directly" detect subsurface oil and gas accumulations. If a subsurface oil or gas accumulation leaks, the leakage may be detected in remotely sensed data because of associated alteration of surface materials (soil, exposed rock, and vegetation). Interest in such a high technology approach to seepage prospecting was stimulated by research results published at the time the three test site investigations were started (for example, see Davis, 1977; Donovan and Dalziel, 1977; Ferguson, 1975; Roberts et al., 1977; Saunders, 1979).

Test site efforts addressing the direct detection approach resulted in two empirical models based on observations made at Patrick Draw and Lost River. The two models are illustrated in Figures 10-10 and 10-11.

The reservoir sandstone of the Patrick Draw oil field pinches out to the west (Figure 10-10a). A western shale facies and overlying shales result in closure for this stratigraphic trap. If it is assumed that the shale cap rock does not have a permeability of absolute zero, reservoir fluids must leak from the Patrick Draw reservoir. Leaking hydrocarbon compounds reaching the surface should locally alter soil chemistry and may be expressed by detectable geochemical/spectral changes at the surface. A soil gas survey revealed anomalously high hydrocarbon concentrations in soils overlying the gas cap of the Patrick Draw reservoir (Figure 10-10b). Anomalously high soil helium and zinc concentrations and high soil pH values were also measured over the gas cap. A tonal anomaly identified in NS-001 images corresponds with this area of anomalous soil geochemistry (Figure 10-10b). Field observations, spectral analysis, and laboratory botanical studies demonstrate that the image tonal anomaly is caused by a decrease in vegetation density and stunting of sage in the anomaly area. Detailed study of the sage indicates that the stunted condition has been chronic, existing over the life span of local sage (over 90 years), and is symptomatic of a zinc deficiency caused by low zinc availability to the sage resulting from high soil pH. These empirical correlations (gas cap area, high hydrocarbon soil gas concentration, high soil pH, high soil zinc, low zinc availability to sage, stunted sage, and multispectral tonal anomaly) suggest an exploration model for seepage prospecting in this type of semiarid environment.

The reservoir sandstone of the Lost River gas field has secondary fracture porosity/permeability. Overlying shales result in closure for this anticlinal trap (Figure 10-11a). If it is assumed that fractures cutting the reservoir sandstone must also penetrate the overlying shale cap rock, gas must leak from the Lost River reservoir. Areal variations in image lineament density (assumed to be the surface expression of subsurface fractures) suggest that this is the case (Paragraph VI.E). Based on the regional tectonic style, fractures should dip to the east and, therefore, fractures cutting the reservoir should intersect the surface as lineaments to the west of the reservoir (Figure 10-11b). A soil elemental geochemical survey suggests anomalously high soil manganese concentrations in the area of maximum lineament density. Hydrogen-sulfide-rich springs also occur in the area of high image lineament density. Vegetation maps of the test site area, prepared using NS-001 multispectral data, demonstrate that local anomalous maple concentrations, confirmed by field observations, also characterize the area of high lineament density (Figure 10-11c). A soil microbe sur-

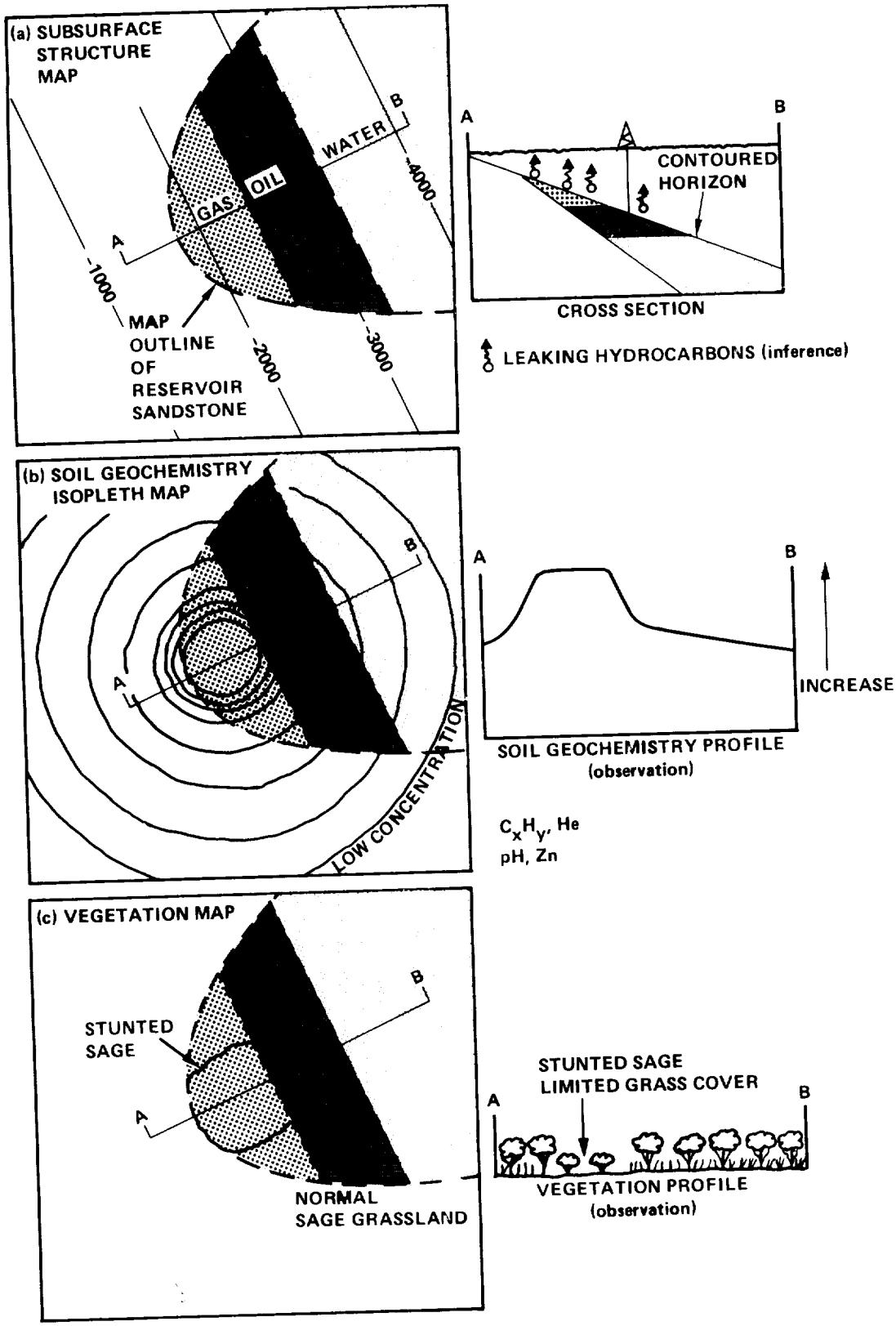

Figure 10-10. Diagrammatic illustrations of the empirical remote sensing exploration model developed in the Patrick Draw, Wyoming, test site study

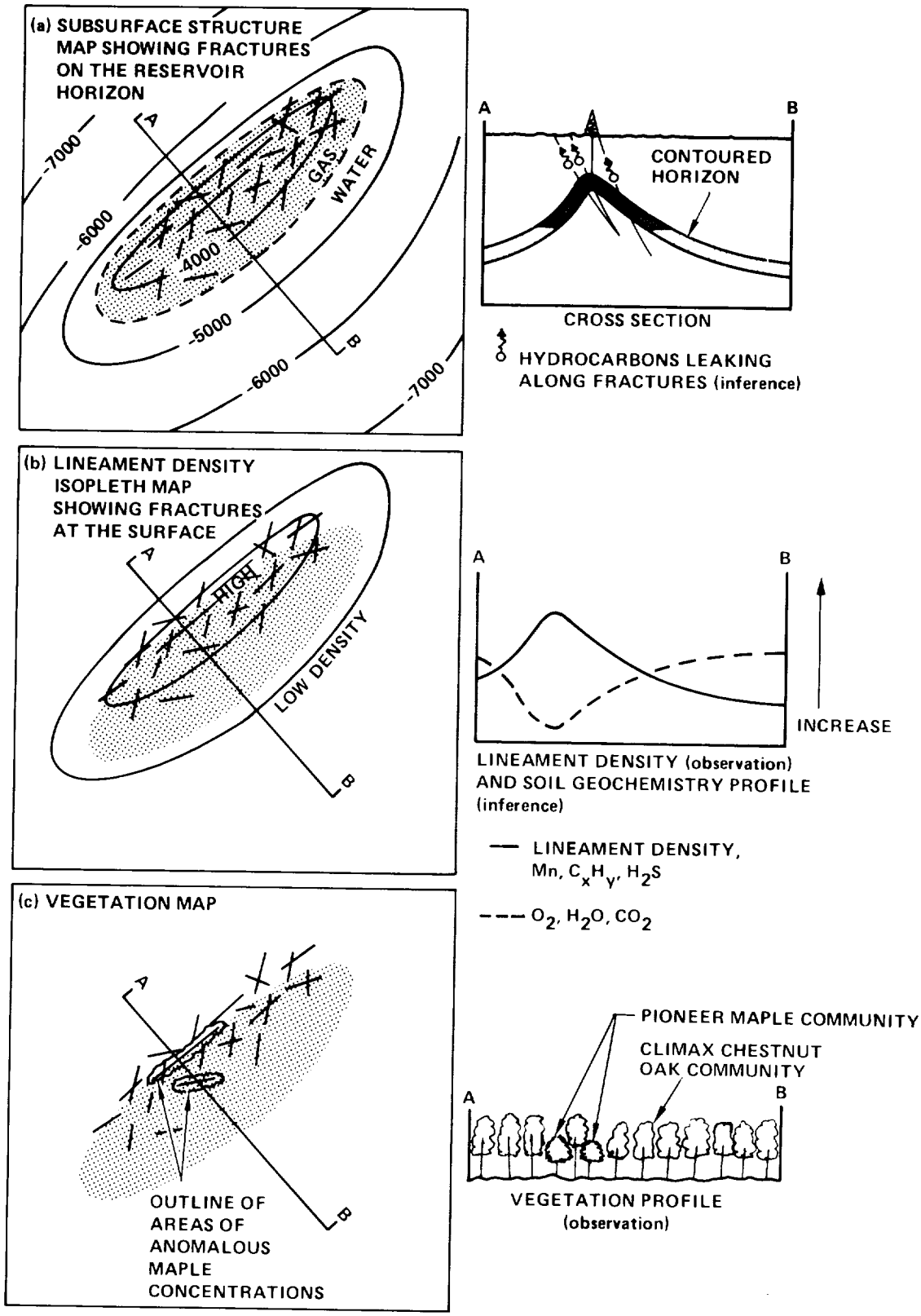

Figure 10-11. Diagrammatic illustrations of the empirical remote sensing exploration model developed in the Lost River, West Virginia, test site study

vey did not find any evidence of hydrocarbon leakage in the test site area, but the results were questionable due to the composition of reservoir fluids. These observations lead to the hypothesis that hydrocarbon and hydrogen sulfide gases leak from the Lost River reservoir along fractures expressed at the surface as lineaments. Seepage results in local changes in soil geochemistry which affect vegetation. Research in vegetation tolerance to methane seeping from artificial landfills demonstrates that, of the tree species occurring at Lost River, maples are the most methane tolerant (Flower et al., 1981; Leone et al., 1977, 1979). According to Flower and coworkers, maples are tolerant of the low soil oxygen, carbon dioxide, and water in regions where these fluids are displaced by seeping methane gas (inferred soil geochemistry, Figure 10-11b). These empirical correlations (subsurface fractured gas reservoir, area of high lineament density, and area of anomalous maple concentration) suggest an exploration model for seepage prospecting in this type of temperate environment.

Both of these results suggest that (1) some reservoirs leak, (2) this leakage results in alteration of soils and vegetation, and (3) this alteration can be detected with NS-001 data. A satisfactory geochemical explanation, which integrates all the observations and inferences summarized in Figures 10-10 and 10-11, has not been formulated. Although suggestive correlations have been documented, *cause–effect* relationships of leaking reservoir hydrocarbons to soil hydrocarbons to soil geochemical alteration to anomalous vegetation have not been proven. Therefore, the proposed models should be considered working models applicable to their respective sites. Hydrocarbon surface seepage may have entirely different expressions in other geological, environmental, and climatic settings. A thorough physical explanation of these relationships requires basic research that does not presently exist and is beyond the scope of the present investigation. Additional basic research is required before unequivocal conclusions regarding the direct hydrocarbon detection problem can be made.

VIII. Conclusions and Recommendations

Remote sensing data provide useful information which can be incorporated into all stages of hydrocarbon exploration in a wide variety of geologic and climatic settings. The ability to delineate regional, structural, and stratigraphic features as well as to provide a data base for more detailed studies, and in some cases to provide geochemical/geobotanical information for the direct detection of leaking hydrocarbons, makes existing and future remote sensing systems valuable exploration tools. Remote sensing methods can be efficiently used to evaluate large areas and are capable of determining prospective exploration targets for further analysis and/or drilling. Production operations can incorporate detailed information obtained from remote sensing data for more effective development drilling programs, particularly in fractured reservoirs. The results demonstrate that, in those areas where geologic, soil, and vegetation information exists, remote sensing data can provide a detailed data base for surficial, structural, stratigraphic, and geochemical/geobotanical analyses of direct value in hydrocarbon exploration. Furthermore, in regions where ground data are limited or lacking, remote sensing data can provide cost effective and timely geologic information.

Remote sensing data are internally consistent, objective, and uninterpreted physical measurements. Their objectivity and their grid-sampling nature make remote sensing measurements a unique type of geological observation or geophysical survey. These raw data can be computer processed to enhance and display in map form surface features of interest to the exploration geologist. They are, thus, a primary and versatile data base which can contribute significantly to the assessment of the hydrocarbon potential of an area.

Existing remote sensing data sets have already had significant impact upon hydrocarbon exploration. To derive the maximum benefit from remote sensing data, the user must understand their physical meaning and recognize both their strengths and their limitations. Remote sensing methods are another tool to be added to those routinely used today in exploration. The effective incorporation of remotely sensed data into the overall exploration program requires the constant involvement of a skilled geologist. The application of remote sensing methods to the solution of specific exploration problems requires broad knowledge of the geologic setting of the site studied, incorporation of any existing geophysical and/or subsurface information, as well as geomorphic, pedologic, and botanical characteristics of the site.

Structural geologic features are readily evident in most remote sensing images. These include previously mapped as well as unmapped structures. Landsat MSS images, with 80-m resolution, exhibit the regional structural framework, particularly at the 1:200,000–1:500,000 scale. Structural interpretation of these data is useful in determining basin boundaries and configurations and can be of particular value in basin evolution studies.

Detailed analysis of NS-001 images can be used to identify subtle structural exploration targets at the 1:48,000 scale. Landsat 4 TM images, with 30-m resolution, should exhibit

structural features at an equivalent scale. The user of these data must be aware of the illumination aspect of a specific image so that structural features, which may be enhanced or suppressed, can be properly interpreted.

Fracture (lineament) density analysis is of particular exploration value in areas where reservoirs are created by secondary fracture porosity and permeability. To effectively delineate specific prospect areas, the regional tectonic style and the orientation of potential stress directions must be known in conjunction with the approximate depth to potential reservoir horizons. The test site results suggest the feasibility of combining detailed fracture analyses from images with actual fracture identifications from subsurface well data to provide information for effective development drilling and well stimulation in regions containing fractured reservoirs.

During the test site investigation it became evident that in many cases geologic, soil, and vegetation information available for the three test sites was often insufficient to fully evaluate image interpretations. The necessary data commonly did not exist either in the open literature or in the information made available by exploration companies participating in the Project. Since the only means of evaluating the validity of image interpretations was by comparison with information acquired from other sources, further site characterization including both field and laboratory analyses, became an important aspect of the Project. Even with these additional data, the available information was often inadequate to unambiguously evaluate the image interpretation results. One example of this aspect of the Project is that of structural interpretations of Coyanosa image data. Not all faults identified in the photogeomorphic interpretations could be evaluated with certainty because of inadequate surface and subsurface geological data. This problem, however, clearly illustrates one of the strengths of remote sensing methods. The exploration geologist's attention can be focused on inadequately or possibly incorrectly mapped areas, which require further geological/geophysical evaluation.

The ability to use NS-001 data to discriminate previously mapped as well as unmapped lithostratigraphic units will provide new information for hydrocarbon exploration. This will be of particular value along the margins of basins for constructing regional depositional models which describe the presence, thickness, and distribution of prospective reservoir facies. When this information is extrapolated to depth and tied to existing subsurface data, the ability to identify potential stratigraphic traps should be significantly improved. Furthermore, detailed stratigraphic information will help determine the thickness, areal extent, and volume of hydrocarbon source rocks. These are important criteria for assessing the hydrocarbon potential of a basin. Stratigraphic information will be of value in determining the basinal sedimentary history, which combined with structural data can assist in determining the timing of hydrocarbon generation, potential migration paths, and prospective trap locations. The ability to map weathered surface materials/soils in detail can provide information on where to apply surface velocity corrections used for processing seismic reflection data.

The value of identifying "tonal anomalies" in multispectral images, presumed to result from hydrocarbon seepage, was investigated. In attempts to understand the physical causes of tonal anomalies and the value of their delineation for hydrocarbon exploration, it became clear that knowledge of the complex surface geochemical–geobotanical systems is insufficient. Evaluation of a tonal anomaly over the subsurface gas cap at Patrick Draw revealed the existence of a previously unrecognized area of stressed vegetation. The relationship of this feature to surface alteration associated with hydrocarbon leakage was suggested by further geochemical–geobotanical studies. A subtle geochemical–geobotanical anomaly was also suggested over the gas accumulation at the heavily vegetated Lost River test site. Tonal anomalies at Coyanosa showed no demonstrable relationship to hydrocarbon seepage. In all cases, increased spectral and spatial resolution provided by NS-001 data yielded enhanced delineation and characterization of tonal anomalies compared with Landsat MSS data.

A crucial factor in the successful exploration application of tonal anomaly mapping will be the ability to determine which features are related to hydrocarbon occurrences. This will require a better understanding of the cause of tonal anomalies and the formulation of exploration models for their evaluation and integration with other exploration data sets. This will require some fundamental research into the spectral characteristics of earth materials including soils, exposed rocks, and vegetation.

In evaluations of geological remote sensing data, the distinction is commonly made between rock-type identification and rock-type discrimination. Analysts find that they cannot identify but can discriminate rocks with remotely sensed data. The term "identification" is synonymous with determination of rock mineralogy and "discrimination" is synonymous with the separation of rocks into distinct image tonal classes that represent unknown rock types. A critical future remote sensing research problem is the development of classifications of earth materials based on remote sensing parameters, i.e., their spectral reflectance and emittance, thermal inertia, and radar scattering properties.

Identification first requires a meaningful classification. Rock identification means applying rock names to earth materials. The name used is selected from a list (classification) based on the type of rock characteristics observed, on an understanding of the cause of the observed characteristics, and on the purpose of the study (Ham and Pray, 1961).

Remote sensing techniques cannot identify image tonal units until classifications of earth materials based on their remote sensing characteristics exist. Research aimed at developing such classifications is essential. Presently available rock classifications were tailored for use by geologists making conventional observations and not for making remote sensing measurements. Rock-type identification with remote sensing measurements is an impossible task if the constraints inherent in presently available classifications are applied to remote sensing data.

Based on the petroleum test case studies, three critical elements involved in remote sensing rock-type classification research are:

(1) The acquisition of laboratory, field, and image spectral data for rocks, soils, and vegetation in many environments.

(2) The analysis of these spectral data by unsupervised classification approaches to identify natural, spectrally defined classes of earth materials.

(3) The investigation of the bedrock–soil–vegetation–atmosphere system (Figure 10-8) to determine the causes of the class distinctions identified in item (2).

Only when a classification of earth materials based on their remote sensing characteristics exists can analysts directly make the step from rock-type discrimination to rock-type identification. Without this, the step from discrimination to identification requires field studies at specific sites.

Geologic interpretation of remote sensing data for petroleum exploration must be applied in the context of an exploration model to be most effective. Two empirical models resulted from the petroleum test site investigations. One is applicable for exploration in densely vegetated, deciduous forest terrain in a humid, temperate environment. The other is applicable for exploration in sparsely vegetated, sage–grassland terrain in a semiarid environment. Both recognize that alteration of vegetation due to soil chemistry changes caused by leaking hydrocarbons can be detected with multispectral remote sensing methods. The ability of advanced sensor systems to resolve detailed geologic features with the aid of more sophisticated data processing and image enhancement techniques will require more elaborate exploration models to be developed and evaluated in other environmental settings. Polar, coastal, and tropical environments were not represented by the three petroleum test sites. Future investigations should evaluate the utility of geologic remote sensing for exploration in other geological and environmental settings.

Geologic information obtained from advanced remote sensing data will have an impact on exploration for commodities other than oil and gas. The improved spatial and spectral resolution of Landsat 4 TM data compared with Landsat MSS data will be of particular value. Detailed lineament/fracture analyses from these data should be applicable in exploration for other subsurface gases and liquids such as carbon dioxide, helium, groundwater, and geothermal fluids that are produced from fractured rocks.

The improved stratigraphic mapping potential of Landsat 4 TM data will be directly applicable in identifying and assessing strata-bound and stratiform ore deposits including copper, zinc, lead, silver, gold, uranium, iron, sulfates and borates (Wolf, 1976), and other sedimentary resources such as coal, oil shale, and tar sand. The identification of potential geochemical and geobotanical alteration associated with these resources will be of additional exploration value.

The ability to perform detailed vegetation community mapping and vegetation cover density mapping will contribute valuable new information to agriculture, forestry, and rangeland studies. Additionally, multitemporal vegetation information could provide valuable data for monitoring cultural activity of all types.

As part of the petroleum test site program, geological, geochemical, botanical, pedological, and aircraft and satellite remote sensing data were acquired and analyzed. This unique collection of information, documented in Sections 11, 12 and 13, makes the three petroleum test sites ideal locations for testing new approaches to geological remote sensing in the future.

In conclusion, the results of the petroleum test case program are promising, but further research is necessary.

References

Auldridge, L. (1979). World reserves holding up despite record production. *Oil Gas J., 77*, 67–74.

Brooks, R. R. (1972). *Geobotany and geochemistry in mineral exploration.* New York: Harper & Row.

Collins, W., S. H. Chang, and J. T. Kuo (1981). *Detection of hidden mineral deposits by airborne spectral analysis of forest canopies* (NASA Final Report, Contract NSG–5222). Washington, D.C.: National Aeronautics and Space Administration.

Cram, I. H. (Ed.) (1971). Future petroleum provinces of the United States—Their geology and potential. *AAPG Mem. 15.*

Davis, S. H., Jr. (1977). The effect of natural gas on trees and other vegetation. *J. Arboric., 3*(8), 153–154.

Department of Energy (1980). *United States crude oil, natural gas and natural gas liquids reserves.* Washington, D.C. (Annual Report)

Donovan, T. J. (1974). Petroleum microseepage at Cement, Oklahoma: Evidence and mechanism. *AAPG Bull., 58*, 429–446.

Donovan, T. J., and M. C. Dalziel (1977). Late diagenetic indicators of buried oil and gas. *U.S. Geol. Surv. Open File Rpt. 77-817.*

Donovan, T. J., I. Friedman, and J. D. Gleason (1974). Recognition of petroleum-bearing traps by unusual isotopic compositions of carbonate-cemented surface rocks. *Geology, 1*, 351–354.

Elachi, C. (1980). Spaceborne imaging radar: Geologic and oceanographic applications. *Science, 209*, 1073–1082.

Enright, R. J. (1981). World oil flow dives, reserves climb. *Oil Gas J., 79*, 83–87.

Ferguson, J. D. (1975). *Surface alteration and mineralization of Permian red beds overlying several oil fields in southern Oklahoma.* Unpublished master's thesis, Oklahoma State University.

Flower, F. B., E. F. Gilman, and I. A. Leone (1981). Landfill gas, what it does to trees and how its injurious effects may be prevented. *J. Arboric., 7*, 43–51.

Froidevaux, C. M. (1980). Radar, an optimum remote sensing tool for detailed plate tectonic analysis and its application to hydrocarbon exploration (an example in Irian Jaya, Indonesia). In *Radar geology: An assessment* (JPL Publication 80-61). Pasadena, California: Jet Propulsion Laboratory, 457–501.

Goetz, A. F. H., and L. C. Rowan (1981). Geologic remote sensing. *Science, 211*, 781–791.

Halbouty, M. T. (1976). Application of Landsat imagery to petroleum and mineral exploration. *AAPG Bull., 60*, 745–793.

Halbouty, M. T. (1980). Geologic significance of Landsat data for 15 giant oil and gas fields. *AAPG Bull., 64*, 8–36.

Ham, W. E., and L. C. Pray (1961). Modern concepts and classifications of carbonate rocks. In W. E. Ham (Ed.), Classification of carbonate rocks, *AAPG Mem. 1*, 2–19.

Hodgson, R. A. (1974). Review of significant early studies of lineament tectonics. In R. A. Hodgson, S. Parker–Gay, Jr., and J. Y. Benjamins (Eds.), *Proceedings of the First International Conference of the New Basement Tectonics*. Salt Lake City: The Utah Geological Association.

Hunt, J. M. (1979). *Petroleum geochemistry and geology*. San Francisco: W. H. Freeman.

Johnston, J. E., and F. J. Janza (1977). The role of remote sensing for energy development. In W. L. Smith (Ed.), *Remote sensing applications for mineral exploration*. Stroudsburg, Pennsylvania: Dowden, Hutchinson and Ross, 199–234.

Kahle, A. B., J. P. Schieldge, J. M. Abrams, R. E. Alley, and C. J. LeVine (1981). *Geologic application of thermal inertia imaging using HCMM data* (JPL Publication 81-55). Pasadena, California: Jet Propulsion Laboratory.

Leone, I. A., F. B. Flower, J. J. Arthur, and E. F. Gilman (1977). Damage to woody species by anaerobic landfill gases. *J. Arboric., 3*(12), 221–225.

Leone, I. A., F. B. Flower, E. F. Gilman, and J. J. Arthur (1979). Adapting woody species and planting techniques to landfill conditions. *Field and laboratory investigations*. (U.S. EPA Report 600/2-79-128)

Link, W. K. (1952). Significance of oil and gas seeps in world oil exploration. *AAPG Bull., 36*, 1505–1540.

McCulloh, T. H. (1973). Oil and gas. In D. A. Brobst and W. P. Pratt (Eds.), United States mineral resources, *U.S. Geol. Surv. Prof. Pap. 820*, 477–496.

Miller, J. B. (1975). Landsat images as applied to petroleum exploration in Kenya. *NASA Earth Resources Survey Symposium* (NASA TM X-58168, 1-B). Houston: Lyndon B. Johnson Space Center, 605–624.

Reeves, R. G. (1975). Manual of remote sensing. *Am. Soc. Photogramm., I & II*.

Roberts, A. A., M. C. Dalziel, L. A. Pogorski, and S. G. Quirt (1977). A possible petroleum helium anomaly in soil gas, Boulder and Weld Counties, Colorado. *U.S. Geol. Surv. Open File Rpt. 76-544*.

Roberts, W. H. (1980). Design and function of oil and gas traps. In W. H. Roberts and R. J. Cordell (Eds.), Problems of petroleum migration, *AAPG Studies in Geology*, No. 10, 217–240.

Rosaire, E. E. (1940). Symposium on geochemical exploration, geochemical prospecting for petroleum. *AAPG Bull., 24*, 1400–1433

Sabins, F. F., Jr. (1978). *Remote sensing: Principles and interpretation*. San Francisco: W. H. Freeman.

Saunders, D. F. (1979). Use of Landsat geomorphic and tonal anomalies in petroleum prospecting. In B. M. Gottlieb (Ed.), *Unconventional methods in exploration for petroleum and natural gas II*. Dallas: Southern Methodist University Press, 63–82.

Siegel, F. R. (1974). *Applied geochemistry*. New York: John Wiley & Sons.

Stewart, H., R. Blom, M. Abrams, and M. Dailey (1980). Rock type discrimination and structural analysis with Landsat and Seasat data: San Rafael Swell, Utah. In *Radar geology: An assessment*. (JPL Publication 80-61). Pasadena, California: Jet Propulsion Laboratory, 151–167.

St. John, B. V. (1981). *Sedimentary basins of the world and giant hydrocarbon accumulations*. Tulsa, Oklahoma: AAPG.

Sweeney, R. E., and I. R. Kaplan (1980). Diagenetic sulfate reduction in marine sediments. *Mar. Chem.*, *9*, 165–174.

The Times (1980). *The Times atlas of the world* (6th ed.). New York: Times Books.

Tissot, B. P., and D. H. Welte (1978). *Petroleum formation and occurrence*. New York: Springer–Verlag.

Vincent, R. K. (1977). Geochemical mapping by spectral ratioing methods. In W. L. Smith (Ed.), *Remote sensing applications for mineral exploration*. Stroudsburg, Pennsylvania: Dowden, Hutchinson and Ross, 251–278.

White, I. C. (1885). The geology of natural gas. *Science*, *5*, 521–522.

Wing, R. S., and J. Mueller (1975). SLAR reconnaissance Mimika–Eilanden Basin, southern trough of Irian Jaya. *NASA Earth Resources Survey Symposium* (NASA TM X-58168, 1-B). Houston: Lyndon B. Johnson Space Center, 599–604.

Wolf, K. H. (Ed.) (1976). Handbook of strata-bound and stratiform ore deposits, 11. *Regional studies and specific deposits* (Vol. 7). New York: Elsevier Scientific Publishing Company.

Bibliography

Doeringsfeld, W. W., Jr., and J. B. Ivey (1964). Use of photogeology and geomorphic criteria to locate subsurface structure. *Mountain Geologist*, *1*(4), 183–195.

Goetz, A. F. H., L. C. Rowan, and M. J. Kingston (1982). Shuttle Multispectral Infrared Radiometer: Preliminary results from the second flight of Columbia. *IEEE Digest, 1982 International Geoscience and Remote Sensing Symposium (IGARSS 82), II*, FA-6-3.1–FA-6-3.6.

Gottlieb, B. M. (Ed.) (1979). *Unconventional methods in exploration for petroleum and natural gas II*. Dallas: Southern Methodist University Press.

Halbouty, M. T. (1968). Giant oil and gas fields in United States. *AAPG Bull.*, *52*, 1115–1151.

Henderson, F. B., III, and G. A. Swann (Eds.) (1976). *Geological remote sensing from space* (LBL Publication 110). Livermore, California: Lawrence Berkeley Laboratory, 1-1–8-2.

Heroy, W. B. (Ed.) (1968). *Unconventional methods in exploration for petroleum and natural gas*. Dallas: Southern Methodist University Press.

Hubbert, M. K. (1967). Degree of advancement of petroleum exploration in the United States. *AAPG Bull.*, *51*, 2207–2227.

Laubmeyer, G. (1933). A new geophysical prospecting method, especially for deposits of petroleum. *Petroleum*, *29*, 1–4.

LeRoy, L. W., D. O. LeRoy, and J. W. Raese (Eds.) (1977). *Subsurface geology*. Colorado School of Mines, Golden.

Levorsen, A. I. (1967). *Geology of petroleum*. San Francisco: W. H. Freeman.

Menard, H. W., (1981). Toward a rational strategy for oil exploration. *Sci. Am.*, *244*(1), 55–65.

Menard, H. W., and G. Sharman (1975). Scientific use of random drilling models. *Science*, *190*(4212), 337–343.

Miller, V. C., and C. F. Miller (1961). *Photogeology*. New York: McGraw–Hill.

Moody, J. D. (1975). Distribution and geological characteristics of giant oil fields. In *Petroleum and global tectonics*. Princeton: Princeton University Press, 307–320.

Nettleton, L. L. (1971). Elementary gravity and magnetics for geologists and seismologists. *SEG, Monograph Series, No. 1*.

Ray, R. G. (1960). Aerial photographs in geologic interpretation and mapping. *U.S. Geol. Surv. Prof. Pap. 373*.

Short, N. (Chairman) (1976). Practical applications of Landsat data for earth resources surveys – Mineral/energy resources. *Mineral and petroleum resources application panel*. Unpublished report prepared for NASA Johnson Space Center Earth Resources Program Office, Houston, Texas.

Slotnick, M. M. (1959). *Lessons in seismic computing*. Tulsa, Oklahoma: SEG.

Sokolov, V. A. (1934). Summary of the experimental work of the gas survey. *Neft. Khoz.*, *27*, 28–34.

Section 11

Patrick Draw, Wyoming, Petroleum Test Case Report

Authors/Editors

Harold R. Lang
Jet Propulsion Laboratory

Willis H. Alderman
AMOCO Production Co.
Denver, Colorado

Floyd F. Sabins, Jr.
Chevron Oil Field Research Company
La Habra, California

Contributors

M. Lee Allison
Donald U. Wise
University of Massachusetts
Amherst, Massachusetts

Kathleen W. Baird
Michael I. Dailey
Barrett N. Rock
Jet Propulsion Laboratory

Anthony R. Barringer
Barringer Resources Inc.
Golden, Colorado

Rhonda Gaylord
Ronald W. Marrs
University of Wyoming
Laramie, Wyoming

Leslie L. Lundell
Atlantic Richfield Corp.
Dallas, Texas

John B. McKeon
Gulf Science and Technology Co.
Pittsburgh, Pennsylvania

Gary L. Prost
Joe R. Applegate
AMOCO Production Co.
Denver, Colorado

Robert J. Reed
David M. Richers
Cities Service Co.
Tulsa, Oklahoma

Robert D. Watson
U.S. Geological Survey
Flagstaff, Arizona

Section 11

Patrick Draw, Wyoming, Petroleum Test Site Report

Contents

I. Introduction 11-1
- A. Site Selection and Objectives 11-1
- B. Test Site Operations 11-1

II. Geographic Setting 11-2
- A. Location and Access 11-2
- B. Climate 11-2
- C. Physiography 11-2

III. Surface Geology 11-2
- A. Introduction 11-2
- B. Previous Work 11-2
- C. Structural Evolution 11-3
- D. Stratigraphy 11-4
  - 1. Fort Union Formation 11-5
  - 2. Fort Union–Wasatch contact 11-5
  - 3. Wasatch Formation 11-10
  - 4. Green River Formation 11-10

IV. Subsurface Geology and Producing Reservoir 11-10
- A. Introduction 11-10
- B. Discovery 11-10
- C. Reservoir Stratigraphy 11-10

V. Vegetation 11-13
- A. Introduction 11-13
- B. Collection and Interpretation of Vegetation Data 11-15
  - 1. Assessment of shrubby and semishrubby vegetation 11-15
  - 2. Assessment of herbaceous vegetation 11-15

PRECEDING PAGE BLANK NOT FILMED

C. Results of Vegetation Sampling 11-15
1. Species distribution 11-15
2. Species diversity 11-18
3. Vegetation cover 11-18

VI. Soils 11-18

VII. Special Field/Laboratory Investigations 11-20
A. Introduction 11-20
B. Analysis of an Area of Abnormal Stunted Sage 11-21
1. Introduction 11-21
2. Field characteristics 11-21
3. Anatomy of stunted sage from Patrick Draw test site 11-29
4. Conclusions 11-32
C. Organic Geochemistry 11-32
1. Introduction 11-32
2. Geologic model 11-33
3. Sample collection 11-34
4. Soil gas chemistry 11-35
5. Conclusions 11-38
D. Helium Soil Gas Survey 11-38
1. Introduction 11-38
2. Methods 11-38
3. Results 11-38
4. Conclusions 11-38
E. Soil Elemental Geochemistry 11-39
1. Introduction 11-39
2. Data acquisition and analysis 11-39
3. Results 11-39
4. Conclusions 11-43
F. Soil Carbon and Oxygen Isotope Survey 11-43
1. Objective 11-43
2. Results 11-43
3. Conclusions 11-45

VIII. Multispectral Remote Sensing Data 11-45
A. Introduction 11-45
1. Preliminary processing 11-46
2. Interpretation 11-47
B. Landsat MSS Data in Reconnaissance Mapping 11-47
C. Spectral Characteristics of Cover Types 11-47
1. Introduction 11-47
2. Spectral characteristics of vegetation 11-47
3. Spectral characteristics of soil/rock 11-52
D. Equivalent NS-001 Band Reflectance Values Obtained From PFRS Spectra 11-54
1. Equivalent NS-001 band values 11-54
2. Equivalent NS-001 band-ratio values 11-54
3. Conclusions 11-57

E. NS-001 Image-Derived Spectra—The Calibration Problem 11-59
1. Introduction 11-59
2. Characteristics of NS-001 data 11-59
3. Calibration of NS-001 data 11-61
4. Conclusions 11-63

IX. NS-001 Image Analysis 11-63
A. Mapping Tonal/Textural Units 11-63
1. Introduction 11-63
2. Results of tonal/textural interpretation of NS-001 data 11-67
3. Conclusions 11-69
B. A Tonal Anomaly Coincident With an Area of Anomalous Vegetation 11-69
1. Introduction 11-69
2. Image characteristics 11-69
3. Interpretation 11-69
C. Geologic Mapping 11-71
1. Introduction 11-71
2. Stratigraphic analysis 11-71
3. Structure 11-72
D. Lineament Analysis 11-73
1. Introduction 11-73
2. Topographic lineament analysis 11-73
3. NS-001 lineament analysis 11-78
E. Vegetation Mapping 11-80
1. Introduction 11-80
2. Discussion 11-80
3. Conclusions 11-81

X. Radar 11-81
A. Introduction 11-81
B. Seasat SAR Data Characteristics and Processing 11-81
C. SAR Interpretation 11-82
D. Summary 11-84

XI. Fraunhofer Line Discriminator—Luminescence Survey 11-84
A. Introduction 11-84
B. Data Analysis 11-87
C. Results 11-87
D. Conclusions 11-90

XII. Summary and Conclusions 11-90
A. "Direct" Detection of Hydrocarbons 11-90
B. Improved Geologic Mapping 11-92
1. Structure 11-92
2. Lineaments 11-92
3. Stratigraphic analysis 11-93
C. Improved Soils and Vegetation Mapping 11-93
D. Use of Multispectral Scanners as Platform-Borne Spectrometers 11-93
E. Spectral Analysis 11-93

Acknowledgments 11-94

References 11-95

Appendixes

A. Results of Hydrocarbon Soil Gas Analyses 11-99

B. Results of Lasertrace® Soil Elemental Geochemistry Analyses 11-107

Figures

11-1. Map showing the location of the Patrick Draw test site in south–central Wyoming 11-2

11-2. Map showing major structural subdivisions of the Cordilleran orogen of the western United States 11-3

11-3. Structural contours on top of the Dakota showing major structural features of south–central Wyoming 11-4

11-4. Published geologic map, Patrick Draw test site 11-6

11-5. Unpublished geologic map, Patrick Draw test site 11-7

11-6. Unpublished photogeologic interpretation, Patrick Draw test site 11-7

11-7. Detailed bedrock stratigraphy and superjacent residual soil mineralogy as observed in exposures in a gas pipeline trench 11-8

11-8. Detailed bedrock stratigraphy and superjacent residual soil elemental geochemistry 11-9

11-9. Generalized E–W stratigraphic diagram illustrating the interfingering relationship of the Green River and Wasatch Formations 11-11

11-10. Regional subsurface structural contour map showing Patrick Draw and adjacent fields 11-12

11-11. Regional W–E structural cross section from surface exposures of the Almond Formation to the Patrick Draw and Table Rock fields 11-13

11-12. General regional lithofacies map for the upper Almond Formation, showing paleogeographic relationships 11-14

11-13. Map showing structure contours on top of Mesa Verde, and isolith of Patrick Draw reservoir sandstone 11-16

11-14. Cross sections illustrating subsurface stratigraphic relations, Patrick Draw oil field 11-17

11-15. Index map showing the locations of sites selected for vegetation analysis, Patrick Draw test site 11-18

11-16. Aerial photograph, acquired October 19, 1978, showing the outline of the area of anomalous stunted sage as recognized in NS-001 multispectral data acquired at the same time 11-26

11-17. Area of anomalous stunted sage 11-27

11-18. Ground photographs: (a) normal sage; (b) anomalous stunted sage 11-28

11-19. Diagram illustrating the availability of nutrients to plants as a function of soil pH 11-30

11-20. Representative leaf cross sections of normal sage and abnormal stunted sage from the Patrick Draw test site 11-31

11-21. Representative stem cross sections of wood of normal sage and wood of stunted sage from the Patrick Draw test site 11-32
11-22. Soil gas anomaly significance map showing combined results of all parameters: adsorbed, absorbed, and free soil gas 11-33
11-23. Aerial photograph mosaic showing the location of endpoints of seven selected lineaments evaluated in a soil gas survey 11-34
11-24. Index map showing the locations of sites sampled in hydrocarbon soil gas survey 11-35
11-25. Sampling devices used in hydrocarbon soil gas survey 11-36
11-26. Index map showing the locations of significant adsorbed soil gas anomaly sites 11-36
11-27. Index map showing the locations of significant absorbed soil gas anomaly sites 11-37
11-28. Index map showing the locations of significant free soil gas anomaly sites 11-37
11-29. Index map showing soil helium gas survey sample sites and results 11-39
11-30. Index map showing the locations of sites sampled in soil elemental geochemistry survey 11-40
11-31. Soil titanium concentration map 11-40
11-32. Soil vanadium concentration map 11-40
11-33. Soil copper concentration map 11-40
11-34. Soil zinc concentration map 11-41
11-35. Soil iron concentration map 11-41
11-36. Soil phosphorus concentration map 11-41
11-37. Soil potassium concentration map 11-41
11-38. Soil nickel concentration map 11-42
11-39. Soil manganese concentration map 11-42
11-40. Soil calcium concentration map 11-42
11-41. Soil sodium concentration map 11-42
11-42. Plot of $\delta^{13}C$ versus $\delta^{18}O$ for soil carbonates from Patrick Draw, Wyoming 11-44
11-43. Carbon isotope values versus methane content measured in adsorbed soil gas 11-45
11-44. Carbon isotope values versus methane content measured in absorbed gas 11-45
11-45. Carbon isotope values versus methane content measured in free soil gas 11-45
11-46. Distribution of carbon isotope values in the vicinity of Patrick Draw oil field 11-46
11-47. Map showing flight-line locations and areal coverage for M^2S, NS-001, and color photographic aircraft data acquired 11-46
11-48. Portion of a published geologic map for the Rock Springs Uplift that is shown in the Landsat MSS subscene, Figure 11-49 11-48

11-49. Landsat MSS image produced using a principal components stretch (VICAR, PGSTR): band 4, blue; band 5, green; and band 7, red (acquired May 13, 1976) 11-49
11-50. Examples of field spectra for major cover types, Patrick Draw test site 11-50
11-51. Comparison of the PFRS field spectra for typical soil and the same soil in shadow 11-51
11-52. Composite diagrammatic laboratory spectrum illustrating major mineral absorption bands affecting NS-001 data 11-52
11-53. Three laboratory spectra illustrating the loss of the calcite absorption band near 2.3 μm when grain size is decreased to $<74\,\mu$m (fine silt/clay) 11-53
11-54. PFRS field spectra exhibiting maximum, minimum, and mean equivalent NS-001 band reflectances 11-55
11-55. Photograph of PFRS field spectrum site 37A, which exhibited the maximum equivalent reflectances of 260 field spectral measurements in all seven NS-001 VNIR bands 11-56
11-56. Photograph of PFRS field spectrum site 36E, which exhibited the minimum equivalent reflectances of 260 field spectral measurements in NS-001 VNIR bands 1, 2, 3, 4, 5, and 6 11-56
11-57. Photograph of PFRS field spectrum site 8F, which exhibited the minimum equivalent reflectances of 260 field spectral measurements in NS-001 VNIR band 4 11-56
11-58. Photograph of PFRS field spectrum site 7G, which exhibited the minimum equivalent reflectances of 260 field spectral measurements in NS-001 VNIR band 7 11-56
11-59. Photograph of PFRS field spectrum site 16A, which exhibited the mean equivalent reflectances of 260 field spectral measurements in all seven NS-001 VNIR bands 11-57
11-60. Field spectra for samples exhibiting maximum equivalent NS-001 VNIR band-ratio values 11-58
11-61. Field spectra for samples exhibiting minimum equivalent NS-001 VNIR band-ratio values 11-58
11-62. A comparison of uncalibrated NS-001 image spectra and equivalent seven-point PFRS-derived spectra for three relatively homogeneous targets in the Patrick Draw test site .. 11-59
11-63. PC spectra for NS-001, Mission 390, line 4 data acquired October 19, 1978 11-61
11-64. Calibration curves used to determine offsets and gains that were applied to NS-001, Mission 390, line 4 data to convert image DN radiance values to equivalent PFRS reflectances .. 11-62
11-65. NS-001, Mission 390, line 4 calibrated image for band 1 11-63
11-66. NS-001, Mission 390, line 4 calibrated image for band 2 11-64
11-67. NS-001, Mission 390, line 4 calibrated image for band 3 11-64
11-68. NS-001, Mission 390, line 4 calibrated image for band 4 11-65
11-69. NS-001, Mission 390, line 4 calibrated image for band 5 11-65
11-70. NS-001, Mission 390, line 4 calibrated image for band 6 11-66
11-71. NS-001, Mission 390, line 4 calibrated image for band 7 11-66

11-72. A comparison of calibrated NS-001 image spectra and equivalent seven-point PFRS-derived spectra for three targets in the Patrick Draw test site 11-67
11-73. NS-001, Mission 407, line 4, August 31, 1979, CRC image 11-68
11-74. Tonal/textural units and dominant image colors recognized in an interpretation of a band 6/7 (blue), 6/1 (green), 3/2 (red) NS-001 CRC image 11-68
11-75. Geometrically rectified NS-001, Mission 390, line 4 PC image 11-70
11-76. Geometrically rectified NS-001, Mission 390, line 4 CRC image 11-70
11-77. Composite NS-001, Mission 390, line 4 photogeologic interpretation of Figures 11-75 and 11-76 11-72
11-78. Location map comparing the spatial relationship of the transition spectral unit to the published mapped contact of the Fort Union/Wasatch Formations and to major soil/vegetation units 11-72
11-79. Side-illuminated image of the Rock Springs, Wyoming, 1° by 2° raised relief map 11-74
11-80. Statistical summary of topographic lineaments 11-75
11-81. Orientations of major topographic lineament sets from each of six different lighting directions 11-76
11-82. Topographic lineament rose diagrams from all lighting directions for six subareas, Rock Springs, 1° by 2° quadrangle 11-76
11-83. Topographic lineaments in the vicinity of the Patrick Draw test site as observed by combining interpretations from six different lighting azimuths 11-77
11-84. NS-001 lineament azimuth histogram for 176 lineaments recognized in the composite geologic interpretation shown in Figure 11-77 11-79
11-85. Photograph (looking NNE) of jointed Wasatch claystone exposed in a gas pipeline trench 11-80
11-86. Image showing variations in percent vegetation cover in the test site area 11-81
11-87. The location of the Patrick Draw test site with respect to Seasat SAR Rev. 789 coverage 11-82
11-88. Components used in split-spectrum (HSI) processing of Seasat SAR data 11-83
11-89. Composite lineament and tonal/textural interpretation of Figure 11-88(a) 11-84
11-90. Key to tone/texture classes for Seasat SAR image (Rev. 789) at the Patrick Draw test site 11-85
11-91. Seasat HSI image 11-86
11-92. NS-001 band 3 image with a luminescence overlay, Patrick Draw test site. Luminescence values at 486.1 nm 11-87
11-93. NS-001 band 3 image with a luminescence overlay, Patrick Draw test site. Luminescence values at 589.0 nm 11-88

11-94. NS-001 band 3 image with a luminescence overlay, Patrick Draw test site. Luminescence values at 656.3 nm 11-88
11-95. Luminescence plotted on a soil manganese concentration map 11-91

Tables

11-1. Stratigraphic summary, Patrick Draw test site 11-5
11-2. X-ray diffraction analysis results illustrating significant mineralogical differences among Wasatch Formation, Transition Member, and Fort Union Formation 11-8
11-3. Percent cover of major vegetation species at selected sites in the Patrick Draw area 11-19
11-4. Chemical analysis of vegetation samples by Lasertrace® 11-20
11-5. Summary of major vegetation types and percent cover at selected sites in the Patrick Draw area 11-21
11-6. Physical aspects of soil units, Patrick Draw test site 11-22
11-7. Botanical aspects of soil units, Patrick Draw test site 11-24
11-8. Ranking correlation among all sample types 11-38
11-9. Ranges of carbon isotope values for various natural carbon sources 11-43
11-10. Carbon and oxygen isotope measurements of soils collected at the Patrick Draw test site 11-44
11-11. Summary of Landsat MSS data, Patrick Draw test site 11-46
11-12. Summary of aircraft multispectral data, Patrick Draw test site 11-46
11-13. NS-001 Thematic Mapper Simulator 11-50
11-14. Mineralogy of Patrick Draw soil/rock determined by XRD analysis of 37 representative surface samples 11-52
11-15. Summary of equivalent NS-001 band reflectance values determined from 260 PFRS field spectra measured at 60 sites 11-54
11-16. Summary of equivalent NS-001 band-ratio values determined from 260 PFRS field spectra measured at 60 sites 11-57
11-17. Significant NS-001 VNIR band ratios for the enhancement and interpretation of images based on the analysis of 260 PFRS spectral measurements at 60 sites 11-59
11-18. Correlation matrices for the seven NS-001 VNIR band data acquired in two overflights of the Patrick Draw test site 11-60
11-19. NS-001 Mission 390, October, 1978, principal components analysis: Eigenvectors of seven VNIR bands for the first three PCs 11-61
11-20. Summary of trends of six lineament sets recognized in a statistical analysis of 176 azimuthal measurements for lineaments shown in Figure 11-77 11-79
11-21. Summary of five lineament sets recognized in the analysis of 176 lineaments shown in Figure 11-77 11-79

11-22. Characteristics of Seasat SAR subscene (Rev. 789) as processed by Gulf Science and Technology Company 11-82
11-23. Summary of the sample sites that show luminescence above background and those elements of rank 3 or greater classified as anomalous 11-89
11-24. Summary of elements that correlate with luminescence as a function of Fraunhofer wavelength 11-89

Plates[1]

11-1. Patrick Draw, Wyoming: Map of test site showing subsurface structure and field sample locations
11-2. Patrick Draw, Wyoming: Soil map of test site
11-3. Patrick Draw, Wyoming: Composite geologic interpretation of geometrically corrected NS-001 data from Mission 390, October 19, 1978
11-4. Patrick Draw, Wyoming: Interpretation of NS-001 data from Mission 390, October 19, 1978, showing traceable bedding units

[1]Plates are contained in Part 3 (envelope) of *The Joint NASA/Geosat Test Case Project.*

Section 11

Patrick Draw, Wyoming, Petroleum Test Site Report

I. Introduction

A. Site Selection and Objectives

The Patrick Draw, Wyoming, test site was selected to evaluate the effectiveness of using remote sensing techniques to detect nonstructural oil fields or stratigraphic traps. Patrick Draw produces oil from a lens of sandstone surrounded by shale and is a typical stratigraphic trap. Because of their lack of structural closure, stratigraphic traps are difficult to recognize by geophysical methods or by standard surface mapping techniques. Recent research has indicated that microseepage of oil and gas can alter the chemistry and mineralogy of surface rocks and soils and can affect vegetation. If surface changes related to such seepage are detectable by remote sensing, they could constitute additional exploration criteria for finding both structural and stratigraphic traps.

The Patrick Draw test site was selected for the following reasons:

(1) The reported surface and subsurface geology of the area is relatively simple and is reasonably well known as a result of surface mapping and exploration and production well drilling.

(2) Cultural disturbance in the area is limited to roads and well sites, which improves the potential for recognizing surface alteration effects.

(3) The area is accessible for fieldwork.

(4) The geology and oil occurrence are typical of much of the Rocky Mountain region; therefore, results at the test site may be widely applicable in this region.

(5) Earlier studies of Landsat Multispectral Scanner (MSS) remote sensing data at Patrick Draw indicated potential utility in exploration (Short, 1976).

B. Test Site Operations

This section describes in detail the investigations conducted during this study. The study began with a review of published and unpublished information and a reconnaissance field trip and overflight in a light airplane. This information was used to plan traverses for sampling soil and vegetation and for acquiring portable field reflectance spectrometer measurements.

Initial remote sensing data consisted of color aerial photographs and Landsat multispectral data that were digitally processed at JPL and by participating Geosat member companies. Subsequently, NASA used the airborne NS-001 Thematic Mapper Simulator to acquire multispectral data that were digitally processed at JPL. The U.S. Geological Survey (USGS) acquired data with the airborne Fraunhofer Line Discriminator. Seasat radar data were also acquired. Interpretation of images by various investigators defined features that were checked on subsequent field trips to the test site.

To evaluate the possibility of hydrocarbon microseepage, a major effort was made to acquire soil and soil gas samples. These samples were analyzed at laboratories of Geosat member companies.

II. Geographic Setting

A. Location and Access

The Patrick Draw test site is in south–central Wyoming, approximately 55 km (35 mi) east of the city of Rock Springs (Figure 11-1). It encompasses approximately 400 km^2 (160 mi^2) in township 18, 19, and 20 N, range 98 and 99 W, Sweetwater County. The coordinates for the test site area are lat. 41°45′ N, long. 108°30′ W; lat. 41°42′ N, long. 108°22′ W; lat. 41°25′ N, long. 108°35′ W; and lat. 41°28′ N, long. 108°40′ W.

A system of dirt and paved oil field lease roads provides access to most of the test site area from the Bitter Creek and Patrick Draw offramps of Interstate Highway 80.

B. Climate

The test site is in a semiarid, intermontane basin typical of western Wyoming. Winds in the area are strong and persistent due to channeling of cold Arctic air through a gap in the Continental Divide in central Wyoming. Summer daytime temperatures can exceed 32° C (90° F), but the mean annual temperature is only 5° C (40° F). Annual precipitation is approximately 20 cm (8 in.), of which 40 percent is snow. Freezing temperatures may occur any time of the year but, on the average, the last spring and the first fall occurrences of freezing temperatures are 60 days apart (Becker and Alyia, 1964).

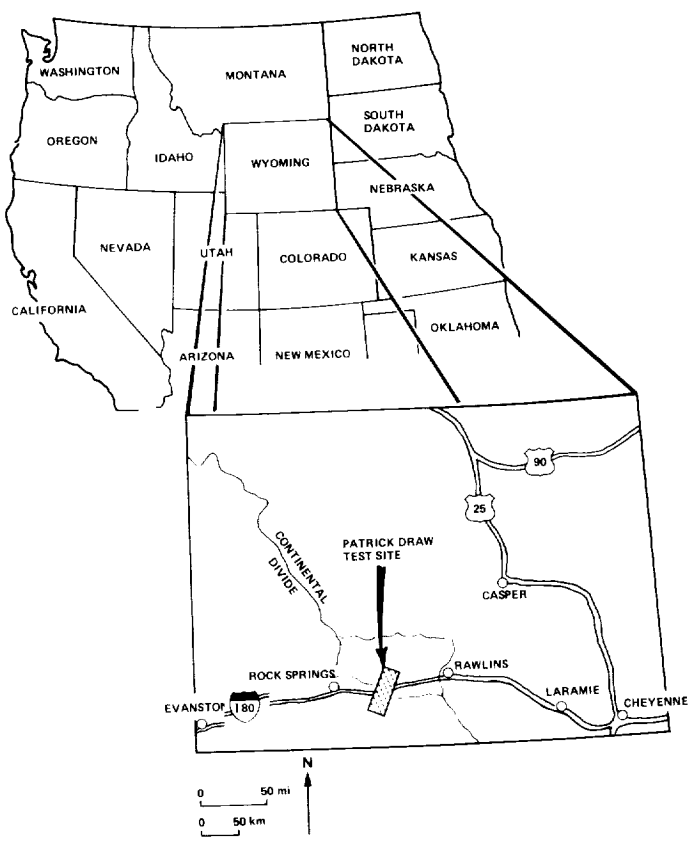

Figure 11-1. Map showing the location of the Patrick Draw test site in south–central Wyoming

C. Physiography

Elevations in the test site area range from 2200 m (6600 ft) to almost 2400 m (7200 ft). Relief is low throughout most of the area, except for the southern one-third where nearly vertical cliffs form the northwest rim of resistant marlstone, sandstone, and shale bluffs. The westernmost edge of the area is badlands, composed of cuestas formed by east-dipping, resistant sandstone beds.

The principal drainage in the area is Bitter Creek, a perennial tributary of the Green River. Bitter Creek enters the test site on the east–central margin and flows in a northwesterly direction to Bitter Creek Station, where it turns to the southwest, paralleling the Union Pacific Railroad bed. West of the test site, Bitter Creek appears superposed—it flows nearly due west and is incised in a direction transverse to the axis of the Rock Springs Uplift.

III. Surface Geology

A. Introduction

All of Wyoming—including the Patrick Draw test site—is located in the unstable foreland of the Rocky Mountains and is flanked on the west by the Cordilleran geosynclinal complex and on the east by the stable cratonic interior (Figure 11-2).

The Patrick Draw oil field is located on the east limb of the Rock Springs Uplift and is in the northwest Washakie Basin, an intermontane subbasin of the greater Green River Basin (Figure 11-3). Except for the transverse Uinta Uplift, a feature of probable late Precambrian origin, all structures shown in Figure 11-3 are primarily the result of a tectonic regime established during the late Cretaceous–Eocene Laramide orogeny (Grose, 1972, p. 36). The stratigraphic and structural evolution of the Patrick Draw test site is therefore ultimately tied to the evolution of the Cordillera.

B. Previous Work

Geologic investigation of the Rocky Mountain region, including the area of the Patrick Draw test site, had its inception with the territorial surveys of Hayden, King, and Powell during the period 1868 to 1878 (King, 1959, p. 93–97). Interest in the coal and petroleum resource potential

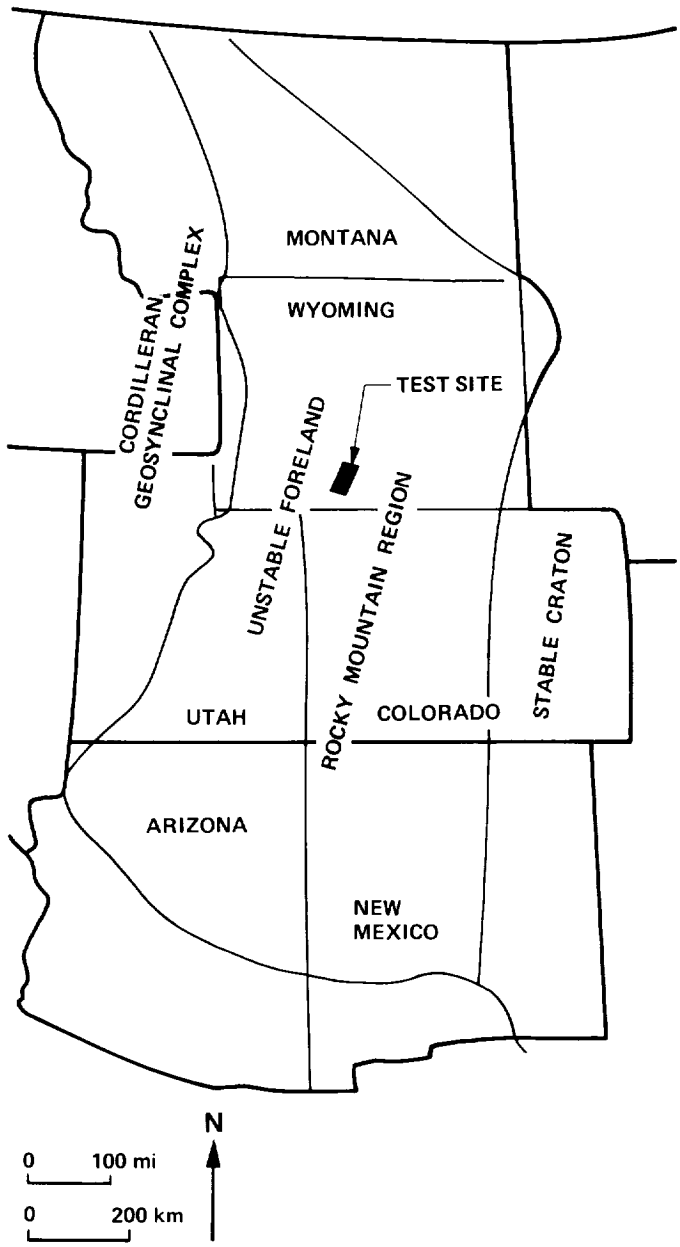

Figure 11-2. Map showing major structural subdivisions of the Cordilleran orogen of the western United States (Grose, 1972, Figure 1, p. 37). The Patrick Draw test site is in the unstable foreland of south-central Wyoming.

of the area east of the Rock Springs Uplift spawned more detailed work in the Patrick Draw region by Schultz (1909, 1910, 1920) and Sears and Bradley (1925). These early studies defined the stratigraphic and structural framework of the test site area.

Davis (1958) prepared a detailed stratigraphic analysis of the Tertiary units exposed at Patrick Draw. Works by Asquith (1970) and Weimer (1966) elucidated the Cretaceous through early Tertiary paleogeographic evolution of the test site area.

Early petroleum development of the Wamsutter Arch area, including the Patrick Draw oil field, was described by Ritzman (1961). Cox (1962) provided a detailed analysis of the structure, stratigraphy, exploration strategy, and petroleum development history and potential of the region. A comprehensive compendium of structural, stratigraphic, reservoir, and discovery data for oil and gas fields of the greater Green River Basin was published by the Wyoming Geologic Association (1979). This publication includes data for the Patrick Draw oil field (p. 274–277) as well as for the neighboring Brady Deep North, Desert Springs, and Table Rock fields. The origin of commercial gas accumulations and the potential for future gas development throughout the Washakie Basin were evaluated by McPeek (1981).

Roehler (1977a) compiled a regional 1:120,000 geologic map of the Rock Springs Uplift, which included the test site area. A comprehensive integration of most published and much unpublished geological information for the entire U.S. Cordillera is provided in the *Geologic Atlas of the Rocky Mountain Region* (Mallory, 1972).

C. Structural Evolution

Skeeters and Hale (1972, p. 274) recognize five Phanerozoic stages in the evolution of that portion of the Cordilleran orogen which includes the Patrick Draw test site:

(1) Paleozoic–Triassic. Stable shelf deposition in an epicontinental sea on the west flank of the stable North American Craton.

(2) Late Triassic–Jurassic. Fluctuating retreat of the epicontinental sea.

(3) Cretaceous. Invasion by an epicontinental North American interior seaway.

(4) Late Cretaceous. Onset of the Laramide orogeny; coincident fluctuating retreat of the epicontinental seaway and mountain building west of the test site.

(5) Paleocene–Eocene. Climax of Laramide orogeny, presumably resulting from E–W compressional forces having their origin in plate interaction on the east Pacific margin (Dewey and Bird, 1970). Development of present structures, including creation of structural/topographic highs that provided detritus for deposition in structural/topographic lows; onset of paludal, lacustrine, and fluvial sedimentation that continued into the Holocene.

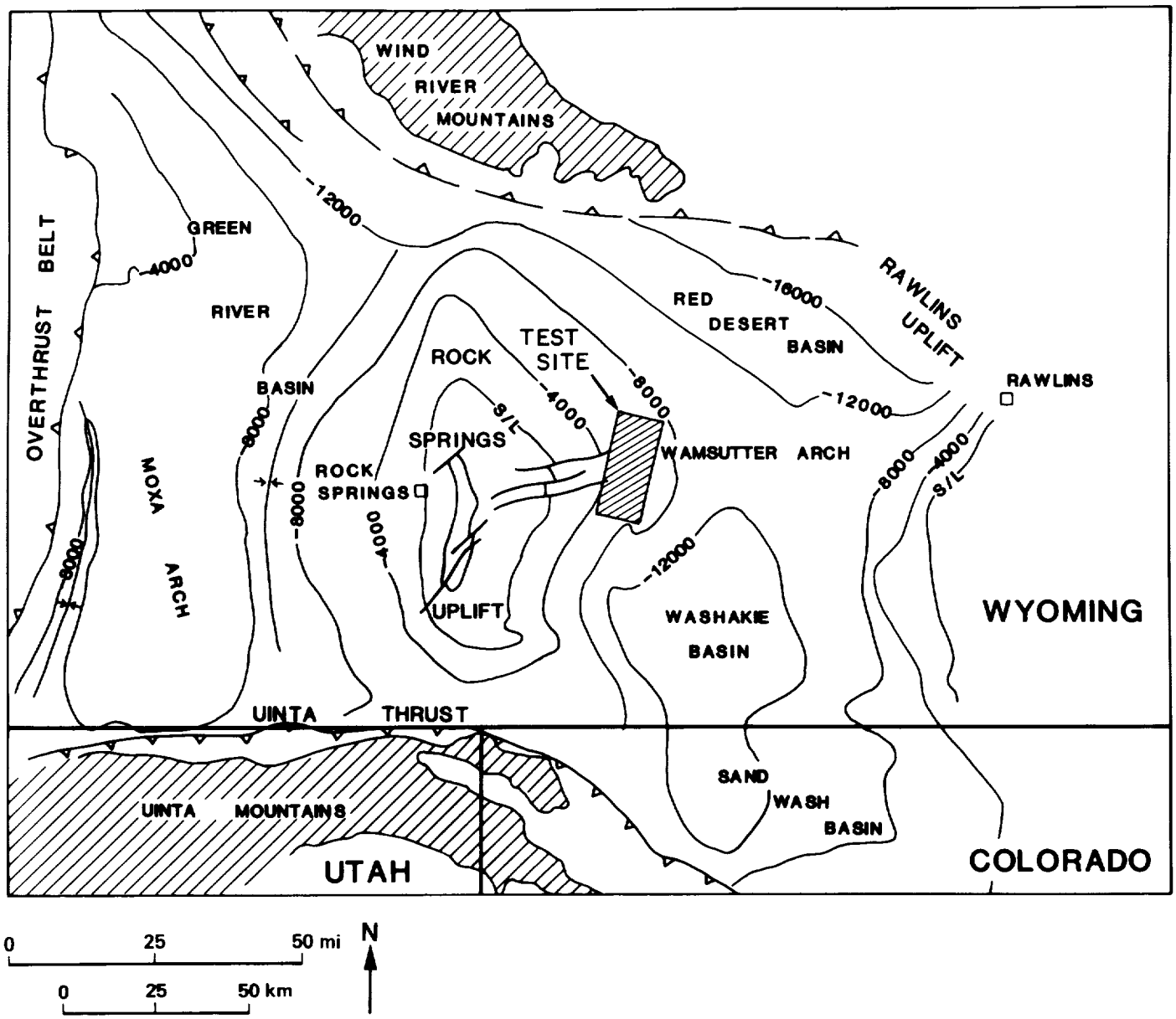

Figure 11-3. Structural contours on top of the Dakota showing major structural features of south–central Wyoming. The Patrick Draw test site is on the east flank of the Rock Springs Uplift. Contours (in feet) on top of the Dakota; datum, sea level (Skeeters and Hale, 1972, Figure 9, p. 275).

All structures shown in Figure 11-3 had their inception during stage 5. The clastic sedimentary rocks exposed at the surface and penetrated by drilling in the Patrick Draw oil field were deposited, lithified, and deformed during this critical stage of Cordilleran evolution. Additionally, the petroleum produced in the test site area was generated, then migrated, and finally was trapped in commercial reservoirs during this period (McPeek, 1981).

The surface structure of the test site area has been mapped (Figure 11-4) as a simple SE-dipping (2°–5°) homocline, cut in the north by an east-trending normal fault of minimal displacement.

D. Stratigraphy

Table 11-1 summarizes important stratigraphic units exposed at the surface or penetrated by drilling in the Patrick Draw test site. Some important characteristics of bedrock units present in the test site are discussed below, in order of decreasing age.

Table 11-1. Stratigraphic summary, Patrick Draw test site[a]

Age	Formation	Maximum Thickness, m	Description
Pleistocene–Holocene	Soil and alluvium	20[b]	Residual silty clay loams, eolian sand, fluvial sand and gravel, and playa deposits
Eocene	Green River	130[b]	Nonmarine, lacustrine sandstone, shale, and marlstone; fossiliferous
	Wasatch	430[b]	Nonmarine, variegated, fluvial and lacustrine, silty sandstone and argillaceous limestone; fossiliferous
Paleocene	Fort Union	400[b]	Nonmarine, fluvial shale, siltstone, calcareous sandstone, and coal
Late Cretaceous	Lance	430	Nonmarine sandstone, carbonaceous shale, lignitic shale, and coal
	Fox Hills	120	Transitional massive sandstone
	Lewis	420	Marine shale, bentonite, and sandstone
	MESAVERDE GROUP: Almond	130	Nonmarine sandstone, silty shale, carbonaceous shale, and coal Includes the Patrick Draw reservoir sandstone
	Ericson	150	Nonmarine, massive sandstone and carbonaceous shale
	Rock Springs	400	Nonmarine, interbedded sandstone, siltstone, carbonaceous shale, and coal
	Blair	600	Transitional, silty shale and sandstone
	Baxter	1200	Marine, soft, dark shale

[a]Compiled and modified from Asquith (1970), Cox (1962), Land (1972), and Roehler (1977b).
[b]Units exposed at the surface in the test site area; others reported in the subsurface.

1. Fort Union Formation. The drab-gray, fine- to medium-grained, feldspathic, carbonate-cemented sandstones of this unit grade into arenaceous limestones and are intercalated with mudstone, coal, and carbonaceous shale (Davis, 1958). These fluvial deposits, derived from surrounding Laramide-induced topographic highs, were deposited in meander systems, floodplains, coal swamps, and a freshwater lake complex centered in the eastern portion of the Washakie Basin (McDonald, 1972). The contact of the Fort Union with the underlying Lance is not exposed in the test site area. The unit varies in thickness from 170 m (500 ft) on the south end of the Rock Springs Uplift to over 1500 m (4500 ft) northeast of the Wamsutter Arch (McDonald, 1972).

2. Fort Union–Wasatch contact. The contact between the Paleocene Fort Union Formation and the Eocene Hiawatha Member of the Wasatch Formation has been mapped in the central portion of the test site area (Figure 11-4). The nature of this contact was described by Davis (1958, p. 25), based on measured sections in and near the Patrick Draw test site:

> Lithologically, the Fort Union–Hiawatha contact may be drawn at the top of the very calcareous units in the Fort Union formation. It is usually necessary to be somewhat arbitrary, for the contact is a gradational one. The uppermost very calcareous units encountered in the Fort Union are relatively extensive laterally and are at least two or three feet thick. The very carbonaceous shales and coals appear within a very short distance below the top bed of the Fort Union. There are no carbonaceous beds of any consequence in the lower Hiawatha Member.

Based on an analysis of this contact throughout the greater Green River Basin, McDonald (1972, p. 248) states:

> The contact of the upper Fort Union with the overlying Wasatch is often difficult or even impossible to ascertain.... The Wasatch generally displays more red coloration and fewer coal beds than the more drab-appearing Fort Union. Toward the basin interiors, however, these criteria become indistinct in places, and

geologists may vary several hundred feet in their placement of the Wasatch–Paleocene boundary.

The problematic nature of this contact in the test site area is demonstrated by differences in its location as mapped by three workers (Figures 11-4, 11-5, and 11-6). Poor exposures and shallow dips make tracing the Wasatch–Fort Union contact difficult. However, in the summer of 1980, exposures in a 2.5-m (9-ft) deep gas pipeline trench provided the first opportunity to locally evaluate the detailed bedrock stratigraphy of this contact, which otherwise is not exposed in the test site area (Plate 11-1).

a. General lithology. The trenched interval spans the Fort Union–Wasatch contact as mapped by Roehler (Figure 11-4). The sequence may be divided into three informal lithostratigraphic units, based on criteria described below and shown in Figure 11-7.

(1) 0–125 m, Fort Union Formation. Light greenish-gray sandstone and claystone contain many intervals of calcareous concretions that commonly coalesce, forming resistant beds, some traceable along strike up to 5 km. Sandstones are generally fine- to medium-grained, friable, and micaceous. Thin 15-cm (6-in.), discontinuous, lignitic coal seams and carbonaceous shale beds are common throughout.

(2) 125–220 m, Transition Member, Fort Union Formation. Dark greenish-gray claystone is tough, fractured, and generally nonresistant. Gypsum fracture filling is common in upper one-half of the unit. A prominent, resistant, 5-m (16-ft) thick carbonate-cemented sandstone bed, which commonly contains septarian nodules, is at the top of the unit, and a dark-gray, thin 15-cm (6-in.) marlstone bed is at the base. Three thin, lignitic coal seams occur in the unit, the thickest, 40 cm (16 in.), near the base. This unit includes the highest occurrence of coal and the highest occurrence of carbonate concretionary sandstone beds.

(3) 220–275 m, Basal Wasatch Formation. This unit includes a variegated sequence of sandstone, siltstone, claystone, and marlstone. Sandstones are typically sideritic and platy. Coal and carbonaceous shale are not present; the unit lacks resistant, ledgeforming concretionary sandstones.

b. Mineralogy based on X-ray diffraction (XRD). Minerals common to all units, in order of decreasing abundance, are quartz, plagioclase (Ab 10–15), K-feldspar (microcline), illite–vermiculite mixtures, calcite, and siderite. Table 11-2 shows the distribution of the most diagnos-

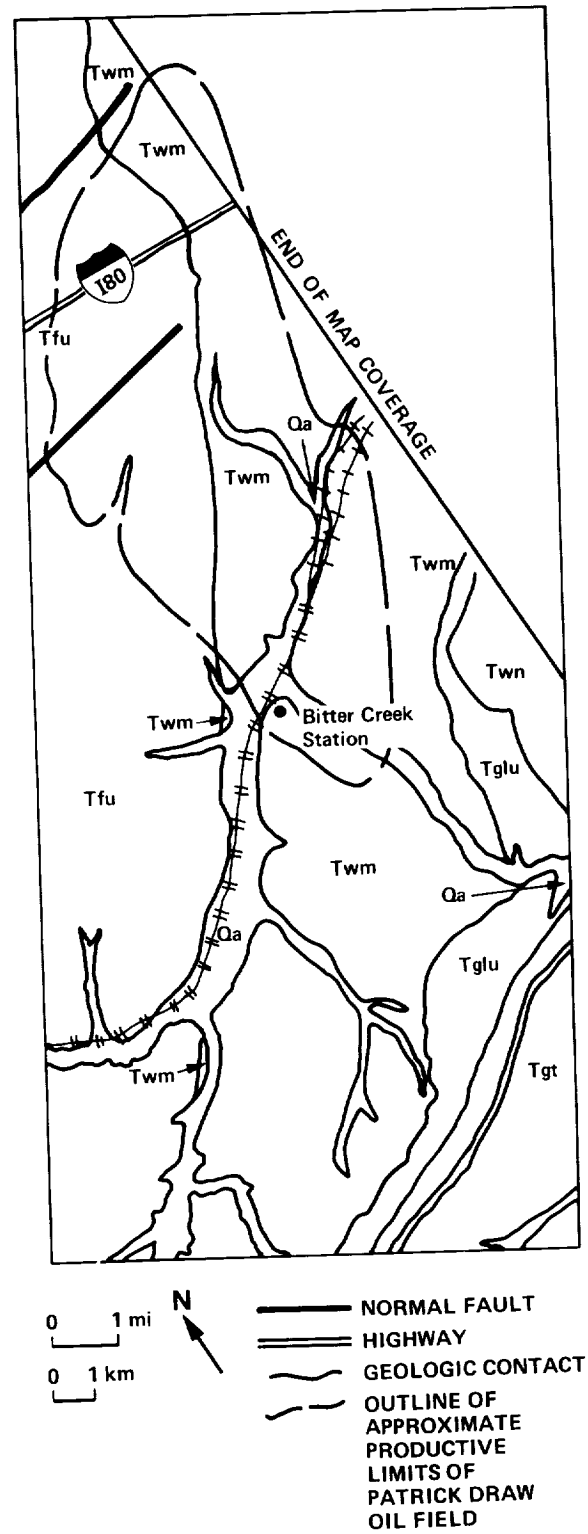

Figure 11-4. Published geologic map, Patrick Draw test site (Roehler, 1977a). The test site is mapped as a SE-dipping homocline cut by a single east-trending normal fault of minimal displacement.

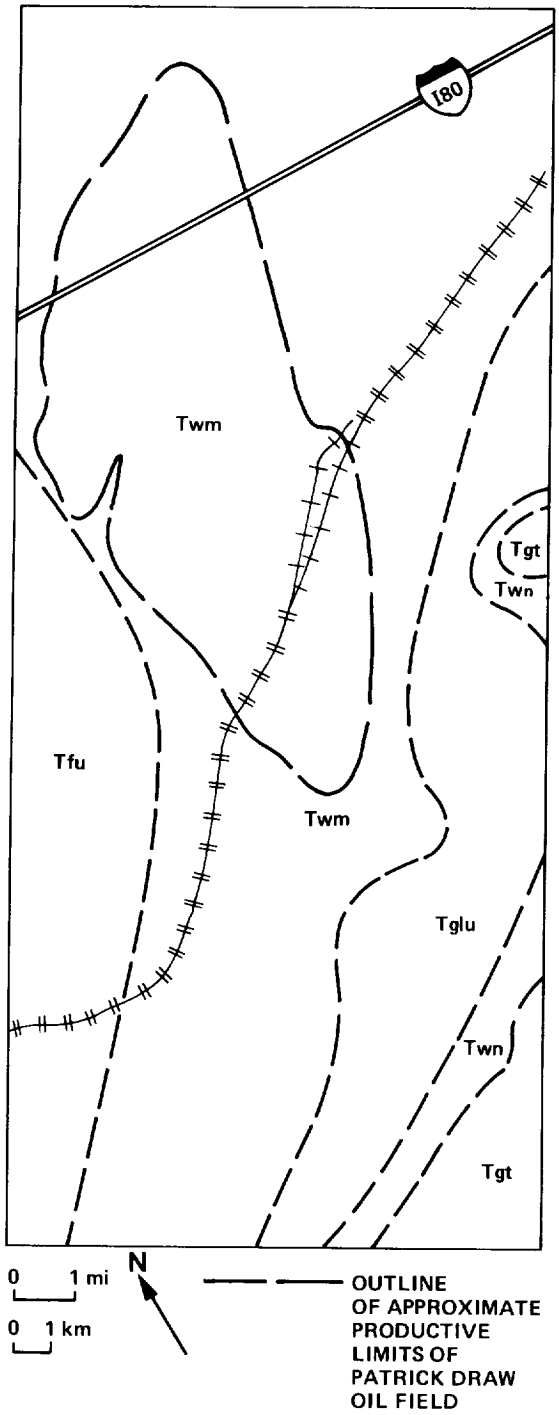

Figure 11-5. Unpublished geologic map, Patrick Draw test site (Davis, 1958, Figure 4, p. 8). Compare to Figures 11-4 and 11-6.

Unit designations for Figures 11-4,11-5, and 11-6:	
Tfu	Paleocene, Fort Union Formation
Twm	Eocene, Wasatch Formation, main body
Tglu	Eocene, Green River Formation, Luman Tongue
Twn	Eocene, Wasatch Formation, Niland Tongue
Tgt	Eocene, Green River Formation, Tipton Tongue
Qa	Pleistocene–Holocene, Alluvium

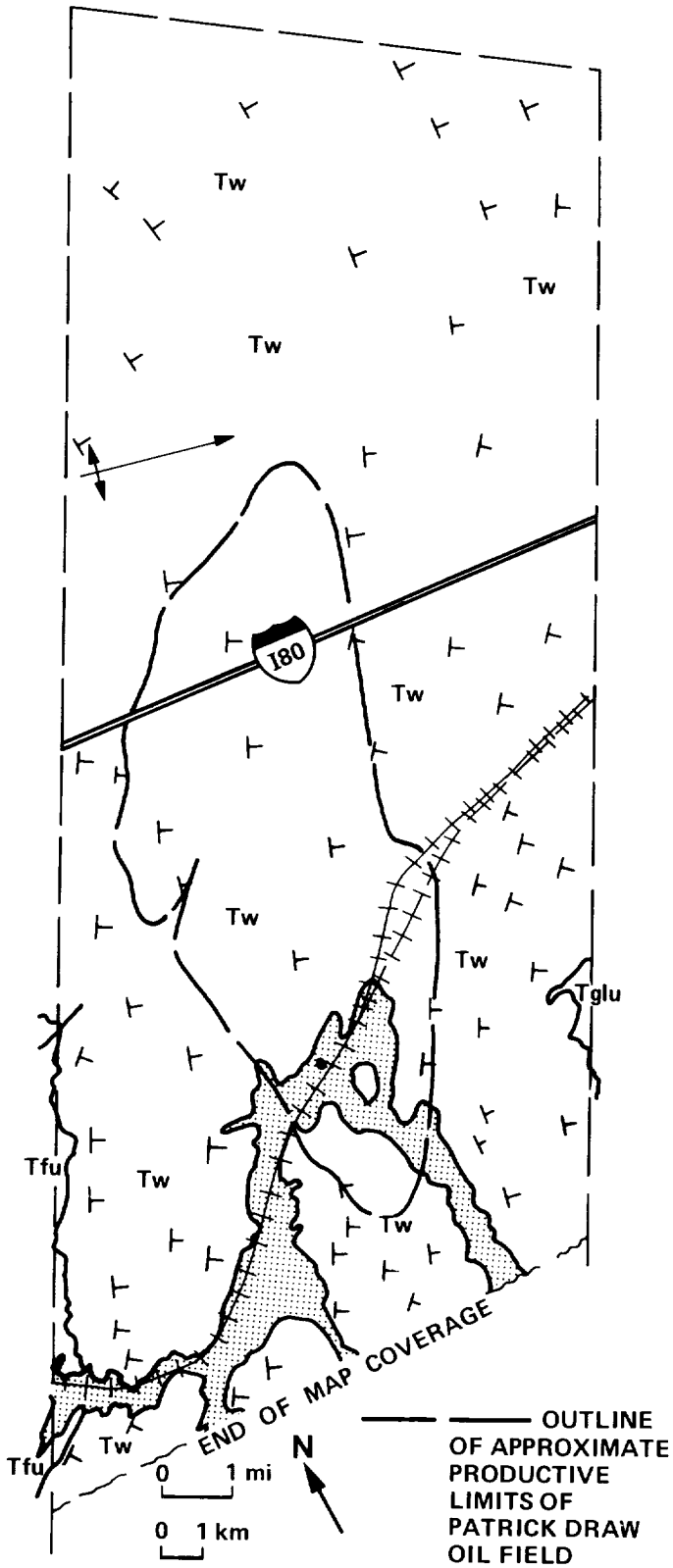

Figure 11-6. Unpublished photogeologic interpretation, Patrick Draw test site (anonymous). Compare to Figures 11-4 and 11-5. Qa is shown with a dot pattern.

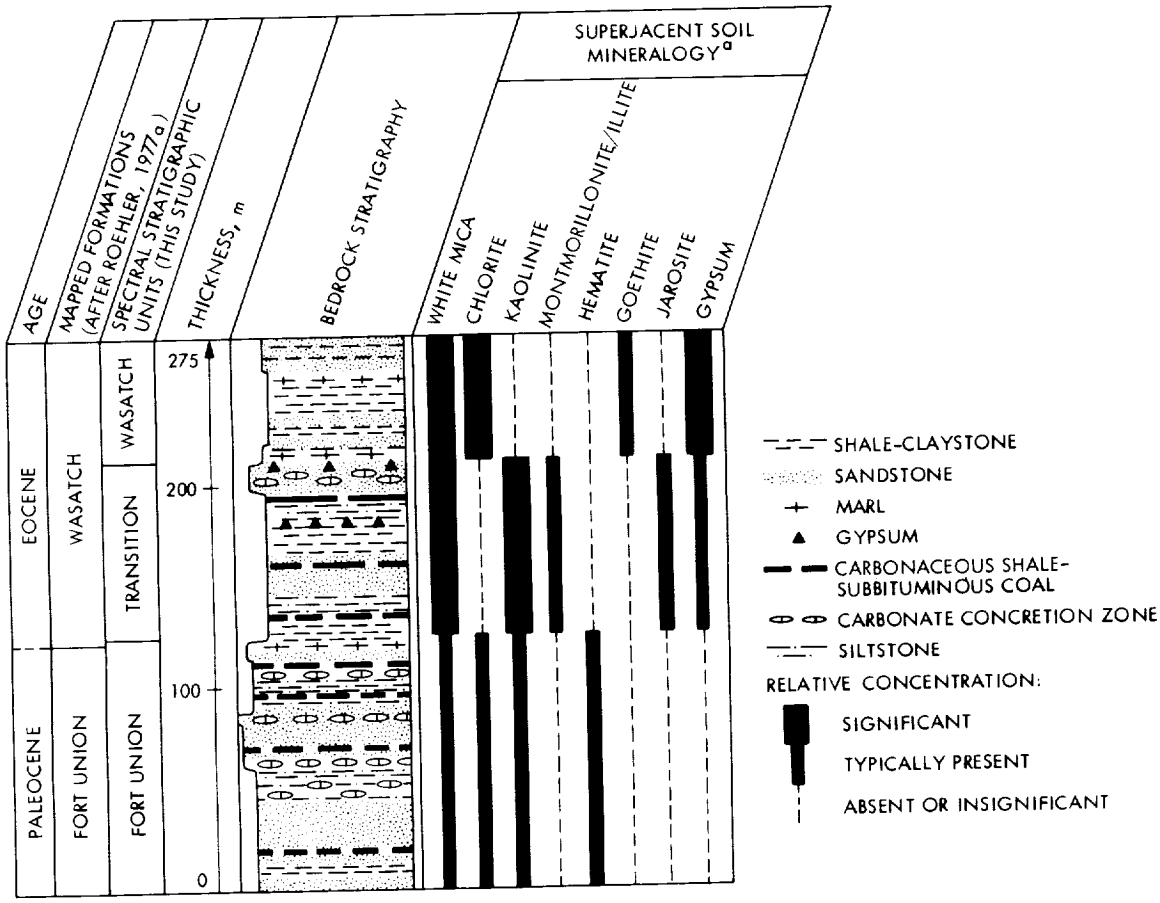

[a] NOTE: ONLY MINERALS HAVING ABSORPTION BANDS IN NS-001 CHANNELS AND VARIABLE IN CONCENTRATION BETWEEN UNITS ARE SHOWN

Figure 11-7. Detailed bedrock stratigraphy and superjacent residual soil mineralogy as observed in exposures in a gas pipeline trench. Units recognized in the present study are compared to those mapped by Roehler (1977a).

Table 11-2. X-ray diffraction analysis results illustrating significant mineralogical differences among Wasatch Formation, Transition Member, and Fort Union Formation

Mineral	Bedrock[a]			Superjacent Soils[a]		
	Wasatch	Transition	Fort Union	Wasatch	Transition	Fort Union
White mica	5	4	5	5	5	4
Chlorite	4		2	4		3
Kaolinite	1	3	2		2	1
Montmorillonite/Illite			1		1	
Calcite	5	5	1	5	4	4
Hematite						1
Goethite	1			1		
Jarosite					1	
Gypsum	2	1	3	2	1	
Siderite	3	1	2	2	2	2

[a] 7 – Very major; 6 – Major; 5 – Minor; 4 – Minor to very minor; 3 – Very minor; 2 – Minor to trace; 1 – Trace

tic minerals associated with each of the three units and their superjacent soils. The relative concentrations shown are based on a qualitative assessment of the relative size of X-ray diffraction peaks.

Mineralogically, the Transition Member and Wasatch Formation are distinct. The Fort Union Formation contains many minerals found in both the Transition Member and Wasatch Formation, but lacks the distinctive mineral suite associated with each.

(1) Bedrock. Goethite is found only in the Wasatch Formation; montmorillonite/illite in the Fort Union Formation. Chlorite and siderite are most abundant in the Wasatch Formation.

(2) Superjacent soil. Montmorillonite/illite and jarosite are restricted to the Transition Member; goethite to the Wasatch Formation; hematite to the Fort Union Formation. Gypsum is found in the Wasatch Formation and Transition Member and is absent in the Fort Union Formation. Kaolinite is present in the Transition Member and Fort Union Formation; chlorite in the Wasatch and Fort Union Formations.

Variations in superjacent soil elemental chemistry also reflect the contact of the Fort Union Formation and the Transition Member. Figure 11-8 summarizes soil elemental geochemical data obtained in a survey of the trench line area (refer to Paragraph VII.E). Concentrations of titanium, copper, zinc, and phosphorus have similar stratigraphic trends. All have maxima in the Fort Union Formation and minima in the Wasatch Formation. Trends in sodium and potassium exhibit minima in the Transition Member. Iron increases downsection. Manganese variation is similar to that of iron, but displays a minimum at the top of the Transition. This difference in iron and manganese trends results in an iron–manganese ratio maximum in the Transition Member.

Some of these trends may be related to bedrock mineralogy. The concentrations of sodium and potassium in superjacent soil are a measure of the amount of feldspar in

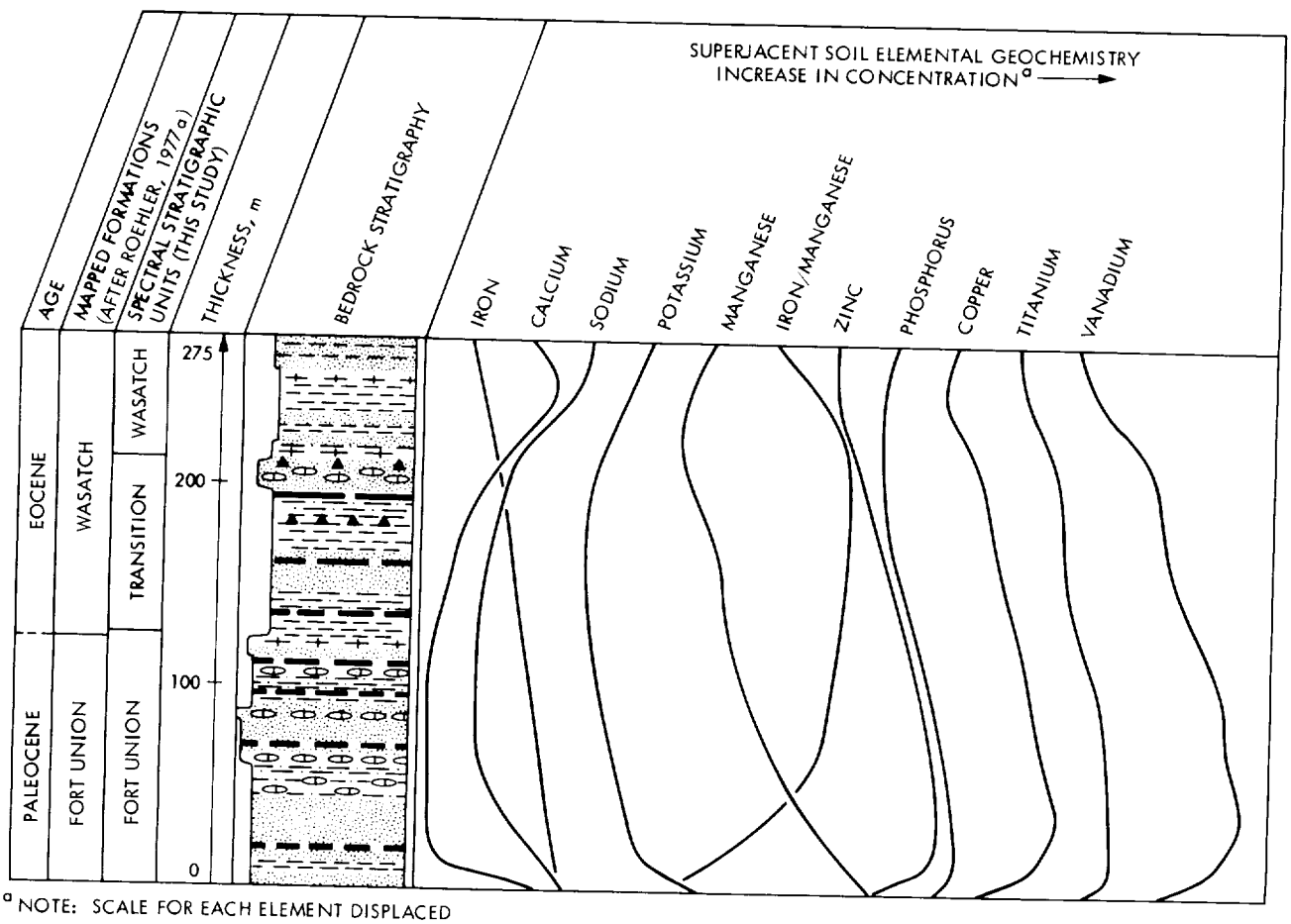

Figure 11-8. Detailed bedrock stratigraphy and superjacent residual soil elemental geochemistry. Compare to Figure 11-7.

bedrock arkosic sandstone, and jarosite and montmorillonite in associated soils. Iron concentration is related to the distribution of jarosite, goethite, hematite, and siderite. Calcium trends are related to the stratigraphic distribution of gypsum, montmorillonite, feldspar, and calcite cement.

3. Wasatch Formation. This dominantly fluvial unit is present throughout the greater Green River Basin. It reaches its maximum thickness south of the test site, in a basin that formed just north of the presumably active Eocene Uinta Thrust Fault (McDonald, 1972, p. 255). Two members of the Wasatch Formation are recognized in the test site area: the Hiawatha Member and the Niland Tongue.

a. Hiawatha Member (Davis, 1958). This basal member has also been referred to as the main body of the Wasatch Formation by Roehler (1977b). It is poorly exposed in the east–central part of the test site. The variegated sandstones, mudstones, and shales of this unit were deposited in fluvial-deltaic environments on the margins of Eocene Lake Gosiute (Bradley, 1964). One of the more characteristic features of the unit is its locally red color: the "Red" of the Red Desert Basin was derived from the color of Wasatch outcrops there (McDonald, 1972). This unit is over 390 m (1280 ft) thick in sections measured south of the test site and contains two persistent, mappable, phosphatic vertebrate fossil-bearing, marlstone marker beds (Roehler, 1977b).

b. Niland Tongue. This member is exposed in the southeastern part of the test site area, where it has a measured thickness of over 120 m (375 ft) (Roehler, 1977b). It forms a tongue of silty, sandy mudstone and mollusk-bearing sandstone, which is overlain by the Tipton shale member and underlain by the Luman Tongue of the Green River Formation (Figure 11-9).

4. Green River Formation. This unit consists of light greenish-gray, fine-grained sedimentary rocks that were deposited in Eocene Lake Gosiute, which at times covered the Green River, Red Desert, Sand Wash, and Washakie Basins (Bradley, 1964). Two members are exposed in the southeastern test site area: the Luman and the Tipton Tongues.

a. Luman Tongue. This member is underlain by the Hiawatha Member and overlain by the Niland Tongue of the Wasatch Formation in the test site area. This brown, resistant sandstone sequence is approximately 120 m (380 ft) thick (Roehler, 1977b).

b. Tipton Tongue. This member is underlain by the Niland Tongue of the Wasatch and represents the highest stratigraphic unit of the Patrick Draw test site. It is 15 m (45 ft) thick in the area and is a drab-brown, flaky oil shale typical of the quiet, deeper water facies of the Green River Formation (Roehler, 1977b).

IV. Subsurface Geology and Producing Reservoir

A. Introduction

The Patrick Draw oil field is a stratigraphic trap that has been affected by Tertiary deformation. Located on the eastern flank of the Rock Springs Uplift, the field is south of a broad structural nose, the Wamsutter Arch, extending from the uplift (Figure 11-10). Extensional faults related to the Rock Springs Uplift trend ENE–E and appear to cut the field in several places.

The oil-producing horizon at Patrick Draw (Figure 11-11) is a sandstone in the Upper Cretaceous Almond Formation of the Mesa Verde Group, at a depth of approximately 1700 m (5500 ft). There is a small updip gas cap. Approximately 250 wells in the field produce 42-degree API oil. The oil has a high associated gas content; most produced gas is reinjected into the gas cap for reservoir pressure maintenance. The estimated ultimate production for the field is approximately 1.2×10^8 bbl.

B. Discovery

The field was discovered in 1959 by exploration geologists who observed that the gas-producing sandstones present in the subsurface at Table Rock field (to the east) were not present on the Rock Springs Uplift (to the west). They correctly deduced that these sandstones must pinch out between the Table Rock field and the Rock Springs Uplift. Because the section dips 4° to 5° to the east and only gas was present at Table Rock, it was assumed that gas might have driven oil updip to the west where the producing sandstones apparently pinch out (Cox, 1962).

C. Reservoir Stratigraphy

Regionally, the marine shale of the Lewis Formation overlies the reservoir sandstones of the Almond Formation (Table 11-1) and provides a cap for the Patrick Draw reservoir sandstone. The generalized lithofacies map (Figure 11-12) shows the relationship of the producing Almond sandstones and their environment of deposition. Stratigraphic relationships indicate that these producing sandstones were deposited in barrier bar or delta environments. Deeper water neritic shales and siltstones, presumably the source beds, apparently bordered the sandstones on the east. To the west, impermeable coastal plain claystones provide

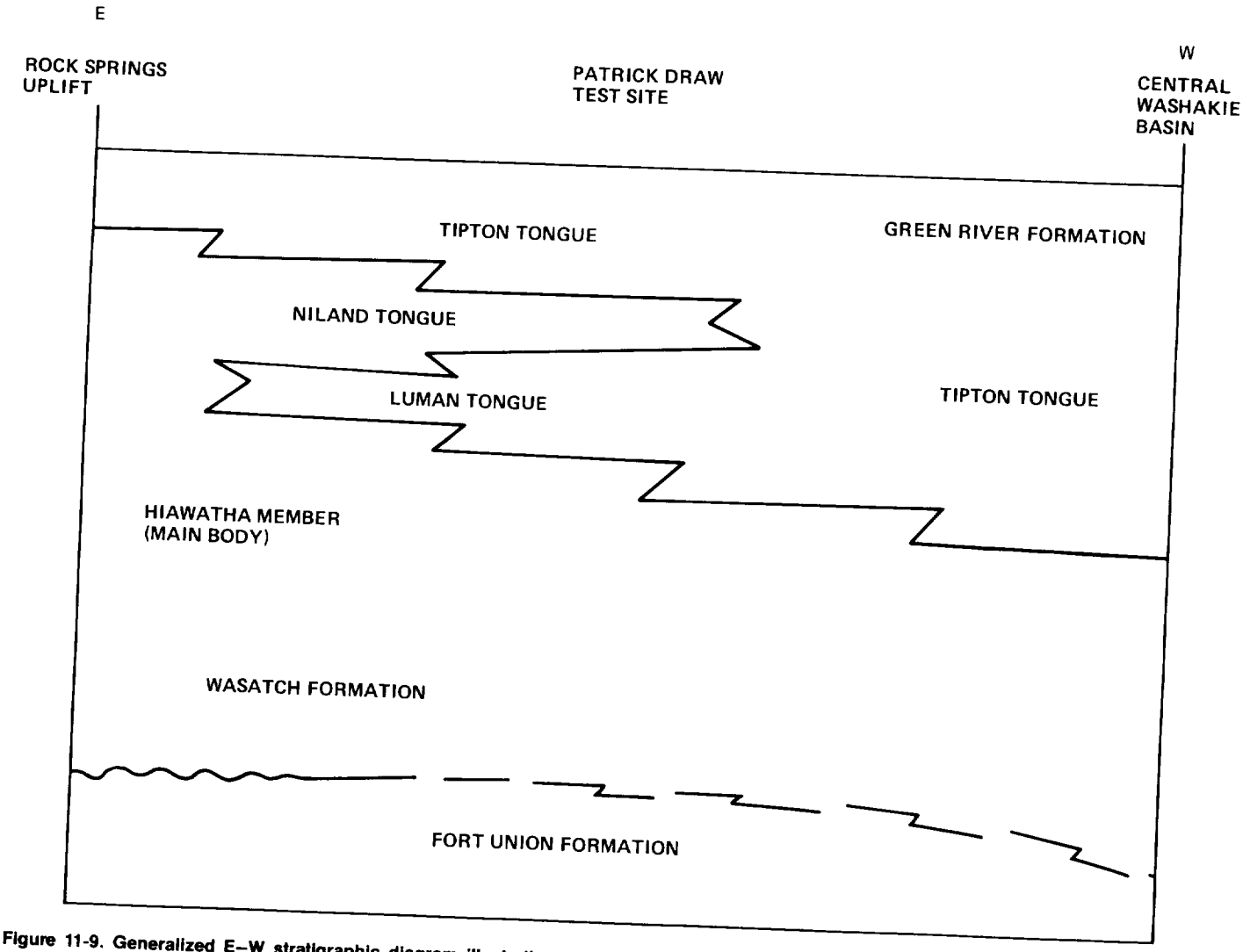

Figure 11-9. Generalized E–W stratigraphic diagram illustrating the interfingering relationship of the Green River and Wasatch Formations (Davis, 1958, Figure 4, p. 8)

a lateral seal to the oil that migrated from the neritic shales into the reservoir barrier bar sandstones (Weimer, 1966).

The Patrick Draw reservoir sandstone trends generally north and has a maximum width of about 6 km (4 mi) (Figure 11-13). The updip parts are tight, however, and the productive part is about 3 km (2 mi) wide and 16 km (10 mi) long. It occurs at the top of the dominantly nonmarine Almond Formation, which consists of coal, carbonaceous shale, siltstone, and thin lenticular sandstones. There are a few thin interbeds of marine shale and siltstone in the upper part of the Almond Formation that pinch out in a landward (northwest) direction.

The reservoir sandstone is overlain by the marine Lewis shale with a sharp contact. Commonly, the bar sandstone is capped by a few feet of oyster-coquina limestone that is tight and resistive on electric logs, as shown in Gulf 6 Chorney State Well of cross-section A-A′ (Figure 11-14). On the isolith map of the Patrick Draw reservoir sandstone (Figure 11-13), there is a narrow NW-trending belt of little or no sandstone that is filled with oyster-coquina limestone, as shown in Forest Oil 39-13-7 Arch Unit Well of cross-section B-B′ (Figure 11-14). This coquina belt is tight and forms a fluid barrier since the oil–water contact is at different elevations on opposite sides. In a landward (northwest) direction, the Patrick Draw reservoir sandstone pinches out into nonmarine shale and coal of the Almond Formation. The bar sandstone persists in a basinward (southeast) direction, although it is thinner and appears to intertongue with marine shale. The Patrick Draw reservoir was a barrier between the coal swamp environment and the open marine environment.

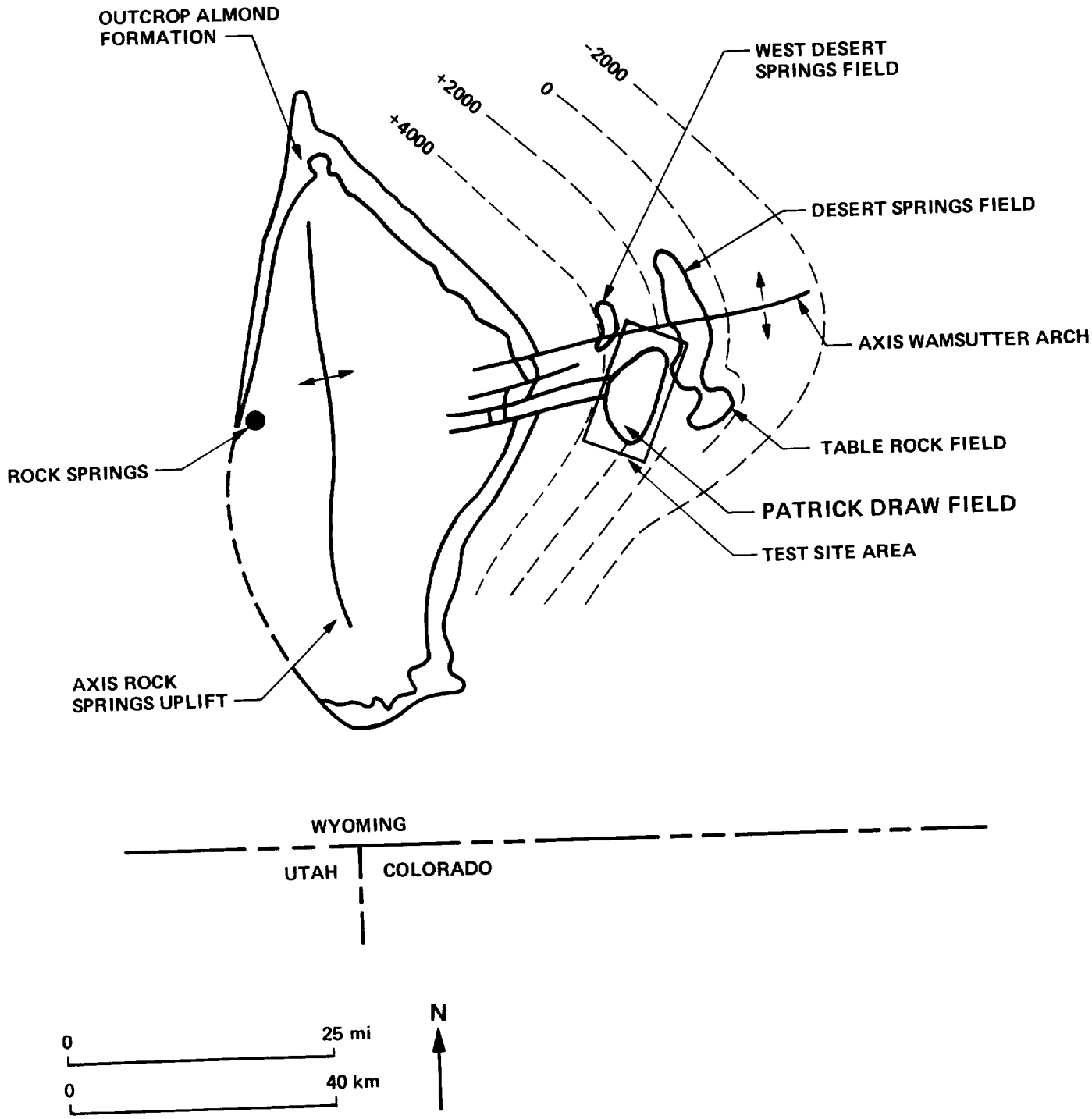

Figure 11-10. Regional subsurface structural contour map showing Patrick Draw and adjacent fields. Contours (in feet) on the top of the Almond Formation; datum, sea level (Weimer, 1966, Figure 2, p. 2151)

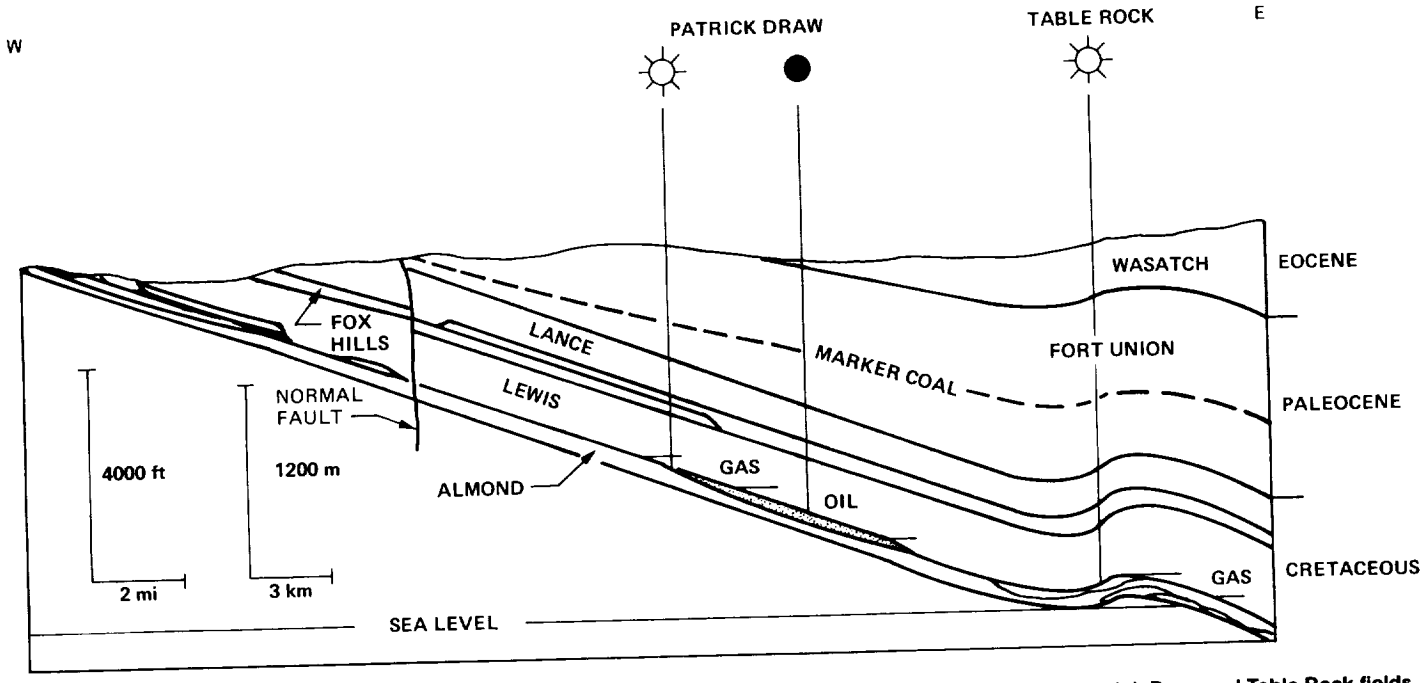

Figure 11-11. Regional W–E structural cross section from surface exposures of the Almond Formation to the Patrick Draw and Table Rock fields (Weimer, 1966, Figure 3, p. 2152).

Northward the bar sandstone pinches out into the Almond Formation. There are additional separate lenticular sandstones in the Almond Formation north of the pinchout of the Patrick Draw reservoir sandstone. Similar lenticular sandstones occur at the Almond Formation outcrops on the Rock Springs Uplift about 20 km (12 mi) west of the north end of the field.

The distribution pattern of the Patrick Draw reservoir sandstone is irregular (Figure 11-14). The Patrick Draw reservoir apparently consists of a number of individual sandstones with a coquina-filled channel cutting across the trend.

The shales of the Upper Cretaceous Lewis Formation mark a marine transgression over the Almond Formation. The Lewis is overlain by the Fox Hills and Lance Formations (Table 11-1), which were deposited during the final marine regression in Late Cretaceous time. The Paleocene Fort Union and Eocene Wasatch Formations complete the subsurface section.

V. Vegetation

A. Introduction

Vegetation is an important factor in the total surface reflectance recorded by imaging sensors. Even in semiarid regions, such as Patrick Draw, vegetation strongly influences the spectral response of imaging sensors. In addition, vegetation can be sensitive to subtle variations in soil chemistry. It was, therefore, considered essential that vegetation in the test site area be examined for variations in species and concentration.

Most of the contrasts in vegetation observed in a reconnaissance survey correlate with soil type, slope, and soil moisture. Consequently, if petroleum-related vegetation anomalies are present at Patrick Draw, they should appear as subtle second-order effects. Species and subspecies identifications and quantitative cover and condition estimates are required to detect such subtle differences.

A complete survey of vegetation in the area was desired, but the cost and time required for such a project were considered prohibitive. Therefore, selected sites that would provide a reasonable representation were surveyed and sampled within the Patrick Draw test site. The intent was to cross correlate results from geologic and soil maps, soil chemistry, laboratory and field spectral analyses, and vegetation samples, and to use image data as a base for extrapolation of the vegetation information from point sample localities to other areas.

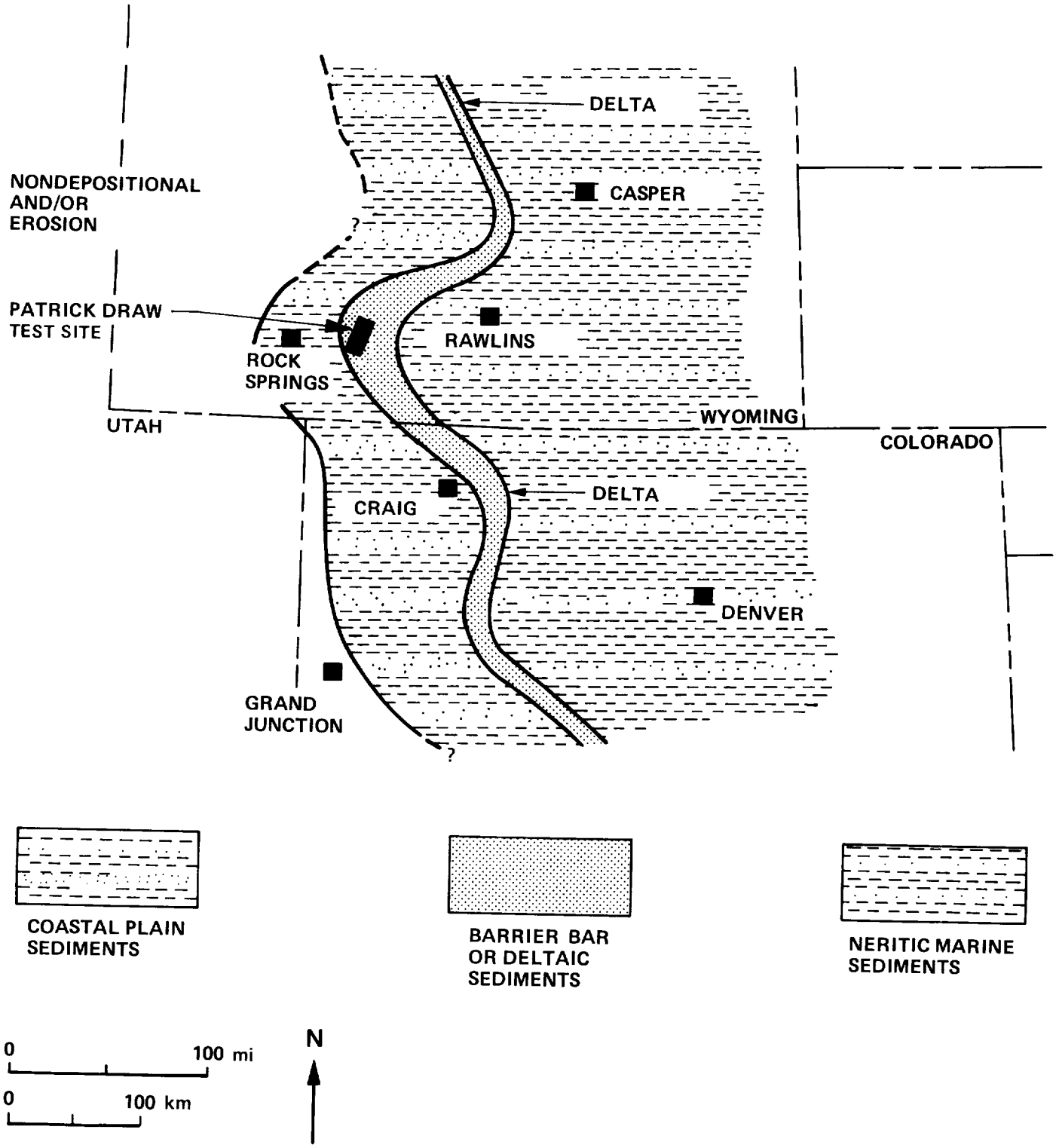

Figure 11-12. General regional lithofacies map for the upper Almond Formation, showing paleogeographic relationships. The Patrick Draw test site was located on the Late Cretaceous Almond delta/barrier bar complex. The Almond delta/barrier bar complex is only locally present along the sinuous trend depicted in the illustration (Weimer, 1966, Figure 16, p. 2173).

B. Collection and Interpretation of Vegetation Data

During the summers of 1979 and 1980, 19 stations in the Patrick Draw test site area were selected for vegetation analysis (Figure 11-15). These sites were relatively undisturbed (i.e., free from recent oil drilling activity, steep slopes, stream cuts, etc.), and local vegetation cover was more or less homogeneous. Five of these sites—A10, A14, A18, A19, and A20—were located on a S–N traverse extending over the length of the Patrick Draw oil field. Seven sites—E10, E14, E15, E17, E18, E19, and E21—were located on an E–W line crossing the northern portion of the field. The primary objective of these analyses was to determine vegetation type and percent cover.

1. Assessment of shrubby and semishrubby vegetation. In August and September 1979 and in May and June 1980, the shrubby and semishrubby vegetation at each of the 19 sites was collected and identified. Percent cover was calculated for all species at each site (Table 11-3).

Cover estimates were made using the line-intercept method of vegetation sampling (Mueller–Dumbois and Ellenberg, 1974). The line-intercept method is a standard sampling method used for shrubby vegetation or vegetation with a well-defined canopy. The method is both accurate and efficient in areas where shrubs or semishrubs dominate. At each site, a 50-m tape was tightly stretched across the tops of the shrubby vegetation in several compass directions. The intervals intercepted by the canopies of each shrubby species were measured and recorded. Total intervals intercepted by all shrubby species were summed and then used to calculate total percent cover.

Ten shrubby and semishrubby species were collected and identified at the 19 stations sampled (Table 11-3). Taxonomic identification of plant specimens was made using Dorn's *Manual of the Vascular Plants of Wyoming* (1977).

For comparison to the vegetation data presented in the Bureau of Land Management (BLM) soil map (Plate 11-2), the 10 shrubby or semishrubby species and their common names are listed below:

Artemisia tridentata, subsp. *tridentata*	Common Big Sagebrush
Artemisia tridentata, subsp. *wyomingensis*	Wyoming Big Sagebrush
Chrysothamnus nauseosus	Rabbit Brush
Chrysothamnus viscidiflorus	Rabbit Brush
Atriplex gardneri[1]	Saltbush or Shad Scale
Eurotia lanata	Winterfat
Atriplex confertifolia[1]	Saltbrush or Shad Scale
Sarcobatus vermiculatus	Greasewood
Tetradymia canascens[1]	Horsebrush
Opuntia polyacantha	Prickly Pear Cactus

[1]Characteristic of alkaline conditions and/or dry, rocky soils.

A simple chemical analysis was used on all collected specimens of *Artemisia tridentata* to facilitate field identification of the three subspecies occurring in the region: *tridentata*, *vaseyana*, and *wyomingensis*. The method used is that reported by Stevens and McArthur (1974). This method was selected over others (such as chromatography) because it is quick and inexpensive. The results of the chemical analyses indicated that all specimens of *Artemisia tridentata* were *Artemisia tridentata*, subsp. *wyomingensis*.

Samples of the dominant shrubby vegetation were also collected at 11 sites and sent to Barringer Resources, Inc., for elemental analysis. The results of these analyses are given in Table 11-4. Based on these limited data, no chemically anomalous samples were identified.

2. Assessment of herbaceous vegetation. In May and June 1980, the herbaceous vegetation at each of the 19 sites was collected; 22 species were identified (Table 11-3).

The Daubenmire (1959) canopy-coverage method of vegetation sampling was used for cover estimates. This canopy-coverage method is particularly useful in western grasslands where the vegetation is of low stature and individual plants often lack a well-defined canopy. A quadrat is placed on the ground at several locations at each sampling site. The percent cover of each species within the quadrat is visually estimated and recorded. The values at each location at a site are then averaged to yield an estimate of the percent cover for each species at the site.

C. Results of Vegetation Sampling

Although the data obtained at the 19 vegetation stations represent only a small portion of the test site area, several observations were made regarding species distribution, species diversity, and percent vegetation cover.

1. Species distribution. Of 32 species collected from the area, four are restricted to the known oil-producing area:

(1) *Artemisia pedatifida* was found only at sites E14 and A19, in the northern part of the producing area.

(2) *Astragalus purshii* was collected only at sites E18 and E19, in the northern Patrick Draw field.

(3) *Xylorhiza glabriuscula* was found only at sites A19 and A20. This species is a known selenium indicator plant.

(4) *Sarcobatus vermiculatus* (greasewood) was collected at three sites—B15, B17, and B19. Greasewood is an indicator of highly alkaline soils.

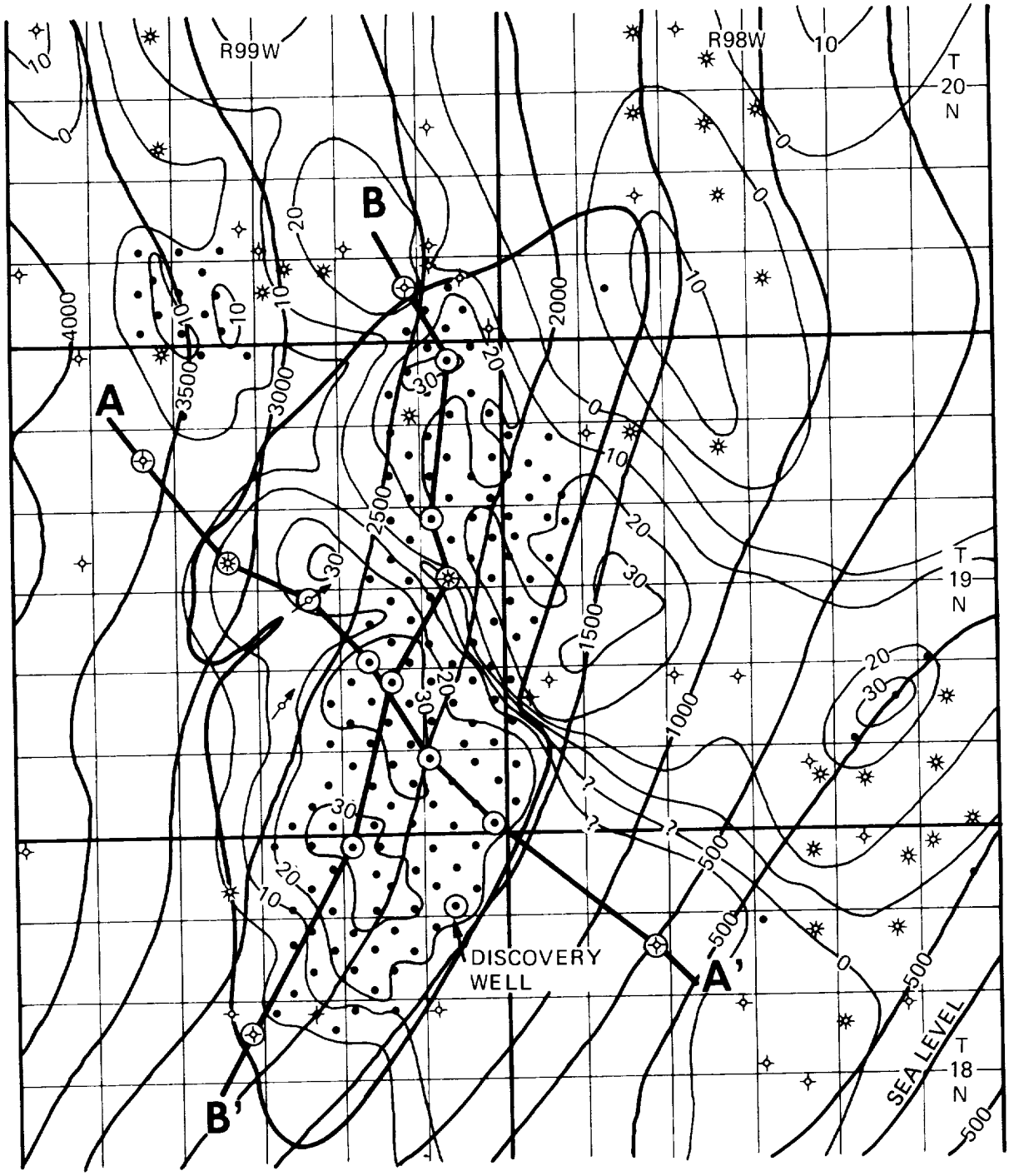

STRUCTURE CONTOURS ON TOP OF MESA VERDE GROUP. CONTOUR INTERVAL = 500 ft

ISOLITH CONTOURS OF PATRICK DRAW SANDSTONE. CONTOUR INTERVAL = 10 ft

APPROXIMATE PRODUCTIVE LIMITS

WELL STATUS (1964)

- PRODUCTIVE GAS
- PRODUCTIVE OIL
- ABANDONED DRY HOLE
- GAS INJECTION WELL

Figure 11-13. Map showing structure contours on top of Mesa Verde, and isolith of Patrick Draw reservoir sandstone (furnished by F. Sabins, Chevron Oil Field Research)

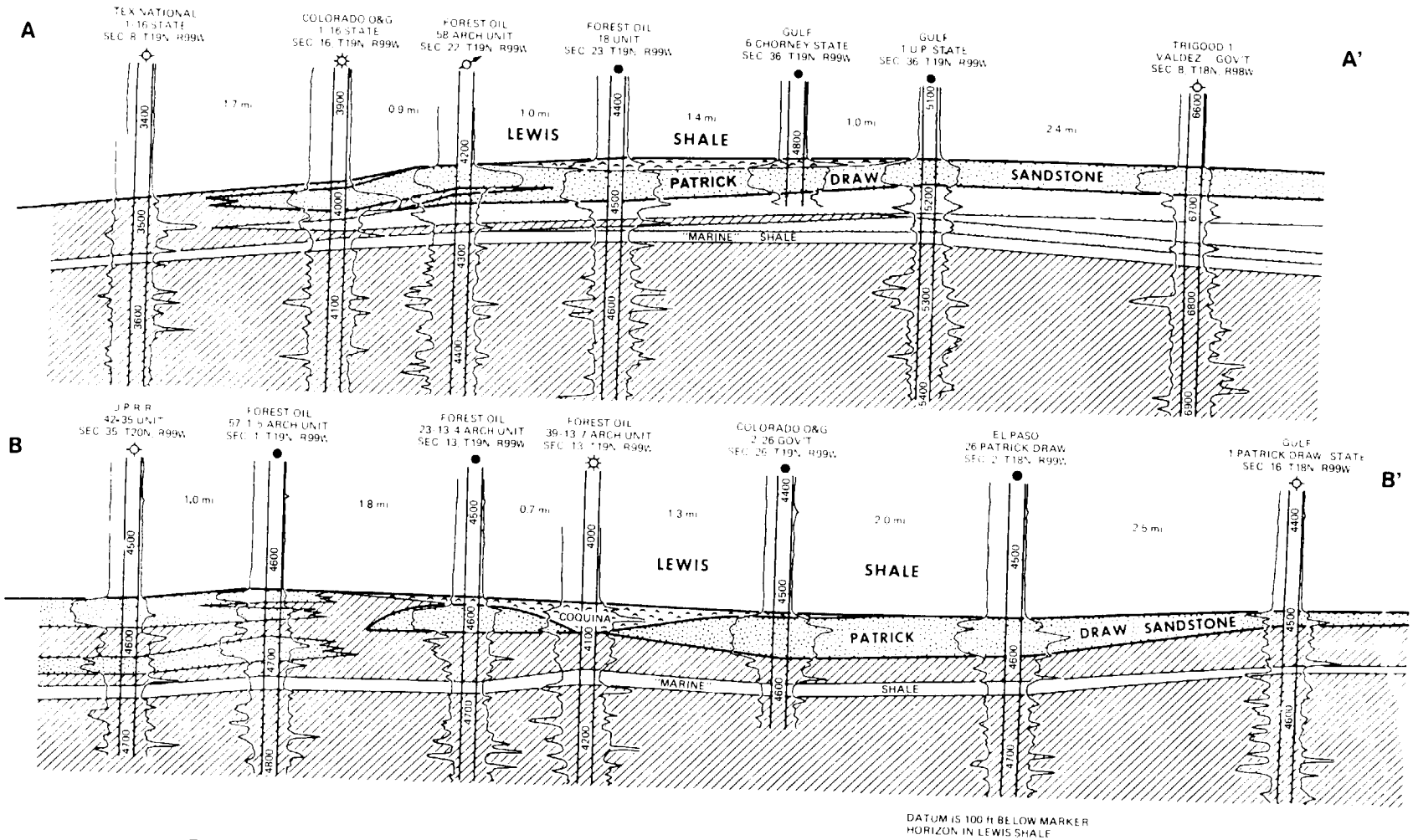

Figure 11-14. Cross sections illustrating subsurface stratigraphic relations, Patrick Draw oil field. Figure 11-13 shows locations of the cross sections (furnished by F. Sabins, Chevron Oil Field Research)

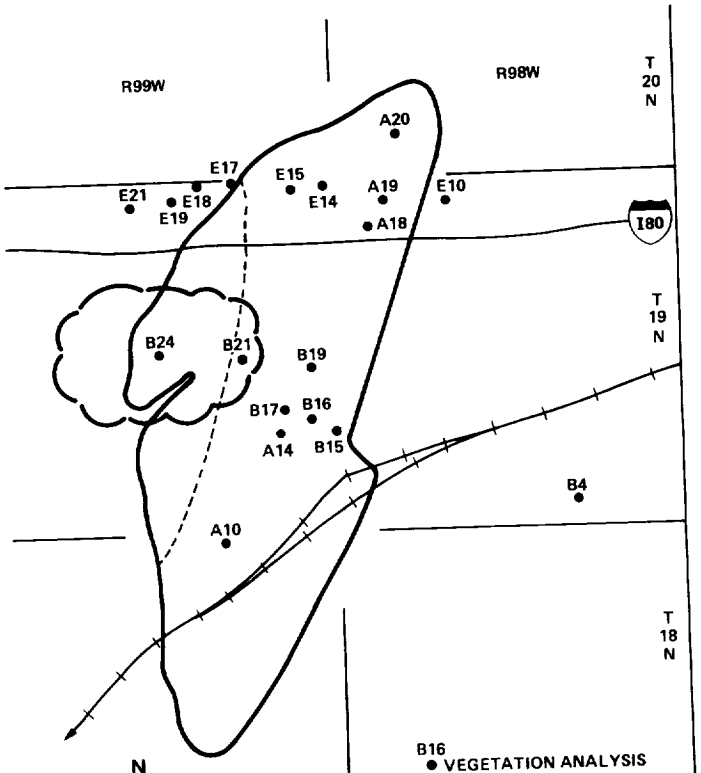

Figure 11-15. Index map showing the locations of sites selected for vegetation analysis, Patrick Draw test site. Outline of the productive limits (solid line) and oil–gas contact (dashed line) are also shown. Site B24 is located near the center of an area of anomalous stunted sage (lobulate outline).

Four other species occur both inside and outside the producing area, but are more abundant within the field:

(1) *Agropyron smithii* was collected at six sites: five (A10, B16, B21, E14, and E15) within the producing field and one (E10) outside the field.

(2) *Artemisia spinescens* was collected at six sites: five (A18, A19, A20, B15, and B16) within the field and one (E10) outside the field.

(3) *Hordeum jubatum* was collected at 10 sites: eight (A10, A14, A19, A20, B15, B16, B17, and B19) within the field and two (E10 and E21) outside the field.

(4) *Oryzopsis hymenoides* was collected at 11 sites: eight (A10, A14, A19, A20, B16, B21, E14, and E15) within the field and three (B4, E10, and E18) outside the field.

Artemisia tridentata, subsp. *wyomingensis*, the dominant shrub throughout most of the area, proved to be the only species common to all sites. The high values for percent cover recorded at sites E17 and E18 (39.8 and 42.7 percent) are attributed to the normal increase in vegetation cover in a broad drainage area.

2. Species diversity. The number of species identified at a site is a measure of species diversity. For the 19 sites analyzed in the Patrick Draw area, the diversity of species is generally greater within the producing area than outside the area (Table 11-5). This relationship probably reflects the general coincidence of the area of production with outcrops of and soils derived from a nonresistant bedrock unit. Apparently, this unit generally parallels Patrick Draw, is more easily eroded than the flanking resistant bedrock units, and is more amenable to the development of soils conducive to a more diverse plant community.

3. Vegetation cover. Data from the 19 vegetation sites indicate vegetation cover for the area ranges from 25 to 59 percent (Table 11-5). This range includes both herbaceous and shrubby cover types. Because herbaceous cover is more seasonally controlled than shrubby cover, and the values for herbaceous cover percentage used in this study were obtained during their peak (May and June), the low vegetation value of 25 percent is probably somewhat high. The low cover value of approximately 5 percent, associated with shrubby vegetation alone (Table 11-5), is therefore a more realistic value for minimal vegetation cover in the Patrick Draw test site area. The spectral influence of 5 to 59 percent vegetation cover must be considered in the analysis of remote sensing data for the Patrick Draw test site.

VI. Soils

Because of the cold, dry, and windy climate, soils in the Patrick Draw test site are generally immature. When exposed, they are subject to rapid erosion (1) by wind, or (2) by water during the occasional torrential rains which accompany thunderstorms. Most soils are genetically related to the subjacent bedrock. Areally, bedrock exposures are relatively insignificant. Residual soils are typically silt loams. Significant local variation exists in both the texture and chemistry of soils in the test site area. Local conditions may favor the development of evaporite crusts on surfaces in low-lying areas and deposits of transported eolian soil in areas sheltered from the prevailing wind.

The Rock Springs office of the Bureau of Land Management completed a soil mapping project covering all of Sweetwater County in August 1981. The mapped area included the Patrick Draw test site. Plate 11-2 is a 1:48,000 soil map of the test site taken from the BLM's original

Table 11-3. Percent cover of major vegetation species at selected sites in the Patrick Draw area

Species[a]	Site, % cover																		
	A10	A14	A18	A19	A20	B4	B15	B16	B17	B19	B21	B24	E10	E14	E15	E17	E18	E19	E21
Agropyron smithii (h)	3.60							3.12			9.14		2.00	0.16	4.06				
Allium textile (h)																			trace
Arabis holboellii (h)																0.06			
Arenaria hookeri (h)			2.34		7.80	1.03		0.10					0.75				0.30		0.63
Artemisia ludoviciana (h)					1.09														
Artemisia nova (h)						1.4													
Artemisia pedatifida (h)				1.88															
Artemisia spinescens (h)			3.67	0.47	5.39		0.50	2.80						0.50					
Artemisia tridentata subp. *tridentata* (s)													3.41						
Artemisia tridentata subp. *wyomingensis* (s)	2.54	14.17	12.03	7.03	5.00	14.39	22.60	5.00	4.43	8.49	2.53	18.32	4.50	21.73	8.27	39.81	42.73	26.28	25.31
Astragalus purshii (h)																			
Astragalus spatulatus (h)					0.47	1.16					0.31		1.38		5.53		0.07	0.31	
Atriplex confertifolia (s)	0.21										1.46	0.29		0.24	1.84			1.34	
Atriplex gardneri (s)	1.16	0.92	0.63	2.34	0.31	0.69	4.31	0.51	16.56	7.06	0.16			0.35					
Chrysothamnus nauseosus (s)								5.30					1.13		0.10				
Chrysothamnus viscidiflorus (s)	0.14					0.26				5.66	0.60	0.20		0.40	2.06	3.27	0.92		
Cordylanthus ramosus (h)												0.12		0.09		8.10	2.34		
Cryptantha flava (h)								1.10											
Cryptantha caespitosa (h)						0.25		0.70											
Eriogonum ovalifolium (h)	0.70	0.30	0.35			0.03					1.40		1.06		2.94			0.47	0.04
Erysimum asperum (h)															0.06				
Eurotia lanata (s)	0.93			2.34		0.51		0.86			0.05		0.56	0.75	0.24			0.07	
Haplopappus armerioides (h)			0.31			1.00									0.08			4.38	
Hordeum jubatum (h)	0.63	5.39		2.50	1.18		7.84	0.10	1.60	2.19			0.75						0.04
Opuntia polyacantha (s)	0.30			1.87		0.73	0.07						0.25	0.14	0.22			0.40	0.21
Oryzopsis hymenoides (h)	12.50	3.43		5.70	0.47	2.84		5.78			6.25		4.13	0.50	8.84		6.02		
Penstemon sp. (h)	0.16				0.23								0.25						
Phlox hoodii (h)	1.40	6.33	3.40	1.64	4.57	4.66		0.08			0.94	2.15	3.91	5.23	1.41		0.70	3.90	4.31
Poa sandbergii (h)	1.10		9.96	10.47	5.98	5.87		0.94	0.35	7.30	5.38	3.79	8.94	3.20	6.66	8.00	6.21	11.20	7.34
Sarcobatus vermiculatus (s)							9.44		18.66	16.55									
Tetradymia canascens (s)													0.50		1.34				
Xylorhiza glabriuscula (h)				0.63	0.67														

[a](s) shrubby, (h) herbaceous.

Table 11-4. Chemical analysis of vegetation samples by Lasertrace®

Element[a]	Site[b], values in ppm										
	A14	B4	B14	B17	B19	B24	E15	E17	E18	E19	E21
Aluminum	1760	3070	1330	247	224	2640	3030	782	566	1030	1050
Calcium	5400	5440	5400	6840	4830	4690	4920	4920	5240	2930	3360
Chromium	5.8	9.1	3.4	2.1	2.0	7.5	8.2	2.4	1.6	3.4	4.2
Cobalt	1.1	1.8	1.7	3.7	1.9	<0.5	1.4	1.6	2.1	1.2	2.3
Copper	7.4	11.8	8.4	6.4	7.0	10.8	8.1	8.5	8.5	6.7	7.2
Iron	1370	2320	875	161	145	1910	2220	572	275	791	791
Lead	3	6	4	1	4	10	3	5	6	7	8
Magnesium	1590	2180	1720	1700	2220	1740	1390	1320	1450	1280	1380
Manganese	63.5	70.8	56.1	140	174	68.1	85.9	44.0	47.8	65.8	55.8
Nickel	4.1	4.9	2.7	1.4	1.3	3.5	4.1	1.9	2.0	1.8	2.5
Phosphorus	1350	1430	1740	1200	1240	1230	1210	1530	1760	960	1240
Potassium	11700	12100	12900	15200	11400	14900	11700	10400	13600	10100	10700
Sodium	968	368	1540	68500	87600	431	322	574	368	300	455
Strontium	41	43	29	22	10	34	32	23	22	22	27
Titanium	17	47	10	5	5	46	37	17	1	14	25
Vanadium	2.78	4.85	2.21	0.83	0.65	4.46	5.12	1.58	1.24	2.03	2.02
Zinc	14.3	20.1	22.0	9.7	7.6	21.7	18.0	25.8	24.0	15.5	14.9

®Lasertrace is a registered trademark of Barringer Resources, Inc.
[a]Silver, beryllium, cadmium, molybdenum, thorium, and zirconium were also analyzed, but concentrations were below Lasertrace® resolution.
[b]*Artemesia tridentata*, subsp. *wyomingensis*, was sampled and analyzed at all sites. In addition, *Sarcobatus vermiculatus* was sampled and analyzed at sites B17 and B19.

1:24,000 map. Tables 11-6 and 11-7 were compiled from the explanatory text accompanying the BLM map.

A review of these data shows that over 60 soil units were mapped in the test site area. These units are separable on the basis of over 30 physical, chemical, and botanical criteria.

Most soils are residual in genesis and are clay–loams in texture. Most transported soils are eolian in genesis and sandy–silty loams in texture. Eolian soils, designated with a stipple pattern in Plate 11-2, are most prevalent in generally linear, E–W-trending areas in the east–central portion of the test site area. The only gravelly soil in the area (unit 465) is confined to terrace deposits associated with the Bitter Creek drainage. Many of the soils are alkaline, but only soils 450 and 344 were described as being, in part, strongly alkaline. The immaturity of soils is supported by the fact that all alkaline soils are associated with calcareous shale bedrock.

If evaluated in conjunction with the vegetation survey results, the data included in Table 11-7 provide insight into major vegetation community distribution patterns. The dominant vegetation communities are shrub grassland and upland salt desert. The wet meadow community is restricted to the upper Bitter Creek drainage; the lowland salt desert community is most prevalent in the lower Bitter Creek drainage, near the western edge of the test site. Based on associated soil, the species most tolerant of chemically inhospitable substrates are greasewood, gardner saltbrush, and bottlebrush squirreltail. These are the only species present in the playa soils of unit 400. Strongly alkaline soils typically do not support large sagebrush.

VII. Special Field/Laboratory Investigations

A. Introduction

Several investigations were conducted to identify any changes in surface materials (soils and vegetation) that might be caused by the migration of hydrocarbons from the Patrick Draw reservoir. The following paragraphs review the results of these studies, which included a detailed field/laboratory evaluation of anomalous vegetation and geochemical surveys in the test site area. The geochemical surveys included a local soil pH survey in the vicinity of anomalous vegetation and soil hydrocarbon gas, soil helium gas, soil elemental geochemistry, and soil carbon isotope surveys of the entire test site area. A review of principles, methods, and results of similar studies conducted elsewhere for explora

Table 11-5. Summary of major vegetation types and percent cover at selected sites in the Patrick Draw area

Station	Site																			Max.	Min.	$\overline{X}$	σ
	A10	A14	A18	A19	A20	B4	B15	B16	B17	B19	B21	B24	E10	E14	E15	E17	E18	E19	E21				
Shrubby species, number	6	2	2	4	2	5	4	4	3	5	5	2	5	6	7	2	2	3	2	7	2	3.7	1.7
Shrubby cover, %	5.3	15.1	12.7	13.6	5.3	16.6	36.4	11.7	39.7	38.8	4.8	18.8	6.9	23.6	14.1	43.1	43.7	28.1	25.5	43.7	4.8	21.2	13.5
Herbaceous species, number	7	4	6	7	10	9	2	9	2	2	6	4	10	6	8	3	6	6	6	10	2	6.00	2.6
Herbaceous cover, %	20.3	15.4	20.0	23.3	27.9	18.2	8.4	14.7	1.9	9.5	23.4	6.1	26.6	9.7	29.6	16.1	15.6	20.3	12.4	29.6	1.9	16.8	7.6
Herbaceous %/ shrubby %	4.0	0.5	1.6	0.6	5.3	1.1	0.2	1.3	0.1	0.3	4.9	0.3	3.9	0.4	2.1	0.4	0.4	0.7	0.5	5.3	0.1	1.5	1.7
Total species, number	13	6	8	11	12	14	6	13	5	7	11	6	15	12	15	5	8	9	8	15	5	9.7	3.4
Total vegetation cover, %	25.4	30.5	32.7	36.9	33.2	34.8	44.8	26.4	41.6	48.3	28.2	24.9	33.5	33.3	43.7	59.2	59.3	48.4	37.9	59.3	24.9	38.0	10.4

$\overline{X}$ –Mean
σ –Standard deviation

tion is provided by Siegel (1974). Additional background information and references to similar studies reported elsewhere are provided in each of the following discussions.

B. Analysis of an Area of Abnormal Stunted Sage

1. Introduction. As a result of field examination of a tonal anomaly first recognized in a preliminary analysis of aircraft-acquired multispectral data, an area of abnormal stunted sage was recognized in the Patrick Draw test site. Figure 11-16 is a normal-color aerial photograph acquired at the same time as the multispectral data in which this tonal anomaly was first recognized (October 1978). The boundary of the multispectral tonal anomaly that corresponds to the distribution of anomalous stunted sage is not detectable in normal-color photography, black-and-white photography, or infrared color photography. The tonal anomaly is barely detectable on Landsat MSS images that were carefully processed with preknowledge of the location of the anomaly.

This tonal anomaly encompasses approximately 5 km^2 (2 mi^2) of sections 14, 15, 16, 21, 22 and 23, T19N, R99W (Figure 11-17). The location corresponds approximately to the center of the gas cap of the underlying Patrick Draw reservoir (Plate 11-1). The only vegetation control site (B24, Figure 11-15) that lies within this area is located in an area where the vegetation is in better condition than in most of the anomalous area. Site B24 was located specifically to avoid areas of stunted sage, which were initially thought to represent areas damaged by fire. Consequently, the vegetation data collected at this station are unfortunately not representative of the stunted vegetation and offer little insight into its character and origin.

To evaluate the possibility that this vegetation anomaly is a microseepage-induced feature, considerable effort was spent in examining this area. The following discussions summarize the results of this analysis.

2. Field characteristics

a. General description. Field inspection of the area was made after the anomaly was first observed on NS-001 Landsat 4 Thematic Mapper Simulator data in 1979. Periodic checks of the area were conducted by various test site team members during the period June 1979 to February 1982. By careful field comparison of sites within and outside the anomaly area, it was determined that the chief contrast was in vegetation condition (Figure 11-18). Generally, sage within the anomalous area is smaller, less dense, and less vigorous than that in the surrounding area. Sage bushes in the anomalous area appear darker due to the restriction of active growth to branch tips. Areas between individual sage bushes are poorer in herbaceous ground cover and they also have a higher density of deep rills than equivalent sites outside the anomalous area. Typically, individual stunted sage bushes occupy elevated mounds, approximately 35 cm (14 in.) high and approximately the same diameter as the sage. Rare "islands" of apparently healthy sage, up to 30 m (90 ft) in diameter, are scattered throughout the anomalous area and are most common on its margin.

Table 11-6. Physical aspects of soil units, Patrick Draw test site[a]

Soil Unit	Chemistry		Texture				Source				Depth, in.		Color				Comments
	Alkaline	Gypsiferous	Loam	Clay	Sand	Silt	Residual	Transported	Eolian	Contains bedrock outcrops	Minimum	Maximum	Yellow	Brown	Gray	Red	
332	■		■		■		■	■			10	40	■	■			
333	■		■					■			40	>60	■				
334	■		■					■			40	>60	■	■			
335	■	■	■	■	■	■	■				<10	20		■	■		
336	■		■	■			■			■	0	20		■	■		
337		■	■	■		■	■				10	40		■	■		
341	■		■	■		■	■			■	0	40		■	■	■	
344	■		■			■		■			40	>60		■			Very strongly alkaline
347	■		■		■			■	■		40	>60	■	■			
349	■		■		■			■	■		40	>60	■	■			
400	■	■		■			■	■			40	>60			■		Playa deposits
402	■		■	■	■			■			20	40		■			
414	■		■		■			■			40	>60		■			
416			■		■		■				20	40		■	■		
417			■		■		■				<10	20		■	■		
422			■	■			■	■			<10	>40		■	■		
429			■		■			■			40	>60	■	■	■		
430			NS														
431			■		■		■				20	40		■			
434				■		■		■			40	>60	■	■			
436			■		■		■	■			20	40	■	■			
438	■		■	■			■				10	40	■	■			
439	■		■		■			■			40	>60	■	■			
440			■	■	■		■	■	■	■	0	40		■	■		
441			■		■		■	■			40	>60		■			
442			■		■			■			40	>60	■	■			
445			■		■			■			40	>60	■	■			
446	■		■	■			■			■	0	20	■	■	■		
447				■		■		■			40	>60	■				
448				■		■		■			40	>60		■		■	
449			■	■		■		■			40	>60	■	■			
450	■		■			■	■				20	40		■			
451			■		■		■			■	0	20	■	■			
452			■		■		■	■		■	0	40	■	■			
453	■		■	■	■	■	■			■	0	10		■	■		
454			■	■		■		■			40	>60		■	■		
455			■		■			■			40	>60		■			
457			NS														
459			■	■	■	■	■			■	0	20	■	■			Mostly bedrock
460							■			■	0	<10			■		Badlands, all bedrock

Table 11-6 (Continued)

Soil Unit	Chemistry		Texture				Source				Depth, in.		Color				Comments
	Alkaline	Gypsiferous	Loam	Clay	Sand	Silt	Residual	Transported	Eolian	Contains bedrock outcrops	Minimum	Maximum	Yellow	Brown	Gray	Red	
461					■		■			■	0	<10					
463	■		■		■		■	■	■		20	>40			■		Bedrock escarpments
464		■	■	■		■	■			■	0	20			■		
465			■	■	■		■	■		■	0	>60			■		
466			■		■		■			■	0	40	■	■			Gravelly
467	■		■		■		■			■	0	20	■	■			
468			■		■		■	■	■	■	0	>40		■			
470			■		■		■		■		20	>40		■			
471	■		■	■	■	■		■	■		40	>60		■			
475	■		■		■			■	■		40	>60		■	■		Sand dunes dominate
476			■		■		■	■	■	■	0	>40		■	■		
479					■			■	■		40	>60		■	■		
480	■		■	■		■		■			40	>60		■			
481			■		■		■	■	■		40	>60	■	■			
482	■		■		■		■	■		■	40	>60		■			
487			■		■		■			■	0	40	■	■			
488			■		■		■			■	0	40	■	■			
492	■		■		■		■	■		■	10	40	■	■			
493	■		■	■	■		■	■		■	0	40	■	■		■	
494			■		■		■	■		■	20	40	■	■			
495	■		■		■		■			■	10	40	■	■			
496			■		■		■	■		■	10	40		■	■		
530			■				■				>10	20	■	■			
817			■				■										

[a]Compiled from BLM soil descriptions.
NS—Not stated.

Table 11-7. Botanical aspects of soil units, Patrick Draw test site[a]

Soil Unit	Potential Species														Potential Community			
	Thick-spike Wheatgrass	Wheatgrass	Needle-and-thread	Indian Ricegrass	Sagebrush	Bluebunch Wheatgrass	Bottlebrush Squirreltail	Gardner Saltbrush	Rhizomatous Wheatgrass	Alkali Sacation	Basin Wildrye	Greasewood	Western Wheatgrass	Wet Meadow	Shrub Grassland	Upland Salt Desert	Lowland Salt Desert
332	■	■	■	■	■	■									■	■	
333	■		■	■	■		■	■							■	■	
334				■		■	■									■	
335				■		■	■	■								■	
336	■		■	■		■	■	■	■						■	■	
337	■		■	■	■		■	■								■	
341				■			■	■	■								■
344								■	■	■	■						■
347			■	■			■								■	■	
349			■	■			■	■									
400														■			
402			NS													■	
414				■			■	■							■		
416	■		■	■	■										■		
417	■		■	■													
422	■		■	■	■		■	■	■						■	■	
429				■			■	■								■	
430[a]			NS														
431	■		■	■	■											■	
434				■		■	■								■		
436			NS														
438				■			■	■								■	
439				■			■	■								■	
440				■			■	■	■							■	
441	■		■	■	■									NS			
442	■		■	■	■										■		
445	■		■	■	■										■		
446				■			■	■	■							■	
447				■			■	■								■	
448				■			■	■								■	
449				■			■	■		■	■	■	■				
450	■		■	■	■										■		
451	■		■	■		■	■								■		
452	■		■	■	■											■	
453				■			■	■	■						■		
454	■		■	■		■											

Table 11-7 (Continued)

Soil Unit	Potential Species													Potential Community			
	Thick-spike Wheatgrass	Wheatgrass	Needle-and-thread	Indian Ricegrass	Sagebrush	Bluebunch Wheatgrass	Bottlebrush Squirreltail	Gardner Saltbrush	Rhizomatous Wheatgrass	Alkali Sacation	Basin Wildrye	Greasewood	Western Wheatgrass	Wet Meadow	Shrub Grassland	Upland Salt Desert	Lowland Salt Desert
455				■			■	■								■	
457[b]			NS														
459				■		■	■	■	■						■	■	
460																	
461[c]			NS														
463	■		■	■			■	■					■		■	■	
464				■			■	■	■							■	
465	■		■	■											■		
466	■		■	■	■										■		
467	■		■	■			■	■	■						■	■	
468	■		■	■	■		■								■		
470	■		■	■	■		■								■		
471			NS											NS			
475	■		■	■	■		■	■							■	■	
476	■		■	■		■	■								■		
479			■	■			■								■		
480				■			■	■								■	
481				■			■	■		■	■	■	■			■	■
482				■			■	■								■	
487	■		■	■	■										■		
488	■		■	■	■										■		
492	■		■	■	■										■		
493	■	■	■	■	■	■									■		
494				■			■	■								■	
495	■		■	■	■										■		
496	■		■	■	■										■		
530	■		■	■	■	■									■		
817	■		■	■		■	■								■		

[a]Compiled from BLM soil description.
[b]No data.
[c]No Vegetation.
NS – Not stated.

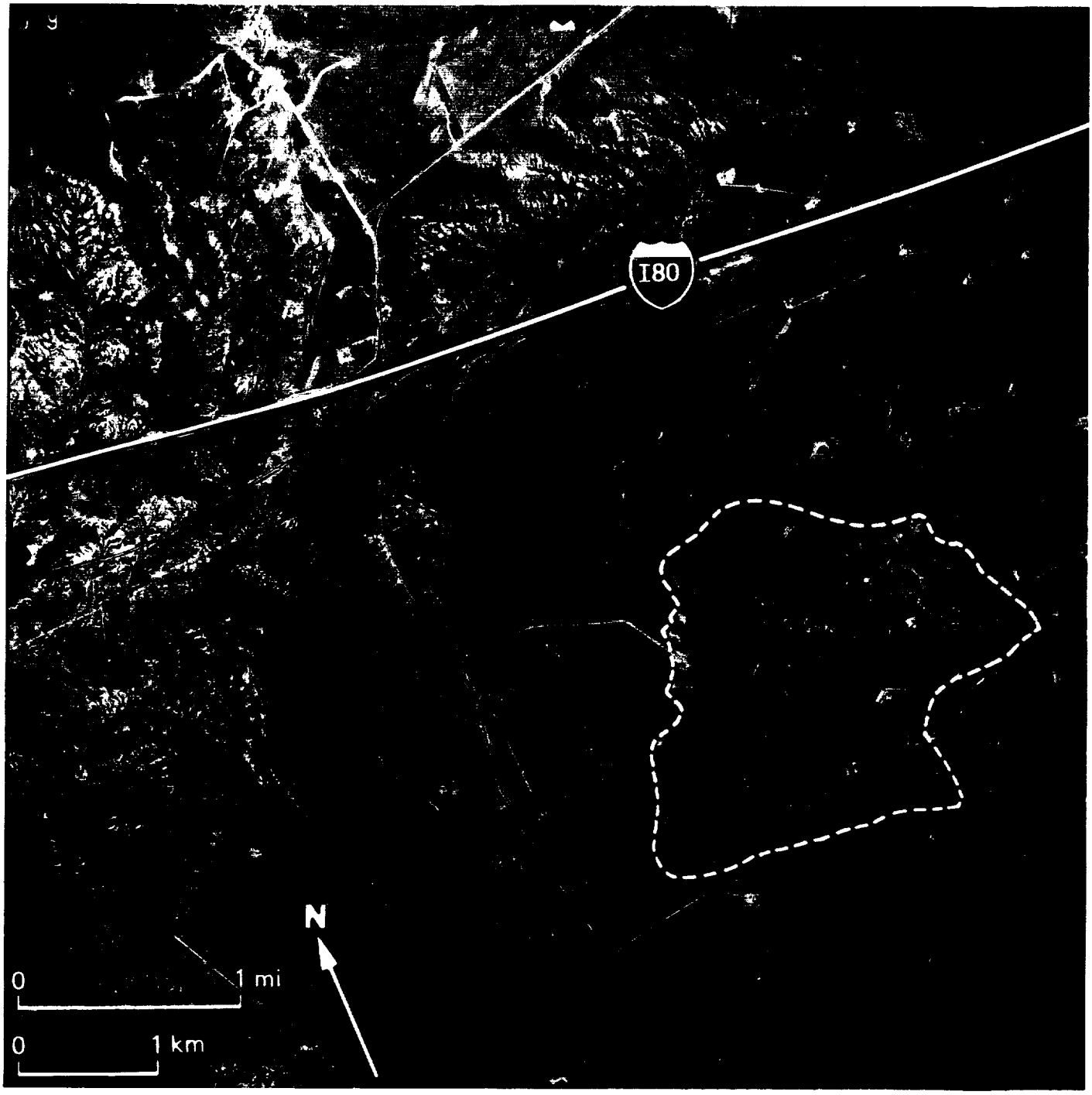

Figure 11-16. Aerial photograph, acquired October 19, 1978, showing the outline of the area of anomalous stunted sage as recognized in NS-001 multispectral data acquired at the same time. This anomalous area is not recognizable in this or other aerial photographic data.

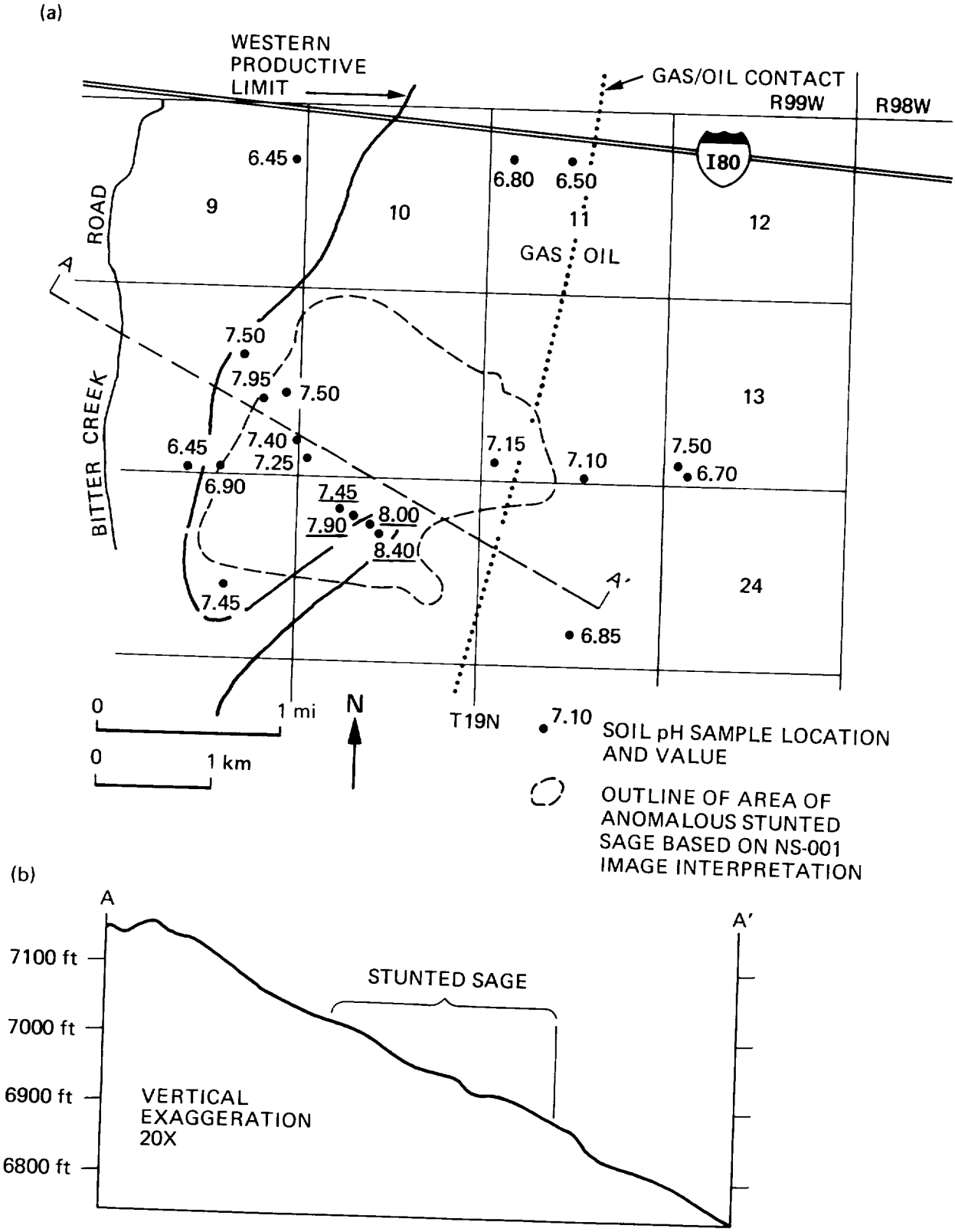

'igure 11-17. Area of anomalous stunted sage: (a) location map; (b) topographic profile. Sample sites for soil pH survey are also shown. Under-ned pH values are mean values for three closely spaced sample sites. Maximum pH value recorded in this survey was 8.55 for a sample in the uite obtained at location 8.40.

(a)

(b)

Figure 11-18. Ground photographs: (a) normal sage; (b) anomalous stunted sage

Figures 11-16 and 11-17(b) show that the boundary of the anomalous area coincides on the south with a prominant drainage and on the west with a subtle decrease in slope apparently associated with a subcropping resistant Fort Union sandstone lens. The northern and eastern boundaries of the anomaly are less well defined topographically.

b. Soils. Soils in the anomalous area were mapped as unit 450 by the BLM (Plate 11-2). The southern boundary of the area of stunted sage corresponds approximately to the southern boundary of a large area characterized by this soil unit. General characteristics of the soil unit are summarized in Tables 11-6 and 11-7. The following information, extracted from the descriptive text accompanying the BLM soil map (1981), gives further insight into the characteristics of soils in the anomalous area:

450—Neosh–Bittercreek complex, 1 to 8 percent slopes. This map unit is on gently sloping upland plains. Slopes are smooth. The native vegetation is mainly shrub grassland. Elevation is 6500 to 7300 feet.

Also included are small areas of Sagecreek in concave swales and Haterton, strongly alkaline, soils on convex surfaces. These inclusions make up about 25 percent of total acreage. The percentage varies from one area to another.

The Haterton, strongly alkaline soil is shallow and well drained. It formed in residuum derived dominantly from shale. Typically, the surface layer is pale yellow loam about 4 inches thick. The substratum is pale yellow loam about 8 inches thick over soft, calcareous shale. Depth to shale bedrock ranges from 10 to 20 inches.

Permeability of the Haterton, strongly alkaline soil is moderate. Available water capacity is about 1.6 to 3.6 inches. Effective rooting depth is 10 to 20 inches. Runoff is medium to rapid, and the hazard of water erosion is moderate to severe.

Based on field observations during the present investigation, soils on the islands of nonstunted sage within the anomalous area appear to be coarser in texture than soils in stunted sage terrain. A comparison to eolian soils mapped by the BLM in the test site area lends credence to the interpretation that these islands occur in areas of stabilized windblown soils within the mapped area of Neosh- Bittercreek complex soils.

c. Reconnaissance soil pH survey. To evaluate the possibility of any soil pH variation associated with the anomalous area, a limited soil pH survey was conducted during the summer of 1980. The results of this survey are summarized in Figure 11-17.

A total of 33 pH samples were collected at 23 sites, 1 outside the anomalous area and 13 inside the area. A samples were analyzed in the laboratory, at least twice, usin standard soil pH analysis procedures as described by Fo et al. (1980, p. 73–77). The greatest variation between re licate runs of the same sample was 0.1 pH units.

To summarize the results of this limited soil pH survey

(1) The range of pH values inside the anomalous ar was 6.90 to 8.55 (mean, 7.60).

(2) The range of pH values outside the anomalous ar was 6. 45 to 7.50 (mean, 6.90).

(3) Six soil samples obtained from healthy islands in the anomalous area had pH values ranging from 6.70 to 7.60 (mean, 7.10). Five adjacent samples (within 7 m [20 ft]) in anomalous sage terrain had pH values ranging from 7.40 to 8.55 (mean, 8.00).

Apparently, alkaline soil conditions are associated with the anomalous area. Figure 11-19 summarizes the reported potential effect of such pH variation on nutrient uptake by plants.

d. Results of soil gas and elemental geochemistry surveys. Soil gas (hydrocarbon and helium) and soil elemental geochemistry surveys conducted during the test site investigation (discussed in detail in Paragraphs VII.C.4 and VII.E of this section) suggest anomalous soil conditions in this area:

(1) The most anomalously high soil hydrocarbon gas sample (R47, Plate 11-1) is located in the approximate center of the stunted sage terrain.

(2) The highest soil helium concentration was obtained for a sample (H31, Plate 11-1) from the approximate center of the stunted sage terrain.

(3) Anomalously high concentrations of titanium, vanadium, copper, and zinc, and low concentrations of calcium and magnesium are associated with soil samples obtained from stunted sage terrain.

3. Anatomy of stunted sage from Patrick Draw test site. Nineteen specimens of sage (*Artemisia tridentata*, subsp. *wyomingensis*) were sampled on September 4, 1981 and February 13–14, 1982. Both normal and stunted sage specimens, consisting of branch tips (15 to 25 cm in length), branch (stem) segments, main trunks, and leaves, were collected and placed in plastic bags, which were then sealed. Initially, the specimens were studied with a stereo dissecting microscope. Typical leaves, stems, and trunks were then hand-sectioned with a razor blade and the thin sections (20 to 50 μm thick) studied at higher magnifications. The following observations were made.

a. Leaf anatomy. In comparison with normal sage leaves collected outside the area of anomalous stunted sage, the leaves from stunted specimens differ in a number of ways (Figure 11-20). The leaves from stunted specimens are smaller than leaves from healthy sage (8 mm versus 11 mm), possess poorly developed palisade layers, have underdeveloped intercellular spaces between mesophyll cells, and lack development of extraxylary fibers in the vascular bundles (veins). The cells of the mesophyll are densely cytoplasmic and dark green. The covering of trichomes (epidermal hairs) is much heavier than that seen in the normal leaves. This syndrome of characters indicates that, based on anatomical structure, these leaves are immature. However, only the oldest leaves (those farthest from the stem tip) were sampled in both the healthy and stunted specimens. If older leaves were produced on the stunted sage plants, they had abscissed prior to the time of collection.

Leaf morphology is essentially the same in both healthy and stunted specimens; however, the leaves of the stunted sage tend to be less lobed than those of the healthy sage. No evidence of chlorosis was seen in the stunted leaves, but this characteristic would be difficult to detect due to the heavy trichome cover associated with these specimens. The small, stunted leaves are clustered in rosette patterns at the tips of short lateral branches. There are far fewer leaves per branch as well. The overall effect of these features is to expose more branch (stem and bark) surface on the stunted sage (when compared to the normal branch/leaf ratio). In the field, in addition to more visible branch, more soil or undergrowth (ground cover) would be seen as well. The combined effects of fewer leaves, stunted leaf development, and heavier trichome cover appears to explain the dark color of stunted sage as observed in the field.

b. Wood anatomy. In an examination of the abnormal sage stem section (Figure 11-21), the following observations were made. In comparison with normal sage wood, the individual growth rings are narrower (an average of 14.8 rings/cm versus 10.5 rings/cm in the healthy sage), with fewer and smaller cells. Individual vessel elements within the growth rings have narrower tangential diameters and thinner walls. The fibers within each growth ring have a lower degree of optical activity (when viewed with crossed Nicols) and are suggestive of possessing gelatinous walls (this same feature is seen in some normal sage stems). Fewer vascular rays are seen.

Examination of growth rings in sections from two stunted sage specimens revealed that the stunted effect can be traced back for a total number of 95 growth rings. If it is assumed that one growth ring is produced per year, the factors causing stunted growth have had an influence for 95 years (dating back to 1887). It is possible that a few false annual rings occur (due to several wet and dry seasons within a one-year period) in the sectioned specimens, but that would be an unusual condition. Comparison of these stem sections with rainfall records would help clarify if the growth rings do represent annual increments. Given the area of the United States from which the samples were collected and the previous studies of sage wood by Diettert (1938), it is assumed that each growth ring represents an annual growth increment.

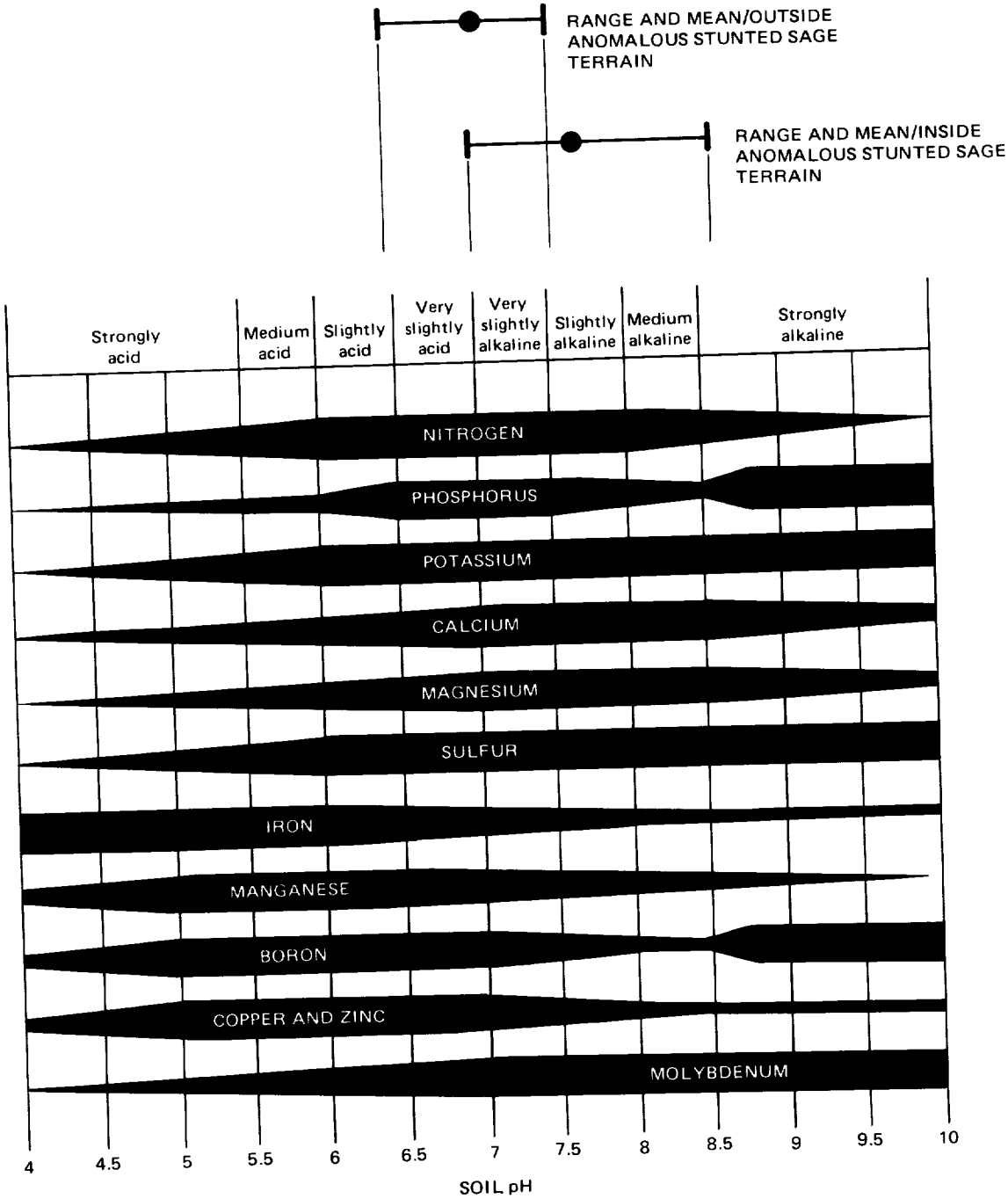

Figure 11-19. Diagram illustrating the availability of nutrients to plants as a function of soil pH (modified from Bidwell, 1974, Figure 10-2, p. 252). The range of soil pH values obtained in a survey of a portion of the Patrick Draw test site is also shown. The range of soil pH values from stunted sage terrain falls in the minimum availability range for phosphorus, iron, boron, copper, and zinc, and decreased availability range for nitrogen.

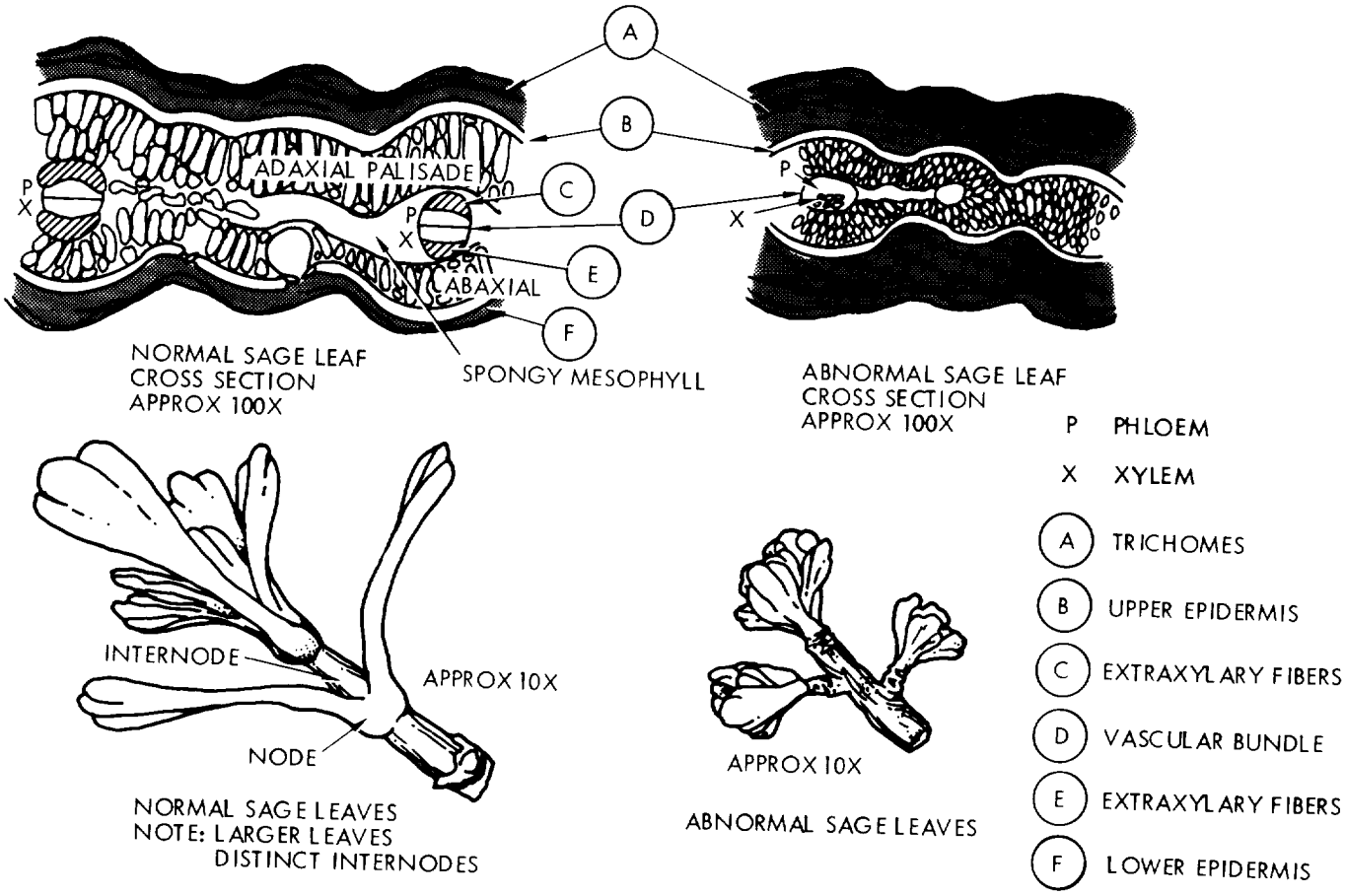

Figure 11-20. Representative leaf cross sections of normal sage and abnormal stunted sage from the Patrick Draw test site. Note the rosette arrangement of small leaves and poorly developed mesophyll (both palisade and spongy), heavy trichome cover, and lack of extraxylary fibers characteristic of the stunted sage.

c. Summary. In a study of the morphology and anatomy of *Artemisia tridentata*, Diettert (1938) describes a number of the features seen in the stunted Patrick Draw sage. Diettert refers to rosette-like clustering of leaves, due to lack of internode elongation, as a common feature that becomes pronounced in plants growing in less-favorable environments. The size and shape of the leaves are influenced by both time of year sampled (this should not be a factor at the Patrick Draw site since normal and stunted specimens were collected at the same time) and local environmental conditions, including soil conditions (plants growing in deep, rich soils and sheltered sites have larger leaves than those found in shallow soils and exposed areas). Diettert also considers that the loss of larger, mature leaves and the retention of arrested embryonic leaves are related to local environmental conditions.

Hewitt (1963) reports that the following characteristics are associated with zinc deficiency in higher plants: smaller leaves ("little leaf" is a common designation for diseases related to zinc deficiencies); clusters or rosettes of leaves at the tips of branches ("rosette of apples" is due to a zinc deficiency) caused by decrease of internodal elongation of the stem; and suppressed or delayed differentiation of leaf tissue at the cellular level. Lack of differentiation in mesophyll tissues and limited development of intercellular spaces in leaf tissues are also cited as characteristic of zinc deficiency.

This syndrome of characteristics precisely matches the leaf anatomy and morphology of the stunted leaf specimens collected at Patrick Draw. Based on wood anatomy, this stunted condition has been chronic (that is, spread over time) rather than acute.

Since zinc is involved in the synthesis of indoleacetic acid (IAA), a plant hormone required for normal growth (cell elongation) and differentiation, it is not surprising that a zinc deficiency leads to a delayed differentiation in leaves and an altered differentiation in wood (due to altered cambial activity in response to changes in IAA levels within

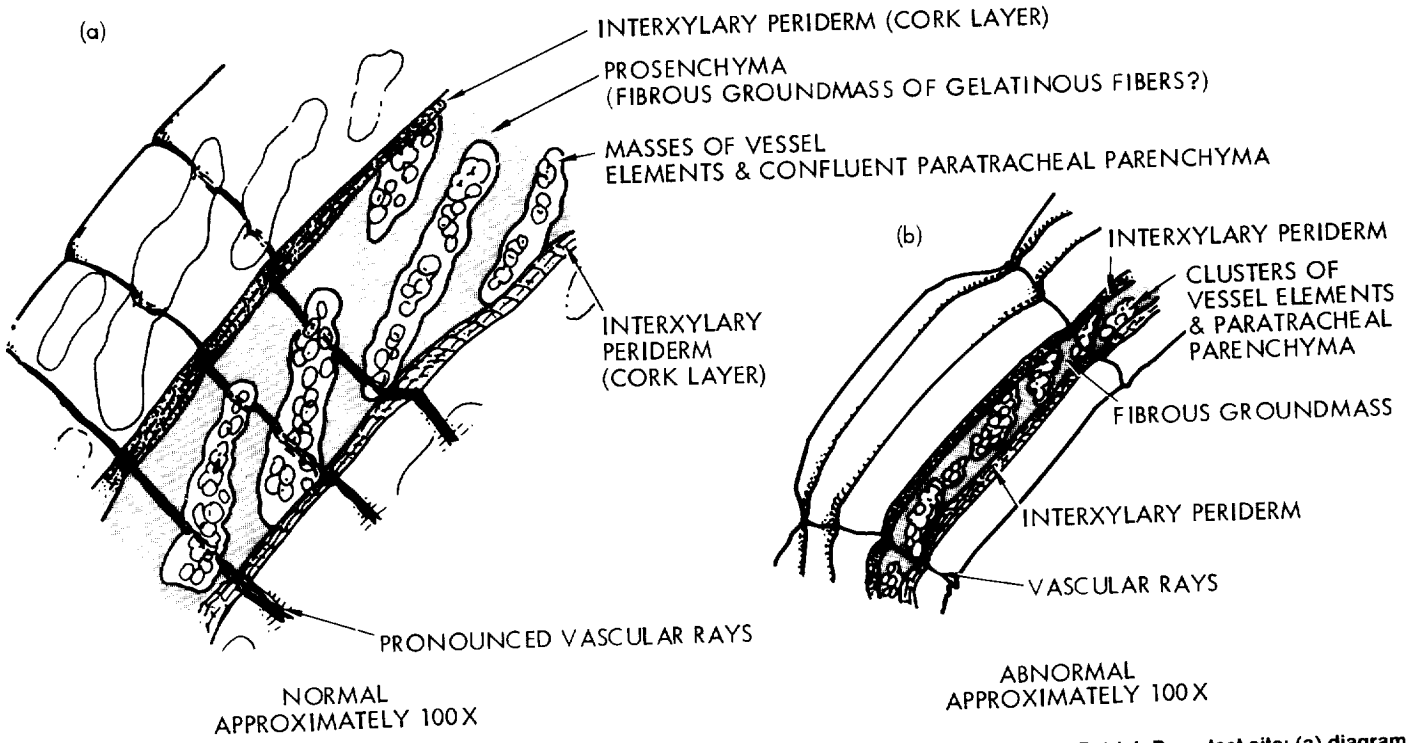

Figure 11-21. Representative stem cross sections of wood of normal sage and wood of stunted sage from the Patrick Draw test site: (a) diagram of the normal sage stem showing a small portion of two annual growth rings of wood (a portion of one ring is illustrated in detail); (b) diagram of the stunted sage stem showing a portion of five annual rings (again, one is illustrated in detail). Note the reduced amount of secondary xylem (wood) tissue produced per annual ring in the abnormal stunted sage.

the plant). The various morphological and anatomical characters described by Diettert (1938) and attributed to adverse environmental conditions are symptomatic of a zinc deficiency. These zinc deficiency symptoms are so unique that they are not likely to be confused with symptoms due to other deficiences (Bidwell, 1974).

Leone et al. (1977) note significant increases in levels of iron, zinc, and ammonia nitrogen in soil samples (both topsoil and subsoil) taken from landfill sites, when compared with soils from sites adjacent to landfills. They propose that such increases of major and trace elements in soils containing landfill gases (high concentrations of methane and carbon dioxide, low concentrations of oxygen) are due to the reducing atmosphere created in the soil by the presence of methane. Similar high soil gas concentrations were recognized in stunted sage terrain at Patrick Draw.

According to Siegel (1974), availability of zinc to plants decreases as soil pH increases over 7.0, becoming essentially unavailable above a pH of 8.5. Field studies of soil pH indicate that within the area of stunted sage, soil pH measurements reach 8.55 (in comparison to a maximum pH of 7.5 for soils outside the stunted area). Elemental analysis of soil samples indicates anomalously high zinc concentrations in soil samples from stunted sage terrain. These data correlate well with Leone's findings (Leone et al., 1977) for zinc levels in soils containing landfill gases. Although high concentrations of zinc are in the solid soil phase, zinc is apparently unavailable (due to high soil pH) to the sage plants, resulting in zinc deficiency symptoms.

4. Conclusions. Field observations, geochemical survey results, and a preliminary anatomical and morphological evaluation of Patrick Draw sage support the premise that stunted, abnormal sage at the test site is the result of adverse environmental conditions resulting in a zinc deficiency. There is no evidence of fungal or bacterial disease, fire damage, or winter kill. The effect has been chronic, extending back for at least 95 years. Correlation of growth rings with weather data would provide useful supplemental information concerning the relationship between growth rings and any local climatic conditions.

C. Organic Geochemistry

1. Introduction. An organic geochemical study of the Patrick Draw test site was conducted during the summer

1980. The purpose of this study was to determine if the moderately deep (1.5 to 2.0 km) Patrick Draw reservoir could be detected by measuring soil gas concentrations that could reflect microseepage of the alkane (C_1 through C_6+) fraction from the hydrocarbon reservoir. There were two objectives for the Patrick Draw organic geochemistry program. The first was to determine if detectable amounts of C_1 through C_6+ hydrocarbons were present as free soil gas and/or as bound (adsorbed and absorbed) soil gas. The second was to determine whether anomalous levels of these hydrocarbons were present in areas in which lineaments had been recognized over the Patrick Draw reservoir.

Interpretation of aerial photographs as well as Landsat MSS and NS-001 images revealed linear features (lineaments) crossing the Patrick Draw test site area. These features were assumed to represent the surface trace of nearly vertical, extensional fractures. Several of these lineaments were postulated from subsurface data to represent fractures which extend to depth and, thus, might provide communications between the reservoir and the surface. Fractures may swell and pinch, resulting in localized microseepage of hydrocarbons along their length; therefore, closely spaced samples were collected along sampling lines located on lineaments. Since fractures commonly occur as subparallel sets, closely spaced samples were also collected along sampling lines crossing lineaments. Additional samples were collected over the adjacent test site area to provide background data.

Values for adsorbed (bound), absorbed (headspace), and free (unbound) hydrocarbon soil gas were determined for 105 sample sites. The adsorbed gas analyses were performed by Phillips Petroleum, Bartlesville, Oklahoma; absorbed gas by Arco, Dallas, Texas; and free soil gas by Cities Service Company, Tulsa, Oklahoma. Data from the three methods revealed similar anomalous values, although sample-to-sample agreement among the three methods was low. This poor agreement probably reflects differences in the clay and carbonate content of the soil samples. Soils with low clay or carbonate content should have higher free gas values, whereas soils with high clay or carbonate content should have more gas in an adsorbed state and, hence, have little free soil gas. Adsorbed gas values should be less susceptible to short-term atmospheric (pressure) changes. Of the three sets of soil gas values, the adsorbed soil gas values revealed the highest correlation for measured concentrations of gas species. Data from the absorbed gas analyses showed the least intersample variability.

Figure 11-22 presents the combined sample anomalies for adsorbed, absorbed, and free soil gas. If a sample possessed anomalous concentrations of a particular gas species in two or more forms (i.e., adsorbed, absorbed, etc.), the sample was considered to be significantly anomalous. Such samples are represented as squares in Figure 11-22. A complete explanation of the ranking scheme used in this study is discussed below. Of the 15 significantly anomalous samples shown in Figure 11-22, nine fell in close proximity to the lineaments. The geological and chemical significance of this distribution is discussed in the following paragraphs.

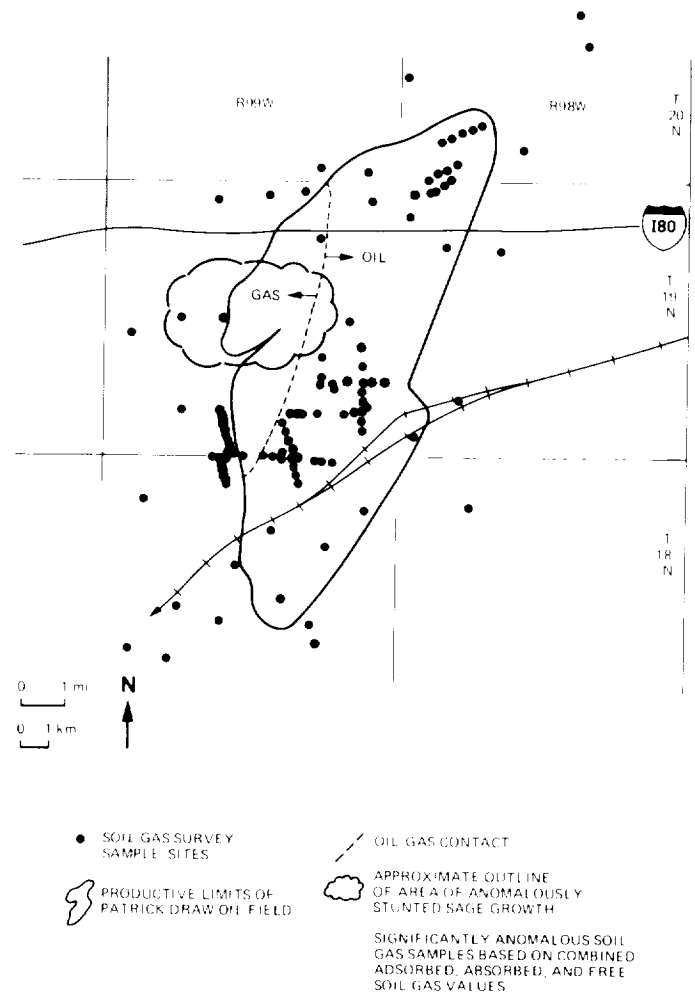

Figure 11-22. Soil gas anomaly significance map showing combined results of all parameters: adsorbed, absorbed, and free soil gas

2. Geologic model. Figure 11-23 shows the location of selected aerial photograph lineaments that were recognized in the test site area. Two lines of evidence lend credence to the interpretation that these features coincide with fractures or faults.

(1) Lineaments 1 and 3 appear to be surface manifestations of faults that cut the reservoir. The surface trace

coincides with discontinuities mapped at depth indicated by as much as 62 m (200 ft) offset of the oil/gas and oil/water contact in the reservoir (McCubbin and Brady, 1963).

(2) The apparent bending and offset of topographic features along lineaments 4, 5, and 6 suggest that these lineaments are also faults. The aerial photograph mosaic shows that these lineaments truncate material similar to the Killpecker Dune Field to the north. These eolian deposits form in linear topographic depressions, which are interpreted to coincide with the trace of faults.

Figure 11-23. Aerial photograph mosaic showing the location of endpoints of seven selected lineaments evaluated in a soil gas survey

Considering the structural location of the Patrick Draw test site with respect to the Wamsutter Arch and Rock Springs Uplift, it seems reasonable to assume that the ENE–E-trending lineaments in the test site are genetically related to similar features exposed on the Rock Springs Uplift (Figure 11-3). Specifically, the ENE–E–W-trending lineaments at Patrick Draw, like those on the Rock Springs Uplift, are postulated to be nearly vertical, extensional fractures or faults.

These fractures and faults may act as potential conduits for leakage of reservoir fluids to the surface. If this is the case, analysis of soil gas samples obtained from these features should show significantly higher values than samples over the rest of the oil field and in the area in general. A sampling program, based on this model, was conducted in 1980 and is described below.

3. Sample collection. The sampling program was designed to obtain suitable samples for adsorbed, absorbed, and free soil gas analysis at each sample site. A soil sample (in excess of 400 g) and four vacuum sample containers (20 cm^3/Vacutainer) of free soil gas were collected at each of the 105 sample sites. To assure maximum coverage of the study area, sites both along selected lineaments and away from selected lineaments were sampled. The lineament sample traverses transected and/or followed the mapped lineaments, whereas the regional sites were randomly located over the remaining test site area. Of the 105 sites sampled, 43 were along lineaments. Sample locations are identified in Figure 11-24. This sample program was determined by the practical considerations of available time and resources.

At each site, a hole 15 cm in diameter was augered to a depth of 0.5 to 1 m. The hole was cleared of loose debris, and a 5-cm inside-diameter barrel sampler was driven into the bottom of the hole to a depth of 1 to 1.5 m (Figure 11-25a). The sampler was then withdrawn and a bottom hole soil sample of approximately 400 g was taken from the end of the barrel and sealed in a metal sample can. Phillips analyzed these canned samples for adsorbed gas; Arco analyzed them for absorbed gas.

Upon removal of the barrel sampler, a gas sampler probe (Figure 11-25b) was immediately driven into the bottom of the hole. Rapid implacement of this probe was necessary to reduce loss of free soil gas. The gas probe consisted of a

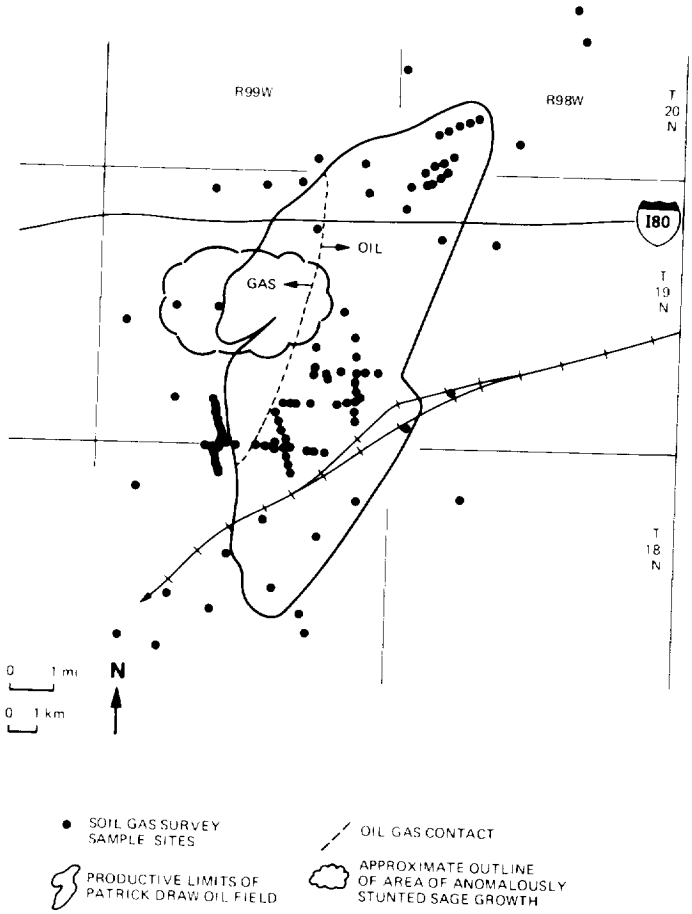

Figure 11-24. Index map showing the locations of sites sampled in hydrocarbon soil gas survey

thick-walled, high-carbon steel tube with a replaceable steel point. The point was helically perforated. These perforations connected to a low-volume conduit tube. The conduit tube, fabricated from 0.8-mm stainless steel capillary tubing, extended from the point of the steel tube and into a chamber recessed in the striking surface tube. At the striking surface end, the conduit tube was cut at an acute angle to form a needle tip capable of perforating the rubber seal on the evacuated sample containers. These evacuated sample containers (Vacutainers) are commonly used for collecting blood samples in medical laboratories. Subsurface gas samples were obtained by impaling the Vacutainers on this needle point. Figure 11-25(c) is a sketch of the probe.

Two Vacutainer sizes were used: 10 and 20 ml. The probe was driven into the sampling hole, and a 10-ml Vacutainer was placed on the probe for 3 minutes to purge the capillary tube of atmospheric gas. This purge Vacutainer was sealed with silicone adhesive and retained. Four successive free soil gas samples of 20 ml each were then collected at 3-minute intervals and sealed.

4. Soil gas chemistry

a. General. The most mobile constituents of a hydrocarbon accumulation include the lighter homologues—methane through butane. Since these compounds volatilize easily, they may migrate from hydrocarbon accumulations along fractures, through diffusion, or in groundwater solution. In some instances, the detection of these volatile compounds at the surface has been used to indicate the presence of accumulations of hydrocarbons at depth. Numerous studies using this phenomenon, conducted with different degrees of success, are described by Debnam (1969), Devine and Sears (1977), Horwitz (1972, 1980), and Kvenvolden and Redden (1980).

The results of the test site survey indicate that adsorbed gas analyses yield useful information for methane through butane (C_1 through C_4). Absorbed gas analyses yield data for C_1 through C_3. Free soil gas analyses yield data for C_1 through C_5+. The tabulated results of these analyses appear in Appendix A.

b. Treatment of data. Each of the three sample types (i.e., adsorbed, absorbed, and free soil gas) contains a variety of gas species (e.g., methane, ethane, propane, etc.). To interpret the significance of these data, the "background" or threshold value of each gas species must be determined for each sample type. Several schemes exist for determining this threshold value; some are more statistically rigorous than others. Four of the most commonly used schemes include setting the threshold for background versus anomaly at (1) two standard deviations above the mean, (2) one standard deviation above the mean, (3) the 97.5 percentile value, and (4) the inflection point of a cumulative frequency plot. To determine the most appropriate method for determining this threshold, the nature of the data, the degree of sampling bias (i.e., whether background and anomalous areas have been equally sampled), and the distribution of the sample sites should be considered. (Refer to the works by Hawks and Webb (1962), Levinson (1974), and Rosenblum (1980) for a complete discussion of techniques available for statistically ranking sample populations.) For this study, each sample population was ranked as follows: samples with soil gas values greater than two standard deviations, 2σ, above the mean, $\bar{X}$, were considered anomalously high. These anomalous samples are represented by squares in Figures 11-26, 11-27, and 11-28. Samples with soil gas values that fell between one and two standard deviations above the mean were plotted as triangles.

In Figure 11-22, the samples are rated according to their overall significance level. A sample is rated as having the highest significance if it has at least two anomalous values

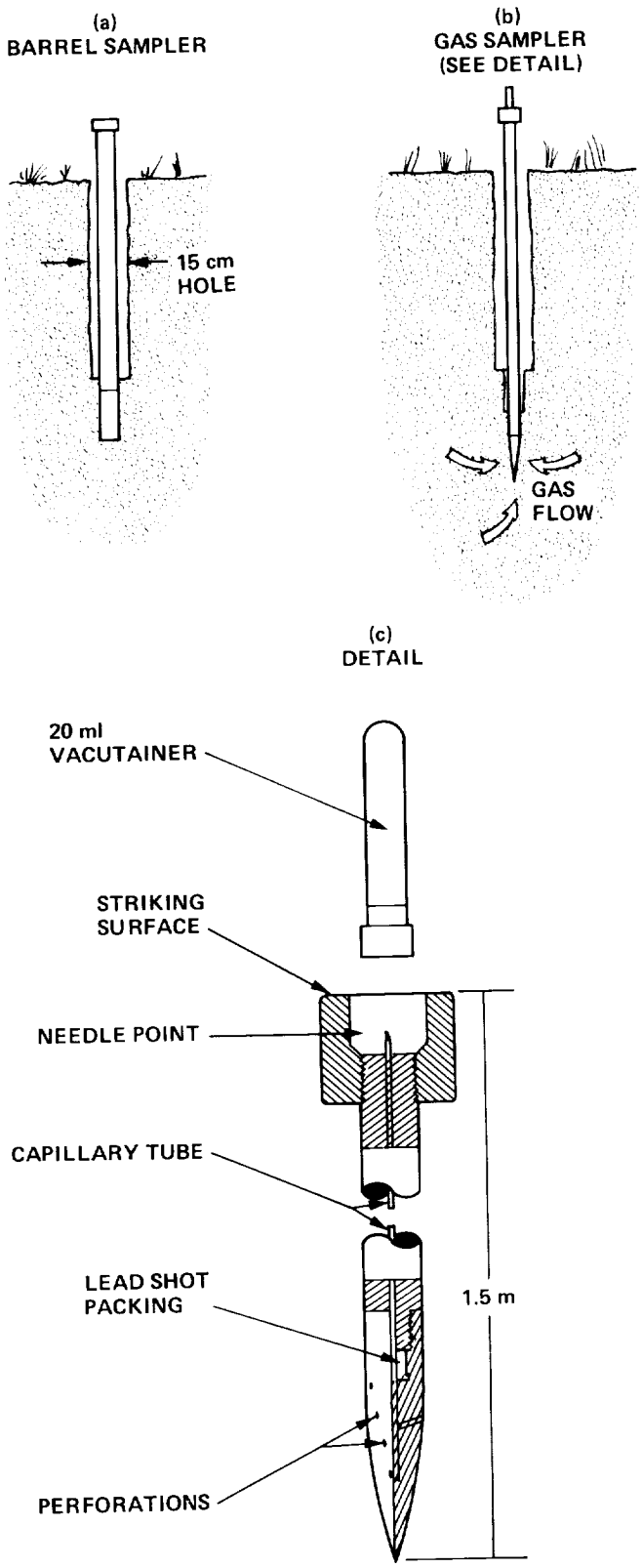

Figure 11-25. Sampling devices used in hydrocarbon soil gas survey

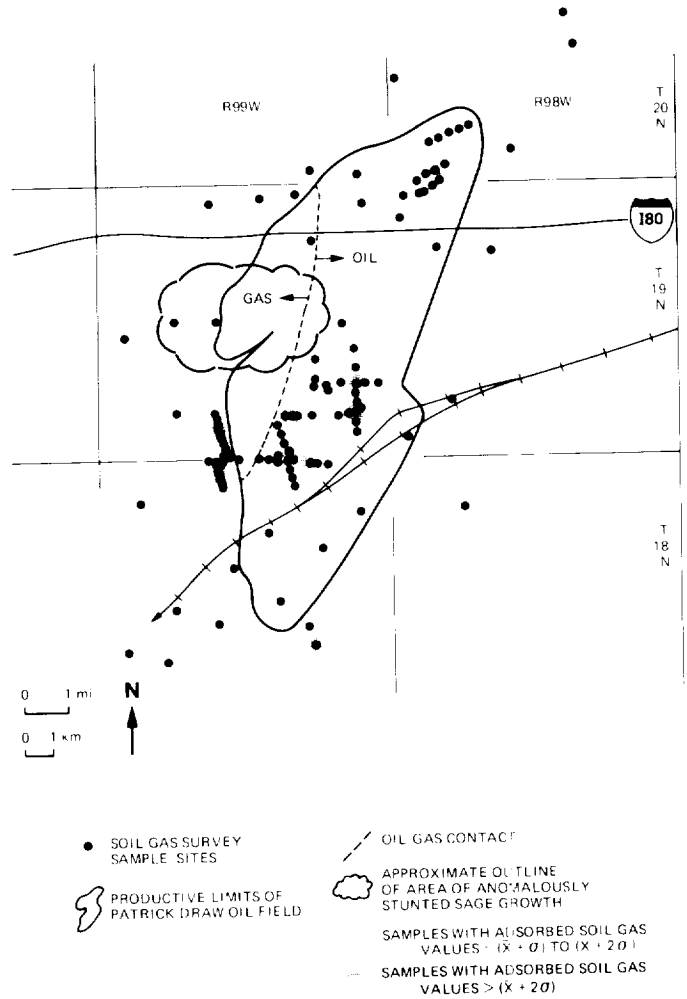

Figure 11-26. Index map showing the locations of significant adsorbed soil gas anomaly sites

(e.g., anomalously high ethane from both absorbed and free soil gas analyses). These samples are identified with squares in Figure 11-22. Samples not satisfying these criteria are considered nonanomalous.

Adsorbed soil gas. Results of the adsorbed gas analyses are summarized in Figure 11-26. Many sample sites showing anomalously high adsorbed gas concentrations coincide with the selected lineament locations. Anomalous values for all geochemical populations (methane, ethane, and propane) fall on or within close proximity to the selected lineaments.

Eight samples are considered anomalous. A comparison of Figures 11-26 and 11-28 reveals no apparent site-to-site correlation between the adsorbed and free soil gas anomalies. This most likely results from variation in the clay and carbonate content of the soils sampled. Clay- or carbonate

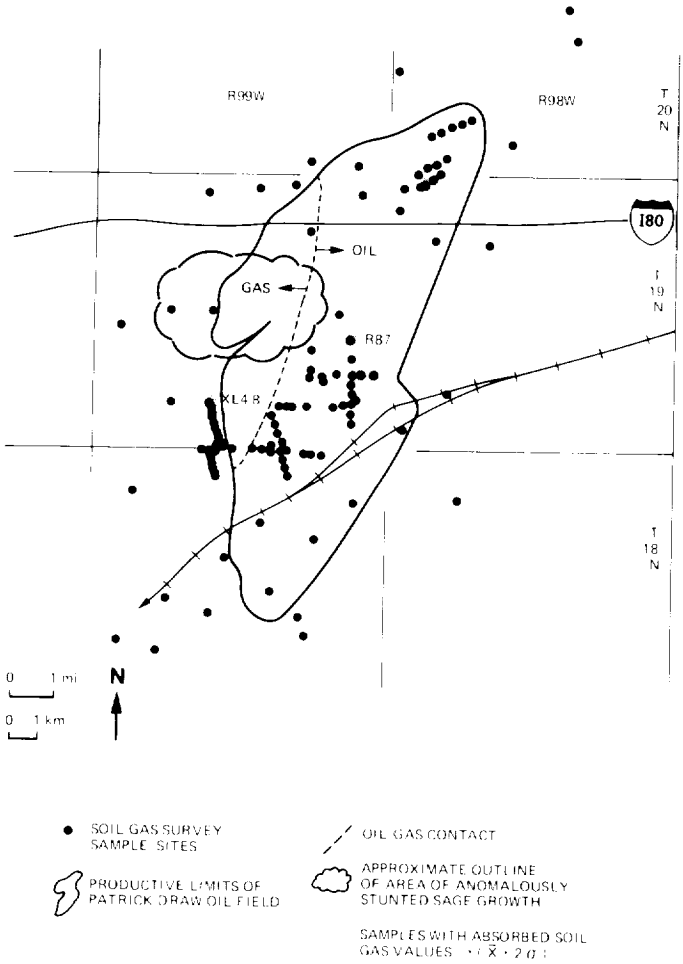

Figure 11-27. Index map showing the locations of significant absorbed soil gas anomaly sites

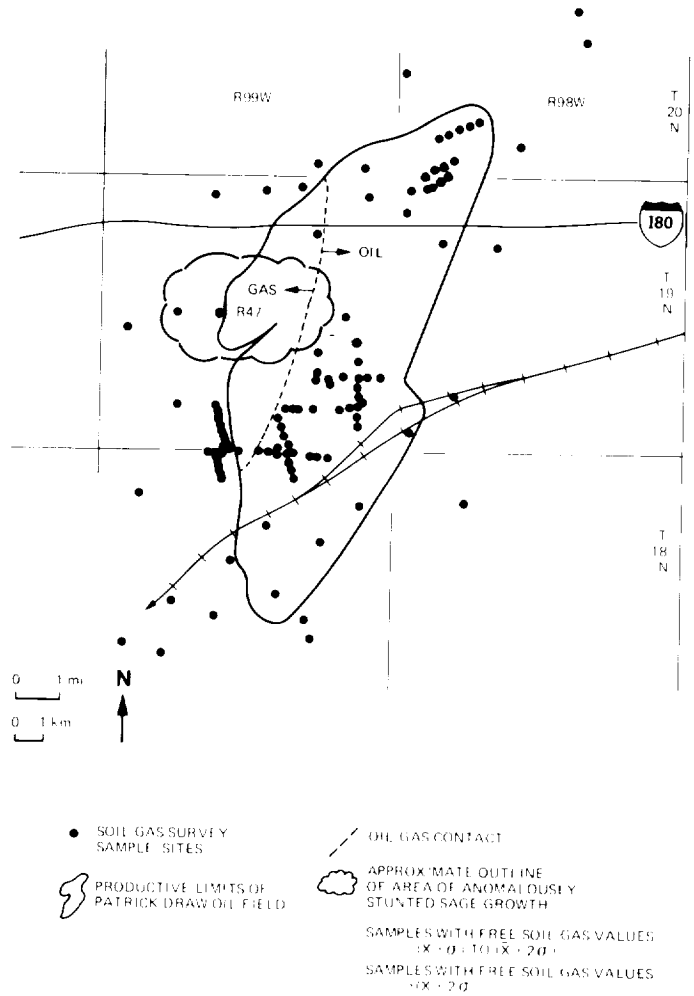

Figure 11-28. Index map showing the locations of significant free soil gas anomaly sites

rich samples should show higher adsorbed gas values than quartz-rich samples. A quartz-rich sample should show higher free soil gas values than a clay- or carbonate-rich sample, which should adsorb hydrocarbons.

Absorbed soil gas. Results of the absorbed gas analyses are summarized in Figure 11-27. In this case, the log values of the analytical results were used to calculate the means and standard deviations because the data are log-normally distributed.

The majority of the absorbed gas samples with methane, ethane, and propane values greater than one standard deviation above the mean occur on lineaments. Samples along lineaments 4 and 5 in Figure 11-23 are consistently high. Two consistent highs that do not appear related to faults or lineaments occur at sites XL4-8 and R87. XL4-8, obtained near the center of the field, also contains one of the highest light hydrocarbon values measured in the free soil gas analysis.

Free soil gas. Results of the free soil gas analyses are summarized in Figure 11-28. In addition to the five parameters analyzed for adsorbed soil gas, the free soil gas samples were also analyzed for C_3+ hydrocarbons. The distribution of anomalies for the various geochemical populations tested in the free soil gas shows more internal scatter than the adsorbed gas values. This variation may reflect short-term fluctuations in atmospheric pressure, sample contamination, or variable migration rates for the different hydrocarbons. Most anomalous values ($\bar{X} + >2\sigma$) are at least an order of magnitude higher than the mean value, and most of the consistently anomalous samples were obtained near lineaments. A recent work by Weisman (1980) notes that geochemical profiles of soil gas yield similar

concentrations over known fields elsewhere in the Western Overthrust Belt.

Of six very significant anomalies, three fall on lineaments over the field. Of the three remaining anomalies, one (site R47) falls on a lineament that extends from the west into the field. This sample, which was several orders of magnitude greater than the average soil gas sample, was obtained from the approximate center of the NS-001 tonal anomaly associated with stunted sage.

5. Conclusions. Table 11-8 lists the number of agreements in the mean ranking classification scheme for the three methods. Adsorbed soil gas and free soil gas values correlate best.

In Figure 11-22, 15 significant anomalies can be seen throughout the study area. Ten of these anomalies are near lineaments (including one on the contact between the Wasatch and Fort Union Formations). This distribution of anomalies is consistent with the hypothesis that these lineaments act as conduits for gases seeping from depth to the surface. Alternately, it may only reflect sample distribution.

Although both adsorbed and free soil gas levels appear to be higher in the vicinity of selected lineaments in the Patrick Draw field, it remains unproven that this technique can be useful in finding reservoirs elsewhere. The results of this study are encouraging, and further work of this nature should be pursued. Most certainly, reduction of the size of a geochemical study with remote sensing data will minimize the time and cost necessary to conduct such surveys. Identification of "leaking" lineaments versus "nonleaking" lineaments, coupled with additional geological information, may be helpful in selecting exploration targets requiring more detailed evaluation with conventional exploration tools.

Table 11-8. Ranking correlation among all sample types[a]

Sample Soil Gas	Methane (CH_4)	Ethane (C_2H_6)	Propane (C_3H_8)
Absorbed–adsorbed	48	44	43
Absorbed–free	50	46	53
Adsorbed–free	37	41	44
All methods in agreement	24	23	23
No methods in agreement	17	17	10

[a]Number of cases in agreement among the three analytical techniques was based on division of results into four classes: (1) sample value less than mean; (2) values between mean and one standard deviation above; (3) values between one and two standard deviations above mean; and (4) samples greater than two standard deviations above mean.

D. Helium Soil Gas Survey

1. Introduction. Most petroleum reservoirs contain helium in concentrations exceeding 100 ppm and, in some cases, exceeding 10,000 ppm. Soil, soil gas, and water can be sampled near the surface for trace amounts of helium that may be leaking from underlying hydrocarbon reservoirs.

2. Methods. To help identify any potential areas of hydrocarbon microseepage in the Patrick Draw test site, 59 soil gas samples were collected and analyzed for helium content. For this reconnaissance survey, the sample distribution included closely spaced sampling along a traverse over the known gas cap and more widely spaced sampling of the remainder of the test site area.

The soil gas sampling procedure used in this survey consisted of extracting a 20-ml gas sample through a hollow probe driven 75 cm into the soil at each sampling site. The low moisture content of Patrick Draw soils provided an excellent sampling medium. The 20-ml samples were each stored in small steel tubes with lead-lined brass caps. Western Systems, Inc., Evergreen, Colorado, analyzed these samples with a mass spectrometer specifically modified for helium analysis. Sensitivity of this instrument is better than 10 ppb.

3. Results. The results of the helium soil gas survey are illustrated in Figure 11-29. These data may be compared to the normal atmospheric helium concentration of 5.24 ppm.

The two highest helium concentrations (9.53 and 7.83 ppm) occur in samples acquired from approximately the center of the area of anomalously stunted sage and coincide approximately with the center of the gas cap of the Patrick Draw field. The soil helium concentrations determined for samples in this area are extremely high; the measured values are as high as Western Systems has measured anywhere. These high values may be the result of leakage along fractures which cut the reservoir, or they may be related to gas reinjection operations.

Values outside the gas cap area are slightly high compared to normal background values. One high value (6.30 ppm) on the southwestern edge of the field outline may suggest a southern extension of the gas cap. Another high value (7.41 ppm) in the east–central part of the field is not easily explained in terms of microseepage from the gas cap.

4. Conclusions. Although reconnaissance in nature, a helium geochemical survey of the test site demonstrates

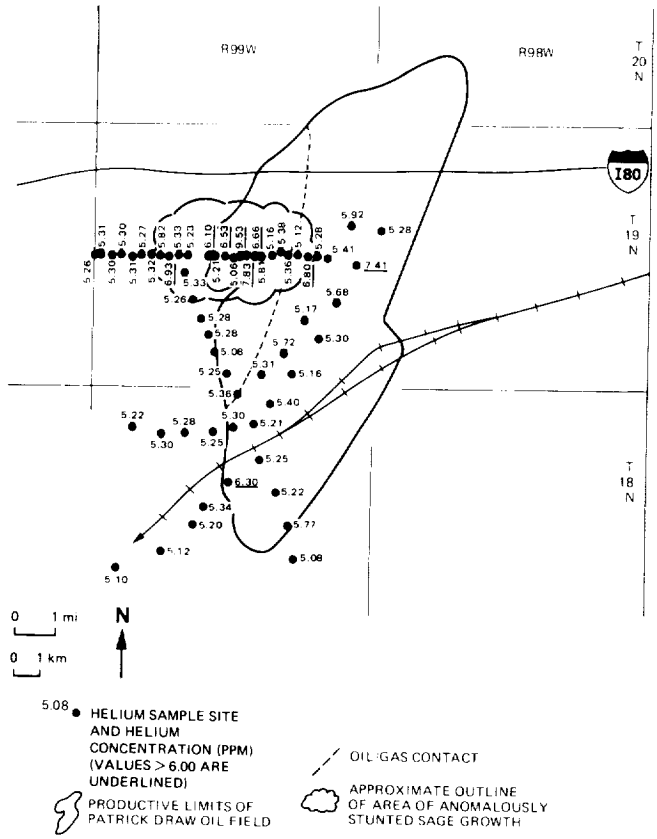

Figure 11-29. Index map showing soil helium gas survey sample sites and results

anomalous values that suggest leakage from the hydrocarbon reservoir. Additional sampling and analysis is recommended. The high soil helium concentrations measured in the area of anomalously stunted sage correlate with other geochemical data in the area. It is possible that bedrock faulting or fracturing has had an influence on helium movement from the reservoir to the surface.

E. Soil Elemental Geochemistry

1. Introduction. The Lasertrace® method of analysis (refer to the Technical Appendix, Section 14) was used to determine the elemental composition of soil samples. The objective was to investigate any possible relationships between soil elemental chemistry and features noted on remote sensing images. In particular, it was hoped to compare geochemical characteristics with tonal anomalies recognized in the analysis of images, which might be related to microseepage of hydrocarbons from the Patrick Draw reservoir.

Dalziel and Donovan (1980) have recognized cases of anomalous concentration, alteration, and distribution of certain elements in soils, bedrock, and vegetation over and adjacent to oil and gas fields. Their geochemical anomalies have been attributed to the effect of hydrocarbon microseepage from the reservoir to the surface.

2. Data acquisition and analysis. Surface soil samples were scooped up with a trowel at 330 undisturbed and uncontaminated sites (Plate 11-1 and Figure 11-30) and stored in paper envelopes. During two weeks in July 1979, 108 samples were collected at approximately 1-km (0.6-mi) spacing along a regional NE–SW traverse and four E–W traverses. During June 1980, two weeks were spent collecting an additional 109 samples on an infilling basis to improve the sample distribution and density. These samples were all obtained from locations adjacent to those drilled and sampled during the soil hydrocarbon gas survey. During the summer of 1981, an additional 113 samples were collected. All 330 samples collected were analyzed by the Lasertrace® method using the same USGS standards. The analytical results (Appendix B) were portrayed in trend surface elemental concentration isopleth map form for interpretation. The Lasertrace® method of analysis used in this program was developed by Barringer Resources, Inc., and is designed for automated multi-element analyses on a mass production basis.

The Lasertrace® method shows some differences in absolute elemental concentration when compared with values obtained in the conventional acid-digestion method of multi-element analysis. Lasertrace® results, however, are reproducible and consistent for detecting relative differences in elemental concentration and are thus useful for detecting geochemical anomalies. The chief merit of the Lasertrace® method is its speed and low analytical cost. It is therefore applicable on a much larger scale than acid-digestion methods.

3. Results. Raw, trend-surface, and trend-residual elemental concentration maps were produced for each of 24 elements. Raw data isopleth maps exhibited excessive small-scale variability, which was an artifact of the sample distribution. Fifth-order trend surface portrayal of the data smoothed these sample distribution-induced artifacts and at the same time preserved the original data. Davis (1973) describes the trend surface approach to automated contouring and smoothing of geological data. Fifth-order trend surface maps for selected elements produced from the Lasertrace® data (Figures 11-31 through 11-41) were evaluated to delineate potential geochemical anomalies for interpretation.

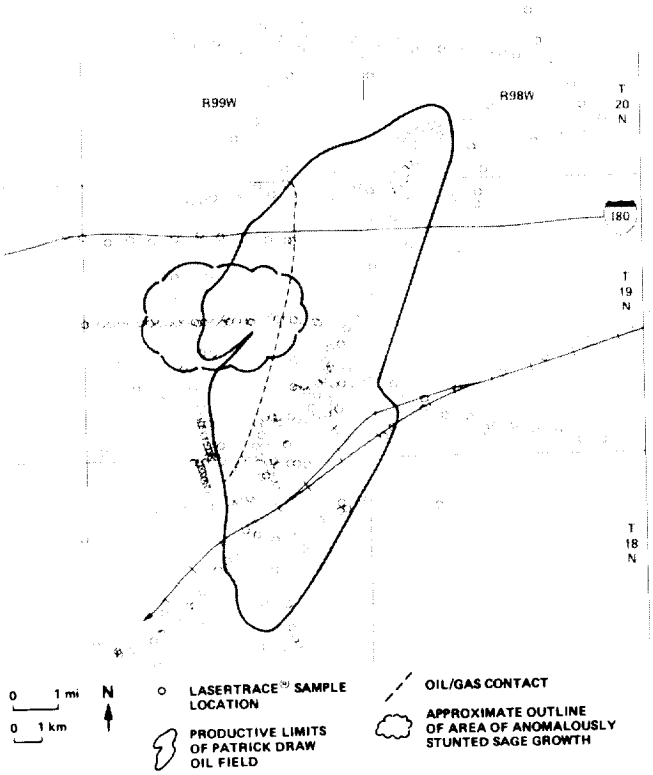

Figure 11-30. Index map showing the locations of sites sampled in soil elemental geochemistry survey

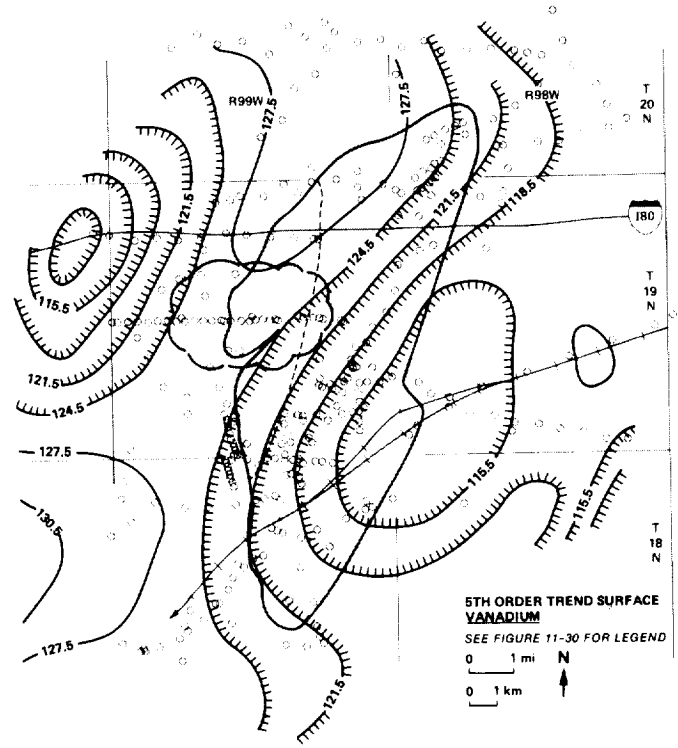

Figure 11-32. Soil vanadium concentration map

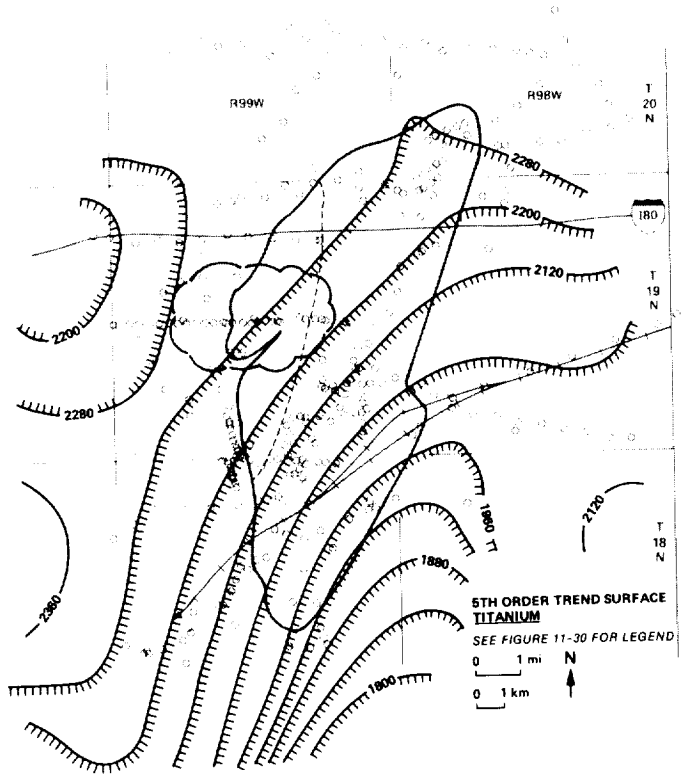

Figure 11-31. Soil titanium concentration map

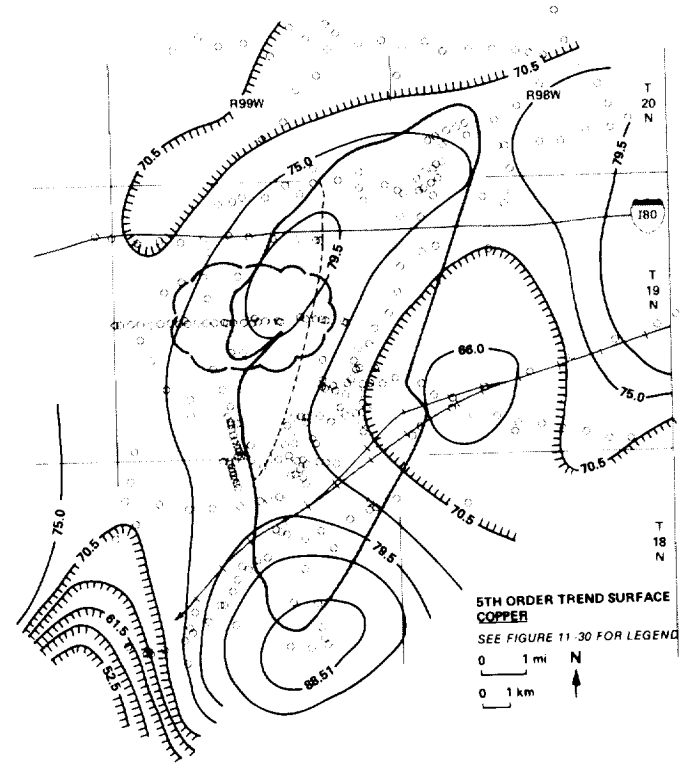

Figure 11-33. Soil copper concentration map

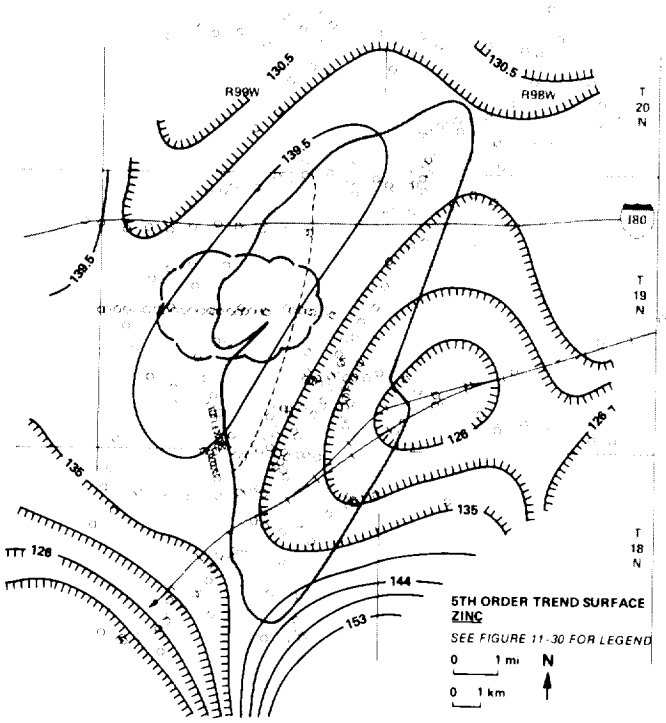

Figure 11-34. Soil zinc concentration map

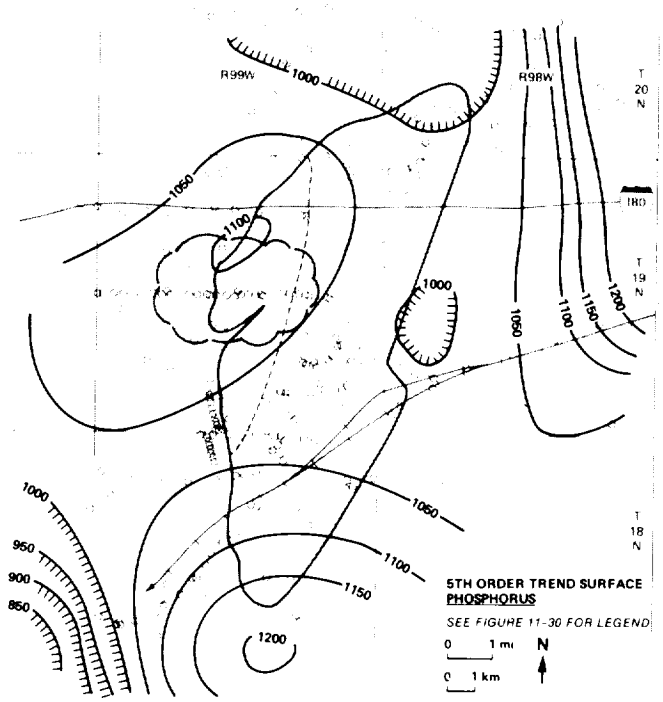

Figure 11-36. Soil phosphorus concentration map

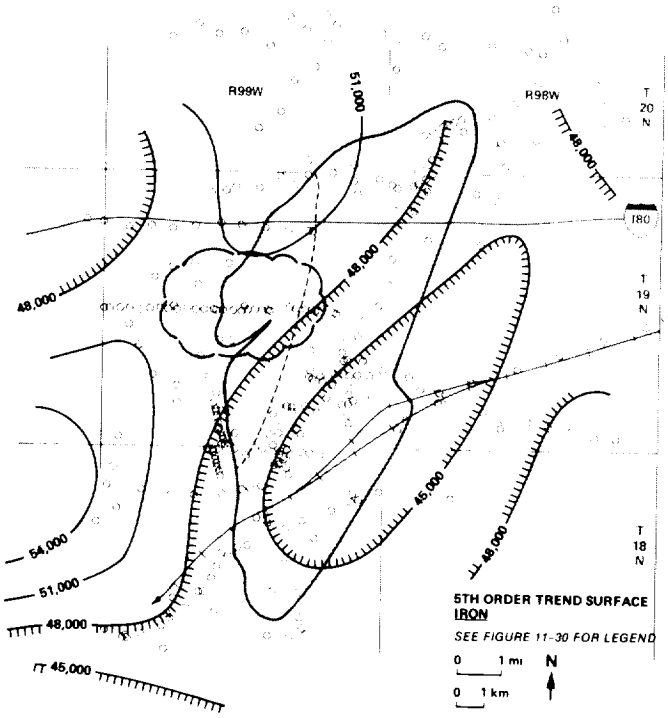

Figure 11-35. Soil iron concentration map

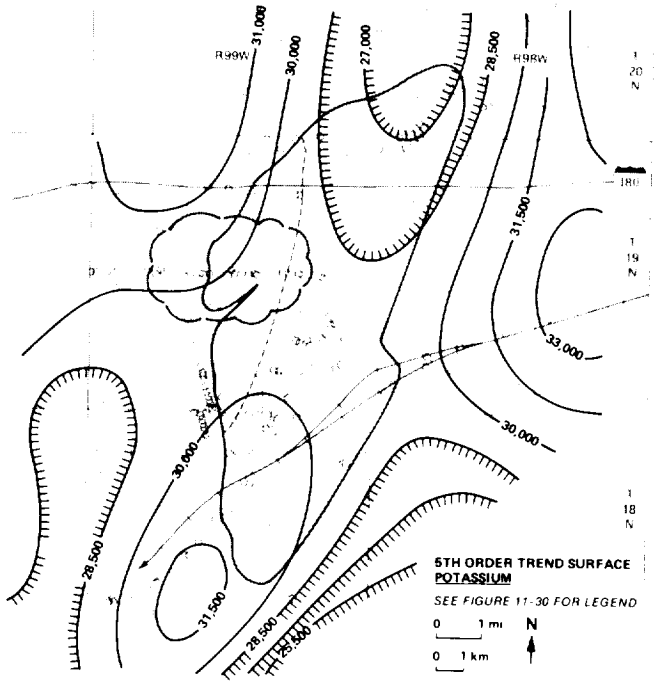

Figure 11-37. Soil potassium concentration map

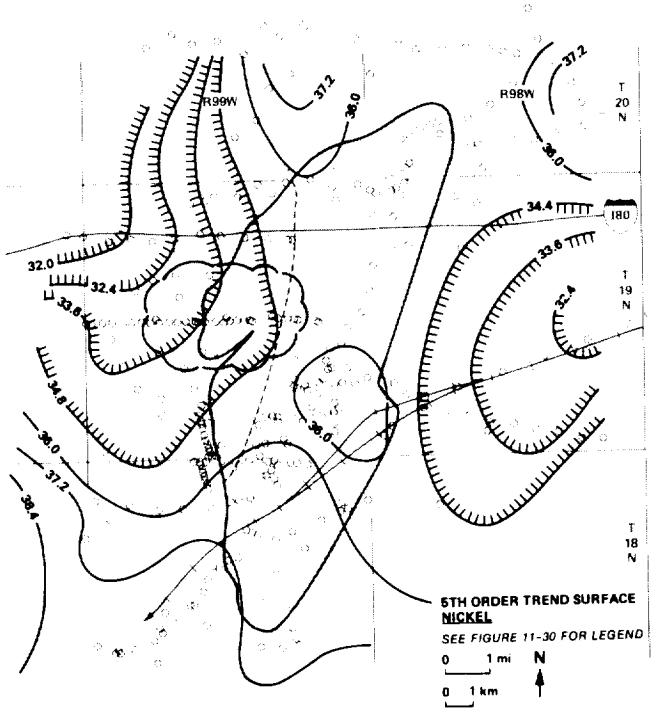

Figure 11-38. Soil nickel concentration map

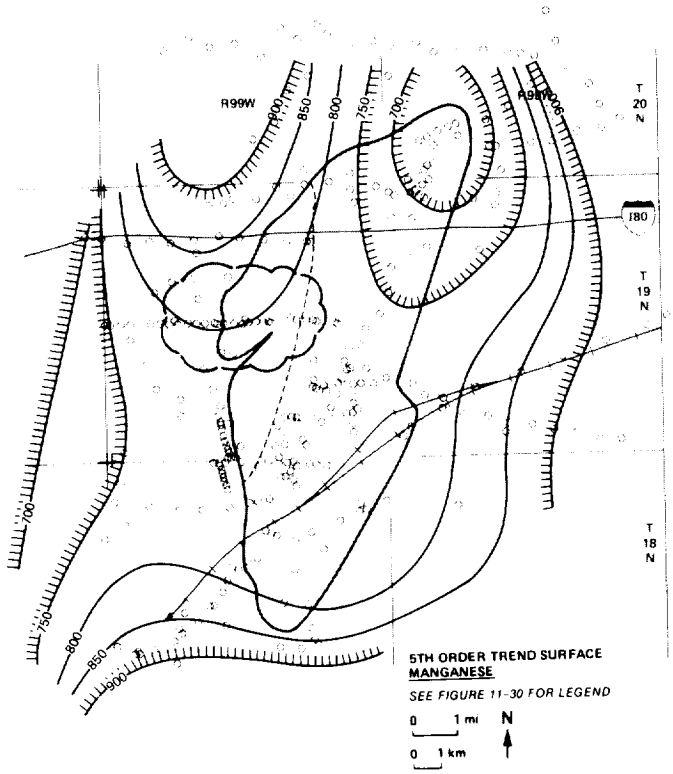

Figure 11-39. Soil manganese concentration map

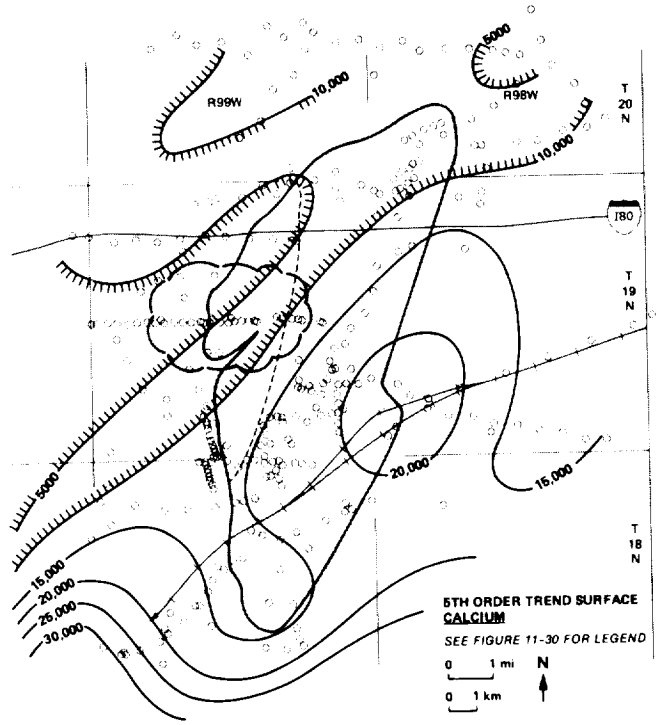

Figure 11-40. Soil calcium concentration map

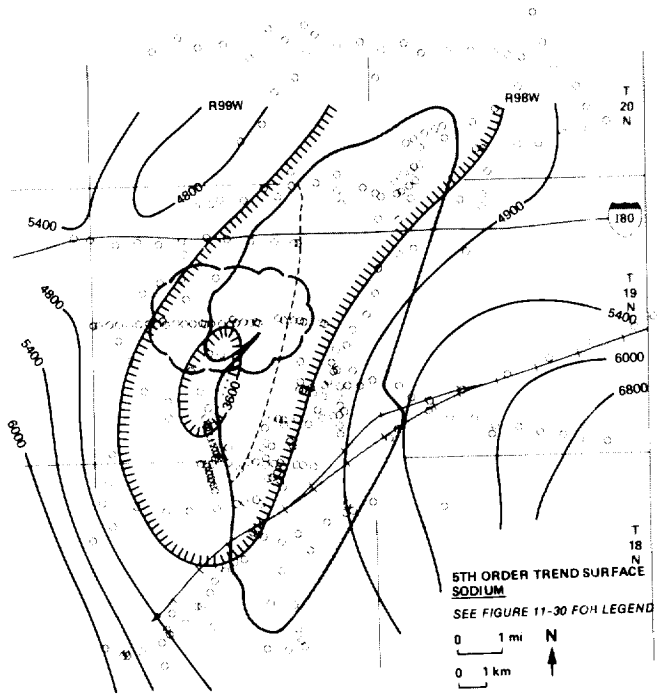

Figure 11-41. Soil sodium concentration map

Low-order (second- or third-order) trend surface maps show a NE–SW trend, which correlates geographically with the contact between the Fort Union and Wasatch Formations. The patterns for high-order (fourth- or fifth-order) trends for some elements, however, appear to correlate with the subsurface distribution of hydrocarbons. Figures 11-31 through 11-41 are examples of selected fifth-order trend surface isopleths in parts per million.

Titanium (Figure 11-31), vanadium (Figure 11-32), copper (Figure 11-33), and zinc (Figure 11-34) all exhibit maximum values in an area of anomalously stunted sage growth that lies above the gas cap of the Patrick Draw reservoir. The concentration of these elements appears to increase in an updip direction from low values east of the field, reaching the highest values near the updip limit of production, before decreasing significantly to the west of the field. A similar trend is exhibited by iron (Figure 11-35), but the locations of the downdip low and updip high are shifted approximately 1.2 km (1 mi) to the west.

Phosphorus (Figure 11-36) shows a maximum concentration in the area of anomalously stunted sage. Potassium (Figure 11-37), nickel (Figure 11-38), and manganese (Figure 11-39) exhibit similar, but less pronounced, maxima.

Calcium (Figure 11-40) and magnesium exhibit minimum concentrations in the area of anomalously stunted sage. Sodium (Figure 11-41) contours show a closed low over the Patrick Draw oil field.

4. Conclusions. Several factors may be responsible for these elemental distributions. Factors include soil variations associated with compositional variations in parent bedrock and chemical/biochemical reactions within the soil. The latter may be directly influenced by hydrocarbon microseepage. The observed anomalies may be indicative of a reducing soil environment created by the presence of hydrocarbon gases in the soil. Metal ions such as copper and zinc tend to form organic complexes and are mobilized in such reducing environments.

Migration of reservoir fluids along faults in the updip area of the Patrick Draw oil field may also be responsible for the direct enrichment of metal ions at the surface. Reservoir pressure may provide the force necessary to move fluids along fractures. These fluids may have high concentrations of metals and gases that are in solution at reservoir pressure and temperature and that are less soluble at surface conditions.

The observed anomalies in soil elemental concentrations over the Patrick Draw oil field are consistent with both direct migration of ions from the reservoir and selective mobilization/immobilization of ions in a gas-enriched soil environment.

F. Soil Carbon and Oxygen Isotope Survey

1. Objective. Hydrocarbons seeping to the surface may be oxidized by certain species of bacteria to ultimately form carbon dioxide and water (Davis, 1967). The carbon dioxide formed may then react with calcium in groundwater to form calcium carbonate, which precipitates and forms calcite cements in near-surface sediments. Calcite resulting from oxidized petroleum may have a distinctive carbon isotope value indicative of the petroleum origin of the carbon. Carbon isotope values for petroleum are considerably more negative than those for carbonates of inorganic origin (Table 11-9).

The concept that carbon isotope values could be used to link the origin of calcite in cemented sandstones to carbon dioxide generated by the oxidation of hydrocarbons was demonstrated by Donovan (1974). His study of the Cement field in Oklahoma demonstrates that microseepage of petroleum occurs over the field and that calcite in cemented sandstones has carbon isotope values which approximate those of petroleum.

Calcite is a common constituent of the soils sampled in the Patrick Draw test site. Carbon isotope values were measured for the calcite in 38 soil samples. A study to determine whether the carbonate resulted from the oxidation of hydrocarbons is described below.

2. Results. Fourteen samples collected during a 1979 field program were analyzed for carbon and oxygen isotope values. Twenty-four additional samples from the 1980 field program were also analyzed. The results for all 38 samples are given in Table 11-10.

Table 11-9. Ranges of carbon isotope values for various natural carbon sources[a]

Source	$\delta^{13}C$ PDB, per mil
Atmospheric CO_2	−7.4 to −6.7
Marine limestone	−4.0 to +4.0
Freshwater limestone	−18.0 to −3.0
Marine plants	−30.0 to −12.0
Terrestrial plants	−29.0 to −23.0
Petroleum	−34.0 to −22.0
Coal	−27.0 to −22.0

[a]From Donovan, 1974.

Table 11-10. Carbon and oxygen isotope measurements of soils collected at the Patrick Draw test site

Year	Sample No.	$\delta^{13}C$ PDB	$\delta^{18}O$ SMOW
1979	A-01	−3.291	19.205
	A-02	−4.825	18.861
	A-03	−5.837	18.285
	A-05	−5.673	18.523
	A-06	−4.530	19.289
	A-07	−3.428	18.166
	B-01	−9.283	10.847
	E-8b	−7.751	19.069
	E-9b	−3.018	21.331
	E-13	−3.169	20.716
	E-20a	0.480	19.427
	Oil-02	−8.754	18.211
	Oil-05	−1.886	20.870
	Dry-12	−4.594	22.259
1980	L1-13	−4.948	16.89
	L2-2	−5.015	18.44
	L3-4	−5.985	22.34
	L3-5	−3.560	15.84
	L3-6	−6.665	18.78
	L4-1	−1.596	18.99
	L4-4	+0.197	16.31
	L5-1	−4.875	15.80
	L5-4	−3.506	17.04
	XL1-6	−4.000	16.08
	XL1-14	−7.198	20.69
	XL2-3	−4.267	20.17
	XL2-4	−0.309	21.57
	LX4-3	−2.379	19.08
	XL4-8	−4.777	18.53
	R1	−2.240	18.55
	R4	−2.307	17.73
	R45	−5.233	15.25
	R47	−2.344	19.66
	R72	−1.977	19.12
	R87	−4.159	18.01
	R95	−4.835	18.66
	R97	−2.236	21.28
	R100	−0.376	16.19

The carbon and oxygen isotopes were measured using Pee Dee belemnite (PDB) as a standard. The oxygen isotopes were converted to standard mean ocean water (SMOW) by the formula:

$$\delta^{18}O\ SMOW = 1.03 \times \delta^{18}O\ PDB + 19.5\%$$

In Table 11-10, carbon isotope values are reported according to the PDB standard, and oxygen values according to the SMOW standard.

Carbon and oxygen isotope values from the Patrick Draw area are plotted on Figure 11-42. This figure also shows the values reported over Cement field by Donovan (1974). Approximate ranges for carbon and oxygen isotopes for a variety of carbonate sources are also plotted on the figure.

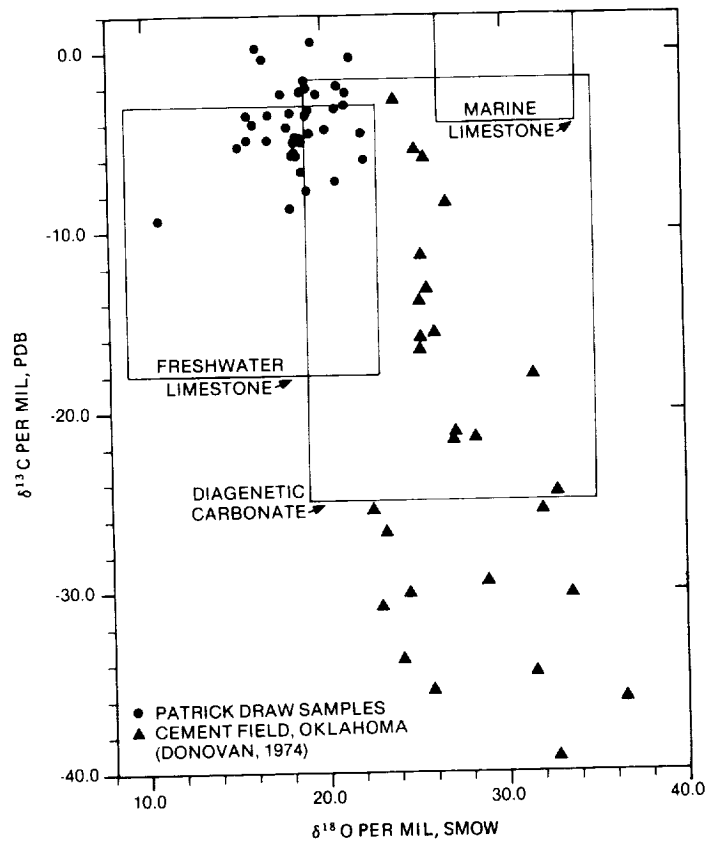

Figure 11-42. Plot of $\delta^{13}C$ versus $\delta^{18}O$ for soil carbonates from Patrick Draw, Wyoming. Values for carbonate cements from the Cement field, Oklahoma, are related to petroleum microseepage. Compositional limits of marine and freshwater limestones and diagenetic carbonates are shown for reference (Donovan, 1974).

Carbon isotopes from carbonates in the soils of the Patrick Draw area are all found to be heavier (more positive) than −10 per mil. This indicates that little, if any, of the carbonate has resulted from the oxidation of hydrocarbons. In contrast, 16 of the 27 samples measured by Donovan for the Cement field have carbon isotope values lighter (more negative) than −20 per mil. Carbon isotope values this light indicate a substantial contribution of isotopically light carbon resulting from the oxidation of petroleum. It has been concluded that there is no positive evidence of petroleum microseepage in the carbon isotope data from soil carbonates in the Patrick Draw area.

The possibility that the soil carbonate resulted from two or more origins must also be considered. If the carbonate contained only a small contribution from oxidized hydrocarbons, then the carbon isotope values would reflect only a slight negative shift from the values associated with the major source of the carbonate. Therefore, in areas with a higher rate of hydrocarbon seepage, the carbon isotopes of

the carbonate might be more negative if the hydrocarbons are being oxidized and incorporated into the carbonate. In order to test this possibility, the carbon isotope values were plotted versus the quantity of methane measured in the soil samples. Soil hydrocarbon content was measured only on the samples taken during the 1980 field season and is reported in Paragraph VII.C.

Figures 11-43, 11-44, and 11-45 show the carbon isotope values versus methane content for the adsorbed soil gas, absorbed soil gas, and free soil gas measurements. Methane was found to be the dominant hydrocarbon in all three types of hydrocarbon measurements. Also, the ethane, propane, and butane concentrations follow the same trend as methane in most of the samples analyzed, so that the methane concentration should be a sufficient indicator of hydrocarbon leakage rates.

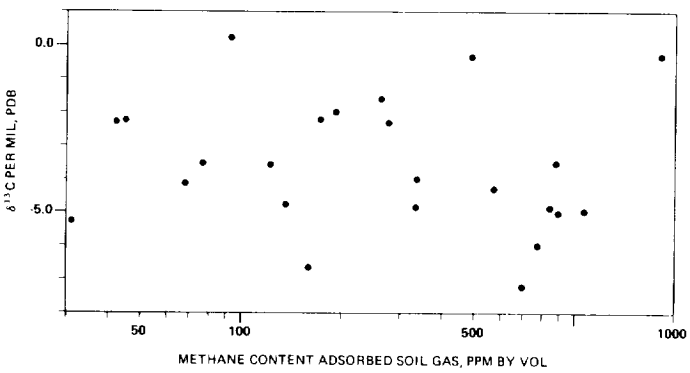

Figure 11-43. Carbon isotope values versus methane content measured in adsorbed soil gas

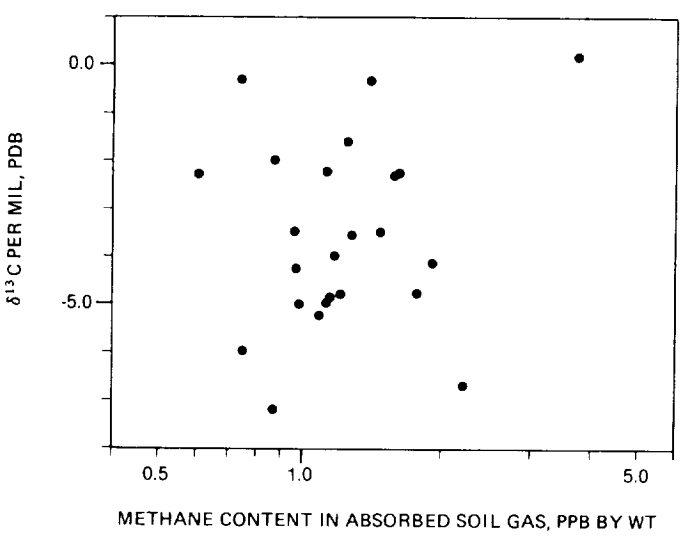

Figure 11-44. Carbon isotope values versus methane content measured in absorbed gas

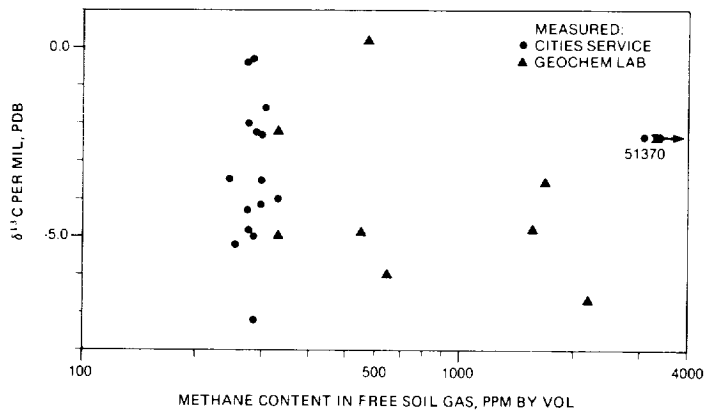

Figure 11-45. Carbon isotope values versus methane content measured in free soil gas

No consistent relationship was found between the carbon isotope values and the hydrocarbon content of the soil gas. This finding indicates that either hydrocarbons are not being oxidized and thus are not contributing to soil carbonate or, if they are, the amount is very minor compared to other sources for the carbonates. The source of the carbonate in the soils appears to be that of a freshwater limestone or caliche. Detrital carbonate from limestone in the Fort Union, Wasatch, and Green River Formations probably contributes carbonate with a freshwater carbon isotope signature to the residual soils.

Figure 11-46 shows the distribution of the carbon isotope values and the oil and gas field boundary. The data were not contoured because the sample distribution was irregular. There does not appear to be any consistent trend in the carbon isotopes and their distribution with respect to the field boundary.

3. Conclusions. Carbon isotope values measured for soil carbonates from the Patrick Draw area indicate either a caliche or detrital freshwater limestone origin for the carbonates. There is no isotopic evidence for hydrocarbon microseepage as was seen by Donovan (1974) over the Cement field in Oklahoma.

VIII. Multispectral Remote Sensing Data

A. Introduction

Multispectral remote sensing data acquired during the test site investigation included Landsat MSS four-band data as well as aircraft NS-001 Thematic Mapper Simulator eight-band and Bendix Modular Multispectral Scanner (M²S) 11-band data. Additionally, color photography was acquired

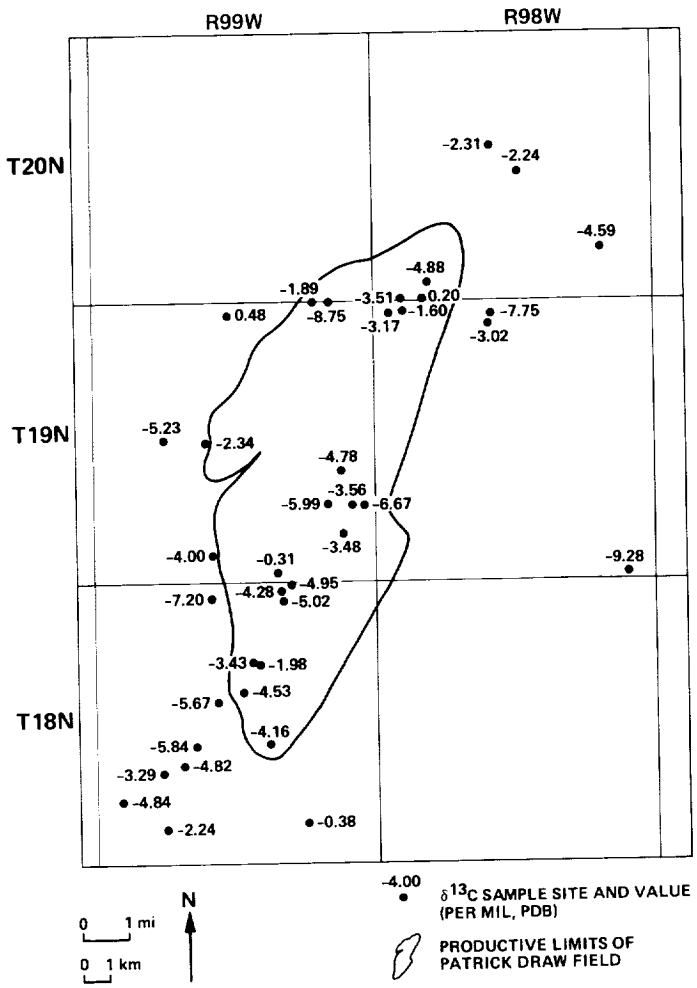

Figure 11-46. Distribution of carbon isotope values (per mil, PDB) in the vicinity of Patrick Draw oil field

during aircraft overflights. All aircraft data were acquired by the NASA–Johnson Space Center. The acquisition dates and selected characteristics of these data are summarized in Tables 11-11 and 11-12. For a discussion of sensor characteristics, refer to the Technical Appendix, Section 14. Flight-line locations and areal coverage for aircraft-acquired data are illustrated in Figure 11-47.

1. Preliminary processing. Preliminary processing of all aircraft-acquired multispectral data was carried out by JPL's Image Processing Laboratory (IPL). A complete list and description of IPL programs used in processing these data is included in the Technical Appendix, Section 14.

During the investigation, JPL retained the master sets of both digital and film data. JPL distributed copies of these data sets to two participating companies for further distribution to other member companies. CONOCO distributed digital data and Gulf distributed image prints.

Table 11-11. Summary of Landsat MSS data, Patrick Draw test site

Date Acquired	Scene Identification
September 15, 1973	1409-17294
September 18, 1974	10787-17195
May 13, 1976	20477-17133

Table 11-12. Summary of aircraft multispectral data, Patrick Draw test site

Date Acquired	Mission	Photography	Multispectral Scanner[a]
August 4, 1978	383	True color	M^2S
October 19, 1978	390	True color	NS-001
August 28, 1979	407	Color infrared	NS-001

[a] Instantaneous field of view for all data is ~15 m.

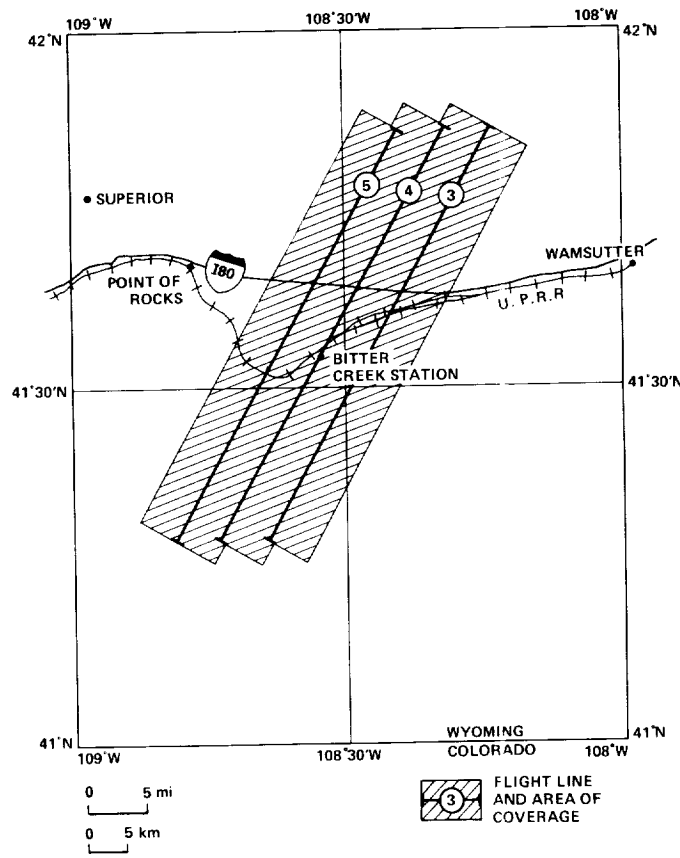

Figure 11-47. Map showing flight-line locations and areal coverage for M^2S, NS-001, and color photographic aircraft data acquired. The area covered by line 4 includes the entire Patrick Draw test site area

2. Interpretation. The multispectral data were processed mainly by JPL and, to a lesser extent, by Gulf Science and Technology and by the University of Wyoming. Analysis and interpretation of the data were performed by all test site team members in group sessions or independently. Because of constraints of personnel, time, and image processing facilities, all remote sensing data sets were not evaluated equally. The greatest analytical attention was given to data that, upon initial examination, demonstrated the greatest potential utility.

NS-001 data acquired on Mission 390, line 4 (Table 11-12, Figure 11-47, and Plate 11-1) were evaluated in the greatest detail. These were the only aircraft multispectral data that were geometrically rectified and registered to a 1:48,000 USGS topographic base. Aircraft data were most commonly interpreted at a scale of 1:48,000; Landsat MSS data at a scale of 1:500,000 or 1:200,000.

The purpose of the multispectral image analysis was to evaluate the utility of these data for hydrocarbon exploration, specifically geologic mapping and the detection of potential microseepage-induced alteration of surface material. The approach used in the analysis of the multispectral data is reflected in the following discussions, which include (1) Landsat MSS data for reconnaissance geologic mapping, (2) spectral characteristics of cover types, and (3) NS-001 image analysis for tonal/textural interpretation, and geologic, lineament, and vegetation mapping.

B. Landsat MSS Data in Reconnaissance Mapping

The utility of Landsat MSS data for mapping major geological features has been well documented (Goetz and Rowan, 1981). The analysis of over 25 Landsat images produced from MSS data acquired on three dates (Table 11-11) supports this observation. At the 1:500,000 or 1:200,000 scale, Landsat MSS image analysis reveals all major structural and stratigraphic units mapped in the test site area. A comparison of the regional published geologic map (Figure 11-48) to a Landsat MSS image (Figure 11-49) illustrates this conclusion. Previously unmapped faults (expressed as linear features or "lineaments"), extensions of previously mapped faults, and unmapped subdivisions of previously mapped stratigraphic units (expressed as bedding-parallel tonal units) may also be delineated in this Landsat MSS image.

C. Spectral Characteristics of Cover Types

1. Introduction. In a series of papers published between 1970 and 1976, Hunt and Salisbury as well as Hunt et al. reported the visible and near-infrared (VNIR) laboratory spectral characteristics of many rocks and minerals. Their work demonstrated the potential utility of VNIR multispectral remote sensing for the discrimination and identification of geological materials. To apply the general empirical and theoretical results of Hunt and Salisbury to the specific problem of VNIR multispectral image enhancement and interpretation at Patrick Draw, a program of field and laboratory spectral measurements and mineralogical analyses was conducted in the test site area. The spectral analysis program emphasized the part of the VNIR spectrum sensed by the NS-001 aircraft scanner so that the potential utility of the Landsat 4 Thematic Mapper (TM) satellite sensor, which the aircraft scanner was designed to simulate, could be evaluated (Table 11-13).

This spectral analysis program included (1) Beckman DK2A spectrophotometer laboratory measurements for samples obtained from 149 sample sites, (2) 260 field reflectance measurements obtained from 60 sites, using JPL's Portable Field Reflectance Spectrometer (PFRS) (Goetz et al., 1975, and the Technical Appendix, Section 14), and (3) 27 Perkin Elmer 330 spectrophotometer laboratory measurements on plant specimens obtained at 10 sites. Additionally, laboratory X-ray diffraction (XRD) mineralogical analysis was performed on 37 samples selected from the field and laboratory sample suite.

Plate 11-3 shows the locations of all field and laboratory spectral and mineralogical sample sites. The site locations and materials sampled at each site were selected to include the major surface cover types of the test site area, including natural vegetation and soil/rock, and materials introduced by man. The results of this investigation are summarized below; only those spectra considered illustrative of significant relationships are included.

2. Spectral characteristics of vegetation. Vegetation covers from 5 to 60 percent of the Patrick Draw test site. Data acquired by the NS-001 multispectral scanner are significantly affected by this vegetation. Knowledge of the spectral characteristics of vegetation is therefore essential information for enhancing and interpreting multispectral images of the test site area.

Figure 11-50 includes typical PFRS reflectance spectra for vegetation (7G, 8F, and E11) and shows the locations of the seven NS-001 VNIR bands. Five of these band locations (1, 2, 3, 4, and 6) were selected specifically for the identification of vegetation species, vigor, and density (Hovis et al., 1975, p. G-7). The significant spectral features for vegetation that occur in the seven VNIR bands of the NS-001 scanner are briefly described below. These observations are summarized from discussions by Hovis et al. (1975), Salomonson et al. (1980), and Weirsma and Landgrebe

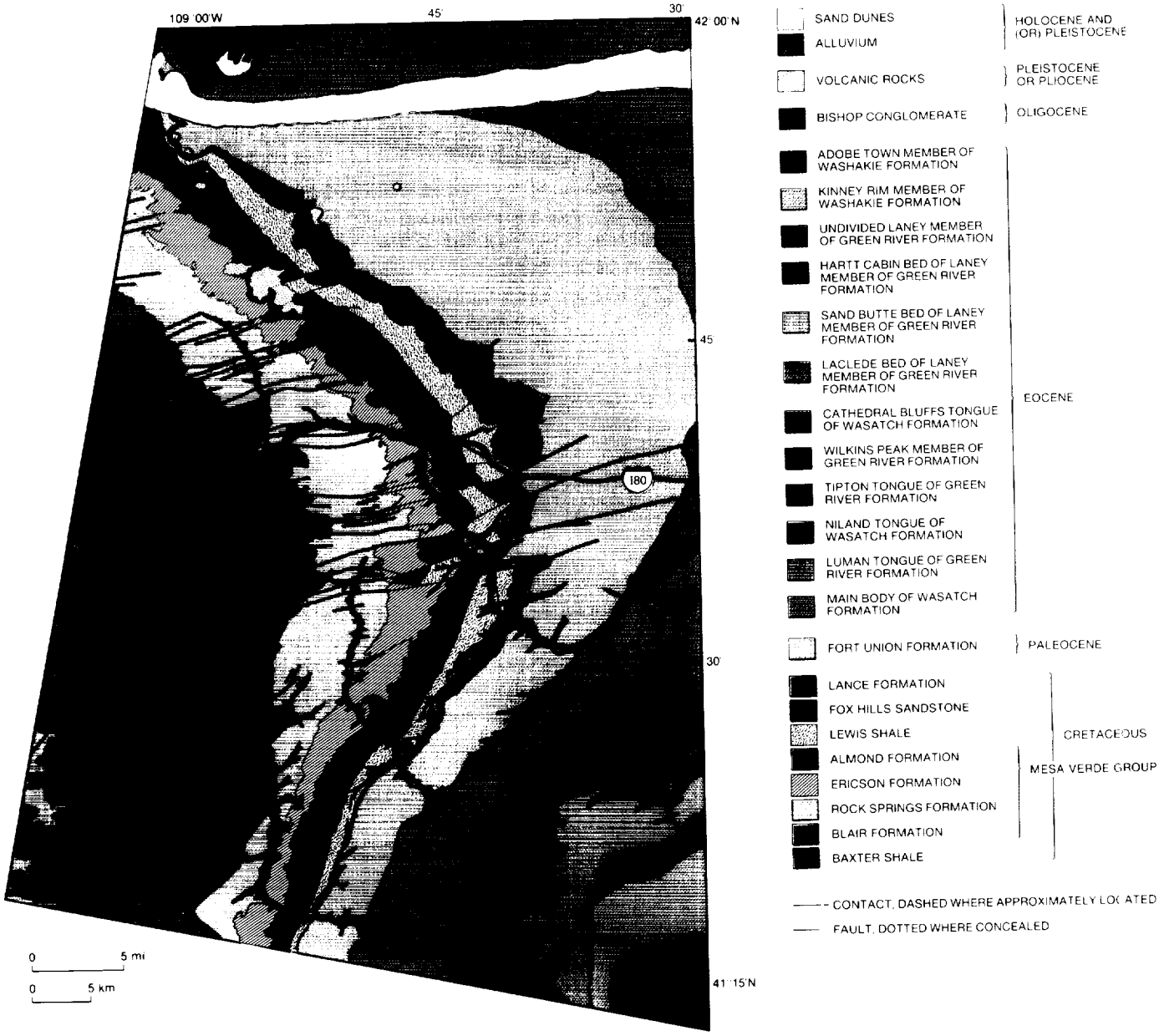

Figure 11-48. Portion of a published geologic map for the Rock Springs Uplift (Roehler, 1977a) that is shown in the Landsat MSS subscene, Figure 11-49

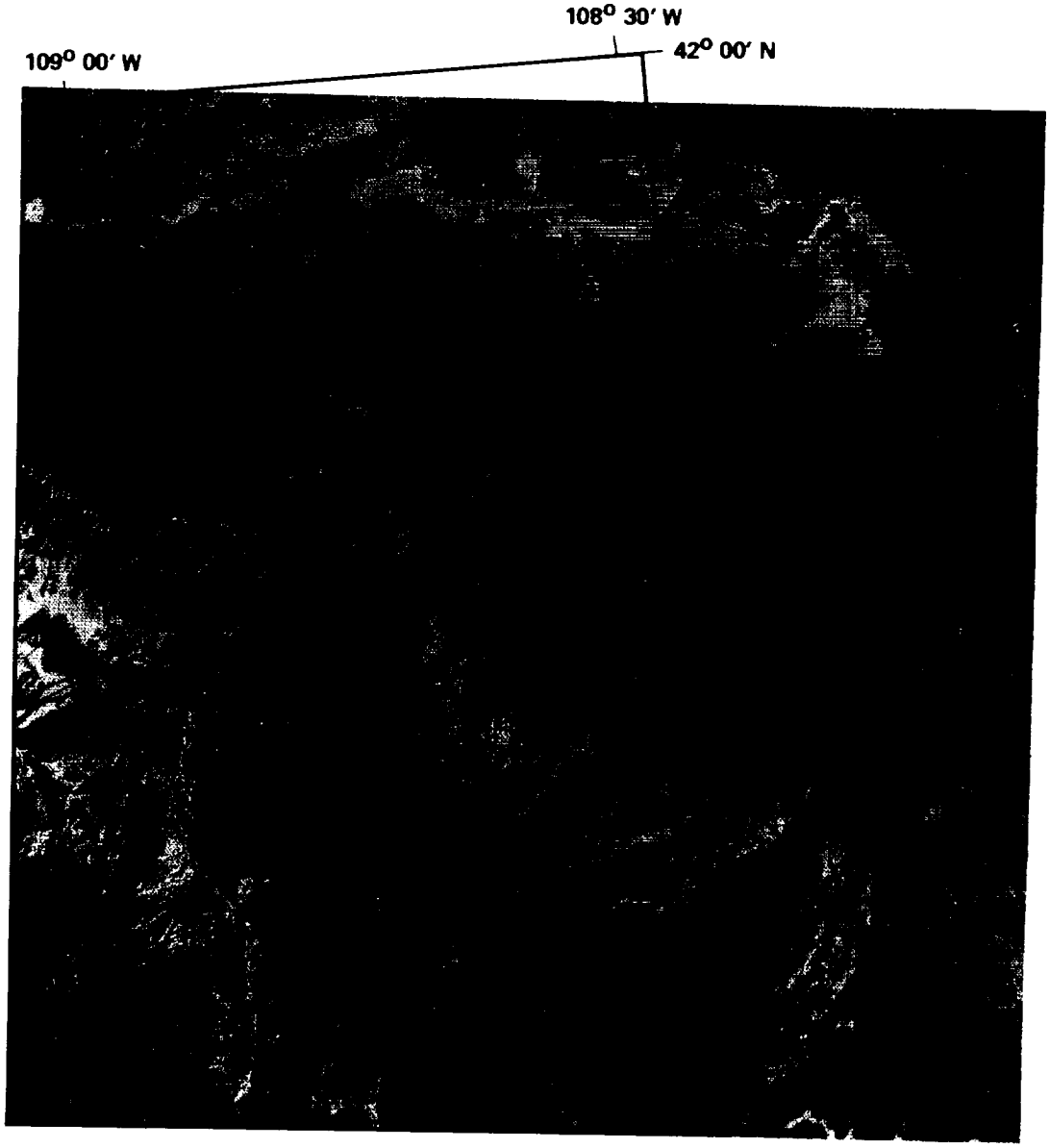

Figure 11-49. Landsat MSS image produced using a principal components stretch (VICAR, PGSTR): band 4, blue; band 5, green; and band 7, red (acquired May 13, 1976). A comparison of this image to Figure 11-48 clearly demonstrates that all geologic features of regional importance are discernible in the Landsat MSS image. All major faults and stratigraphic contacts may be delineated; additionally, unmapped stratigraphic contacts (expressed as tonal/textural boundaries) and possible unmapped faults and extensions of mapped faults (expressed as lineaments) may also be recognized. Solid outline shows area of geologic map (Figure 11-48); dashed outline is area covered by aircraft-acquired multispectral data, line 4.

C-2

Table 11-13. NS-001 Thematic Mapper Simulator

Band	Wavelength Interval, μm	Approximate Channel Center, μm	Equivalent Landsat 4 TM Band
1	0.45–0.52	0.49	1
2	0.52–0.60	0.56	2
3	0.63–0.69	0.66	3
4	0.76–0.90	0.83	4
5	1.00–1.30	1.15	None
6	1.55–1.75	1.65	5
7	2.08–2.35	2.22	7
8	10.4–12.5	11.5	6

(1980), and from analysis of laboratory and PFRS vegetation spectra obtained by JPL.

Band 1 (0.45–0.52 μm). Centered at approximately 0.49 μm, this band includes the visible blue; contains absorption features due to chlorophyll and carotinoid concentrations; useful for differentiating conifers and deciduous vegetation.

Band 2 (0.52–0.60 μm). Centered at approximately 0.56 μm, this band includes the visible green; contains a reflectance peak due to chlorophyll concentration; sensitive to green pigmentation in healthy vegetation and, therefore, useful for the assessment of vegetation vigor.

Band 3 (0.63–0.69 μm). Centered at approximately 0.66 μm, this band includes the visible orange and red; contains a maximum chlorophyll absorption band; useful for species differentiation.

Band 4 (0.76–0.90 μm). Centered at approximately 0.83 μm, this band contains a reflectance peak sensitive to leaf area, vegetation density, and biomass; useful for species identification.

Band 5 (1.00–1.30 μm). Centered at approximately 1.15 μm, this band contains several diagnostic absorption bands; sensitive to leaf area.

Band 6 (1.55–1.75 μm). Centered at approximately 1.65 μm, this band is located within an absorption feature characteristic of leaf water-mass.

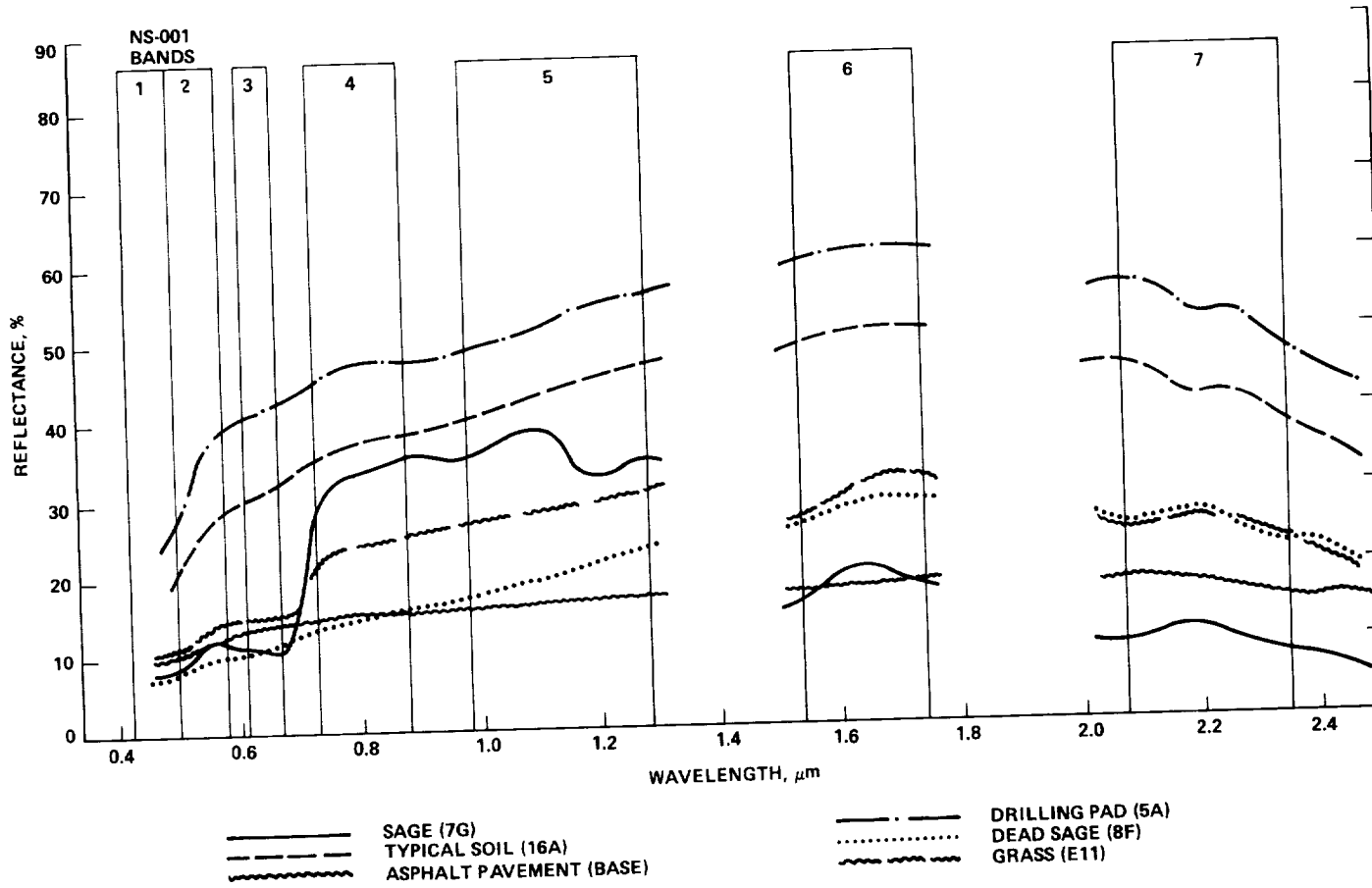

Figure 11-50. Examples of field spectra for major cover types, Patrick Draw test site. Spectra acquired at locations shown in Plate 11-3 using JPL's PFRS.

Band 7 (2.08–2.35 μm). Centered at approximately 2.22 μm, this band is located within an absorption feature characteristic of leaf water-mass.

A comparison of the vegetation and soil spectra shown in Figure 11-50 demonstrates that the reflectance values in all bands are typically higher for soil than for vegetation. Spectra for vegetation and soil exhibit the greatest disparity in bands 6 and 7, and the least disparity in bands 4 and 5. Maximum reflectance values typically occur in bands 4 or 5 for vegetation and in bands 6 or 7 for soils. In some cases, the reflectance of vegetation in bands 4 or 5 may exceed the reflectance of soil.

The shadow of plants will contribute to the lowered albedo of vegetated terrain. The dominant vegetation type at Patrick Draw is sage. Associated with each bush, except for the situation of vertical solar elevation or 100 percent sage cover, is a shadow. The spectral effect of this vegetation-shadow component is illustrated by the two PFRS spectra shown in Figure 11-51. These spectra indicate a 13 percent decrease in albedo for typical Patrick Draw soil in a sage shadow. The significance of this effect is illustrated by the observation that a surface with 80 percent sage cover (1-m bushes with 1-m spacing) and a 60° solar elevation (typical for the time of NS-001 acquisition at Patrick Draw) will be seen by an aircraft or satellite sensor as 100 percent sage and sage-shadow cover.

The relative spectral contribution of plant material and plant shadow is dependent on both plant density (percent cover) and plant geometry. In the case of Patrick Draw vegetation, there are two distinct plants in terms of geometry: sage and grass. Because of the broader leaf area of sage compared with grass (as viewed from above by a sensor), dense sage should have a smaller shadow component compared with dense grass cover in conditions of near-vertical illumination. This should result in lower albedo and less distinct carotinoid, chlorophyll, and leaf-water spectral features for dense grass cover compared with sage. This relationship is illustrated by comparing the PFRS spectra of dense green grass (E11) to that of green sage (7G) in Figure 11-50.

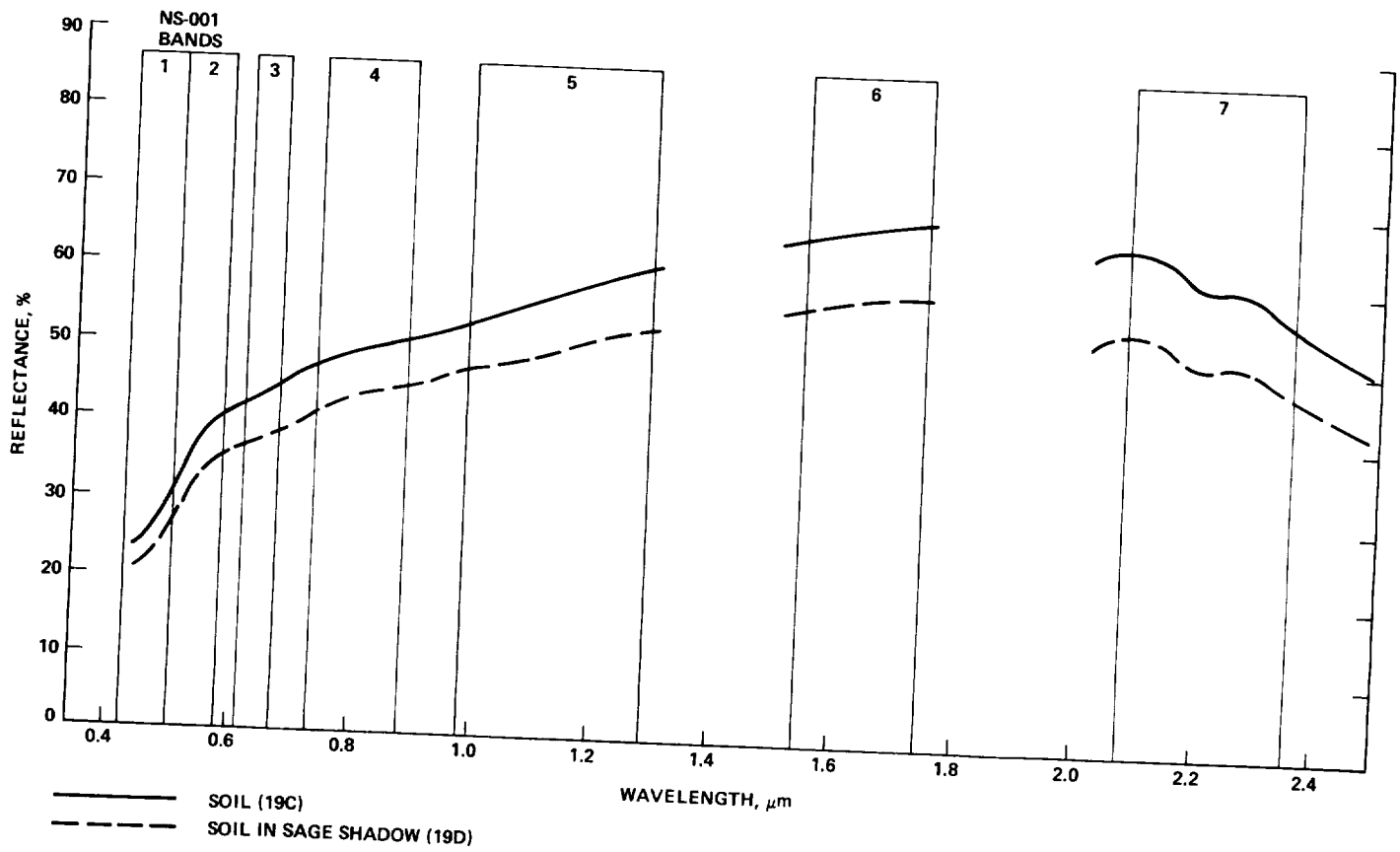

Figure 11-51. Comparison of the PFRS field spectra for typical soil and the same soil in shadow

3. Spectral characteristics of soil/rock

a. Mineralogy. The laboratory spectral measurements of Hunt and Salisbury as well as Hunt et al. (1970 to 1976) demonstrated that many minerals have spectral absorption bands in the VNIR that are caused by crystal lattice electronic and vibrational processes which are related to composition. To establish which minerals in the multimineralic soils and clastic sedimentary rocks exposed in the Patrick Draw test site have spectral absorption features capable of affecting NS-100 sensor response, a mineralogical and spectral analysis investigation was conducted.

Table 11-14 lists the minerals identified in XRD analyses of 37 selected surface samples from the Patrick Draw test site. This suite of 21 minerals is considered to represent the major mineral constituents of the soils and rocks exposed in the test site area. Sixteen of the minerals listed in Table 11-14 are characterized by absorption bands in that portion of the VNIR spectrum measured by the NS-001 scanner. Figure 11-52 is a composite diagrammatic laboratory spectrum showing the locations and relative depths of major absorption bands identified in 149 DK2A laboratory spectra. The locations of the seven NS-001 VNIR bands are also shown as a guide for the prediction of the response of this sensor to some of the minerals listed in Table 11-14.

Table 11-14. Mineralogy of Patrick Draw soil/rock determined by XRD analysis of 37 representative surface samples

Mineral	Formula
Albite[a]	$NA(AlSi_3O_8)$
Alunite	$KAl_3(SO_4)_2(OH)_6$
Biotite	$K(MgFe)_3(AlSi_3O_{10})(OH)_2$
Calcite	$CaCO_3$
Chlorite	$(MgFeAl)_6[(AlSi)_4O_{10}](OH)_2$
Fluorapatite[a]	$Ca_5(PO_4)_3F$
Goethite	$FeO(OH)$
Gypsum	$Ca(SO_4) \cdot 2H_2O$
Hematite	Fe_2O_3
Hornblende	$Ca_4Na_2(MgFe)_8(AlFe)_2(Al_4Si_{12}O_{44})(OH,F)_4$
Illite	$K(Al_4 \cdot Fe_4 \cdot Mg_4 \cdot Mg_6)(AlSi_7O_{20})(OH)_4$
Jarosite	$KFe(SO_4)_3(OH)_6$
Kaolinite	$Al_2(Si_2O_5)(OH)_4$
Microcline[a]	$K(AlSi_3O_8)$
Montmorillonite	$X(AlMg)_2[(AlSi)_4O_{10}](OH)_2$
Muscovite	$KAl_3(AlSi_3O_{10})(OH)_2$
Plagioclase[a]	$(CaNa)[(AlSi)_4O_8]$
Pyrite	FeS_2
Vermiculite	$Mg_3(Si_4O_{10})(OH)_2 \cdot H_2O$
Quartz[a]	SiO_2
Siderite	$FeCO_3$

[a]Mineral without absorption features in NS-001 bands.

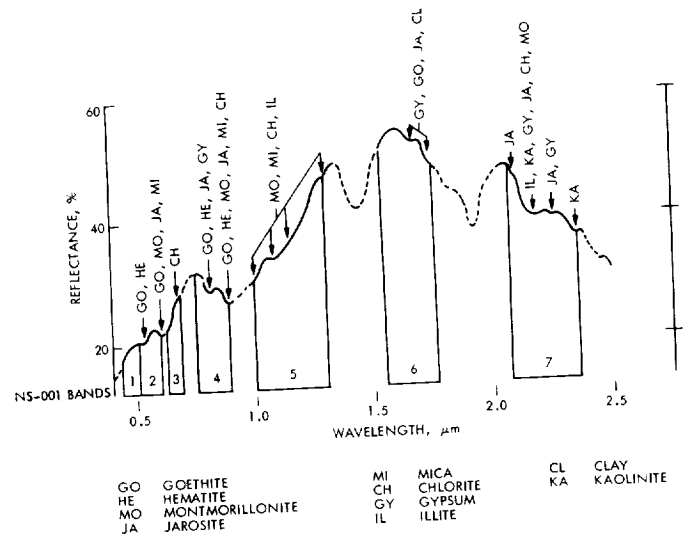

Figure 11-52. Composite diagrammatic laboratory spectrum illustrating major mineral absorption bands affecting NS-001 data. Absorption feature identifications are after Hunt and Salisbury as well as Hunt et al. (1970 to 1976).

Of the samples analyzed at Patrick Draw, only five ions, radicals, and molecules—Fe^{+2}, Fe^{+3}, HOH, OH , and CO_3^{-2}—cause the absorption features shown in Figure 11-52. A review of the chemical formulas of minerals listed in Table 11-14 and consideration of the multimineralic nature of Patrick Draw soil and rock demonstrate that unique mineral identification is almost impossible using spectral reflectance data from the seven NS-001 VNIR channels alone. Furthermore, comparison of the depths and locations of absorption bands shown in Figure 11-52 to the depths and locations of absorption features associated with vegetation (Figure 11-50; 7G, 8F, and E11) demonstrates the significant potential for confusion in the analysis of the spectra of mineral and vegetation mixtures. This observation is consistent with the conclusion of Siegal and Goetz (1977, p. 195) in their modeling of the spectral response of soil/vegetation mixtures:

> Naturally occurring vegetation significantly masks and alters the spectral response of earth materials. The significance of vegetative cover depends primarily on the amount and type of vegetation and the spectral reflectance of the ground.

b. Soil/rock grain size. Variations in soil or rock grain size may result in significant variations in the spectral response of soils and rocks. Grain-size-induced variations in visible spectral response have long been recognized by the hand-specimen mineralogist. Finely powdered material tends to be lighter colored (has higher albedo in the

visible spectrum) than coarse material. This visible albedo effect has been used in the so-called "streak test" of hand-specimen mineralogy. This albedo increase with decreasing particle size was reported by Adams and Filice (1967). They noted that there are also wavelength-dependent changes associated with the decrease in particle size below 0.5 mm (medium sand). They attribute such wavelength-dependent, grain-size-induced changes to the relative contribution of the diffuse and specular component of reflected energy.

Fine particulate materials (<20 μm in diameter, i.e., fine silt and clay) form reflecting surfaces with a larger specular component when compared to coarser materials. Apparently, the Rayleigh criterion for a smooth surface is realized with such particle diameter at higher wavelengths of the VNIR (Beckman and Spizzichino, 1963, p. 9). Less diffuse energy (the absorbed component) is available for interaction within the reflecting material. This results in a decrease in the net amount of incident energy available for absorption and a decrease in the depth of absorption bands characteristic of the material.

The practical significance of these relationships is illustrated in Figure 11-53. Sample 8514, a light-gray clay soil from the central portion of the test site area, was found to be primarily calcite based on XRD and acid digestion. The laboratory spectrum for this sample lacked the characteris-

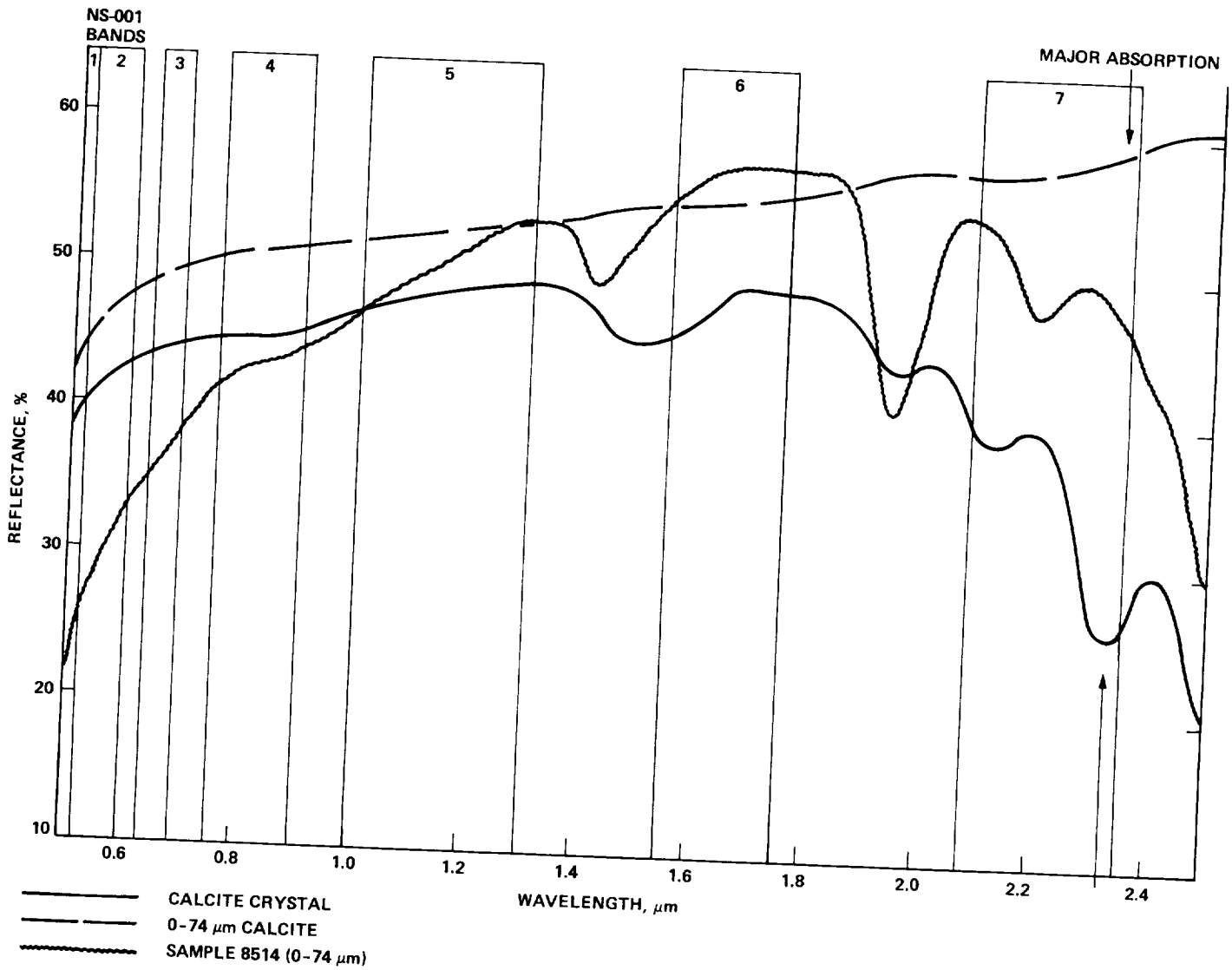

Figure 11-53. Three laboratory spectra illustrating the loss of the calcite absorption band near 2.3 μm when grain size is decreased to <74 μm (fine silt/clay)

tic CO_3^{-2} absorption band near 2.3 μm. Sieve analysis of grain size revealed that this sample was composed of particles <74 μm in diameter (fine silt and clay). Also shown on this figure are the spectra of a calcite crystal and a <74-μm powder obtained from grinding the crystal. Comparison of these curves reveals a loss of the diagnostic calcite absorption band. According to Hunt and Salisbury (1970b, p. 26) this gain-size-dependent phenomenon is most significant for materials with high refractive indices, such as calcite.

D. Equivalent NS-001 Band Reflectance Values Obtained From PFRS Spectra

To evaluate the response of the NS-001 sensor to surficial material in the Patrick Draw test site, PFRS field spectral data were used to determine equivalent NS-001 band reflectance values. This information, in conjunction with laboratory spectral and mineralogical data, may be used as a guide for the optimal enhancement and interpretation of NS-001 raw band images for the test site area.

1. Equivalent NS-001 band values. Equivalent NS-001 band reflectance values were obtained from each of the 260 PFRS spectra. This was accomplished by determining the average interval reflectance for each of the seven NS-001 VNIR bands in each of the 260 PFRS spectra. These data were tabulated and used to determine band reflectance maximum and minimum, band-ratio maximum and minimum, ranges, means, and standard deviations.

Table 11-15 and Figure 11-54 summarize the raw band equivalent PFRS spectra for all field samples, except those for asphalt pavement. Figures 11-55 through 11-59 are photographs of the five PFRS spectral sample sites included in Figure 11-54.

As would be expected from the general relationships described above, maximum reflectance values in all bands occur in a soil spectrum (37A) and minimum reflectance in vegetation (36E, 8F, 7G). The lowest value occurs in band 1 (6.6 percent for sage sample 36E) and the highest value in band 6 (81.6 percent for soil sample 37A). The PFRS spectrum most closely exhibiting the mean value in all seven raw bands is soil sample 16A. The maximum range in values occurs in band 6 and the minimum range in band 1. These relationships predict that the highest NS-001 band values are diagnostic of soil/rock and the lowest values are diagnostic of vegetation.

2. Equivalent NS-001 band-ratio values. A well-established processing technique for recognizing absorption bands in multispectral remote sensing data involves the creation of band-ratio images. Color ratio composite (CRC) images enhance reflectance differences in material and subdue slope effects (Goetz and Rowan, 1981).

To predict the NS-001 band-ratio response of surface material at Patrick Draw, equivalent band-ratio values were calculated using the equivalent PFRS band values described above. This information, in conjunction with laboratory spectral and mineralogical data, may be used as a guide for the optimal enhancement and interpretation of NS-001 ratio images for the test site area.

Table 11-16 and Figures 11-60 and 11-61 summarize the 21 equivalent NS-001 VNIR band-ratio values calculated using the PFRS spectra from Patrick Draw. A maximum ratio value of 3.7 was obtained for band 5/1 in sample 7G (green sage); a minimum ratio value of 0.1 was obtained for band 7/5 in sample 7I. Of the 260 PFRS spectra measured at 60 sites, only five exhibit all maximum ratio values and six exhibit all minimum ratio values.

A review of Table 11-16 reveals that the maximum or minimum values for several ratios are represented by the same samples, e.g., 4B and 36E for band-ratios 2/1 and

Table 11-15. Summary of equivalent NS-001 band reflectance values determined from 260 PFRS field spectra measured at 60 sites

Equivalent NS-001 Band	Approximate Channel Center, μm	Reflectance Value, %, From PFRS Spectra (Sample Number)				
		Maximum	Minimum	Range	Mean	Standard Deviation
1	0.49	42.0 (37A)	6.6 (36E)	35.4	19.1	7.3
2	0.56	53.0 (37A)	7.0 (36E)	46.0	25.7	9.6
3	0.66	58.2 (37A)	7.8 (36E)	50.4	30.4	11.0
4	0.83	63.0 (37A)	15.4 (8F/36E)	47.6	37.7	9.5
5	1.15	70.0 (37A)	18.2 (36E)	51.8	43.3	9.8
6	1.65	81.6 (37A)	17.4 (36E)	74.2	48.6	13.1
7	2.22	77.0 (37A)	10.8 (7G)	66.2	41.4	13.5

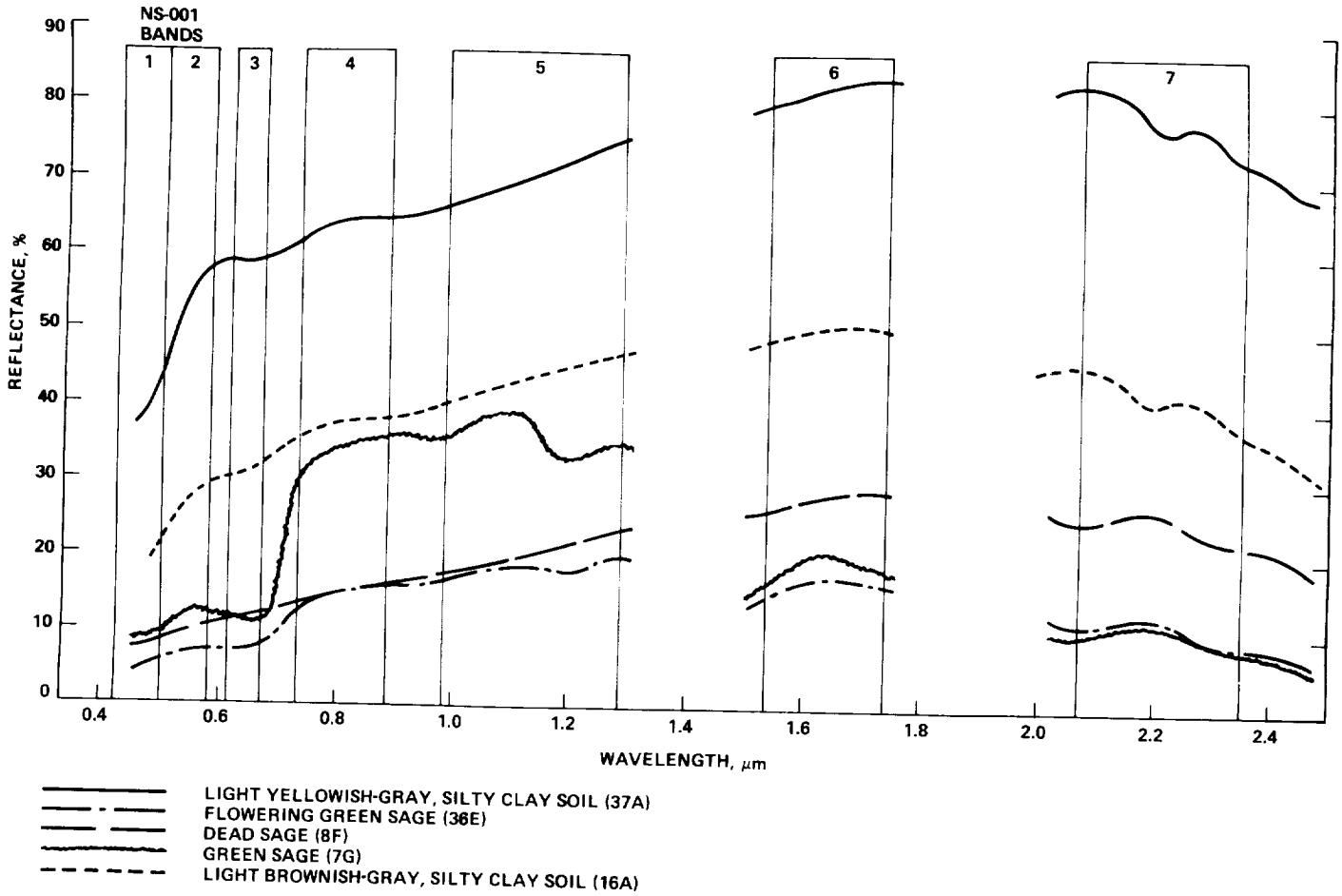

Figure 11-54. PFRS field spectra exhibiting maximum, minimum, and mean equivalent NS-001 band reflectances (see Table 11-15). The spectrum for the light brownish-gray, silty clay soil (16A) exhibits the mean equivalent reflectances in the seven NS-001 VNIR bands. Figures 11-55 through 11-59 are photographs of the sample sites where these spectra were acquired.

3/1, and 8F and 7G for band-ratios 7/3, 5/4, 6/4, 7/4, 6/5, and 7/5. For ratios showing the same samples with minimum and maximum values, the ratio exhibiting the largest range of values is considered most "significant" in terms of its potential usefulness for discriminating among different surface materials. Ratios with minimum or maximum values that do not differ from the mean by more than one standard deviation are not considered significant. On the basis of these two measures of significance and an evaluation of field descriptions and XRD mineralogical analyses of the PFRS samples, the following observations were made:

(1) Band-ratios 2/1 and 3/1 are equivalent; band-ratio 3/1 values are more significant because of the larger range of values. High values occur in reddish-brown, sandy, Fe^{+3}-bearing calcareous and kaolinitic soils of the lower Bitter Creek drainage (4B). Low values occur in sage (36E).

(2) Band-ratios 6/1 and 6/2 are equivalent; band-ratio 6/1 values are more significant because of the larger range of values. High values occur in gypsiferous, quartz-poor soil (34D). Low values occur in micaceous, quartz-rich soil (38E).

(3) Band-ratios 7/1, 7/2, 7/3, 5/4, 6/4, 7/4, 6/5 and 7/5 are equivalent; band-ratio 7/2 values are most significant because of the largest range of values. High values occur in dead sage (8F/G). Low values occur in healthy, green sage (7G/I).

(4) Band-ratio 6/3 exhibits high values in dead sage (8G) and low values in micaceous, quartz-rich soil (38E).

(5) Band-ratio 7/6 exhibits high values in clay-poor, quartz-rich soil (21B) and low values in healthy sage (7G).

Table 11-17 summarizes these relationships.

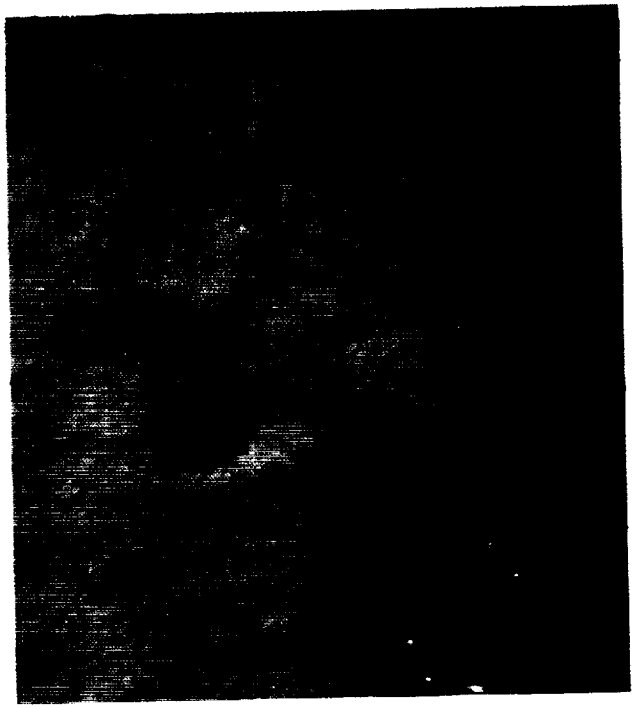

Figure 11-55. Photograph of PFRS field spectrum site 37A, which exhibited the maximum equivalent reflectances of 260 field spectral measurements in all seven NS-001 VNIR bands (see Table 11-15 and Figure 11-54)

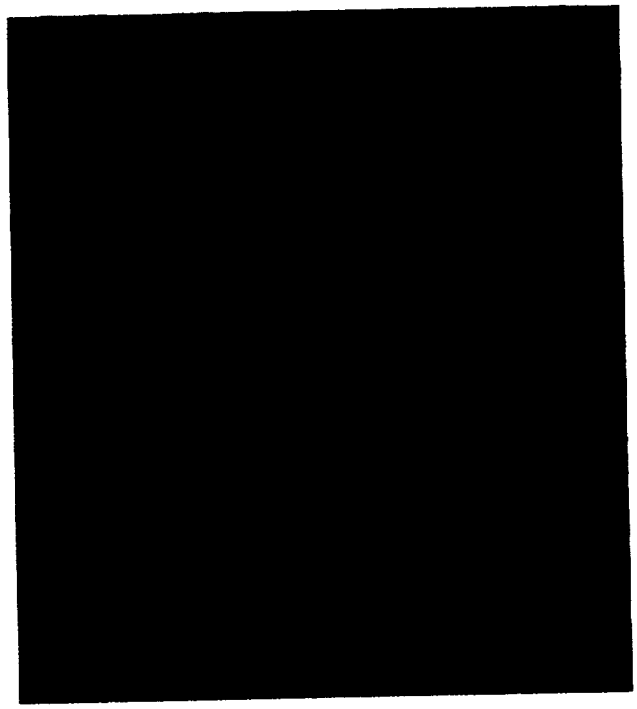

Figure 11-57. Photograph of PFRS field spectrum site 8F, which exhibited the minimum equivalent reflectances of 260 field spectral measurements in NS-001 VNIR band 4 (see Table 11-15 and Figure 11-54). Sage from area of stunted sage is shown.

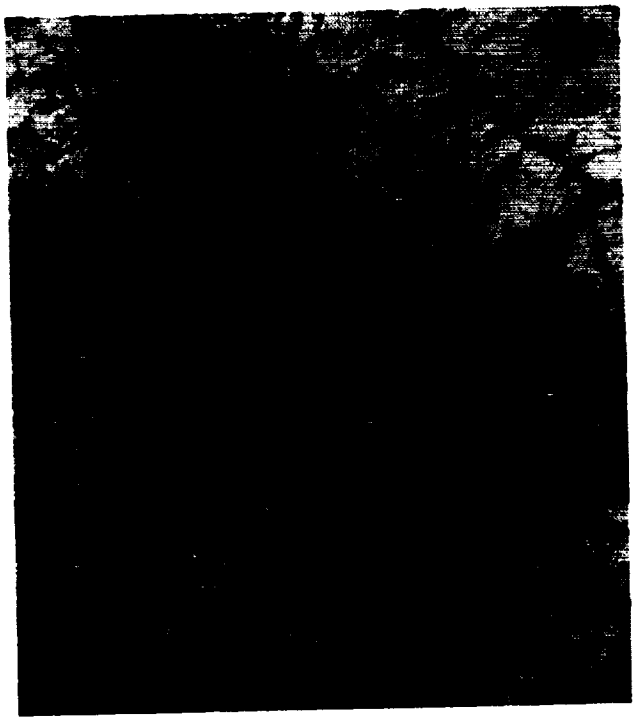

Figure 11-56. Photograph of PFRS field spectrum site 36E, which exhibited the minimum equivalent reflectances of 260 field spectral measurements in NS-001 VNIR bands 1, 2, 3, 4, 5, and 6 (see Table 11-15 and Figure 11-54). Healthy sage is shown.

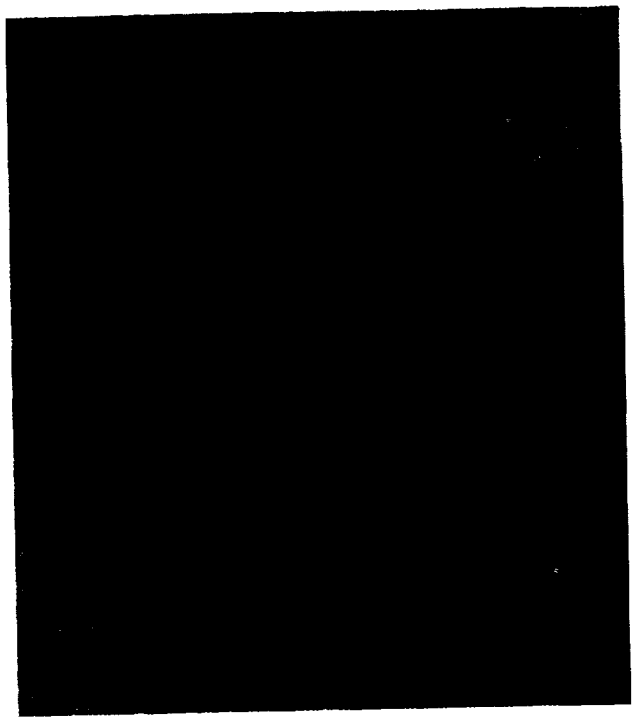

Figure 11-58. Photograph of PFRS field spectrum site 7G, which exhibited the minimum equivalent reflectances of 260 field spectral measurements in NS-001 VNIR band 7 (see Table 11-15 and Figure 11-54)

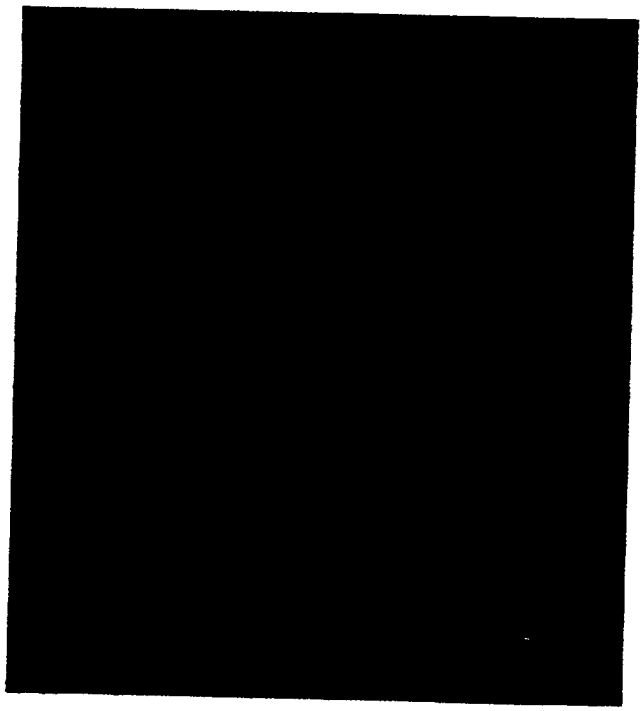

Figure 11-59. Photograph of PFRS field spectrum site 16A, which exhibited the mean equivalent reflectances of 260 field spectral measurements in all seven NS-001 VNIR bands (see Table 11-15 and Figure 11-54)

3. Conclusions. The analysis of PFRS/laboratory spectra for the Patrick Draw test site demonstrates that:

(1) Reflectance values in all seven NS-001 VNIR bands (albedo) tend to be lower in vegetation than in soil or rock.

(2) The most useful spectral information for the characterization of surface material is the location and depth of diagnostic absorption bands. In NS-001 images, such absorption features might best be portrayed by selected band-ratio color composites. An evaluation of equivalent NS-001 band-ratio values obtained from 260 PFRS spectra reveals that only five of the 21 possible NS-001 VNIR band ratios have the greatest potential for discriminating cover materials in the test site area. No ratio values may be uniquely attributed to a single surficial material.

(3) Variation in soil and rock spectra is minimal when compared with soil/rock versus vegetation variations. Spectral variability due to variations in vegetation density mask absorption features attributable to changes in soil/rock mineralogy.

Table 11-16. Summary of equivalent NS-001 band-ratio values determined from 260 PFRS field spectra measured at 60 sites

Equivalent NS-001 Band Ratio	Ratio Value From PFRS Spectra (Sample Number)				
	Maximum	Minimum	Range	Mean	Standard Deviation
2/1	1.7 (4B)	1.1 (36E)	0.6	1.4	0.1
3/1	1.9 (4B)	1.2 (36E)	0.7	1.6	0.2
4/1[a]	3.6 (7G)	1.5 (35F/37A)	2.1	2.2	0.8
5/1[a]	3.7 (7G)	1.6 (35F)	2.1	2.5	0.9
6/1	3.5 (34D)	1.9 (38E)	1.6	2.7	0.5
7/1	3.0 (8F/G)	1.2 (7G)	0.8	2.2	0.4
3/2[a]	1.3 (34D)	1.0 (7G)	0.3	1.2	0.2
4/2[a]	2.9 (7G)	1.1 (35F)	0.8	1.6	0.6
5/2[a]	2.9 (7G)	1.2 (35F)	1.7	1.8	0.6
6/2	2.8 (34D)	1.4 (38E)	1.4	2.0	0.3
7/2	2.5 (8F)	0.9 (7G)	1.6	1.7	0.3
4/3[a]	3.0 (7G)	1.1 (35F)	1.9	1.4	0.6
5/3[a]	3.0 (7G)	1.1 (38E)	1.9	1.6	0.6
6/3	2.4 (8G)	1.3 (38E)	1.1	1.7	0.3
7/3	2.2 (8F)	0.9 (7G)	1.3	1.4	0.2
5/4	1.4 (8G)	1.0 (7G)	0.4	1.2	0.1
6/4	1.8 (8F)	0.6 (7G)	1.2	1.3	0.2
7/4	1.7 (8F)	0.3 (7G)	1.4	1.1	0.3
6/5	1.4 (8F)	0.6 (7G)	0.8	1.1	0.2
7/5	1.2 (8F)	0.1 (7G/I)	1.1	0.9	0.2
7/6	1.0 (21B)	0.6 (7G)	0.4	0.8	0.1

[a]Not considered significant: range of values not more than one standard deviation above and below the mean.

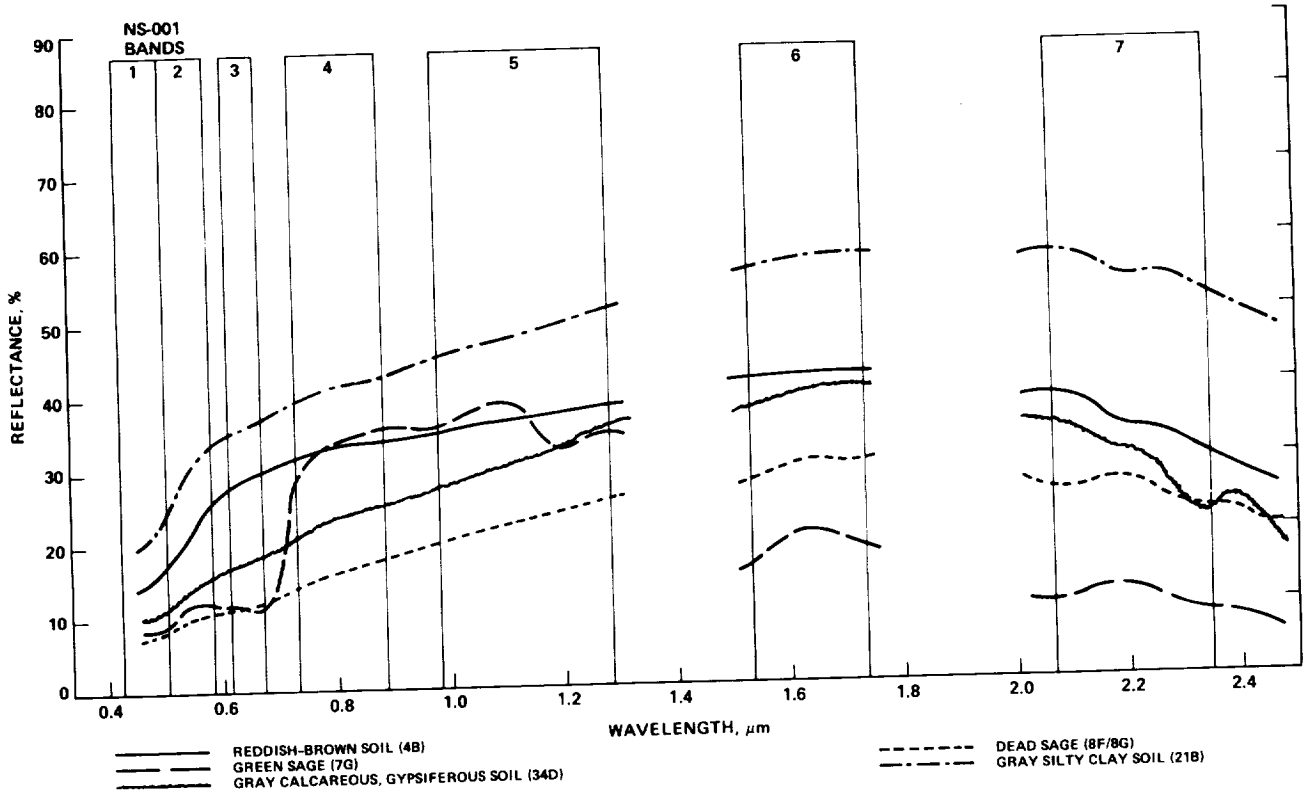

Figure 11-60. Field spectra for samples exhibiting maximum equivalent NS-001 VNIR band-ratio values (see Table 11-16)

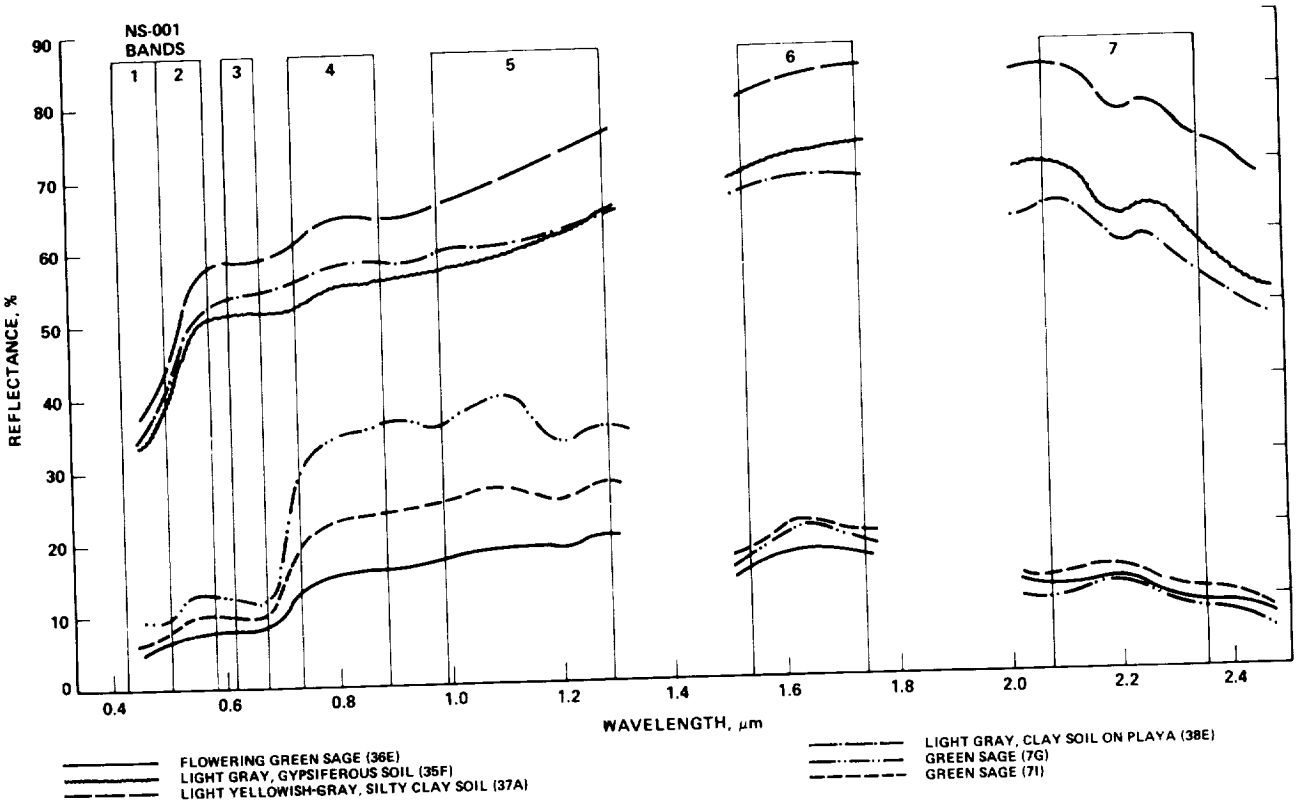

Figure 11-61. Field spectra for samples exhibiting minimum equivalent NS-001 VNIR band-ratio values (see Table 11-16)

Table 11-17. Significant NS-001 VNIR band ratios for the enhancement and interpretation of images based on the analysis of 260 PFRS spectral measurements at 60 sites

NS-001 Band Ratio	Interpretation	
	High Values	Low Values
3/1	Fe^{+3}-bearing soil and/or no green vegetation	Green vegetation and/or soil lacking Fe^{+3}
6/1	Gypsiferous (HOH-bearing) quartz-poor soil and/or mica-poor (OH - lacking) soil	Quartz-rich micaceous (OH - bearing) soil and/or gypsum-poor (HOH-lacking) soil
7/2	Dead vegetation and/or lack of green vegetation	Green vegetation and/or lack of dead vegetation
6/3	Dead vegetation and/or quartz-poor soil lacking mica (OH lacking)	Quartz-rich micaceous (OH - bearing) soil and/or lack of dead vegetation
7/6	Quartz-rich soils (poor in OH , CO_3^{-2}, or HOH) and/or no green vegetation	Green vegetation and/or quartz-poor (OH , CO_3^{-2}, or HOH-bearing) soil

E. NS-001 Image-Derived Spectra—The Calibration Problem

1. Introduction. One strategy in spectral analysis is to use field and laboratory spectra as a guide for enhancing and interpreting multispectral images. Field and laboratory spectral analysis of the Patrick Draw test site was based on over 400 spectral measurements at over 200 sites. NS-001 multispectral data acquired in each of two overflights, however, include spectral measurements at over 3 million sites (picture elements or pixels) in the test site area.

2. Characteristics of NS-001 data. The NS-001 scanner records VNIR spectral data as uncalibrated radiance values scaled from 0 to 255 digital numbers (DNs). Prior to their use in producing images, data from each band are routinely processed for gradient removal and "stretched." The gradient removal is presumed to remove atmospheric and illumination aspect effects or at least normalize these effects for the scene. The initial stretch is an offset and gain applied to the raw data so that it fills the 255 DN range available for each band. The uncalibrated nature of these initially processed data is illustrated in Figure 11-62, which compares uncalibrated image-derived spectra and PFRS spectra from three more or less spectrally homogeneous locations in the test site. The disparity in both form and magnitude of these three pairs of spectra is in part due to (1) the differences in the gain and offset for the detectors for each band and (2) the gain and offset applied in the initial stretch. A potential pitfall in the routine application of the preliminary stretch is demonstrated by the saturation (DN = 255) in all bands for the image-derived spectrum for the playa. The original raw NS-001 data for this location were not saturated in any band. Such a processing artifact must be avoided to preserve all the radiometric information acquired by a scanner.

During each of the two NS-001 overflights of the Patrick Draw test site, the scanner measured average radiance in each of the bands at over 3 million 18.5-m (60.5-ft) by 18.5-m locations (pixels). The minimum surface target dimensions for one pixel to represent a known area of homogeneous reflectance on the ground is approximately

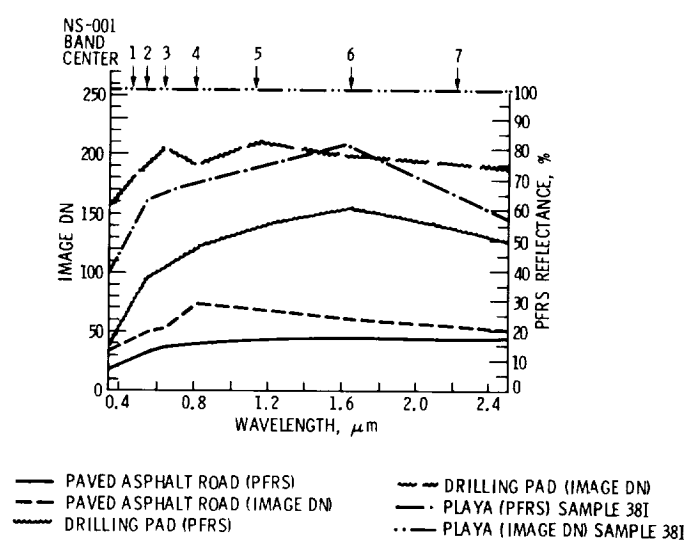

Figure 11-62. A comparison of uncalibrated NS-001 image spectra and equivalent seven-point PFRS-derived spectra for three relatively homogeneous targets in the Patrick Draw test site (from Mission 390, line 4, data acquired October 19, 1978)

55.5 m (181.5 ft) by 55.5 m (3 by 3 pixels). Surficial cover at Patrick Draw includes cultural, vegetation, soil, and bedrock elements of variable spectral character. Field spectral measurements clearly demonstrate that nowhere in the test site do spectrally homogeneous elements cover areas equivalent to 3 by 3 pixels. All spectral measurements made by the scanner were, therefore, obtained for mixtures of spectral classes. It is practically impossible to measure in the field the spectrum of a single pixel area whose radiance was measured by the scanner. At best, the 200-cm^2 area sampled for a PFRS spectrum can only characterize a single point in the mixed spectral continuum sampled by the sensor.

Statistical analysis provides some insight into the nature of the NS-001 spectral data acquired at Patrick Draw. Table 11-18 includes the correlation matrices for the data acquired in the two NS-001 overflights of the test site area. These data clearly demonstrate the high correlation of all bands for both flights. Although acquired during different seasons, in different years, both matrices are in agreement. This agreement may be considered evidence for consistency in the scanner's radiance measurements. The greatest difference between the two matrices is the lower correlation between bands 2 and 5, 2 and 6, and 2 and 7 for Mission 407 data. This decrease in correlation may be attributed to an increase in vegetation influence for these August data.

The histograms for each of the seven VNIR band DN values in the initially processed data for both flights are Gaussian distributions. This lends credence to the observation that the scanner measured radiance values in a single spectral population or in a population composed of a spectral continuum composed of mixed spectral end members.

Table 11-18. Correlation matrices for the seven NS-001 VNIR band data acquired in two overflights of the Patrick Draw test site

NS-001 Band	1	2	3	4	5	6	7
	Mission 390, Line 4, October 19, 1978						
1	1.00						
2	0.97	1.00					
3	0.95	0.99	1.00				
4	0.88	0.93	0.92	1.00			
5	0.87	0.91	0.94	0.92	1.00		
6	0.89	0.91	0.94	0.88	0.97	1.00	
7	0.89	0.90	0.92	0.84	0.92	0.97	1.00
	Mission 407, Line 4, August 28, 1979						
1	1.00						
2	0.97	1.00					
3	0.91	0.93	1.00				
4	0.88	0.90	0.94	1.00			
5	0.81	0.84	0.90	0.94	1.00		
6	0.80	0.83	0.90	0.87	0.93	1.00	
7	0.82	0.83	0.87	0.83	0.85	0.91	1.00

Principal components analysis provides additional insight into the nature of NS-001 data. (A complete discussion of this multivariate statistical technique is presented by Davis, 1973.)

Table 11-19 summarizes the seven VNIR-band eigenvectors for the first three principal components (PCs) determined for Mission 390 NS-001 data. Also included are percent variance explained by each PC. The numerical values for the eigenvectors are rather low for all bands. This reflects the high correlation among the bands. Over 85 percent of the variance in the NS-001 data is associated with the first three PCs.

Understanding the physical meaning of these new variables is aided by interpreting the PC spectra shown in Figure 11-63 according to the spectral characteristics of Patrick Draw cover types discussed above. The first PC is approximately equally and positively correlated with all bands. It may be considered an approximation of the mean radiance value for all seven bands or a measure of albedo of the surface material. Over 63 percent of the variance of the NS-001 data is explained by this first PC. Apparently, most of the spectral variability of Patrick Draw cover may be attributed solely to variation in albedo. This observation is consistent with the high interband correlations shown in Table 11-18. The greatest variation in albedo for surface materials at Patrick Draw is associated with soil/rock (high albedo) and vegetation (low albedo). An increase in the first PC, therefore, is largely a measure of an increase in the contribution of the soil/rock spectral component or a decrease in the vegetation spectral component.

The second PC is most positively correlated with band 7. It is also positively correlated with bands 6 and 5. Negative correlations are associated with bands 1, 2, 3, and 4. This PC will vary in a manner similar to band ratios having bands 5, 6, and 7 in the numerator and bands 1, 2, 3, and 4 in the denominator. These relationships support the interpretation that V2 is a measure of the soil/rock spectral contribution; an increase in the second PC is a measure of an increase in the contribution of the soil/rock spectral component. The 11 percent variance explained by this component may be considered a measure of the contribution of "pure" soil/rock spectral classes to the variance of these NS-001 data.

The third PC is positively correlated with band 4, where the highest eigenvector seen in Table 11-19 occurs. It is

Table 11-19. NS-001 Mission 390, October, 1978, principal components analysis: Eigenvectors of seven VNIR bands for the first three PCs

Variance Explained, %	PC	Eigenvectors for Indicated NS-001 Band						
		1	2	3	4	5	6	7
63.7	V1	0.3825	0.4048	0.4085	0.3748	0.3526	0.3511	0.3672
11.3	V2	−0.3468	−0.3608	−0.1682	−0.3329	0.3063	0.4652	0.5476
10.2	V3	−0.4992	−0.1883	−0.0724	0.6819	0.3884	0.0448	−0.3033
Σ85.2								

also positively correlated with band 5 and negatively correlated with bands 1, 2, and 7. The overall form of this third PC spectrum is analogous to the spectral reflectance curve for vegetation. These relationships support the interpretation that V3 is a measure of the vegetation spectral contribution; an increase in the third PC is a measure of an increase in the contribution of the vegetation spectral component. The 10 percent variance explained by this component may be considered a measure of the albedo-independent contribution of pure vegetation spectral classes to the variance of these scanner data.

3. Calibration of NS-001 data. To use the NS-001 sensor as an airborne spectrometer, scanner radiance data must be converted to reflectance—the uncalibrated DN radiance values must be converted to calibrated reflectance values. Gillespie and Kahle (1977, p. 987–988) developed an approach that used PFRS field spectral data to calibrate M²S aircraft data at Pisgah Crater, California. Prost (1980, p. 899) used the same approach with laboratory spectral data to calibrate aircraft scanner data at Gold Acres, Nevada. In the Gillespie and Kahle approach, scanner DN values for at least two ground locations of known reflec-

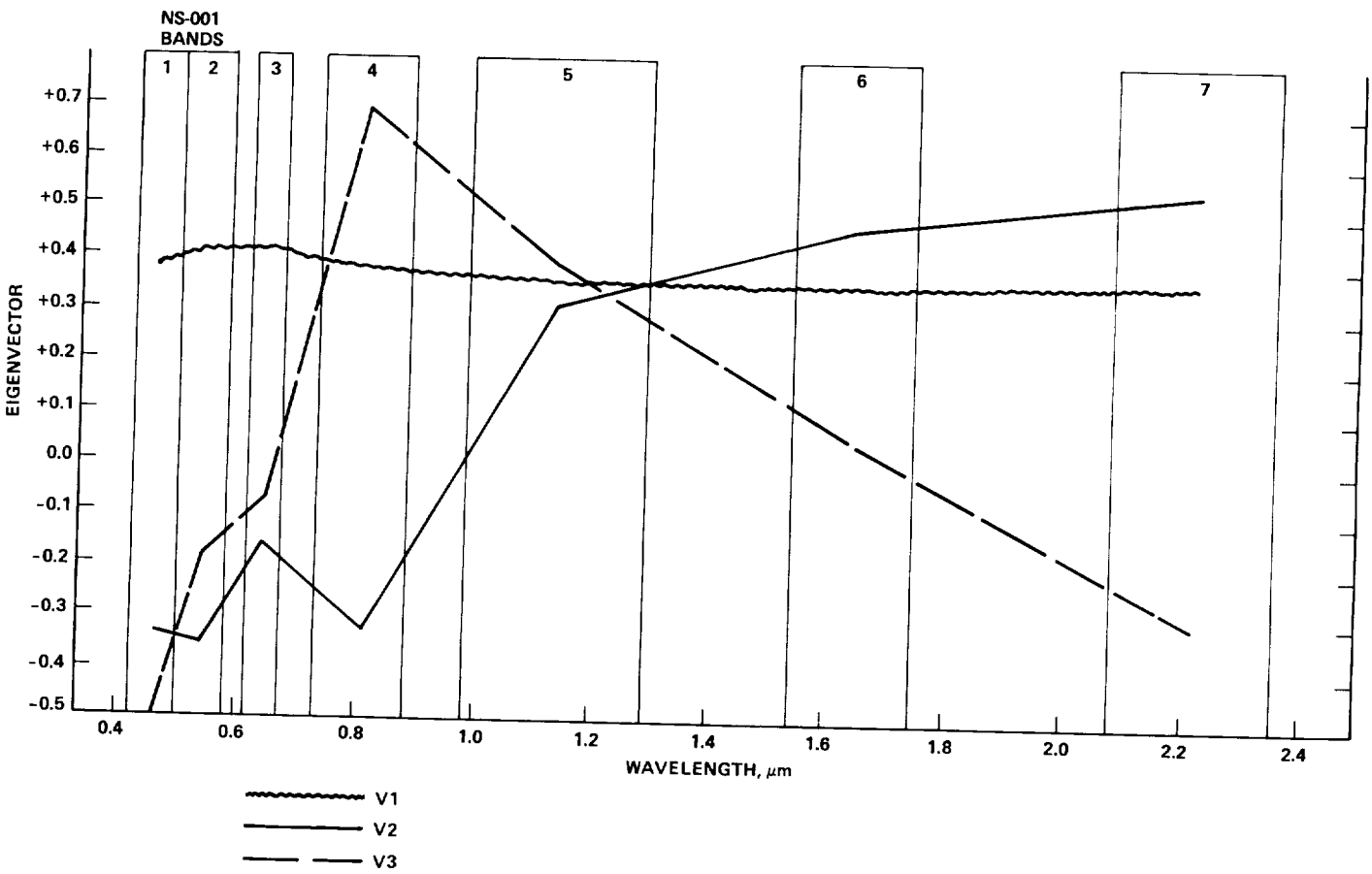

Figure 11-63. PC spectra for NS-001, Mission 390, line 4 data acquired October 19, 1978. Spectra were constructed by connecting eigenvector values for each PC plotted at band centers. V1 is the first PC; V2, second; and V3, third.

tance in each band (based on PFRS or laboratory spectral data) are mathematically forced to yield equivalent reflectance values by applying an offset and gain (linear stretch) determined from a scatterplot of DN versus known reflectance. This stretch is then applied to the DN values of all pixels to yield calibrated DN values which are equal to PFRS or laboratory reflectance. A potential pitfall in such an approach is the inherent assumption that the "true" reflectance of any pixel can be determined by laboratory or PFRS spectral measurements. The nature of most areas of the Earth's surface, including Patrick Draw, inhibit the ability to determine the true reflectance spectrum of any real ground area represented by any pixel. The primary inhibiting factors include:

(1) Lack of spectral homogeneity at the pixel-area scale due to the mixing of numerous spectral phases such as different soils and rocks, vegetation, shadows, etc.

(2) Temporal- and aspect-dependent spectral variability due to atmosphere, soil moisture, state of vigor and composition of vegetation, slope, specular reflectance effects, and solar illumination conditions.

The significance of these factors is obviously site specific. Evaluation of these factors for Patrick Draw demonstrated that calibration of NS-001 data could only be accomplished by a modified Gillespie and Kahle approach.

After gradient removal, data from the geometrically corrected NS-001 Mission 390, line 4 were linearly stretched with the restriction that no DN values be decreased to 0 nor increased to 255. Analysis of the histograms for all seven VNIR band data revealed that their distributions were all Gaussian. It was assumed that:

(1) The atmospheric and illumination aspect effects had been effectively removed or at least normalized in gradient processing.

(2) The NS-001 detector response was linear.

(3) The PFRS spectral sample was statistically representative of the scanner spectral population.

Based on these assumptions, calibration stretches for each band of the Patrick Draw NS-001 data were determined from least squares fits of scatterplots of minimum, mean, and maximum DN (from the histograms of the linearly stretched data) versus minimum, mean, and maximum PFRS reflectance (from Table 11-15). These scatterplots are shown in Figure 11-64. The goodness of fit for these regressions is considered evidence that the assumptions made in this calibration procedure were correct for the Patrick Draw data.

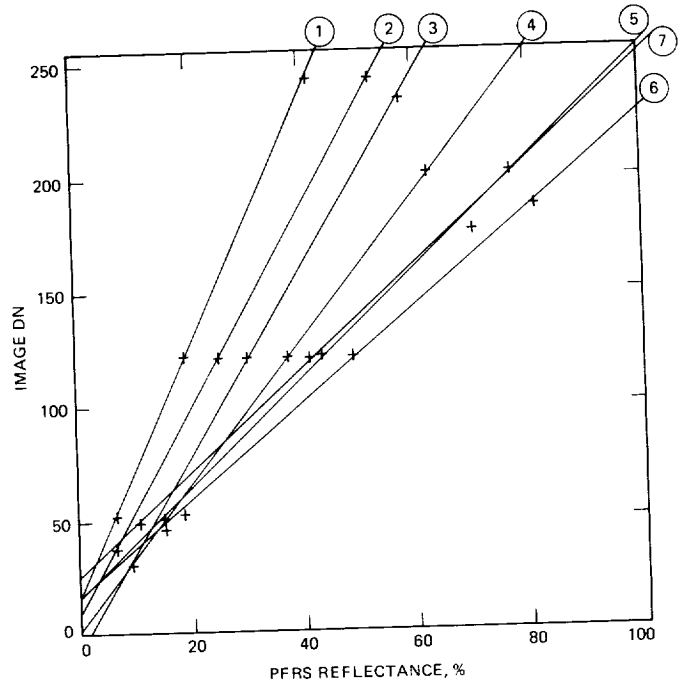

Figure 11-64. Calibration curves used to determine offsets and gains that were applied to NS-001, Mission 390, line 4 data to convert image DN radiance values to equivalent PFRS reflectances. Least squares fits of minimum, mean, and maximum equivalent PFRS reflectance versus minimum, mean, and maximum image DN radiance in each band were used to produce the seven straight-line calibration curves shown. Points used in the calibration are indicated by cross symbol.

To put these data in a form that would be useful in image analysis, seven images were prepared, which display equivalent PFRS reflectance for the NS-001 data in 5 percent reflectance color slices (Figures 11-65 through 11-71). To further test the validity of these calibration stretches reflectance spectra for several locations were determined from the seven calibrated images and were compared to PFRS spectra obtained at the same location (Figure 11-72). The similarity of equivalent spectra pairs is apparent. Differences are considered a measure of the 5 percent precision of the image portrayal of reflectance and the inability to determine the true reflectance for any pixel based on PFRS data. These results are considered further empirical evidence for the validity of the initial assumptions and the calibration approach used.

This approach to calibration provides an effective procedure for image calibration and an efficient strategy for the acquisition of field spectra. In operation, the procedure would involve the following steps:

(1) Acquire scanner data over the site of interest, maintaining onboard detector offset and gain so that DN 0 and DN 255 are not recorded in any channel

(2) Preprocess scanner data, with gradient removal and an initial linear stretch, to maintain the DN 0 and DN 255 exclusion.

(3) Examine histograms for each channel, and select optimal DN values in each for calibration (e.g., if histograms are Gaussian: minimum, mean, and maximum DN values).

(4) Prepare an image for each band which alarms the ground location of all pixels exhibiting the optimal DN values determined in item (3).

(5) Acquire appropriate field-band reflectance values for the alarmed locations.

(6) Prepare DN versus reflectance scatterplots; determine offset and gain for each channel.

(7) Apply calibration stretch to each channel.

4. Conclusions. Effective image calibration can be accomplished even in areas such as Patrick Draw where the "true" reflectance spectrum for any pixel area cannot practically be determined. The utility of calibrated data does not reside in the superiority of calibrated images for discrimination of geologic materials; calibration is nothing more than a stretch—a stretch *not* designed to optimize separation. The utility of calibrated data resides only in their portrayal of the original scanner data in a form that may be compared directly to field or laboratory spectra. With calibrated data, the "true" spectra of units identified in images, which have been optimized for discriminating geologic materials, can be retrieved from the scanner data. Calibrated multispectral data provide a direct means for characterizing surface composition from established principles of spectral reflectance.

IX. NS-001 Image Analysis

A. Mapping Tonal/Textural Units

1. Introduction. One method of image analysis consists of an interpreter visually examining an image print and tracing the outline of each distinctive tonal/textural area observed. Tonal/textural units portrayed by the image data are thus subjectively defined. The image itself is considered an unlabeled map that objectively portrays the distribution of surface materials. The physical meaning (labels) of units recognized by the interpreter is determined by comparison to available ancillary information, such as geologic, soil, topographic, and vegetation maps, field examination, and laboratory/field spectral measurements. Even if the interpreter is not able to rigorously establish, on the basis of spectral evidence, the cause-and-effect relationship between cover characteristics and image units, the

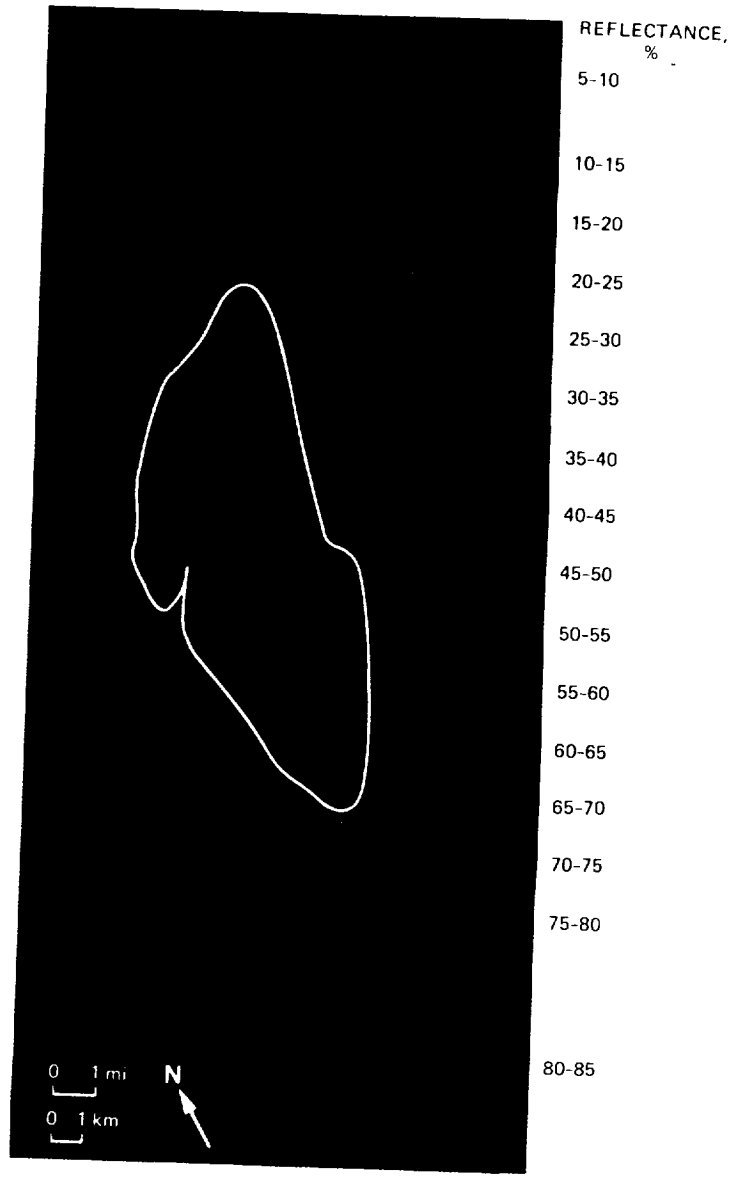

Figure 11-65. NS-100, Mission 390, line 4 calibrated image for band 1. Equivalent PFRS reflectance is scaled using 5 percent reflectance color slices, which are displayed in dark blue (5–10 percent), medium blue (10–15 percent), etc., to flesh tone (80–85 percent) as shown on the color bar. Offset and gain used for this calibration are illustrated in Figure 11-64.

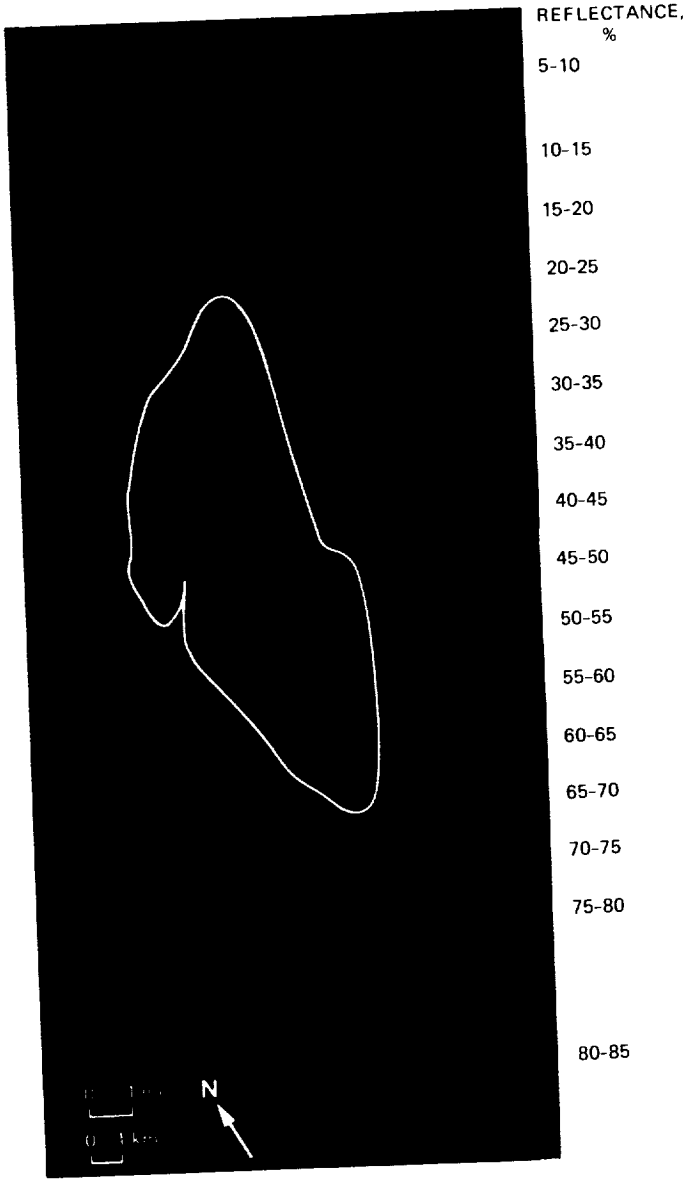

Figure 11-66. NS-001, Mission 390, line 4 calibrated image for band 2. Refer to Figure 11-65 for explanation.

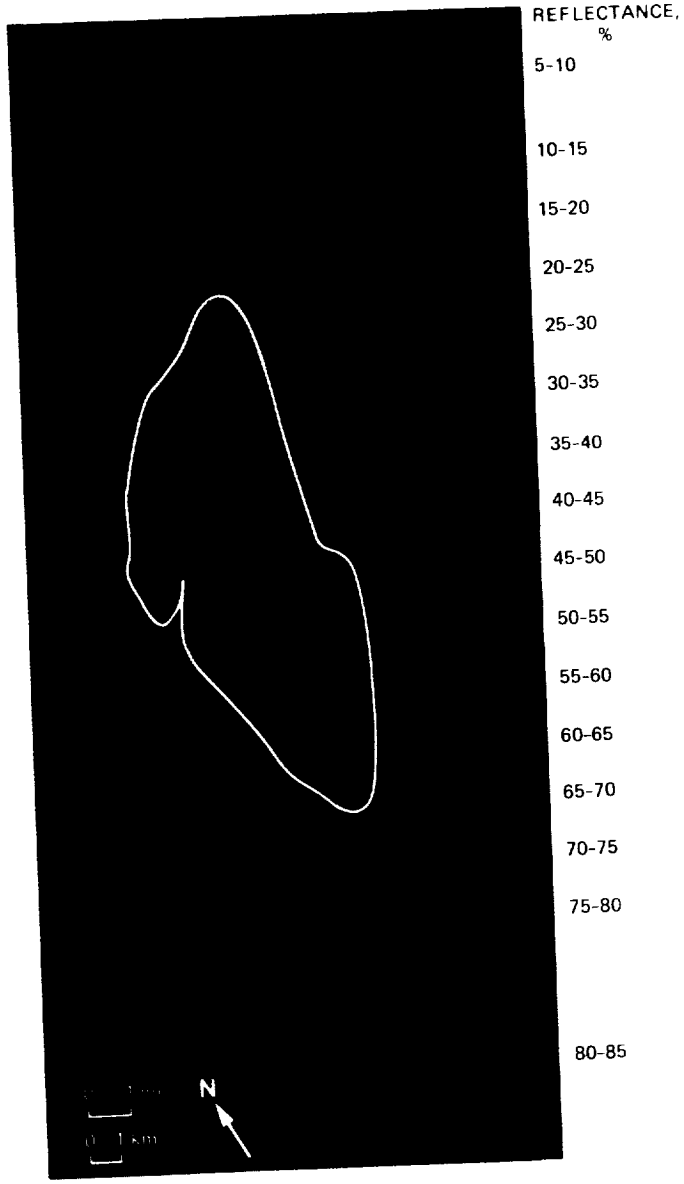

Figure 11-67. NS-001, Mission 390, line 4 calibrated image for band 3. Refer to Figure 11-65 for explanation.

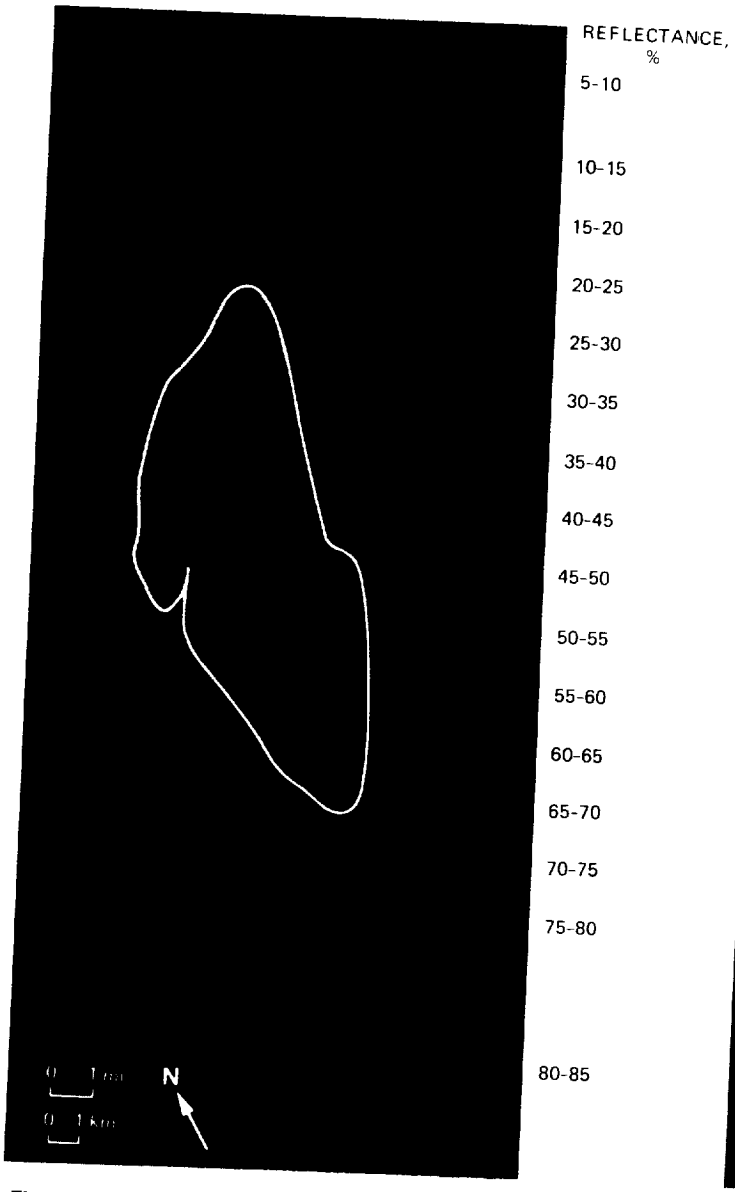

Figure 11-68. NS-001, Mission 390, line 4 calibrated image for band 4. Refer to Figure 11-65 for explanation.

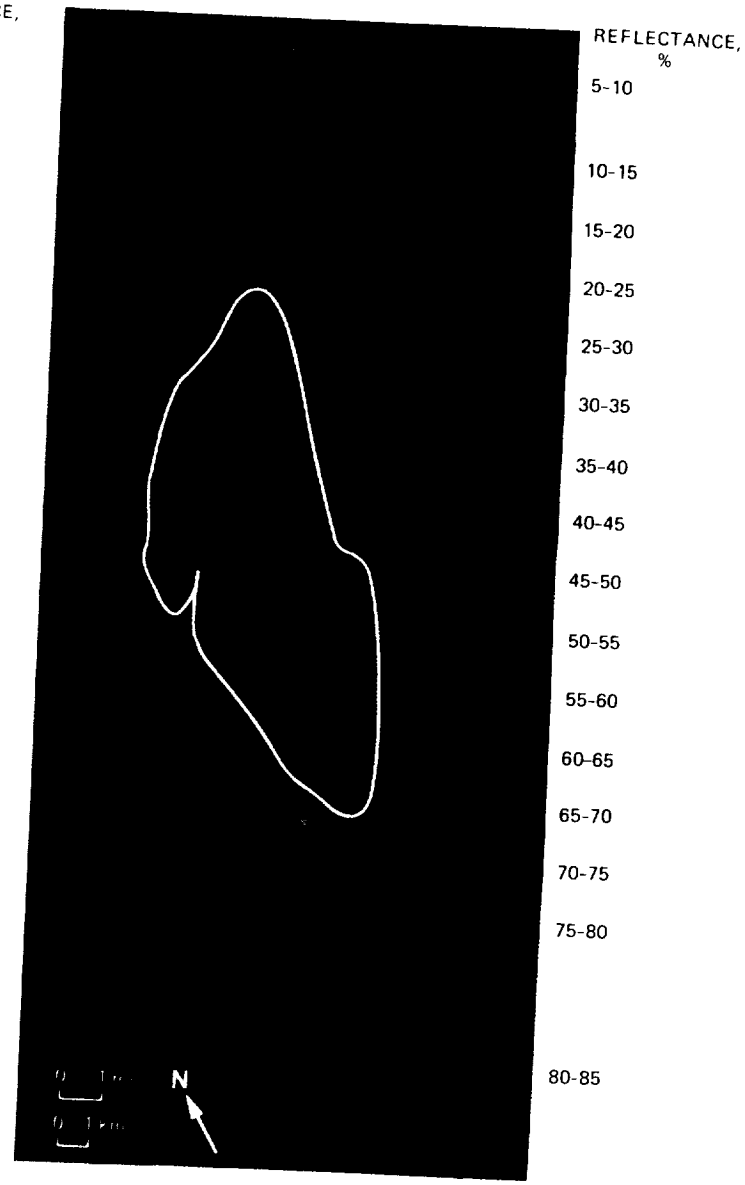

Figure 11-69. NS-001, Mission 390, line 4 calibrated image for band 5. Refer to Figure 11-65 for explanation.

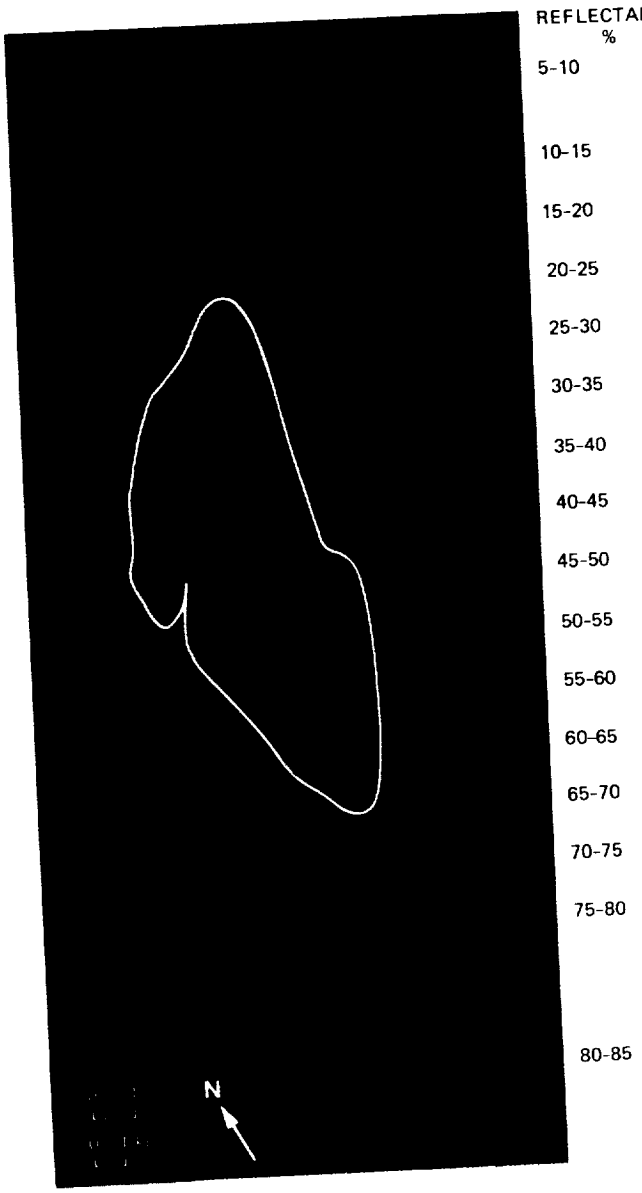

REFLECTANCE, %

5-10
10-15
15-20
20-25
25-30
30-35
35-40
40-45
45-50
50-55
55-60
60-65
65-70
70-75
75-80
80-85

Figure 11-70. NS-001, Mission 390, line 4 calibrated image for band 6. Refer to Figure 11-65 for explanation.

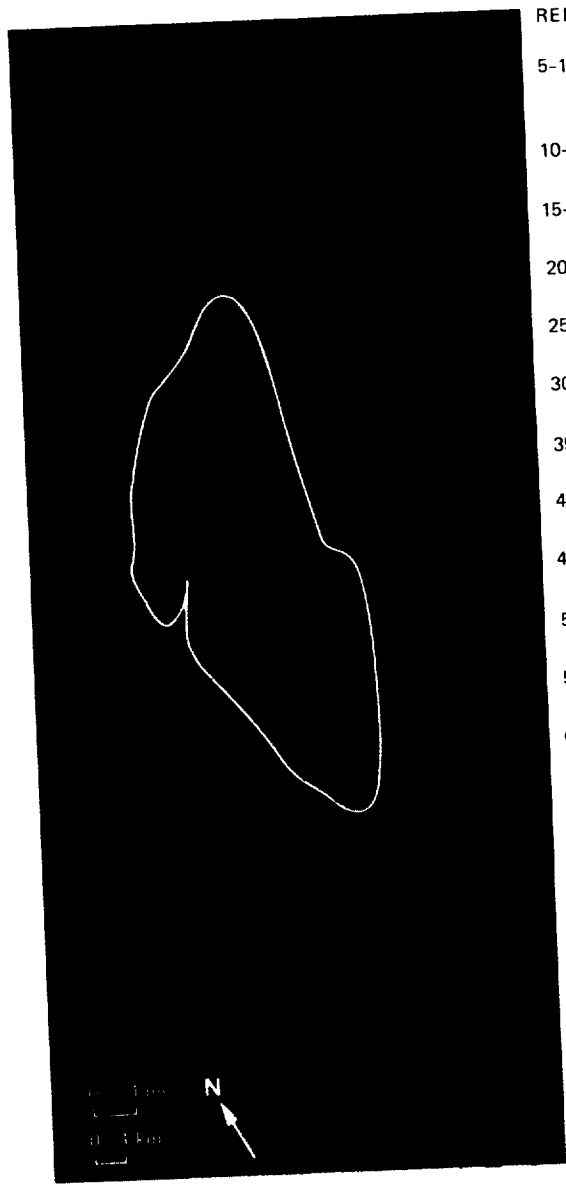

REFLECTANCE, %

5-10
10-15
15-20
20-25
25-30
30-35
35-40
40-45
45-50
50-55
55-60
60-65
65-70
70-75
75-80
80-85

Figure 11-71. NS-001, Mission 390, line 4 calibrated image for band 7. Refer to Figure 11-65 for explanation.

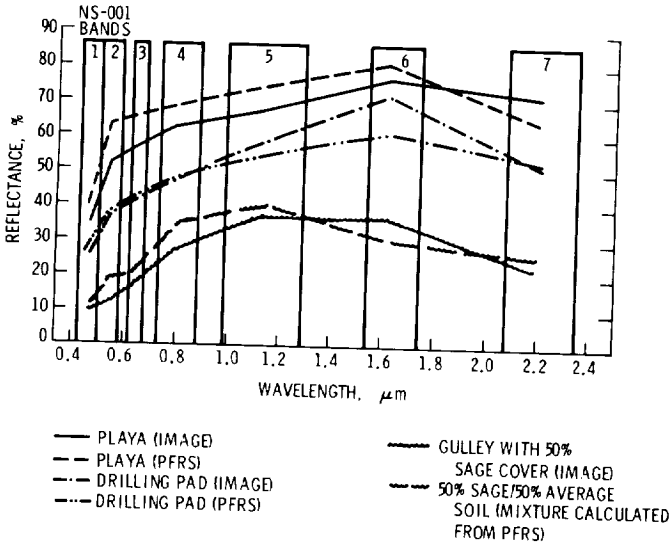

Figure 11-72. A comparison of calibrated NS-001 image spectra and equivalent seven-point PFRS-derived spectra for three targets in the Patrick Draw test site. The PFRS spectra shown for the playa and drilling pad represent averages from multiple field spectral measurements; the soil sage PFRS spectrum was calculated using typical soil and typical sage PFRS spectra, which were mathematically mixed using the model of Siegal and Goetz (1977).

image interpretation is still considered a portrayal of differences between and variations within cover classes. Each unit recognized is assumed to be the unique result of the combined influence of rock, soil, vegetation, moisture, surface texture, topography, etc. If, by comparison to the available ancillary data, the cause of a unit cannot be accounted for, the unit is commonly referred to as an "anomaly."

2. Results of tonal/textural interpretation of NS-001 data. During the Patrick Draw test site investigation, the approach described above was used to interpret many NS-001 images. One such image and the resulting interpretation are illustrated in Figures 11-73 and 11-74, respectively.

The NS-001 ratios used in producing the Figure 11-73 color ratio composite (CRC) image were selected based on a *preliminary* examination of the spectral characteristics of Patrick Draw cover types as illustrated in Figures 11-50 and 11-52. The band-ratio 3/2 (image red) should be higher in soil/rock than in vegetation (Figure 11-50); the presence of hematite and/or goethite in soils/rocks should also result in higher ratio values (Figure 11-52). Band-ratio 6/1 (image green) is largely a measure of albedo; increased vegetation is characterized by lower ratio values (Figure 11-50). Band-ratio 6/7 (image blue) should be higher in vegetation than in soil/rock (Figure 11-50). The presence of clay-bearing soil/rock, however, should also increase ratio values (Figure 11-52).

On the basis of these spectral considerations, comparisons to other ancillary data, and field examination, the image analyst provided the following explanation for the 18 tonal/textural units recognized in Figure 11-73:

(1) Brown. All ratios approximately equal and relatively low; slightly lower values in band 1 or slightly higher values in band 6. Represents barren areas of relatively low albedo: areas of bare rock in shadows and areas of dark exposed soil near the railroad track.

(2) Pink–magenta. High values for all ratios; 6/1 values somewhat higher and 6/7 somewhat lower than 3/2. Areas of relatively well-exposed, dry, red or yellow soil or rock.

(3) Red. High 3/2 values and lower 6/7 and 6/1 values. Areas of yellow or red clay-rich soil most common along the valley of Bitter Creek.

(4) Indigo. Low values for all ratios; 6/7 values somewhat higher. Areas of very little soil/rock exposures (covered by relatively dense sage) and/or very high clay content in exposed soil/rock. Areas of relatively well-developed moist soil.

(5) Lavender. High values for all ratios; 6/1 values somewhat lower. Areas of fairly heavy vegetation cover with clay-rich soil. Most common along Patrick Draw where relief is low and soil moisture is high.

(6) Pale pink. Similar to item (2), but with somewhat higher values for all ratios. Areas of relatively well-exposed red or yellow soils in the southeastern Bitter Creek drainage.

(7) Mixed turquoise/green. Higher values for all ratios; dominated by high values in band 6. Dry areas of moderate vegetation cover; dip slopes of resistant units within the Fort Union Formation on the west side of the image area.

(8) Sky blue. High values for all ratios; dominated by high 6/7 values. Protected areas with high soil moisture and well-developed vegetation cover; side slopes of major drainage.

(9) Dark blue–violet. Low values for all ratios; 6/7 values somewhat higher. Areas of heavy vegetation; similar to those described for item (8), but partially shadowed.

Figure 11-73. NS-001, Mission 407, line 4, August 28, 1979, CRC image: ratio of bands 6/7, displayed in blue; 6/1, green; and 3/2, red. This image was used for the tonal/textural interpretation illustrated in Figure 11-74.

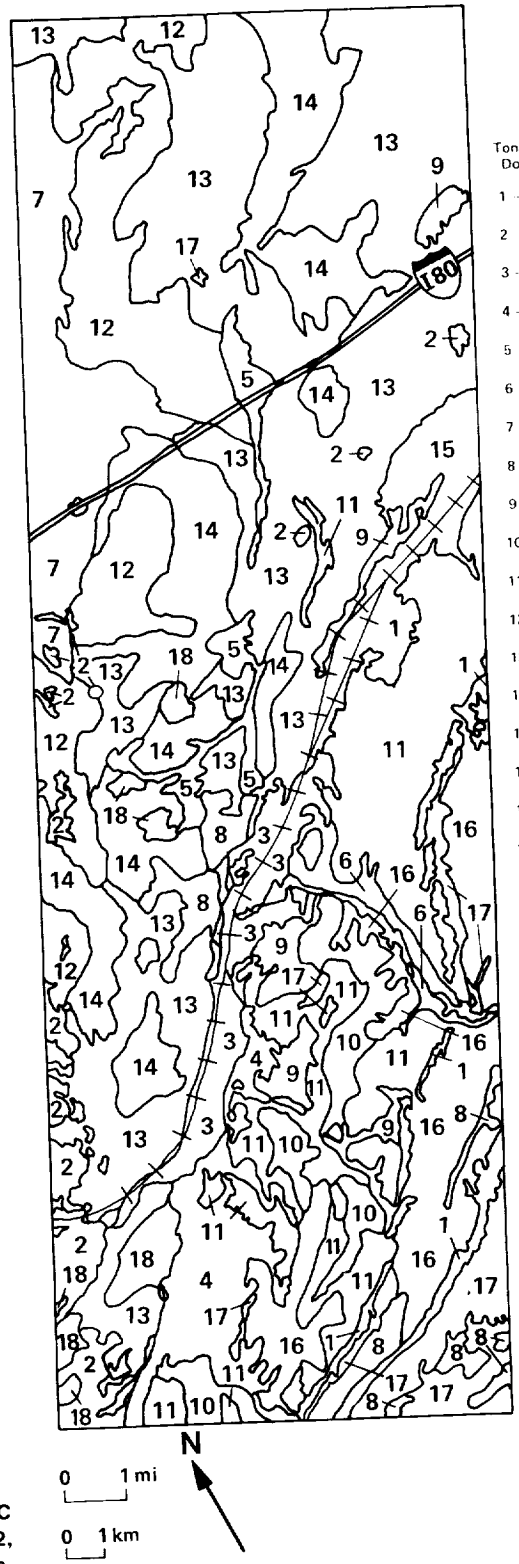

Tonal/Textural Unit And Dominant Image Color

1 – brown
2 – pink-magenta
3 – red
4 – indigo
5 – lavender
6 – pale pink
7 – mixed turquoise/green
8 – sky blue
9 – dark blue to violet
10 – yellow and yellow green
11 – mixed blue/yellow/green
12 – yellow gray
13 – mixed yellow/blue
14 – mixed purple/pink
15 – violet
16 – tawny yellow
17 – white
18 – gold
Unlabeled – variable

Figure 11-74. Tonal/textural units and dominant image colors recognized in an interpretation of a band 6/7 (blue), 6/1 (green), 3/2 (red) NS-001 CRC image (Figure 11-73)

(10) Yellow and yellow green. High values in band 1 and in the 6/1 ratio. Relatively sparsely vegetated areas of light-colored, clay-poor, sandy, poorly developed soils. Topographically high interstream areas.

(11) Mixed blue/yellow/green. Relatively small-scale intermixing of items (8), (9), (10), resulting in a mottled texture. Areas of variable vegetation cover and irregular topography.

(12) Yellow gray. Topographically smooth, relatively sparsely vegetated areas; characterized by dry calcareous soils, which will not support vigorous vegetation.

(13) Mixed yellow/blue. Areas similar to item (11), but with more abrupt cover changes. Dissected terrain where intermixed shale and sandy soils are exposed. Locally, heavily vegetated in low, flat subareas where moisture is available.

(14) Mixed purple/pink. A mottled mixture of items (2) and (10). Areas of sparse vegetation and irregular topography.

(15) Violet. Similar to item (4), but with a slightly higher 3/2 component. High percentage of herbaceous compared to shrubby vegetation cover.

(16) Tawny yellow. High values for all ratios. Light-colored, calcareous, clay-rich soil/rock with sparse vegetation cover.

(17) White. Similar to item (16), but with higher values in all ratios. Essentially unvegetated areas of calcareous bare rock exposure.

(18) Gold. Moderate values for all ratios; 6/7 lowest. Areas of poorly developed, yellow or tan, clay-poor soils with little vegetation cover.

3. Conclusions. A comparison of soil unit characteristics (Tables 11-6 and 11-7) and distribution (Plate 11-2) to tonal/textural units recognized in this NS-001 image interpretation (Figure 11-74) demonstrates the correlation between image units and soil units. The subdivision of some areas in the tonal/textural interpretation, which are not subdivided in the soil map, is considered an indication of the sensitivity of the multispectral data for discriminating local variations in surface cover. NS-001 images may be interpreted to delineate subtle areal changes in soil characteristics that are not always identified using conventional field soil mapping procedures alone.

Even in relatively sparsely vegetated areas such as Patrick Draw, vegetation has a significant influence on the colors and textures perceived in the multispectral image interpretation. Explanation of each of the 18 units recognized in the tonal/textural interpretation of an NS-001 CRC image required consideration of the vegetation component; nine of the units recognized were interpreted to be dominated by vegetation influence.

B. A Tonal Anomaly Coincident With an Area of Anomalous Vegetation

1. Introduction. Early in the NS-001 image interpretation phase of the test site investigation, a tonal anomaly was recognized that coincides with an area of anomalous stunted sage. The field/laboratory evaluation of this anomaly is discussed in Paragraph VII.B, and the image characteristics of this feature are described below.

2. Image characteristics. The hand-shaped outline of unit 12, south of Interstate Highway 80, near the west edge of Figure 11-74, coincides approximately with the outline of a tonal anomaly recognized in many NS-001 images. This unit was considered anomalous because of its lack of areal correlation with previously mapped geologic, soil, or vegetation units. Examination of available aerial photographs and Landsat MSS images revealed that this anomaly was not detectable in these data. NS-001 images in which the anomaly was most easily recognized and its image characteristics include:

(1) PC image (A in Figure 11-75). Anomaly is an area of high PC 2 and PC 3 values (yellow in a region of green).

(2) CRC image (Figure 11-76). Anomaly appears as an area of high 6/1 in an area of higher 3/2 (green in a region of yellowish green).

(3) Color ratio slice (4/2, Mission 390). Anomaly exhibits lower ratio values than surrounding area.

(4) Color ratio slice (6/7, Mission 390). Anomaly exhibits higher ratio values than surrounding area.

(5) Calibrated images (Figures 11-65 through 11-71). Anomaly is best displayed in Figure 11-71 (band 7) where it appears as a yellow area surrounded by green; i.e., the anomaly has approximately 5 percent higher reflectance than the surrounding area.

3. Interpretation. Based on the image characteristics of the anomaly and on the spectral characteristics of Patrick Draw cover types, the anomaly defines an area of less dense and less vigorous vegetation in an area of high albedo soils with a higher concentration of minerals with absorption features in NS-001 band 7 (Figures 11-50 and 11-52).

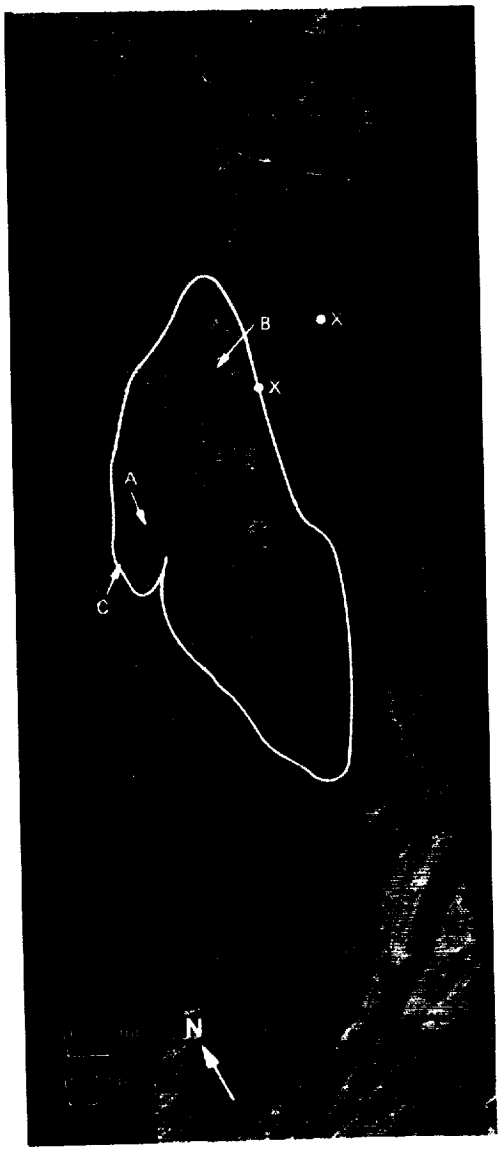

Figure 11-75. Geometrically rectified NS-001, Mission 390, line 4 PC image: the first PC is displayed in red; the second, green; and the third, blue. *A* shows the location of a tonal anomaly (a yellow-toned area in a region of green) which coincides with the areal distribution of anomalous stunted sage. *B* points to a distinct tonal unit (pink tone in a region of green) which has a sinusoidal, generally NNE–SSW trend. *C* identifies an apparent thin bedding unit (pink line on yellow/green background). Points labeled *X* identify the endpoints of a lineament discussed in Paragraph IX.D.

Figure 11-76. Geometrically rectified NS-001, Mission 390, line 4 CRC image: band 3/2, displayed in red; 6/1, green; and 6/7, blue. The features identified in Figure 11-75 are also recognizable in this image.

C. Geologic Mapping

1. Introduction. To evaluate the utility of NS-001 multispectral data for geologic mapping, selected geometrically rectified images from Mission 390 data were interpreted using photogeologic/geomorphic analysis procedures. Figures 11-75 and 11-76 are two of the images used in this analysis. Elements of this interpretation included key bed tracing, stratigraphic analysis, structural geologic interpretation, and lineament analysis. Results are summarized in Figure 11-77 and Plates 11-3 and 11-4. The utility of NS-001 data for geologic mapping is illustrated by comparing these interpretations to Figures 11-4, 11-5, and 11-6. Significant results of this photogeologic analysis are discussed in the following paragraphs.

2. Stratigraphic analysis. Preliminary interpretation indicated the presence of a distinct spectral unit trending NNE–SSW through the central portion of the test site area (B in Figure 11-75). Images in which this unit was recognized and its characteristics include:

(1) PC image (Figure 11-75): PC 1, red; PC 2, green; PC 3, blue. Higher values in all bands than adjacent units; highest in PC 1.

(2) CRC image (Figure 11-76): 3/2, red; 6/1, green; 6/7, blue. Higher values in all bands than adjacent units; highest in 3/2 and 6/7.

(3) Single-band calibrated images (Figures 11-65 through 11-71). Higher values in all bands than adjacent units, but less in bands 2, 5, and 7.

On the basis of these characteristics, the unit could be traced through the entire image area. Because of its proximity to the mapped Fort Union/Wasatch contact (Figure 11-4), it was designated the Transition Member (Figure 11-77). The question was posed: Does this unit represent the surface expression of an unmapped, bedrock, lithostratigraphic unit? To answer this question, a detailed evaluation of the unit was conducted in the area of its best development (type area) in the central portion of the Patrick Draw test site (Figure 11-78).

The area was mapped in the field (Figure 11-4) in as much detail as possible given the paucity of bedrock exposures. To the west of the stratigraphically lower boundary of the image-defined unit, the east-dipping contact of the early Tertiary Fort Union and Wasatch Formations was traced. The image-derived unit appears to be a transitional facies in the lower part of the mapped Wasatch Formation.

An analysis of the soil map (Plate 11-2) and descriptive soil information (Tables 11-6 and 11-7) reveals significant correlation between soil and vegetation boundaries and transitional spectral unit boundaries (Figure 11-78). Soils outside the spectral unit are dominated by sage-bearing silty and sandy loams; soils within the spectral unit by grass-bearing gypsiferous clay loams.

A 2.5-m-deep gas pipeline trench excavated across the area was noted during the fieldwork in July 1980. This trench provided an opportunity to log the detailed bedrock stratigraphy of the Fort Union/Wasatch contact (Figure 11-7). The transition unit includes less resistant and generally finer-grained material than the Wasatch or Fort Union Formations. It is the only bedrock unit containing gypsum in megascopic form. It includes the thickest and highest stratigraphic occurrence of coal and the highest stratigraphic occurrence of carbonate concretionary beds. The spectral transition unit thus represents the surface expression of a separable bedrock unit as used in standard field stratigraphic practice.

To determine the cause of the NS-001 image characteristics of the transition unit, a field sampling and analysis program was conducted in the summer of 1980. At 35 locations shown in Figure 11-78, field spectral measurements were made. A total of 140 spectra were collected, representing all major cover types and mixtures. At each of the 35 locations, a representative soil sample was taken for XRD mineralogical analysis and laboratory spectral analysis (with a Beckman DK2A). These data, discussed in Paragraph VIII.C, were used to establish which minerals and cover types occurring in the Patrick Draw area have spectral absorption features capable of affecting NS-001 band values. The high albedo for the transition unit in the seven NS-001 bands results from the absence of significant sage cover (Figures 11-50 and 11-78). This also contributes to the high 6/1 and 3/2 ratios associated with the unit. The low albedo contrast in bands 2, 5, and 7 is the result of absorption features in these bands associated with kaolinite, montmorillonite, jarosite, and gypsum (Figures 11-7 and 11-52). These minerals also contribute to high 6/7 values associated with the unit.

These results demonstrate the value of multispectral data for detailed stratigraphic analysis. Since multispectral data are sensitive to subtle vegetation and mineralogical changes not otherwise discernible, multispectral images are useful for mapping established units and defining new lithostratigraphic units. With the aid of ancillary field and laboratory spectral data and mineralogical analysis of residual soils, image spectral units can be directly related to bedrock lithology.

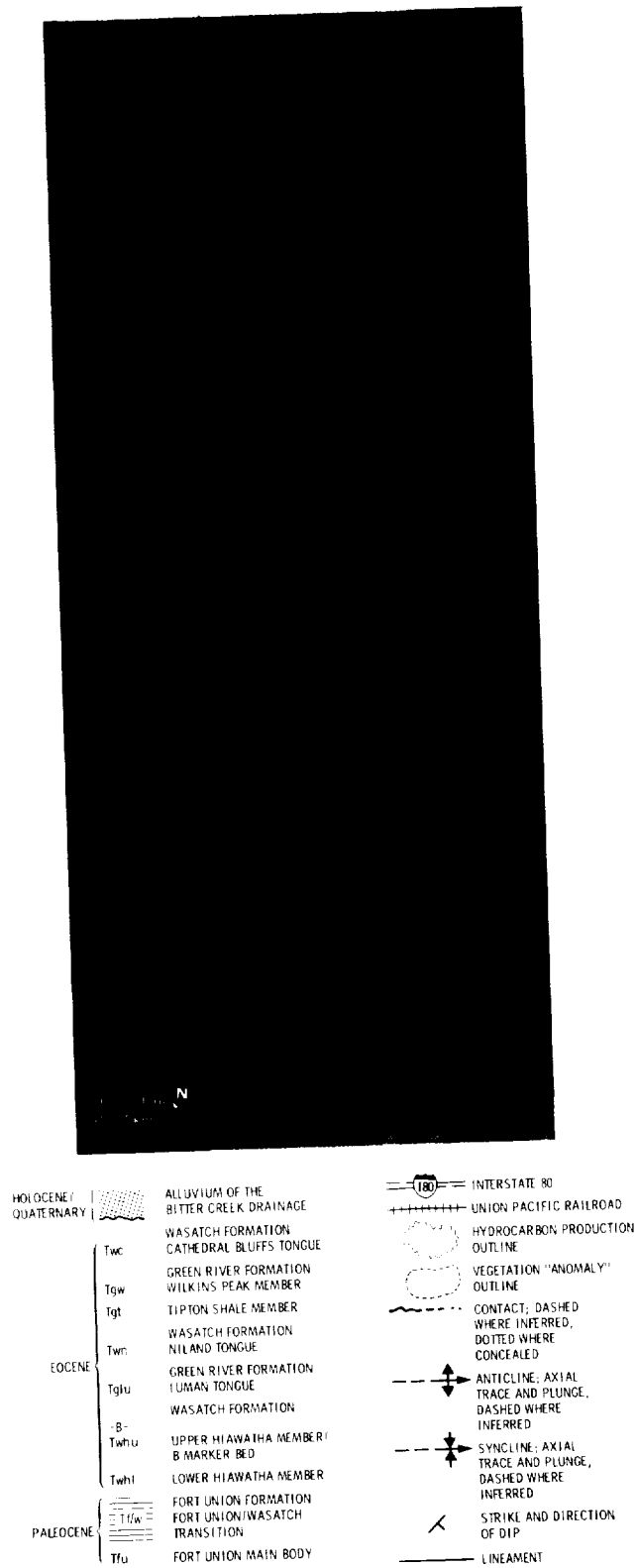

Figure 11-77. Composite NS-001, Mission 390, line 4 photogeologic interpretation of Figures 11-75 and 11-76. The interpretation is plotted on the PC image base shown in Figure 11-75.

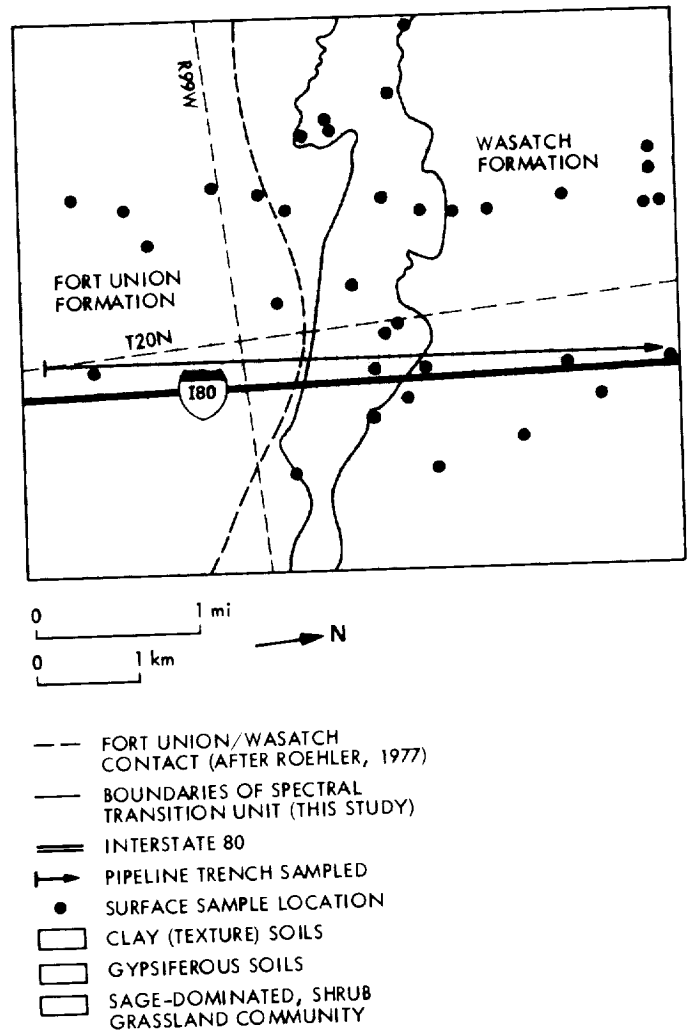

Figure 11-78. Location map comparing the spatial relationship of the transition spectral unit to the published mapped contact of the Fort Union/Wasatch Formations and to major soil/vegetation units. This figure is approximately centered at location *B* shown in Figure 11-75. Also shown are field and laboratory spectral and mineralogical sample locations. Bedrock exposures of the stratigraphic interval included in this area were studied in the gas pipeline trench interval shown.

3. Structure. As part of the photogeologic interpretation of NS-001 data, key beds were traced (Plate 11-4). These traces were used with 1:48,000 topographic contour maps to determine the dip and strike of bedding units (Figure 11-77 and Plate 11-3). This information provided greater structural information for the test site area than is available using field methods (Figures 11-4 and 11-5) or interpretation of standard color aerial photographs (Figure 11-6). Six subtle folds, not recognized on available maps, are clearly delineated. The northernmost anticline (Figure 11-77) coincides approximately with the trace of the Wamsutter Arch (Figure 11-10). The NE-trending anticline–syncline couplet coincides in trend and in location with the

projection of the Pennsylvanian Brady Deep North field structure, which has been mapped in the subsurface (Wyoming Geologic Association, 1979) approximately 8 km (5 mi) south of the structure shown in Figure 11-77. Field examination of this feature confirmed the image interpretation. The SE-trending anticline on the eastern edge of Figure 11-77 reflects the subsurface structure of the Table Rock field (Figure 11-10). The two ESE-trending synclines shown on the western edge of Figure 11-77 are less well defined and may be alternately interpreted as minor faults.

These results demonstrate the utility of geometrically registered NS-001 data for structural mapping. Structures too subtle to be recognized using surface mapping methods alone and not recognized in the subsurface map of the Patrick Draw field because of the coarse (1000-ft) contour interval are clearly delineated.

D. Lineament Analysis

1. Introduction. The advent of satellite image data resulted in the recognition that large numbers of linear features (lineaments) could be recognized on images regardless of scale or sensor type. Unfortunately, the linear features recognized tend to change with season, vegetation, lighting azimuth, sensor wavelength, scale, and resolution. Multiple observers viewing the same images often fail to recognize the same feature. Consequently, the utility of lineament analysis is the subject of considerable debate, even though lineaments are generally regarded as some manifestation of topographic and vegetative enhancement of linear fracture traces. A lineament study was performed for the Patrick Draw test site to identify linear features that could be attributed to variations in surface topography alone.

2. Topographic lineament analysis. Because the poor quality of digital terrain data for the test site area precluded detailed analysis, a study of the terrain information contained in the raised relief map of the Rock Springs, Wyoming, 1° by 2°, 1:250,000 quadrangle was undertaken. The effect of lighting on this relief map was studied. As with the analysis of digital terrain data, the method also eliminates vegetative and seasonal effects. Use of the reverse or underside of the raised relief map eliminates printing, contour, and cultural clutter, and it permits the analyst to study the relief of a surface of constant albedo. The photographic image of the underside of the raised relief map is corrected by inverting the negative before printing. Lineament directions are highlighted by shadow effects associated with differing lighting angles. These directional biases are suppressed by combining observations performed on images that have been illuminated from different directions. The identification of lineaments is in part subjective. The reproducibility of lineament trends may be evaluated by examining the patterns resulting from the same image being interpreted with differing azimuths of illumination. Lines oriented 30° ± 15° in azimuth on either side of the lighting azimuth are enhanced; lines parallel (± 15°) to the lighting azimuth are suppressed.

The area represented by the Rock Springs, Wyoming, 1° by 2° quadrangle (Figure 11-79) includes three physiographic regions: the broad dome of the Rock Springs Uplift which trends north–south through the center of the quadrangle; the Green River Basin with the Green River and Flaming Gorge as major elements of topography in the western third; and the Washakie Basin in the south and the Red Desert Basin in the north of the eastern third.

a. Method. Topographic lineaments were drawn on images of the Rock Springs Quadrangle for six different lighting azimuths (30°, 60°, 90°, 300°, 330°, and 360°) with an illumination of 8.5° from the horizontal for all images. Approximately 300 lines were drawn for each of the six images. The lines were digitized and processed using a computer program developed by Donald Wise of the University of Massachusetts and Francesco Salvini of the University of Rome. The program fits Gaussian curves to peaks on azimuth-frequency histograms. Resulting curves smooth the data and are used to quantify height, width, and location of the various azimuthal peaks. These plots are then normalized to the same height for the largest peak and plotted in both histogram and rose diagram format. The analysis is done for cumulative number of lines and for cumulative lengths. The rose diagram is plotted with data for cumulative numbers of lines on the upper half and cumulative lengths of lines on the lower half.

b. Results. Figure 11-80 illustrates the azimuth-frequency histograms for all six lighting directions added together and shows a cumulative plot for the 1860 lineaments detected, many of which are multiple recognitions of the same feature on different images. Each of the single lighting azimuth plots indicates a suppression of lineament trends parallel to the lighting direction. However, many of the peaks are easily correlated from plot to plot. The cumulative plot enhances these recurring directions and suppresses by dilution any trends appearing on only one or two of the diagrams.

The degree of reproducibility of lineament trends among the various plots is best judged in Figure 11-81. Peaks from the Gaussian fits of Figure 11-80 were characterized as strong, moderate, or weak and were plotted at their appropriate azimuth on Figure 11-81. The suppression of lineaments parallel to the lighting azimuth and the enhancement

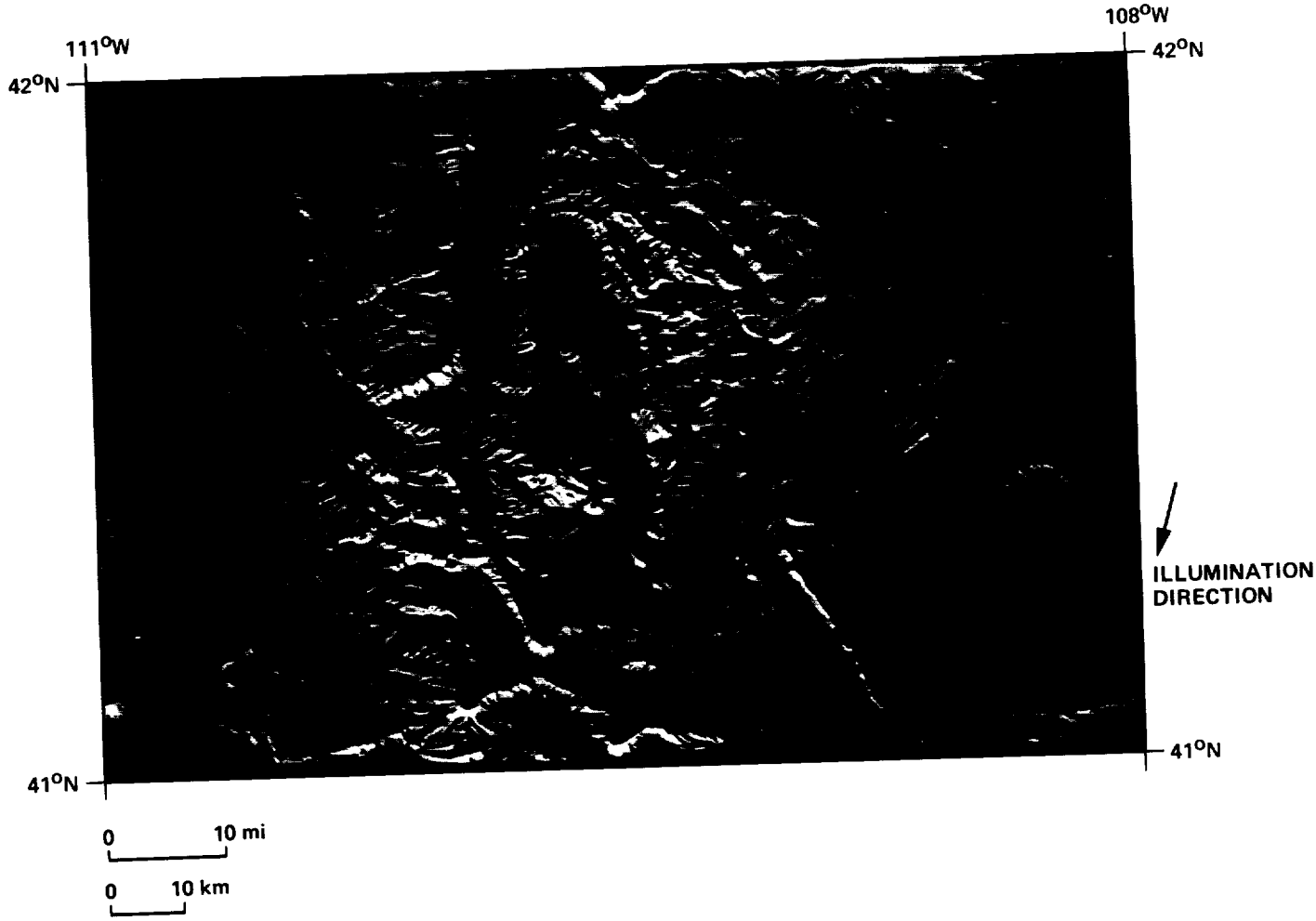

Figure 11-79. Side-illuminated image of the Rock Springs, Wyoming, 1° by 2° raised relief map

of lineaments up to 45° on either side of that direction are indicated by the zone marked "least reliable data." Comparison of the peaks identified on the individual plots with those on the cumulative plot indicates that similar lineament trends were detected on most of the images. The strongest trends appear in spite of the effect of unfavorable lighting azimuths.

Nine lineament trends, indicated by letters A through I in Figures 11-80 and 11-81, appear to be reproducible from topography alone and appear to be detectable with reasonable independence of the lighting azimuth. These directions are assumed to correlate with real elements of the structural grain. The strongest trends (069°, 333°, 318°, and 085°) appear as well-defined azimuthal trends. Other trends, particularly north–south and 280°–300° trends, may be composed of two overlapping and/or less well-defined lineament sets.

Figure 11-82 illustrates the extent to which the cumulative results of the analysis are local versus regional. The individual rose diagrams represent cumulative plots for all lighting directions for azimuths within a 35-km radius of the center of each plot location. The plot on the northeast includes the Patrick Draw test site. The fact that most of the major peaks can be identified across the image suggests that they are regional rather than local features. Density of observable lineaments varies markedly across the image, and probably reflects variations in surface rock type. The highest lineament density appears in the Rock Springs Uplift area, whereas the lowest density is in the Red Desert area, which includes the Patrick Draw test site. Areas of low lineament density correspond to areas of low topographic relief.

Examination of the areal distribution of the peaks in Figure 11-82 reveals some of the reasons for difficulties in

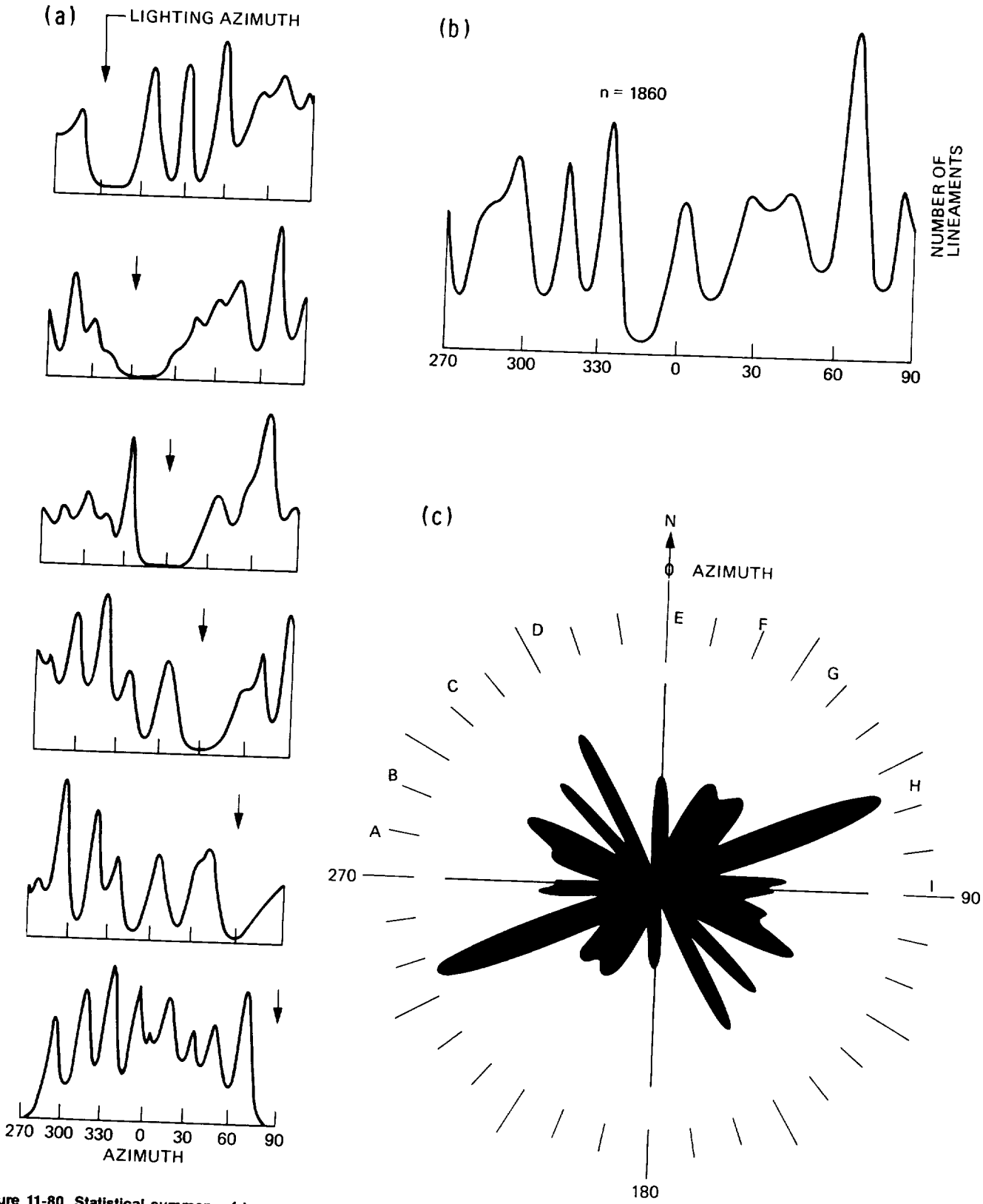

Figure 11-80. Statistical summary of topographic lineaments: (a) smoothed Gaussian histograms illustrating trends in topographic lineament density obtained for each of six lighting directions; (b) cumulative smoothed Gaussian histogram for the six lighting directions combined; (c) rose diagram for the cumulative data

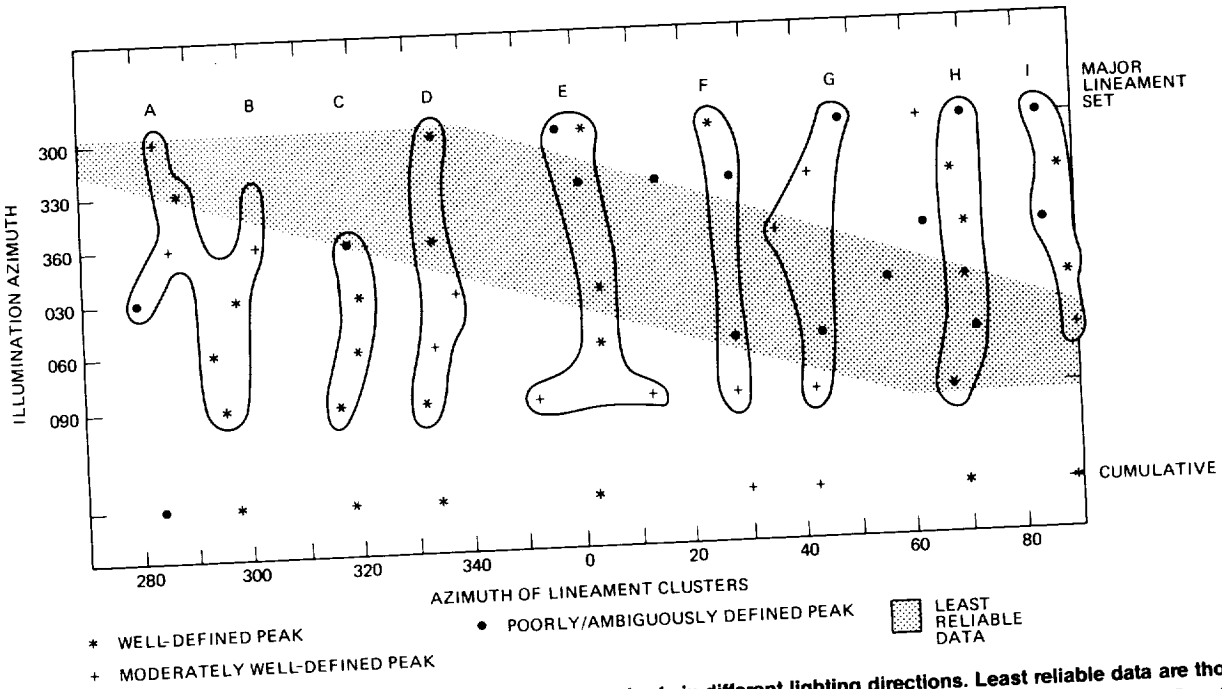

Figure 11-81. Orientations of major topographic lineament sets from each of six different lighting directions. Least reliable data are those within ±45° of the lighting azimuth. Reproducibility of a given set may be judged by its recurrence in many different lighting azimuths. Trends labeled "cumulative" were obtained from the 1860 data points for all six lighting azimuths.

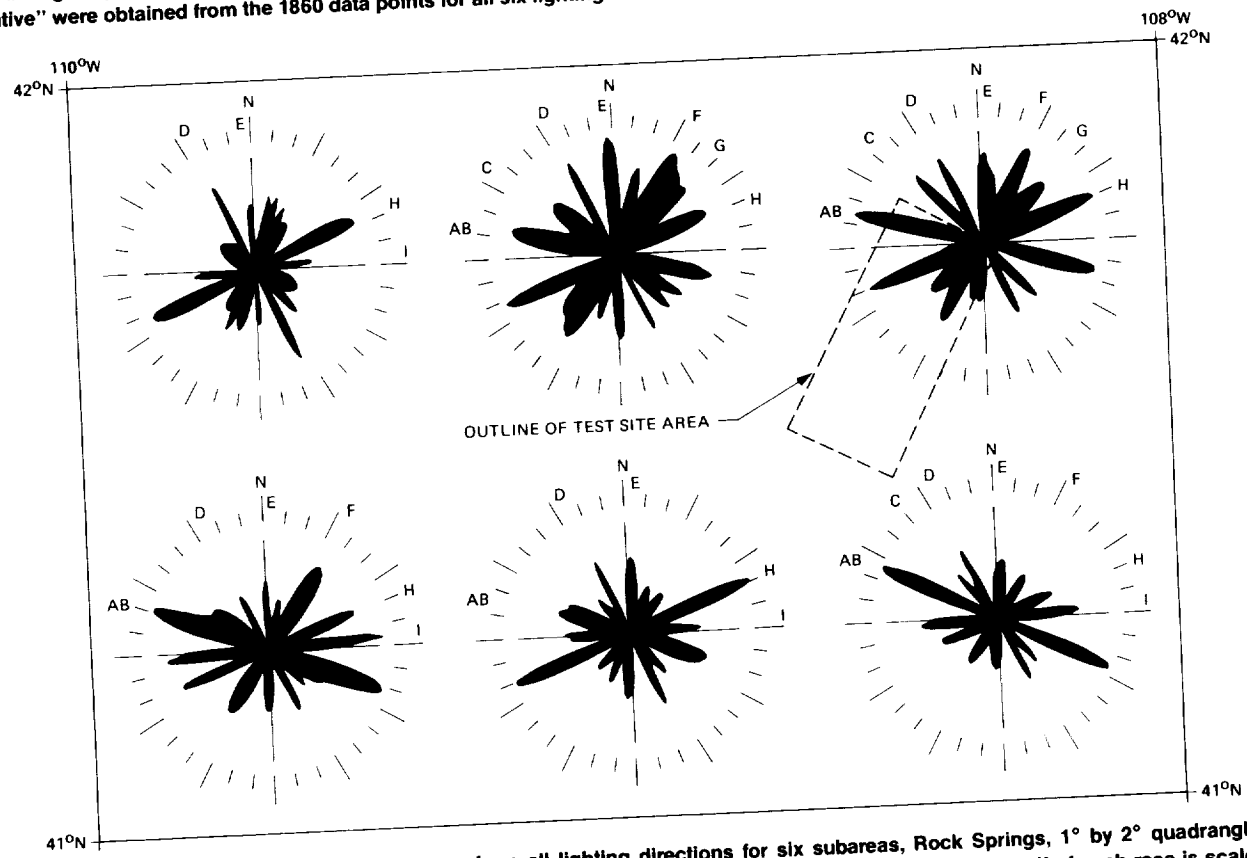

Figure 11-82. Topographic lineament rose diagrams from all lighting directions for six subareas, Rock Springs, 1° by 2° quadrangle (Figure 11-79). The center of each rose is located at the center of each of the 35-km-radius areas analyzed. The top half of each rose is scaled for cumulative number of lineaments and the bottom half for cumulative length of lineaments. Major lineament concentration directions are indicated by letter in each of the rose diagrams.

representing some of the peaks of Figure 11-81 by simple vertical stacking of data. Peaks such as F and G are only locally developed. E and AB range through approximately 10° azimuth, and AB does not appear in the northwest corner.

The regions in which lineament trends are developed may be correlated with other structural features and orientations and may provide clues to both the orientation and timing of associated stress fields. The following observations and possible interpretations are derived from Figure 11-82 in the context of regional structure as discussed in Paragraph III.C:

Set D (333°). A regional trend producing a sharp peak on the smoothed histograms. This set may be an extension fracture system striking normal to the present minimum compressive stress direction of 060° azimuth. This orientation agrees well with Zoback and Zoback's (1980) report of minimum regional compression in this area.

Set E (north–south). Most prominent in Rock Springs Uplift area and the area to the east, but weakly developed to the west. Its localization in and parallelism with the axis of the Rock Springs Uplift suggest an origin by extensional fracturing associated with the development of that structure and the basins to the east.

Set H (070°). Most prominent of the regional trends, although not as consistent a trend as set D. It is parallel to the trend of mapped faults in the area. The orientation of this regional peak suggests an extensional origin of late Laramide age. Just as D may reflect the outcrop traces of the present regional sigma 1/sigma 2 plane, this prominent set may represent extensional features developed parallel to regional traces of the sigma 1/sigma 2 field of Laramide deformation.

Set I (085°). Marked by relatively subtle topographic expression. It is best developed in the west and south, and is parallel to the Uinta Uplift. It is interpreted as a family of distal effects representing extensional fracturing parallel to the axial trend of the Uinta Uplift.

Set AB (280°–300°). A prominent but less consistent trend than those described above. It is not recognized in the northwest portion of the quadrangle. Eastward it appears to bifurcate into two azimuth directions (285° in the northeast and 295° in the southeast). This pattern suggests minor regional curvature of a major stress trajectory. One possibility, deserving further examination, is that this set represents the effects of the stresses of the Overthrust Belt just to the WNW pushing ESE into a foreland region. As in the interpretation of D and H above, these lines would represent the regional traces of the sigma 1/sigma 2 plane of that tectonic episode.

Set C (315°–320°). Seems better defined at the east end of the quadrangle, but is reasonably prominent in the entire test site area. No interpretation has been made for origin or age.

Set F (030°). Appears at least weakly developed throughout much of the area, but is most strongly developed in the northeast, north–central, and southwest parts of the quadrangle. No interpretation has been made as to origin or age.

Set G (040°–045°). Poorly defined but most apparent in the northern and eastern portion of the quadrangle. No interpretation has been made as to origin or age.

c. Topographic lineaments near the Patrick Draw Test site. Figure 11-83 illustrates the trends of topographic lineament traces in the vicinity of the Patrick Draw test site. Different authors, or even the same author on different days,

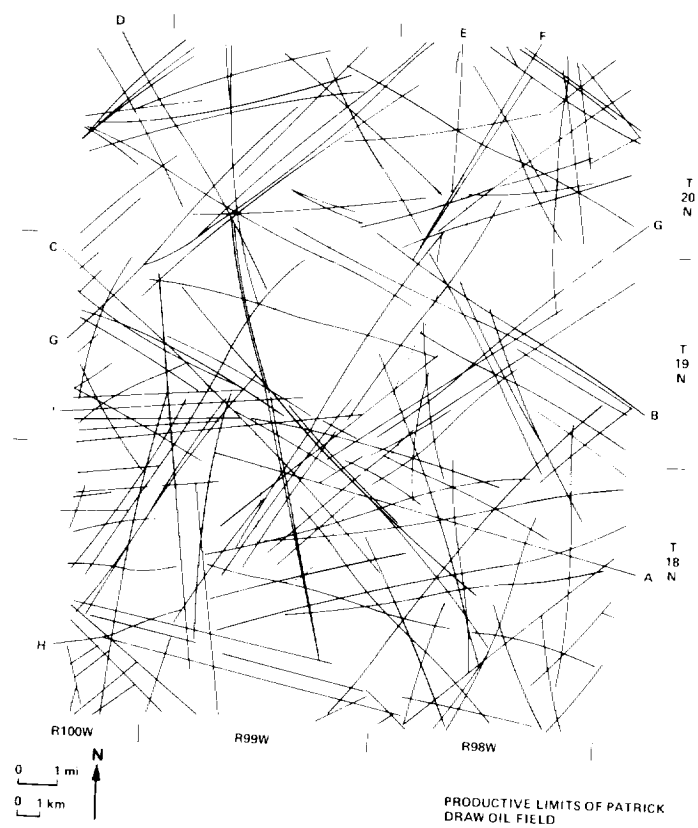

Figure 11-83. Topographic lineaments in the vicinity of the Patrick Draw test site as observed by combining interpretations from six different lighting azimuths. A single lineament has the potential of appearing six times in this illustration. Several of these multiple recognitions are evident. Examples of individual lineaments associated with each of the major regional sets are labeled *A–I*, corresponding to the designations of Figure 11-81.

will draw a lineament trace at different locations on the same image. One time the line will be drawn on one side of a valley, another time on the other side or in the valley center. What remains relatively constant and reproducible is the azimuth of the line drawn, rather than its precise location. Thus, the present analysis emphasizes lineament trends rather than the absolute locations of lineaments.

Figure 11-83 includes all lineaments drawn on six different lightings of the test site. Thus, a single lineament conceivably could be represented by up to six nearly coincident lines. The near coincidence of some of the lines may reflect the same lineament being identified on several images at about the same location or may demonstrate the existence of closely spaced, parallel lineaments. All eight of the major topographic lineament sets described above are present in the Patrick Draw test site area.

d. Discussion and conclusions. Based on topography alone, eight lineament trends can be identified in the Rock Springs region. The objectivity of their detection may be evaluated by examining their reproducibility on variously lighted topographic images of the same area. Differing sets have differing degrees of parallelism, intensity of development and relationship in map distribution, and orientation to the large-scale tectonic elements of the area. Based on these clues, the eight topographic lineament trends are interpreted to be subtle extensional features, mostly zones of more intense jointing related to regional stress trajectories. They are interpreted as the outcrop of the sigma 1/sigma 2 plane for two tectonic environments: (1) broad warping as in the Rock Springs and Uinta Uplifts and (2) traces of past or present maximum compressive stress trajectories during regional compressive events. For the Patrick Draw test site, four of the trends seem best developed. Because these trends are due to topography alone, some of them will certainly appear in the analyses of remote sensing data.

3. NS-001 lineament analysis. In the geologic interpretation of NS-001 data shown in Figure 11-77, 176 lineaments are identified. An examination of Figure 11-77 and the histogram of lineament azimuth measurements obtained from this interpretation (Figure 11-84) reveals two dominant lineament trends. A generally E–W trend, perpendicular to the solar azimuthal plane, is represented by lineaments throughout the image area; a generally N–S trend, parallel to the solar azimuthal plane, is best represented by lineaments in the southern one-third of the image.

A statistical analysis of azimuth measurements for 176 lineaments shown on Figure 11-77 (Table 11-20) supports the existence of these two dominant populations and reveals the existence of four other populations within the two. Three subpopulations are within the E–W-trending set A: A′, A″, and A‴. A and A′ are statistically inseparable since both have the same mean value. A″ and A‴ are significantly different from A, and A′ is significantly different from A″ and A‴. Based on these relationships, set A is considered an artifact of combining the statistically "real" lineament sets A′, A″, and A‴. The N–S-trending lineament set B contains a subdominant population B′. B and B′ are considered to be two statistically "real" populations.

In Table 11-21, the five "real" lineament trends are ranked according to the number of lineaments included in each. The effect of illumination-aspect enhancement of lineament trends that are transverse to the solar azimuth is apparent in the dominance of set A′, which contains over 55 percent of the lineaments identified.

A comparison of the azimuthal means and ranges for the lineament trends recognized in the NS-001 data to those trends recognized in topographic data reveals that the five NS-001 trends coincide with five of the topographic trends. Three of these trends also correspond to the orientation of major structural elements (Figure 11-3) in the Patrick Draw vicinity.

Set A′ (N 87° E). Corresponds to topographic set I (N 85° E); has approximately the same orientation as the Wamsutter Arch and numerous normal faults mapped by Roehler (1977a), which are transverse to the axis of the Rock Springs Uplift. This is suggestive of extensional cross-fracturing genetically related to the Rock Springs Uplift.

Set B (N 1° E). Corresponds to topographic set E (N 0° E); has approximately the same orientation as the axis of the Rock Springs Uplift. This is suggestive of parallel axial fracturing genetically related to the Rock Springs Uplift.

Set A″ (N 67° W). Corresponds to topographic set AB (N 60° W to N 80° W). The relationship to structural elements in the region is rather obscure but, based on similar trends, may be related to the Overthrust Belt to the west or the Wind River Uplift to the north.

Set B′ (N 24° E). Corresponds to topographic set F (N 30° E). The relationship to known structural elements in the region is obscure.

Set A‴ (N 51° W). Corresponds approximately to topographic set C (N 45° W to N 40° W). The relationship to known structural elements in the region is obscure.

Additional insight into the meaning of at least one of these lineament trends was afforded by observations in a

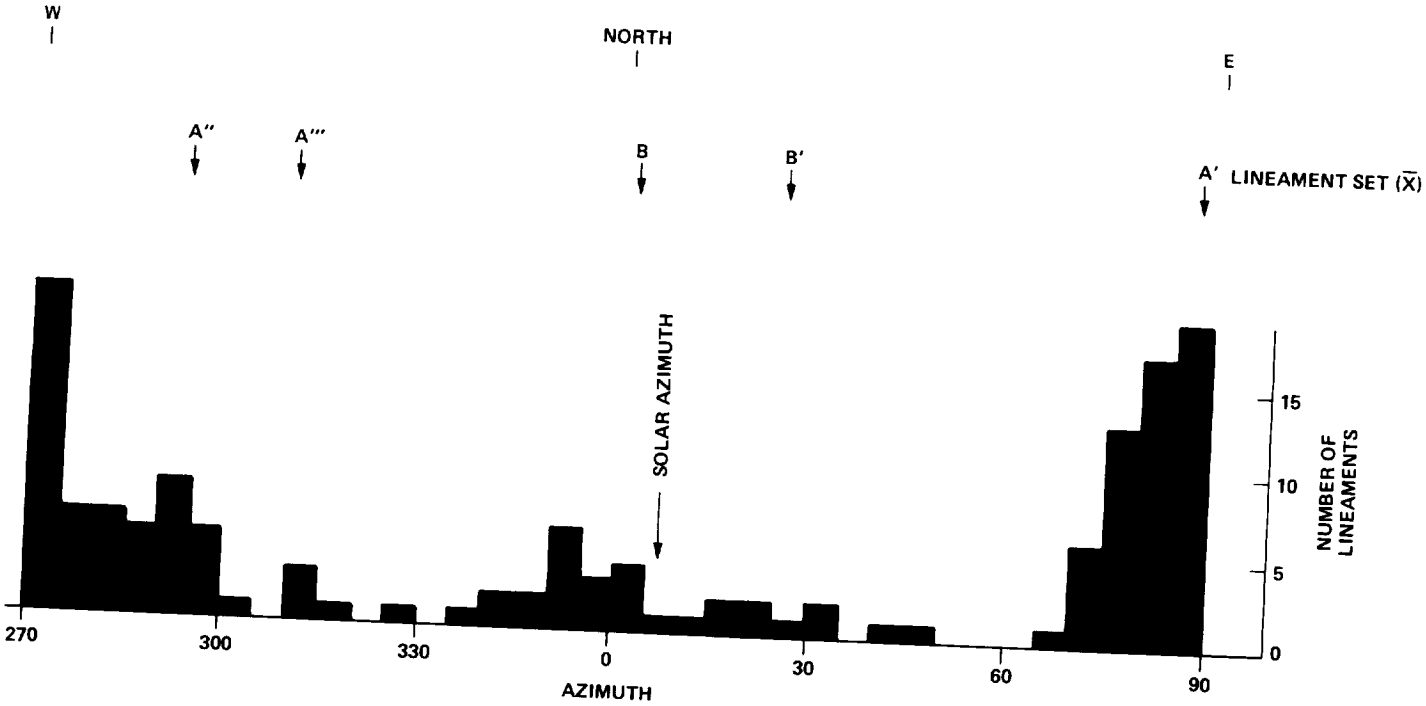

Figure 11-84. NS-001 lineament azimuth histogram for 176 lineaments recognized in the composite geologic interpretation shown in Figure 11-77

Table 11-20. Summary of trends of six lineament sets recognized in a statistical analysis of 176 azimuthal measurements for lineaments shown in Figure 11-77

Set	Number	$\overline{X}$ (azimuth), degrees	σ, degrees	Range, degrees	τ_d[a]	F-Test Significance Level
A	110	86.4	10.7	90	0.71 (A–B)	>99.5
A′	101	87.2	3.5	39	0.43 (A′–A″)	>99.5
A″	22	292.5	5.4	20	0.24 (A–A″)	99.5
A‴	6	308.8	5.0	29	0.33 (A″–A‴)	>99.5
B	32	1.0	22.3	90	0.71 (A–B)	>99.5
B′	12	23.5	12.8	46	0.25 (B′–B)	99.5

[a]Modified T-test:

$$\tau_d = \frac{\overline{X}_1 - \overline{X}_2}{w_1 + w_2}$$

Table 11-21. Summary of five lineament sets recognized in the analysis of 176 lineaments shown in Figure 11-77. Sets are ranked according to number of lineaments included, and illumination aspect effects are indicated. Equivalent topographic lineament sets are also shown.

Rank	Set	Trend (azimuth), degrees	Illumination Aspect		Equivalent Topographic Set
			Enhanced	Suppressed	
1	A′	87	+		I
2	B	1		+	E
3	A″	293	+		AB
4	B′	24			F
5	A‴	309	+		C

gas pipeline trench that was excavated across the test site area. A jointed claystone in the Wasatch Formation was exposed in the trench at a location coincident with the location of one of the lineaments included in set A′ (Figure 11-85). The jointed interval was approximately 10 m wide and was characterized by closely spaced, vertical planar joints striking N 85° E. Sandy laminae in the claystone were not offset by the joints. This 10-m interval was the only exposure of jointed bedrock observed in the trench; it was also the only location at which the trench crossed a lineament recognized in NS-001 images. These observations lend credence to the interpretation that lineaments seen in the NS-001 images represent restricted localities of fractured bedrock.

E. Vegetation Mapping

1. Introduction. The vegetation study discussed in Paragraph V included an evaluation of percent vegetation cover at 19 sites in the test site area (Table 11-5). Fifteen of these sites are within the image area of NS-001, Mission 390, line 4, October 19, 1978 (Plate 11-1). To evaluate the utility of these image data for vegetation analysis, the seven VNIR raw band data were used as variables in a supervised percent vegetation cover classification. The 15 vegetation study sites and eight other sites (five unvegetated areas—a playa, drilling pad, paved road, and two dirt roads—and three dense vegetation areas—drainages with more than 50 percent sage cover) were used as training areas for VICAR programs STATS and FASTCLAS to produce a supervised classification image (Figure 11-86). These VICAR programs are described in the Technical Appendix, Section 14.

2. Discussion. Both field evaluation and comparison to color infrared (CIR) aerial photography demonstrate that Figure 11-86 is an accurate portrayal of variations in vegetation density in the image area. The area of anomalous stunted sage appears red (1 to 10 percent vegetation cover) in a region characterized by yellow (21 to 30 percent vegetation cover). Thus, this image provides evidence that the area of anomalous stunted sage is characterized by a decrease in vegetation cover of at least 10 percent. The "type area" for the Fort Union/Wasatch transition unit (Figure 11-75) is shown in Figure 11-86 to be characterized by more unvegetated areas (black) than adjacent Fort Union strata to the west or Wasatch strata to the east. The supervised classification image is considered a valid portrayal of variations in percent vegetation cover, which has direct application to botanical study and to geologic mapping.

Additionally, this image provides critical information for separating the vegetation and soil/rock components for spectral analysis studies. Data from Figure 11-86 can be used in a simple unmixing calculation that extracts image soil/rock spectra from mixed pixels, provided calibrated image data (such as Figures 11-65 through 11-71) are available. For any pixel, the percent vegetation cover is determined from Figure 11-86. The average reflectance for vegetation in a particular band may be estimated from PFRS or equivalent spectral data. The total reflectance for the

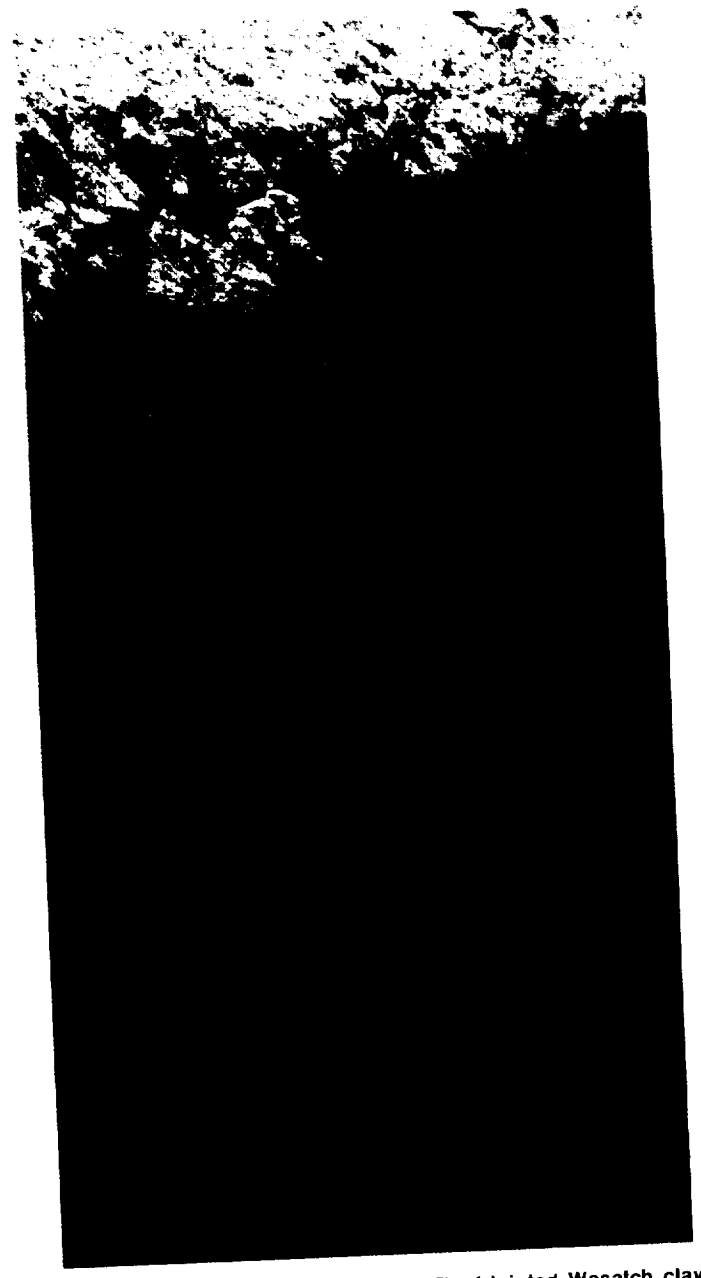

Figure 11-85. Photograph (looking NNE) of jointed Wasatch claystone exposed in a gas pipeline trench. The jointed interval coincides in location with the trench intersection of lineament *X*–*X* identified in Figure 11-75; the strike of the joint planes shown (N 85° E) coincides with the trend of the *X*–*X* lineament.

pixel in a particular band can be extracted from the calibrated image data. Thus, using the simple Siegal and Goetz (1977) mixing model:

$$r_S = \frac{(r_P)100 - (v)(r_V)}{100 - v}$$

where r_S = soil/rock reflectance (%) in a particular band for the pixel

r_P = total reflectance (%) in a particular band for the pixel determined from calibrated image data

v = vegetation cover (%) for the pixel determined from the supervised percent vegetation cover image

r_V = vegetation reflectance (%) in the band from appropriate field/laboratory spectra

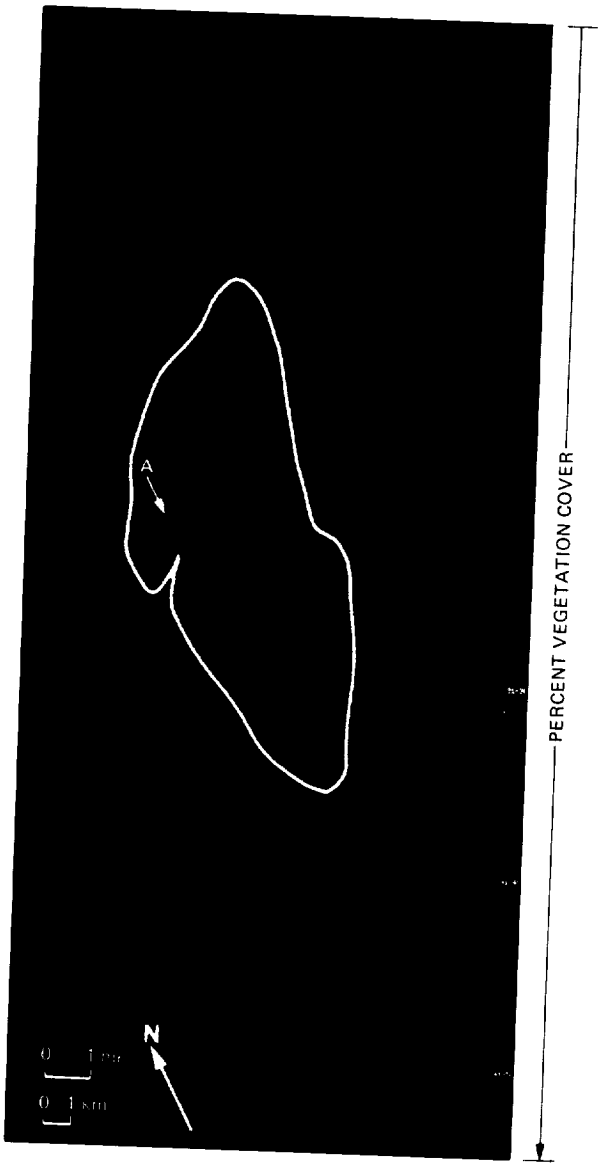

Figure 11-86. Image showing variations in percent vegetation cover in the test site area. The seven VNIR band data from Mission 390, line 4, and 23 training areas were used in VICAR programs STATS and FASTCLAS to produce this supervised classification map. *A* shows the approximate center of the area of stunted sage.

3. Conclusions. NS-001 VNIR band data can be used as variables with limited ground-control training areas to produce supervised classification images that portray areal variations in percent vegetation cover. Such supervised classification images provide information directly applicable to geobotany and also may be used with calibrated image data to quantitatively solve the problem of unmixing the vegetation and soil/rock spectral components in multispectral image data.

X. Radar

A. Introduction

Seasat Synthetic Aperture Radar (SAR) data were acquired at the Patrick Draw test site area during two overpasses: Rev. 738 on August 17, 1978 and Rev. 789 on August 21, 1978. When digital tapes from both passes were first processed, it was discovered that the Patrick Draw test site was in the far range of the Rev. 738 data where the signal-to-noise ratio and data range are both low; therefore, the SAR data of Rev. 789 were selected for further computer processing by both JPL's and Gulf's remote sensing centers.

B. Seasat SAR Data Characteristics and Processing

The SAR data for Rev. 789 cover the entire Rock Springs Uplift area. Figure 11-87 shows that the test site is located at the north or near range of the image. Although approximately one-third of the test site is not contained within the image, most of the Patrick Draw field is.

Gulf processed the portion of the SAR image that included the test site. Table 11-22 summarizes the characteristics of the data. Spatial processing of the data with a 3 by 3 median filter improved the image quality by suppressing the extreme local noise or speckle that is so common in most radar data. Test site team members received copies of a black-and-white version of the filtered SAR data, with a linear contrast stretch, for interpretation.

JPL processing of the SAR data focused on the use of spatial information, both in terms of enhancement (split-spectrum) and classification (texture analysis). Hue, saturation, and intensity (HSI) split-spectrum processing capitalizes on the fact that tone variations in a radar image are governed by variations in surface relief which occur over a

wide range of spatial scales. Large-scale (low spatial frequency) variations in image tone are related to variations in surface roughness (vegetation and rock type), whereas small-scale (high spatial frequency) variations in image tone are dominated by slope effects. An additional component is radar speckle, which is especially evident at the highest spatial frequencies.

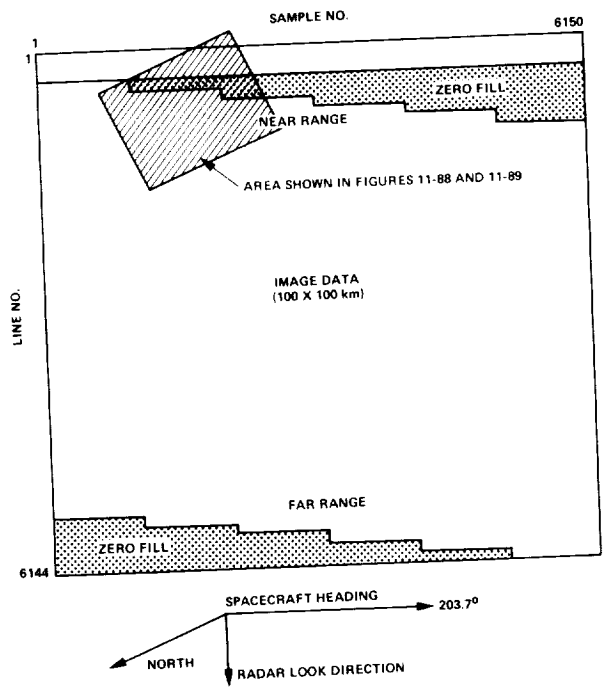

Figure 11-87. The location of the Patrick Draw test site with respect to Seasat SAR Rev. 789 coverage

Table 11-22. Characteristics of Seasat SAR subscene (Rev. 789) as processed by Gulf Science and Technology Company

Parameter	Value
Wavelength, cm	23 (L band)
Spacecraft heading, deg	203.7
Look direction, deg	113.7
Look angle (from vertical), deg	20
Date	August 21, 1978
Number of lines	1280
Number of samples	2048
Data range (8 bit)	
Minimum	2
Maximum	253
Image DN statistics	
Mean	31.8
Variance	200
Median	30
Mode	26
Filter used	3 by 3 median
Contrast stretch used	Linear
Pixel size used (approximate registration at 1:48,000), m	17 by 17

To separate and encode these physical mechanisms, the input scene was filtered into high-pass (HP) and low-pass (LP) images; then the LP image was used to encode hue, the HP image was used to modulate intensity, and the image saturation was varied interactively. Figure 11-88 shows the components that contribute to the color image. A variety of black-and-white images was also made from HP-filtered SAR data (Figure 11-88a).

C. SAR Interpretation

Interpretations for lineaments and tone/texture from the SAR images described in the previous paragraphs were compiled as an overlay on a 1:48,000 print of Figure 11-88(a) (see Figure 11-89 for interpretation). Lineament analyses were made by several geologists. To assure consistency in analysis, seven tone/texture classes were established. The tone characteristic refers to the average gray level of the black-and-white image over an area approximately 2 by 2 km in size and is either dark, medium, or bright. The texture characteristic is a measure of the granularity or homogeneity of the same area and is either rough, medium, or smooth. Figure 11-90 provides a key to the tone/texture classes. All areas that are rough in texture are bright in tone. This relationship results in part from the fact that dark (black) surfaces can only be smooth textured. The boundaries drawn between classes are approximate but do delineate areas of different radar return in both the black-and-white and color (HSI) versions.

The SAR tone/texture map and image were compared to interpretations from the remotely sensed data and to ground observations. This comparison helps to further elucidate the physical meaning of the SAR classes.

The SAR classes are best correlated with local topographic relief, slope, and slope aspect. Areas of bright tone and rough texture on the SAR image (Class A) include the prominent north-trending ridge of 45- to 60-m (150- to 200-ft) relief south of Bitter Creek, the west escarpment of Table Rock Plateau, and the rugged hills along the western edge of the study area. All portions within these areas that slope to the southeast (or face the look-direction of the SAR sensor) have the brightest radar return. The medium-toned areas are mostly restricted to areas of moderate to gentle slope, approximately 20 m/km (100 ft/mi) and less, that face in all directions, whereas the darkest toned areas include areas of moderate to steep slope, approximately 40 m/km (200 ft/mi) and more, that face northwest. On a local scale, negative or positive terrain features such as gullies or dunes appear in the image data as areas of rough or medium texture. In short, a major part of the radar return may be attributed to terrain relief.

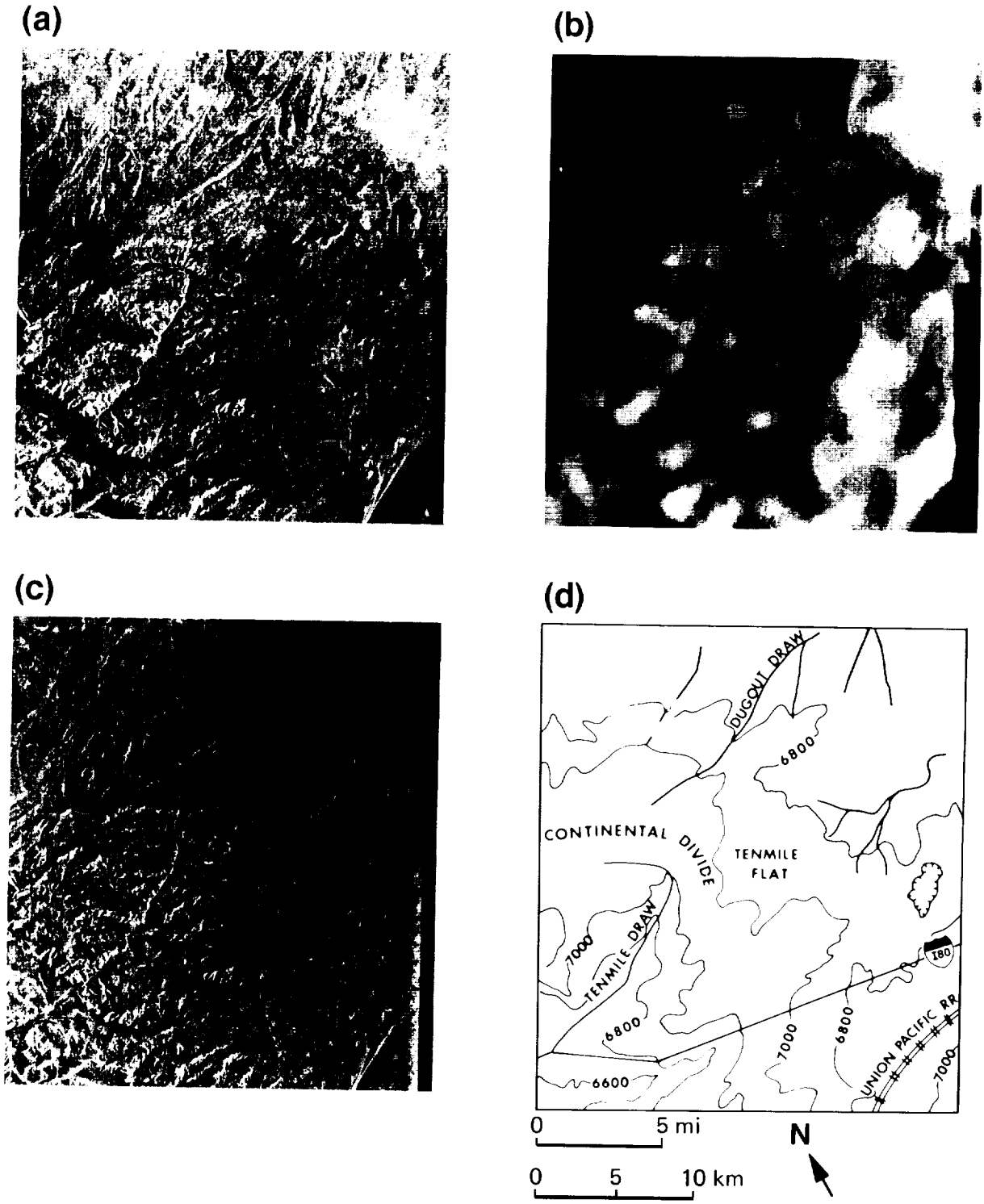

Figure 11-88. Components used in split-spectrum (HSI) processing of Seasat SAR data: (a) HP-filtered data; (b) LP-filtered data; (c) HSI image; (d) major geographic features in image area

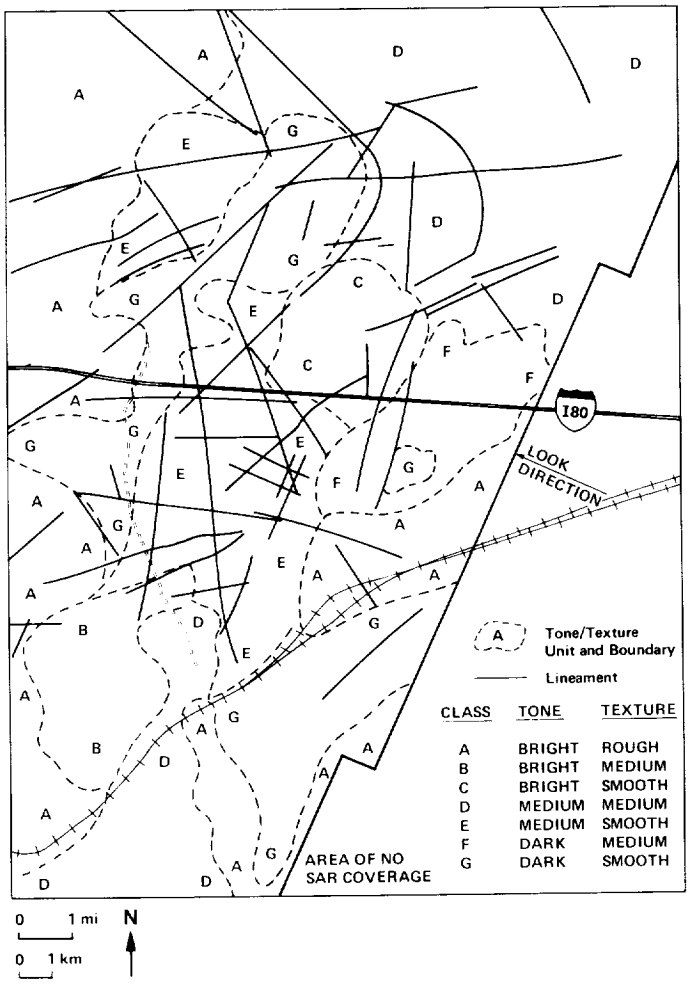

Figure 11-89. Composite lineament and tonal/textural interpretation of Figure 11-88(a). Original interpretation was made at a scale of 1:48,000. Figure 11-90 shows the key used in textural classification.

All but one SAR class (bright tone, medium texture) are present both on and off the field. In addition, the field boundary is not coincident with any significant portion of the SAR class boundaries. The vegetation anomaly, which was first recognized in NS-001 images, is located within a much larger SAR class of medium tone and smooth texture. There is no feature in the radar image data that is coincident with the vegetation anomaly boundary.

A comparison was made between the BLM soil map and the SAR image. No significant pattern or correlation emerges from this comparison. There is no physical attribute of the soil units, which includes chemical, texture (grain size), provenance, depth, color, and potential plant species, that uniquely identifies one of the seven SAR tone/texture classes. The strongest correlation was that all soils with an eolian source were located in areas on the SAR image with the roughest texture in each tone class.

Problems in SAR image interpretation encountered in this study stem from two factors:

(1) Radar generates extremely strong returns from gullies and other relatively small topographic features. These specular scattering variations are restricted to high spatial frequencies since slopes of the requisite steepness (20°) are rare for large topographic features in the Patrick Draw area. The bright returns swamp the subtle low-frequency scattering variations that are associated with changes in vegetation density.

(2) The image scale used (1:48,000) is too large for detection of subtle low-frequency tone variations at normal viewing distance (approximately 1 m). The spatial frequency response of the human visual system decreases significantly at low frequencies. The optimum viewing distance for kilometer-scale tone variations at 1:48,000 scale is over 10 m.

The split-spectrum process yields a color image largely free of these problems. The filtering operation separates topographic from vegetation (surface scattering) effects. Since hue is perceived best at low spatial frequencies, the hue and intensity encoding optimizes the scene in relation to the spatial frequency response of the human visual system. The color image in Figure 11-91 clearly shows the surface expression of the Wamsutter Arch, while retaining high-frequency visual cues associated with minor drainages.

D. Summary

Comparison of SAR data with other remote sensing data revealed little correlation between radar return (backscattering) and variations in solar reflectance. Microwave images obtained in the area appeared to be dominated by variations in surface topography. It is possible that the removal of the topographic component, perhaps through registration with digital terrain data, may enhance a signal now masked by topography and so provide a better correlation with other data sets. This topographic masking can be stripped out very effectively by splitting the scene spectrum into high- and low-frequency components. These components may then be encoded as intensity and hue, respectively, yielding a color image that shows regional structural features such as the Wamsutter Arch.

XI. Fraunhofer Line Discriminator—Luminescence Survey

A. Introduction

The U.S. Geological Survey acquired aircraft luminescence data of selected areas in the Patrick Draw test site on

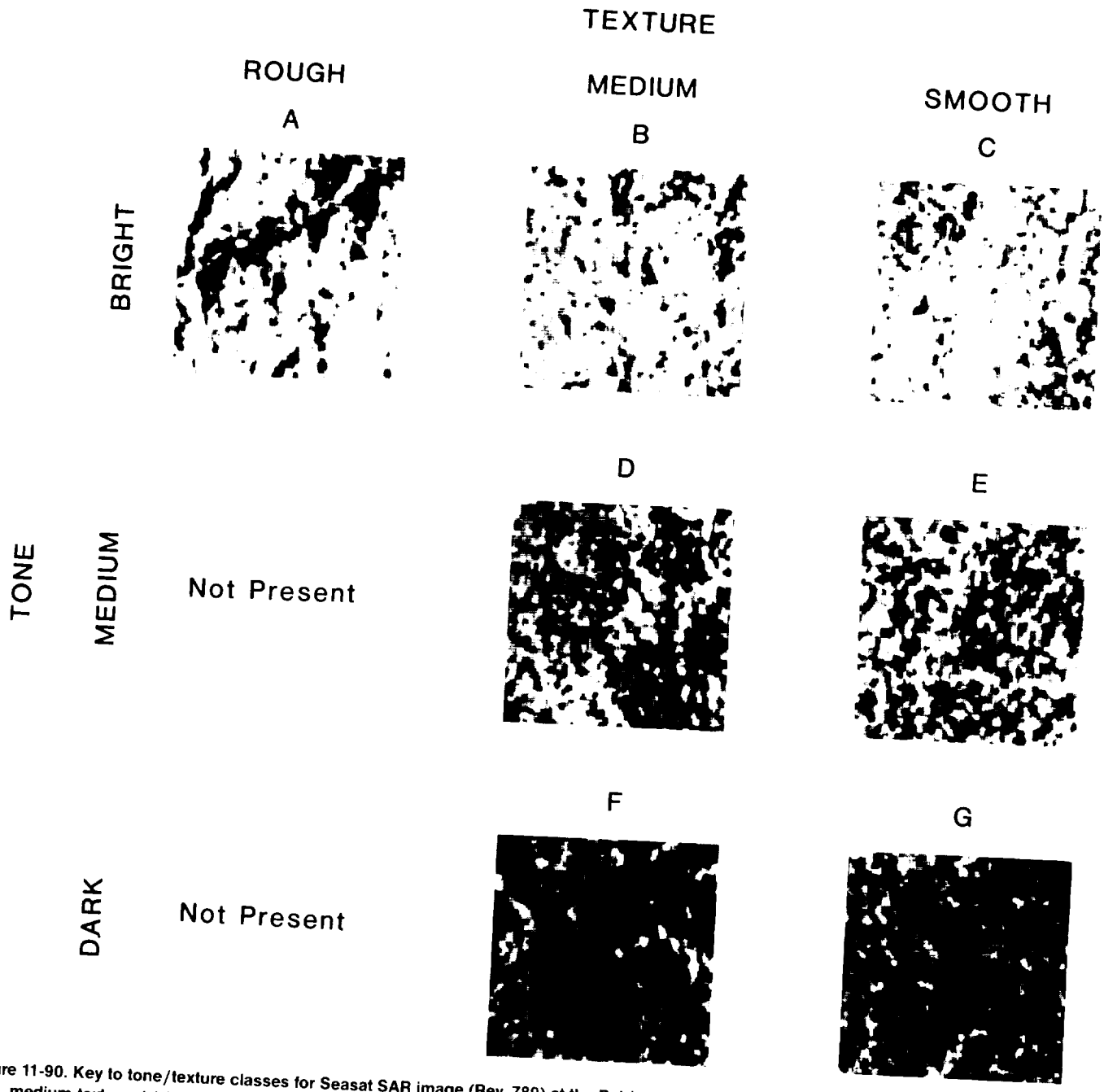

Figure 11-90. Key to tone/texture classes for Seasat SAR image (Rev. 789) at the Patrick Draw test site: (a) bright tone, rough texture; (b) bright tone, medium texture; (c) bright tone, smooth texture; (d) medium tone, medium texture; (e) medium tone, smooth texture; (f) dark tone, medium texture; (g) dark tone, smooth texture. Image samples are at a scale of 1:48,000.

August 4, 1980, with the Fraunhofer Line Discriminator (FLD) (refer to the Technical Appendix, Section 14, for a discussion of this sensor). The objective in acquiring FLD data was to determine if luminescence anomalies could be detected in areas within the test site and to correlate these anomalies with other measurements as described elsewhere in this report.

Six traverses with the airborne FLD were made over the Patrick Draw field; three at an operating wavelength of 656.3 nm, two at 486.1 nm, and one at 589.0 nm. The location of five of these traverses is shown in Plate 11-1. Traverse six is oriented in an E–W direction, approximately 1.5 km (1 mi) to the north of the area shown in Plate 11-1. Overlays of luminescence values in discrete intervals from

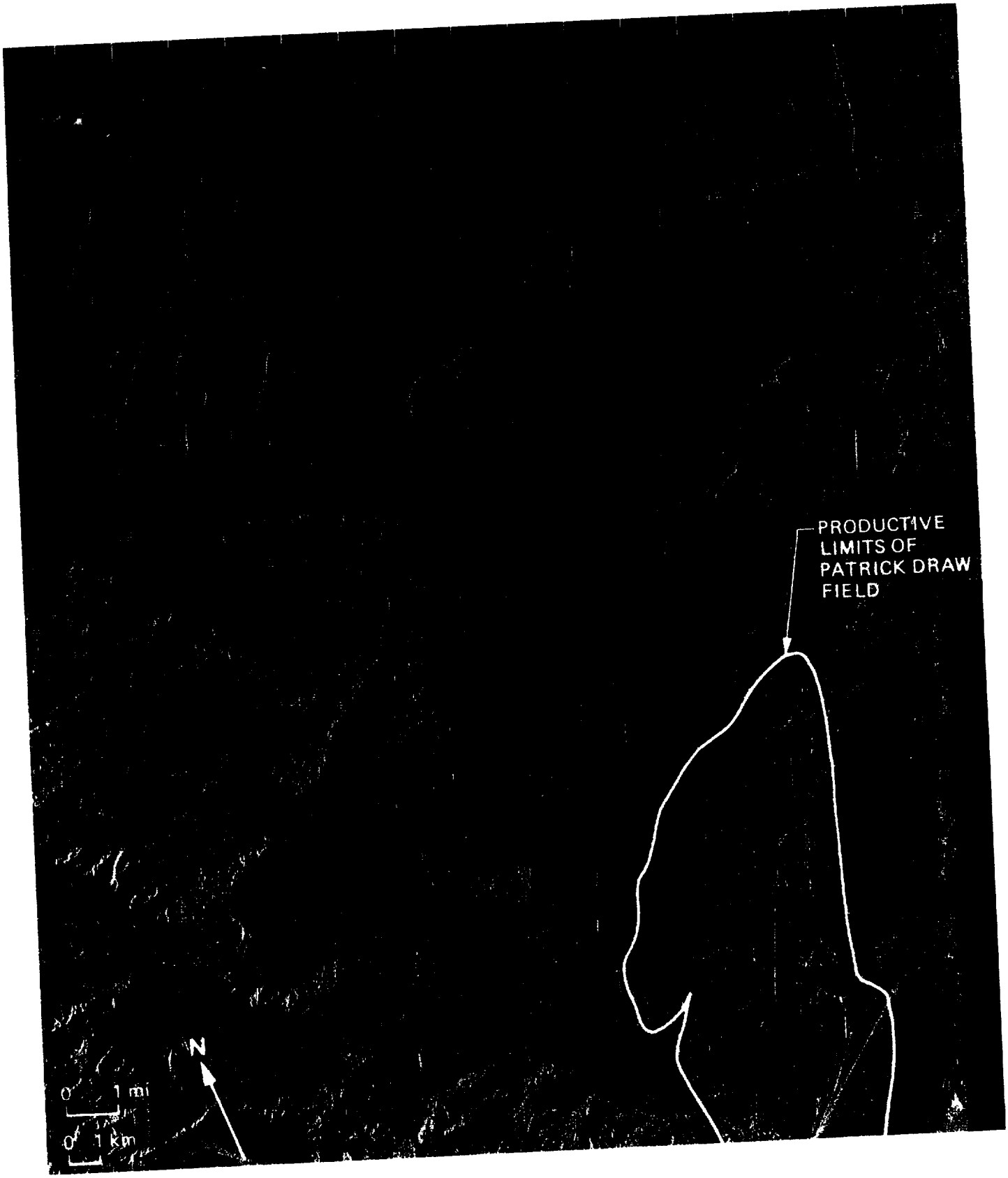

Figure 11-91. Seasat HSI image

1.5 to 2.5 (green), 2.5 to 3.5 (orange), and 3.5 to 4.5 (red) ppb rhodamine WT equivalence are shown in Figures 11-92, 11-93, and 11-94 for the five traverses.

Each of the three Fraunhofer wavelengths produces a different luminescence in response to the geochemistry/mineralogy of the materials image by the FLD. Of the three wavelengths, 656.3 nm, located on the shoulder of the chlorophyll-a band, could be expected to reveal stressed vegetation within the image area. The 656.3-nm wavelength might also be used to correlate luminescence with calcite cements, as was demonstrated in laboratory and field measurements on samples of calcite-cemented sandstones collected in the Cement, Oklahoma, oil field (Donovan et al., 1975).

In the following discussion, luminescence at each Fraunhofer wavelength is compared to the geochemistry of materials measured in the field and discussed in Paragraph VII.E. The combined luminescence/geochemistry data set is limited due to the lack of geochemical sampling sites in all of the FLD image areas. Even with this restriction, it was possible to correlate elemental geochemistry and luminescence at each Fraunhofer wavelength.

B. Data Analysis

To correlate luminescence with geochemistry, the mean of all geochemical surface samples for each element was determined, and each sample was ranked against the mean and standard deviation of the entire sample population. Values less than the mean were given rank 1; between the mean and one standard deviation above the mean, rank 2; between one and two standard deviations above the mean, rank 3; and greater than two standard deviations above the mean, rank 4. Since only a limited number of geochemical sample sites were available for correlating element concentration with luminescence, it was not possible to perform a multiple regression analysis to simultaneously correlate all elements against luminescence. Therefore, a simple linear regression analysis was performed for each element, and the 12 elements showing the strongest correlation were selected for multiple regression analysis.

C. Results

Table 11-23 is a summary of those sample sites that show luminescence above background and those elements of rank 3 or 4 which are classified as geochemically anomalous.

Table 11-24 lists elements versus the wavelength that produced a positive correlation with luminescence. The percent of total luminescence (value in parentheses) is a

Figure 11-92. NS-001 band 3 image with a luminescence overlay, Patrick Draw test site. Luminescence values at 486.1 nm (ppb rhodamine WT equivalence) are 1.5 to 2.5 (green), 2.5 to 3.5 (orange), and 3.5 to 4.5 (red).

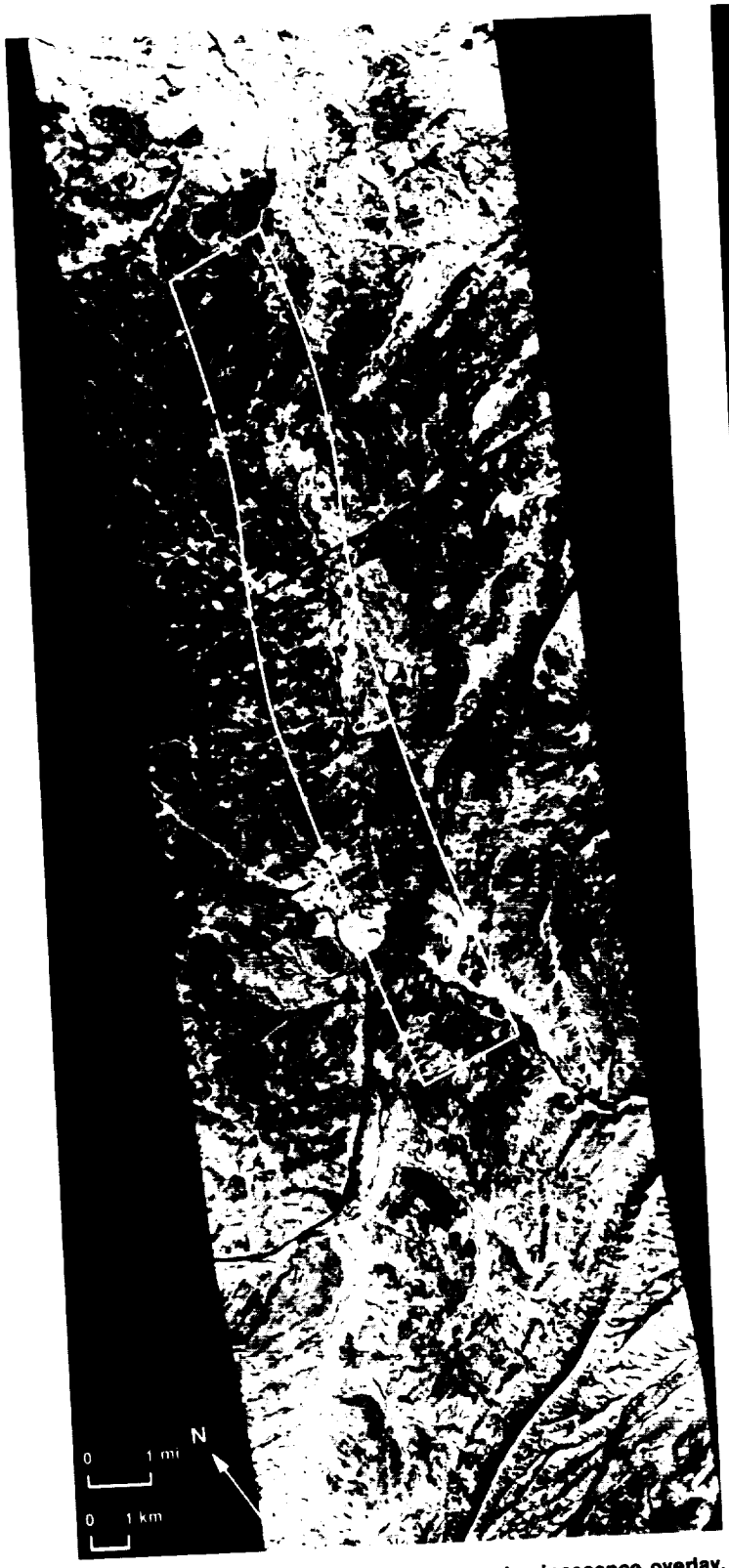

Figure 11-93. NS-001 band 3 image with a luminescence overlay, Patrick Draw test site. Luminescence values at 589.0 nm (ppb rhodamine WT equivalence) are 1.5 to 2.5 (green), 2.5 to 3.5 (orange), and 3.5 to 4.5 (red).

Figure 11-94. NS-001 band 3 image with a luminescence overl
Patrick Draw test site. Luminescence values at 656.3 nm (ppb r
damine WT equivalence) are 1.5 to 2.5 (green), 2.5 to 3.5 (orang
and 3.5 to 4.5 (red).

Table 11-23. Summary of the sample sites that show luminescence above background and those elements of rank 3 or greater classified as anomalous. Any additional descriptive features known on the site are also included.

Site[a]	Description	Soil Unit[b]	Luminescence, nm[c]		
			486.1	589.0	656.3
L1-9	Mn = 3	438	2.5	NM	NM
1-11	Mn, P = 4; Al = 3; high Fe, low C; Wasatch	438	2.5		NM
1-12	Mn = 4	438	2.5	1.75	NM
1-13	Mn, Mg, Pb, Cu = 3; siderite, $CaCO_3$, Wasatch	438	2.5		
1-15	Mn, Cu = 4; Pb, Mg, V = 3	438–439	2.5	3.5	2.5
2-4	K = 3; $CaCO_3$, kaolinite, midtransition	333	1.75	1.75	NM
2-6	Mn = 4; B, V = 3	332			2.5
3-1	Mn, P = 3	449	1.75	2.5	NM
3-2	Cu = 4; Al, Sr, Ti, V = 3	335		2.5	1.75
3-3	Cu, Al, Ti, V = 4	335	1.75	1.75	2.5
3-5	Cr, Fe, Ni, Soil gas = 4, Co, Mn, Mo, Zn, P, B, V = 3	335	NM	NM	3.5
3-6	Soil gas = 4; Mn, Ni, P = 3	449			3.5
4-4	Soil gas = 3, $CaSO_3$; kaolinite, midtransition	447		1.75	1.75
5-4	Soil gas = 3; Cu, Be, Zn = 3	450	NM	2.5	NM
6-1	Mn = 3	450	NM	1.75	NM
6-2	Co, Mn, Mo, P, B = 3; $CaCO_3$ coal bed at base of transition	450–335	NM	3.5	NM
6-3	Be = 4	333	NM	2.5	NM
6-5	Ti = 3	333	NM	2.5	3.0
XL2-1	P, B = 3; shale between $CaCO_3$ beds, coal layers	466	3.5	1.75	NM
2-4	D, V = 3; coal, midtransition	438	1.75	1.75	NM
4-4	Mn = 3	332	NM	NM	1.75
4-6	CR = 4; Go, Fe, Pb, Mg, Mn, Ni, Ag, Be, Ba, Zn = 3; $CaCO_3$, jarosite, gypsum, siderite	335		4.0	
4-7	Cu, Co = 3; $CaCO_3$, top of transition				
R35		449	NM	1.75	
41	Mn = 3; coal and limestone	438	NM	NM	1.75
47	Soil gas, Mn = 4, Si = 3	438	NM	NM	1.75
72	Soil gas, Mn, Sr, Ba, P, B = 3	332	NM	NM	2.50
93	Mn, Cu, Ni, P = 3; $CaCO_3$ bed, top of transition	416	2.5	NM	NM
		466	4.0	NM	NM

[a]Refer to Plate 11-1 for location.

[b]Refer to Tables 11-6 and 11-7 for description.

[c]NM indicates no measurement.

11-24. Summary of elements that correlate with luminescence as a function of Fraunhofer wavelength

Wavelength, nm	Element (%)[a]
486.1	Beryllium (44)
	Phosphorus (20)
	Boron (17)
	Nickel (11)
589.0	Barium (45)
	Molybdenum (13)
	Carbon (13)
656.3	Phosphorus (30)
	Boron (19)
	Vanadium (16)
	Lead (12)
	Nickel (11)

[a]The value in parentheses is the percent of total variance of luminescence data explained by the soil concentration of the element.

measure of the contribution of each element to the regression. Those elements showing less than 10 percent contribution are not included.

Luminescence at the Patrick Draw test site is generally low at all three wavelengths, with only occasional highs. Of interest are the highs at 656.3 nm occurring in vegetation, particularly in the area of stunted sage described in Paragraph VII.B.

At the 486.1-nm wavelength (Figure 11-92), flight lines 1 and 2 show different luminescence profiles, but both reveal a series of anomalies (2.5 to 3.5 ppb rhodamine WT equivalence) just east and south of Bitter Creek Station. This is an area in which marl beds are exposed. North to northeast of Bitter Creek Station in T19N R99W, sections 12 and 13, is a luminescence region of 2.5 to 4.5 ppb rhodamine WT equivalence. This is a region of coal-bearing clay

soils. Most of the luminescence highs are associated with alkaline, loam clay soils with vegetation in an upland salt desert community. Results of a multiple regression analysis show beryllium (44 percent), phosphorus (20 percent), boron (17 percent), and nickel (11 percent) as the elements that correlate best with luminescence. The percentage of the contribution of each element to total luminescence is given in parentheses in Table 11-24.

At 589.0 nm (Figure 11-93), most of the luminescence highs occur in the Fort Union/Wasatch transition unit described in Paragraph IX.C.2. Sample sites A12 and L1-15 (Plate 11-1) both show luminescence of 3.5 to 4.5 ppb rhodamine WT equivalence. In addition, the area of clay and gypsiferous soils just east of sample sites A16 and A18 and sites L6-2 through L6-5 show luminescence highs from 2.5 to 4.5 ppb. An area in the Desert Springs oil field just west of sample sites G7 and R4 also shows values from 2.5 to 4.5 ppb. Multiple regression analysis indicates barium (45 percent) is the strongest correlator with luminescence at this wavelength.

At 656.3 nm (Figure 11-94), along the south to north flight line, the marl beds east and south of Bitter Creek Station are somewhat lower in luminescence (1.5 to 2.5 ppb) than at 486.1 nm. Again, many of the highs north of Bitter Creek Station occur in the Fort Union/Wasatch transition unit, with the area from site A14 to B16 showing luminescence from 2.5 to 3.5 ppb. Sites L3-1, L3-2, and L3-3 show luminescence from 1.5 to 2.5 ppb. Farther to the north in the clay and gypsiferous soils, from site A16 to L6-3, a band of luminescence from 1.5 to 4.5 ppb exists mainly along the western edge of the Fort Union/Wasatch transition unit. Along the west to east flight line, a number of 2.5 to 4.5 ppb luminescence highs occur from site B20 to B25, mainly in and along major drainages. This is the area of anomalous stunted sage discussed in Paragraph VII.B. This area appears to coincide with the maximum density and thickness of resistant Fort Union carbonate-cemented sandstone beds. The area is bounded on the north, south, and east by major drainages and on the west by exposures of a resistant, carbonate-cemented sandstone lens. Results of multiple regression analysis indicate phosphorus (30 percent), boron (19 percent), vanadium (16 percent), lead (12 percent), and nickel (11 percent) as those elements most strongly correlated with luminescence in this wavelength. The area to the east of the area of anomalous stunted sage shows 2.5 to 4.5 ppb luminescence highs occurring in T19N, R98W, section 18. This is an area of shrub grassland containing bedrock outcrops. It is impossible to know what actually contributes to luminescence highs in this area without additional field and laboratory analysis. No laboratory or field luminescence measurements were obtained during the test site investigation. However, it is interesting to note that trend surface analysis of soil elemental concentrations (described in Paragraph VII.E) shows that manganese trend patterns are similar to the anomalous pattern of luminescence at 656.3 nm in this area and elsewhere in the Patrick Draw test site (Figure 11-95).

D. Conclusions

Many of the luminescence highs occur in the Fort Union/Wasatch transition unit. This could be due to exposures of coal and gypsum in this zone. Marl beds appear to be slightly higher in luminescence than carbonate-cemented sandstone beds throughout the Patrick Draw area, although both are above background luminescence.

Correlation of luminescence with geochemical elements at Patrick Draw is complicated by the paucity of sites where both geochemical/mineralogical and luminescence data were acquired. It was not possible to perform multiple regression analysis on all 24 geochemical elements simultaneously. With the limited number of observations, an abbreviated multiple regression analysis was attempted. The elements that showed the highest correlation with luminescence are phosphorus, boron, beryllium, barium, vanadium, and nickel.

Manganese at site R47 is above the threshold value tha could be expected to activate luminescence in calcite an could be reponsible for some of the luminescence high along the W–E 656.3-nm flight line. Although manganes does not appear as one of the elements that correlates wit luminescence, the pattern of luminescence at 656.3 n closely fits the pattern of soil manganese concentration fro trend surface analysis. The lack of correlation from th multiple regression analyses may be due to the limite number of observations.

Some pronounced luminescence highs occur in the ar of anomalously stunted sage. This apparent correlation m be physically caused by the luminescence properties of so that are better exposed due to lower vegetation density the sage anomaly area. Field and laboratory studies a essential, however, to clearly establish if correlation betwe stunted vegetation and luminescence exists at Patrick Dra

XII. Summary and Conclusions

A. "Direct" Detection of Hydrocarbons

Solving the problem of "direct" detection of hydro bons by remotely sensing surface alteration associated v microseepage involves three questions:

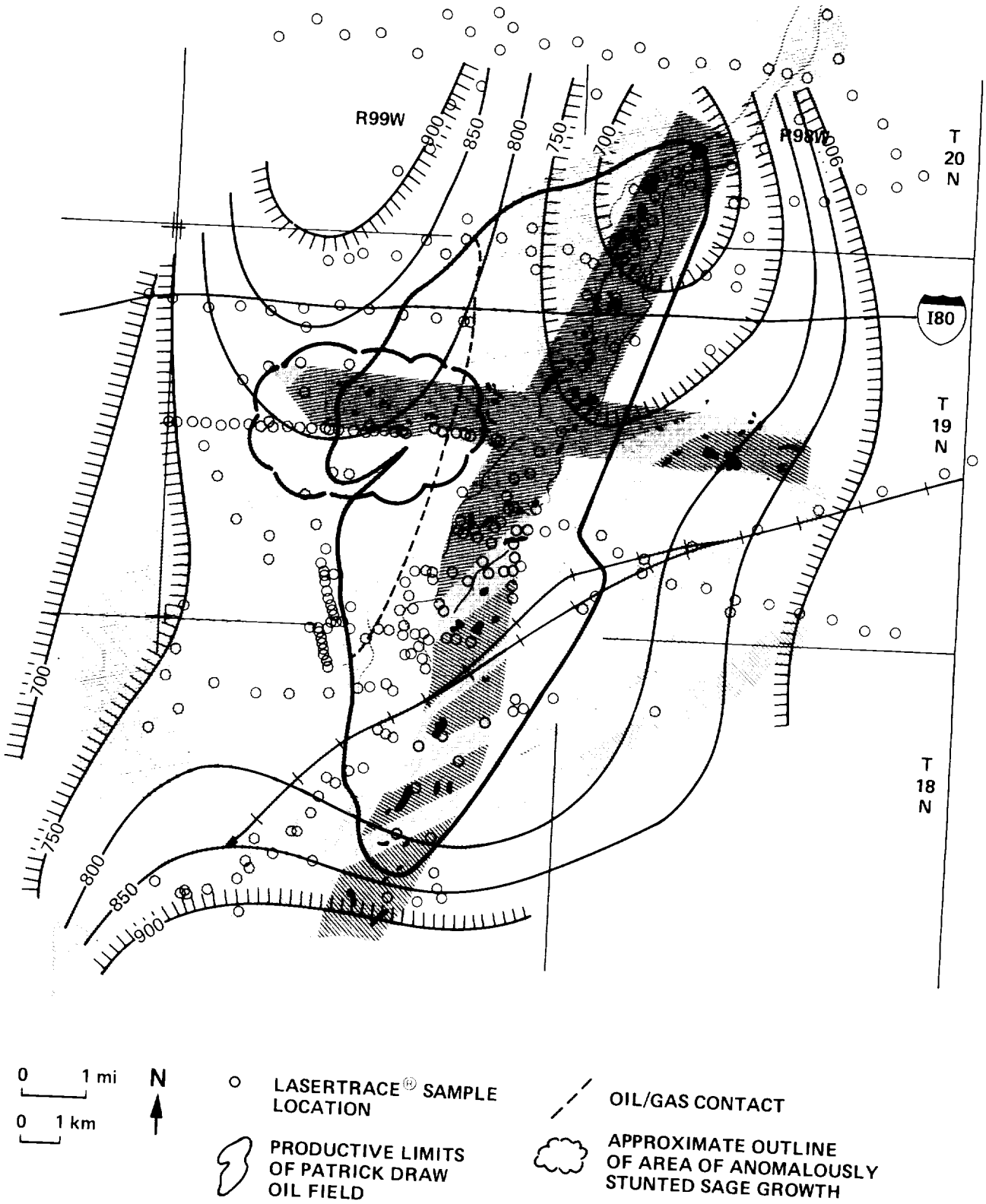

Figure 11-95. Luminescence plotted on a soil manganese concentration map. Luminescence values at 656.3 nm (ppb rhodamine WT equivalence) are 1.5 to 2.5 (green), 2.5 to 3.5 (orange), and 3.5 to 4.5 (red).

(1) Does the reservoir leak?

(2) Do leaking hydrocarbons alter surface material?

(3) Can this alteration be detected by remote sensing?

A hydrocarbon soil gas survey of Patrick Draw revealed anomalously high concentrations of hydrocarbons in soil samples obtained on selected lineaments and in one sample obtained from the approximate center of the surface location of the gas cap of the reservoir. A helium soil gas survey indicated similar high concentrations of helium in soil samples from the gas cap area. These results suggest that the Patrick Draw reservoir may leak in the gas cap area. This leakage may be concentrated along lineaments that represent zones of bedrock fracturing connecting the reservoir and the surface.

A soil elemental geochemical survey revealed high titanium, vanadium, copper, and zinc concentrations in soil samples from locations overlying the gas cap of the Patrick Draw reservoir. Soil pH values in the gas cap area were also high compared to adjacent areas. These high soil pH and elemental concentrations may represent alterations of soil geochemistry due to microseepage of hydrocarbons from the gas cap region of the Patrick Draw reservoir.

A tonal anomaly recognized in the interpretation of NS-001 Thematic Mapper Simulator images corresponds in location with the approximate center of the underlying gas cap of the Patrick Draw reservoir and with areas of high soil hydrocarbon gas, high soil helium gas, high soil pH, and high elemental concentrations noted above. Field examination of this tonal anomaly revealed that it corresponds to an area of anomalous stunted sage. Laboratory anatomical evaluation of stunted sage specimens from this area demonstrates that stunting has been chronic in the area for at least 95 years (predates development of the Patrick Draw oil field). The anatomical and morphological characteristics of the stunted sage are symptomatic of a zinc nutrient deficiency. This deficiency may be the result of locally high soil pH which can effectively block zinc uptake.

The aerial correspondence of high soil hydrocarbon gas concentrations, high helium soil gas concentrations, high soil elemental concentrations, high soil pH, and stunting of sage (first recognized as an NS-001 image tonal anomaly) suggests that the Patrick Draw reservoir leaks. This leakage results in alteration of soils and associated vegetation, and this alteration can be detected using NS-001 remote sensing data. A satisfactory geochemical explanation that integrates the observations, however, has not been proposed. Further evaluation of this problem is required before unequivocal conclusions regarding the "direct" detection problem in the Patrick Draw area can be made. Although suggestive *correlations* have been documented, the *cause-and-effect* relationship of gas cap to soil gas to soil geochemical alteration to stunted sage has not been proven.

B. Improved Geologic Mapping

With the aid of limited ground observations, geometrically rectified NS-001 Thematic Mapper Simulator images can be interpreted to produce 1:48,000 geologic maps of the Patrick Draw area. Such maps are superior to those presently available in both structural and stratigraphic detail. This type of information should have wide application to petroleum exploration.

1. Structure. Detection of jointing, faulting, and folding may be used to locate targets for the application of the more expensive conventional exploration tools and the development of models of basin evolution. The interpretation of Landsat MSS images of the test site area reveals the presence of all-important structures recognized in published 1:250,000 geologic maps of the eastern Rock Springs Uplift and Washakie Basin. The interpretation of NS-001 Thematic Mapper Simulator images at a scale of 1:48,000 reveals broad E–W- and NW-trending folds, with too little closure to be detectable in subsurface structure maps available for the Patrick Draw field. The northernmost anticline plunges to the east and lies on the Wamsutter Arch. The southernmost north-trending syncline–anticline couplet lies on trend with the axial traces of similar structures shown in subsurface contours on the productive horizon at the North Brady field. This structure was not recognized in a commercial photogeological interpretation, but is clearly evident in a reinterpretation of the stereo-photography and field observations.

2. Lineaments. Lineament analysis by remote sensing methods is a tedious process but can yield reproducible results. Five major trends in lineament orientation (azimuths 87, 1, 293, 24, and 309) were consistently recognized in the analysis of Landsat MSS, topographic, NS-001, and radar images. Lineament data are demonstrated to be useful for two purposes in exploration:

(1) Field evidence at Patrick Draw suggests that NE-trending lineaments recognized in NS-001 data cor respond in location with areas of joint-induced bed rock fracturing. The soil hydrocarbon gas samplin program for the 1980 field season was designed t concentrate on lineament targets determined in preliminary analysis of remote sensing data. Th approach made the sampling effort more econom cal than would have been possible using availab published geologic data alone for sample site selectio

(2) An important aspect of image lineament analysis is the map area over which given lineament sets are observed. The relationship of this map pattern to other structures of known age and origin in the Patrick Draw area gives important clues as to the timing and the stress orientations that generated the lineament trends. The areas in which lineament trends occur indicate the limits of the region affected by the structural disturbance and its associated stress field.

These remotely sensed data have obvious implications for hydrocarbon exploration. The area affected by a given lineament trend can help localize general search areas. Additionally, lineament analysis could aid in determining the timing and direction of organic fluids migration from source beds to final entrapment. This requires detailed knowledge about the paleo-stress fields, which provide selective directions of fracture plumbing for fluid migration. The present study suggests the possibility of using lineament analysis to identify paleo-stress orientations and related fracture orientations, to link these features to geologically datable structures, and finally to map the area of influence and relative intensity of dated paleo-stress orientations.

3. Stratigraphic analysis. The ability to recognize and trace stratigraphic units at the surface is essential for the preparation of isopach, facies, and other stratigraphic maps. This information, if integrated with subsurface data, may be used to locate sites for potential stratigraphic traps and to develop models of basin evolution. The recognition of a previously unmapped lithostratigraphic unit—the Fort Union/Wasatch transition unit (based on NS-001 Thematic Mapper Simulator image interpretation)—is evidence of the improved stratigraphic capabilities of these data when compared to standard field methods. Additionally, individual poorly exposed beds, which are difficult if not impossible to trace using standard field techniques, are traceable on NS-001 images up to 10 km.

C. Improved Soils and Vegetation Mapping

Tonal/textural interpretation of NS-001 Thematic Mapper Simulator images provided an economic means for establishing the distribution of surficial materials in the Patrick Draw area. Discrimination of soil units correlates well with BLM soil maps, which required years of fieldwork to prepare. A supervised percent vegetation classification image, using NS-001 band data as variables and limited training areas obtained from field vegetation analysis, provided an accurate map of areal variations in vegetation cover. The detail of this image, which results from the grid-sampling nature of multispectral data, could not have been practically obtained using standard field vegetation mapping techniques. Geochemical and geological investigations of the area demonstrate that these vegetation data reflect variations in substrate geochemistry, which add to the understanding of the area's geology. Additionally, if combined with calibrated image data, the supervised percent vegetation image can be used to estimate the contribution of soil/rock and vegetation spectra within individual image pixels.

D. Use of Multispectral Scanners as Platform-Borne Spectrometers

Aircraft and satellite multispectral scanners encode grid-sampled radiance values from the Earth's surface. Solar radiation passes through the atmosphere, interacts with the surface, passes through the atmosphere between the surface and the sensor, and is recorded by the instrument as DN radiance values. To exploit the potential use of multispectral scanners as spectrometers, atmospheric and illumination-aspect-dependent and instrument gain- and offset-dependent corrections must be applied to instrument DN radiance values. An empirical approach to this problem was successfully used for NS-001 Thematic Mapper Simulator scanner data from the Patrick Draw test site. An empirically derived function was first used to remove the scan-line brightness gradient from the original scanner data. This procedure effectively normalized the atmospheric- and illumination-aspect-dependent scene variation. To convert the resulting gradient-corrected DN values to equivalent reflectance values, a modified version of the Gillespie and Kahle (1977) approach for determining gain and offset was used. Based on the observation that the distribution of gradient-corrected DN values was Gaussian, the minimum, mean, and maximum values were extracted from the NS-001 scene and plotted against the similar values determined from the large representative collection of PFRS data from the same area. This plot provided a linear transformation relating DN values to PFRS reflectance. With these calibrated data, the "true" spectra of units recognized in other images, which have been processed to optimize unit separation, can be retrieved from the scanner data.

E. Spectral Analysis

One of the primary goals of multispectral remote sensing is to use scanner data to identify surface materials. Analysis of field and laboratory spectral data and image spectral data for the Patrick Draw test site demonstrates that in mixed soil/rock/vegetation terrain this goal is not accomplished. Mixing several spectral components in the scanner-acquired radiance data typically precludes unique identification of materials.

Acknowledgments

Patrick Draw test site fieldwork, image analysis, interpretation, and reporting were done as a team effort by 38 individuals. Their time, financial support, and laboratory work were provided by 24 organizations representing government, industry, and academia. The authors express sincere appreciation to the individuals listed below and to the organizations they represent. Their participation in discussion, fieldwork, and laboratory analyses contributed substantially to the successful completion of the Project.

Participant	Affiliation (during test site study)
Ron Alley	JPL
Ward Austin	Pacific Energy & Minerals
Ralph Baker	Phillips Petroleum
Gary Bible	Phillips Petroleum
Aderbal Correa	CONOCO
William Duchscherer	Geochemical Surveys
Janet Earle	Champlin Petroleum Company
Robert Foote	Geodata International
William Hemphill	USGS
Robert Huguenin	University of Massachusetts
Jeremy Hutt	Barringer Resources
David Kahler	Dynatech Corporation
James Klein	Phoenix Geophysics
Robert Maynard	SUNOCO Energy Development
Michael McGuire	AMOCO Production Company
Walter Merschat	Gulf Science and Technology Company
Richard Michael	Earth Satellite Corporation
Paul Nadeau	The Anschutz Corporation
Harry Stewart	JPL
Jose Valdes	University of Massachusetts
Robert Vincent	Geospectra Corporation

References

Adams, J. B., and A. L. Filice (1967). Spectral reflectance 0.4 to 2.0 microns of silicate rock powders. *J. Geophys. Res., 72,* 5705–5728.

Asquith, D. O. (1970). Depositional topography and major marine environments, Late Cretaceous, Wyoming. *AAPG Bull., 54,* 1184–1224.

Becker, C. F., and J. D. Alyia (1964). Precipitation probabilities in Wyoming. *Agric. Exp. Stn. Univ. Wy. Bull. 416.*

Beckman, P., and A. Spizzichino (1963). *The scattering of electromagnetic waves from rough surfaces.* New York: Macmillan.

Bidwell, R. G. S. (1974). *Plant physiology.* New York: Macmillan.

Bradley, W. H. (1964). Geology of Green River and associated Eocene rocks in southwestern Wyoming and adjacent parts of Colorado and Utah. *U.S. Geol. Surv. Prof. Pap. 496A.*

Bureau of Land Management (1981). *Preliminary soils map, Sweetwater County, Wyoming.* (Rock Springs, Wyoming, maps and explanatory text)

Cox, J. E. (1962). Patrick Draw field and adjacent areas, Sweetwater County, Wyoming. *Billings Geol. Soc. Paper No. 1,* 1–17.

Dalziel, M. C., and T. J. Donovan (1980). Biogeochemical evidence for subsurface hydrocarbon occurrence, Recluse oil field, Wyoming: Preliminary results. *U.S. Geol. Surv. Circ. 837.*

Daubenmire, R. (1959). A canopy coverage method of vegetational analysis. *Northwest Sci., 33,* 43–64.

Davis, J. B. (1967). *Petroleum microbiology.* New York: American Elsevier Scientific Publishing Company.

Davis, J. C. (1973). *Statistics and data analysis in geology.* New York: John Wiley & Sons.

Davis, R. W. (1958). *Stratigraphy of the Wasatch Formation, east flank of the Rock Springs Uplift, Sweetwater County, Wyoming.* Unpublished master's thesis, University of Wyoming, Laramie.

Debnam, A. H. (1969). Geochemical prospecting for petroleum and natural gas in Canada. *Geol. Surv. Can. Bull. 117,* 1–27.

Devine, S. B., and H. W. Sears (1977). Soil hydrocarbon geochemistry, a potential exploration tool in the Cooper Basin, Australia. *J. Geochem. E., 8,* 397–414.

Dewey, J. F., and J. M. Bird (1970). Mountain belts and the new global tectonics. *J. Geophys. Res., 75,* 2625–2645.

Diettert, R. A. (1938). The morphology of *Artemisia tridentata* Nutt. *Lloydia, 1,* 3–74.

Donovan, T. J. (1974). Petroleum microseepage at Cement, Oklahoma—Evidence and mechanism. *AAPG Bull., 58,* 51–64.

Donovan, T. J., A. R. Barringer, R. S. Foote, and R. D. Watson (1975). Low-altitude remote sensing experiments at Cement and Davenport oil fields, Oklahoma. *Proceedings of the Annual SEG Meeting,* Denver.

Dorn, R. P. (1977). *Manual of the vascular plants of Wyoming.* New York: Garland Publishers.

Foth, H. D., L. V. Withee, H. S. Jacobs, and S. J. Thien (1980). *Laboratory manual for introductory soil science.* Dubuque, Iowa: Wm. C. Brown Publishing Company.

Gillespie, A. R., and A. B. Kahle (1977). Construction and interpretation of a digital thermal inertia image. *Photogr. E. R., 43,* 983–1000.

Goetz, A. F. H., F. C. Billingsley, A. R. Gillespie, M. J. Abrams, E. M. Squires, E. M. Shoemaker, I. Lucchitta, and D. P. Elston (1975). *Applications of ERTS images and image processing to regional geologic problems and geologic mapping in northern Arizona* (JPL Technical Report 32-1597). Pasadena, California: Jet Propulsion Laboratory.

Goetz, A. F. H., and L. C. Rowan (1981). Geologic remote sensing. *Science, 211,* 781–791.

Grose, L. T., (1972). Tectonics. In W. W. Mallory (Ed.), *Geologic atlas of the Rocky Mountain region.* Denver: Rocky Mountain Association of Geologists, 34–44.

Hawks, H. E., and J. S. Webb (1962). *Geochemistry in mineral exploration.* New York: Harper & Row.

Hewitt, E. J. (1963). The essential nutrient elements: Requirements and interactions in plants. In F. C. Steward (Ed.), *Plant physiology, a treatise* (Vol. III). New York: Academic Press.

Horwitz, L. (1972). Vegetation and geochemical prospecting for petroleum. *AAPG Bull., 56,* 925–940.

Horwitz, L. (1980). Near-surface evidence of hydrocarbon movement from depth. In W. H. Roberts and R. J. Cordell (Eds.), Problems of petroleum migration, *AAPG Stud. Geol.* (No. 10), 241–269.

Hovis, W., J. Nichols, A. Potter, and F. Thomson (1975). *Landsat-D Thematic Mapper technical working group final report* (Report No. JSC-09797). Houston: Lyndon B. Johnson Space Center, Appendixes A–H.

Hunt, G. R., and J. W. Salisbury (1970a). Visible and near-infrared spectra of minerals and rocks: I. Silicate minerals. *Mod. Geol., 1,* 283–300.

Hunt, G. R., and J. W. Salisbury (1970b). Visible and near-infrared spectra of minerals and rocks: II. Carbonates. *Mod. Geol., 2,* 23–30.

Hunt, G. R., and J. W. Salisbury (1976). Visible and near-infrared spectra of minerals and rocks: XI. Sedimentary rocks. *Mod. Geol., 5,* 211–217.

Hunt, G. R., J. W. Salisbury, and C. J. Lenhoff (1971a). Visible and near-infrared spectra of minerals and rocks: III. Oxides and hydroxides. *Mod. Geol.*, *2*, 195–205.

Hunt, G. R., J. W. Salisbury, and C. J. Lenhoff (1971b). Visible and near-infrared spectra of minerals and rocks: IV. Sulphides and sulphates. *Mod. Geol.*, *3*, 1–14.

Hunt, G. R., J. W. Salisbury, and C. J. Lenhoff (1972). Visible and near-infrared spectra of minerals and rocks: V. Halides, phosphates, arsenates, vanadates and borates. *Mod. Geol.*, *3*, 121–132.

Hunt, G. R., J. W. Salisbury, and C. J. Lenhoff (1973). Visible and near-infrared spectra of minerals and rocks: VI. Additional silicates. *Mod. Geol.*, *4*, 85–106.

King, P. B. (1959). *The evolution of North America.* Princeton, New Jersey: Princeton University Press.

Kvenvolden, K. A., and G. D. Redden (1980). Hydrocarbon gas in sediment from the shelf, slope and basin of the Bering Sea. *Geochim Cosmochim Acta*, *44*, 1145–1150.

Land, C. B., Jr. (1972). Stratigraphy of Fox Hills sandstone and associated formations, Rock Springs Uplift and Wamsutter Arch area, Sweetwater County, Wyoming: A shoreline-estuary sandstone model for the Late Cretaceous. *Colo. Sch. Mines Q.*, *62*(2).

Leone, I. A., F. B. Flower, J. J. Arthur, and E. F. Gilman (1977). Damage to woody species by anaerobic landfill gases. *J. Arboric.*, *3*, 221–225.

Levinson, A. A. (1974). *Introduction to exploration geochemistry.* Wilmette, Illinois: Applied Publishing.

Mallory, W. W. (Ed.) (1972). *Geologic atlas of the Rocky Mountain region.* Denver: Rocky Mountain Association of Geologists.

McCubbin, D. G., and M. J. Brady (1963). Depositional environment of the Almond reservoirs, Patrick Draw field, Wyoming. *Mt. Geol.*, *6*, 3–36.

McDonald, R. E. (1972). Eocene and Paleocene rocks of the southern and central basins. In W. W. Mallory (Ed.), *Geologic atlas of the Rocky Mountain region.* Denver: Rocky Mountain Association of Geologists, 243–256.

McPeek, L. A. (1981). Eastern Green River Basin: A developing giant gas supply from deep, overpressured Upper Cretaceous sandstones. *AAPG Bull.*, *65*, 1078–1098.

Mueller–Dumbois, D., and H. Ellenberg (1974). *Aims and methods of vegetation ecology.* New York: John Wiley & Sons.

Prost, G. (1980). Alteration mapping with airborne multispectral scanners. *Econ. Geol.*, *75*, 894–906.

Ritzman H. R. (1961). Geology and occurrence of oil and gas, Wamsutter Arch, Wyoming. *AAPG Mem. 2*, 188–195.

Roehler, H. W. (1977a). Geologic map of the Rock Springs Uplift and adjacent areas, Sweetwater County, Wyoming. *U.S. Geol. Surv. Open File Rep. 77-242.*

Roehler, H. W. (1977b). Geologic quadrangle map, Sand Butte rim NW quadrangle, Wyoming. *U.S. Geol. Surv. Bull. GQ-1362.*

Rosenblum, S. (1980). *The anomaly-ratio concept in geochemical exploration.* Soc. of Min. Engr. AIME. (Preprint 80-6)

Salomonson, V. V., P. L. Smith, Jr., A. B. Park, W. C. Webb, and T. J. Lynch (1980). An overview of progress in the design and implementation of Landsat-D systems. *IEEE Trans. Geosci. Rem. Sens., GE-18*(2), 137–145.

Schultz, A. R. (1909). The northern part of the Rock Springs coal field, Sweetwater County, Wyoming. *U.S. Geol. Surv. Bull. 341,* 256–282.

Schultz, A. R. (1910). The southern part of the Rock Springs coal field, Sweetwater County, Wyoming. *U.S. Geol. Surv. Bull. 381,* 214–281.

Schultz, A. R. (1920). Oil possibilities in and around Baxter Basin in the Rock Springs Uplift, Wyoming. *U.S. Geol. Surv. Bull. 702.*

Sears, J. D., and W. H. Bradley (1925). Relations of the Wasatch and Green River Formations in northwestern Colorado and Southern Wyoming, with notes on oil shale in the Green River Formation. *U.S. Geol. Surv. Prof. Pap. 132,* 93–107.

Short, N. (Chair) (1976). *Practical applications of LANDSAT data for earth resources surveys—Mineral/energy resources.* Unpublished report prepared by the Mineral and Petroleum Application Panel for NASA–Lyndon B. Johnson Space Center, Earth Resources Program Office, Houston, Texas.

Siegal, B. S., and A. F. H. Goetz (1977). Effects of vegetation on rock and soil type discrimination. *Photogr. E. R., 43,* 191–196.

Siegel, F. R. (1974). *Applied geochemistry.* New York: John Wiley & Sons.

Skeeters W. W., and L. A. Hale (1972). Southern Wyoming. In W. W. Mallory (Ed.), *Geologic atlas of the Rocky Mountain region.* Denver: Rocky Mountain Association of Geologists, 274–276.

Stevens, R., and E. D. McArthur (1974). A simple field technique of identification of some sagebrush taxa. *J. Range Man., 27*(4), 325–326.

Weimer, R. J. (1966). Time-stratigraphic analysis and petroleum accumulations, Patrick Draw field, Sweetwater County, Wyoming. *AAPG Bull., 50,* 2150–2175.

Weirsma, D. J., and D. A. Landgrebe (1980). Analytical design of multispectral sensors. *IEEE Trans. Geosci. Rem. Sens., GE-18*(12), 137–145.

Weisman, T. J. (1980). Developments in geochemistry and their contribution to hydrocarbon exploration. *Proceedings of the 10th World Petroleum Congress,* Bangkok, *2,* 369–386.

Wyoming Geologic Association (1979). *Wyoming Oil and Gas Field Symposium, Greater Green River Basin.* Casper, Wyoming, 274–277.

Zoback, M. L., and M. Zoback (1980). State of stress in the conterminous United States. *J. Geophys. Res., 85,* 6113–6156.

Appendix A
Results of Hydrocarbon Soil Gas Analyses

Adsorbed hydrocarbon soil gas values

ID	C_1*	C_2*	C_3*	iC_4*	nC_4*	P/M*10^3	%WET
L1-1	76.800	5.900	1.700	0.500	0.600	22.135	8.024
L1-2	9.000	0.200	0.0	0.200	0.0	0.0	4.255
L1-3	49.300	2.400	1.000	0.200	0.300	20.284	7.331
L1-4	106.000	5.900	2.300	0.500	0.800	21.698	8.225
L1-5	166.800	8.600	3.400	0.800	1.200	20.384	7.743
L1-6	22.600	0.800	0.300	0.0	0.0	13.274	4.641
L1-7	589.000	21.400	6.200	2.800	2.100	10.526	5.076
L1-8	38.800	2.200	0.900	0.200	0.400	23.196	8.706
L1-9	318.400	18.300	6.900	1.700	2.500	21.671	8.453
L1-10	212.700	17.500	5.500	1.100	1.800	25.858	0.780
L1-11	441.100	22.800	8.400	2.100	3.000	19.043	7.604
L1-12	154.000	7.700	3.200	0.800	1.100	20.779	7.674
L1-13	1068.800	51.800	20.800	5.000	7.500	19.461	7.375
L1-14	188.900	8.400	3.500	0.900	1.300	18.528	6.946
L1-15	477.800	25.800	10.200	2.700	3.800	21.348	8.168
L1-16	381.600	20.700	8.100	1.900	2.900	21.226	8.092
L2-1	161.400	10.000	3.700	0.800	1.300	22.924	8.916
L2-2	893.600	42.700	15.700	3.700	5.500	17.569	7.053
L2-3	180.900	9.000	3.600	0.900	1.400	19.900	7.610
L2-4	533.100	26.900	10.300	2.300	3.700	19.321	7.496
L2-5	21.500	1.400	0.400	0.200	0.300	18.605	9.664
L2-6	92.800	3.600	1.300	0.500	0.400	14.009	5.882
L2-7	282.400	19.100	7.100	1.600	2.600	25.142	9.719
L3-1	229.500	11.700	4.800	1.200	1.800	20.915	7.831
L3-2	117.600	5.500	1.900	0.500	0.600	16.156	6.741
L3-3	2.600	0.100	0.0	0.0	0.0	0.0	3.704
L3-4	776.100	44.700	16.400	3.600	5.400	21.647	8.371
L3-5	122.800	4.900	1.900	0.0	0.600	15.472	5.084
L3-6	159.900	9.300	3.600	0.900	1.400	22.514	8.681
L4-1	262.400	14.900	6.200	1.400	2.300	23.628	8.635
L4-2	67.400	3.800	1.500	0.400	0.500	22.255	8.424
L4-3	53.800	2.700	1.100	0.400	0.400	20.446	7.877
L4-4	92.900	5.000	2.000	0.400	0.700	21.529	8.020
L5-1	847.600	32.300	11.800	3.000	4.200	13.922	5.707
L5-2	46.000	2.400	0.900	0.300	0.400	19.565	4.000
L5-3	260.100	21.900	7.500	1.300	2.500	28.835	11.319
L5-4	77.400	7.700	2.700	0.500	1.000	34.884	15.526
L6-1	4.300	0.200	0.100	0.0	0.0	23.256	6.522
L6-2	194.000	11.700	5.100	1.400	2.000	26.289	9.430
L6-3	6.600	0.400	0.200	0.100	0.0	30.303	9.589
L6-4	40.600	1.900	0.700	0.200	0.200	17.241	6.881
L6-5	75.300	3.800	1.500	0.500	0.600	19.920	7.834
XL1-1	63.600	5.100	2.200	0.400	0.700	34.591	11.667
XL1-2	339.900	224.800	9.800	2.000	3.700	28.832	10.600
XL1-3	191.000	11.700	5.100	1.100	1.800	26.702	9.550
XL1-4	23.900	3.900	2.400	0.300	0.900	100.418	23.885
XL1-5	154.700	10.500	4.500	0.800	1.600	29.089	10.110
XL1-6	337.00	7.100	9.400	2.200	3.400	27.840	9.955
XL1-11	120.200	6.300	2.600	0.200	1.000	21.631	7.751
XL1-12	192.700	10.500	4.200	0.900	1.400	21.796	8.107
XL1-13	147.300	9.500	3.600	0.200	1.300	24.440	8.905
XL1-14	698.100	46.700	17.800	4.000	5.900	25.498	9.631
XL1-15	192.500	10.600	4.400	1.100	1.700	22.857	8.464
XL1-16	16.100	0.900	0.300	0.100	0.200	18.634	8.523
XL1-17	377.800	22.400	9.100	2.000	3.300	23.087	8.876
XL2-1	446.200	24.100	9.000	2.200	3.300	20.170	7.962
XL2-2	576.900	28.000	10.600	2.300	3.700	18.374	7.176
XL2-3	572.600	31.300	11.800	2.800	4.100	20.608	8.031
XL2-4	1816.100	65.300	22.400	4.800	7.600	12.334	5.224
XL2-5	156.900	9.000	3.200	0.700	1.100	20.395	8.192
XL2-6	154.300	7.800	3.100	0.700	1.200	20.091	7.660
XL2-7	307.200	24.000	6.300	1.000	2.200	20.508	9.833
XL3-1	99.300	5.000	2.000	0.500	0.700	20.141	7.628
XL3-2	186.300	9.600	3.900	0.900	1.500	20.934	7.863
XL4-1	599.900	22.600	8.400	1.800	2.900	14.002	5.617
XL4-2	270.700	17.300	6.700	1.400	2.500	24.751	9.343
XL4-3	880.800	40.100	15.600	3.600	5.400	17.711	6.843
XL4-4	216.600	11.600	4.400	0.800	1.700	20.314	7.869
XL4-5	331.00	24.100	8.300	1.500	2.800	25.076	9.981
XL4-6	10.300	0.600	0.200	0.0	0.0	19.417	7.207
XL4-7	318.000	18.600	6.900	2.200	2.400	21.698	8.647
XL4-8	136.300	8.000	3.000	0.800	1.000	22.010	8.585
R-1	44.800	2.100	0.900	0.300	0.400	20.089	7.629
R-4	42.100	2.400	1.100	0.300	0.300	26.128	8.874
R-9	255.700	15.600	6.800	1.900	2.700	26.594	9.551
R-13	482.100	27.800	10.000	2.400	3.700	20.743	8.204
R-17	318.400	18.300	7.500	1.700	2.700	23.555	8.663
R-18	299.100	14.900	6.200	1.500	2.400	20.729	7.714
R-19	195.300	8.700	3.700	0.800	1.300	18.945	6.911
R-24	31.000	1.800	1.000	0.300	0.400	32.258	10.145
R-27	55.900	3.400	1.600	0.400	0.600	28.623	9.693
R-28	9.300	0.300	0.200	0.0	0.0	21.505	5.102
R-29	352.700	21.000	9.300	1.900	3.500	26.368	9.191
R-32	97.500	4.900	2.200	0.500	0.700	22.564	7.845
R-35	268.300	13.400	5.300	1.200	2.000	19.754	7.546
R-36	415.200	18.400	8.100	1.900	3.000	19.509	7.031
R-41	9.900	0.300	0.300	0.100	0.0	30.303	6.604
R-45	31.500	2.300	1.200	0.200	0.400	38.095	11.517
R-47	275.300	13.600	5.400	1.400	1.900	19.615	7.493
R-52	682.700	32.600	11.600	2.700	2.600	16.991	7.014
R-56	10.800	0.700	1.100	0.0	0.100	101.852	14.961
R-60	537.100	25.100	9.700	2.400	3.700	18.060	7.076
R-69	95.400	4.200	1.700	0.400	0.400	17.870	6.745
R-72	191.100	22.500	9.600	2.800	4.300	50.235	17.071
R-74	278.300	14.200	5.700	1.500	2.300	20.481	7.848
R-76	348.200	22.100	9.300	3.400	5.900	26.709	10.002
R-79	342.700	23.800	9.600	2.700	3.800	28.015	10.429
R-81	307.800	16.100	7.000	2.200	2.900	22.742	8.393
R-85	375.500	21.800	9.800	3.200	4.100	26.099	9.387
R-87	68.100	5.400	3.000	0.500	0.800	44.053	12.468
R-91	306.000	30.100	12.800	4.000	5.500	41.830	14.620
R-93	104.400	4.900	2.000	0.500	0.700	19.157	7.200
R-95	335.500	18.400	7.600	2.000	3.000	22.655	8.458
R-97	173.000	10.200	3.900	1.000	1.300	22.543	8.659
R-100	489.700	45.100	18.300	5.200	7.200	37.370	13.404
R-101	128.400	7.400	2.800	0.500	1.000	21.807	8.351

*ppm (vol).

Absorbed hydrocarbon soil gas C_1–C_3 data

ID	C_1*	C_2*	C_3*
L1-1	1.08	0.03	0.04
L1-2	0.61	0.02	0.02
L1-3	0.87	0.02	0.02
L1-4	0.55	0.02	0.02
L1-5	0.97	0.02	0.03
L1-6	1.25	0.05	0.05
L1-7	1.17	0.10	0.08
L1-8	0.95	0.03	0.04
L1-9	1.56	0.10	0.05
L1-10	0.95	0.04	0.04
L1-11	1.08	0.04	0.04
L1-12	1.24	0.06	0.04
L1-13	1.13	0.04	0.04
L1-14	0.72	0.02	0.02
L1-15	1.31	0.07	0.04
L1-16	1.04	0.05	0.06
L2-1	0.92	0.03	0.02
L2-2	0.98	0.03	0.04
L2-3	0.97	0.02	0.03
L2-4	0.96	0.03	0.02
L2-5	0.96	0.04	0.04
L2-6	1.19	0.04	0.03
L2-7	0.63	0.02	0.02
L3-1	1.46	0.05	0.06
L3-2	1.97	0.07	0.07
L3-3	1.33	0.05	0.06
L3-4	0.75	0.03	0.02
L3-5	1.26	0.05	0.03
L3-6	2.16	0.13	0.12
L4-1	1.24	0.06	0.07
L4-2	1.74	0.06	0.04
L4-3	2.89	0.11	0.10
L4-4	3.73	0.14	0.11
L5-1	1.14	0.04	0.03
L5-2	3.36	0.14	0.13
L5-3	1.21	0.05	0.04
L5-4	1.45	0.10	0.21
L6-1	1.22	0.04	0.05
L6-2	1.14	0.03	0.03
L6-3	2.11	0.05	0.06
L6-4	0.91	0.02	0.02
L6-5	2.51	0.06	0.08
XL1-1	1.13	0.04	0.05
XL1-2	1.10	0.03	0.03
XL1-3	1.48	0.04	0.05
XL1-4	1.67	0.04	0.06
XL1-5	1.31	0.03	0.04
XL1-6	1.16	0.03	0.04
XL1-11	1.04	0.03	0.03
XL1-12	0.76	0.02	0.02
XL1-13	0.83	0.02	0.03
XL1-14	0.87	0.02	0.02
XL1-15	1.39	0.06	0.06
XL1-16	1.05	0.02	0.04
XL1-17	0.90	0.02	0.03
XL2-1	1.59	0.08	0.06
XL2-2	0.66	0.03	0.03
XL2-3	0.97	0.10	0.19
XL2-4	0.74	0.03	0.04
XL2-5	0.65	0.03	0.02
XL2-6	1.24	0.05	0.04
XL2-7	1.66	0.06	0.05
XL3-1	0.95	0.03	0.02
XL3-2	1.21	0.09	0.05
XL4-1	0.77	0.04	0.04
XL4-2	0.46	0.02	0.02
XL4-3	0.96	0.05	0.03
XL4-4	1.37	0.07	0.07
XL4-5	1.23	0.04	0.03
XL4-6	1.41	0.06	0.05
XL4-7	1.51	0.07	0.05
XL4-8	1.72	0.23	0.39
R-1	1.59	0.08	0.08
R-4	0.61	0.03	0.02
R-9	1.12	0.03	0.03
R-13	1.06	0.04	0.04
R-17	0.83	0.02	0.04
R-18	1.24	0.06	0.08
R-19	1.83	0.09	0.07
R-24	1.31	0.10	0.13
R-27	1.58	0.07	0.05
R-28	1.51	0.07	0.06
R-29	1.58	0.07	0.04
R-32	1.18	0.06	0.04
R-35	1.34	0.10	0.05
R-36	1.31	0.02	0.02
R-41	1.13	0.05	0.04
R-45	1.09	0.05	0.05
R-47	1.56	0.07	0.05
R-52	1.14	0.05	0.04
R-56	1.09	0.07	0.09
R-60	1.44	0.07	0.05
R-69	1.28	0.05	0.04
R-72	0.87	0.04	0.04
R-74	1.23	0.05	0.04
R-76	1.35	0.06	0.04
R-79	1.06	0.05	0.04
R-81	1.24	0.06	0.06
R-85	1.47	0.06	0.05
R-87	1.87	0.28	0.44
R-91	1.59	0.09	0.07
R-93	1.00	0.04	0.03
R-95	1.20	0.06	0.04
R-97	1.12	0.06	0.07
R-100	1.38	0.06	0.04
R-101	1.36	0.05	0.03

*ppb by weight (nanograms of gas per gram of soil sample).

C_5+ free soil gas data[a]

ID	C_1*	C_2*	C_3*	iC_4*	nC_4*	C_5+*	P/M×10^3	%WET
L2-2	284	7.7	0.6	--	--	444.9	2.11	2.84
L4-3	257	7.1	0.6	--	--	459.7	2.33	2.90
L5-3	322	9.3	0.8	--	--	638.7	2.48	3.04
L5-4	299	9.0	0.8	--	--	691.2	2.68	3.17
L6-1	283	8.4	0.7	--	--	497.7	2.47	3.12
L6-4	252	7.7	0.7	--	--	625.4	2.78	3.23
XL1-1	310	8.6	0.7	--	--	485.9	2.26	2.91
XL1-3	285	7.9	0.6	--	--	527.5	2.11	2.90
XL1-4	302	8.6	0.7	--	--	556.8	2.32	2.99
XL1-5	323	8.8	0.7	--	--	605.1	2.17	2.86
XL1-6	331	19.1	7.7	2.9	3.4	509.1	23.26	9.09
XL1-11	333	--	0.7	--	--	461.7	2.09	0.21
XL1-12	308	7.8	0.6	--	--	510.7	1.95	2.65
XL1-13	284	8.7	0.8	--	--	654.6	2.82	3.24
XL1-14	265	8.4	0.8	--	--	495.2	2.80	3.12
XL1-15	270	8.0	0.7	--	--	459.9	2.59	3.12
XL1-17	272	8.3	0.8	--	--	532.9	2.94	3.24
XL2-1	159	4.8	--	--	--	390.4	--	2.36
XL2-2	267	7.5	0.5	--	--	423.0	1.87	2.91
XL2-3	273	8.1	0.6	--	--	525.4	2.20	3.09
XL2-4	254	8.1	0.4	--	--	444.6	1.41	2.91
XL2-5	265	7.5	0.5	--	--	520.6	1.88	2.92
XL2-6	254	7.2	0.5	--	--	464.1	1.97	2.94
XL2-7	216	5.3	0.4	--	--	413.1	1.85	2.57
XL3-1	268	7.6	0.7	--	--	424.8	2.61	3.00
XL3-2	309	8.2	0.6	--	--	589.1	1.94	2.78
XL4-1	308	8.4	0.7	--	--	601.6	2.27	2.87
XL4-3	245	7.3	0.5	--	--	441.0	2.04	3.09
XL4-4	269	7.7	0.6	--	--	505.3	2.23	2.59
XL4-5	292	8.4	0.6	--	--	508.7	2.06	2.59
XL4-6	284	8.1	0.6	--	--	479.7	2.11	2.97
XL4-7	279	7.9	0.7	--	--	477.4	2.51	2.39
R-1	291	--	0.7	--	--	441.1	2.41	0.24
R-4	300	8.9	0.8	--	--	692.7	2.67	3.15
R-9	284	8.5	0.7	--	--	630.3	2.46	3.14
R-13	266	8.1	0.7	--	--	559.4	2.63	3.20
R-17	269	--	0.7	--	--	437.7	2.60	0.26
R-18	308	8.2	0.6	--	--	576.8	1.95	2.78
R-19	305	9.0	--	--	--	572.5	3.93	3.24
R-24	307	8.6	0.7	--	--	515.3	2.28	2.94
R-27	298	8.8	0.8	--	--	467.6	2.68	3.12
R-28	295	8.7	0.6	--	--	460.9	2.03	3.06
R-29	309	9.0	0.8	--	--	511.4	2.59	3.07
R-32	279	7.8	0.6	--	--	632.8	2.15	2.92
R-35	277	8.2	0.7	--	--	672.6	2.53	3.11
R-36	279	8.4	0.7	--	--	566.5	2.51	3.16
R-41	252	7.0	0.4	--	--	461.9	1.59	2.58
R-45	254	6.7	0.7	--	--	451.5	2.76	2.83
R-47	51370	4401	1448	516.6	242.8	567.1	28.11	11.09
R-52	220	6.6	0.4	--	--	398.9	1.82	3.08
R-56	279	8.2	0.8	--	--	514.4	2.87	3.12
R-60	248	7.1	0.5	--	--	426.5	2.02	2.99
R-69	263	8.0	0.6	--	--	515.5	2.28	3.17
R-72	275	7.8	0.7	--	--	471.8	2.55	3.00
R-74	277	7.6	0.6	--	--	453.0	2.17	2.88
R-76	264	7.3	0.5	--	--	533.5	1.89	2.87
R-79	320	9.1	0.7	--	--	541.3	2.19	2.97
R-81	299	8.3	0.8	--	--	586.0	2.68	2.95
R-85	322	8.5	0.7	--	--	583.2	2.17	2.78
R-87	298	9.0	0.8	--	--	664.3	2.18	3.18
R-91	282	8.1	0.8	--	--	422.1	2.84	3.23
R-93	271	8.3	0.8	--	--	634.9	2.95	3.25
R-95	278	8.6	0.7	--	--	584.6	2.52	3.24
R-100	275	8.2	0.8	--	--	501.7	2.91	3.17
R-101	298	9.0	0.8	--	--	508.5	2.68	3.18

[a]Cities Service Laboratories.
*ppm (vol).
--indicates below detection limits.

C_1–C_5+ free soil gas data[a]

ID	C_1*	C_2*	C_3*	iC_4*	nC_4*	C_5+*	P/M•10^3	%WET
L1-1	218.1	5.3	2.8	0.0	71.3	379.4	12.84	26.7
L1-2	397.0	16.5	5.7	0.0	124.3	597.2	14.36	27.0
L1-3	463.8	23.9	8.4	0.0	145.1	686.9	18.11	27.7
L1-4	511.2	18.0	9.1	0.0	165.0	503.4	17.80	27.3
L1-5	520.7	22.7	7.8	0.0	176.5	526.6	14.98	28.5
L1-6	498.6	19.8	6.6	0.0	189.5	600.1	13.24	30.2
L1-7	482.3	21.7	7.4	0.0	167.2	517.6	15.34	28.9
L1-8	460.2	20.2	6.6	0.0	139.5	434.2	14.34	26.6
L1-9	488.1	26.1	8.7	0.0	150.2	700.4	17.82	27.5
L1-10	239.2	7.1	3.0	0.0	63.8	271.7	12.54	23.7
L1-11	535.6	20.6	6.1	0.0	173.5	596.1	11.39	27.2
L1-12	469.9	25.2	8.0	0.0	155.0	792.1	17.02	28.6
L1-13	333.8	19.3	6.0	0.0	120.4	363.3	17.97	30.4
L1-14	344.1	11.7	4.8	0.0	115.7	406.2	13.95	27.8
L1-15	311.2	10.8	4.3	0.0	99.7	320.6	13.82	27.0
L1-16	489.3	25.4	7.9	0.0	153.9	651.4	16.14	27.7
L2-1	555.1	21.6	6.2	0.0	138.3	567.7	11.17	23.0
L2-2	566.8	28.9	8.7	0.0	144.5	529.3	15.35	24.3
L2-3	530.7	26.4	7.8	0.0	141.3	643.3	14.70	24.9
L2-4	439.4	15.3	6.4	0.0	113.1	424.8	14.57	23.5
L2-5	467.9	21.9	7.2	0.0	123.3	354.8	15.39	24.6
L2-6	486.3	21.2	6.7	0.0	117.3	395.6	13.78	23.0
L2-7	515.7	25.9	12.9	0.0	138.1	558.5	25.01	25.5
L3-1	626.2	31.8	10.2	0.0	203.6	8.4	16.29	28.2
L3-2	626.7	29.2	9.7	0.0	210.7	829.9	15.48	28.5
L3-3	626.6	26.6	7.8	0.0	206.2	860.3	12.45	27.8
L3-4	647.5	24.2	7.2	0.0	205.8	652.6	11.12	26.8
L3-5	1690.0	39.8	18.6	0.0	509.8	1365.3	11.01	25.2
L3-6	2202.4	77.1	29.5	0.0	633.4	1740.0	13.39	25.2
L4-1	495.5	37.9	12.3	0.0	228.7	515.2	24.82	36.0
L4-2	559.3	29.9	9.3	0.0	197.0	851.8	16.63	29.7
L4-3	510.2	20.0	8.9	0.0	165.7	481.4	17.44	27.6
L4-4	571.1	33.3	10.7	0.0	186.3	788.4	18.74	28.7
L5-1	548.6	30.5	9.6	0.0	186.1	621.7	17.50	29.2
L5-2	625.6	34.2	10.6	0.0	214.8	886.1	16.94	29.3
L5-3	517.6	27.9	9.0	0.0	166.0	658.0	17.39	28.2
L5-4	454.0	18.9	8.3	0.0	148.9	100.6	18.28	28.0
L6-1	579.7	29.3	9.6	0.0	194.4	419.1	16.56	28.7
L6-2	615.9	31.4	11.3	0.0	177.9	814.6	18.35	26.4
L6-3	545.6	21.8	9.3	0.0	163.2	565.7	17.05	26.3
L6-5	394.5	15.0	6.8	0.0	114.5	486.9	17.24	25.7
XL1-3	392.8	11.7	5.2	0.0	111.6	325.4	13.24	24.7
XL4-2	537.0	29.0	14.1	0.0	141.7	640.1	26.26	25.6
XL4-8	1559.8	53.5	21.6	0.0	353.3	1093.9	13.85	21.6
R-41	469.1	26.9	8.5	0.0	130.5	524.9	18.12	26.1
R-97	330.5	15.1	9.3	0.0	92.6	377.5	28.14	26.2

[a]Geochem Lab, Inc.
*ppm (vol).

Mean ranked adsorbed gas values

ID	C_1*	C_2*	C_3*	iC_4*	nC_4*
L1-1	-0.69	-0.82	-0.81	-0.70	-0.81
L1-2	-0.94	-1.11	-1.16	-0.95	-1.15
L1-3	-0.79	-0.94	-0.96	-0.95	-0.98
L1-4	-0.58	-0.66	-0.69	-0.70	-0.70
L1-5	-0.35	-0.45	-0.46	-0.45	-0.47
L1-6	-0.89	-1.06	-1.10	-1.12	-1.15
L1-7	1.21	0.55	0.13	0.38	0.03
L1-8	-0.85	-0.95	-0.98	-0.95	-0.93
L1-9	0.21	0.31	0.27	0.30	0.26
L1-10	-0.18	0.23	-0.02	-0.20	-0.14
L1-11	0.66	0.66	0.59	0.63	0.54
L1-12	-0.40	-0.52	-0.50	-0.45	-0.53
L1-13	3.00	2.93	3.17	3.05	3.08
L1-14	-0.27	-0.47	-0.44	-0.37	-0.42
L1-15	0.80	0.90	0.96	1.13	0.99
L1-16	0.44	0.50	0.52	0.47	0.49
L2-1	0.37	-0.34	-0.39	-0.45	-0.42
L2-2	2.35	2.22	2.11	1.97	1.95
L2-3	-0.30	-0.42	-0.41	-0.37	-0.36
L2-4	1.01	0.98	0.98	0.80	0.94
L2-5	-0.89	-1.01	-1.08	-0.95	-0.98
L2-6	-0.63	-0.84	-0.89	-0.70	-0.93
L2-7	0.07	0.37	0.31	0.22	0.32
L3-1	-0.12	-0.21	-0.16	-0.12	-0.14
L3-2	-0.54	-0.69	-0.77	-0.70	-0.81
L3-3	-0.96	-1.12	-1.16	-1.12	-1.15
L3-4	1.91	2.37	2.34	1.68	2.12
L3-5	-0.52	-0.74	-0.77	-1.12	-0.81
L3-6	-0.38	-0.40	-0.41	-0.37	-0.36
L4-1	-0.00	0.04	-0.13	0.05	0.15
L4-2	-0.72	-0.85	-0.85	-0.78	-0.87
L4-3	-0.77	-0.91	-0.94	-0.78	-0.93
L4-4	-0.63	-0.73	-0.75	-0.78	-0.76
L5-1	2.18	1.40	1.29	1.38	1.22
L5-2	-0.80	-0.94	-0.98	-0.87	-0.93
L5-3	-0.01	0.59	0.40	-0.03	0.26
L5-4	-0.69	-0.52	-0.60	-0.70	-0.59
L6-1	-0.96	-1.11	-1.14	-1.12	-1.15
L6-2	-0.25	-0.21	-0.10	0.05	-0.02
L6-3	-0.95	-1.09	-1.12	-1.03	-1.15
L6-4	-0.82	-0.97	-1.02	-0.95	-1.04
L6-5	-0.69	-0.83	-0.85	-0.70	-0.81
XL1-1	-0.74	-0.72	-0.71	-0.78	-0.76
XL1-3	-0.26	-0.21	-0.10	-0.20	-0.14
XL1-4	-0.89	-0.82	-0.66	-0.87	-0.64
XL1-5	-0.40	-0.30	-0.23	-0.45	-0.25
XL1-6	0.28	0.61	0.79	0.72	0.88
XL1-11	-0.53	-0.63	-0.62	-0.95	-0.59
XL1-12	-0.26	-0.30	-0.29	-0.37	-0.36
XL1-13	-0.43	-0.40	-0.41	-0.95	-0.42
XL1-14	1.62	2.53	2.54	2.22	2.18
XL1-15	-0.26	-0.29	-0.25	-0.20	-0.19
XL1-16	-0.91	-1.05	-1.10	-1.03	-1.04
XL1-17	0.45	0.63	0.73	0.55	0.71
XL2-1	0.68	0.76	0.71	0.72	0.71
XL2-2	1.17	1.07	1.04	0.80	0.94
XL2-3	1.15	1.33	1.29	1.22	1.16
XL2-4	5.77	3.99	3.50	2.88	3.14
XL2-5	-0.39	-0.42	-0.50	-0.53	-0.53
XL2-6	-0.40	-0.51	-0.52	-0.53	-0.47
XL2-7	0.17	0.76	0.15	-0.28	0.09
XL3-1	-0.61	-0.73	-0.75	-0.70	-0.76
XL3-2	-0.28	-0.37	-0.35	-0.37	-0.31
XL4-1	1.25	0.65	0.59	0.38	0.49
XL4-2	0.03	0.23	0.25	0.05	0.26
XL4-3	2.30	2.01	2.09	1.88	1.90
XL4-4	-0.17	-0.22	-0.25	-0.45	-0.19
XL4-5	0.26	0.76	0.56	0.13	0.48
XL4-6	-0.94	-1.08	-1.12	-1.12	-1.15
XL4-7	0.21	0.33	0.27	0.72	0.20
XL4-8	-0.47	-0.50	-0.54	-0.45	-0.59
XL5-2	0.29	0.82	0.88	0.55	0.94
R-1	-0.81	-0.96	-0.98	-0.87	-0.93
R-4	-0.82	-0.94	-0.94	-0.87	-0.98
R-9	-0.02	0.10	0.25	0.47	0.37
R-13	0.82	0.99	0.92	0.88	0.94
R-17	0.21	0.31	0.40	0.30	0.37
R-18	0.14	0.04	0.13	0.13	0.20
R-19	-0.25	-0.44	-0.39	-0.45	-0.42
R-24	-0.86	-0.98	-0.96	-0.87	-0.93
R-27	-0.77	-0.86	-0.83	-0.78	-0.81
R-28	-0.94	-1.10	-1.12	-1.12	-1.15
R-29	0.34	0.52	0.77	0.47	0.82
R-32	-0.61	-0.74	-0.71	-0.70	-0.76
R-35	0.02	-0.07	-0.06	-0.12	-0.02
R-36	0.57	0.32	0.52	0.47	0.54
R-41	-0.94	-1.10	-1.10	-1.05	-1.15
R-45	-0.86	-0.94	-0.91	-0.95	-0.93
R-47	0.05	-0.06	-0.04	0.05	-0.08
R-52	1.56	1.43	1.25	1.13	1.45
R-56	-0.93	-1.07	-0.94	-1.12	-1.10
R-60	1.02	0.84	0.86	0.88	0.94
R-69	-0.62	-0.79	-0.81	-0.78	-0.81
R-72	-0.26	0.64	0.84	1.22	1.28
R-74	0.06	-0.01	0.02	0.13	0.15
R-76	0.32	0.61	0.77	1.72	1.05
R-79	0.30	0.74	0.84	1.13	0.99
R-81	0.17	0.14	0.29	0.72	0.49
R-85	0.42	0.58	0.88	1.55	1.16
R-87	-0.72	-0.70	-0.54	-0.70	-0.70
R-91	0.16	1.23	1.50	2.27	1.95
R-93	-0.59	-0.74	-0.75	-0.70	-0.76
R-95	0.27	0.32	0.42	0.55	0.54
R-97	-0.33	-0.32	-0.35	-0.28	-0.42
R-100	0.85	2.41	2.65	3.22	2.47
R-101	-0.50	-0.54	-0.58	-0.70	-0.59

*In standard deviation units from the mean.

Mean ranked absorbed soil gas values

ID	C_1*	C_2*	C_3*
L1-1	-.36	-.64	-.27
L1-2	-3.68	-.90	-.61
L1-3	-.78	-.90	-.61
L1-4	-1.42	-.90	-.61
L1-5	-.58	-.90	-.44
L1-6	-.02	-.13	-.10
L1-7	-.18	1.15	.41
L1-8	-.62	-.64	-.27
L1-9	.60	1.15	-.10
L1-10	-.62	-.385	-.27
L1-11	-.36	-.385	-.27
L1-12	-.04	.13	-.27
L1-13	-.26	-.385	-.27
L1-14	-1.08	-.90	-.61
L1-15	.10	.385	-.27
L1-16	-.44	-.13	.07
L2-1	-.68	-.64	-.61
L2-2	-.56	-.64	-.27
L2-3	-.58	-.90	-.44
L2-4	-.60	-.64	-.61
L2-5	-.60	-.385	-.27
L2-6	-.14	-.385	-.44
L2-7	-1.26	-.90	-.61
L3-1	.40	-.13	.07
L3-2	1.42	.385	.24
L3-3	.14	-.13	.07
L3-4	-1.02	-.64	-.61
L3-5	-0-	-.13	-.44
L3-6	1.80	1.92	1.085
L4-1	-.04	.13	.24
L4-2	.96	.13	-.27
L4-3	3.26	1.41	.75
L4-4	4.94	2.18	.92
L5-1	-.24	-.385	-.44
L5-2	4.20	2.18	1.25
L5-3	-.10	-.13	-.27
L5-4	.38	1.15	2.61
L6-1	-.08	-.385	-.10
L6-2	-.24	-.64	-.44
L6-3	1.70	-.13	.07
L6-4	-.70	-.50	-.61
L6-5	2.50	.13	.41
XL1-1	-.26	-.385	-.10
XL1-2	-.32	-.64	-.44
XL1-3	.44	-.385	-.10
XL1-4	.82	-.385	.07
XL1-5	.10	-.64	-.27
XL1-6	-.20	-.64	-.27
XL1-11	-.44	-.64	-.44
XL1-12	-1.00	-.90	-.61
XL1-13	-.86	-.90	-.44
XL1-14	-.78	-.90	-.61
XL1-15	.26	.13	.07
XL1-16	-.42	-.90	-.27
XL1-17	-.72	-.90	-.44
XL2-1	.66	.64	.07
XL2-2	-1.20	-.64	-.44
XL2-3	-.58	1.15	2.27
XL2-4	-1.04	-.64	-.27
XL2-5	-1.22	-.64	-.61
XL2-6	-.04	-.13	-.27
XL2-7	.80	.13	-.10
XL3-1	-.62	-.64	-.61
XL3-2	-.10	.90	-.10
XL4-1	-.98	-.385	-.27
XL4-2	1.60	-.90	-.61
XL4-3	-.60	-.13	-.44
XL4-4	.22	.385	.24
XL4-5	-.06	-.385	-.44
XL4-6	.30	.13	-.10
XL4-7	.50	.385	-.10
XL4-8	.92	4.49	5.66
R1	.66	.64	.41
R4	-1.30	-.64	-.61
R9	-.28	-.64	-.44
R13	-.40	-.385	-.27
R17	-.86	-.90	-.27
R18	-.04	.13	.41
R19	1.14	.90	.24
R24	.10	1.15	1.25
R27	.64	.385	-.10
R28	.50	.385	.07
R29	.64	.385	-.27
R32	-.16	.13	-.27
R35	.16	1.15	-.10
R36	.10	-.90	-.61
R41	-.26	-.13	-.87
R45	-.34	-.13	-.10
R47	.60	.385	-.10
R52	-.24	-.13	-.27
R56	-.34	.585	.58
R60	.36	.385	-.10
R69	.04	-.13	-.27
R72	-.78	-.585	-.27
R74	-.06	-.13	-.27
R76	.18	.13	-.27
R79	-.40	-.13	-.27
R81	-.04	.13	.07
R85	.42	.13	-.10
R87	1.22	5.77	6.51
R91	.66	.90	.24
R93	-.52	-.385	-.44
R95	-.12	.13	-.27
R97	-.28	.13	.24
R100	.24	.13	-.27
R101	.20	-.13	-.44

*In standard deviation units from the mean.

Mean ranked free soil gas values

ID	C_1*	C_2*	C_3*	C_5**	P/M*1000	%WET
L1-1	-1.01	-1.67	-1.365	-.74	-.92	-.11
L1-2	-.50	-.71	-.73	.01	-.51	.02
L1-3	-.31	-.08	-.13	.32	.51	.31
L1-4	-.17	-.58	.02	-.31	.42	.14
L1-5	-.14	-.18	-.27	-.23	-.34	.64
L1-6	-.21	-.45	-.55	.02	-.81	1.34
L1-7	-.25	-.265	-.35	-.26	-.24	.805
L1-8	-.32	-.59	-.53	-.55	-.515	-.15
L1-9	-.24	.11	-.07	.37	.43	.22
L1-10	-.95	-1.51	-1.32	-1.11	-1.00	-1.35
L1-11	-.10	-.36	-.64	.01	-1.51	.10
L1-12	-.29	.03	-.22	.68	.21	.68
L1-13	-.68	-.47	-.66	-.80	.47	1.43
L1-14	-.65	-1.12	-.93	-.65	-.62	.35
L1-15	-.74	-1.20	-1.04	-.94	-.66	.02
L1-16	-.23	.05	-.24	.20	-.03	.31
L2-1	-.05	-.27	-.62	-.09	-1.37	-1.64
L2-2	-.01	.35	-.07	-.22	-.24	-1.10
L2-3	-.12	.14	-.27	.17	-.42	-.98
L2-4	-.38	-.81	-.57	-.58	-.45	-1.44
L2-5	-.295	-.25	-.40	-.82	-4.02	-.98
L2-6	-.24	-.31	-.51	-.68	-.67	-1.64
L2-7	-.16	.09	.855	-.12	2.38	-.61
L3-1	.16	.60	.26	-2.02	.01	.515
L3-2	.16	.38	.15	.81	-.21	.64
L3-3	.16	.15	-.27	.92	-1.03	-.35
L3-4	.22	-.05	-.40	.20	-1.39	-.07
L3-5	3.19	1.28	2.11	2.66	-1.42	-.73
L3-6	4.65	4.47	4.50	3.95	-.77	-.73
L4-1	-.22	1.12	.72	-.27	2.33	3.75
L4-2	-.03	.44	.06	.89	.11	1.14
L4-3	-.17	-.41	-.02	-.39	.33	.27
L4-4	-.0002	.73	.37	.67	.68	.72
L5-1	-.06	.49	.13	.10	.34	.93
L5-2	.16	.80	.35	1.01	.19	.97
L5-3	1.58	.70	.035	1.56	.31	.515
L5-4	.69	-.50	.035	2.24	.55	.43
L6-1	.07	.385	.13	-.27	.09	.72
L6-2	.13	.56	.50	.76	.57	-.23
L6-3	-.07	-.26	.06	-.10	.22	-.27
L6-4	-1.14	-.31	-.08	1.39	-.07	.10
L6-5	-.50	-.84	-.49	-.37	.27	-.52
XL1-1	1.12	.26	-.08	-1.24	-.20	-.13
XL1-3	.145	31.45	-.20	.12	-.23	-.14
XL1-4	.81	.26	-.08	.50	-.18	-.075
XL1-5	1.62	.39	-.08	-1.37	-.22	-.17
XL1-6	1.93	6.91	7.97	.63	5.08	4.48
XL1-11	-2.01	--	-.04	-.74	-.24	-2.15
XL1-12	.22	-.06	-.20	.15	-.24	-.11
XL1-13	.11	.32	.035	1.77	-.06	.11
XL1-14	.18	.13	-.03	-.42	-.06	.02
XL1-15	-.44	-.12	-.08	-.71	-.11	.02
XL1-17	-.36	.07	.03	.97	-.03	.11
XL2-1	-3.20	-2.15	--	-1.66	--	-.545
XL2-2	.11	-.31	-.20	-.12	-.23	-.13
XL2-3	-.32	-.06	-.20	-.05	-.21	--
XL2-4	.11	-.06	-.43	-.96	-.41	-.13
XL2-5	-.59	-.44	-.31	.03	-.29	-.13
XL2-6	-1.06	-.63	-.31	-1.11	-.27	-.11
XL2-7	-2.54	-1.83	-.43	-.76	-.30	-.59
XL3-1	-.52	-.37	-.08	.97	-.11	-.07
XL3-2	1.08	.01	-.20	.92	-.28	-.23
XL4-1	1.04	.13	-.04	-1.08	-.19	-.16
XL4-2	-.10	.36	1.12	.16	2.72	-.56
XL4-3	-.94	-.56	-.20	-.76	-.18	+(-.14)
XL4-4	-.48	-.31	-.20	-.09	-.20	-.075
XL4-5	.42	.13	-.20	2.26	-.25	-.075
XL4-6	.11	-.06	-.20	-.50	-.23	-.09
XL4-7	-.09	-.18	-.08	-.53	-.13	-.075
XL4-8	2.82	2.45	2.77	1.72	-.65	-2.22
R-1	.38	--	-.08	-1.00	-.16	-2.13
R-4	.73	.45	.02	-.10	-.09	.03
R-9	.11	.20	-.08	1.45	-.15	.04
R-13	-.59	-.06	-.08	-.30	-.10	.08
R-17	-.48	--	-.08	-.04	-.11	-2.11
R-18	1.04	.01	-.20	.76	-.27	-.23
R-19	.92	.51	--	.70	.22	-.11
R-24	1.00	.26	-.08	-1.22	-.19	-.11
R-27	.65	.39	.02	-.13	-.09	.02
R-28	.53	.32	-.20	-.75	-.25	-.07
R-29	1.08	.51	.03	-1.05	-.11	-.02
R-32	-.09	-.25	-.20	1.48	-.22	-.13
R-35	-.17	.01	-.08	2.00	-.13	.015
R-36	-.09	.13	-.08	.62	-.13	.05
R-41	1.14	-.75	-.43	-.73	-.36	-.58
R-45	-1.06	-.94	-.08	-.87	-.80	-.19
R-47	1987.12	2780.26	1663.48	-.84	6.30	5.97
R-52	-2.38	-1.01	-.43	-1.55	-.31	-.01
R-56	-.09	.01	.03	1.89	-.04	.02
R-60	-1.29	-.69	-.31	-1.19	-.26	-.07
R-69	-.71	-.12	-.20	-.04	-.19	.06
R-72	-.24	-.25	-.08	-.61	-.12	-.07
R-74	-.15	-.37	-.20	.09	-.22	-.1
R-76	-.67	-.56	-.31	.195	-.29	-.1
R-79	1.51	.58	-.08	.30	-.21	-.0
R-81	.69	.07	.035	.88	-.09	-.1
R-85	1.58	-.20	-.08	.84	-.22	-.2
R-87	.65	.51	.03	.53	-.09	.0
R-91	.03	-.06	-.035	-.17	-.05	.0
R-93	-.40	.07	.035	1.51	-.02	.1
R-95	-.13	.26	-.08	.86	-.15	.1
R-97	-.69	-.83	.06	-.75	3.22	-.
R-100	-.24	.01	.03	1.12	.05	.
R-101	.65	.51	.02	-.13	-.09	-

*In standard deviation units from the mean.

Appendix B
Results of Lasertrace® Soil Elemental Geochemistry Analyses

Soil elemental values[a]

ID	Ca	Cu	Fe	Mn	Ni	P	K	Na	Ti	V	Zn
A1	28880	88.0	44190	780	40.8	985	28490	4697	2322	130	132
A2	29030	79.4	46130	883	38.7	1151	31500	6108	2519	120	126
A3	38950	81.9	42890	936	38.5	924	30850	5589	2227	120	114
A4	22920	71.0	42260	772	39.1	992	31470	5308	2147	117	117
A5	24950	75.0	44920	718	36.1	965	31510	5554	2064	122	115
A6	33690	75.5	43820	800	36.8	983	30090	4636	2020	120	120
A7	29360	72.8	46270	1088	37.8	1139	31300	5038	2125	128	128
A8	12570	63.3	46890	583	39.3	879	28960	3635	2106	142	135
A9	16420	73.3	44730	886	35.8	1048	29750	4013	2281	132	126
A10	61530	83.9	43640	1761	40.4	1221	28760	4042	1894	119	131
A11	7586	78.2	47070	739	36.6	1093	31130	3831	2401	127	135
A12	14960	53.8	67580	716	42.1	1069	25480	7417	2127	140	126
A13	12580	68.5	43580	805	34.5	1126	32920	4034	2497	120	124
A14	11640	77.8	51070	792	37.2	1066	31980	3623	2339	128	127
A15	4211	83.3	48950	700	35.6	1094	28640	3575	2406	125	126
A16	2871	71.4	48350	704	39.2	1070	29330	3556	2140	127	146
A17	7698	76.4	40540	363	33.2	926	19890	2466	2358	131	124
A18	1909	77.6	53120	537	43.2	1046	27700	3116	2454	135	207
A19	14280	91.1	47890	638	42.3	1071	24230	3063	2309	133	145
A20	7851	73.8	50170	365	37.9	920	27910	5222	1900	117	138
A21	2845	76.6	52160	927	33.2	1032	29880	3503	2454	136	139
A22	10930	128.6	51720	603	38.3	1129	27670	3577	1977	123	151
A23	3712	92.3	52880	674	37.1	1112	29770	3439	2354	136	143
A24	3769	73.5	54610	822	34.7	1185	30160	4168	2275	133	128
A25	3041	58.0	48850	1004	31.6	1215	32490	4252	2280	114	123
B1	21210	53.9	52040	820	41.2	1010	31030	8495	2055	109	109
B2	10730	82.5	46390	1346	30.3	1240	31900	6856	2206	116	122
B3	15640	70.5	45170	930	33.3	980	34200	6012	2122	118	131
B4	11220	93.9	48210	641	32.6	909	34050	6844	2280	119	115
B5	15710	69.9	46800	877	34.3	1163	31940	5515	2040	127	124
B6	29810	38.9	39720	905	31.6	798	26100	7224	1563	97	92
B7	20460	59.0	44400	916	31.0	1075	28300	5115	2055	116	118
B9	21800	70.3	45440	841	34.9	1112	30380	5976	1955	116	120
B10	6392	54.4	41630	877	32.6	1054	31190	7389	1844	107	106
B11	17460	75.0	42080	860	32.8	1281	33810	7486	1863	112	125
B12	3930	22.8	33050	442	21.0	639	26860	9449	1415	85	76
B13	19990	65.9	45060	810	36.4	1040	33170	5832	2083	122	134
B15	11750	67.4	46520	613	28.3	833	35470	6297	2170	110	105
B16	40280	35.7	49780	1470	32.9	968	26160	8055	1809	103	99
B17	10500	51.0	45250	740	27.7	987	31380	5481	2203	111	114
B18	18550	80.8	70150	604	45.2	1246	25160	6390	2260	176	120
B19	6353	71.1	47460	569	31.1	1014	30090	4555	2362	128	128
B20	19430	82.9	49930	769	34.1	993	29940	4772	2173	123	143
B21	15890	70.2	45780	931	32.8	1106	31330	4787	2068	128	136
B22	20800	61.8	46180	604	28.5	905	25480	6273	1960	109	113
B23	5141	62.4	43660	965	30.0	1116	30100	5238	2058	114	117
B24	3089	92.4	48090	786	35.5	1038	31260	3739	2394	132	139
B25	7678	79.5	50300	1078	38.5	1319	33650	4250	2288	125	139
D1	8390	123.6	44350	946	35.0	1149	27860	4151	2098	116	178
D2	16070	94.2	47940	1126	37.6	1310	28700	4281	2063	123	146
D3	8912	108.4	50720	840	40.0	1425	26690	3472	1981	142	167
D4	9818	124.1	46500	959	33.7	1198	31220	4635	2129	115	132
D26	15570	63.5	49730	730	36.1	1123	29030	4779	1960	115	142
D27	20350	83.4	48000	686	33.8	1104	28830	4201	2050	128	127
D28	16000	94.2	47770	807	36.1	1150	32310	5337	1979	120	128
D29	14930	87.2	47640	887	34.2	1178	33390	5490	2153	123	126
D31	15160	71.4	43670	981	32.8	1248	31430	5494	2024	117	129
D32	18320	86.9	47980	806	37.1	1148	32140	5301	2067	119	120
D34	20370	77.5	47990	937	35.7	1085	30450	5052	1947	122	138
D35	14360	83.4	48440	787	34.4	1066	31590	4440	1963	123	148
D36	18670	76.7	45280	918	35.2	1216	33090	5476	2106	116	134
D37	6820	64.5	51640	806	32.1	1237	31170	4933	2096	133	142
D38	10360	105.2	47480	778	33.0	1238	33500	5029	2073	117	162
D39	21880	74.6	46430	1037	31.6	1182	31080	5508	1859	110	123

[a]In ppm.

ID	Ca	Cu	Fe	Mn	Ni	P	K	Na	Ti	V	Zn
E5	11670	63.2	45680	971	34.0	1123	34120	4864	2097	117	121
E6	11050	42.4	44410	722	27.9	872	24640	6722	1770	103	99
E7	3185	77.8	48300	983	32.9	983	32900	5162	2362	117	129
E8	2874	71.0	45860	700	31.6	1001	33520	4690	2415	110	130
E9	3420	70.6	47640	986	34.9	1389	33730	4520	2415	118	130
E10	6518	63.9	45990	1217	31.6	1060	31770	4310	2329	110	116
E11	21450	74.3	45560	1047	48.1	1078	33380	5037	2217	117	132
E12	26780	74.3	46150	646	42.0	1074	24760	3595	2287	117	134
E13	5304	90.1	54860	716	35.3	1138	29680	4196	2620	142	140
E14	2770	74.5	53000	805	37.9	1024	29700	4050	2416	131	139
E15	42310	83.7	54000	705	38.8	1193	21780	3349	2114	135	115
E16	26090	62.2	48880	1188	35.9	1134	28920	3751	2136	116	116
E17	2705	67.5	51230	919	31.3	1000	28540	4308	2532	126	125
E18	2545	72.3	48520	690	32.9	900	31310	3680	2345	128	141
E19	2806	69.9	53040	1179	36.9	1124	31840	4572	2487	128	143
E20	31590	56.9	50640	1051	35.8	1090	32360	4392	2113	109	115
F1	13770	45.1	50050	615	40.4	777	27780	7315	2197	120	104
F2	12850	69.7	48000	794	39.5	1084	31250	5101	2336	132	128
F3	23150	72.9	47500	793	43.8	1021	31200	5187	2240	125	116
F4	28590	63.4	47300	1199	37.8	1178	31520	4883	2266	118	123
F5	19380	70.4	48710	1120	36.0	1311	30590	5257	2269	120	129
F6	27420	66.1	44610	489	43.7	952	30960	4885	2109	130	119
F7	16940	72.9	48550	813	41.2	1161	33990	6166	2197	124	115
F8	19740	67.5	47730	933	38.5	1069	29600	6528	2001	116	108
F9	21970	66.2	44660	963	35.3	1073	31460	5375	2395	117	109
F10	46780	55.1	47510	1571	37.9	1552	27180	7362	1759	92	109
F11	57010	72.0	57640	1269	38.7	1069	25780	6171	1933	103	109
F13	13950	80.1	46750	553	40.1	971	31860	11150	2230	137	122
F14	12630	60.2	44040	323	39.3	640	29400	4634	2454	148	124
F15	14090	65.3	45910	556	41.6	884	31080	10530	2245	138	115
F16	11240	75.0	60250	928	43.3	928	33070	9145	2276	130	119
G1	5405	75.2	48260	1067	37.7	1100	33320	6203	2537	117	134
G2	7687	72.4	50030	1083	41.5	1259	36420	5573	2411	127	135
G3	3540	70.5	50670	1029	38.5	1315	31450	4832	2356	117	135
G4	3540	81.1	50230	1249	35.4	1170	30910	4940	2463	124	129
G5	5158	76.5	44610	1035	31.9	886	23040	4341	2674	120	118
G6	14760	68.5	50070	889	38.3	1022	29880	4501	2165	123	119
G7	6186	60.1	48500	1011	34.6	1073	30920	4339	2438	120	120
G8	2692	65.3	52780	968	38.4	949	29240	4381	2389	125	124
G9	2284	60.4	57630	918	39.5	924	30660	4634	2468	134	141
G12	6328	72.4	56300	724	41.3	1124	28090	3473	2316	142	140
G13	20800	73.1	53800	820	39.6	1077	28320	3259	2204	131	129
G14	4896	64.4	54170	1034	36.7	1047	29100	5328	2464	133	123
G15	32570	46.7	51790	681	38.4	1003	24690	3422	2378	149	115
G16	13470	46.1	43900	858	32.0	890	27600	6106	2057	112	104
G17	12550	83.1	53850	834	37.3	973	30750	4156	2323	128	125
G18	3764	75.6	53320	903	37.2	968	31700	4583	2482	133	137
L1-1	3185	88.7	42670	464	34.7	968	23860	2364	2203	128	194
L1-2	3566	164.1	44800	515	55.0	1500	33050	4804	2124	138	274
L1-3	8665	83.0	44130	599	36.1	982	29610	3444	2270	127	138
L1-4	6391	78.6	42470	537	37.0	829	27750	3034	2270	123	165
L1-5	7390	86.4	46530	555	38.1	877	28560	2960	2220	135	152
L1-6	6405	95.7	44520	508	38.4	920	30800	3177	2283	137	182
L1-7	39530	117.3	49530	522	41.1	1227	30010	3887	2240	131	139
L1-8	39760	93.5	42150	926	36.9	1115	28860	2647	2135	113	126
L1-9	9050	89.3	45500	857	37.0	1102	29640	3323	2340	123	138
L1-10	11110	76.2	39660	455	31.0	819	27200	2599	2050	126	147
L1-11	9306	84.8	49310	1055	40.9	1352	29500	3597	2224	131	173
L1-12	12650	77.3	43030	885	34.3	1096	31240	3363	2235	123	141
L1-14	29720	93.7	44820	1409	38.5	1109	30540	4113	2070	121	143
L1-15	23290	79.4	42290	959	35.1	1067	33160	4392	2175	116	131
L1-16	19350	82.0	42080	984	38.3	1126	34100	4677	2226	109	151
L2-1	10670	88.8	40690	523	34.0	1000	32670	3298	2016	116	167
L2-2	7370	65.5	41160	394	34.3	680	31080	2745	1926	118	120
L2-3	5842	93.1	43360	612	36.5	946	32460	3581	2209	122	137
L2-4	5821	80.5	43530	805	35.9	1073	34880	3837	2294	123	140
L2-5	71350	60.7	42540	882	37.3	1049	26960	4009	1739	111	120
L2-7	36800	87.7	37640	2346	61.5	1683	26050	3489	1287	92	167
L3-1	7196	67.9	45350	790	37.2	1170	30740	4310	2254	116	138

ID	Ca	Cu	Fe	Mn	Ni	P	K	Na	Ti	V	Zn
L3-2	4034	156.8	35100	230	34.3	866	17110	2113	2516	158	183
L3-3	1743	160.7	37450	112	27.5	852	15640	2336	2727	203	179
L3-4	11410	88.8	41860	718	33.9	989	24140	3123	2300	136	134
L3-5	14390	77.6	55330	1001	45.6	1148	25240	4660	2290	137	173
L3-6	8981	63.2	42350	715	34.9	1054	31680	4961	2360	114	120
L4-1	36820	60.7	47100	553	34.2	837	25630	8420	1912	118	134
L4-2	5733	84.8	41540	365	31.2	831	21820	2650	2353	128	132
L4-3	3936	87.3	41540	334	27.5	894	22370	2128	2522	131	132
L4-4	3344	82.2	45390	494	31.6	943	25010	2605	2330	129	155
L5-1	2727	83.7	45820	665	36.3	1012	25380	3859	2222	120	154
L5-2	4817	87.5	43530	348	32.5	803	19090	2449	2296	132	162
L5-3	7751	107.2	44100	345	34.9	921	23950	2657	2263	128	171
L5-4	4306	98.9	42140	454	38.6	881	25470	2818	2044	126	186
L6-1	2764	72.6	49180	896	35.8	1039	27810	3435	2246	128	141
L6-2	3595	70.8	47290	739	35.3	1157	33250	4476	2250	126	140
L6-3	2173	76.6	43660	573	31.3	903	28350	3382	2257	124	153
L6-4	2352	84.2	47730	325	28.6	885	24850	2636	2353	135	140
L6-5	3421	80.5	46520	422	27.4	997	26540	3611	2272	129	130
R-1	3469	71.8	42550	358	26.8	794	24370	3111	2270	117	110
R-4	3483	55.5	45630	755	28.5	1038	30290	4620	2186	117	128
R-9	2530	72.9	48170	835	35.4	983	30150	4415	2491	127	138
R-13	16330	59.3	42280	1086	34.9	1015	27400	3652	1984	106	126
R-17	4525	70.5	48150	1088	31.1	1119	31340	4297	2284	121	136
R-18	6052	56.5	53930	722	32.3	1114	24310	3342	2278	145	119
R-19	15200	57.7	60590	787	44.7	963	25600	3341	2157	147	140
R-24	3689	66.5	46470	802	34.4	919	31380	3891	2261	115	127
R-27	2013	59.2	44570	739	30.0	855	33240	4080	2200	111	125
R-28	2014	64.4	54090	718	35.0	943	30720	3319	2304	132	142
R-29	2722	64.3	46610	712	36.7	980	28680	3544	2159	116	158
R-32	3370	72.2	47910	683	36.0	1051	32100	3776	2231	127	157
R-35	15290	74.3	49450	545	39.1	1035	24290	4089	1927	124	154
R-36	24100	68.8	45220	629	37.6	867	27190	4139	1896	115	144
R-41	5778	81.5	50430	815	38.8	1101	26320	3647	2146	128	153
R-45	2514	77.1	50220	643	38.3	1015	31210	2957	2407	130	144
R-47	3770	76.8	51370	1015	36.6	1237	31580	3216	2246	126	153
R-52	20050	79.5	45080	729	38.9	1005	30880	4797	1904	120	149
R-56	17060	82.4	51620	701	38.7	1175	26410	3331	2351	143	153
R-60	10670	80.0	48530	902	37.4	997	32130	4247	2106	129	137
R-72	21220	68.1	46110	1006	36.7	1293	32480	4280	2001	122	147
R-74	13160	55.4	43680	871	31.3	1133	30830	4494	2084	114	120
R-76	24300	70.7	45630	711	39.8	1020	26720	3889	1862	118	132
R-79	20280	66.1	42950	904	34.5	1087	31450	4681	1936	107	120
R-81	23400	69.6	42870	851	34.2	998	31340	4672	1935	110	119
R-85	26150	70.6	45810	886	37.1	1061	29870	4415	2203	119	128
R-87	22080	61.6	42460	480	38.3	886	25580	2866	1906	155	132
R-91	23140	70.1	45970	687	37.8	1124	27330	4580	2027	119	129
R-93	19580	75.5	42550	838	40.2	1008	30140	4832	1954	123	136
R-95	24320	71.4	44400	727	33.8	893	32280	4523	1969	119	126
R-97	9658	86.4	45030	919	35.4	1058	34470	4981	2393	125	135
R-100	28720	88.9	47830	763	39.0	1119	26460	4024	1658	124	181
R-101	4449	62.9	50010	707	37.2	972	27060	3974	2006	129	158
U1	6330	87.9	52360	988	32.2	1124	30860	5031	2226	126	136
U2	567	78.0	51440	942	30.6	1273	28880	4866	2213	124	125
U3	3681	99.9	48920	541	29.4	857	26830	3519	2259	138	129
U4	3234	64.9	52400	1011	33.3	1195	28590	4654	2204	125	138
U5	7465	97.0	51780	1029	32.4	1164	33740	4689	2367	125	131
U6	5953	80.1	52210	995	33.7	1178	30210	4780	2189	122	132
U7	5423	76.3	48430	702	34.7	1035	31350	3680	2158	123	122
U8	11130	91.5	56690	1007	35.5	1320	25850	3910	2151	125	117
U9	5227	75.1	52300	964	31.0	1104	32290	4227	2288	122	136
U10	26270	61.0	52540	1018	34.8	1096	28010	3390	1980	115	139
U11	4633	78.0	53110	1064	35.3	1234	28890	3455	2185	123	133
U12	4927	83.0	52170	910	33.6	1098	31200	3673	2255	125	144
U13	2480	75.7	51990	732	36.3	1046	30630	3750	2248	130	141
U14	5119	83.9	51480	975	35.8	1103	33390	4024	2257	126	146
U15	2645	70.5	50820	680	33.8	1028	31140	3428	2212	122	135
U16	2436	69.3	50400	1041	32.9	1121	28600	3931	2216	116	149
U17	2187	70.4	51350	1086	32.4	1107	30470	4675	2369	122	133
U18	2475	86.7	49500	719	34.9	994	29770	3422	2164	126	140

ID	Ca	Cu	Fe	Mn	Ni	P	K	Na	Ti	V	Zn
U19	2549	71.7	55650	668	34.4	996	27910	3958	2316	127	142
U20	1899	74.6	49360	650	31.5	949	28820	4461	2305	120	139
U21	2985	78.3	45700	566	26.8	894	27220	3176	2267	121	128
U22	1971	75.6	51910	710	31.6	991	29620	4818	2306	121	146
U23	2278	69.7	44770	599	32.3	982	30470	4012	2142	121	147
U24	2736	83.8	49900	681	33.1	1079	28980	3902	2187	126	151
U25	10480	62.1	46140	537	36.1	949	26380	3639	1926	121	142
U26	7824	88.0	46020	753	31.2	1054	27170	4967	2078	121	116
U27	18230	92.0	51500	668	39.3	1172	31670	3887	2398	134	129
U28	6136	75.8	50230	872	32.7	991	29690	4493	2333	127	126
U29	5673	76.0	49550	668	31.6	979	30840	4628	2342	125	135
U30	3098	82.1	50490	819	31.5	1087	28690	4334	2281	121	147
U31	3455	75.4	51360	1068	33.6	1268	32810	4558	2265	123	136
U32	12880	75.1	47810	863	30.9	1015	31800	3982	2152	117	123
U33	16300	65.6	47370	889	29.8	1146	30430	4855	2176	117	113
U34	5601	72.1	49420	724	33.7	1079	31240	3671	2177	121	136
U35	3167	77.8	45240	650	30.1	1027	29260	3380	2155	118	133
U36	1883	80.3	48990	742	31.9	974	31380	4559	2348	116	141
U37	2881	71.3	55270	1038	33.5	1150	29950	4024	2264	120	150
U38	2494	75.5	52720	1306	33.5	1223	30560	5046	2422	121	160
U39	2309	69.7	51990	874	28.8	1271	32660	5486	2491	119	141
U40	2646	76.7	51820	734	31.5	1070	30650	5016	2314	121	159
U41	3952	67.9	45300	704	29.1	1026	34170	4146	2251	116	136
U42	5361	75.7	51200	1150	31.0	1199	33940	4695	2354	121	155
U43	10040	62.3	46610	730	30.0	1036	28590	4501	2025	114	121
U44	4777	67.3	45610	563	32.0	1002	31340	4348	2126	120	124
U45	2792	75.0	53120	933	34.9	1121	30340	4718	2313	125	145
U46	2535	74.4	45550	501	29.6	1191	33960	4201	2313	115	132
U47	7867	84.4	44240	429	28.4	872	34750	5626	2256	113	110
U48	3584	83.4	57960	1045	36.0	1080	32340	4196	2292	128	155
U49	2807	78.3	53330	987	34.6	1069	31280	4011	2343	124	147
U50	2260	80.4	54710	1024	33.0	1096	34720	4701	2433	122	154
U51	2946	94.6	53460	995	32.4	1282	32590	4387	2387	120	156
U52	14470	85.2	48840	827	33.3	1077	31180	3846	2336	128	131
U53	13820	77.7	49280	681	34.4	975	33190	4269	2173	132	128
U54	8943	76.7	50490	747	32.7	1005	32320	4740	2335	125	121
U55	8760	83.7	49290	637	33.4	981	31880	4619	2407	125	121
U56	4339	66.0	61360	832	37.5	1304	28920	4391	2502	132	156
U57	2729	67.6	60110	915	37.1	1185	29560	3937	2674	154	156
U58	6388	74.3	52020	702	37.4	1056	29420	4097	2566	140	139
U59	15350	68.4	49100	722	31.1	962	33060	5686	2521	119	115
U60	4954	70.7	49500	807	33.2	1004	31580	4974	2289	117	130
U61	10940	63.9	63290	1058	34.8	1283	30550	5018	2619	142	142
U62	9518	74.7	54560	993	38.6	1157	27500	5006	2465	130	137
U63	4159	78.5	54590	874	32.8	1031	31710	4306	2366	123	145
U64	2916	92.7	54650	964	35.8	1096	33350	4364	2423	127	153
U65	2164	79.3	52960	977	39.4	999	32290	4402	2470	124	152
U66	2009	73.9	53550	586	37.2	882	32380	4770	2428	123	142
U67	2207	74.4	52140	824	37.3	1013	31910	4662	2319	117	143
U68	1993	80.4	52780	658	39.9	925	32800	4017	2335	123	142
U69	3143	83.6	51430	756	36.5	1121	32840	4433	2367	132	137
U70	4340	72.6	58820	758	39.9	1017	30010	3705	2639	147	142
U71	1904	66.5	56540	814	39.3	975	32810	5268	2536	131	139
U72	13120	77.2	52880	1025	35.5	1089	32390	3894	2339	127	135
XL1-1	4406	70.5	47660	725	34.4	981	27780	3030	2246	127	150
XL1-2	8465	76.4	47600	692	36.8	1039	27040	3297	2148	119	152
XL1-3	11460	77.2	47180	611	38.6	957	29010	2587	2256	130	153
XL1-4	8026	75.0	42130	273	27.0	805	20160	1721	2397	130	125
XL1-5	3333	71.3	59710	1153	38.4	1290	27830	4290	2432	147	169
XL1-6	23340	57.4	54500	1092	44.7	1293	25440	2902	2230	127	145
XL1-11	3009	77.6	50680	881	36.6	1066	31930	3613	2299	128	135
XL1-12	2819	76.9	54650	941	39.6	1140	32500	3753	2359	139	146
XL1-13	21180	80.9	50600	777	37.7	1013	31110	2805	2241	135	133
XL1-14	6209	87.7	49770	401	36.2	877	28110	4061	2306	145	128
XL1-15	10930	68.1	44320	811	31.9	1182	30800	4694	2230	115	118
XL1-16	6193	66.1	46050	668	34.3	1045	29710	5030	2174	118	122
XL1-17	6965	58.9	48770	948	36.3	1222	27150	3837	2268	120	145
XL2-1	11780	67.0	46570	631	38.7	1156	36020	3784	2158	136	134
XL2-2	25390	61.3	41050	604	37.9	861	29220	3921	1816	120	117

ID	Ca	Cu	Fe	Mn	Ni	P	K	Na	Ti	V	Zn
XL2-3	23280	72.3	43290	774	40.2	990	29950	3600	1973	120	129
XL2-4	25540	70.1	42060	724	36.0	902	28350	3076	1969	123	128
XL2-5	10230	103.5	37190	415	39.2	761	21290	2310	2217	126	149
XL2-6	7791	71.7	41730	584	36.9	920	32710	3942	2318	120	121
XL2-7	3901	84.5	43470	303	32.8	896	21710	2424	2109	122	148
XL3-1	13650	71.7	44400	691	45.4	1026	30820	3790	2193	116	131
XL3-2	8915	76.5	47130	676	35.2	970	33690	4101	2326	130	126

Section 12

Lost River, West Virginia, Petroleum Test Site Report

Authors/Editors

Harold R. Lang
Jet Propulsion Laboratory

John B. Curtis
John S. Kovacs
Columbia Gas System Service Corp.
Columbus, Ohio

Contributors

Gary A. Cooke
Aurelio A. DeGasparis
Gulf Science and Technology Co.
Pittsburgh, Pennsylvania

John B. Davis
Mobil Research and Development Co.
Dallas, Texas

Kathleen W. Baird
John P. Ford
Catherine J. LeVine
Barrett N. Rock
Jet Propulsion Laboratory

Section 12

Lost River, West Virginia, Petroleum Test Site Report

Contents

I. **Introduction** 12-1

II. **Geographic Setting** 12-1
- A. Location and Access 12-1
- B. Climate 12-1
- C. Physiography and Drainage 12-2

III. **Geologic Setting** 12-3
- A. Stratigraphy 12-3
  - 1. Rockwell Formation 12-3
  - 2. Hampshire Formation 12-3
  - 3. Chemung Formation 12-4
  - 4. Brallier Formation 12-4
  - 5. Marcellus Formation 12-4
  - 6. Oriskany Sandstone 12-4
  - 7. Silurian and Ordovician strata 12-5
- B. Structure 12-5
  - 1. Introduction 12-5
  - 2. Regional setting 12-5
  - 3. Test site 12-5
- C. Development of the Lost River Gas Field 12-5

IV. **Soils** 12-7

V. **Surface Geochemistry** 12-8
- A. Rock/Soil Geochemistry 12-12
  - 1. Chemung mineralogy/elemental geochemistry 12-12
  - 2. Soil mineralogy/elemental geochemistry 12-12
  - 3. Soil manganese geochemistry 12-12
  - 4. Conclusions 12-12
- B. Soil Bacteria 12-13

PRECEDING PAGE BLANK NOT FILMED

VI. Field and Laboratory Vegetation Studies 12-15
A. Introduction 12-15
B. Lichens 12-16
C. Mycorrhizal Fungi 12-17
1. Introduction 12-17
2. *In vivo* study 12-17
3. *In vitro* study 12-20
4. Conclusions 12-20
D. Higher (Vascular) Plants 12-21

VII. Multispectral Image Analysis and Interpretation 12-23
A. Introduction 12-23
B. NS-001 Image Analysis for Vegetation Discrimination 12-27
1. General spectral characteristics of vigorous vegetation 12-27
2. Botanical significance of NS-001 band data 12-30
3. Characteristics of NS-001 spectral data 12-30
4. Evaluation of NS-001 band and band-ratio data for vegetation mapping 12-33
5. Vegetation classification maps using NS-001 data 12-39
6. Determination of optimal NS-001 vegetation classification 12-43
C. Conclusions 12-46

VIII. Field Evaluation of NS-001 Supervised Vegetation Maps 12-48
A. Introduction 12-48
B. Accuracy of Supervised NS-001 Vegetation Classification Maps 12-48
C. Comparison of the Two Classifications 12-52
D. Anomalous Vegetation Distribution 12-53
E. Conclusions 12-58

IX. Photogeologic Interpretation of Aircraft Multispectral Data 12-58
A. Introduction 12-58
B. Results 12-58
C. Conclusions 12-60

X. Lineament Analysis of Multispectral Data 12-60
A. Introduction 12-60
B. Landsat MSS Lineament Analysis 12-61
C. Landsat MSS Lineament Density Analysis 12-61
D. NS-001 Lineament Density Analysis 12-65
1. NS-001 lineament density trend surface 12-71
2. Geologic model 12-73

XI. Radar Analysis 12-74
A. Introduction 12-74
B. Seasat SAR Images 12-74
C. Airborne SAR Images 12-77
D. Recommendations 12-77

XII. Conclusions and Recommendations 12-79
A. Spectral Analysis in Vegetated Terrain 12-79
B. Vegetation Classification Images 12-79
C. Lineament Density Analysis 12-79
D. Exploration Strategy 12-79
E. Direct Detection of Hydrocarbons 12-79
F. Mycorrhizal Fungi 12-79
Acknowledgments 12-81
References 12-82
Appendixes
A. Lost River Rock and Soil Analyses 12-87
B. Ground Vegetation Analysis Methods 12-93
C. Lost River Statistics for Trend Surface Analysis of NS-001 Lineament Density Values 12-95

Figures

12-1. Location map showing the geology of the Lost River test site, Hardy County, West Virginia 12-2
12-2. General topography of the Lost River test site 12-3
12-3. Schematic block diagram illustrating a physical interpretation for CSDs 12-5
12-4. Subsurface structural contour map of the top of the Onandaga or equivalent 12-6
12-5. NW–SE cross section through the central part of the Lost River gas field, based on seismic, well, and surface geologic data 12-7
12-6. Stratigraphic, lithologic, and mechanical logging data available for discovery well 9058 12-9
12-7. Map showing sample sites for preliminary soil mineralogy/elemental geochemistry survey 12-13
12-8. Map showing sample sites for soil manganese elemental geochemistry survey 12-14
12-9. Map showing sample sites for soil microbiology survey 12-15
12-10. Diagrammatic representation of first-year seedling of Chestnut Oak (*Quercus prinus*) showing the relative positions of the taproot, lateral roots, and clubroots 12-18
12-11. Topographic data for area over the center of the gas field 12-19
12-12. Diagrammatic representation of the *in vitro* experimental design for exposing roots of Chestnut Oak seedlings to migrating soil gases 12-21
12-13. Comparison of a 0.1-acre circular sample plot and a 15-m pixel 12-23
12-14. Preliminary field vegetation map 1—an area within the boundary of Lost River State Park 12-24
12-15. Preliminary field vegetation map 2—an area over the southern portion of the gas field 12-25
12-16. Preliminary field vegetation map 3—an area over the central portion of the gas field 12-26

12-17. Preliminary field vegetation map 4—an area at the northern end of the gas field 12-27
12-18. TC and CIR ground photography, Chestnut Oak leaves 12-28
12-19. Overview: looking east from the southern end of Big Ridge 12-29
12-20. Map showing flight-line locations and areal coverage for M²S, NS-001, and color photographic aircraft data acquired at the Lost River test site 12-31
12-21. Examples of field spectra for major cover types 12-32
12-22. PC spectra for NS-001, Mission 407, line 1 data acquired September 19, 1979 12-34
12-23. PC spectra for NS-001, Mission 431, line 1 data acquired October 21, 1980 12-35
12-24. NS-001 bands 2 (blue), 3 (green), and 4 (red) image of the Lost River test site (Mission 431, line 1) as seen in mid-October 12-36
12-25. NS-001, Mission 431, line 1, October 21, 1980 color composite image: bands 3 (blue), 4 (green), and 6 (red) 12-36
12-26. NS-001, Mission 431, line 1, October 21, 1980 color ratio slice image: band-ratio 2/3 12-37
12-27. NS-001, Mission 431, line 1, October 21, 1980 color ratio composite image: band-ratios 4/3 (green), 4/5 (blue), and 5/7 (red) 12-37
12-28. Tonal/textural unit interpretation of NS-001 bands 2, 3, and 4 color composite image 12-38
12-29. Tonal/textural unit interpretation of NS-001 bands 3, 4, and 6 color composite image 12-39
12-30. Tonal/textural unit interpretation of NS-001 band-ratio 2/3 color slice image 12-40
12-31. Tonal/textural unit interpretation of NS-001 band-ratios 4/3, 4/5, and 5/7 color composite image 12-41
12-32. DN color key used for tonal/textural unit interpretations 12-42
12-33. Outlines of 35 training areas used in the supervised vegetation classification map plotted on the NS-001 band 4 image 12-43
12-34. Outlines of 20 training areas in the northern part of the test site used in the supervised vegetation classification map 12-44
12-35. Outlines of 15 training areas in the southern part of the test site used in the supervised vegetation classification map 12-45
12-36. Supervised vegetation classification map produced using NS-001 (Mission 431) bands 2, 3, 4, 5, and 7 in the following combinations: 2, 3, 4, 4/5, 5/7 12-46
12-37. Supervised vegetation classification map produced using NS-001 (Mission 431) bands 3, 4, 5, and 6 in the following combinations: 6, 3/5, 4/5, 5, 3/6 12-48
12-38. Field of mean correct classification for eight BMD stepwise discriminant analyses of training areas used in the supervised vegetation classification map 12-49
12-39. Aerial CIR and NS-001 images of the area covered by preliminary field vegetation map 3 12-51

12-40. Maple anomaly sites 12-54
12-41. Stress symptoms in vegetation occurring at the Funkhouser maple anomaly sites 12-56
12-42. M^2S, Mission 399, line 1, April 20, 1979 color composite image 12-59
12-43. Composite geologic interpretation from aircraft multi-spectral data 12-59
12-44. High-contrast stretch, Landsat MSS bands 4 (blue), 5 (green), and 7 (red) color composite image 12-62
12-45. Regional Landsat MSS lineament interpretation 1 12-63
12-46. Regional Landsat MSS lineament interpretation 2 12-64
12-47. Regional Landsat MSS lineament density isopleth map from an analysis of interpretation 1 12-66
12-48. NS-001 band 4, 5 by 5 high-pass filter image used in lineament analysis 12-67
12-49. NS-001 band 4 shift image: shift direction –2 lines, 4 samples 12-68
12-50. NS-001 band 4 shift image: shift direction 4 lines, 2 samples 12-68
12-51. NS-001 band 4 shift image: shift direction 0 lines, 5 samples 12-69
12-52. NS-001 band 4 shift image: shift direction 5 lines, 0 samples 12-69
12-53. NS-001 band 4 shift image: shift direction –4 lines, 2 samples 12-70
12-54. NS-001 band 4 shift image: shift direction 2 lines, 4 samples 12-70
12-55. Composite band 4 NS-001 lineament interpretation plotted on a band 8 high-pass filter image base 12-72
12-56. Composite NS-001 lineament density isopleth map from an analysis of Figure 12-55 12-72
12-57. Comparison of lineament density trends from the Lost River test site analysis to joint and CSD trends recognized by Wheeler 12-73
12-58. Results of trend surface analysis of NS-001 lineament density data using the entire grid array 12-74
12-59. Results of trend surface analysis of NS-001 lineament density data excluding biased perimeter values 12-74
12-60. Fifth-degree lineament density trend surface plotted on an NS-001 band 8 high-pass filter image base 12-75
12-61. Typical domal structure exhibiting crestal fracturing, north dome of Kettleman Hills oil field, California 12-76
12-62. Diagram showing the geometry of Seasat SAR coverage 12-77
12-63. Comparison of Seasat SAR optically correlated images showing effects of illumination direction 12-78
12-64. Aircraft X-band SAR image; look-direction (S 63° E) is approximately perpendicular to the Ridge and Valley trend . . . 12-80
12-65. Aircraft X-band SAR image; look-direction (S 28° W) is approximately parallel to the Ridge and Valley trend 12-80

Tables

12-1. Stratigraphic units exposed at the surface and penetrated in the subsurface, Lost River test site 12-4
12-2. Driller's log from well 9058 12-8
12-3. Typical gas composition at well 9058 12-8
12-4. Well data—Lost River gas field 12-10
12-5. Characteristics of soils occurring in the Lost River test site .. 12-11
12-6. Methane-oxidizing bacterial colonies in soil samples from the Lost River test site 12-16
12-7. List of lichens and mosses identified in the Lost River area .. 12-16
12-8. Mycorrhizal data from the Lost River test site 12-18
12-9. Partial flora of the Lost River test site
(a) Woody angiosperms and gymnosperms 12-22
(b) Vascular cryptograms 12-22
12-10. Summary of aircraft-acquired multispectral data, Lost River test site 12-30
12-11. Summary of Landsat-acquired MSS data, Lost River test site 12-30
12-12. Correlation matrices for the seven NS-001 VNIR band data acquired in two overflights of the Lost River test site ... 12-32
12-13. Matrix of correlation change (October to September) for the seven NS-001 VNIR band data acquired in two overflights of the Lost River test site 12-33
12-14. NS-001 principal components analysis: eigenvectors of seven VNIR bands for the first three PCs 12-33
12-15. Discriminant function results: bands 2, 3, 4, 4/5, 5/7 12-47
12-16. Discriminant function results: bands 2, 3, 4, 4/5, 5/6 12-47
12-17. Discriminant function results: bands 1, 2, 3, 4, 5, 6, 7 12-47
12-18. Discriminant function results: band-ratios 1/6, 1/7, 2/7, 3/6, 3/7, 4/6, 4/7, 5/6, 5/7, 6/7 12-47
12-19. Discriminant function results: bands 6, 3/5, 5, 2/4, 4/5, 1/3, 4/6, 5/6, 3/5 12-47
12-20. Summary of results of eight BMD stepwise discriminant analysis runs showing minimum number of variables for maximum correct classification of 10 vegetation groups 12-48
12-21. Percentage of vegetation cover at the Lost River test site 12-49
12-22. Summary of vegetation cover percentage data for the Lost River test site 12-50
12-23. Major cover types of Lost River State Park, their areal extent in acres, percent of the forests of the state park they comprise, and number of stands sampled 12-50
12-24. Description of vegetation classes recognized at the Lost River test site 12-52
12-25. Soil conditions typical for selected woody species occurring at the Lost River test site 12-55
12-26. Relative tolerance of woody species to landfill conditions ... 12-57
12-27. Summary of shift image geometry for lineament analysis ... 12-71

12-28. Characteristics of available SAR image coverage of the Lost River test site 12-76
A-1. Lost River Chemung rock bulk chemistry 12-88
A-2. Lost River Chemung rock <2-μm fraction trace metal chemistry 12-89
A-3. Lost River Chemung rock reducing, acid-leachate chemistry 12-89
A-4. Lost River soils reducing, acid-leachate chemistry 12-90
A-5. Lost River soils oxidizing leachate chemistry 12-90
A-6. Lost River soils reducing, acid-leachate manganese concentration 12-91
C-1. Statistics for trend surface analysis of NS-001 lineament density values using an entire 9- by 24-point value array . . . 12-96
C-2. Statistics for trend surface analysis of NS-001 lineament density values using a 7- by 22-point value array, which excludes biased perimeter values 12-96

Plates[1]

12-1. Lost River, West Virginia: Drainage map
12-2. Lost River, West Virginia: Seismic structure interpretation
12-3. Lost River, West Virginia: Soils map

[1]Plates are contained in Part 3 (envelope) of *The Joint NASA/Geosat Test Case Project.*

Section 12
Lost River, West Virginia, Petroleum Test Site Report

I. Introduction

The Lost River gas field is the easternmost of the three petroleum test sites. It lies in the Ridge and Valley Province of the Appalachian Basin (Fenneman, 1938), a region now undergoing renewed exploration activity as the "Eastern Overthrust Belt" (Crow, 1981; McCaslin, 1981). The Columbia Gas Transmission Corporation discovered and developed the field during the 1960s and has produced approximately 14 billion cubic feet (BCF) of gas from the Lower Devonian Oriskany Sandstone reservoir.

Structurally, the field has been well defined, occurring on a NE–SW-trending anticline. The primary porosity and permeability of the Oriskany reservoir are low; fracturing associated with thrust faults and associated folds is apparently responsible for the creation of an adequate gas reservoir. Additionally, fractures may provide potential avenues for the migration of natural gas from the reservoir to the surface.

The Lost River test site differs from the two other petroleum test sites in three significant ways: (1) it is located in a structurally complex thrust sheet, (2) it is heavily covered with vegetation, and (3) it is located above a simple anticlinal gas reservoir rather than above an oil reservoir or a complex of oil and gas reservoirs. These attributes make the Lost River test site a challenging area to test new approaches to geologic remote sensing.

The principal objectives of the study were:

(1) To investigate the utility of remote sensing for lithologic and structural mapping in an area of near total vegetation cover.

(2) To determine if surface features (structural, vegetative, or geochemical) exist that may be correlated with the gas reservoir.

(3) To develop techniques to detect such features by remote sensing.

II. Geographic Setting

A. Location and Access

The Lost River test site is in east–central Hardy County, West Virginia (Figure 12-1 and Plate 12-1). No major roads cross the test site, but access to it can be gained by traveling on any of several township roads west from West Virginia Highway 259.

The test site is approximately bounded on the north by West Virginia Highway 55, on the south by Lost River State Park, on the west by South Branch Mountain (Helmick Rock), and on the east by the Lost River. This northeasterly canted rectangular area encompasses approximately 200 km^2. The corner coordinates of the test site are lat. 39°10′ N, long. 78°50′ W; lat. 39°05′ N, long. 78°40′ W; lat. 38°50′ N, long. 78°45′ W; and lat. 38°55′ N, long. 79°00′ W.

B. Climate

The test site is in the temperate, semihumid zone of the Central Appalachians. It lies in a rain shadow as demonstrated by the average annual precipitation of approximately 40 in., the lowest for any area in West Virginia. Prevailing winds in the test site area are from the west (Sturm, 1977, p. 128).

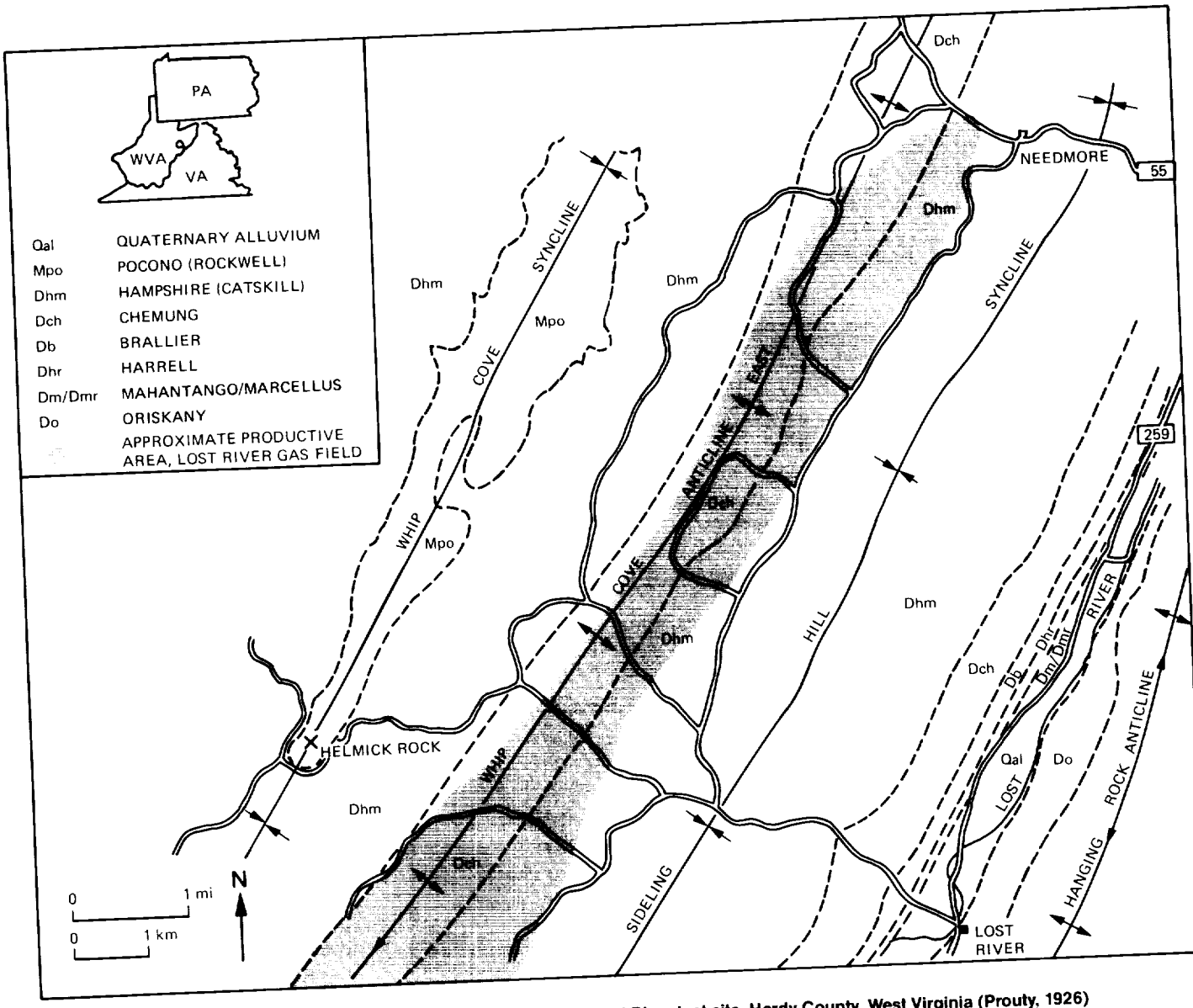

Figure 12-1. Location map showing the geology of the Lost River test site, Hardy County, West Virginia (Prouty, 1926)

C. Physiography and Drainage

Lost River gas field is located in a valley at an average elevation of approximately 2000 ft above sea level (Figure 12-2). Ridges on the east (Big Ridge) and the west (Helmick Rock) average about 1000 ft higher.

Plate 12-1 illustrates the drainage pattern in the test site area and shows the location of major cultural and physiographic features. The topography of the area is typical of the Ridge and Valley Province, characterized by parallel NE-trending ridges and valleys. Ridges are commonly dissected by transverse water gaps. These relationships result in the development of the trellis drainage pattern, which characteristic of the Ridge and Valley Province. On the bas of drainage pattern and texture, the test site may be divid into six drainage subareas. As shown in Plate 12-1, the subareas are:

(A) An area of relatively coarse-textured, poorly dev oped dendritic to rectangular patterned drainage.

(B) An area of relatively coarse-textured, more less radial-patterned drainage composed of fo dendritic-patterned drainage systems.

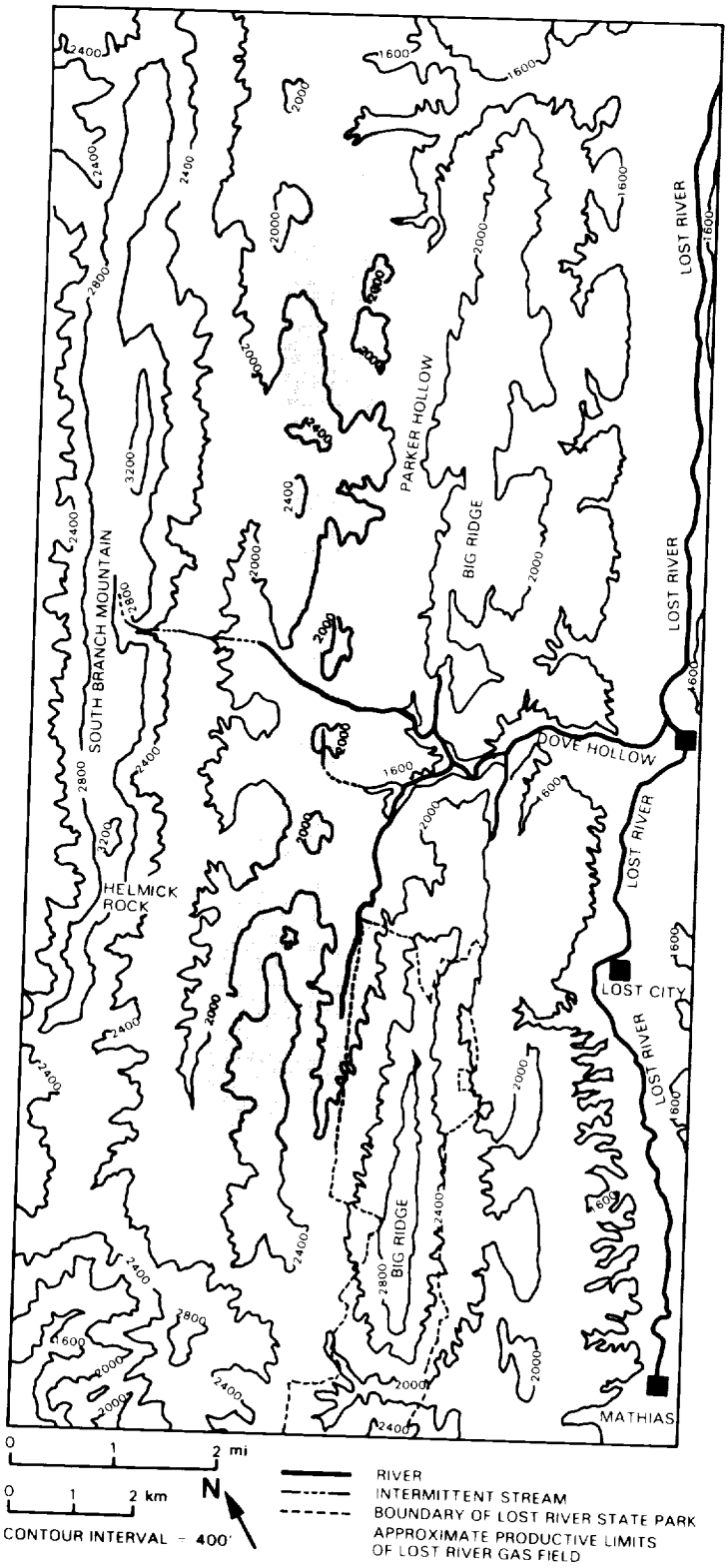

Figure 12-2. General topography of the Lost River test site

(C) An area of two opposing, relatively fine-textured parallel-patterned drainage systems separated by NE-trending South Branch Mountain. The symmetry of this drainage area is disrupted in the southwest by the nearly due-north-trending major drainage of the south fork of the Potomac River and its tributary, Stony Run.

(D) An area exhibiting the best development of the medium-textured trellis drainage pattern that is most characteristic of the Ridge and Valley Province.

(E) An area with drainage characteristics that grade from those of area (C) in the northwest to those of area (D) in the southeast.

(F) An isolated area of medium-textured centripetal drainage pattern.

III. Geologic Setting

A. Stratigraphy

Table 12-1 summarizes the stratigraphy of the Paleozoic sequence exposed at the surface and penetrated in the subsurface of the Lost River test site. The youngest unit that crops out in the area is the Early Mississippian Rockwell Formation (Ludlum, 1952). The Devonian is the most widespread system exposed in the northwest Ridge and Valley Province. Locally exposed Devonian strata include the Hampshire, Chemung, Brallier, Harrell, Mahantango, Marcellus, Needmore, and Oriskany.

Except for the blanket strandline deposits of the Oriskany sandstones, all exposed strata were deposited in paludal, tidal flat, and deltaic environments of the westward prograding Catskill delta complex (Kummel, 1961, p. 110). Some significant characteristics of selected units are discussed below, in order of increasing age. This information is extracted from Chen (1980), except as noted.

1. Rockwell Formation. Outcrops of resistant, blocky, jointed, light brownish-gray sandstones mapped by Prouty (1926) on South Branch Mountain are assigned here to the basal member of the Pocono Group. Similar strata capping the southwest end of Big Ridge were assigned to this unit by Sturm (1977, p. 120). Field observations made during the present investigation support Sturm's interpretation and also indicate that this unit caps the southwestern end of Short Mountain. The Rockwell has a reported thickness of 100 m (350 ft) in the test site vicinity (Ludlum, 1952). Because of their resistance to chemical weathering, these strata are by far the best exposed in the test site area.

Table 12-1. Stratigraphic units exposed at the surface and penetrated in the subsurface, Lost River test site[a]

System	Series	Group/Formation[b]	
Mississippian	Lower	Rockwell Formation (Pocono)[c]	
Devonian	Upper	Hampshire Formation (Catskill)[c] Chemung Formation[c] Brallier Formation (Portage)[c]	
	Middle	Harrell Shale (Genesee)[c] Mahantango Formation (Hamilton)[c] Marcellus Formation[c]	
		Onesquethaw Group (Huntersville)	Onandaga Limestone Huntersville Chert Needmore Shale[c]
	Lower	Oriskany Sandstone[c]	
Silurian	Upper	Helderberg Group Tonoloway Formation Wills Creek Formation Williamsport Formation	
	Middle	McKenzie Formation Rochester Shale Keefer Sandstone Rose Hill Formation	
	Lower	Tuscarora Sandstone	
Ordovician	Upper	Juniata Formation Oswego Formation	
	Middle	Martinsburg Formation	

[a] From Cardwell, 1971, p. 1250.
[b] If different, designation of Prouty, 1926, is shown in parentheses.
[c] Units exposed at the surface; others reported in the subsurface.

2. Hampshire Formation. The most ubiquitous unit in the test site area, this monotonous sequence of fine- to coarse-grained red clastic rocks has a reported thickness of over 1000 m (3500 ft) (Ludlum, 1952). These rocks exhibit cross-bedding, mud cracks, and ripple marks. Although the nonresistant Hampshire is usually mapped on the basis of the red color of superjacent residual soils, resistant sandstone members locally crop out and form ridges in the central test site area.

3. Chemung Formation. This clastic sequence is approximately 1500 m (4700 ft) thick in the test site area. The upper part of the Chemung is transitional with the Hampshire and consists of interfingering green to brown marine and red nonmarine beds. The middle section is a sequence of buff to brown, fine- to medium-grained marine sandstones. The lower Chemung consists of two sandstone units separated by a shale. The upper sandstone is red to green, massive, and flaggy, and locally includes a basal conglomerate. The lower sandstone is typically massive and locally conglomeratic. The intervening shale section is olive to brown and includes thin siltstone and sandstone intercalations.

4. Brallier Formation. The reported local thickness of these strata is approximately 800 m (2500 ft) (Ludlum, 1952). This sequence of light olive-gray to medium-gray micaceous shale includes minor siltstone and sandstone beds which increase in number upwards.

5. Marcellus Formation. The reported thickness of this monotonous sequence of dark-gray to black carbonaceous shale exceeds 125 m (400 ft) (Ludlum, 1952). Calcareous concretions which locally merge to form thin, lenticular beds

occur irregularly in the Marcellus. The unit is gradational with both the overlying Mahantango and underlying Needmore. The incompetent nature of these strata is demonstrated by the tendency of the Marcellus to tightly deform, forming small-scale surface folds.

6. Oriskany Sandstone. In exposures on the east margin of the test site, the massive, medium-grained, fossiliferous, calcareous sandstones of this marine unit have a thickness of 80 m (265 ft) (Ludlum, 1952). Minor quartz–pebble conglomerate beds also occur in the Oriskany. The unit is typically light gray to blue–gray on fresh surfaces and weathers to reddish brown or dull orange. In outcrop, the sandstone exhibits cross-bedding and well-developed conjugate jointing. Subsurface data from the Lost River gas field demonstrate that the Oriskany is an extremely tight reservoir sandstone having a primary porosity of 2.5 percent and a permeability of less than 0.1 md.

7. Silurian and Ordovician strata. The dominantly marine carbonates, shales, sandstones, and cherts of the Silurian and Ordovician Systems are not exposed in the test site, but have been penetrated in the subsurface. These strata are exposed in the northwestern portion of the Ridge and Valley Province on the limbs and cores of large anticlines.

B. Structure

1. Introduction. The Lost River test site is in the Appalachian Mountain Belt. Since the pioneering investigations by Hall and Dana in the 1800s, understanding fold mountain belts elsewhere has largely been based on the Appalachian model (see, for example, King, 1959, p. 41–66; Wyllie, 1971, p. 211–217, 258, 366–372). A complete discussion of the structural evolution of such an intensely studied region is beyond the scope of the present investigation. Only those aspects of Appalachian evolution considered directly pertinent to the test site study are discussed below. For a more detailed discussion of the regional structural setting of the Lost River gas field, refer to Cardwell (1971, 1974), Kulander and Dean (1978), and Patchen (1969).

2. Regional setting. The test site is in the east–central Ridge and Valley structural subprovince of the Appalachian Fold Belt, approximately 32 km (20 mi) east of the Allegheny structural front and 65 km (40 mi) west of the crystalline Blue Ridge Anticlinorium (King, 1959, p. 43–54). This part of the Appalachians is characterized by relatively short-wavelength folding associated with thrusting from the southeast. Structural strike is generally northeast, asymmetric folds face northwest, and thrust faults dip southeast. These features are principally the result of deformation associated with the Permian Allegheny orogeny (King, 1959, p. 66).

The Ridge and Valley structural subprovince is considered a type area for development of the so-called "thin-skinned" tectonic style (Cook et al., 1979; Gwinn, 1964). Thin skin refers to the major décollement horizons that extend through this region. In the test site vicinity, major décollement horizons are in shale intervals of the Middle Cambrian, Middle Ordovician, and Middle to Upper Devonian strata.

Important structures have recently been recognized in the Ridge and Valley Province and are referred to as cross-strike discontinuities (CSDs) by Wheeler (1980). CSDs are considered to be the surface expression of décollement ramps oriented transverse to the regional structural grain and, as such, were also recognized by Kulander and Dean (1978) and Sites (1978). The nature of CSDs is illustrated in Figure 12-3. Surface evidence of their presence is the alignment of disruptions of the strike-parallel pattern such as fold terminations, zones of increased joint density, water and wind gaps, and "long Landsat photolineaments" (Wheeler, 1980, p. 2175).

3. Test site. Early mapping of Hardy County by the West Virginia Geological Survey (Prouty, 1926) clearly shows the location of the Whip Cove Anticline east (Figure 12-1). The location of the anticline was recognized by using field mapping techniques. The complexity of this structure, however, was later revealed by seismic surveys by Columbia Gas during the early 1960s (Plate 12-2) and subsurface well-log interpretation (Figure 12-4).

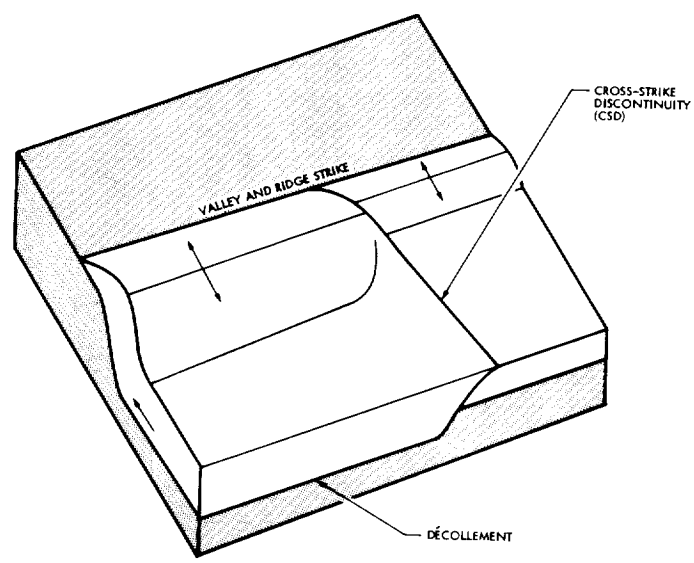

Figure 12-3. Schematic block diagram illustrating a physical interpretation for CSDs. Note actual sense of displacement on the CSD shown is unresolved.

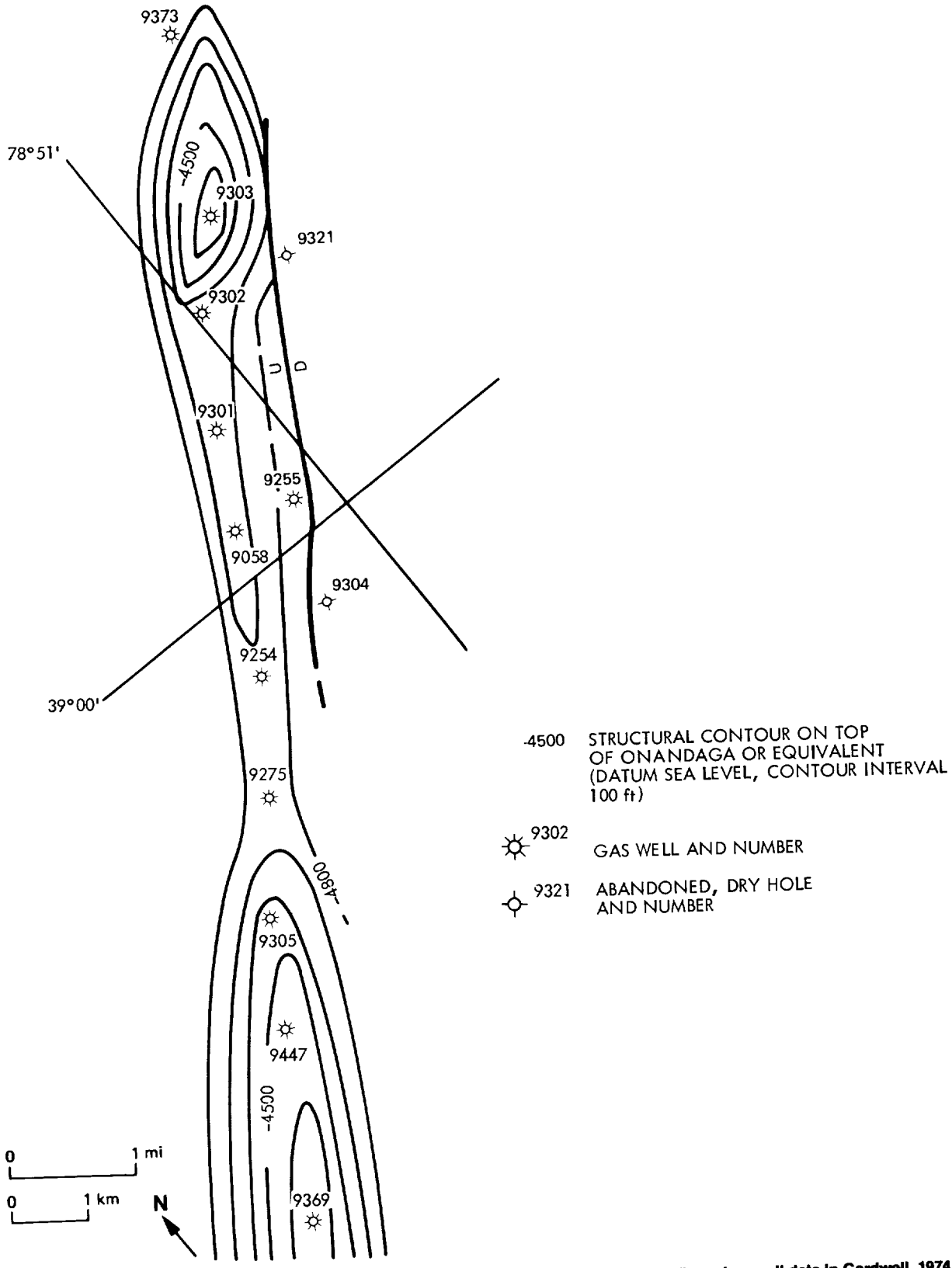

Figure 12-4. Subsurface structural contour map of the top of the Onandaga or equivalent (based on well data in Cardwell, 1974, Figure 13, p. 39)

Columbia Gas gathered single-fold, dynamite source, analog-recorded seismic data along several cross-strike profiles, totaling 50 km (30 mi). An interpretation of these data (Plate 12-2) shows the structure on top of the Oriskany Sandstone. In this interpretation, the anticlinal reservoir is cut by NE-striking thrust faults. The absence of strike-parallel seismic lines precluded the recognition of transverse-strike faulting. Besides having general closure, the anticline is composed of three faulted, domal highs.

The minimum depth of the Oriskany is approximately 1800 m (6000 ft) below the surface (1300 m [4300 ft] below sea level). West of the field, the Oriskany deepens; in the Whip Cove Syncline, 5 km (3 mi) west of the gas field, the Oriskany lies approximately 1800 m (6000 ft) below sea level. Eight km (5 mi) east of the gas field, the Oriskany crops out on the southwest limb of Hanging Rock Anticline. Between the gas field and the Hanging Rock Anticline, the subsurface structure is poorly defined. No wells have been drilled in this area, and the seismic data are noisy and severely affected by reflection migration due to the steeply dipping beds.

Figure 12-5 is a NW–SE cross section through the center of the gas field. Formations above the Oriskany are not shown in this seismic interpretation because no beds within them provide continuous mappable reflections. The structure within the Devonian shale sequence is unknown. The thicknesses of Devonian formations shown on the cross section were obtained from well data.

C. Development of the Lost River Gas Field

The Lost River gas field was discovered in 1962 by Columbia Gas, based on seismic and surface geological data. The driller's log, stratigraphy, and gas composition for the discovery well 9058 are shown in Table 12-2, Figure 12-6, and Table 12-3, respectively. Between 1962 and 1965, 12 more wells, 10 productive and 2 dry, were drilled during field development (Table 12-4). The two dry holes were drilled on the southeast limb of the anticline and may be isolated from the gas reservoir by faulting (Plate 12-2 and Figure 12-4).

Most of the wells were subjected to acid treatment. Initial open flow ranged from 1.5 to 44 thousand cubic feet (MCF) of gas per day. The average initial reservoir pressure was 2200 psi. Today the reservoir pressure is approximately 900 psi. According to Cardwell (1974, p. 38), the ultimate yield of the field is 13.8 BCF. The field is now used for gas storage.

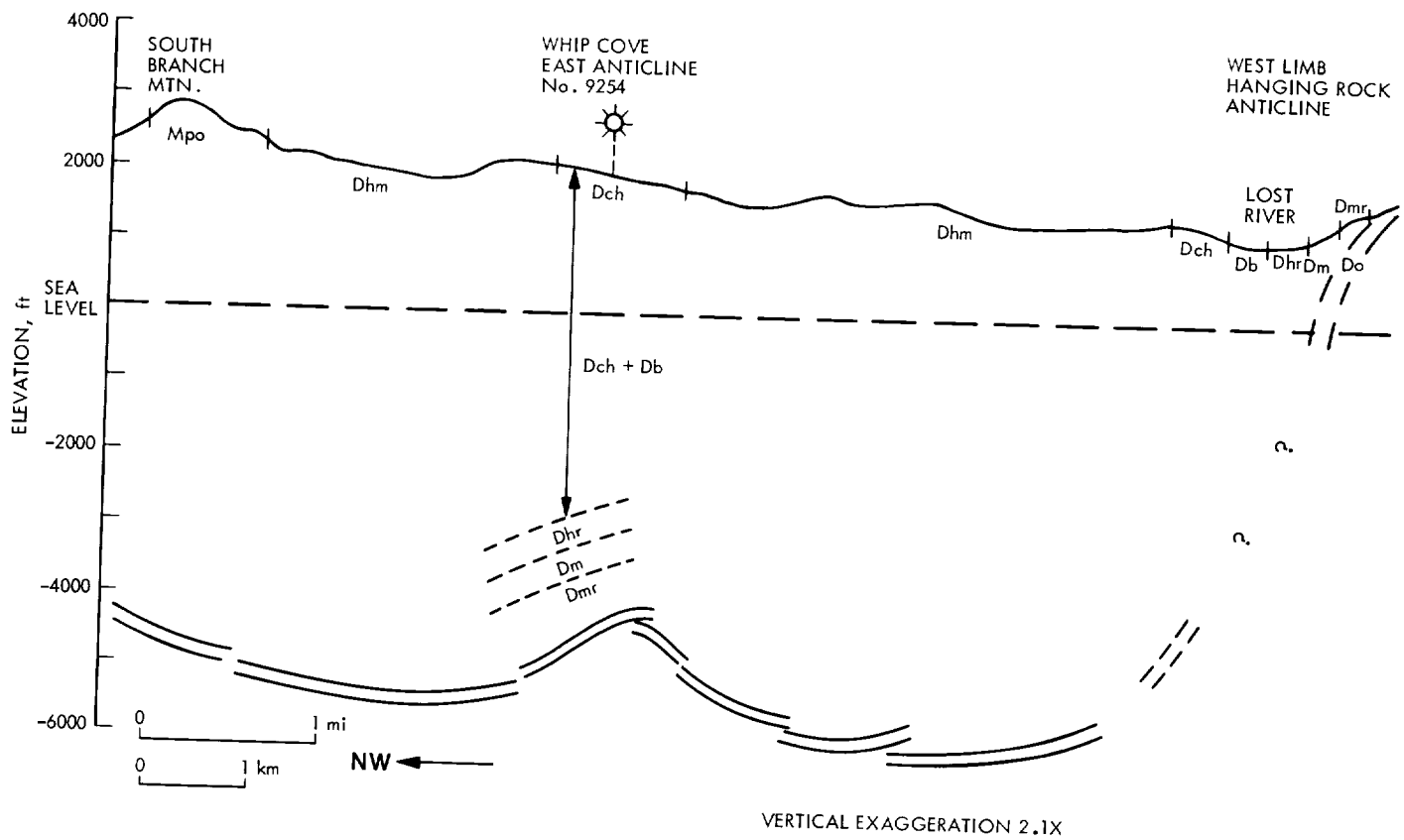

Figure 12-5. NW–SE cross section through the central part of the Lost River gas field, based on seismic, well, and surface geologic data

Table 12-2. Driller's log from well 9058[a]

Stratigraphic Name[b]	Top, ft	Bottom, ft	Test Results
Chemung–Brallier	0	4,710	Water at 49 ft
Harrell Shale	4,710	5,010	Water at 115 ft
Hamilton Shale	5,010	5,800	Water at 150 ft (50 barrels per day)
Marcellus Shale	5,800	6,630	
Metabentonite		6,630	Gas show at 6,782–6,800 ft
Needmore Shale	6,630	6,756	
Oriskany Sand	6,756	6,980	Gas at 6,838–6,845 ft 24/10 Mercury 2-in. 762 MCF
Helderberg Lime	6,980	7,550	Salt water at 8,930 ft, filled up 1,200 ft in 75/8-in. hole, 48,000 ppm chloride
Tonoloway–Wills Creek	7,550	8,645	
Williamsport–Bloomburg	8,645	8,700	
McKenzie Formation	8,700	8,890	
Keefer Sand	8,890	8,930	Hole plugged back from 10,584 to 6,887 ft
Clinton Shale	8,930	9,350	
Clinton Sand	9,350	9,580	Bridge plug set at 6,894 ft with 7 ft of cal seal
Juniata Formation	9,580	10,247	
Oswego Sand	10,247	10,400	Oriskany perforated from 6,788–6,804 ft 6,836–6,860 ft 6,874–6,880 ft four shots per ft
Martinsburg Formation	10,400	10,584	Original open flow—24/10 Mercury, 2-in. 762 MCF
Total depth		10,584	Acidized December 18, 1961 with 300 gal MCA and 10,000 gal 15% HCl (6,000 gal retarded and 4,000 gal regular) and 130 MCF nitrogen Final open flow—4,555 MCF—Oriskany 48 hours, 2,310 psi

[a]Elevation: 1,965.02 ft Gr., 1,976.05 ft RKB.
Contractor: Lohmann & Johnson.
[b]As reported.

IV. Soils

Table 12-5 summarizes the characteristics of soils mapped in the test site area by the Soil Conservation Service (1979). The distribution of these soils is illustrated in Plate 12-3.

A review of these data reveals that, with the exception of rare bedrock outcrops, all soils in the test site area are loams. Most are acidic due to the area's humid climate and adequate precipitation and have well-developed vegetation cover. Most soils tend to be youthful due to their relatively rapid downslope movement on the area's commonly steep slopes (Sturm, 1977, p. 125). Except in drainage bottoms

Table 12-3. Typical gas composition at well 9058

Component	Volume, %
Methane	98.04
Ethane	0.50
Propane	0.20
Isobutane	0.01
N. Butane	0.01
Isopentane	0.004
N. Pentane	0.01
Hexane	0.003
Nitrogen	1.21

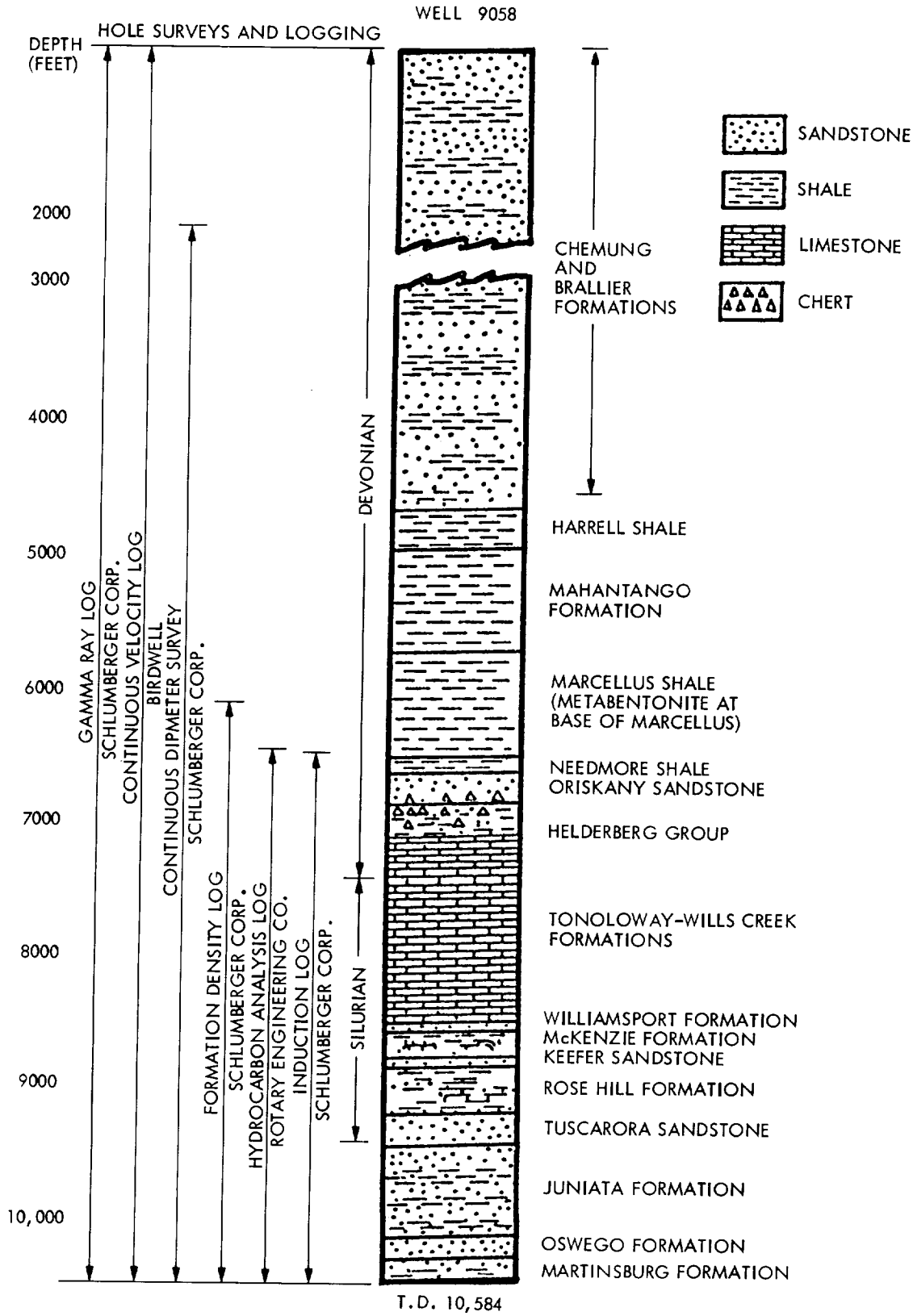

Figure 12-6. Stratigraphic, lithologic, and mechanical logging data available for discovery well 9058

Table 12-4. Well data—Lost River gas field

Well Number	Farm	Elevation, ft above sea level		Total Depth, ft	Oriskany, ft				Open Flow, MCF		Surface Shut-In Pressure, psi	Oriskany, ft below sea level
		Ground	RKB		Top	Bottom		Thickness	Before	After		
9058	Anna Baughman	1,965.02	1,976.50	10,584	6,764	6,991		227	1,008	4,555	2,310	4,788
9254	Grover C. Miller	2,070.94	2,083	7,215	6,981	7,210		229	3,500	6,000	2,310	4,898
9255	H. L. Wilkins	1,868.42	1,880	7,100	6,838	7,066		228	Mud	3,700	2,310	4,958
					6,634	6,760		126				
9275	John H. Miller	1,689.18	1,701	7,045	6,760	6,776	16	368	39,200	Not treated	2,310	4,933
				(Fault zone)	6,776	7,002		226				5,075
9301	C. P. Wilkins	2,054.86	2,066	7,020	6,756	7,005		249	Est. 150	1,500	2,310	4,690
					6,871	6,962		91				
9302	Ethel Teets et al.	2,084.05	2,096	7,250	6,962	6,976	14	331	Est. 75	2,316	2,310	4,775
				(Needmore)	6,976	7,202		226				4,881
9303	Jasper T. Combs	1,841.12	1,852	6,507	6,263	6,485		222	Mud	36,081	2,310	4,411
9304	V. Whetzel	1,854.66	1,866	7,695	7,309	7,628		319	Show	Show		5,443
					6,416	6,654		238				
9305	Harry Combs et al.	1,701.96	1,718	6,785	6,654			344	10,285	44,000	2,340	4,698
				(Fault zone)	6,654	6,760		106				4,936
9447[a]	Grover Funkhouser	2,455.51	2,468	7,356	7,020	7,316		296	1,517	1,750	1,965	4,552
9321	Wm. J. B. Orr et al.	1,977.59	1,994.59	7,500	7,206	7,438		232	Show	Not treated		5,211
9369	Blanch Hamilton	2,211.47	2,228.47	6,920	6,644	6,875		231	6,191	13,170	1,952	4,416
9373	Kenneth Funkhouser et al.	1,640.24	1,657.24	6,927	6,587	6,886		299	474	4,824	1,440	4,930

[a] Formerly Sun Oil Company well F-36195.

Table 12-5. Characteristics of soils occurring in the Lost River test site[a]

Designation (Plate 12-3)	Series	pH			Texture					Maximum Depth to Bedrock, in.	Water Capacity				Color					Vegetation		
		Alkaline	Neutral	Acid	Loam	Clay	Silt	Sand	Gravel		Very Low	Low	Moderate	High	Yellow	Brown	Red	Black	Gray	Crops	Forest	Pasture
4	Tioga			■	■			■		>60				■	■	■				■		
13	Massanta	■			■					>60				■		■				■		
14	Alluvial		■	■	■			■		>60		■				■					■	■
20	Allegheny			■	■					>60			■	■		■				■	■	■
22	Monongahela			■	■		■			>60			■			■				■	■	■
25	Tygart			■	■			■		>60				■		■			■	■		■
27	Purdy			■	■		■			>60				■		■			■	■		■
30	Laidig Channery			■	■					>60			■			■			■	■	■	■
31	Buchanan Channery			■	■					>60		■				■			■	■	■	■
42	Very Stony			■	■					-			■			■			■		■	■
43	Buchanan Stony			■	■				■	>60			■			■		■			■	■
62	Murrill Variant			■	■			■		>48			■	■		■			■	■	■	■
63	Chagrin–Calvin Channery		■	■	■		■			>60		■	■	■		■	■			■	■	■
64	Berks Channery			■	■		■			40	■	■				■	■			■	■	■
65	Dekalb–Lehew Channery			■	■					40	■	■						■		■	■	■
90	Dekalb–Hazelton–Lehew			■	■			■		72	■	■	■					■			■	
131	Ernest			■	■		■			>60			■			■			■	■	■	■
140	Alluvial		■	■	■				■	>60	■					■			■		■	■
166	Berks–Weikhert			■	■		■			40	■	■			■	■				■	■	■
180	Basher			■	■			■		>60				■		■				■		
339	Rock outcrop/ talus	■	■	■		Pocono Sandstone				0			■		■				■		■	

[a]Modified from descriptions supplied by the Hardy County Office of the U.S. Department of Agriculture, Soil Conservation Service.

where soil thickness may exceed 2 m (60 in.), soils are typically less than 25 cm (10 in.) thick. Bedding slopes tend to be steeper and, hence, have shallower soil accumulations than dip slopes.

The residual nature of nonalluvial soils is demonstrated by the red color of the most ubiquitous soil, 64, where it overlies the red mudstones of the Hampshire Formation, and its brown color, where it overlies the brown shales and sandstones of the Chemung.

The prevailing westerly winds in the test site area (Sturm, 1977, p. 128) result in more variable temperatures and enhanced mechanical weathering on west-facing slopes. Stony soils, 42 and 43, therefore are more extensive on the west-facing slopes, where large bedrock fragments are shed from cliff-forming outcrops of resistant Rockwell (Pocono) sandstones.

V. Surface Geochemistry

A. Rock/Soil Geochemistry

To identify any changes in surface geochemistry that might be attributed to the vertical migration of natural gas from the reservoir, Gulf Science and Technology Company conducted a limited inorganic geochemical survey of the Lost River test site. This survey includes X-ray diffraction mineralogical analysis and atomic absorption elemental analysis of 30 Chemung rock samples and 86 soil samples.

1. Chemung mineralogy/elemental geochemistry. Thirty rock samples were obtained from on-gas field and off-gas field outcrops of the Chemung. These samples were analyzed by X-ray diffraction and atomic absorption. The results of the atomic absorption analysis are summarized in Appendix A, Tables A-1, A-2, and A-3.

The Chemung outcrops sampled were interbedded sandstones and siltstones. The X-ray diffraction analyses indicated that clay content ranged from 5 to 50 percent; feldspar, typically less than 10 percent; and the remainder, quartz. Pyrite and carbonate, if present, were below detection limits (3 percent for pyrite and 1 percent for carbonate).

Atomic absorption determination of bulk-rock concentrations for 11 elements exhibited a high positive correlation with aluminum concentration and, hence, with clay content. Sodium, manganese, copper, lead, and zinc concentrations exhibited poorer correlation with aluminum, indicating that these elements are either associated with the nonclay phase, or their concentrations are dependent on clay type rather than on amount. No statistically significant difference in elemental concentration was noted for Chemung rock samples obtained from on-field versus off-field locations.

2. Soil mineralogy/elemental geochemistry. Sixteen soil samples were obtained during a preliminary survey along a traverse that crossed the Lost River gas field (Figure 12-7). Samples were collected at depths of 5 to 15 cm (2 to 6 in.) below the surface.

X-ray diffraction analysis revealed that the soils sampled are primarily clay and quartz, with minor amounts of feldspar. Pyrite and carbonate, if present, were below detection limits.

Samples were subjected to both acid-reducing and oxidizing leaching to remove both the nonclay and nonquartz fractions. The results of atomic absorption elemental analysis of these leachates are summarized in Tables A-4 and A-5. In the acid-reducing leachate samples, iron, aluminum, cobalt, and copper concentrations exhibit positive correlation. These elements are probably present in the soils as oxides. Samples with highest concentrations of these elements were obtained from soils that overlie the red Hampshire Formation and probably reflect parent-rock chemistry. The concentrations of calcium, magnesium, and especially manganese in soils appear independent of the underlying bedrock formations. These elements are probably present in the soil in the form of trace amounts of carbonate. Highest concentrations for these elements are generally restricted to samples collected over the Lost River gas field. To further evaluate this apparent over-the-field geochemical anomaly, further sampling and atomic absorption analyses for manganese were conducted.

3. Soil manganese geochemistry. The concept that manganese is mobile in acid-reducing subsurface waters (transported in solution from a hydrocarbon reservoir?) and immobile in neutral or alkaline surface waters (precipitated in soils overlying a reservoir?) is consistent with Dalziel and Donovan's (1980) recognition of anomalously high soil manganese concentrations over oil fields. The approach of reduced waters to the surface in the Lost River test site is suggested by the presence of hydrogen sulfide-rich springs at Lost River State Park (Ludlum, 1952, p. 18–20). The presence of insoluble manganese oxide coatings on stream pebbles and boulders in the test site and elsewhere in the Appalachians (Carpenter and Hays, 1978) indicates that manganese does not travel far in Appalachian surface waters.

Seventy soil samples were collected, treated with an acid-reducing leach, and the leachates analyzed by atomic

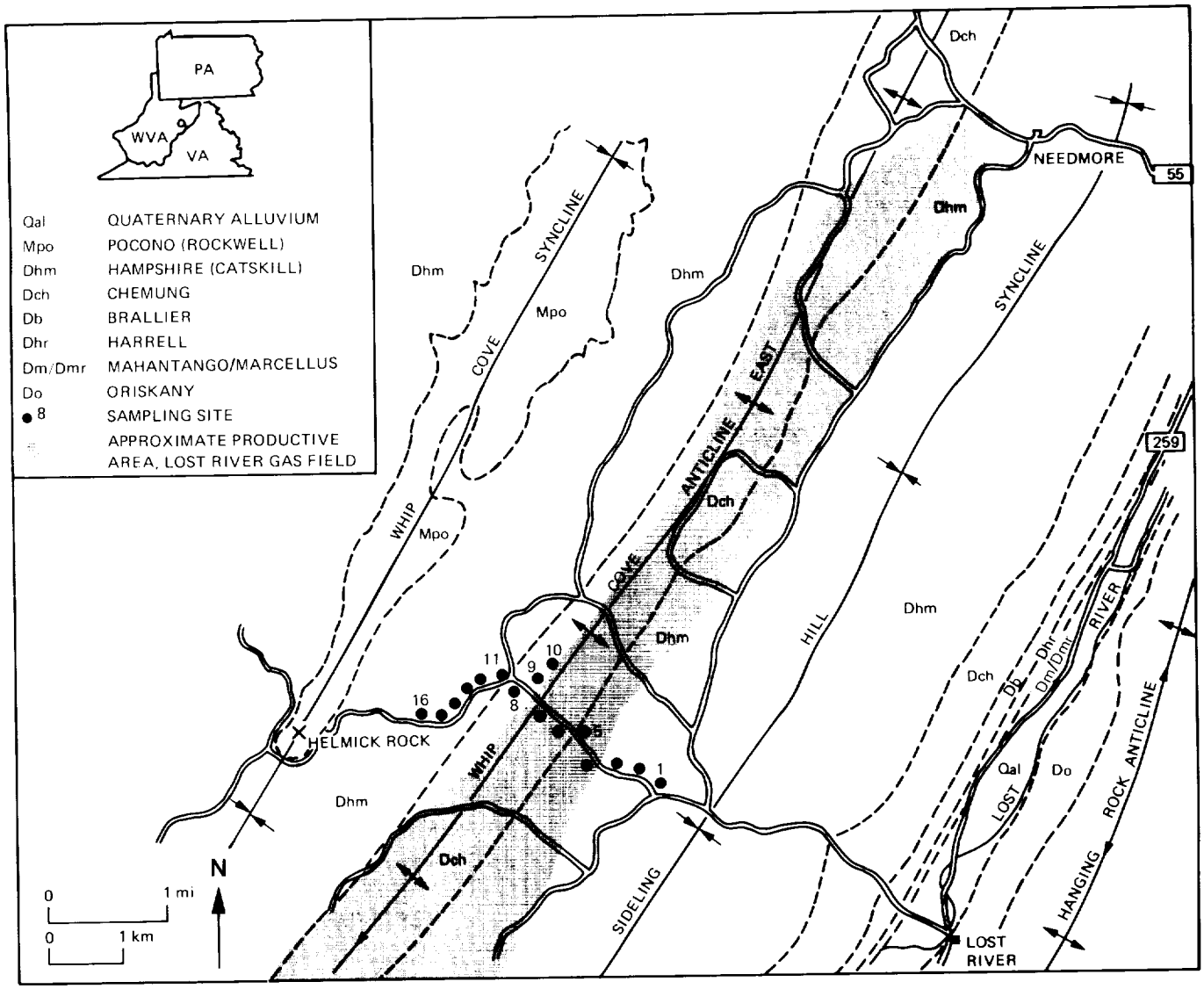

Figure 12-7. Map showing sample sites for preliminary soil mineralogy/elemental geochemistry survey

absorption to determine manganese concentration. Analytical results are tabulated in Table A-6 and are shown graphically in Figure 12-8.

4. Conclusions. Enhanced concentrations of soil manganese were discovered in the vicinity of the Lost River gas field. However, further sampling is required to establish the areal extent of this apparent manganese "anomaly." Geochemical analysis of the rocks from which the soils were derived is also needed in order to determine the source of the manganese found in the soils.

B. Soil Bacteria

Davis (1967) has demonstrated that ethane-oxidizing bacteria thrive in soils where natural gas seepage occurs. The Mobil Oil Corporation has developed an exploration method based upon the identification of soils rich in ethane-oxidizing bacteria. Since the Oriskany reservoir is faulted and fractured in the Lost River gas field, natural gas seepage may occur in the vicinity of the field. In an attempt to identify potential gas seeps in the Lost River test site, Mobil conducted a reconnaissance soil microbiological study.

On May 14 and 15, 1979, 52 soil samples were collected in the area for bacteriological analysis. The samples were taken at a depth of 25 to 30 cm (10 to 12 in.) below the level of grass roots and major organic matter accumulation. Samples were collected at intervals of approximately 0.3 km (0.2 mi) along two traverses crossing the field (Figure 12-9). To avoid contamination, sampling sites were away from roads.

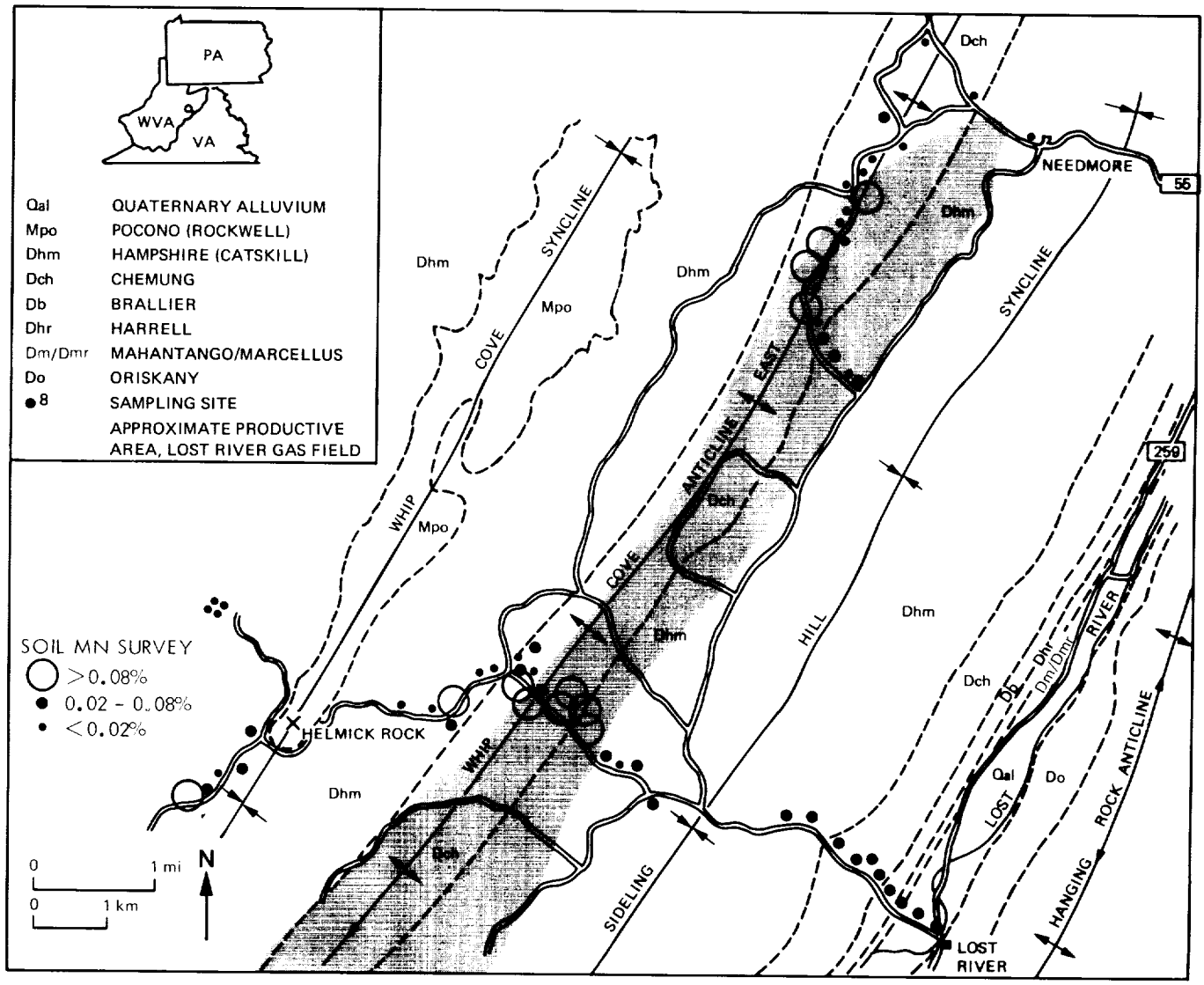

Figure 12-8. Map showing sample sites for soil manganese elemental geochemistry survey

Bacteriological analysis of the samples for both methane- and ethane-oxidizing bacteria was begun on May 18, 1979. Each soil sample was dried and homogenized, and a 0.1-g aliquot was sprinkled as evenly as possible on the surface of a mineral salts agar medium in a petri dish. Three 52-sample sets were prepared in this manner. Each set was incubated in a desiccator at 28° C: one in an atmosphere of 40 percent methane in air; one in 40 percent ethane in air; and one in air only. Each petri dish was examined for bacterial colonies after 7 days, 14 days, and finally after 28 days of incubation.

Except for a few bacterial colonies in the methane- and air-incubated sample 34W, negligible bacterial growth was observed at 7 days and 14 days. After 28 days, 10 methane-incubated samples showed bacterial colonies. The numbers of bacterial colonies observed for these 10 samples are listed in Table 12-6. No significant bacterial growth was observed in the ethane-incubated samples.

Five of the 10 samples with methane-oxidizing bacterial colonies were collected near a gas well (24W, 34W, and 47W) or near a pipeline (25P and 29P). The other five samples with methane-oxidizing bacterial colonies (38, 40, 43, 44, and 46) were collected in a small area characterized by an especially organic-rich soil under heavy grass growth (a likely source of biogenic methane).

Based on prior experience, only two soil samples had sufficiently high methane-oxidizing bacterial counts to be

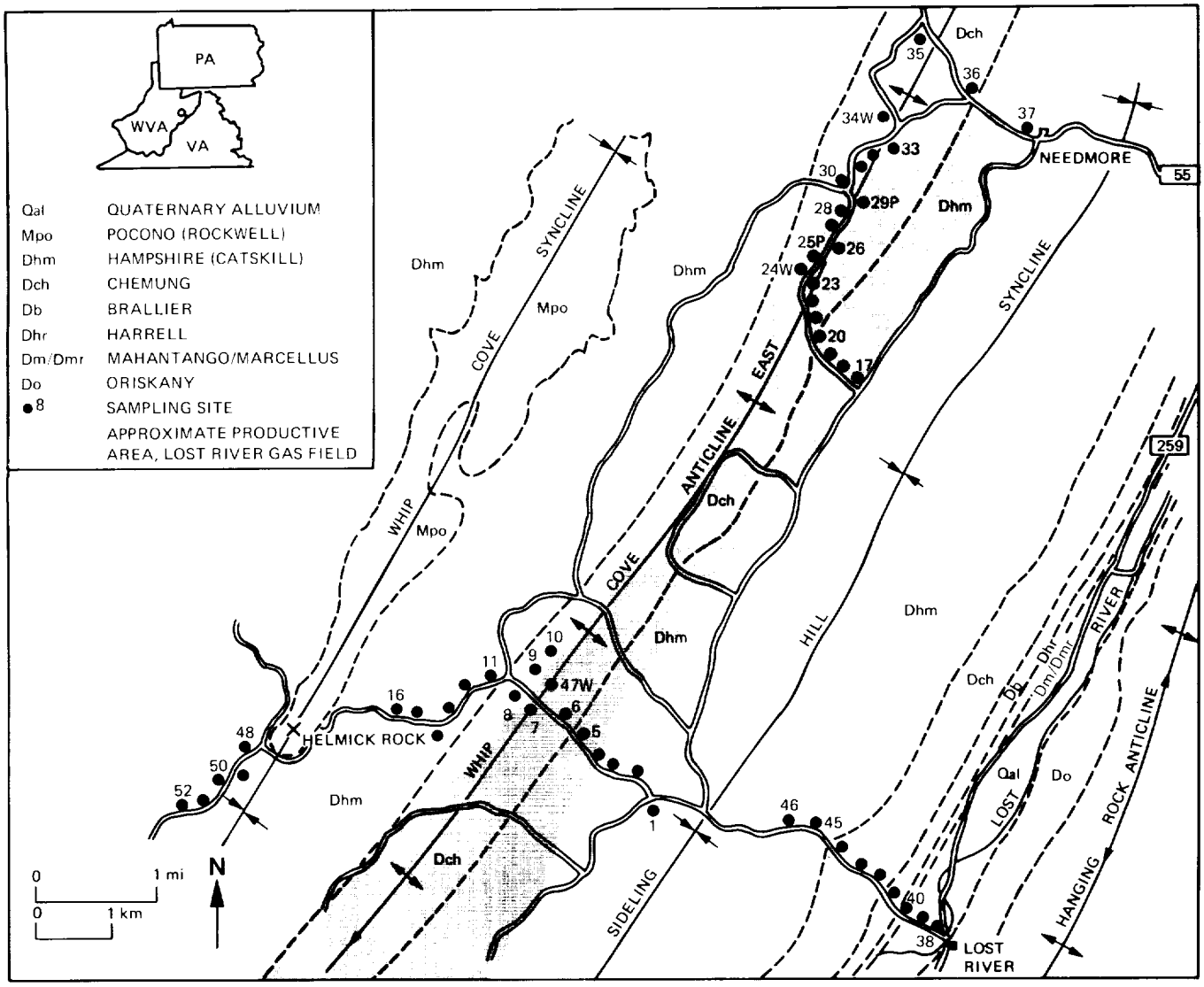

Figure 12-9. Map showing sample sites for soil microbiology survey

considered indicative of gas seepage: sample 34W, collected near a gas well (942 colonies), and sample 25P, collected near a gas pipeline (167 colonies). Their high bacterial counts were interpreted to be the result of contamination due to gas field operations and not due to natural gas seepage.

The complete absence of any ethane-oxidizing bacteria colonies in the 52 samples studied might suggest that natural gas seepage is not occurring over the Lost River gas field (Davis, 1967). However, since ethane concentration in the Lost River reservoir is extremely low (Table 12-3), it is unlikely that gas seeping from such a reservoir would carry sufficient ethane to support extensive colonies of ethane-oxidizing bacteria in soils overlying the gas field. More detailed bacteriological sampling was not recommended in the test site area unless other methods demonstrate natural gas seepage and confirmation by the soil microbe technique is desired.

VI. Field and Laboratory Vegetation Studies

A. Introduction

Because the Lost River test site is heavily forested, considerable effort was devoted to developing an understanding of the plants occurring in the area. If methane microseepage may be expressed by anomalous distributions of species and/or communities, the normal distribu-

Table 12-6. Methane-oxidizing bacterial colonies in soil samples from the Lost River test site

Sample Number	Number of Bacterial Colonies[a]		
	Methane	Air Control	Ethane
24W	17	0	0
25P	167	0	0
29P	10	0	0
34W	942	0	0
38	6	0	0
40	7	0	0
43	12	0	0
44	8	0	0
46	17	0	0
47W	3	0	0

[a]Only 10 of 52 soil samples showed hydrocarbon oxidizing bacteria; i.e., the other 42 samples had no significant colonies.

tion patterns must be determined before such anomalous patterns can be recognized.

Field vegetation studies were conducted on the following dates: May 16–19, August 5–9, and October 20–23, 1979; June 10–12, July 6–31, and October 15–19, 1981. The 1979 studies were aimed at identifying plants occurring in the area, determining normal distribution patterns, and establishing training areas for supervised vegetation classifications using multispectral remote sensing data. The results of these studies are summarized below. The 1981 studies were aimed primarily at evaluating the accuracy of supervised image classifications. These results are summarized in the discussion of image analysis (Paragraph VIII). The botanical nomenclature of Strausbaugh and Core (1978) was adopted for the botanical studies.

B. Lichens

Lichens are a symbiotic association between a fungus and an alga. Studies on the growth and distribution of lichens, as influenced by environmental factors, have demonstrated the so-called "city effect," in which both vigor and distribution of lichen populations are adversely affected by atmospheric pollutants (Hale, 1974). The city effect on Long Island, N.Y., has been traced as much as 65 km (40 mi) eastward on the island from the center of Brooklyn.

Although temperature and humidity are important factors affecting the vigor and density and/or distribution of lichen populations, specific atmospheric pollutants (carbon monoxide and sulfur dioxide) also have an effect on lichen growth (Ahmadjian, 1967; Hale, 1974). Sensitivity of lichens to environmental factors suggests that this group of plants may be affected by the presence of hydrocarbons (or gases associated with them) in the soil and/or atmosphere over gas and oil fields. Accordingly, as part of the initial field vegetation assessment, the density and vigor of lichen populations at the Lost River site were evaluated.

The method adopted for the lichen distribution study was visual estimation of the lichen cover on soil, rocks, and tree trunks on randomly selected plots both on and off the gas field. An attempt was made to keep factors such as elevation, exposure, slope, and habitat as comparable as possible among plots. The percent cover was estimated and, where possible, the genus and/or species was identified. Table 12-7 includes a list of lichen species identified.

The results of this preliminary survey indicate that no significant variation exists among plots sampled relative to position on- or off-field. Features such as population density, relative diversity, and state of health are rather constant at all sites. It is interesting to note that the greatest

Table 12-7. List of lichens and mosses identified in the Lost River area[a]

Common Name	Species
Crutose lichens	*Caloplaca* sp.
	Lecanora sp.
	Lecidea sp.
Foliose lichens	*Cetraria oakesiana*
	Parmelia caperata
	P. cumberlindia
	P. flaventior
	P. rudecta
	P. stuppea
	P. subrudecta
	Peltigera canina
	Physia halei
	Physicia pulverulenta
	P. stellaris
	P. tenella
	Sticta weigelii
	Umbilicaria spp.
Fruticose lichens	*Cladonia furcata*
	C. squamosa
	C. unicialis
Mosses	*Atrichum* sp.
	Dicranum scoparium
	Hypnum sp.
	Leucobryum albidum
	L. glaucum
	Polytricum commune
	P. strictum

[a]Identification by C. W. Klingensmith.

species diversity was seen at Lee Sulfur Spring (at this site, mineralized groundwater rich in sulfur occurs at the surface) in the Lost River State Park.

In summary, based on limited sampling, factors such as exposure to light, humidity, spore sources, wind, and substrate availability are as important in the observed lichen distribution as are the levels of possible atmospheric and soil pollutants that exist in the Lost River area.

C. Mycorrhizal Fungi

1. Introduction. Mycorrhizal fungi are the fungal component of a symbiotic association between the roots of a higher plant and a fungus. Soil factors affecting the vigor and/or distribution of mycorrhizal fungi have a pronounced influence on the vigor and/or distribution of the host. The fungal component of the symbiosis provides an absorbing surface (in place of root hairs) through which available water is absorbed by the host. The fungus also produces organic acids that are involved in the chemical weathering of soil particles (Henderson and Duff, 1963). Availability to the host of essential nutrients such as phosphorus is directly related to the availability and state of health of the host's symbiotic fungus (Raven et al., 1976). These fungi are so essential to forest trees that they should be considered an indispensable part of the host's functional root system (Hacskaylo, 1972). As will be noted in the discussion of *Cenococcum graniforme,* some fungi are less efficient than others in providing their hosts with an adequate amount of water and essential nutrients.

Based on the assumption that fungi may be influenced by high soil hydrocarbon levels, a study of the fungal components of oak mycorrhizae was undertaken at the test site. Because most of the broadleaved canopy cover occurring at Lost River consists of species of oak, it was felt that any factor influencing the fungal component of an oak's root association would likely have a detectable influence on the overall condition of the forest canopy. Because the fungal component of the mycorrhizae is in direct contact with the soil, hydrocarbon seepage could be expected to have an effect which might be detected in remotely sensed data.

2. *In vivo* study. Root collections (for the purpose of studying the mycorrhizal association in selected oak species) were made at seven sites (four on and three off the gas field—Table 12-8). Roots from five first-year seedlings of Chestnut Oak (*Quercus prinus*) were collected per site. The youngest root tips were studied in the field after soil had been removed by rinsing in water, and only healthy mycorrhizal "clubroots" and associated lateral roots (Figure 12-10) were removed and preserved (placed immediately in the killing and fixing preservative FFA—5% Formalin, 5% acetic acid, and 90% EtOH [70% aqueous solution]). Preserved specimens were then dehydrated, embedded in paraffin, and sectioned on a rotary microtome. Microscopic thin sections were then studied in an attempt to detect any variation in the amounts and/or kinds (genera or species) of fungi present and the state of health of host root tissue. Results are summarized in Table 12-8.

A total of 21 specimens of root associations were studied. In 15 specimens, at least two different fungi occur, forming ectotrophic associations (the fungal filaments or hyphae simply growing between the host root's cortical parenchyma cells, rather than into them via haustoria). In the remaining specimens a single type of fungus is seen, again in an ectotrophic association with the host root tissue. One kind of fungus is common to all specimens and has been tentatively identified as *Cenococcum graniforme*; the other fungi remain unidentified. All fungi studied possess septate hyphae (filaments).

Cenococcum graniforme, a common widespread mycorrhiza-forming fungus in tree species (Mikola, 1970), is known to occur in oaks (Trappe and Quinard, 1966) and is frequently present in heavily shaded forests with nutrient-poor soils that typically offer poor conditions for the development of other fungal species (Kay, 1975). These conditions (heavily shaded, nutrient-poor soils) describe those found at Lost River. *C. graniforme* is described in the literature (Dominik, 1959) as a "black form" of an ectotrophic mycorrhizal-forming fungus because of its characteristic darkly pigmented septate hyphae. Based on the anatomical characteristics of the hyphae, the single fungus occurring in all oak roots from the Lost River site appears to be *C. graniforme.*

The occurrence of a single mycorrhizal fungus in some of the root tissue, in particular the relatively vigorous and competitive *Cenococcum graniforme,* may be significant. According to Marks and Foster (1967) and Robinson (1971), the occurrence of *C. graniforme* in a host, to the exclusion of other fungal species, suggests adverse soil conditions (enabling the more competitive fungus to survive at the expense of others). In addition, these authors indicate that in this condition (*C. graniforme* only), the host of such a mycorrhizal association may be adversely affected because *C. graniforme* is apparently less efficient as a symbiont than other species of mycorrhizal fungi.

Of the six oak specimens containing the single species (*Cenococcum graniforme*), five were collected from on-field sites (four specimens from Site C, one specimen from Site 1; Figure 12-11). The single off-field specimen came from Site B in Lost River State Park.

Table 12-8. Mycorrhizal data from the Lost River test site

Specimen Number	Site	On-Field or Off-Field	Host Tissue	Fungi		Soil Color
				Cenococcum graniforme	Other	
1	A–State Park	Off	Living	■	■	Red
2			Living	■	■	Red
3			Living	■	■	Red
4	B–State Park	Off	Living	■	■	Brown
5			Living	■		Brown
6			Living	■	■	Brown
7			Living	■	■	Brown
15	E–Road to Mathias	Off	Living	■	■	Red
16			Living	■	■	Red
17			Living	■	■	Red
18			Living	■	■	Red
8	C–Camp Branch Road	On	Dead	■		Red
9			Dead	■		Red
10			Dead	■		Red
11			Living	■		Red
12	D–Road to Helmick Rock	On	Living	■	■	Brown
13			Living	■	■	Brown
14			Living	■	■	Brown
19	F–Road to Gas Well	On	Living	■	■	Brown
20			Living	■	■	Brown
21	I–Crider's Woods	On	Dead	■		Red

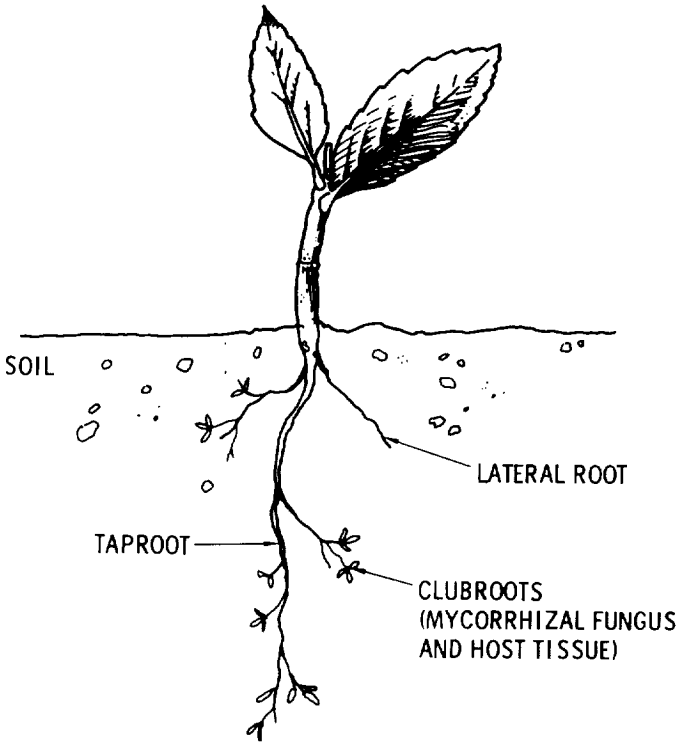

Figure 12-10. Diagrammatic representation of first-year seedling of Chestnut Oak *(Quercus prinus)* showing the relative positions of the taproot, lateral roots, and clubroots (site of mycorrhizal fungal symbiosis)

All roots containing the fungi are typical clubroots associated with ectotrophic mycorrhizal associations. All of those collected off the field possess living clubroots with healthy fungi (as seen under the microscope). Of those specimens collected on the field, four possess hollow, necrotic (dead) clubroots consisting of little more than a central vascular strand surrounded by a persistent epidermal layer. The absence of cortical tissue gives these clubroots an inflated appearance. Three of these specimens were collected at the same site (Site C, Figure 12-11) in soils overlying Hampshire shales along Camp Branch Road, on an east-facing slope. The fourth was collected in the same soil type. An adequate explanation for these necrotic clubroots is not available because microtechnical problems associated with sectioning these roots made it impossible to determine if destruction of the cortical tissue was indeed due to the presence of fungus. The circumstantial evidence is in favor of this view, however, since all four specimens possessed only *Cenococcum graniforme*, known to be an aggressive fungus. Such a condition (destruction of living host cortical tissue) would certainly have an adverse influence on the host trees. Remember that the observations of the *in vivo* mycorrhizal roots in this report were made of young seedlings (first- or second-year seedlings) and not of mature trees.

Based on a limited study of mycorrhizae associated with young seedlings of *Quercus prinus* (Chestnut Oak), a slightly

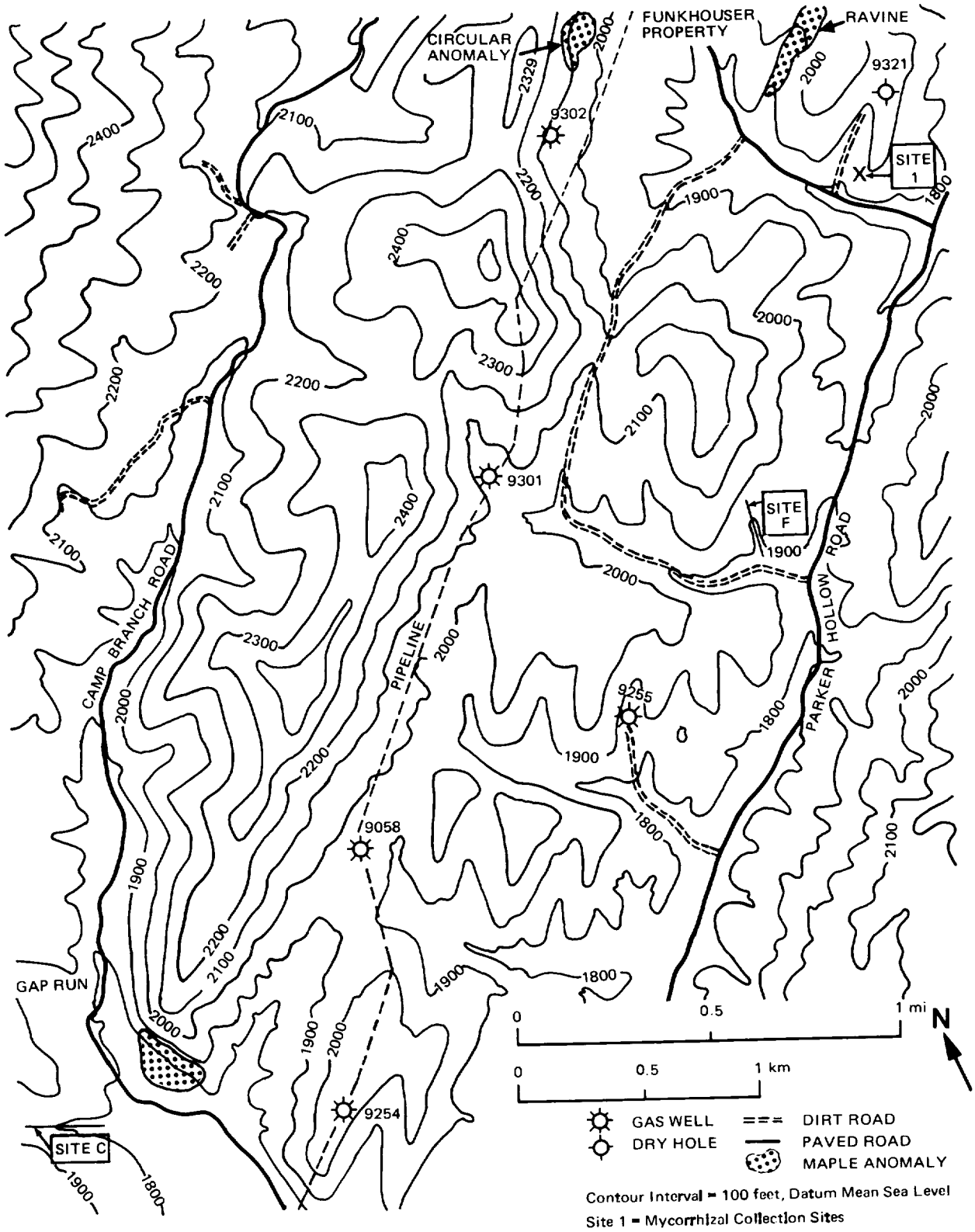

Figure 12-11. Topographic data for area over the center of the gas field. Note collection sites (Sites C, F, and 1) for mycorrhizal root study. The pipeline (NNE-trending dashed line) lies roughly over the crest of the Whip Cove Anticline (based after USGS Needmore and Lost City 7.5-min Quadrangle).

greater diversity of fungal species occurs off-field when compared with on-field specimens. The dominance of the aggressive fungus species *Cenococcum graniforme*, possibly to the detriment of host tissue, is associated with on-field sites. Such an occurrence suggests that the soil conditions at certain on-field sites (Sites C and 1) are more adverse to mycorrhizal development than those typically found at the off-field sites studied.

3. *In vitro* study. Since Chestnut Oak is a common member of the forest community at Lost River and study of seedlings from the test site indicates that Chestnut Oak forms a mycorrhizal association with at least two species of fungi, it was of interest to determine what effect, if any, methane had on this host–fungus relationship.

An experimental study of effects of methane on oak seedlings and/or mycorrhizae grown *in vitro* was conducted. Beginning early in March 1980, acorns of Chestnut Oak (*Quercus prinus*) were germinated and the seedlings grown in pots under two different experimental conditions. In one set, air from a laboratory air jet was introduced into the bottom of the pots (Figure 12-12). Rate of air flow was established by a simple "bubble count" method. The plants exposed to air were considered the control (measuring the drying effect of the air moving through the soil on the root systems). Five seedlings were exposed to these conditions. In a second set of plants, methane (commercial natural gas) from a laboratory gas jet was introduced into the soil, again using the same "bubble count" method of flow rate control. Four seedlings were grown under these experimental conditions. A flow rate of approximately 10 bubbles per minute was maintained in both groups.

Both the control group and the experimental group were illuminated with a combination of fluorescent and incandescent light sources (to insure maximum growth by proper spectral balance in the illumination source). In all cases, the seedlings were from acorns of Chestnut Oak collected at the Lost River test site, grown in soil taken from the test site (both were collected during the October 1979 field trip to the area). The seedlings were watered daily and fertilized twice a week with a dilute solution of Rapidgro™ commercial plant food.

In May, when the seedlings were approximately six weeks old, true color (TC) and false-color infrared (CIR) photographs were taken of each plant as well as of individual leaves from each specimen. Continuous growth rate records (including height, rate of internode elongation, and number and size of leaves) were maintained throughout the experiment. Roots were collected for study of mycorrhizae.

Plants from the set exposed to methane demonstrated an increased vigor and growth rate when compared with the control plants. This observation, based on growth rate data, is reinforced by the CIR photographs taken. Plants exposed to methane had leaves appearing a darker red in the CIR photographs (indicative of a more vigorous and healthy green as seen in true color). Unfortunately, the population size of both sets of plants was too small to produce statistically significant results.

Root samples from both control and experimental seedlings were studied to determine the condition of the mycorrhizae in each. The control roots showed only limited development of mycorrhizal associations in two of the three root sets collected (possibly due to the drying effect of the air moving through the soil). The third control root showed no fungal development. Only a single species of fungus (*Cenococcum graniforme*) was identified in the two roots possessing the association.

The three root sets from the experimental plants showed more extensive development of mycorrhizae (as indicated by the extent of fungal hyphae development in association with the clubroots). In addition, one of the root sets contained two different species of fungi. The fungus common to all five roots containing fungi (both control and experimental plants) was *Cenococcum graniforme* (the other fungus appears to be the same as that seen in field specimens).

These data suggest that low levels of methane in the soil are not inhibitory to fungal growth and/or mycorrhizal formation. Methane may, in fact, have a stimulatory effect on the fungal component of a mycorrhizal association. The increased vigor of the fungus could result in an increased vigor of the host, especially since no evidence of inflated hollow roots was seen in any of the root systems. Of those four seedlings exposed to methane, one died within two weeks of germination (none of the control plants died). Unfortunately, no root samples were collected from the dead seedling. It is tempting to speculate that the methane may have stimulated the growth of the fungus to the point of causing destruction of the host root tissue, which in turn, caused the death of the seedling.

4. Conclusions. The *in vivo* study of mycorrhizae from both on-field and off-field sites suggests that differences in fungal diversity and fungal vigor exist in the Lost River test site. Such differences may influence both the distribution and vigor of host plants occurring in the area. *In vitro* data indicate that small amounts of methane in soil will neither inhibit the growth of Chestnut Oak seedlings nor inhibit formation of mycorrhizal associations between the oak root and fungus. Considerably more information is required before broad

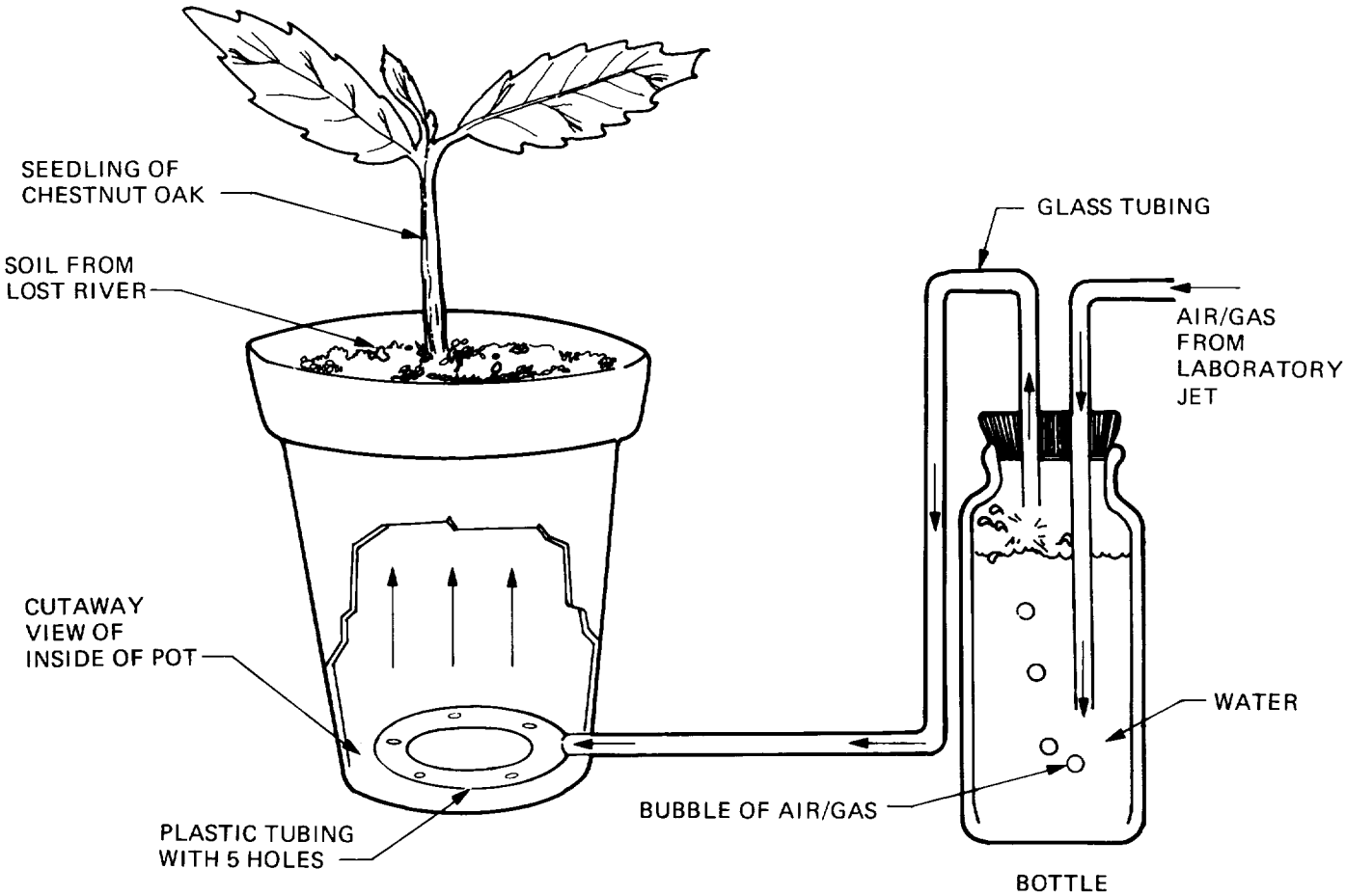

Figure 12-12. Diagrammatic representation of the *in vitro* experimental design for exposing roots of Chestnut Oak seedlings to migrating soil gases (either methane or ambient air)

conclusions can be drawn from these observations. Thus, there is need for detailed study of the mycorrhizae occurring at the Lost River test site.

D. Higher (Vascular) Plants

Detailed vegetation analyses of forested areas were conducted using the modified 0.1-acre circular plot method (Appendix B) as suggested by Lindsey et al. (1958). This method has been shown to be an efficient and accurate means of describing woody habitats (James and Shugart, 1970) and an accurate way of determining woody plant dominance, as expressed by basal area, for the site sampled (Kulow, 1965). In addition to being quick and accurate, this method allows for collection of data that can be compiled into a reasonably complete woody flora (Table 12-9) as well as determination of precise percent vegetation cover. The size of the sample plot is significant (Figure 12-13). A 0.1-acre circle (11.3-m/37-ft radius) is a close approximation of a single 15-m pixel (the average instantaneous field of view [IFOV] of aircraft multispectral data acquired for the test site).

August 1979 fieldwork provided detailed vegetation analyses (0.1-acre circular plots at 36 analysis sites), both on-field and off-field, at four field vegetation mapping areas (Plate 12-1 and Figures 12-14 through 12-17) considered typical for topography and vegetation. Field data were compared with the work of Sturm (1977) at the Lost River State Park. This field period was also used to look for areas exhibiting abnormal stress symptoms which might be expressed during periods of potential drought (late summer). As a result of these field vegetation analyses, general vegetation distribution patterns were established.

October 1979 fieldwork provided photographic ground standards (both TC and CIR) for identification of species and species associations on aerial CIR photographs.

Table 12-9. Partial flora of the Lost River test site

(a) Woody angiosperms and gymnosperms

Species[a]	Common Name	Frequency of Occurrence[b]
Acer rubrum	Red Maple	S
A. pennsylvanicum	Striped Maple	S
A. saccharum	Sugar Maple	S
Amelanchier arborea	Service Berry	S
Betula lenta	Sweet or Black Birch	S
Carpinus caroliniana	American Hornbeam	S
Carya glabra	Pignut Hickory	C
C. tomentosa	Mockernut Hickory	S
Castanea dentata	American Chestnut	S
Cercis canadensis	Red Bud	S
Cornus florida	Flowering Dogwood	C
Crataegus sp.	Hawthorn	S
Fagus grandifolia	American Beech	S
Gaylussacia baccata	Huckleberry	C
Hamamelis virginiana	Witch Hazel	S
Juglans cinerea	Butternut	R
J. nigra	Black Walnut	R
Juniperus virginiana	Red Cedar	R
Kalmia latifolia	Mountain Laurel	C
Liquidambar styraciflua	Sweet Gum	S
Liriodendron tulipifera	Tulip Poplar	S
Magnolia acuminata	Cucumber tree	S
Nyssa sylvatica	Black Gum	C
Ostrya virginiana	Hop Hornbeam	S
Pinus echinata	Shortleaf Pine	C
P. pungens	Table Mountain Pine	C
P. rigida	Pitch Pine	C
P. strobus	White Pine	S
P. virginiana	Virginia Pine	C
Platanus occidentialis	Sycamore	S
Populus tremuloides	Aspen	S
Prunus serotina	Black Cherry	S
Quercus alba	White Oak	C
Q. coccinea	Scarlet Oak	C
Q. ilicifolia	Scrub Oak	C
Q. marilandica	Black Jack Oak	R
Q. palustris	Pin Oak	C
Q. prinus	Chestnut Oak	C
Q. rubra	Red Oak	S
Q. stellata	Post Oak	S
Q. velutina	Black Oak	S
Rhododendron maximum	Rhododendron	S
Rhus copallina	Winged Sumac	R
R. toxicodendron	Poison Ivy	S
R. typhina	Staghorn Sumac	R
Robinia pseudoacacia	Black Locust	S
Sambucus canadensis	Elderberry	S
Sassafras albidum	Sassafras	C
Tilia americana	Basswood	S
Tsuga canadensis	Hemlock	C
Vaccinium spp.	Blueberry	C
Viburnum acerifolium	Maple-Leaf Arrow Wood	R

[a]Nomenclature follows that used in Strausbaugh and Core (1978).
[b]C – common, occurring at most sites of similar topography and habitat
S – scattered in occurrence
R – rare

(b) Vascular cryptograms

Common Name	Species
Club mosses	*Lycopodium clavatum*
	L. lucidulum
	L. obscurum
	L. tristachyum
Ferns	*Adiantum pedatum*
	Asplenium platyneuron
	A. resiliens
	Dryopteris marginalis
	D. spinulosa
	Osmunda cinnomomea
	O. claytoniana
	Polypodium virginianum
	Polystichum acrostichoides
	Pteridium aguilinum
	Thelypteris noveboracensis
Horsetails	*Equisetum arvense*
	E. hyemale
	E. sylvaticum

A comparison of September and October aerial CIR photography indicated that the greatest discrimination among species of woody vegetation occurring at the Lost River site is possible with October photographs acquired at the peak of fall foliage display. The technique of comparing aerial CIR photographs with TC and CIR ground photographs of species and species associations was useful for field mapping species/species communities.

In TC photographs, Chestnut Oaks appear gray–brown (brown on the upper leaf surface, gray–brown on the lower leaf surface), while in CIR they appear dark green. In the early fall (mid-September), the Chestnut Oak leaves begin to curl (note Figure 12-18), possibly due to their occurrence at potentially xeric (dry) sites (generally ridge tops and west-facing slopes), and thus appear fine-textured when seen from a distance (Figure 12-19). This combination of characteristics (dark green in CIR and fine textural appearance when compared with other broadleaf woody vegetation) allows the interpreter to locate stands of Chestnut Oak (on the aerial CIR) along ridge tops and west-facing slopes over much of the field.

Using the same techniques, the Red Oak–Scarlet/Pin Oak complex, the other oaks (White Oaks, Black Oaks and mixes of these with Chestnut and Scarlet–Pin Oaks), maples, hickory, and birch (all having a similar CIR signature) and evergreens (several species of pines plus Hemlock) can be recognized on the aerial photography. Preliminary field vegetation maps for four areas (Figures 12-14 through 12-17) were prepared using these vegetation discrimination

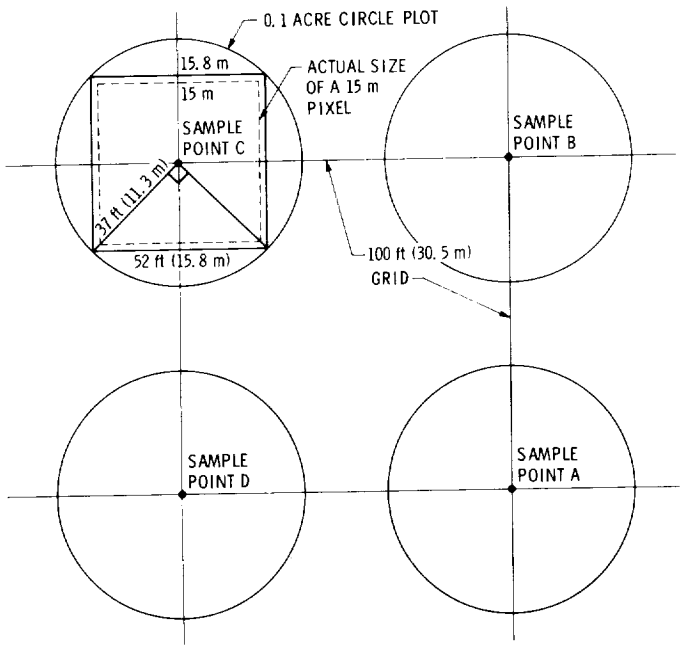

Figure 12-13. Comparison of a 0.1-acre circular sample plot and a 15-m pixel (the average IFOV of aircraft multispectral data acquired at the test site). The diagram shows four sample plots arranged on the 100-ft (30.5-m) grid used for field vegetation analysis.

techniques assisted by laboratory examination of CIR aerial photographs with a stereo zoom transfer scope.

As a result of the Lost River field botanical studies, the major broadleaf, deciduous, needle-leaf evergreen and broadleaf evergreen vegetation types have been documented in terms of their repeated association with specific topographic and/or physiographic features characterizing the test site. When compared with the various types of forest cover occurring in West Virginia (Core, 1966), the woody vegetation found at the test site represents a typical oak–hickory–pine forest, characteristic of the Ridge and Valley Province of the state. The preliminary field vegetation maps (Figures 12-14 through 12-17) were compared with Sturm's (1977) map for the Lost River State Park and were found to agree with his vegetation assessment of the area.

Fully 90 percent of the broadleaf trees of the forest canopy are a type of oak (Table 12-9) with various species associated with local topography. At lower elevation (to approximately 2400 ft) Chestnut Oaks predominate along the tops of ridges and west-facing slopes, with Red Oaks and Scarlet/Pin Oaks more common along the bottoms of ravines (scattered Scarlet/Pin Oaks may also occur in stands of Chestnut Oaks on slopes and ridges). White Oak and Black Oak, not as common, occur scattered throughout ravines, slopes (primarily east-facing), and ridges. The remaining hardwoods in the area consist of maples (*Acer*), hickory (*Carya*), Tulip Poplars (*Liriodendron*), Black Gum (*Nyssa*), birch (*Betula*), Sassafras (*Sassafras*), and others. The Red Maples and Tulip Poplars generally occur at the bottoms of ravines and at the base of water gaps, while the hickory, Sweet Gum, Sugar Maples, birch, and Sassafras are scattered at the higher elevations. The understory in the hardwood forest is generally broadleaf evergreen such as Laurel (*Kalmia* and *Rhododendron*) along with Dogwood (*Cornus*), Sweet Gum (*Liquidambar*), Red Maple, Black Gum, and Sassafras. Woody ground cover (shrubs) consists of a number of species of blueberries (*Vaccinium*), huckleberries (*Gaylussacia baccata*), and Scrub Oak (*Quercus ilicifolia*).

Pines (*Pinus*) occur where sandstone and shale bedrock are exposed, the pines thriving largely due to lack of competition from broadleaf trees in such xeric, shallow soil conditions. The common pines at this type of site are the Table Mountain Pine, the Long Needle Pine, and the Pitch Pine. These pines occur primarily on eroded slopes of water gaps and in eroded areas associated with the ridges and ravines. Pitch Pine and Virginia Pine are also common in mixed (pine–hardwood) scrub growth associated with old abandoned fields and recently timbered areas. Hemlock (*Tsuga*) occurs along valley floors and is always associated with stream banks. In the limestone ridges to the east of the gas field, Red Cedar (*Juniperus*) commonly grows in old pasture sites.

At the higher elevations (generally above 2400 ft along Big Ridge and South Branch Mountain) both Sugar Maple and birch (*Betula lenta*) become more common, to the point of dominance at many sites. Sugar Maple occurs most commonly on east-facing slopes, while birch grows selectively on the south-facing slopes of E–W-oriented ravines (especially along the west-facing slope of South Branch Mountain). This is somewhat surprising since birch apparently out-competes the pines at these sites, occurring at the most xeric sites (exposed bedrock and loose talus on south-facing slopes).

VII. Multispectral Image Analysis and Interpretation

A. Introduction

Multispectral remote sensing data acquired during the test site investigations included Landsat Multispectral Scanner (MSS) four-band data and aircraft NS-001 Thematic Mapper Simulator eight-band and Bendix Modular Multispectral Scanner (M^2S) 11-band data. Additionally, color photography was acquired during aircraft overflights.

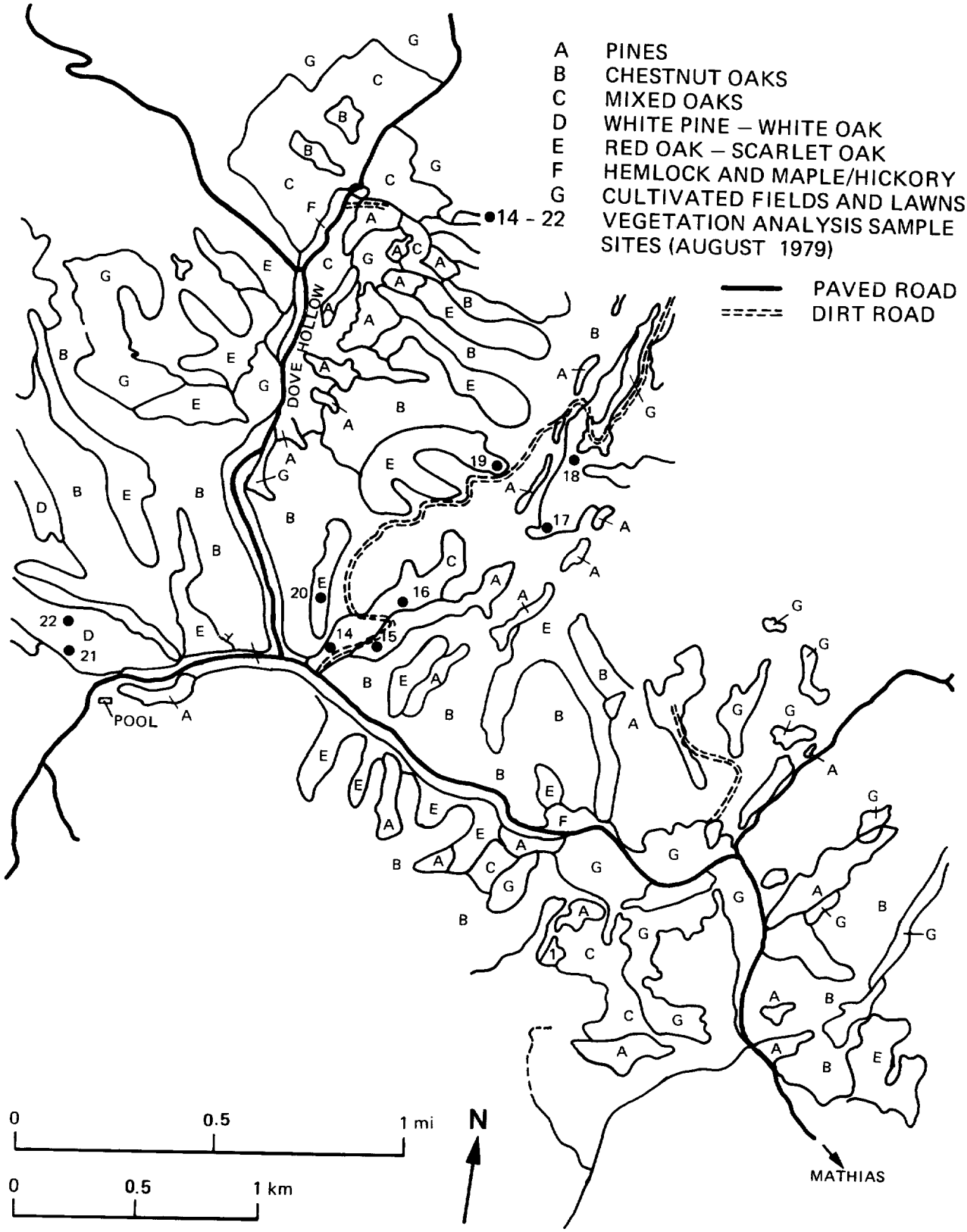

Figure 12-14. Preliminary field vegetation map 1—an area within the boundary of Lost River State Park (note location on Plate 12-1). This map was produced for comparison with a similar product which depicted vegetation of the State Park (Sturm, 1977).

A PINES
B CHESTNUT OAKS
C MIXED OAKS
D WHITE PINE – WHITE OAK
E RED OAK – SCARLET OAK
F HEMLOCK AND MAPLE/HICKORY
G CULTIVATED FIELDS AND LAWNS
● 23 - 32 VEGETATION ANALYSIS SAMPLE SITES (AUGUST 1979)
☼ GAS WELL
PAVED ROAD

0 0.5 1 mi
0 0.5 1 km
N

Figure 12-15. Preliminary field vegetation map 2—an area over the southern portion of the gas field (note location on Plate 12-1)

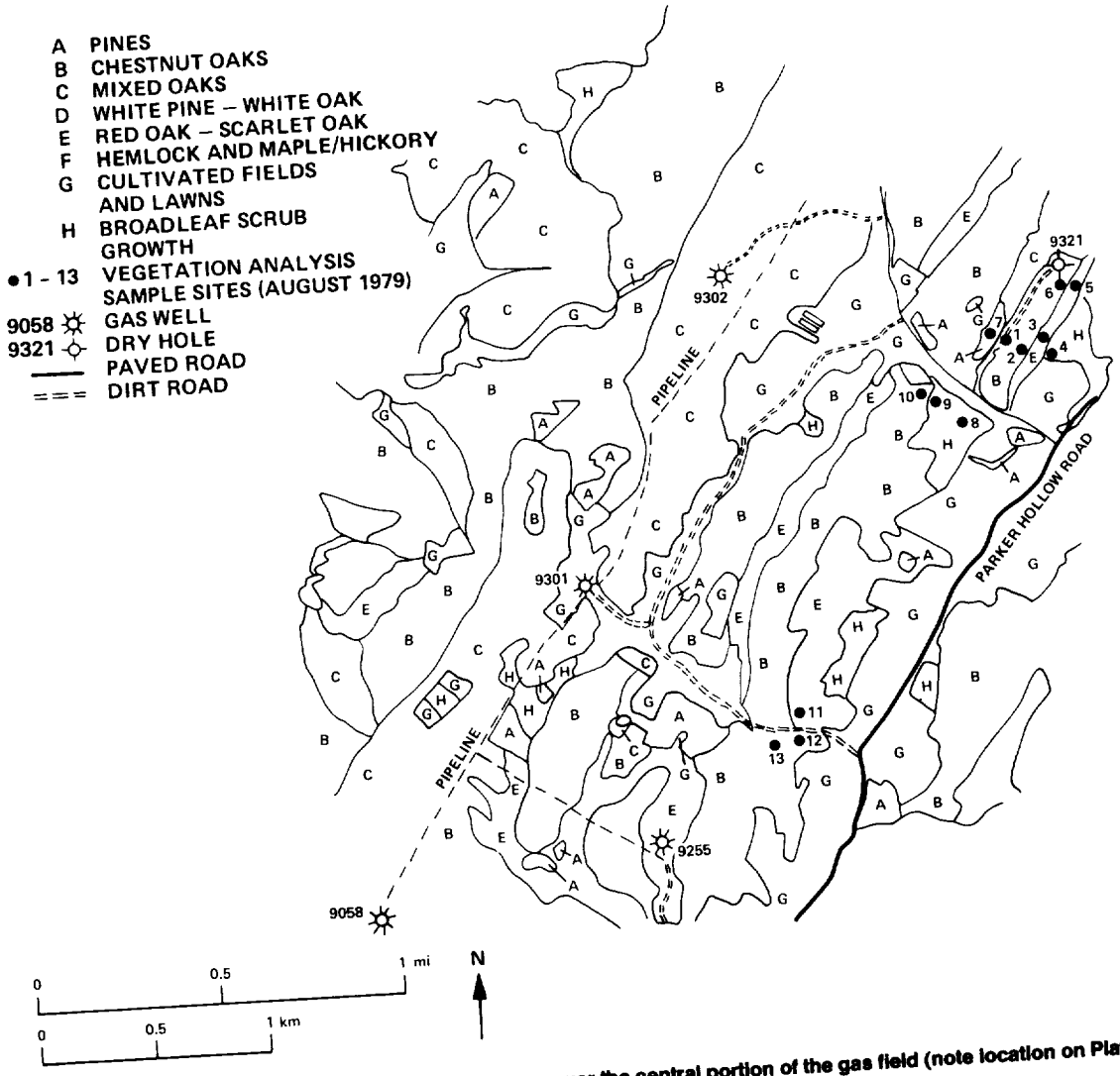

Figure 12-16. Preliminary field vegetation map 3—an area over the central portion of the gas field (note location on Plate 12-1)

All aircraft data were acquired by Johnson Space Center (JSC). The acquisition dates and selected characteristics of these data are summarized in Tables 12-10 and 12-11. For a more complete discussion of sensor characteristics, refer to the Technical Appendix, Section 14. Flight-line locations and areal coverage for aircraft-acquired data are illustrated in Figure 12-20.

Preliminary processing of all aircraft-acquired multispectral data was carried out by JPL's Image Processing Laboratory (IPL). A complete list and description of IPL programs used in processing these data are included in the Technical Appendix, Section 14.

Further multispectral data processing for interpretation was carried out by both IPL and the Gulf Science and Technology Company, Pittsburgh. Analysis and interpretation of the data were performed by all test site team members in common sessions or independently. Because of resource constraints of personnel, time, and image-processing facilities, all multispectral data sets were not equally evaluated. Data that upon initial examination demonstrated the greatest utility were given the greatest analytical attention.

NS-001 data acquired on Mission 431, line 1 (Table 12-10, Figure 12-20, and Plate 12-1) were evaluated in the greatest detail. All aircraft data were interpreted at a scale of 1:48,000; Landsat MSS data at a scale of 1:500,000 or 1:200,000.

The principal purpose of image analysis was to evaluate the utility of multispectral data for geologic mapping and

C-3

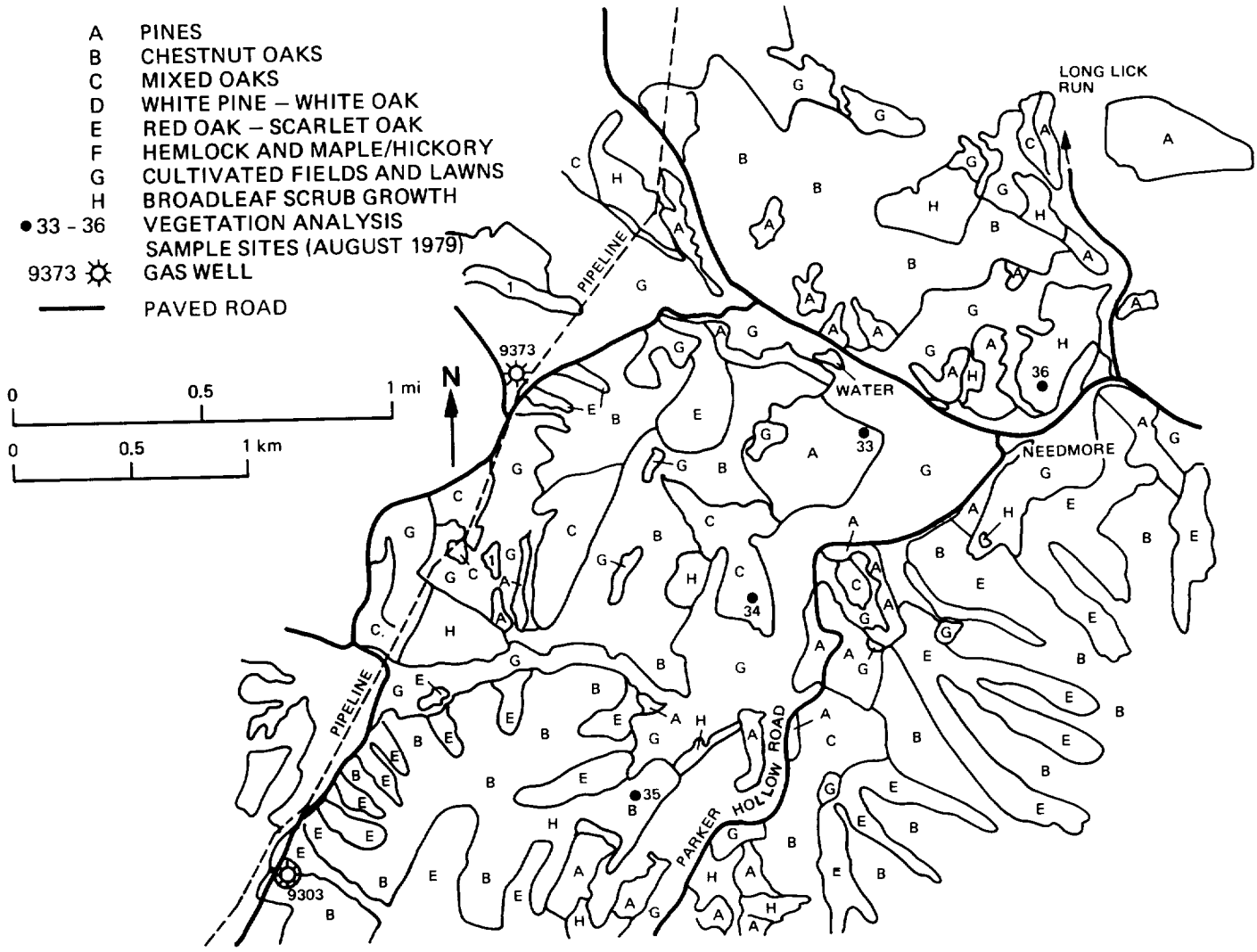

Figure 12-17. Preliminary field vegetation map 4—an area at the northern end of the gas field (note location on Plate 12-1)

hydrocarbon exploration in terrain dominated by vegetation cover. The approach used in the analysis of the multispectral data is reflected in the following discussions, which include the spectral characteristics of cover types, spectral analysis of NS-001 data, supervised classification of NS-001 data for vegetation mapping, photogeologic interpretation of aircraft multispectral data, and Landsat MSS/NS-001 lineament density analysis.

B. NS-001 Image Analysis for Vegetation Discrimination

1. General spectral characteristics of vigorous vegetation. Indigenous and cultivated vegetation dominate the Lost River test site. Data acquired by the NS-001 multispectral scanner are essentially a response to this vegetation, locally modified by topographic and illumination-aspect effects.

Figure 12-21 includes examples of field spectra acquired with JPL's Portable Field Reflectance Spectrometer (PFRS) for major vegetation types occurring in the test site and shows the locations of the seven NS-001 bands in the visible and near infrared (VNIR). Five of these band locations (1, 2, 3, 4, and 6) were selected specifically for the identification of vegetation species, vigor, and density (Hovis et al., 1975, p. G-7). The significant spectral features for vegetation which occur in the seven VNIR bands of the NS-001 are briefly described below. The observations are summarized from discussions by Hovis et al. (1975), Salomonson et al. (1980), and Wiersma and Landgrebe (1980), and the analysis of laboratory and PFRS field spectra obtained by JPL.

Band 1 (0.45–0.52 μm). Centered at approximately 0.49 μm, this band includes the visible blue; contains

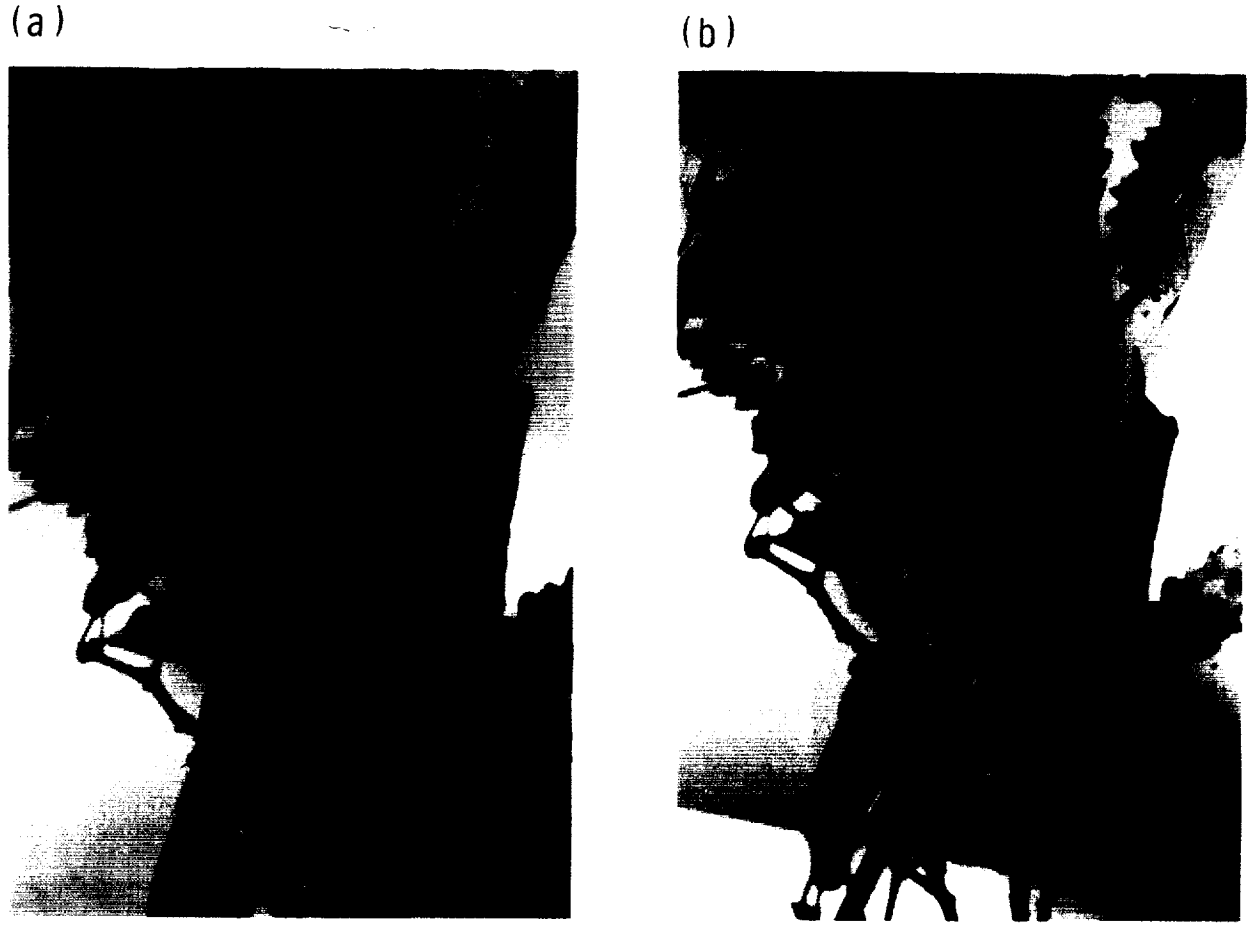

Figure 12-18. TC and CIR ground photography (taken October 20–23, 1979): (a) Chestnut Oak leaves, TC. Note the curling typical of this species of oak in the fall; (b) Chestnut Oak leaves, CIR. Note the very subtle color difference (slightly greener) when compared with the TC photography. More colorful species (Red Oak, Sugar Maple, Red Maple, etc.) demonstrate greater differences (in TC and CIR) when compared with the muted colors of most of the oaks.

absorption features due to chlorophyll and carotenoid concentrations useful for deciduous/coniferous differentiation.

Band 2 (0.52–0.60 μm). Centered at approximately 0.56 μm, this band includes the visible green; contains a reflectance peak due to chlorophyll concentration; sensitive to green pigmentation in healthy vegetation and therefore useful for the assessment of vegetation vigor.

Band 3 (0.63–0.69 μm). Centered at approximately 0.66 μm, this band includes the visible orange and red; contains the maximum chlorophyll absorption band; useful for species differentiation and determination of state of vigor.

Band 4 (0.76–0.90 μm). Centered at approximately 0.83 μm, this band contains a reflectance peak sensitive to leaf area, vegetation density, and biomass; useful for species identification and determination of state of vigor.

Band 5 (1.00–1.30 μm). Centered at approximately 1.15 μm, this band contains the greatest fine spectral structure, including both reflectance and absorption bands; sensitive to leaf area.

Band 6 (1.55–1.75 μm). Centered at approximately 1.65 μm, this band is located within an absorption feature characteristic of leaf water-mass.

Band 7 (2.08–2.35 μm). Centered at approximately 2.22 μm, this band is located within an absorption feature attributed to water molecules within a leaf.

A comparison of the vegetation and soil spectra shown in Figure 12-21 demonstrates that the reflectance values in all bands are typically higher in soil than in vegetation. The two cover types exhibit the greatest disparity in bands 6 and 7 and the least disparity in bands 4 and 5. Maximum reflectance values typically occur in bands 4 or 5 for vigor-

(a)

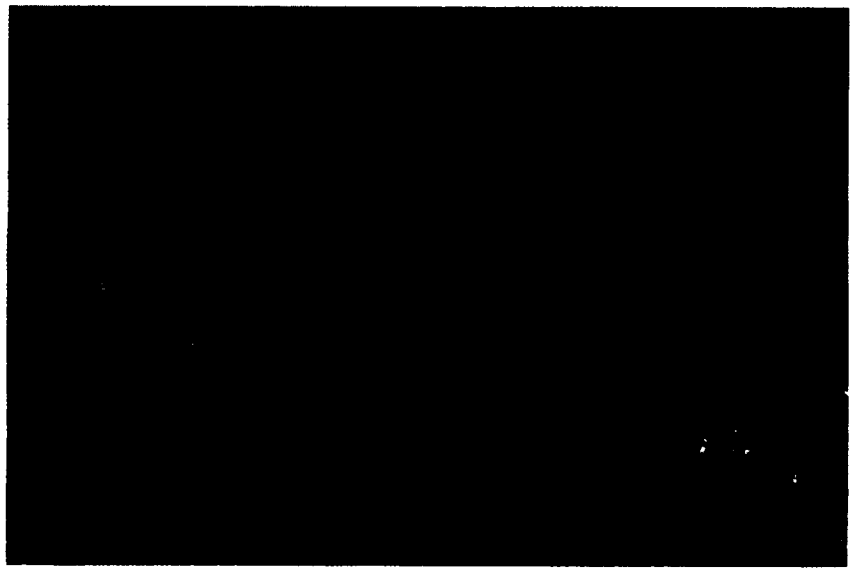

(b)

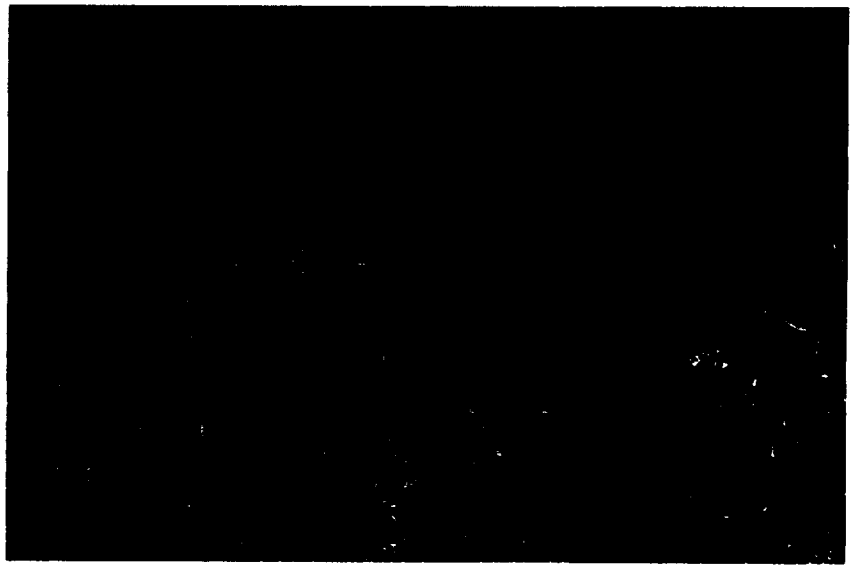

Figure 12-19. Overview: (a) looking east from the southern end of Big Ridge (Lost River State Park), TC. Due to the large number of oaks in this portion of West Virginia, the fall foliage display is muted; (b) looking east from the southern end of Big Ridge, CIR. Note the haze-penetration characteristics of CIR. Also note that the Chestnut Oak stands on the west-facing slopes appear dark green and fine-textured (due to leaf curling).

Table 12-10. Summary of aircraft-acquired multispectral data, Lost River test site

Date	Mission	Lines	Multispectral Scanner[a]
April 20, 1979	399	1 and 2	M^2S[b]
September 19, 1979	407	1 and 2	NS-001[c]
October 21, 1980	431	1 and 2	NS-001[c]

[a]IFOV for all data ~15 m; CIR photography acquired on all flights.
[b]Modular Multispectral Scanner.
[c]NS-001 Thematic Mapper Simulator.

ous vegetation and in bands 6 or 7 for soils. Locally, the reflectance of vegetation cover in bands 4 and 5 may exceed that of nonvegetation cover.

2. Botanical significance of NS-001 band data. NS-001 data were acquired at the Lost River test site at two phenologic stages—late summer vegetative growth (September) and senescence or fall foliage display (October). These data provide information concerning absorption bands due to photoactive plant pigments, chlorophyll-a and chlorophyll-b, and the accessory carotenoid pigments, carotene and xanthophyll. Relative absorption by the pigments will be reflected in NS-001 data, with the greatest absorption in NS-001 band 3 occurring in September data (at the test site, the foliage is still green in mid-September). Absorption in NS-001 band 1 should be roughly the same in both sets of data due to similar concentrations of carotenoid pigments (these carotenoid pigments become visible in certain deciduous species in the fall simply because they are no longer masked by chlorophylls). The relative amounts of carotenoids versus chlorophylls for each phenologic stage should be similar among various species, however, with the greatest amount of variation in ratios of pigment concentration (expressed by the NS-001 band-ratio 1/3) occurring in October.

Data from bands 4, 5, 6, and 7 relate to internal leaf structure (cellular arrangement and intercellular space configuration) and internal leaf moisture (relative humidity of the atmosphere occupying the intercellular spaces of the mesophyll as well as the amount of water imbibed in the cell walls of mesophyll cells). Band 4 may contain some pigment-related information (possibly fluorescent emission of chlorophyll-a) since reflectance in this band drops dramatically with the onset of senescence and/or decay of chlorophyll pigments. Increased variation in reflectance for bands 4 and 5 can be expected during fall foliage display, but both should remain correlated.

Table 12-11. Summary of Landsat-acquired MSS data, Lost River test site

Date	Scene Identification	Solar Elevation
October 15, 1973	8145915230500	34
February 27, 1976	8240115102500	33
April 30, 1976	8537714430500	49
October 18, 1976	8263515034500	34
April 16, 1977	8281514560500	48

Reflectance in band 5 should remain high for both overflights. Data from this band may be related to the basic molecular structure of the cellulosic and hemicellulosic components of the cell wall. Data from band 7 should be more variable relative to phenologic stage of vegetative tissue, due largely to their correlation with amounts of tissue water. Low correlations between bands 5 and 7 would be expected in October data.

To take maximum advantage of the vegetation discrimination capability of the NS-001 sensor, data were acquired over the test site on October 21, 1980. This date was chosen in response to preliminary analyses of M^2S and NS-001 data acquired in April 1979 and September 1979, respectively. Images produced from these data, acquired in early spring and late summer, were less than optimal for vegetation discrimination when compared to conventional field and aerial CIR photographic data. Based on field observations in the test site area by the site botanist and observations in other areas as discussed by Canney et al. (1979), it was concluded that multispectral data acquired early in the autumnal leaf color-change cycle should have the maximum vegetation species and vigor discrimination potential.

3. Characteristics of NS-001 spectral data. During each of two NS-001 overflights of the Lost River test site, the scanner measured average radiance in each band for over 3 million 15- by 15-m (50- by 50-ft) areas (pixels). These data provide a significant sample of the spectral characteristics of surface cover materials (predominantly vegetation). Table 12-12 summarizes interband correlations for the data acquired in the two overflights. These data reveal relatively high, positive interband correlations for both flights. Although the NS-001 data were acquired during different seasons (phenologic stages) in different years, both correlation matrices are surprisingly similar. In both, the highest interband correlations are for band pairs 1 and 2 and 4 and 5. Band pairs 2 and 3, 2 and 6, 3 and 7, 4 and 6, and 5 and 6 also exhibit high correlations. These relationships imply spectral redundancy in each of these band pairs in vegetated terrain. Band pair 1 and 5 correlations are the same in both matrices, demonstrating the seasonal independence of reflectance variability in these two spectral intervals. The lowest correlation is that of band pair 1 and

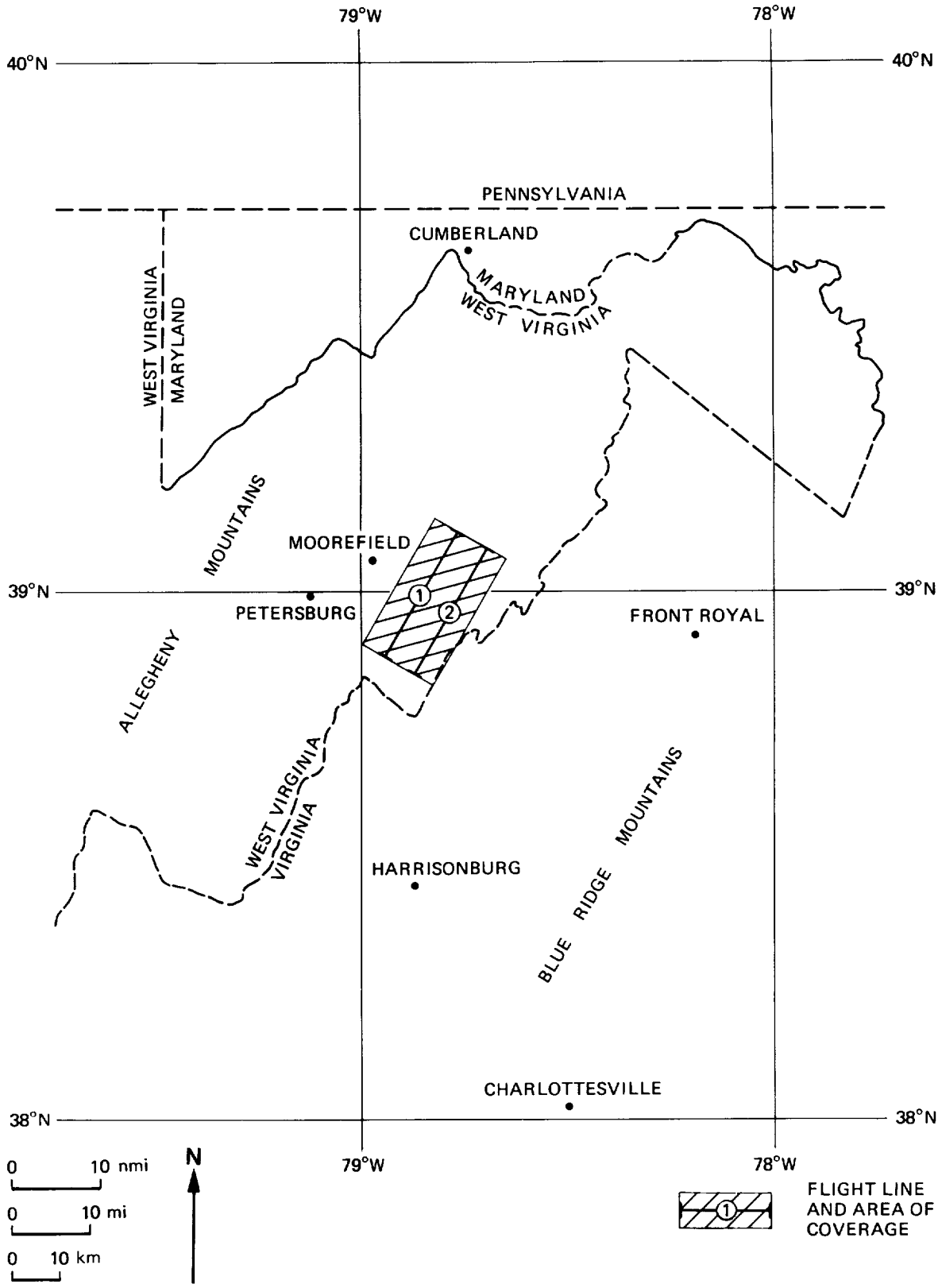

Figure 12-20. Map showing flight-line locations and areal coverage for M²S, NS-001, and color photographic aircraft data acquired at the Lost River test site

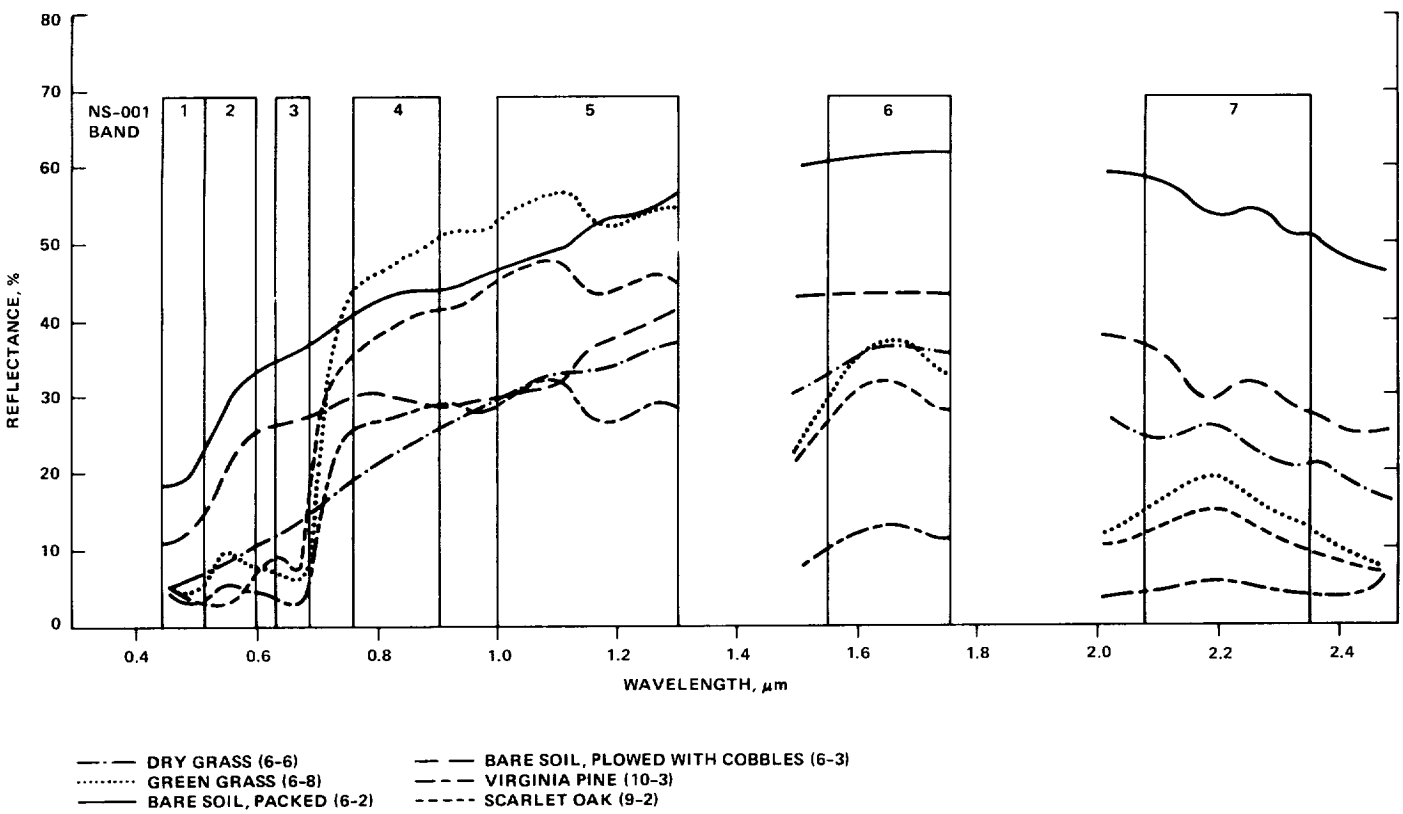

Figure 12-21. Examples of field spectra for major cover types. Spectra were acquired in October 1981, using JPL's PFRS. Positions of NS-001 bands are indicated; the vertical height shown is arbitrary.

Table 12-12. Correlation matrices for the seven NS-001 VNIR band data acquired in two overflights of the Lost River test site

Band	1	2	3	4	5	6	7
	Lost River, Mission 407, Line 1, September 19, 1979 Mean Interband Correlation Coefficient: 0.77						
1	1.00						
2	0.97	1.00					
3	0.90	0.94	1.00				
4	0.55	0.64	0.60	1.00			
5	0.53	0.63	0.60	0.98	1.00		
6	0.75	0.84	0.86	0.83	0.87	1.00	
7	0.75	0.82	0.87	0.68	0.69	0.89	1.00
	Lost River, Mission 431, Line 1, October 21, 1980 Mean Interband Correlation Coefficient: 0.72						
1	1.00						
2	0.95	1.00					
3	0.73	0.83	1.00				
4	0.63	0.75	0.70	1.00			
5	0.53	0.61	0.51	0.91	1.00		
6	0.80	0.82	0.77	0.80	0.80	1.00	
7	0.64	0.71	0.90	0.61	0.44	0.77	1.00

5 for the September data and band pair 5 and 7 for the October data. These low correlations may be interpreted as indications that maximum spectral information (variance) resides in the data acquired in these three bands.

Table 12-13 summarizes the changes in interband correlation for the two overflights. The magnitude of these changes is presumably a measure of the magnitude of seasonal changes in the spectral variability of vegetation. Interband correlation is generally lower in the October data. This decrease in correlation demonstrates an increase in spectral heterogeneity. The greatest decrease is in band pairs 5 and 7 and 1 and 3. Others showing relatively large decreases are 6 and 7, 3 and 5, 3 and 6, 2 and 3, 2 and 7, 1 and 4, and 1 and 6.

Principal components analysis provides a statistical tool for gaining insight into the nature of NS-001 data. (A complete discussion of this multivariate technique is beyond the scope of the present study; refer to Davis (1973) for such a discussion.)

Table 12-13. Matrix of correlation change (October to September) for the seven NS-001 VNIR band data acquired in two overflights of the Lost River test site[a]

Band	1	2	3	4	5	6	7
1	0.00						
2	−0.02	0.00					
3	−0.17	−0.11	0.00				
4	0.08	0.11	0.10	0.00			
5	0.00	−0.02	−0.09	−0.07	0.00		
6	0.05	−0.02	−0.09	−0.03	−0.07	0.00	
7	−0.11	−0.11	0.03	−0.07	−0.23	−0.12	0.00

[a]Mean interband correlation coefficient change: −0.05.

Table 12-14 summarizes the seven NS-001 VNIR band eigenvectors for the first three principal components (PCs) for data acquired in the two Lost River overflights. Also included is the percent variance explained by each PC. Eigenvectors are rather low for all bands in both data sets. This reflects the high interband correlations noted above. In both sets of data, over 95 percent of the variance in the NS-001 data is associated with these three new variables. Interpretation of the physical meaning of these new variables is aided by examination of the PC "spectra" shown in Figures 12-22 and 12-23.

The first PC is approximately equally, positively correlated with all NS-001 VNIR bands. It may be considered an approximation of the "mean" radiance value for the seven bands or a measure of the albedo variation in the site's dominantly vegetated cover. In both cases, over 75 percent of the variance of the NS-001 data is explained by this first PC. Apparently, most of the spectral variability at Lost River may be attributed solely to variations in albedo. This observation is consistent with the high interband correlations shown in Table 12-12. The magnitude of the eigenvectors demonstrates that variation in band 2 data is most important in September (late summer to early fall at this test site, prior to fall foliage change) and variation in bands 5 and 6 data is most important in October (peak autumn foliage display).

The second PC for both data sets is positively correlated with bands 4 and 5 and negatively correlated with bands 1, 2, and 3. The overall form of the two spectra for this second PC is analogous to the typical spectral reflectance curve for vegetation; differences in the two spectra may reflect seasonal differences in the spectral characteristics of the vegetation cover at Lost River. The 14 percent variance explained by this component may be considered a measure of the albedo-independent contribution of "pure" vegetation spectral classes to the variance of these scanner data.

The third PC for both data sets is most positively correlated with band 7, and to a lesser extent with bands 6 and 3. Negative correlation is associated with bands 1 and 2. The contribution of this third PC may therefore be attributed to materials which would have high values in NS-001 band ratios involving the digital number (DN) values for bands 7, 6, or 3 in the numerator and 1 or 2 in the denominator. These relationships lend credence to the interpretation that this third PC is a measure of the contribution of the nonvegetated (bare-ground) spectral component. The 5 percent or less variance explained by this component may be considered a measure of the contribution of pure, bare-ground spectral classes to the variance of these scanner data.

4. Evaluation of NS-001 band and band-ratio data for vegetation mapping. Initially, four images were produced

Table 12-14. NS-001 principal components analysis: eigenvectors of seven VNIR bands for the first three PCs

Variance Explained, %	PC	NS-001 Band 1	2	3	4	5	6	7
		Lost River, Mission 407, Line 1, September 19, 1979						
81	1	0.411	0.465	0.401	0.342	0.346	0.390	0.255
14	2	−0.432	−0.325	−0.286	0.536	0.564	0.170	−0.023
3	3	−0.472	−0.248	0.385	−0.317	−0.103	0.417	0.532
Σ98								
		Lost River, Mission 431, Line 1, October 21, 1980						
77	1	0.319	0.348	0.339	0.397	0.469	0.454	0.280
14	2	−0.305	−0.271	0.381	0.288	0.684	−0.024	−0.370
5	3	−0.614	−0.396	0.389	0.149	0.013	−0.032	0.540
Σ96								

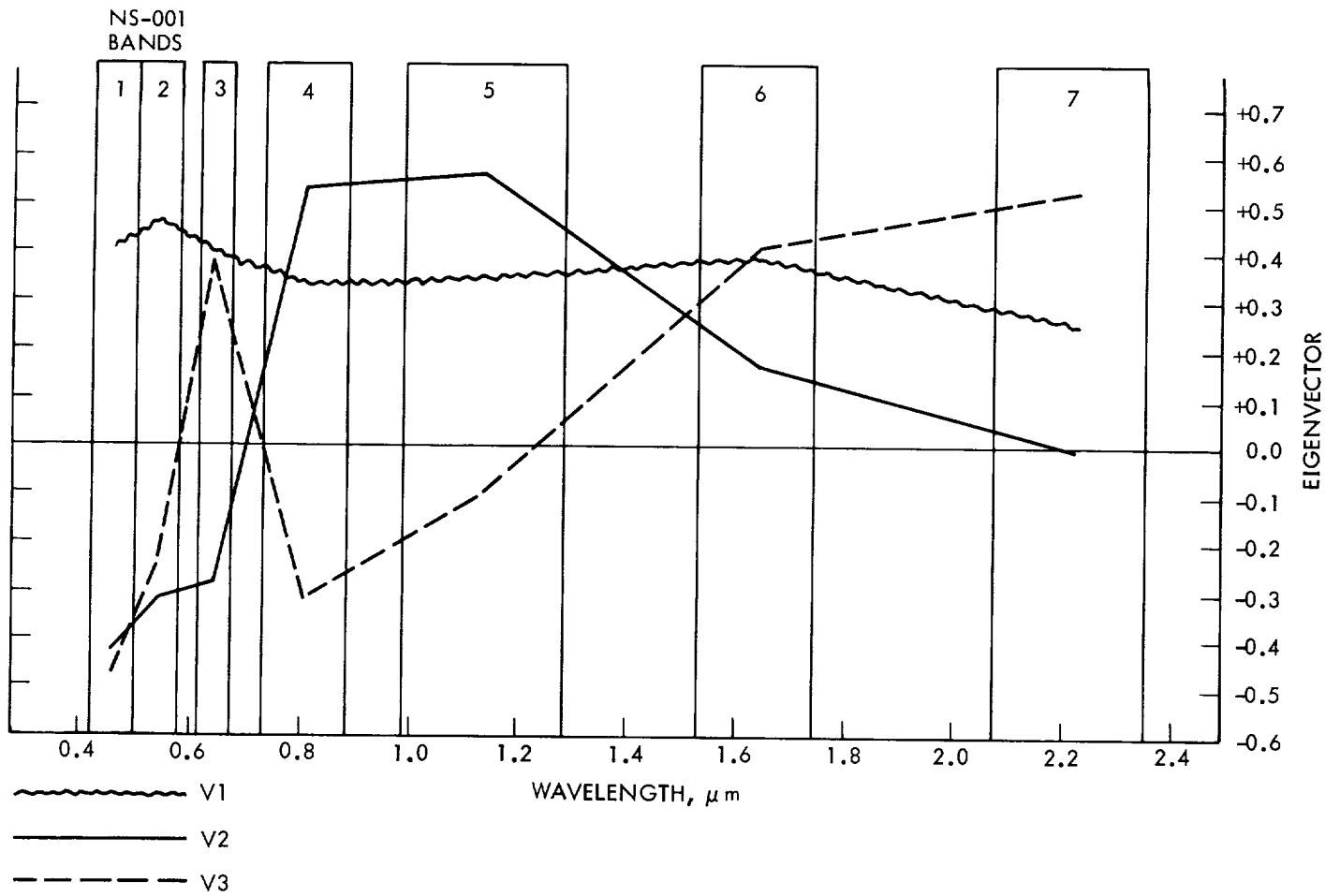

Figure 12-22. PC spectra for NS-001, Mission 407, line 1 data acquired September 19, 1979. Spectra were made by connecting eigenvector values for each PC plotted at band centers.

from the October NS-001 data in an attempt to optimize vegetation discrimination (Figures 12-24 through 12-27). To test the utility of these images for vegetation discrimination, an interpreter lacking botanical training visually delineated tonal/textural units in preliminary field vegetation map area 3 (Figures 12-28 through 12-31). Average DN values were determined for the delineated units by visually interpreting colors with the aid of the color mixing key shown in Figure 12-32. The test site botanist had prepared a preliminary vegetation map of this area using field observations aided by CIR aerial photography (Figure 12-16). A comparison of these interpretations provided (1) the opportunity to evaluate these four NS-001 images and (2) a basis for recommending the optimal processing of these data for vegetation discrimination. The results of this evaluation are discussed below.

A comparison of the preliminary field vegetation map (Figure 12-16) to the image interpretations (Figures 12-28 through 12-31) reveals that units recognized in the vegetation map are commonly subdivided in the image interpretations. Eight species and species community units were used to prepare the preliminary field vegetation map. The greater detail of the NS-001 image interpretations may be a measure of the scanner's sensitivity to subtle variations in vegetation vigor and density, which were not considered in the preparation of the vegetation map.

By comparing the preliminary field vegetation map to the four image interpretations, the image interpreter determined that the bands 2, 3, and 4 image (Figure 12-24) is the best of the four for species and species community discrimination. This is not surprising since the bands used were selected to simulate aircraft CIR photographic images which aided in the preparation of the field vegetation map. The image interpreter's units 1, 2, 3, 3′, and 6 (Figure 12-28) correspond to fields, pastureland, and lawns; unit 5 corre-

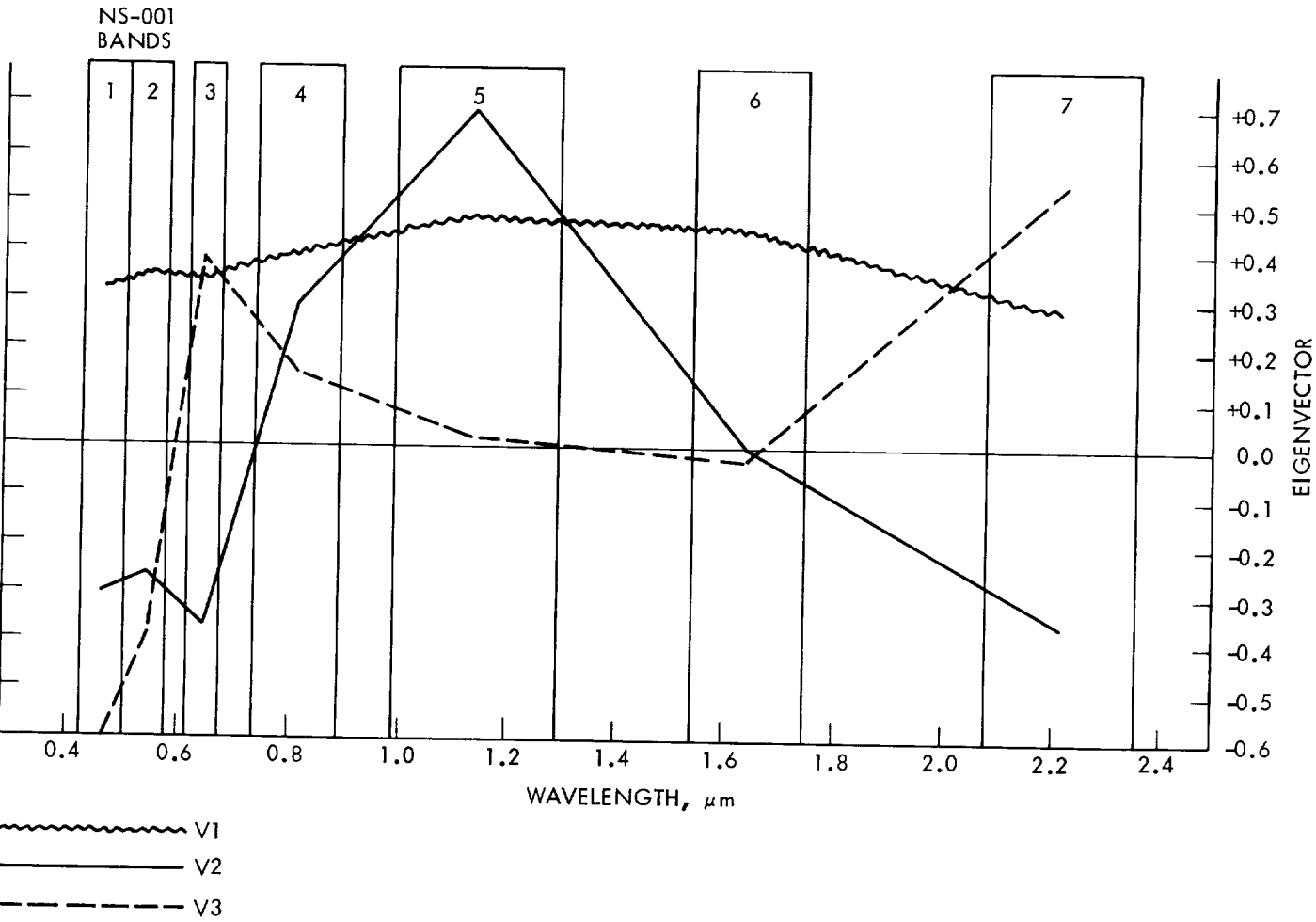

Figure 12-23. PC spectra for NS-001, Mission 431, line 1 data acquired October 21, 1980. Spectra were made by connecting eigenvector values for each PC plotted at band centers.

ponds to Evergreen; unit 8 corresponds to Chestnut Oak; nd the unlabeled unit corresponds to Scarlet Oak and Red)ak.

The bands 3, 4, and 6 color composite image (Figure 2-25) is the poorest for species identification. Bands used or this image were selected primarily to approximate an M²S image that was used for geologic interpretation. The nage interpreter identified nine units in this color composite (Figure 12-29). Unit 1 includes both Chestnut Oak nd Evergreen. The other units show little correspondence species or species communities.

The band-ratio 2/3 color slice image (Figure 12-26) hibits little species discrimination. This ratio was selected measure variations in vegetation vigor by displaying riations in the chlorophyll reflectance feature at 0.56 μm d the associated absorption feature at 0.66 μm. High values of this ratio should be associated with low albedo, green, chlorophyll-bearing material, and low values with high albedo, nongreen, chlorophyll-poor material. The image interpreter recognized four units (Figure 12-30). An unexpected characteristic of this image is that linear features (lineaments) not apparent in other images are accentuated. These lineaments are typically defined by linear "greenness" boundaries, characterized by relatively greener areas on their north side. Rarely, the reverse occurs. This attribute may be explained by the tendency for higher evergreen concentrations on south-facing, xeric (dry) slopes and higher deciduous (nongreen in October) concentrations on north-facing, mesic (wet) slopes. Some of the greenness lineaments are apparently due to such cultural artifacts as active and inactive field and property boundaries as well as old logging boundaries. Subtle linear trends are apparently highlighted by subtle changes in vegetation vigor and species distribution.

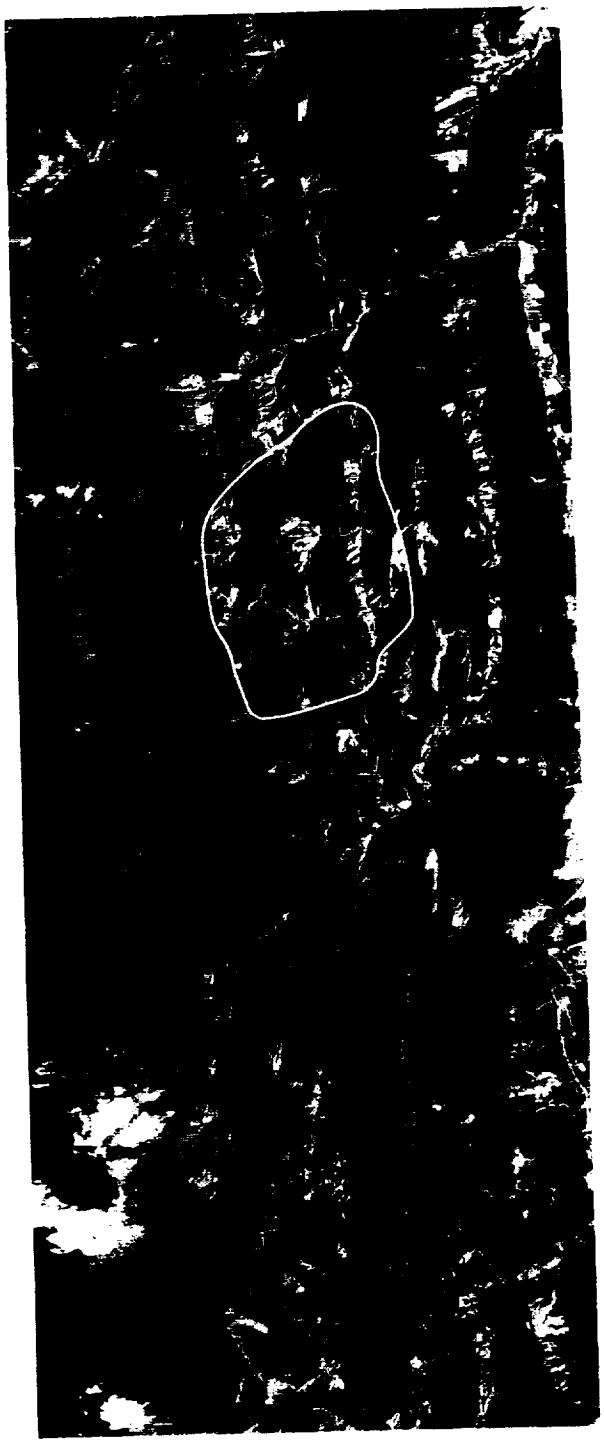

Figure 12-24. NS-001 bands 2 (blue), 3 (green), and 4 (red) image of the Lost River test site (Mission 431, line 1) as seen in mid-October. These color assignments simulate CIR aerial photography. The area of detailed tonal/textural interpretation is outlined.

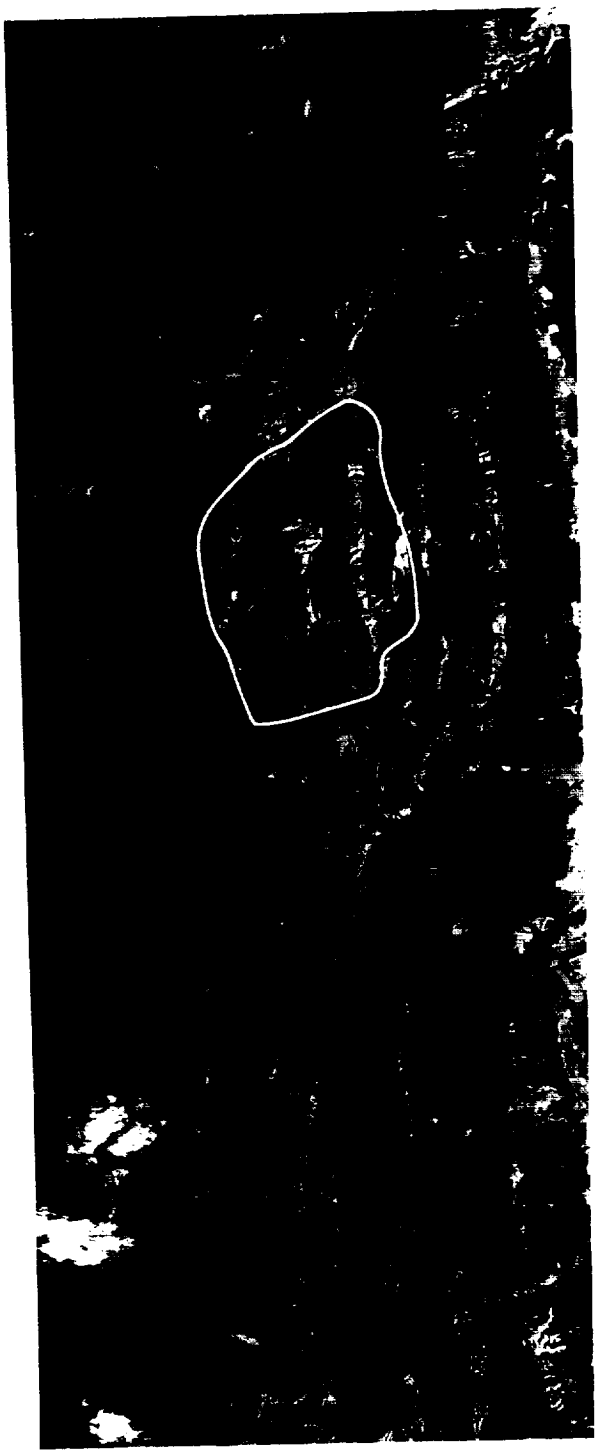

Figure 12-25. NS-001, Mission 431, line 1, October 21, 1980 c
composite image: bands 3 (blue), 4 (green), and 6 (red). The are
detailed tonal/textural interpretation is outlined.

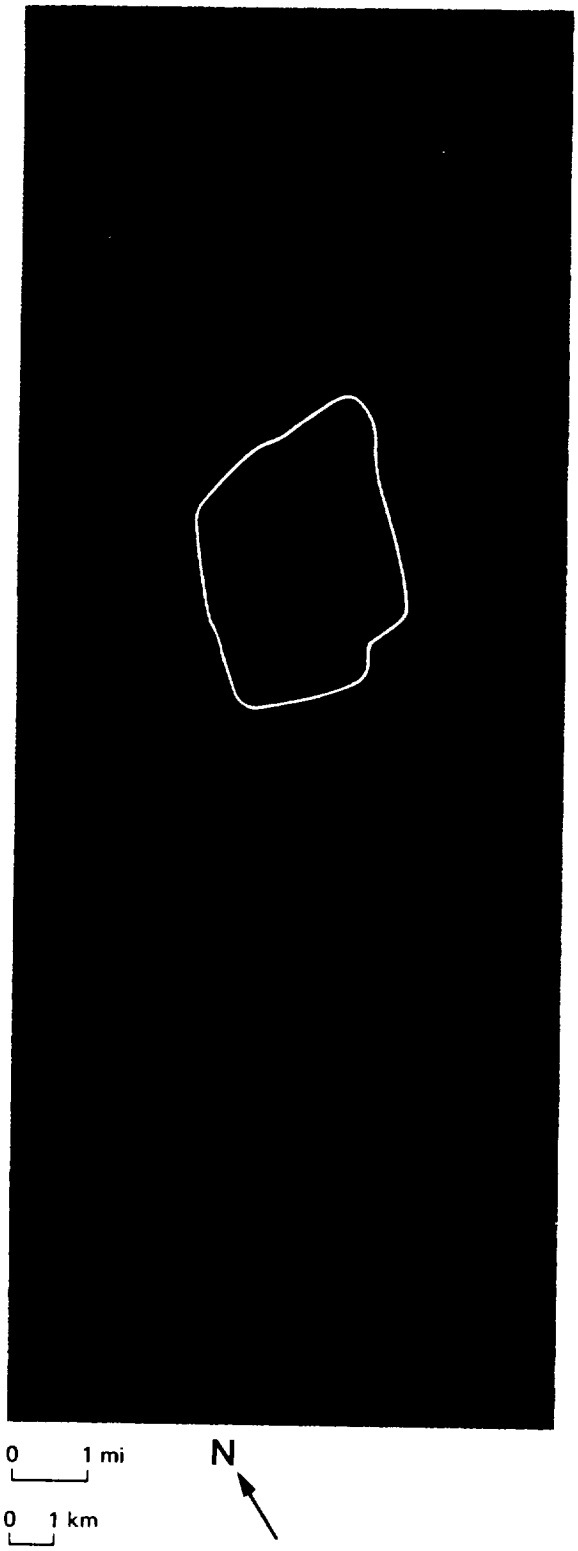

Figure 12-26. NS-001, Mission 431, line 1, October 21, 1980 color ratio slice image: band-ratio 2/3. The increase in ratio values is displayed by color changes from brown to orange to yellow to green. The area of detailed tonal/textural interpretation is outlined.

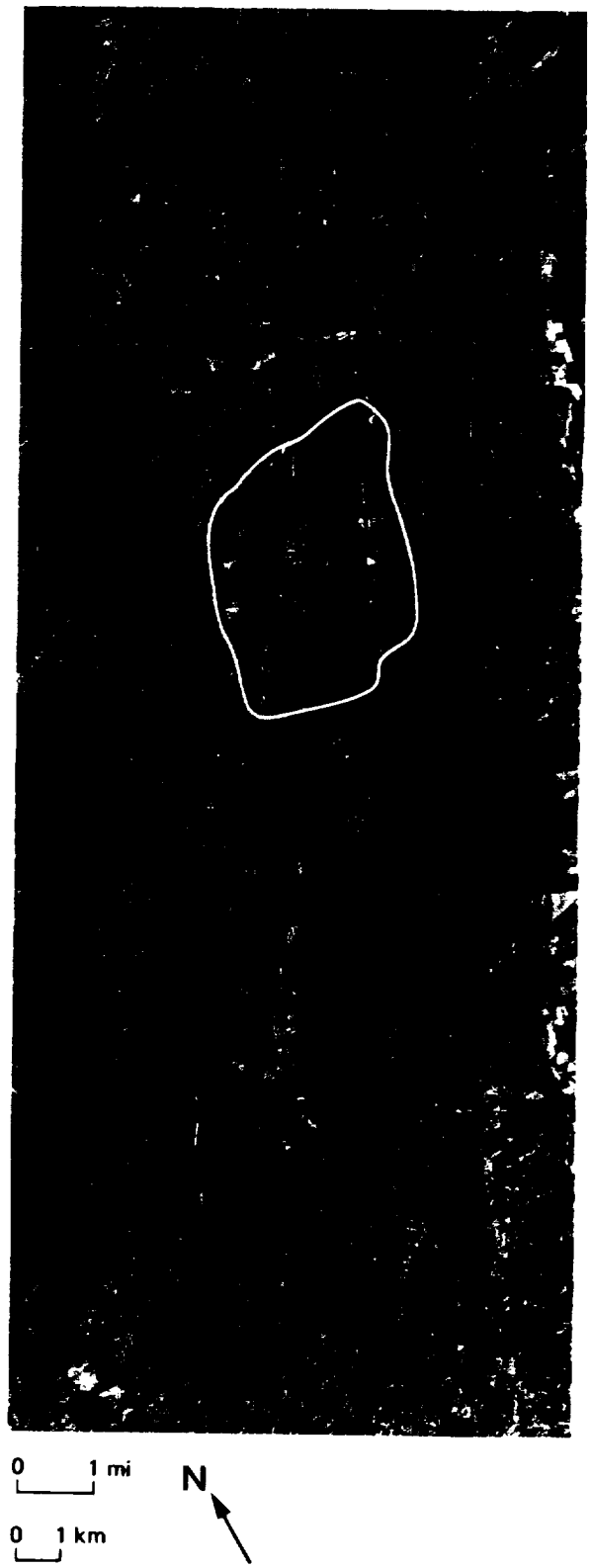

Figure 12-27. NS-001, Mission 431, line 1, October 21, 1980 color ratio composite image: band-ratios 4/3 (green), 4/5 (blue), and 5/7 (red). The area of detailed tonal/textural interpretation is outlined.

UNIT #	BAND DN VALUES 2 (BLUE)	3 (GREEN)	4 (RED)
1	250	250	250
2	250	240	240
3	180	210	240
3'	150	160	210
4	20	60	240
5	0	40	70
6	130	250	250
8	80	120	120
UNLABELED	110	190	220

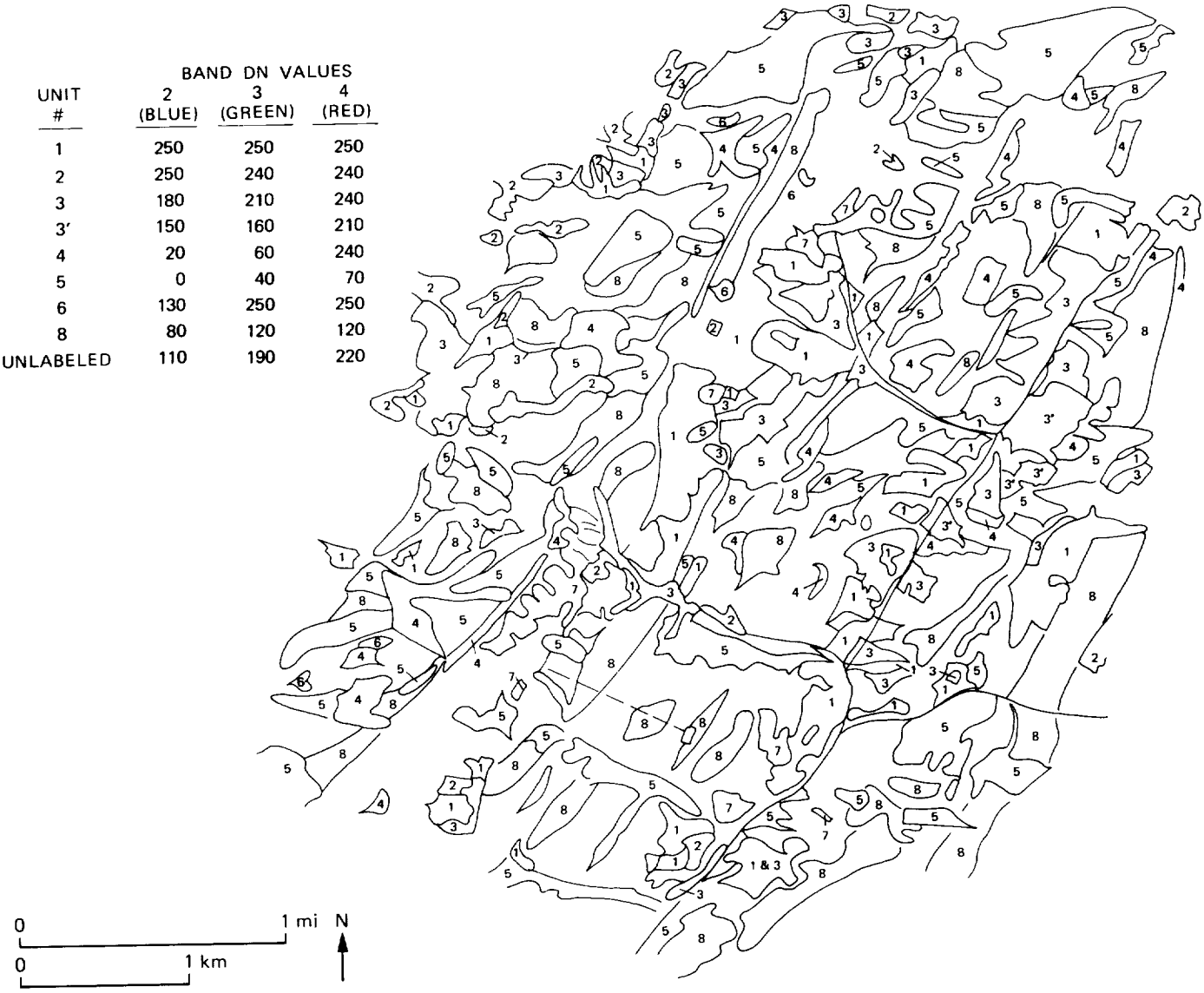

Figure 12-28. Tonal/textural unit interpretation of NS-001 bands 2, 3, and 4 color composite image (Figure 12-24) for preliminary field vegetation map 3. DN values listed are approximate and were assigned by the interpreter by comparing image colors to a DN color key.

The band-ratios 4/3, 4/5, and 5/7 used for the Figure 12-27 color ratio composite image were selected to measure the amount of chlorophyll (band-ratio 4/3), green vegetation biomass (band-ratio 4/5), and general vegetation vigor (band-ratio 5/7). Substantial striping in the original band 7 data resulted in linear artifacts in the band-ratio 5/7 image plane. The image interpreter recognized eight units (Figure 12-31). Some areas having high values in the 4/5 plane (such as unit 6) are Evergreen. Band-ratios 4/5 and 5/7 may be used to separate Chestnut Oaks from other oaks. Chestnut Oaks have high 4/5 values and low 5/7 values. The image interpreter's units 1, 2, 3, and 6 are all Evergreen. Units 1 and 3 are characterized by low 4/5 and variable 5/7 values; units 2 and 6 are characterized by high 4/5 values. These relationships are not readily explainable but may in part reflect shadow effects and variations of evergreen vigor and density.

The foregoing analysis leads to the conclusion that NS-001 bands 2, 3, and 4 and band-ratios 4/5 and 5/7 are useful for the discrimination of vegetation species in the Lost River test site. A supervised classification map using these five variables and training areas furnished by the site botanist should provide useful vegetation distribution information for the test site area.

UNIT #	BAND DN VALUES 3 (BLUE)	4 (GREEN)	6 (RED)
1	0	80	50
1'	60	140	115
2	110	200	120
2'	110	210	175
3	110	220	215
4	145	230	240
5	180	165	195
6	70	120	240
7	145	240	255

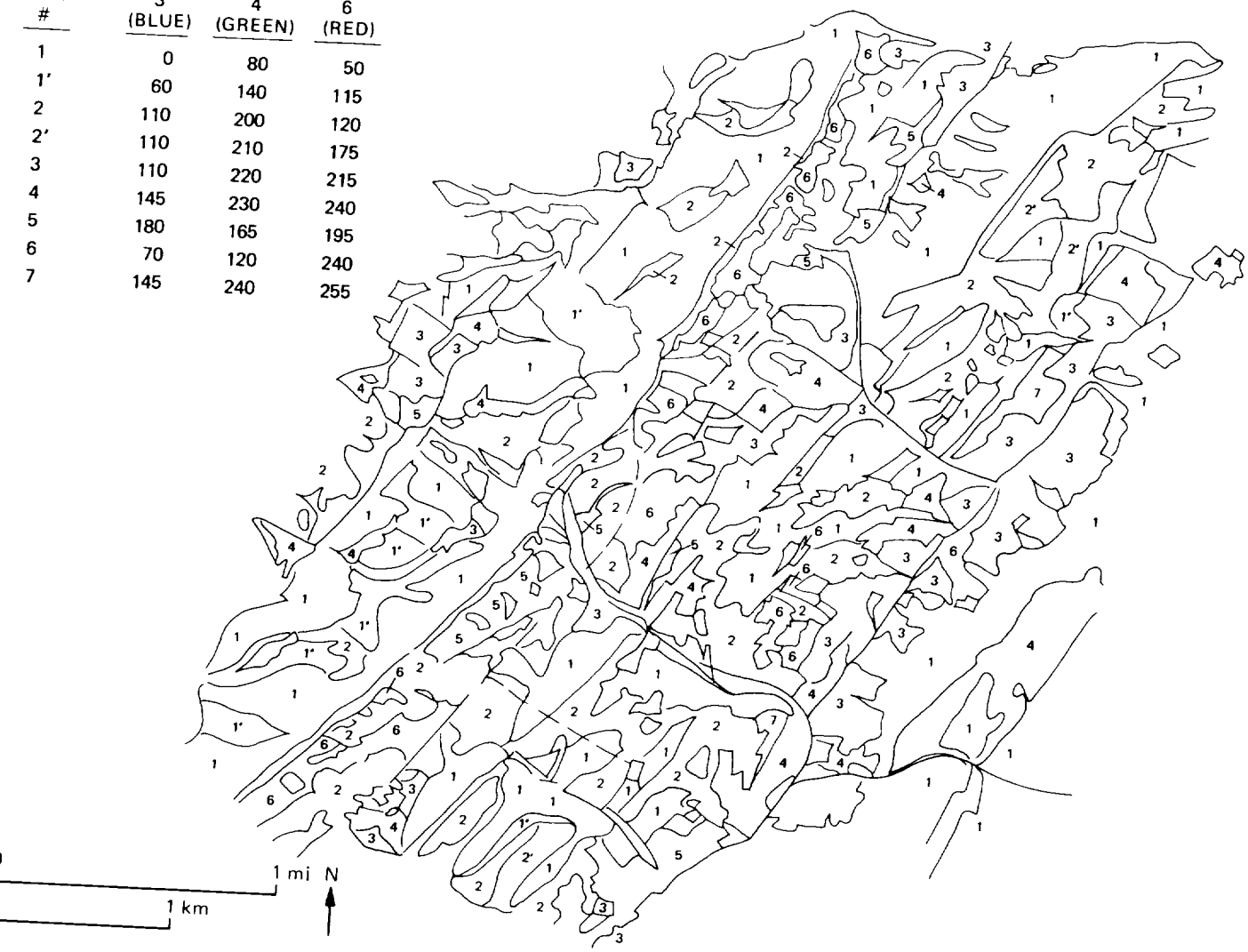

Figure 12-29. Tonal/textural unit interpretation of NS-001 bands 3, 4, and 6 color composite image (Figure 12-25) for preliminary field vegetation map 3

5. Vegetation classification maps using NS-001 data. As result of the preliminary analysis discussed above, the oduction of an accurate vegetation classification from -001 Mission 431 data was considered possible. An initial empt was made at Gulf Science and Technology Com- ny, using their IDIMS image-processing system. In an eractive session, the site botanist selected 11 training areas resenting nine vegetation classes for use in a supervised sification. The nine vegetation classes included the seven egories used for preparing the preliminary field vegeta- maps (Figures 12-14 through 12-17) plus two field and/ awn classes. NS-001 data from Mission 431 bands 2, 3, 4 and band-ratios 4/5 and 5/6 were used as variables roduce two images that portrayed the distribution of the nine vegetation classes. (Band-ratio 5/7 was replaced with 5/6 because of striping in the band 7 data.) One image produced was an unfiltered version of the classification; the other, a 3 by 3 median-filtered version. Analysis of the two versions revealed:

(1) Much useful vegetation information was lost in the filtered version.

(2) Significant misclassification occurred in shadowed areas of both images.

In an attempt to correct these problems, another interactive session was conducted at JPL's IPL. On an NS-001 image displayed to mimic CIR photography (Figure 12-24),

Figure 12-30. Tonal/textural unit interpretation of NS-001 band-ratio 2/3 color slice image (Figure 12-26) for preliminary field vegetation ma

the site botanist designated 35 training areas for 10 vegetation classes. Figures 12-33, 12-34, and 12-35 show the locations and class designations for the training areas. The Oak class of the Gulf classification was modified. White Oaks and Mixed Oaks were combined in an Other Oak class, Scarlet Oaks and Red Oaks were combined in a Scarlet Oak class, and a Shaded Chestnut Oak class was defined (in an attempt to eliminate shadow effects). In addition, new classes were defined: Maple (including all species that exhibit yellow or yellow–orange fall foliage; thus, this class includes Sugar and Red Maples as well as hickories, birch, and Sassafras), Soil (plowed fields, cut crops, drivew dirt roads, etc.), and Scrub (old field successional gr including evergreen and broadleaf members). All pines hemlocks were grouped together in an Evergreen c These data were used in the VICAR programs STATS FASTCLAS to produce two new supervised veget classification maps using NS-001 variables:

(1) Band 2, 3, and 4 and band-ratios 4/5 and 5/6

(2) Bands 2, 3, and 4 and band-ratios 4/5 and 5/7 ure 12-36)

UNIT #	DN RATIO VALUES 4/3 (GREEN)	4/5 (BLUE)	5/7 (RED)
1	150	80	220
2	110	180	60
3	130	80	20
4	220	110	170
5	130	110	170
6	140	250	120
7	250	250	250
UNLABELED	160	80	250

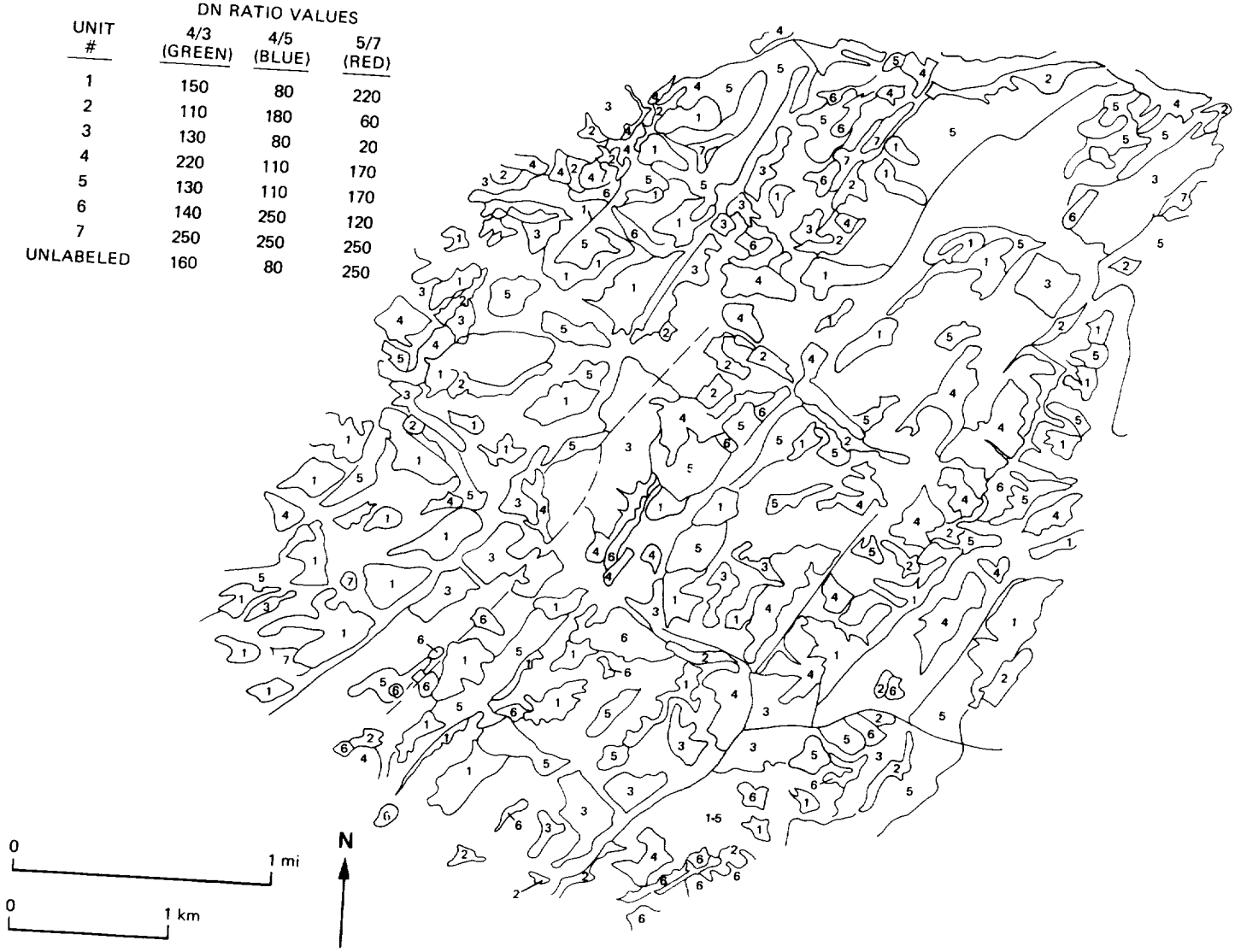

Figure 12-31. Tonal/textural unit interpretation of NS-001 band-ratios 4/3, 4/5, and 5/7 color composite image (Figure 12-27) for preliminary field vegetation map 3

A comparison of the two new versions demonstrated that there was no striping problem in the band-ratio 5/7 version, and that this version contained fewer unclassified or obviously misclassified pixels.

Training area data from the two classification maps were lso used as input for the VICAR version of the UCLA 3MD stepwise discriminant function analysis. The results f this analysis, summarized in Tables 12-15 and 12-16, ive insight into the two classification maps. According to ese tables, the two classifications are equivalently accu- te. A review of Table 12-15 shows that class samples con- ining a total of 3474 pixels were used in the discriminant analysis. The number of training pixels per class ranged from 41 (Scarlet Oak) to 1025 (Chestnut Oak). This in- equality of training sample size should result in a classifica- tion bias that emphasizes large classes at the expense of small classes. Based on training area statistics alone, both sets of variables yielded similar results. In step 5, the most accurately classified group was Field 1 (98 percent), and the least accurately classified group was Other Oak (31 percent). Chestnut Oak and Chestnut Oak Shaded were commonly confused, an error of no consequence for vege- tation mapping purposes. The most significant misclassifi- cations indicated by the BMD analysis were Evergreen as Scrub; most Other Oak as Scarlet Oak; Maple as Scarlet Oak; Soil as Chestnut Oak Shaded; and Scrub as Evergreen.

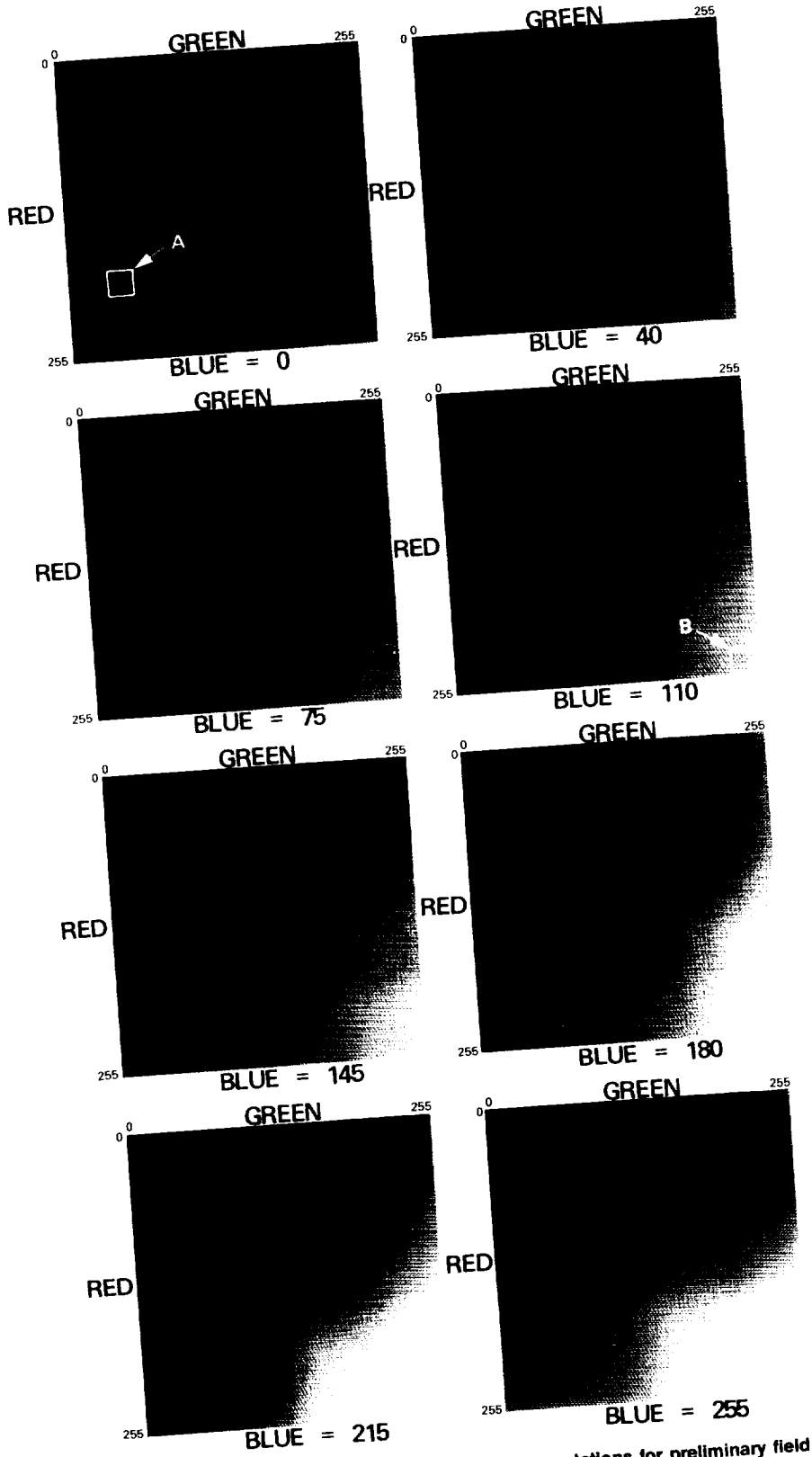

Figure 12-32. DN color key used for tonal/textural unit interpretations for preliminary field vegetation map 3. An interpreter would assign DN red ~190, green ~60, blue ~0 to a red-toned image area corresponding in color to A; red ~255, green ~255, blue ~110 to a yellow-toned image area corresponding in color to B.

6. Determination of optimal NS-001 vegetation classification

a. Introduction. In an attempt to more rigorously select an optimal combination of NS-001 bands and ratios for mapping vegetation, an approach using UCLA BMD discriminant function analysis was tested. Ideally, discriminant analysis using the seven VNIR bands and 21 ratios for the 35 training areas as variables could indicate an optimal combination for assigning training pixels to vegetation classes. Because of inherent constraints in the JPL VICAR preprocessor program, which makes image DN data compatible with this BMD program, there is a limit of 10 input variables. This restriction made it impossible to rigorously apply BMD discriminant analysis to the set of 28 NS-001 variables. Since there are more than 1.3×10^7 ways to choose 10 objects from a group of 28, it was not feasible to analyze all possible combinations. The only practical solution to this dilemma was to reduce the number of combinations. If, after some of the original variables were excluded according to some selection criterion, fewer than 10 remained, the BMD discriminant analysis could be used, although some of its usefulness would be lost. If more than 10 remained, it would be impossible to choose the 10 best variables to be used as input without defeating the purpose of the analysis.

b. Analysis. As a first step in the reduction process, the raw bands were considered separately. The results of this analysis are summarized in Table 12-17. In order of decreasing importance, the three best NS-001 bands for vegetation classification of these Lost River data are bands 6, 3, and 5. Interestingly, Conel et al. (1978, p. 5-33) demonstrated that data equivalent to band 6 data were also the best raw band data for the classification of a suite of rock spectra from Utah and Wyoming.

For the next step in the discriminant analysis, some initial screening of the NS-001 band ratios was required. The choice of 10 of the 21 ratios for this step was based on their histograms for the training areas. Those ratios that exhibited non-Gaussian (multimodal) distributions were identified. Ten of the 21 ratios exhibited multimodal distributions. Table 12-18 summarizes the results of this step in the discriminant analysis. Of the selected ratios, the four best, in order of decreasing importance, are 1/6, 3/6, 4/6, and 5/6. Interestingly, these ratios all contain band 6, further emphasizing the significance of this band for vegetation classification at the Lost River test site.

Five more steps in the reduction process involved discriminant analyses using the remaining ratios in various combinations with the three raw bands and four ratios

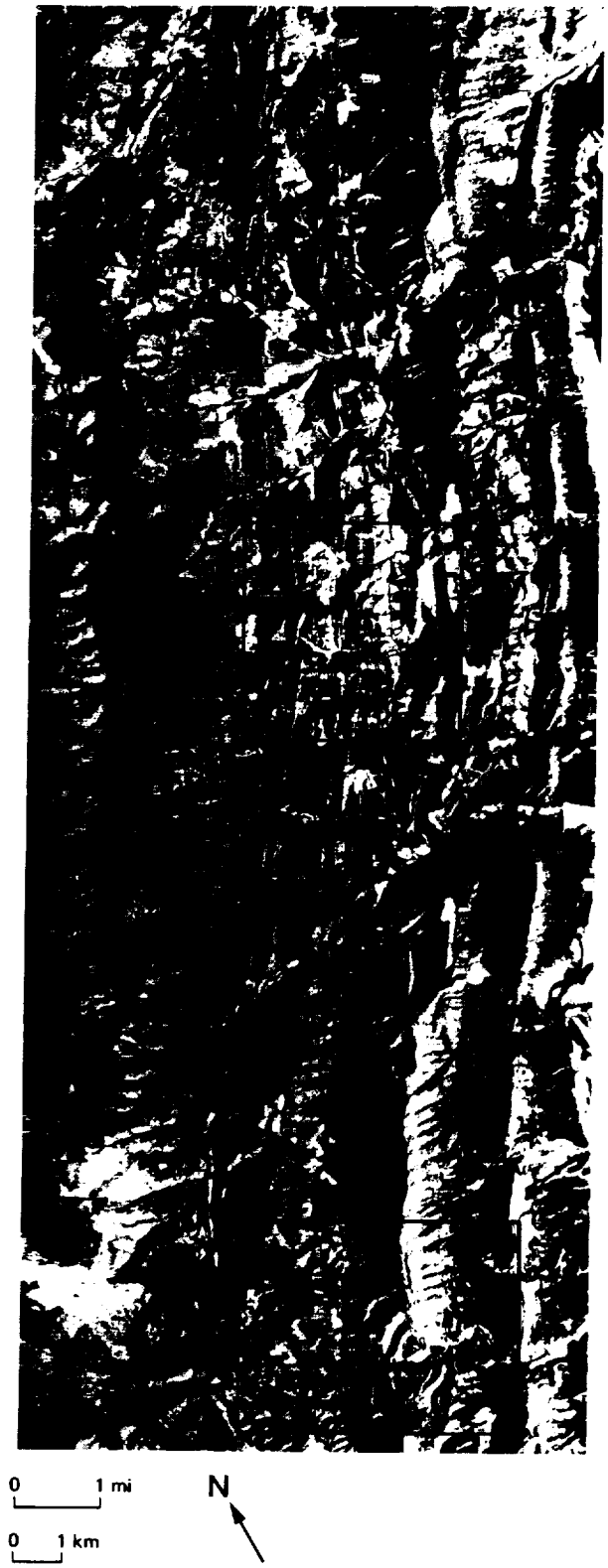

Figure 12-33. Outlines of 35 training areas used in the supervised vegetation classification map plotted on the NS-001 band 4 image. Areas outlined are enlarged and shown in Figures 12-34 and 12-35.

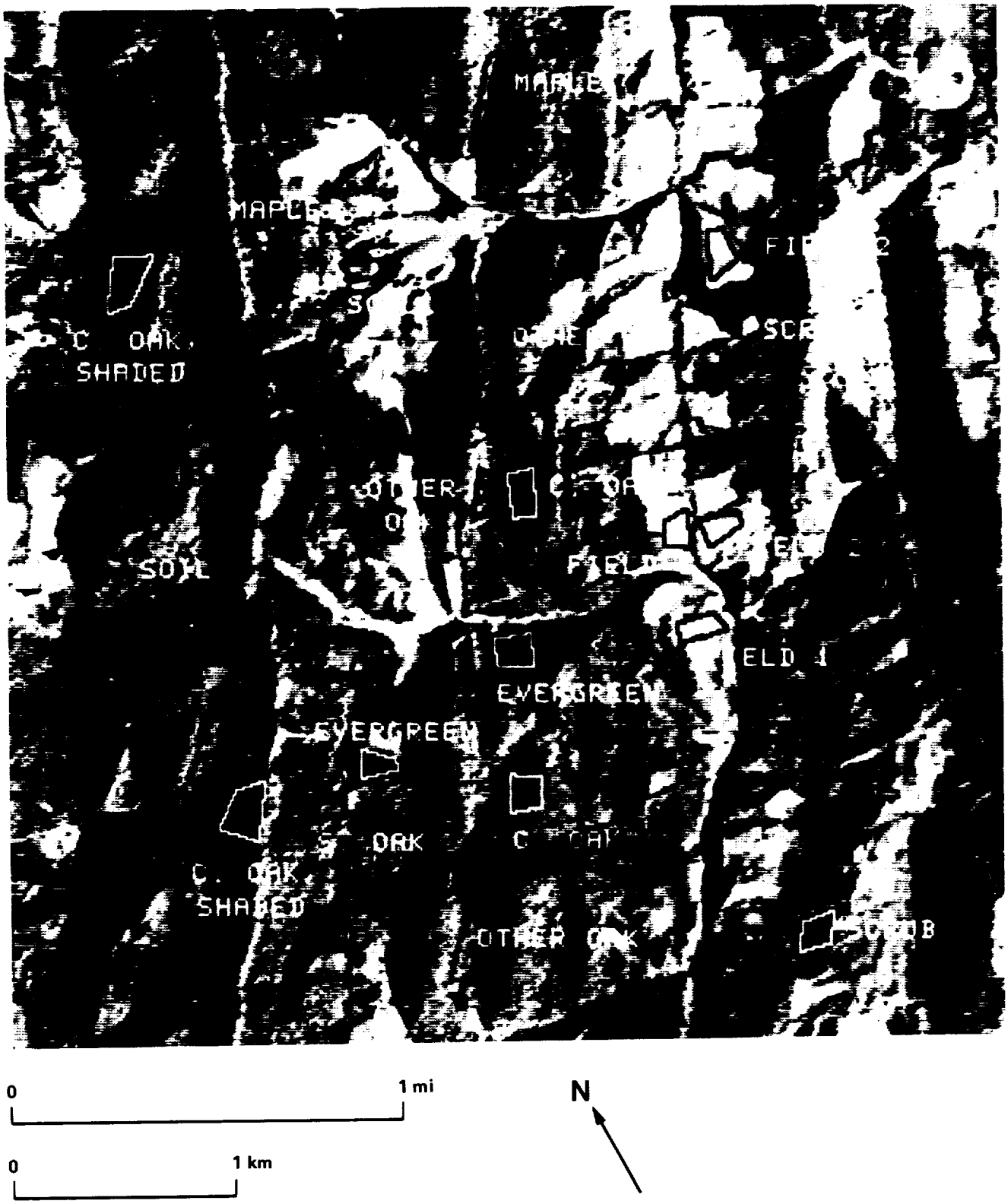

Figure 12-34. Outlines of 20 training areas in the northern part of the test site used in the supervised vegetation classification map

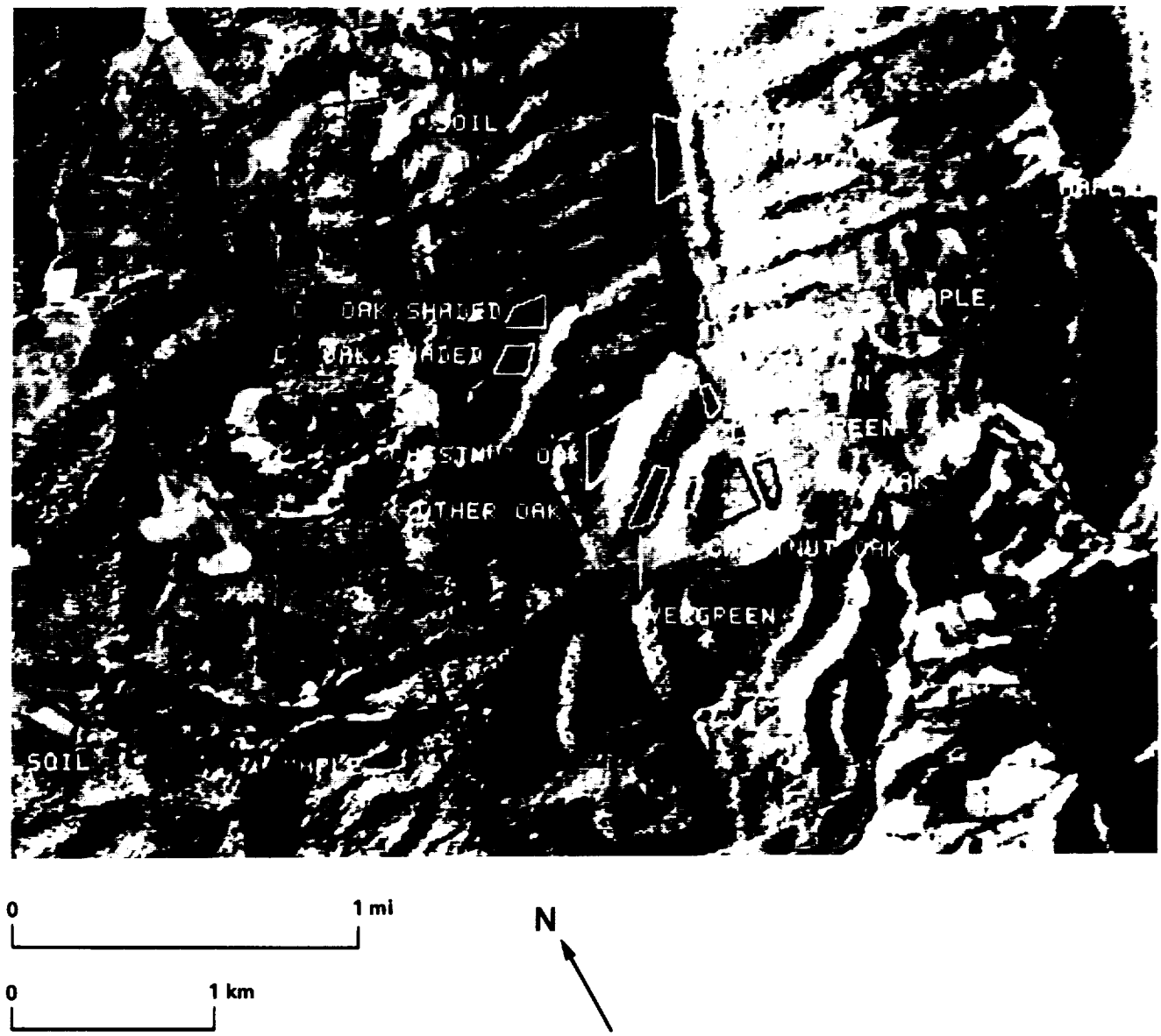

Figure 12-35. Outlines of 15 training areas in the southern part of the test site used in the supervised vegetation classification map

selected above. The optimal five-variable classification determined in this procedure is summarized in Table 12-19. Based on this analysis, the five best of the original 28 variables are, in order of decreasing importance, 6, 3/5, 4/5, 5, and 3/6. These variables were used in the VICAR programs STATS and FASTCLAS to produce a supervised vegetation classification map (Figure 12-37).

The BMD training area statistics for the Figure 12-37 classification, summarized in Table 12-19, indicate that the most accurately classified groups are Field 1 (99 percent) and Field 2 (98 percent); the least accurately classified are Other Oak (27 percent). The most significant misclassifications indicated by the BMD analysis are Evergreen as Scrub; Chestnut Oak as Other Oak; Scarlet Oak as Other Oak; most Other Oak as Chestnut Oak or Scarlet Oak; Maple as Scarlet Oak or Other Oak; Soil as Chestnut Oak Shaded; and Scrub as Evergreen.

A preliminary field comparison of Figure 12-37 (the 6, 3/5, 4/5, 5, and 3/6 classification) to Figure 12-36 (the 2, 3, 4, 4/5, and 5/7 classification), in the area of the prelimi-

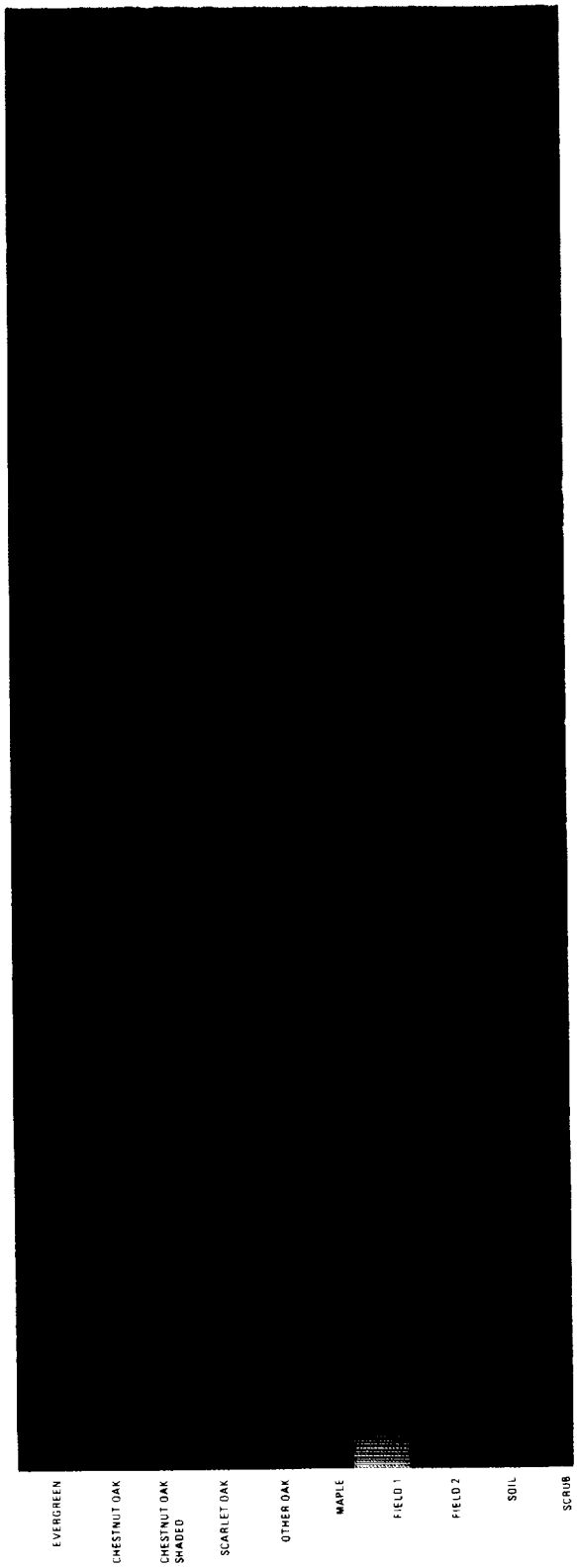

Figure 12-36. Supervised vegetation classification map produced using NS-001 (Mission 431) bands 2, 3, 4, 5, and 7 in the following combinations: 2, 3, 4, 4/5, 5/7. Note the color key at the bottom of the image.

nary field vegetation map 3 (Figure 12-16), demonstrated that both images provide an accurate classification of the forest cover. Somewhat surprisingly, the version that was considered best by the site botanist, based on a qualitative field comparison, is the first classification, which was not based on the more "rigorous" BMD selection of optimal bands for vegetation classification. This implies that the difference in classification accuracy indicated by the training area statistics for the two (step 5, Table 12-15 versus Table 12-19) is not significant (70 versus 71 percent mean percentage correct).

Review of training area classification accuracy from the eight BMD discriminant analyses provides insight into the "optimal" band selection problem. Table 12-20 shows the maximum correct classification for each of the 10 vegetation classes. All classification maxima occur when five or fewer variables are included, even though six steps were used in two of the BMD runs. Band 6 is ubiquitous, again adding credence to its usefulness in vegetation classification.

Figure 12-38 shows the field of mean class correct classification versus number of variables entered for all steps of the eight BMD stepwise discriminant analyses. The distribution shown implies that optimal overall classification is accomplished with *any* four to five input variables, and may explain the apparent equivalence of the "subjectively" selected five-variable vegetation classification and the "rigorously" selected version. This apparent classification optimization with five variables was also noted by Conel et al. (1978, p. 5-37–5-41) in a discriminant analysis of a suite of rock spectra from Utah and Wyoming.

Alternately, the equivalency of the two classifications may demonstrate:

(1) Inability to objectively test all possible combinations of variables due to computing limitations

(2) Inaccuracies in the original training area designations

(3) Classification bias due to unequal class sizes

C. Conclusions

An analysis of two supervised vegetation classifications using training area statistics from NS-001 Mission 431 data acquired for the Lost River test site demonstrates that:

(1) Simple NS-001 band-ratio or composite band-ratio images provide inadequate information for forest vegetation mapping.

(2) NS-001 band 6 is the best single band for classification purposes.

(3) Optimal forest vegetation classification accuracy is provided by supervised classification processing using five NS-001 bands and band ratios as input variables.

(4) The loss of information due to 3 by 3 filtering of the 15-m data acquired for this study implies that spatial resolution finer than 45 m is needed for accurate forest vegetation classification.

(5) Although a BMD discriminant approach for optimal NS-001 variable selection may be useful, the VICAR preprocessor restriction of 10 input variables severely limits its applicability to these data. An image processing version of this program, for use with NS-001 data, should accept 28 input variables.

Table 12-15. Discriminant function results: bands 2, 3, 4, 4/5, 5/7

Lost River Vegetation Analysis — NS-001
BMD Discriminant Function — Mission 431
Band and Band-Ratio Input Variables: 2, 3, 4, 4/5, 5/7

Group/Total Pixels	Vegetation Correctly Classified, %				
	Step 1[a]	Step 2[b]	Step 3[c]	Step 4[d]	Step 5[e]
Evergreen/352	65	62	78	76	77
Chestnut Oak/1025	1	65	61	62	62
Chestnut Oak Shaded/593	57	53	76	76	77
Scarlet Oak/41	39	29	49	51	54
Other Oak/508	0	29	30	31	31
Maple/99	24	26	41	72	72
Field 1/168	85	87	98	98	98
Field 2/174	50	84	88	93	94
Soil/298	80	80	80	81	81
Scrub/216	22	23	49	52	53
Mean Percent Correct	42	54	65	69	70

Variable entered, μm: [a]0.66 [b]0.83/1.15 [c]0.83 [d]0.56 [e]1.15/2.22

Table 12-16. Discriminant function results: bands 2, 3, 4, 4/5, 5/6

Lost River Vegetation Analysis — NS-001
BMD Discriminant Function — Mission 431
Band and Band-Ratio Input Variables: 2, 3, 4, 4/5, 5/6

Group/Total Pixels	Vegetation Correctly Classified, %				
	Step 1[a]	Step 2[b]	Step 3[c]	Step 4[d]	Step 5[e]
Evergreen/352	65	62	78	76	77
Chestnut Oak/1025	1	65	61	62	62
Chestnut Oak Shaded/593	57	53	76	76	77
Scarlet Oak/41	39	29	49	51	54
Other Oak/508	0	29	30	31	31
Maple/99	24	26	41	72	72
Field 1/168	85	87	98	98	98
Field 2/174	50	84	88	93	94
Soil/298	80	80	80	81	81
Scrub/216	22	23	49	52	53
Mean Percent Correct	42	54	65	69	70

Variable entered, μm: [a]0.66 [b]0.83/1.15 [c]0.83 [d]0.56 [e]1.15/1.65

Table 12-17. Discriminant function results: bands 1, 2, 3, 4, 5, 6, 7

Lost River Vegetation Analysis — NS-001
BMD Discriminant Function — Mission 431
Band Input Variables: 1, 2, 3, 4, 5, 6, 7

Group/Total Pixels	Vegetation Correctly Classified, %		
	Step 1[a]	Step 2[b]	Step 3[c]
Evergreen/352	75	70	75
Chestnut Oak/1025	45	40	38
Chestnut Oak Shaded/593	28	70	81
Scarlet Oak/41	22	10	42
Other Oak/508	9	30	13
Maple/99	24	37	71
Field 1/168	98	99	96
Field 2/174	58	95	97
Soil/298	47	79	80
Scrub/216	14	35	24
Mean Percent Correct	42	57	62

Variable entered, μm: [a]1.65 [b]0.66 [c]1.15

Table 12-18. Discriminant function results: band-ratios 1/6, 1/7, 2/7, 3/6, 3/7, 4/6, 4/7, 5/6, 5/7, 6/7

Lost River Vegetation Analysis — NS-001
BMD Discriminant Function — Mission 431
Band-Ratio Input Variables: 1/6, 1/7, 2/7, 3/6, 3/7, 4/6, 4/7, 5/6, 5/7, 6/7

Group/Total Pixels	Vegetation Correctly Classified, %			
	Step 1[a]	Step 2[b]	Step 3[c]	Step 4[d]
Evergreen/352	13	10	36	68
Chestnut Oak/1025	18	22	66	68
Chestnut Oak Shaded/593	74	72	69	74
Scarlet Oak/41	0	73	29	46
Other Oak/508	6	32	23	29
Maple/99	12	60	52	63
Field 1/168	70	88	99	98
Field 2/174	32	80	97	97
Soil/298	81	81	81	80
Scrub/216	80	36	63	60
Mean Percent Correct	32	55	62	68

Variable entered, μm: [a]0.49/1.65 [b]0.66/1.65 [c]0.83/1.65 [d]0.15/1.65

Table 12-19. Discriminant function results: bands 6, 3/5, 5, 2/4, 4/5, 1/3, 4/6, 5/6, 3/5

Lost River Vegetation Analysis — NS-001
BMD Discriminant Function — Mission 431
Band and Band-Ratio Input Variables: 6, 3/5, 5, 2/4, 4/5, 1/3, 4/6, 5/6, 3/5

Group/Total Pixels	Vegetation Correctly Classified, %				
	Step 1[a]	Step 2[b]	Step 3[c]	Step 4[d]	Step 5[e]
Evergreen/352	75	73	72	73	72
Chestnut Oak/1025	45	37	60	59	65
Chestnut Oak Shaded/593	28	48	85	82	86
Scarlet Oak/41	22	44	54	46	46
Other Oak/508	9	17	32	27	27
Maple/99	24	45	49	69	68
Field 1/168	98	99	99	98	99
Field 2/174	58	93	94	99	98
Soil/298	47	80	80	80	79
Scrub/216	14	43	63	66	69
Mean Percent Correct	42	58	69	70	71

Variable entered, μm: [a]1.65 [b]0.66/1.15 [c]0.83/1.15 [d]1.15 [e]0.66/1.65

Next variable to be entered, if continued to next step: band-ratio 2/4

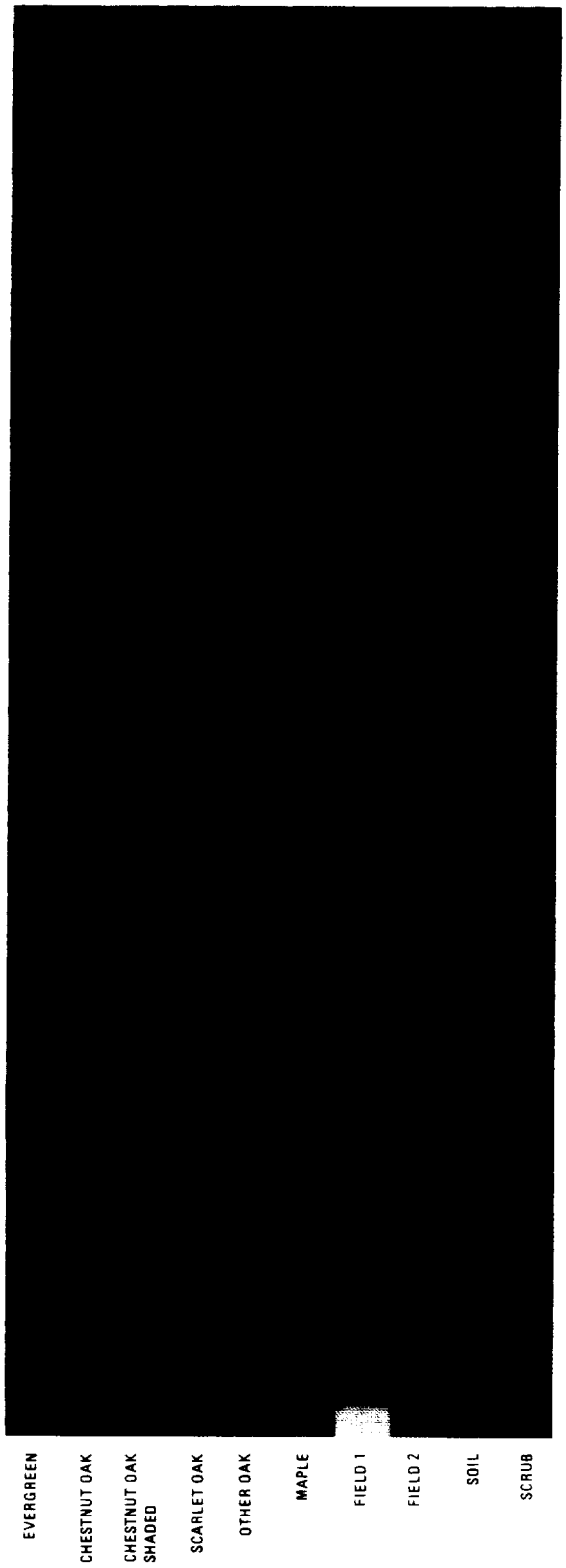

Figure 12-37. Supervised vegetation classification map produced using NS-001 (Mission 431) bands 3, 4, 5, and 6 in the following combinations: 6, 3/5, 4/5, 5, 3/6. Note the color key at the bottom of the image.

Table 12-20. Summary of results of eight BMD stepwise discriminant analysis runs showing minimum number of variables for maximum correct classification of 10 vegetation groups

Group	Maximum Correct Classification, %	Variables Included, bands and band ratios
Evergreen	76	6, 3/5, 5, 4/6, 5/6
Chestnut Oak	68	1/6, 3/6, 4/6, 5/6
Chestnut Oak Shaded	95	6, 3/5, 5, 4/6, 5/6
Scarlet Oak	73	1/6, 3/6
Other Oak	38	6, 3/5, 4/5, 2/4, 1/3
Maple	75	6, 3/5, 5
Field 1	99	6, 3/5
Field 2	99	6, 3/5, 4/5, 5
Soil	81	1/6
Scrub	69	6, 3/5, 4/5, 5, 3/6

VIII. Field Evaluation of NS-001 Supervised Vegetation Maps

A. Introduction

The evaluation of the accuracy of the two NS-001 vegetation classifications, discussed above, was based primarily on training area statistics. In June, July, and October 1981, field botanical evaluations were made to determine the accuracy of the two images. Additionally, two areas of anomalous vegetation identified on the images were studied in the field.

B. Accuracy of Supervised NS-001 Vegetation Classification Maps

Table 12-21 presents percent vegetation cover for the entire test site based on numbers of pixels assigned to each of the vegetation classes in the two supervised NS-001 vegetation classifications (Figures 12-36 and 12-37). Two sets of percentage figures are given for each vegetation classification: the first set is the raw percent figure (including unclassified pixels); the second set is the normalized percentage for each vegetation class (percent of total classified pixels representing each vegetation class with unclassified pixels removed).

Percent values of vegetation cover determined from the image classification (Table 12-21) and those based on field observations are in close agreement. Based on a preliminary field assessment made during the first year of the study, the site is approximately 80 percent forested: oaks comprise approximately 90 percent of the broadleaf forest members, and Chestnut Oaks are the most common forest

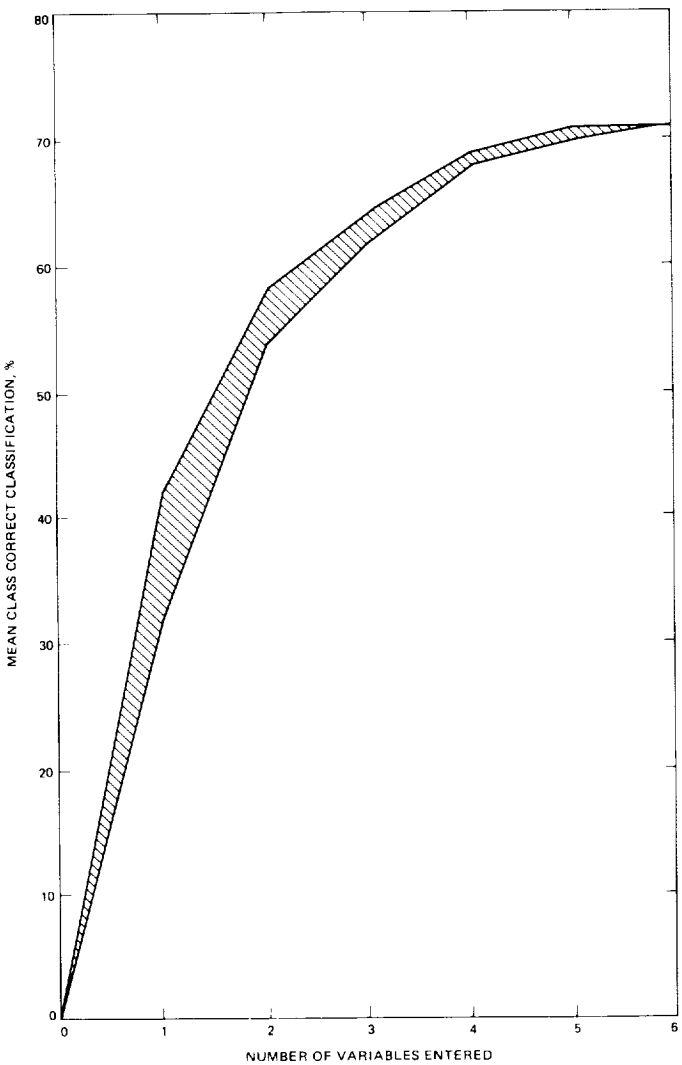

Figure 12-38. Field of mean correct classification for eight BMD stepwise discriminant analyses of training areas used in the supervised vegetation classification map

tree, representing about 40 percent of the mature trees. Table 12-22 shows the following data for Figures 12-36 and 12-37, respectively: 82 and 85 percent forest cover; 86 and 88 percent of the broadleaf forest cover are oaks, and of the forest trees, 50 and 42 percent are Chestnut Oaks. A comparison of data in Tables 12-21 and 12-22 with those in Table 12-23 (from Sturm, 1977, for Lost River State Park only) shows close agreement. It is concluded that the data presented in Tables 12-21 and 12-22 are an accurate representation of the actual vegetation cover at Lost River.

The distribution of forest cover types on the two supervised NS-001 vegetation classification maps is similar (for comparison, see Figure 12-39). In July 1981, 0.1-acre circle plot analyses were conducted at 289 forested sites to check the classification accuracy. Analysis sites were selected based on study of the two classifications; areas determined to be of interest were then located in the field and analyzed. Analyses at another 36 sites were also available from data acquired during preliminary botanical studies of the test site. Approximately 90 percent of the sites analyzed were dominated by the type of vegetation indicated by class assignments on one or both supervised classification images.

Of the total number of pixels per image, only 7 to 8 percent are unclassified (Table 12-21). Of the unclassified pixels, the vast majority are associated either with clouds or fields. Because the purpose of the image classifications was to determine the distribution of forest cover types, little effort was made to develop classifications that would discriminate among the many field and pasture conditions occurring at the site.

Table 12-24 presents a description for each of the vegetation classes recognized on the supervised NS-001 vegetation classification maps for the Lost River test site. In

Table 12-21. Percentage of vegetation cover at the Lost River test site

NS-001 Bands Used in Supervised Vegetation Classification	Occurrence of NS-001 Supervised Vegetation Classes, % of total										
	Unclassified	Evergreen	Chestnut Oak	Chestnut Oak Shaded	Scarlet Oak	Other Oak	Maple	Field 1	Field 2	Soil	Scrub
Figure 12-36 (bands 2, 3, 4, 4/5, 5/7)											
Percentage[a]	6.9	3.6	20.1	18.3	9.7	16.6	8.3	1.2	2.0	5.7	7.6
Normalized percentage[b]		3.9	21.8	19.8	10.5	18.0	9.0	1.3	2.2	6.2	8.2
Figure 12-37 (bands 6, 3/5, 4/5, 5, 3/6)											
Percentage[a]	8.4	3.8	19.8	13.2	12.0	20.2	9.1	1.0	1.3	5.6	5.6
Normalized percentage[b]		4.1	21.7	14.4	13.1	22.1	9.9	1.1	1.4	6.1	6.1

[a]Percentage of pixels over the entire field assigned to this class.
[b]Normalized percentage for each class (i.e., unclassified pixels removed).

Table 12-22. Summary of vegetation cover percentage data for the Lost River test site

Vegetation Class	Figure 12-36, % cover	Figure 12-37, % cover
Forest Cover	82	85
Total Fields	4	2
Fields and Soil	11	9
Chestnut Oak[a]	50	42
Scarlet/Pin Oak[a]	13	15
Other Oak[a]	22	26
Maple[a]	11	12
Evergreen[a]	5	5
Total Oaks[b]	86	88

[a] Percentage of total forest categories represented by this class (Field 1, Field 2, Soil, and Scrub not considered).
[b] Percentage of broadleaf trees represented by oaks (Evergreen, Field 1, Field 2, Soil, and Scrub not considered).

Table 12-23. Major cover types of Lost River State Park, their areal extent in acres, percent of the forests of the state park they comprise, and number of stands sampled[a]

Cover Type	Acreage	Percentage	Number of Stands Sampled
Pine	209	6.7	4
Chestnut Oak	1103	35.6	4
Mixed Oak	923	29.6	4
White Oak/White Pine	85	2.6	b
Red Oak	764	24.5	7
Hemlock/Hardwood	32	1.0	b

[a] Taken from Sturm (1977, p. 133).
[b] Unsampled cover type.

addition to describing the various species associations, Table 12-24 also presents classification problems associated with each class.

One of the consistent misclassifications in both supervised classifications is the incorrect classification of many areas in shadow as Evergreen. This is not surprising since evergreens occurring at Lost River (several species of pines plus hemlock) display very low reflectance in all NS-001 bands, a feature which is likely due to low reflective surface of leaves (needlelike in both genera) coupled with a large shadow component associated with individual tree crowns.

The addition of the Chestnut Oak Shaded class for the Figure 12-36 and 12-37 classifications improved the classification accuracy when compared with the original Gulf version. Fewer shadows were misclassified as Evergreen, and distribution patterns of Chestnut Oak shown on the Figure 12-36 and 12-37 classification maps were more accurate portrayals of actual ground conditions.

Evergreens are misclassified as Scrub because scrub growth frequently consists of young evergreens and/or Black Locust (which present low reflectance in all bands due to small leaflets of compound leaves and a large shadow component). Many of the areas classed as Scrub are mixes of pine and broadleaf trees; thus, the scrub image class includes a variety of pine/hardwood associations.

The other consistent classification problem recognized during field evaluation involves considerable variation in cover composition at sites classified as Scarlet Oak or Other Oak. The areas classed as Scarlet Oak frequently have a sizable component (20 to 40 percent) of Chestnut Oak and/or White Oak. In a similar manner, Scarlet Oaks are a common component in areas classified as Other Oak (a class originally designated for mixes of White Oak and Black Oak) or Chestnut Oak. Further detailed field evaluation could provide more precise training area designations to help alleviate this type of classification problem.

Based on field studies, the two most widely occurring species of oak over the entire study area are the Chestnut Oak and the Scarlet/Pin Oaks. These two species nearly always occur together, with the Chestnut Oak predominating on the ridge top and west-facing slopes, while the Scarlet/Pin Oaks predominate in valleys and bottomland. Frequently, the areas classed as Other Oak on both classification images are more correctly a mix of Chestnut Oak, Scarlet/Pin Oaks, and White Oak. Field data suggest that the class Other Oak should be renamed Mixed Oak.

The areas classed on both vegetation classification maps as Chestnut Oak are seldom pure stands of Chestnut Oak. Scarlet/Pin Oaks are commonly found in association with Chestnut Oaks, with White Oaks and an occasional Black Oak also occurring at these sites. Chestnut Oaks do predominate at these sites, however, and the class designation remains appropriate.

The Scrub category is the least accurately assigned class in either classification. Since this category is botanically the least well defined (scrub growth may consist of any number and/or combination of locally available "weed" trees such as pines, Red Maple, and Black Locust), such a result is to be expected. In many cases, the mixed broadleaf and evergreen community immediately surrounding a stand of evergreen is classed as Scrub. The low reflectance values associated with both pines and Black Locust lead to misclassification of the latter as Evergreen (especially in Figures 12-36 and 12-39c). Shadowed evergreen/hardwood

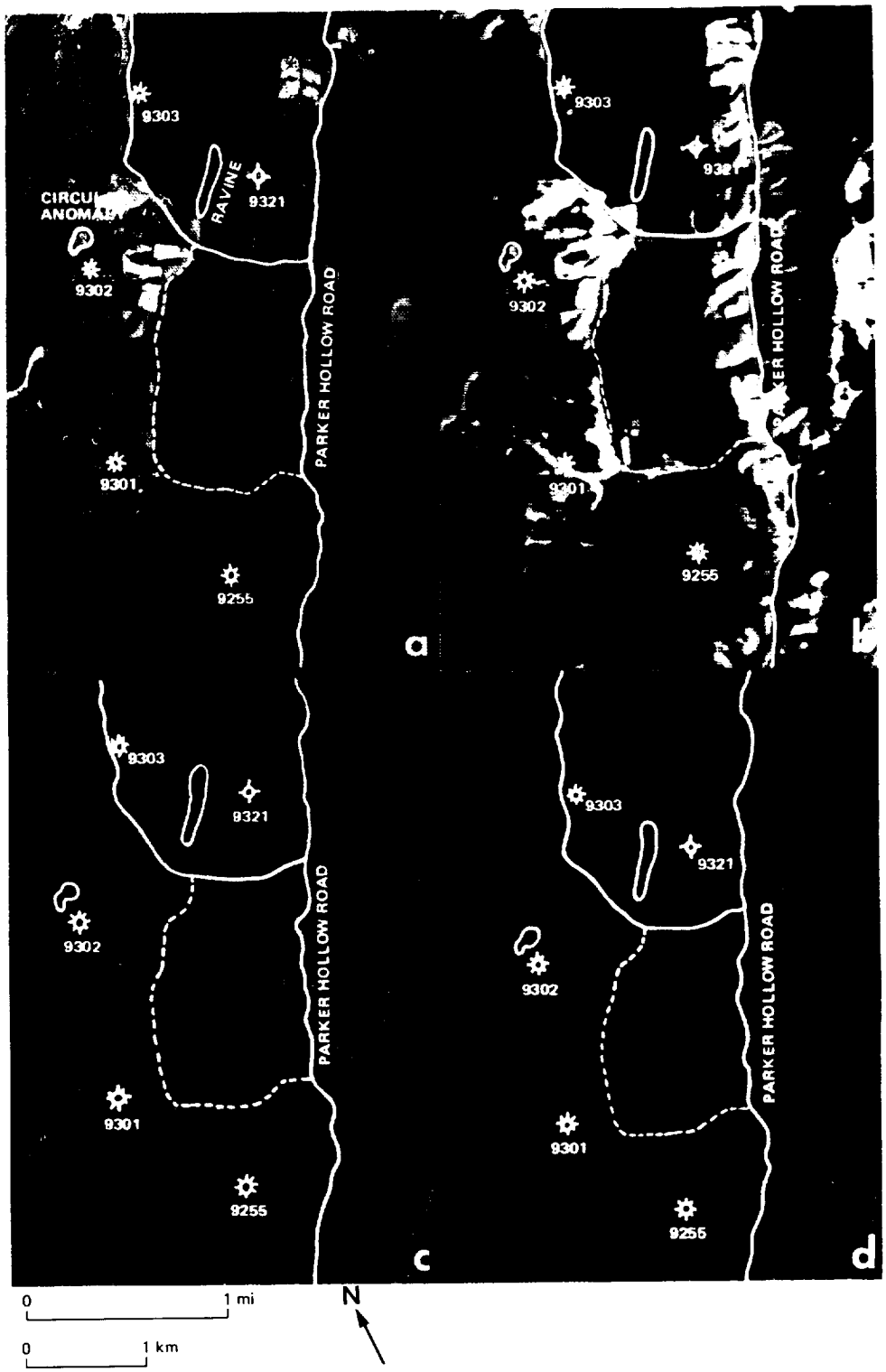

Figure 12-39. Aerial CIR and NS-001 images of the area covered by preliminary field vegetation map 3 (all data derived from October 21, 1980 overflight, Mission 431): (a) aerial CIR. Note subtle variations in color and texture denoting distribution of Chestnut Oaks (greenish, fine-textured canopy), Evergreens (dark reddish-brown, very fine texture), Other Oaks (light brown, somewhat coarse-textured), and Maples (yellow; note anomaly sites); (b) NS-001 bands 2, 3, and 4, designed to simulate the aerial CIR photograph. Note how subtle color differences seen in CIR are enhanced in this image (Chestnut Oaks are now distinct from Other Oaks and within Other Oaks, differences are seen that allow separation of Scarlet Oaks from the remaining oaks); (c and d) supervised vegetation classification maps produced using bands 2, 3, 4, 5, 6, and 7 in the following combinations: (c) 2, 3, 4, 4/5, 5/7, and (d) 6, 3/5, 4/5, 5, 3/6. Note the similarities and differences between the two.

Table 12-24. Description of vegetation classes recognized at the Lost River test site

Class	Description	Problems
Evergreen	Any needle-leaf conifer. Most commonly a species of pine (see Table 12-9a); but may also include Hemlock and Red Cedar. Limited hardwood species may also occur in stands of forest trees recognized in this class.	Shadows included in this class. Some Evergreens are included in the Scrub class.
Chestnut Oak	A forest stand dominated (50 percent or more) by mature trees (6-in. dbh or greater) of Chestnut Oak. Common associates are Scarlet/Pin Oaks and White Oaks. Seldom does *Quercus prinus* occur in pure stands (90 to 100 percent).	Some areas included in this class should be classed as Other Oak.
Chestnut Oak Shaded	Same as above (Chestnut Oak), but shaded as seen in aerial data acquired October 21, 1980 (Mission 431). Since the Chestnut Oaks commonly occur on steep west-facing slopes (partly shaded when the data were acquired), development of this class greatly improved the accuracy of the vegetation images.	None
Scarlet Oak	Includes both Red Oak and Scarlet/Pin Oaks as the dominant species. Commonly includes Chestnut Oak and White Oak. Never occurs in pure stands at this site. Common in ravine bottoms and valleys but may also be found on slopes. This is the second most heterogeneous species association.	Due to the complex nature of this heterogeneous class, this may be classed as Other Oak.
Other Oak	The most heterogeneous class found on the site. This class is assigned to any mixed oak association. Commonly represents mixes of White Oak, Chestnut Oak, and Scarlet/Pin Oak. Any mix of oak in which no single species predominates (50 percent or more) is likely to be so classed. Should be designated Mixed Oak.	Too heterogeneous. Areas that should be classed as Chestnut Oak are placed here.
Maple	Since maples, hickory, Sassafras, and birch all exhibit similar fall foliage coloration (yellow to orange), all of these genera are grouped in this class. Common on east-facing slopes and bottoms of valleys and ravines.	This category is not accurately assigned. In both maps, fields with some growth are classed here.
Field 1	Any field with a high albedo—usually the result of drying or brown stubble (much of the pastureland in late October). Many of these types of field are unclassified, especially in the second vegetation map (Figure 12-37).	This field type is not accurately classed—commonly unclassed (black pixels) or classed as Soil.
Field 2	Fields with living, green plant cover. Commonly lawns and grazed pasturelands. This is a very heterogeneous category and could be broken into two or three classes.	This field type may be classed as Maple. May also be unclassed. Too variable in signature.
Soil	Any area where bare soil and/or rock is exposed. Commonly driveways, dirt roads, plowed fields, and outcrop sites. Has the highest albedo of all the classes.	Commonly confused with clouds or Field 1.
Scrub	Any mix of evergreen and woody broadleaf vegetation. Represents a common but temporary stage in succession at this site. Commonly old fields or areas of previous lumbering activities.	This vegetation category may be classed as Evergreen. May also be unclassed (black pixels).

mixes may be classed either as Scrub or Evergreen, depending on the extent of shadow effect.

The Maple class should be subdivided for a more accurate representation of actual species distribution. As stated previously, Sugar Maple, hickory, and birch all exhibit similar reflectance spectra during fall foliage display at Lost River. For example, Red Maple ranges in color from orange to red and, thus, may be classed with Scarlet Oak. In the future, an attempt should be made to discriminate among these taxa, based on textural variation, slight spectral variations, and elevation and/or slope characteristics.

Both NS-001 supervised vegetation classification maps are approximately 90 percent accurate in the assignment of forest areas. Correct assignment of Field and Soil classes is approximately 70 percent. Most classification errors are the result of either shadow effects or inadequacies of the original training area designations.

C. Comparision of the Two Classifications

A field comparison was also made between the two supervised NS-001 vegetation classification maps (Figures 12-36 and 12-37). Each classification has advantages and disadvantages.

Figure 12-39 provides a comparison of four images used for vegetation mapping. All four cover an area roughly equivalent to the preliminary field vegetation map 3 (Fig-

ure 12-16). Figure 12-39 may be used to make direct comparisons between Figures 12-36 and 12-37.

Figure 12-36 recognizes more Chestnut Oak, primarily at shaded sites. These same sites tend to be classed as Other Oak and/or Scarlet Oak in Figure 12-37. Field checks of these sites showed that varying amounts of Chestnut Oaks, Scarlet/Pin Oaks, and White Oaks are present.

Figure 12-36 does the best job of classifying fields accurately. More fields are recognized, especially Field 1 (dry fields exhibiting high albedo), on this map. Figure 12-37 frequently does not recognize this type of field, displaying it either as Soil or Unclassified. Some Field 2 areas (fields or pastures with green vegetation cover) that are correctly classified in Figure 12-36 are misclassified as Maple in Figure 12-37. Figure 12-36 tends to classify weedy fields (heavy herbaceous weed cover) as Scrub, while Figure 13-37 fails to classify them at all. Neither classification does an adequate job of classifying fields, but Figure 12-36 is better than Figure 12-37.

Figure 12-37 classifies more areas as Maple, but as indicated above, many of these areas are actually fields (Field 2 type). More restricted distribution of maples is displayed in Figure 12-37 at the higher elevations, and this seems to represent a more accurate portrayal of ground conditions.

Figure 12-37 has more unclassified pixels (8.4 versus 6.9 percent for Figure 12-36), mostly associated with fields. Most unclassified pixels in Figure 12-36 are clouds (these same areas are classed as Soil in Figure 12-37) and cloud shadows. The combined effect of these various misclassifications is that Figure 12-36 more accurately displays Chestnut Oak and Field classes, while Figure 12-37 more correctly displays the higher elevation distribution of Maple.

The two classification maps are best used in combination. Based on fieldwork, Figure 12-36 presents a slightly more accurate representation of ground conditions, but there s little significant difference between the two maps (as can e seen by comparing Figures 12-39c and 12-39d).

. Anomalous Vegetation Distribution

At two sites, anomalously high concentrations of maples e displayed on the two supervised vegetation images in area referred to as the Funkhouser study site (much of e property included within this site is owned by Charles nkhouser; see Figure 12-11).

The two NS-001 supervised vegetation classification maps gures 12-39c and 12-39d) show a linear pattern of maple parallel to a narrow ravine (running NE–SW) at this site. A detailed field study (80 vegetation analysis plots) of this ravine confirmed a concentration of Red Maples, corresponding roughly with the bottom of the ravine and the immediate (within 100 ft) west-facing slope (61 percent of the circular plots along the bottom of the ravine were dominated by Red Maple, as were 66 percent of the plots on the west-facing slope).

At most plot sites dominated by Red Maple, the trees are approximately 15 to 20 years old and occur in clumps (clones). Extensive cloning has occurred at many of the plot sites as a result of earlier logging activities, with 10 or more trunks (stump sprouts) commonly occurring per clone, each cluster surrounding an old stump. The number of growth rings on the old stumps indicates that the original maples were approximately 30 years old when cut (thus heavy concentrations of Red Maple have occurred at this site for approximately 45 to 50 years). The heavy growth of maples at this site forms dense thickets in the ravine and to the east. This area, indicated in Figures 12-11 and 12-39(a) as "ravine," is seen in a low-altitude aerial view in Figure 12-40(a).

These field observations suggest that the Red Maple (normally a weed tree and, thus, commonly replaced by climax vegetation such as oak) has been well established at this site for at least 45 years. When the Funkhouser ravine locality is compared with other similar sites (550- to 615-m elevation; narrow NE–SW ravine surrounded by 30 to 60 percent slope; identical soils), such a high concentration of maples is indeed unusual. Vegetation analyses conducted at three similar sites indicate mixed oak communities are typical.

Initially, it was assumed that the anomalous linear concentration of maple at the Funkhouser ravine locality represented a cultural feature such as a logging site, old field, or farm road. The fact that an old farm road, leading to a hunting blind, follows the eastern edge of the ravine bottom would seem to support this assumption. Discussions with the landowner concerning recent logging activities suggest that the ravine site had been selectively logged (only the large, valuable timber removed) in the late 1950s or early 1960s. Stumps and cloning along the ravine bottom and to the east are certainly evidence of recent limited logging activities at the site.

The farm road appears to be currently used only up to the hunting blind (one-third of the way up the ravine, beginning from the southwest end), and is heavily overgrown above this point. Study of black-and-white aerial photographs (acquired October 10, 1959) accompanying the

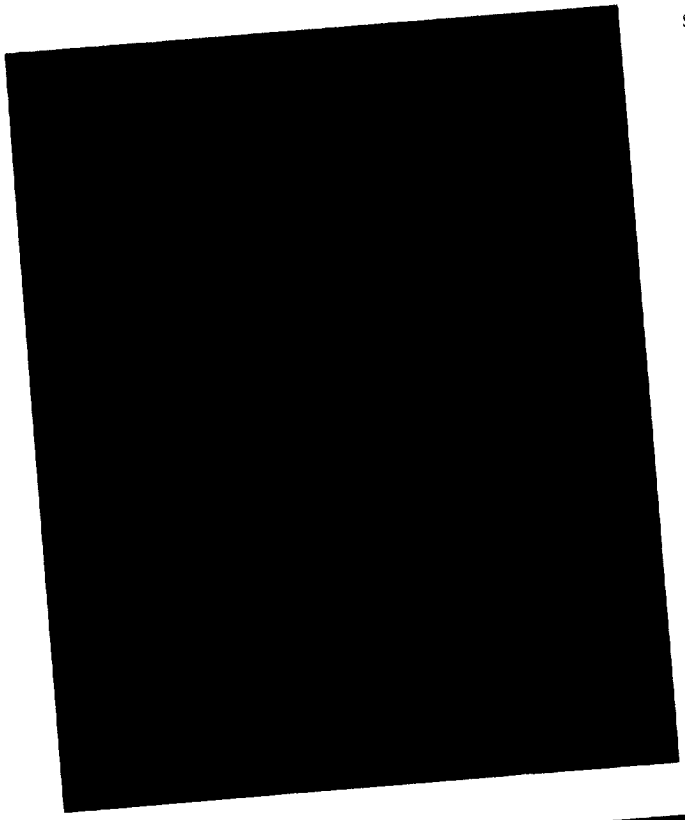

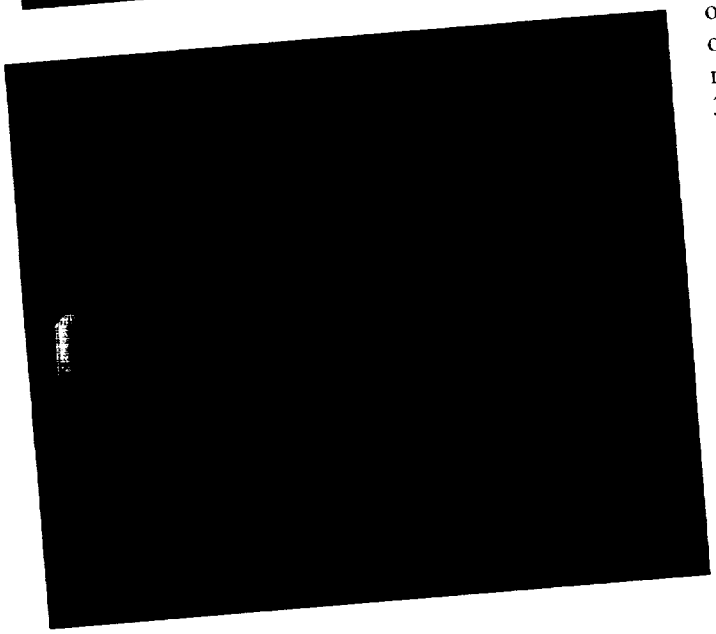

Figure 12-40. Maple anomaly sites (both photographs were taken October 15–19, 1981): (a) the Funkhouser ravine site seen from the air, looking northeast. Note the linear strip of defoliated trees (insect predation) and the slight show of color (muted due to overcast conditions); (b) the Funkhouser circular anomaly site seen from the ground, looking northwest. Colors of the maples appear brighter here in comparison to (a) due to the full-sun condition. Note the tree (a White Oak) in the foreground, defoliated by insects. (The same silo is seen in both pictures.)

soils survey for Hardy County (Soil Conservation Service, 1979) gives no evidence of extensive logging or disturbance associated with the farm road at the ravine site prior to 1959 (assuming that all regrowth at this site has occurred since 1935 when a 15-year period of heavy logging throughout the test site ended). The maple and oak stumps seen at the site are probably the result of limited logging since 1959 (those stumps determined to have been 30 years old when cut would have been cut around 1965). There is evidence of limited logging (stumps) seen above the hunting blind, but the large number of mature, valuable timber trees growing above the blind suggests that much less logging occurred along the northern two-thirds of the ravine. To the north of the ravine, extensive and recent (1974 according to Mr. Funkhouser) logging has occurred, resulting in widespread scrub growth (Black Locust) above the anomaly site (classed as Evergreen in Figure 12-39c and as Scrub in Figure 12-39d).

Since the disturbance due to logging must be post-1959 (approximately 1965), the extent of regrowth of maple at the ravine is surprising. The road is narrow (0.2 to 2.5 m wide), and in no case should disturbance of the canopy due to road activity exceed 4 to 6 m on either side of the road. The maples extend for 45 to 60 m, mostly to the east of the road and ravine bottom. The most extensive stands of maple occur above (north of) the hunting blind where most maples and other woody species are large and at least 30 years old (and in some cases 70 years old).

In the October CIR aerial photograph (Figure 12-40a), some opening in the canopy along the farm road is seen, but few maples are seen at these openings. Most of the maples occur to the north and east of these openings. It is clear that the maples are well established at this site and have been so since 1935 (possibly earlier). It is concluded that the anomalously high concentration of maples at this site is not related to the road or recent (1965) logging activities and may be related to some feature(s) other than cultural.

The soil type at this site is Berks Channery (Plate 12 and Table 12-5), a well-drained, silt-loam soil of shallow depth (5 to 12 cm deep). It is rated as having a low to very low water-holding capacity, is acidic, and is poor for farming. Soil at the site is very sandy and/or rocky. This is the same soil type found extensively over much of the gas field. The slope on the west side of the ravine is steeper (35 to 50 percent) and rockier, while the eastern side has a more gentle slope (25 to 35 percent) with few exposed rocks.

Red Maples are not selective in terms of soil-type preference (Table 12-25), occurring in soils ranging from swa

clays to the more xeric sandy loams of the hardwood forests (Core, 1966). Although Red Maple apparently does best in swampy, wet areas, it also occurs on hillsides and ridges throughout West Virginia (Core and Guthrie, 1977). It is a common pioneer plant associated with secondary plant succession in recently cleared areas and is also a common associate with the more permanent climax species (various oaks and hickories) characteristic of the Ridge and Valley region of the state (Core, 1966).

According to the two supervised NS-001 vegetation classification maps, maples are commonly scattered in their distribution, preferring east-facing slopes and higher ridge tops (above 740 m), and seldom form pure stands except at higher elevations. The pure stands of maple seen on the east sides of South Branch Mountain and Big Ridge, which have been field checked, are composed of Sugar Maple rather than Red Maple.

Since the soil type at this site is typical for the entire field, it would seem unlikely that the occurrence of high concentrations of Red Maple is controlled solely by soil type. The higher soil moisture conditions at the ravine bottom (a spring is located near the hunting blind) are likely to be more favorable for all plant growth, as demonstrated by a dense undergrowth of grape vines, huckleberries, Black Locust, and a variety of herbaceous weeds (including numerous unidentified species of *Aster* and grass) at survey sites located in the ravine bottom. The Red Maples, however, occur on the east side of the ravine and above (north of) the wet areas of the ravine bottom.

Since obvious factors such as recent cultural disturbance, topography, slope aspect, soil moisture, and soil type do not appear as likely causes of the anomalous Red Maple distribution at the Funkhouser site, other possible causes were considered.

Many of the leaves of trees (Red Maple and hickory) and herbaceous weeds growing in the ravine area exhibited some degree of fall foliage coloration and/or nutrient deficiency symptoms (Figure 12-41) in mid- to late July (July 20 to 24, 1981). In the same ravine, many of the oaks to the west of the maple clones had been heavily predated by insects, to the extent that these oaks could be recognized from a distance (Figure 12-40a and 12-40b) because of the denuded appearance. The spring and early summer of 1981 were times of heavy predation and partial defoliation of oaks and other tree species by insect larvae over much of eastern West Virginia. This, however, was the most severely affected site in the Lost River test site area. A flight in a small aircraft over the site on October 16, 1981 revealed a large linear swath to the west of the ravine that was severely affected by insect damage (Figure 12-40a). Such features (early foliage display and predisposition to insect damage) may be indications of stress.

During collection of soil samples for geochemical analysis from the ravine site, extensive development of white fungal mycelia was seen in the soil and on stumps at a number of sample plots. Local residents consider the ravine as an excellent area for collecting mushrooms. Mycorrhizal fungi apparently thrive at this site, perhaps to the extent that host tissues are damaged, resulting in the observed stress symptoms.

Table 12-25. Soil conditions typical for selected woody species occurring at the Lost River test site

Species[a]	Soil Conditions[b]
Black Gum	Wet, imperfectly drained soils; common on borders of swamps.
White Pine	Sandy, well-drained upland sites; rarely in swamps.
Basswood	Rich, moist woodland soils.
Sycamore	Rich bottomlands; often on borders of streams and lakes.
Red Maple	Wet swamps to dry, upland forests; rarely on dry rocky hillsides.
Pin Oak	Rich, moist soils on borders of swamps and river bottomlands.
Sweet Gum	Rich river bottomlands and borders of swamps and wet swales.
Rhododendron	Well-drained upland slopes; common in acidic soils, rare in swamplands.

[a]The species cited here are included because of their relative tolerance or intolerance of landfill conditions (including methane-rich soil gases) according to Flower et al. (1981).

[b]The soil conditions cited are typical of soil conditions or general habitats in which these species commonly occur (Sargent, 1965).

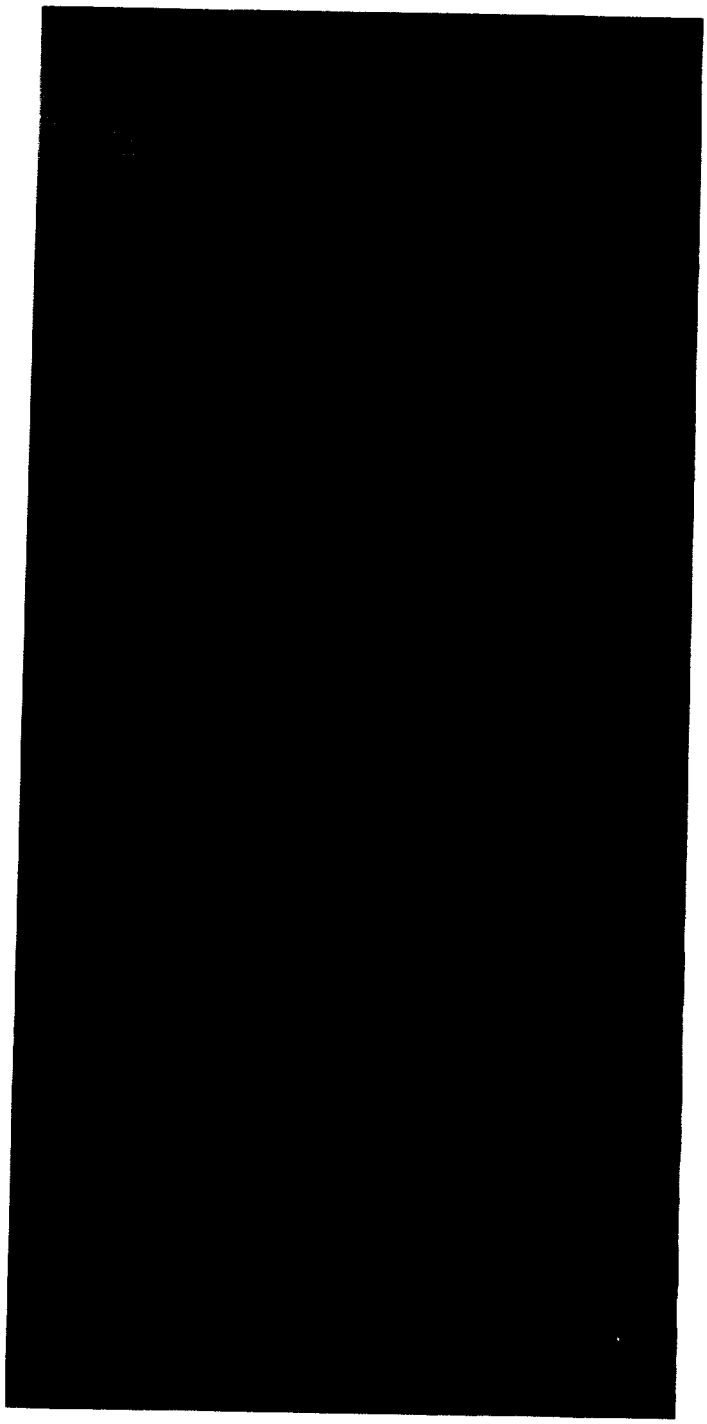

Figure 12-41. Stress symptoms in vegetation occurring at the Funkhouser maple anomaly sites (all photographs were taken July 22, 1981): (a) early foliage display in Red Maples, due to premature anthocyanin development in leaves; (b) interveinal chlorosis in both younger and older leaves of herbaceous ground cover (*Aster*, unidentified), possibly due to nutrient deficiencies such as magnesium or potassium; (c) darkening (reddening) of older (lower) leaves and stems and chlorosis of younger (upper) leaves, possibly due to an iron deficiency

Since the distribution of tree species may be the direct result of their mycorrhizal fungal component's selective ability to inhabit local soils, the anomalous distribution of maples at the Funkhouser ravine may be related to soil conditions selectively favoring one fungal form over another. Although Red Maple is known to form mycorrhizal associations (Medve, 1971), they are very different from those formed with oaks. The fungus associated with Red Maple roots is a nonseptate, filamentous form belonging to the *Phycomycetes* (Medve, 1971) and thus is similar to the fungus noted by Davis (1967) as capable of oxidizing gaseous hydrocarbons.

It may also be reasonable to consider that the soil factors influencing plant distribution at the Funkhouser ravine have a strictly negative effect. If this is the case, survival of a weed tree such as Red Maple at the site, largely to the exclusion of oaks, would be expected since weed trees must be able to tolerate a variety of adverse soil and light conditions in their role as pioneer plants reclaiming previously disturbed areas. The fact that the various oaks at Lost River do not function as pioneer plants attests to their intolerance of such factors.

The two NS-001 supervised vegetation maps depict a second site of high maple concentration on the Funkhouser property. This area is a small circular zone of pure maple (Figures 12-39 and 12-40b) on an east-facing slope. Field examination of the area in July 1981 confirmed that a heavy growth of Sugar Maple occurs at this site. As noted previously, Sugar Maple is a common tree at higher elevations. The approximate elevation of this site is only 650 m (1950 ft). The occurrence of dense stands of Sugar Maple here is therefore considered anomalous. The circular arrangement is unusual but not unique for the entire test site (another similar arrangement occurs southeast of the state park). Based on field observation, the circular pattern does not relate to obvious cultural activity such as old field boundaries, sugar bush (maple syrup) development, or gas well drilling. The maples at this site are mature and appear healthy. This Sugar Maple stand is within 460 m (1475 ft) of a producing gas well (well 9302) and within 154 m (465 ft) of a gas line.

Other concentrations of maple (either Sugar Maple or Red Maple) occur at a number of sites investigated in July 1981. Notable among these are Site C (Figure 12-11; area of collection of mycorrhizal clubroots exhibiting unusual characteristics in oak seedlings) and near well 9303 (a producing well approximately 0.9 km [0.5 mi] north of the Funkhouser sites [Plate 12-1]). Both sites show unusually high concentrations of maturing Red Maples. At each site, the maples are 15 to 20 years old and occur in the margin

of forest surrounding cultural activity (an actively cultivated field and the well site, respectively).

If methane is one of the soil factors influencing distribution of tree species at the two maple anomaly sites, its effect may be the result of anaerobic soil conditions. Leone and others (Flower et al., 1981; Gilman et al., 1981; Leone et al., 1977) relate the influence of landfill gases (up to 60 percent methane, 40 percent carbon dioxide, and trace amounts of certain exotic gases) on tree species to the development of an anaerobic soil atmosphere in the root zone. Methane is not seen as having a direct toxic effect.

A high degree of species and genus variability exists relative to tolerance of oxygen-deficient soils. Since concentrations of landfill gases (methane and carbon dioxide) increase in the soil atmosphere with increasing depth (Flower et al., 1981), shallow-rooted vegetation can tolerate sites from which deep-rooted species have been excluded. Oaks produce deep taproot systems (Raven et al., 1976). Field observations indicate that maples in the Lost River area are shallow rooted (many maples were uprooted, due to shallow root systems, by an ice storm that occurred in 1977, while oaks were not).

Table 12-26 (from Flower et al., 1981) presents woody tree species arranged in order of their tolerance to landfill conditions. Leone et al. (1979) report that Red Maples are more tolerant of soils fumigated with simulated landfill gases than are Sugar Maples. Red Maples are also known to be good tolerant, surviving for prolonged periods in the anaerobic conditions of water-saturated soils. Pin Oaks (Flower et al., 1981) and Black Oaks (Leone et al., 1977) are also less tolerant to landfill gases than are Red Maples. Thus, Red Maples are expected to occur at sites from which oaks and other species have been excluded by anaerobic soil conditions.

Of the tree species studied by Leone and her coworkers, *Nyssa sylvatica* (Black Gum, Sour Gum, Tupelo, or Swamp Tupelo) is cited (Table 12-26) as the most tolerant of the anaerobic root environment caused by landfill gas. This species occurs widely throughout the test site, both on and off the gas field. Where it occurs, it normally forms a low shrub thicket as understory growth below the typical oak-hickory canopy. Seldom does it achieve any significant size in the Lost River area (80 percent of the *Nyssa* seen at vegetation analysis plot sites were small trees and shrubs under 10 cm in diameter at breast height [dbh]). Black Gum trees with trunks exceeding 10 cm dbh occur at less than 5 percent of the analysis plots studied in July 1981. Of the large Black Gum trees at these sites, 80 percent occur either at the two maple anomaly sites or at sites along the gas pipeline or near gas wells. Since *Nyssa* is noted as commonly occurring in saturated soils on borders of swamps and streams (Sargent, 1965), its tolerance of landfill gas conditions is undoubtedly the result of its ability to survive anaerobic soil environments.

Table 12-26. Relative tolerance of woody species to landfill conditions[a]

Species	Rank[b]
Black Gum[c]	1
Japanese Yew	2
Japanese Black Pine	3
Ginkgo	4
White Pine[c]	5
Bayberry	6
Norway Spruce	7
American Basswood[c]	8
American Sycamore[c]	9
Red Maple[c]	10
Hybrid Poplar (rooted cuttings)	11
Pin Oak[c]	12
Sweet Gum[c]	13
Honey Locust	14
Green Ash	15
Euonymus	16
Hybrid Poplar (saplings)	17
Weeping Willow	18
Rhododendron[c]	19

[a] From Flower et al., 1981, p. 50.
[b] Rank 1 = best growth when landfill plot is compared to control plot, i.e., most tolerant to landfill conditions; 19 = least tolerant to landfill conditions (in the case of Rhododendron, all specimens on landfill plot died).
[c] Species occurring at the Lost River test site.

The so-called lower fungi (*Phycomycetes*) are more tolerant of saturated, imperfectly drained soils than are the higher fungi (*Ascomycetes* and *Basidiomycetes*). Since Red Maple forms a mycorrhizal association with members of the *Phycomycetes* and oaks require members of the *Basidiomycetes*, relative tolerance of anaerobic soils by Red Maple is likely to be related to its fungal component's tolerance of such conditions.

Although a number of factors influencing the distribution of maples and oaks at the Lost River test site have been identified, other unidentified factors may exist. Topography, elevation, and slope aspect have an influence, as do cultural activity and soil microenvironment. Indirect evidence (concentrations of Red Maples and Black Gum) suggests that localized anaerobic soil conditions exist over the Lost River gas field. Future studies should be aimed at developing a better understanding of the soil microenvi-

ronment (through both geochemical and biological analyses) and of its effect on the forest cover distribution at the Lost River test site.

One shortcoming of the present botanical evaluation of anomalous species distribution portrayed in NS-001 supervised image classifications is the lack of data for areas that are well off the Lost River gas field. Since Sugar Maples normally occur at the higher elevations in this portion of West Virginia, it is not possible to locate comparable areas (narrow ravines, 550-m [1650-ft] elevation, etc.) within the test site that are outside the productive limits of the Lost River gas field. Given the lack of botanical data from similar sites of known hydrocarbon microseepage elsewhere, it is not possible to predict the boundaries of the Lost River gas field on the basis of the distribution of tree species. Comparable sites to the west of the test site, which are not near known gas fields, should be studied, and a detailed investigation of the influence of hydrocarbons on vegetation should be conducted.

E. Conclusions

The remotely sensed detection of subtle distributional anomalies such as those seen at Lost River may prove to be of considerable value for biogeochemical prospecting for sites of hydrocarbon microseepage. Vegetation distributional anomalies in the form of high concentrations of maples are noted at sites where the more typical oak–hickory climax (successional) species should occur. It is suggested that anaerobic soil conditions may be the cause of these anomalies.

Anomalous distribution of weed trees, in response to anaerobic soil conditions generated by methane-rich soil gases, represents the response of plants to long-term soil conditions. Use of weed tree indicators should not be site specific since areas with differing environmental conditions all have characteristic climax and weed species. Thus, the approach should have broad application on a worldwide basis. Prerequisite to the use of such an approach will be an improved understanding of what constitutes weed trees versus climax forest members for a particular site, as well as recognition of past cultural activities in the area.

IX. Photogeologic Interpretation of Aircraft Multispectral Data

A. Introduction

To evaluate the utility of multispectral data for geologic mapping in vegetated terrain, selected NS-001 and M^2S images were interpreted using aerial photographic/geomorphic (Thornbury, 1965, p. 224–240) analysis procedures. Images shown in Figures 12-24 through 12-27, 12-36, 12-37, and 12-42 were interpreted at 1:48,000 scale. A composite of these seven interpretations is illustrated in Figure 12-43.

B. Results

A comparison of the published geologic map for the tes site area (Figure 12-1) to the composite interpretatior (Figure 12-43) illustrates that structural and stratigraphi features shown in Figure 12-1 are also delineated in Figur 12-43. The composite image interpretation also contain geologic information not shown on the published map.

On the basis of their tonal/textural and geomorphi expression, all previously mapped stratigraphic units ca be recognized in the multispectral images. Additionall several ridge-forming marker beds (resistant sandstone within the Hampshire Formation are traceable on the mu tispectral images. The distinct tonal/textural characteri tics of the Rockwell Formation, which according to th published map occurs only along the axis of the Whip Co Syncline, also appear on the northeast and southwest en of the Sideling Hill Syncline. This image-determined co rection of the mapped distribution of the Rockwell Form tion was confirmed by field observations.

No faults are shown on the published map. On the ba of offsets of key beds and fold axes, a conjugate set of fau is revealed by the image data. The two fault sets (shown dashed lines, "transverse structures," in Figure 12-43) ha trends of approximately N 80°E and N 30°W. On the ba of their relatively straight trace across topography, th structures are nearly vertical. Model experiments by Dul (1980) resulted in the development of a geometrica equivalent conjugate fault set. According to Dube experiments, these conjugate faults are transcurrent in nat and form after the initiation of folding. Similarly, the c jugate system illustrated in Figure 12-43 is interpretec represent transcurrent faulting associated with stress de oped late in the Allegheny orogeny. This interpretatio consistent with Zoback and Zoback's (1980) analysis of state of stress in the Ridge and Valley regions as a whol

A comparison of the locations of fold axes in the p lished map to the image interpretation demonstrates the map is a simplified version of the image interpreta Widths of axial traces plotted on Figure 12-43 reflect va tion in axial locations as determined in the seven in interpretations. Wells of the Lost River gas field are loc near the surface trace of the Whip Cove Anticline as trayed in both the published and image-interpreted logic maps.

0 1 mi

0 1 km

N

Figure 12-42. M²S, Mission 399, line 1, April 20, 1979 color composite image: band 4 is displayed in blue; band 6, green; and band 9, red

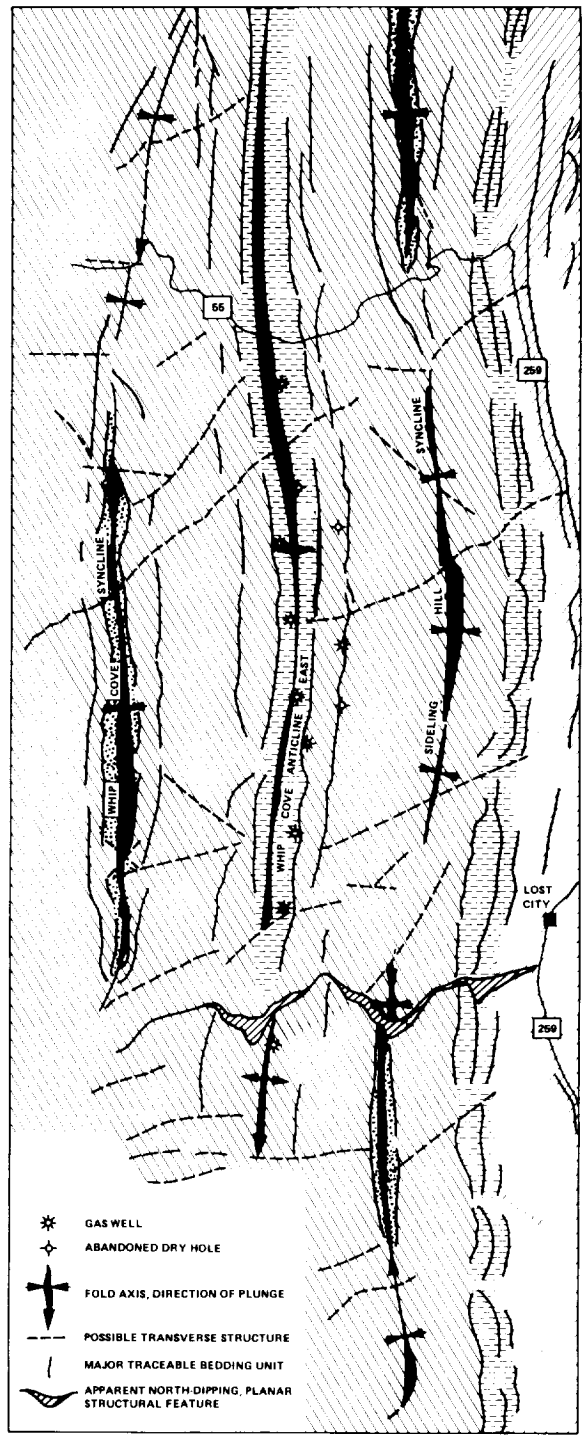

Figure 12-43. Composite geologic interpretation from aircraft multispectral data. Compare to the published geologic map, Figure 12-1. The dot pattern is equivalent to Rockwell (Pocono); right-sloping diagonal, Hampshire (Catskill); dashed, Chemung; and left-sloping diagonal, Brallier and older.

One of the most interesting structures recognized in the image interpretation is the apparent north-dipping planar structure shown in Figure 12-43. On the basis of a three-point dip and strike solution using the trace of this feature and elevation data, the surface has a strike of N 60°W and dips approximately 40°N. Projection of the surface to depth results in an intersection with the Oriskany reservoir approximately coincident with the location of the north end of a southern structural high recognized in the subsurface (Figure 12-4 and Plate 12-2). Field examination of the north end of Big Ridge (Plate 12-1) at the surface location of the trace of this structure revealed fractured shale with slickensides on joint surfaces having approximately the same orientation as that predicted in the image analysis. On the basis of these observations, this planar feature is interpreted to be a major shear surface associated with a CSD type of structure (refer to Paragraph III.B.2), which may cut the Oriskany reservoir at depth.

C. Conclusions

A photogeologic analysis of aircraft multispectral data acquired in the Lost River test site investigation (1) verified that previously mapped geologic features could be discriminated and (2) resulted in new stratigraphic and structural information. These results illustrate the utility of multispectral data for geologic mapping in areas of dense vegetation cover.

X. Lineament Analysis of Multispectral Data

A. Introduction

Commercial hydrocarbon accumulations at Lost River and at other sites in the Eastern Overthrust Belt are apparently confined to areas of enhanced development of secondary fracture porosity at depth (Patchen, 1969). Aerial photograph and Landsat MSS image lineaments in the Appalachian Basin have been interpreted as manifestations of bedrock fracture (Werner, 1976). The preparation of lineament maps and the analysis of areal variation in lineament density and orientation at the surface may, therefore, be a potential means to remotely determine locations of and areal variations in secondary fracture porosity. Such analysis may provide information for the identification of favorable oil and gas exploration targets.

Lineaments are relatively long and generally straight tonal or textural features considered to be manifestations of geologic structure. Although the geologic meaning of individual image lineaments is commonly obscure, many have been identified as topographic expressions of faults, fault zones or systems, or zones of intense jointing.

Two significant biases have been recognized in evaluations of image lineament interpretations.

(1) Operator bias. Lineament interpretations for one image by different interpreters (or one interpreter on different dates) commonly exhibit significant variation in the location and length of individual lineaments.

(2) Image bias. Lineament interpretations for one area using remote sensing data obtained at different times commonly exhibit significant variation in the location, length, and trend of individual lineaments.

Siegal (1977) conducted an experiment that compared lineament interpretations of five geologists who each interpreted five images of the same area. His rigorous statistical comparison of the 25 interpretations clearly documents operator and image subjectivity in determining lineament location, length, and orientation. For the Lost River test site study, it was thought that these biases might be minimized (or at least recognized and evaluated) by using multiple interpreters and multitemporal images for lineament analysis.

To evaluate the utility of lineament analysis for oil and gas exploration in regions of secondary fracture porosity, a study of image lineaments was conducted in the Lost River area. The purpose of this investigation was to:

(1) Evaluate the effects of operator and image bias in lineament analysis and if possible develop methods to obviate such bias.

(2) Determine the relationship of productive areas and subsurface structures to image lineaments.

(3) Develop techniques of lineament analysis optimized for exploration in the Ridge and Valley Province.

(4) Compare results to those of other investigations in the Ridge and Valley Province.

(5) Develop an exploration model that integrates the results above and provides a geologic rationale for the application of lineament analysis in the Ridge and Valley Province and other fold mountain belts characterized by anticlinal reservoirs with fracture porosity.

If lineaments represent a surface manifestation of subsurface fractures, lineament analysis may additionally provide information for the location of potential sites of hydrocarbon microseepage and associated vegetation or soil/bedrock alteration.

3. Landsat MSS Lineament Analysis

Sixteen Landsat MSS images produced from data obtained on five different dates (Table 12-11) were compared for lineament content. A high-contrast, band 4, 5, 7 color composite image for April 16, 1977 appeared to be most suitable for lineament interpretation (Figure 12-44). A 1:500,000 positive color print of the scene was interpreted independently by two observers. Both used the same procedure. All lineaments over 2 km long (6-mm image length) were annotated on a transparent overlay. Each interpreter spent 8 hours to complete the interpretation. The two interpretations (Figures 12-45 and 12-46) were then digitized and stored on magnetic tape for computer analysis.

A qualitative comparison of these two lineament interpretations reveals both similarities and differences. Both interpretations recorded two major lineament trends; one generally NE–SW and one NW–SE. The NE–SW-trending set appears numerically dominant. This set approximately parallels the structural strike of the Central Appalachian Mountains and may reflect the strike of major fold axes and axial-parallel joints, faults, and bedding units. The NW–SE-trending set may reflect the strike of features that are transverse to the Appalachian structural grain, including alignments of fold-axis terminations and cross-axial joints and faults.

On the basis of lineament density, both annotations may be interpreted to show three lineament domains with NE–SW-trending boundaries. The eastern one-half of both interpretations represents a domain of minimum lineament density. This area includes the western portion of the Blue Ridge Province of the central Appalachians. Most of the western half of both interpretations represents a domain of maximum lineament density. This area encompasses most of the Ridge and Valley Province (the so-called "Eastern Overthrust Belt"). The western edge of the area appears to be a domain of intermediate lineament density and coincides approximately with the eastern Allegheny Plateau Province.

The Figure 12-45 interpretation appears to contain more lineaments than Figure 12-46. Although many lineaments are approximately replicated in the two interpretations, three types of variation are apparent:

(1) Lineaments identified by one interpreter are not consistently identified by the other. This reflects individual perceptual bias in lineament recognition.

(2) Few lineaments are exactly coincident in the two interpretations. This may be due to individual decisions to locate lineaments in the middle of or on the edge of a linear textural or tonal feature of finite width.

(3) Lengths of otherwise coincident lineaments are commonly unequal in the two interpretations. This may be the result of individual decisions to connect or not connect series of aligned, linear textural or tonal features.

These qualitative results are in agreement with Siegal's (1977) statistical evaluation of operator bias in lineament interpretation.

C. Landsat MSS Lineament Density Analysis

It was thought that the operator bias recognized in the qualitative comparison of Figures 12-45 and 12-46 might be obviated by evaluating relative areal variations in lineament density or orientation rather than absolute lineament location, length, or number. To evaluate the utility of lineament density analysis, the same 5-km grid was registered to each of the two lineament interpretations. The number of lineaments and lineament intersections was determined for a 10- by 10-km area centered at grid intersections. This procedure resulted in two arrays of 1183 lineament and lineament intersection values for each interpretation. These four data sets were used to statistically compare the two interpretations and to evaluate relative areal variations in lineament and lineament intersection density.

The grid and sampling area dimensions were chosen in response to the conclusions of Kulander and Dean (1978) and Wheeler (1980). Both investigations identify distinct, generally linear swarms of increased lineament density that are transverse to the Appalachian structural grain and are approximately 8 km wide. Both investigations provide evidence that these swarms coincide with areas of increased bedrock fracturing. Wheeler (1980) uses the term "cross-strike discontinuity" (CSD) for such structural features at high angles to the regional strike. He proposes an exploration strategy for the Eastern Overthrust Belt, which postulates that sites of lineament intersection within CSDs are optimal exploration targets.

A linear regression analysis (Davis, 1973, Program 5.3, p. 199) using the 1183 lineament density values from the Figure 12-45 interpretation as the independent variable, x, and the equivalent values from Figure 12-46 as the dependent variable, y, was performed. The resulting least squares fit was

$$y = 0.63x + 1.23$$

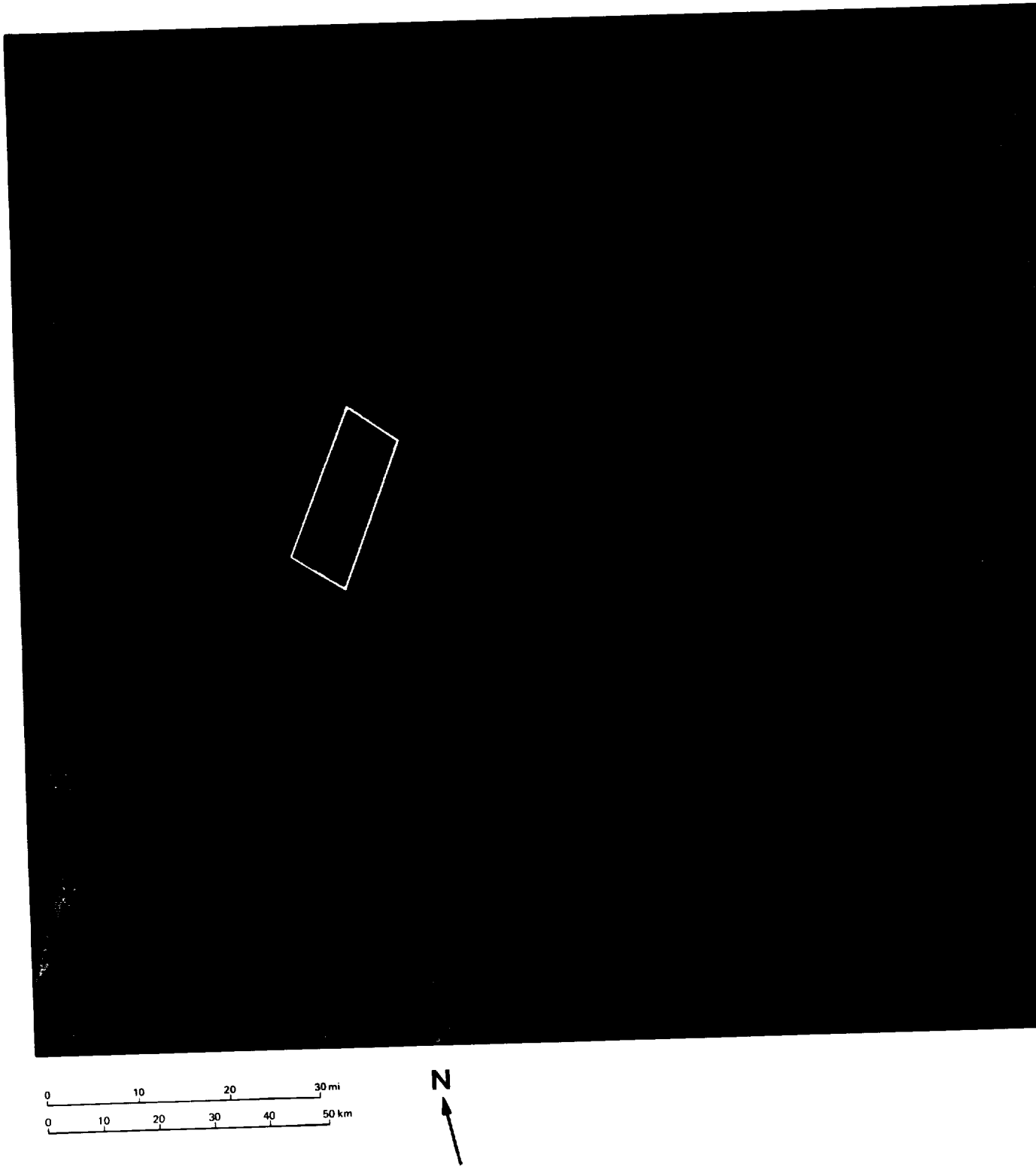

Figure 12-44. High-contrast stretch, Landsat MSS bands 4 (blue), 5 (green), and 7 (red) color composite image (April 16, 1977). A 1:500,000 of this image was used for regional lineament analysis. The area covered by Lost River NS-001 line 1 data is outlined.

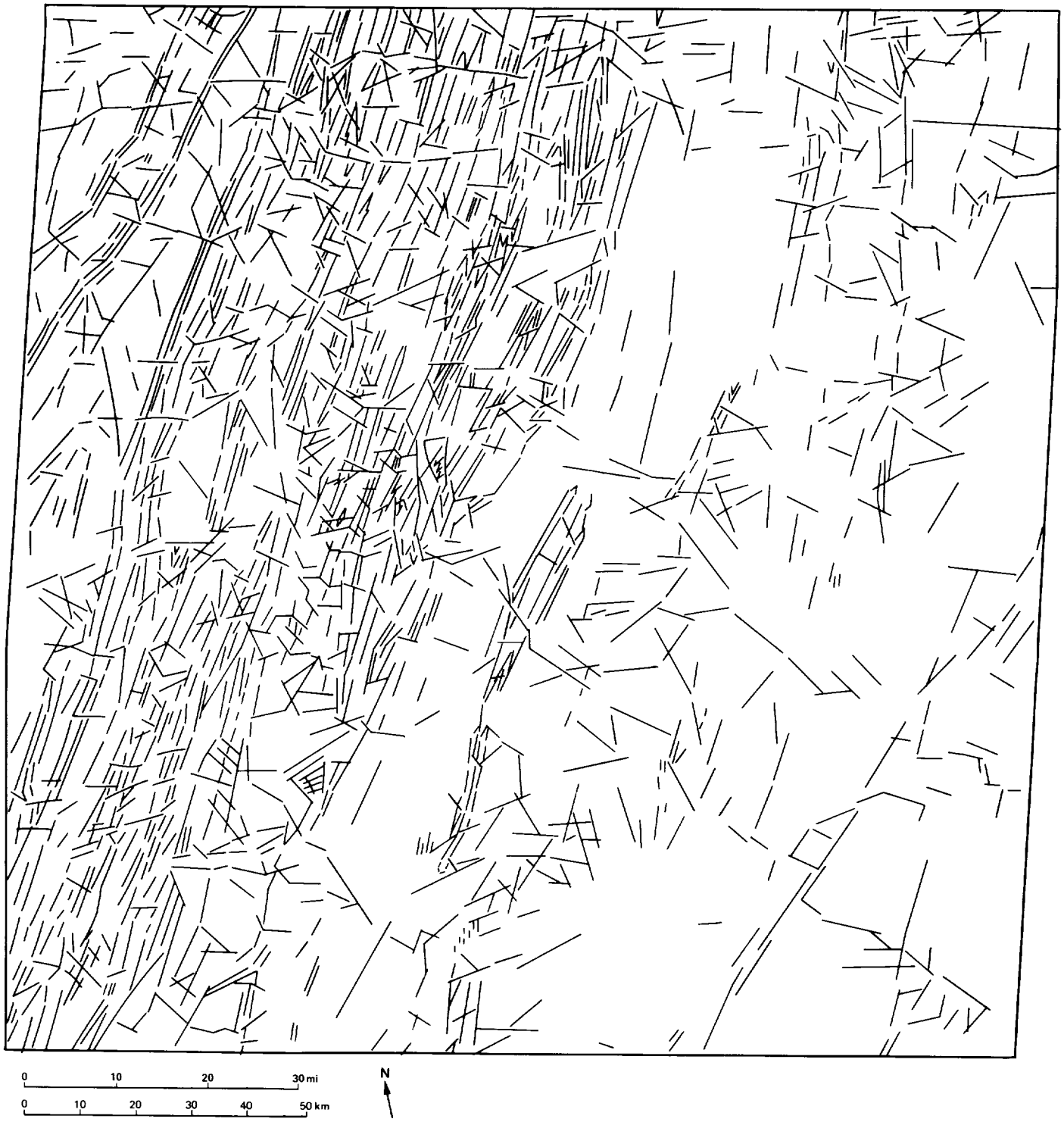

Figure 12-45. Regional Landsat MSS lineament interpretation 1

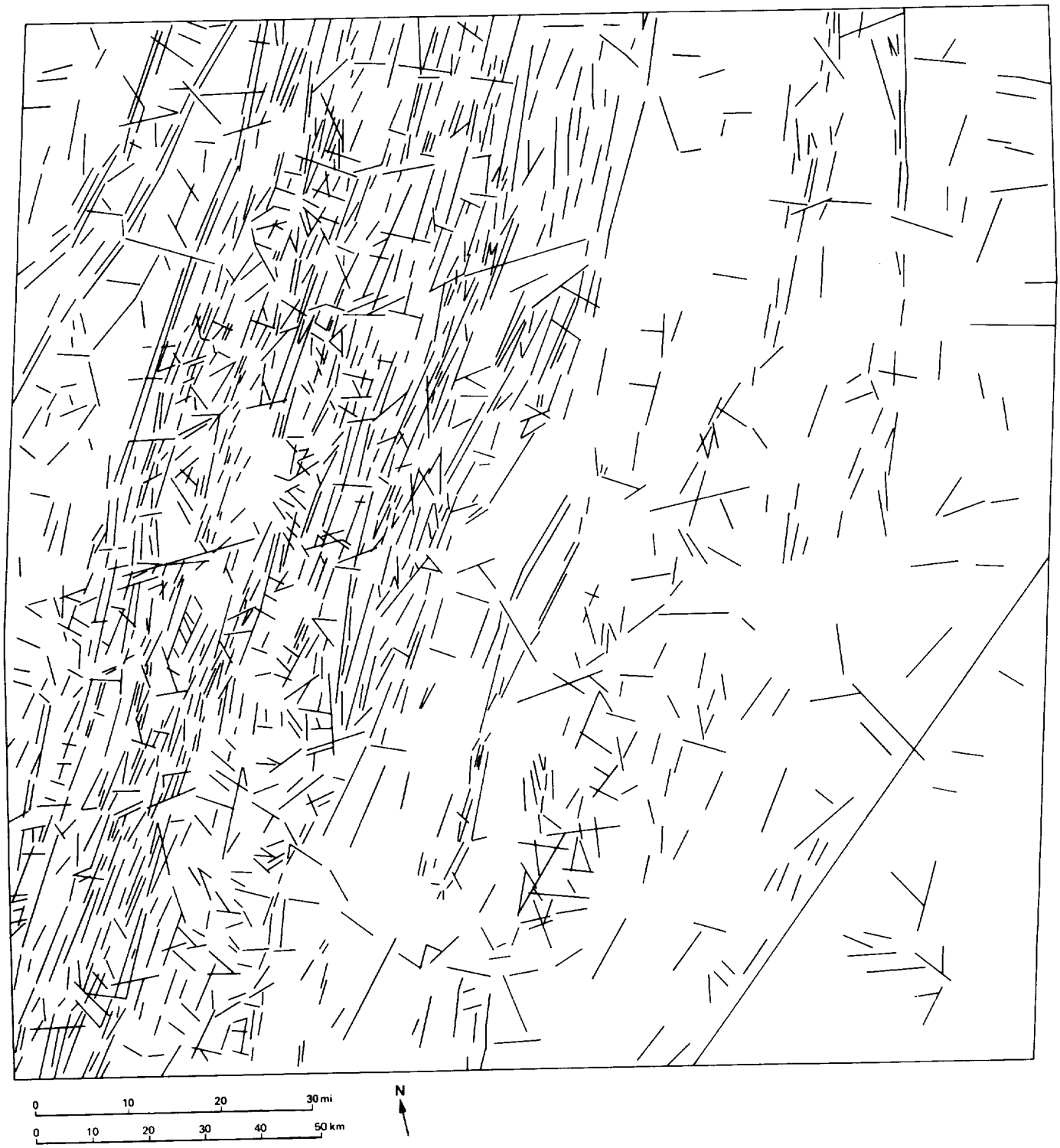

Figure 12-46. Regional Landsat MSS lineament interpretation 2

This regression yielded a goodness of fit of 0.62 and a correlation coefficient of 0.79. An F-test supports the significance of the regression at the >99.95 percent confidence level. These results lend statistical credence to the results of the qualitative comparison of the two lineament interpretations and demonstrate the following:

(1) The interpretations of Figures 12-45 and 12-46 differ in the number of lineaments recognized; Figure 12-45 values are systematically higher than those of Figure 12-46.

(2) For analysis of relative areal variation in lineament density, the interpretations of Figures 12-45 and 12-46 are statistically equivalent.

(3) This equivalence indicates that this approach yields repeatable operator-independent results.

Wheeler's (1980) exploration strategy implies that lineament intersection density is a more useful parameter than lineament density for exploration in the Eastern Overthrust Belt. Conceptually, one would expect the two parameters to have a high, positive correlation. To test this hypothesis, a linear regression of the 1183 lineament density values, x, and lineament intersection values, y, from Figure 12-45 was performed. The resulting least squares fit was

$$y = 0.46x - 1.36$$

This regression yielded a goodness of fit of 0.86 and a correlation coefficient of 0.93. An F-test supports the significance of the regression at the >99.99 percent confidence level. These results lend statistical credence to the inferred equivalence of lineament density and lineament intersection density data.

Four contour maps were prepared from the four lineament density and lineament intersection density arrays produced from Figures 12-45 and 12-46. The four maps show the same highs and lows and trends of high and low values. These results are consistent with the qualitative and statistical inference of equivalency of the two lineament interpretations and high positive correlation of lineament density and lineament intersection density.

Figure 12-47, prepared from the lineament density value array of Figure 12-45, is an example of one of these four equivalent contour maps. The number of lineaments/100 km^2 varies from 0 to 45. Several locations of high lineament density and trends in lineament density are quite apparent:

(1) The area may be divided into three broad lineament density domains. Highest lineament density values are confined to a generally N 35° E trending region that encompasses most of the western portion of the figure. This region is flanked by domains of lower lineament density.

(2) The largest area of maximum lineament density (red) is located in the west–central portion of the figure.

(3) The west–central high is located on a N 33° E trending domain of relatively high lineament density values; this domain contains a second area of maximum lineament density approximately 35 km to the northeast.

(4) Another domain of relatively high lineament density values trends N 3° E and includes a third high approximately 15 km to the northeast of the west–central high.

(5) A domain of relatively high lineament density values trending N 47° W is approximately 20 km south of the west–central high.

Figure 12-47 also shows the locations of gas fields, exploratory wells, and CSD-type features. The Lost River gas field is located on the western flank of the west–central lineament density high. The Inkerman gas field, the most productive field shown, is also located on the west flank of a lineament density high. The relationship of other gas fields to lineament density is not obvious, and the paucity of exploratory wells precludes evaluation of most of the areas of high lineament density.

The trend of Wheeler's Petersburg CSD is not apparent in the lineament density data, although the west–central high is located approximately on the CSD. The trend of the Parsons CSD parallels the N 47°W trending domain of high lineament density south of the west–central high. Wheeler's location for this CSD, however, is approximately 10 km south of the lineament density trend. The relationship of other CSD-type features to the areal variation in lineament density is not obvious.

D. NS-001 Lineament Density Analysis

The results of Landsat MSS lineament density analysis appear to provide useful information for determining regional fracture patterns in the Eastern Overthrust Belt. An equivalent analysis of NS-001 aircraft data for the Lost River test site may provide fracture information at an appropriate scale for direct comparison to subsurface geophysical and well data.

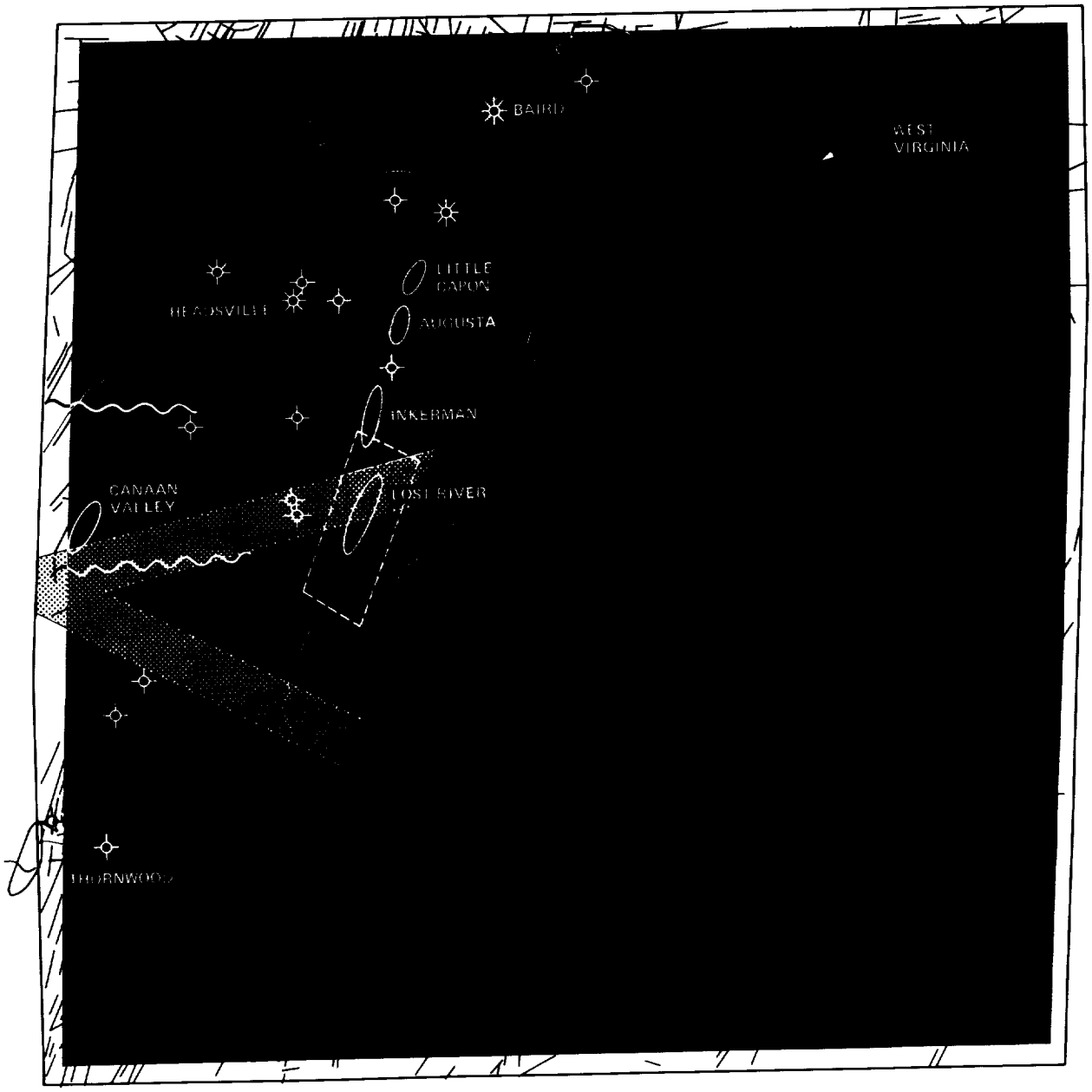

HUNTERVILLE-ORISKANY FIELDS AND DEEP WILDCATS (AFTER PATCHEN, 1969, FIG. 1)

- GAS WELL
- GAS SHOW
- DRY HOLE
- GAS FIELD

MAJOR TRANSVERSE STRUCTURAL FEATURES

- LINEAMENT ZONE (AFTER KULANDER AND DEAN, 1978, FIG. 9)
- PETERSBURG AND PARSONS CSDs (AFTER WHEELER, 1979, FIG. 1)
- AREA COVERED BY NS-001, MISSION 431, LINE 1, OCTOBER 21, 1980

0 10 20 30 40 50 km

0 10 20 30 mi

N

Figure 12-47. Regional Landsat MSS lineament density isopleth map from an analysis of interpretation 1 (Figure 12-45). Lineament densi expressed in number of lineaments/100 km^2; color assignments: gray (0–1), light blue (2–10), dark blue (11–15), dark green (16–20), light g (21–25), yellow (26–30), orange (31–40), red (>40).

A comparison of the two sets of NS-001 images acquired for Lost River indicated that data from the October 21, 1980 overflight revealed lineaments best. Plate 12-1 shows the area covered by line 1 of this overflight. The line covers the entire Lost River gas field. Preliminary evaluation of images produced from these October NS-001 data demonstrated that a positive black-and-white, 5 by 5 high-pass filter (with 100 percent feedback) version of the band 4 data was the most informative rendition (Figure 12-48).

As discussed above, there is a "time-of-image-acquisition" bias in lineament interpretation. An obvious factor contributing to this bias is illumination aspect. Shadowing of linear features preferentially highlights lineaments oriented transverse to the solar azimuthal plane. Lineaments oriented parallel to the illumination direction are subdued. The illumination geometry for the October 21, 1980 NS-001 data should emphasize E–W-trending lineaments and subdue N–S-trending lineaments.

To obviate this bias, six versions of the band 4 high-pass (contrast enhanced) data were produced (Figures 12-49 through 12-54). Each was processed to enhance lineaments of a known trend. In the computer, six identical pairs of high-pass data were superposed and then deregistered ("shifted") by six different line and sample offsets (Table 12-27). Shifted data were then added together and rescaled. This procedure resulted in a unique, artificially induced bias in the lineaments emphasized by each of the six images. Lineaments trending parallel to the shift direction are subdued; those transverse to the shift direction are enhanced. This procedure is a computer application of a photographic enhancement procedure described by Weller (1970).

A comparison of Figures 12-51 and 12-52 clearly illustrates this phenomenon. In Figure 12-52, with a N 32° E shift, NE-trending lineaments are suppressed; in Figure 12-51, with a N 58° W shift, NE-trending lineaments are enhanced. The analysis of lineament density using a composite lineament interpretation obtained from these six images should minimize the illumination geometry bias of the NS-001 data. Illumination biased trends should be diluted and "real" trends revealed. Problems of operator bias may be minimized by using multiple observers in preparing the composite interpretation.

To test the utility of such an approach, the six shift images, printed at 1:48,000, were interpreted by six independent observers. Each interpreter annotated two images. The result was two independent lineament interpretations for each of the six images. These 12 lineament annotations were then plotted on the same base to produce a composite (Figure 12-55).

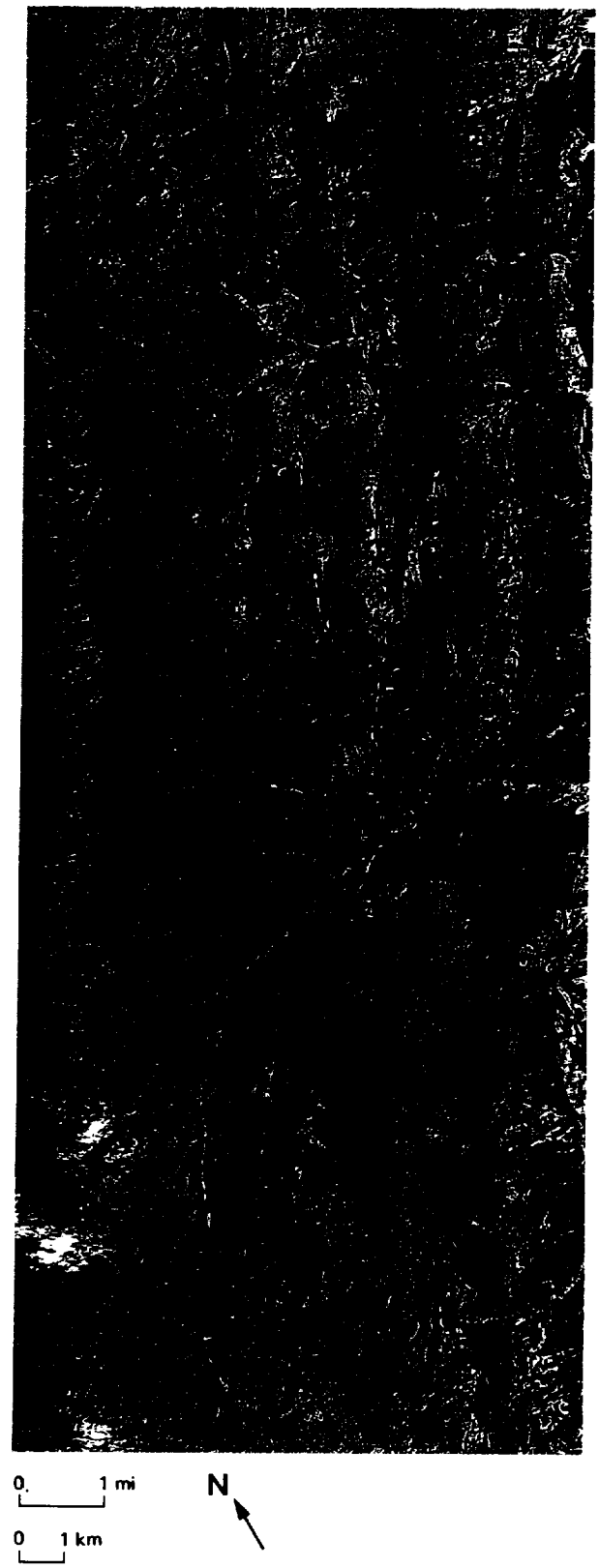

Figure 12-48. NS-001 band 4, 5 by 5 high-pass filter image used in lineament analysis (data acquired October 21, 1980, Mission 431, line 1)

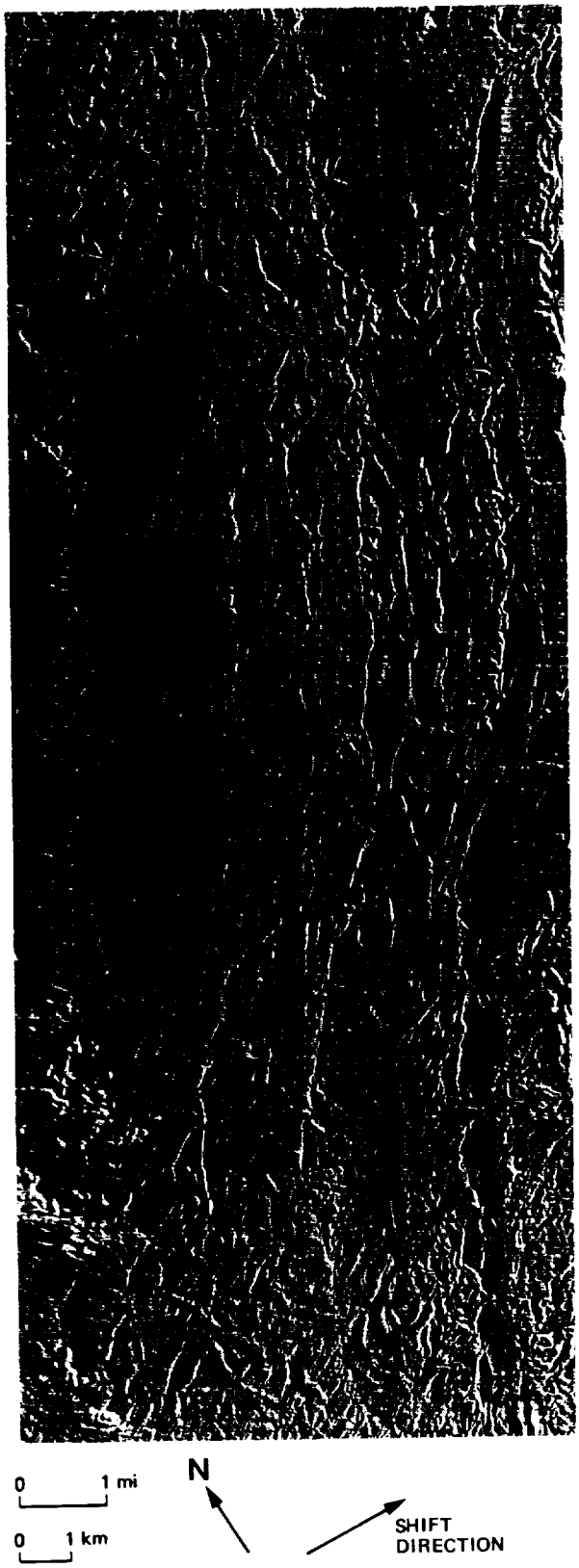

Figure 12-49. NS-001 band 4 shift image: shift direction 2 lines, 4 samples

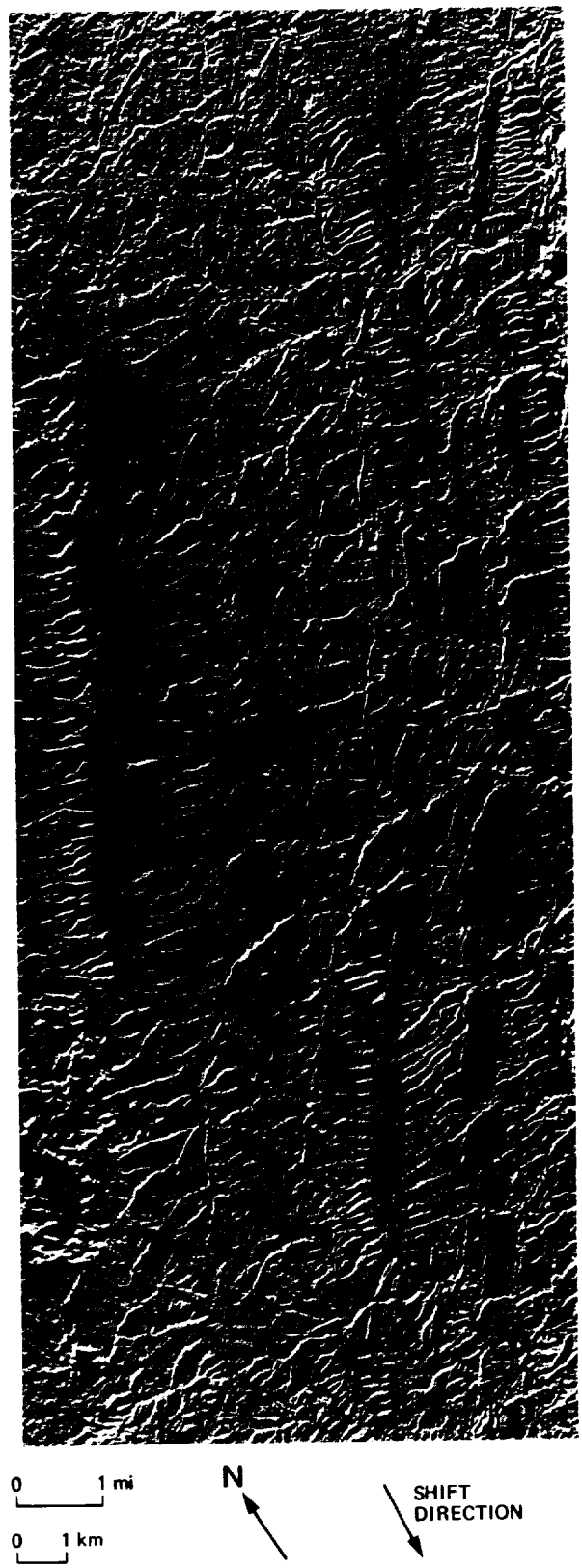

Figure 12-50. NS-001 band 4 shift image: shift direction 4 lines, 2 samples

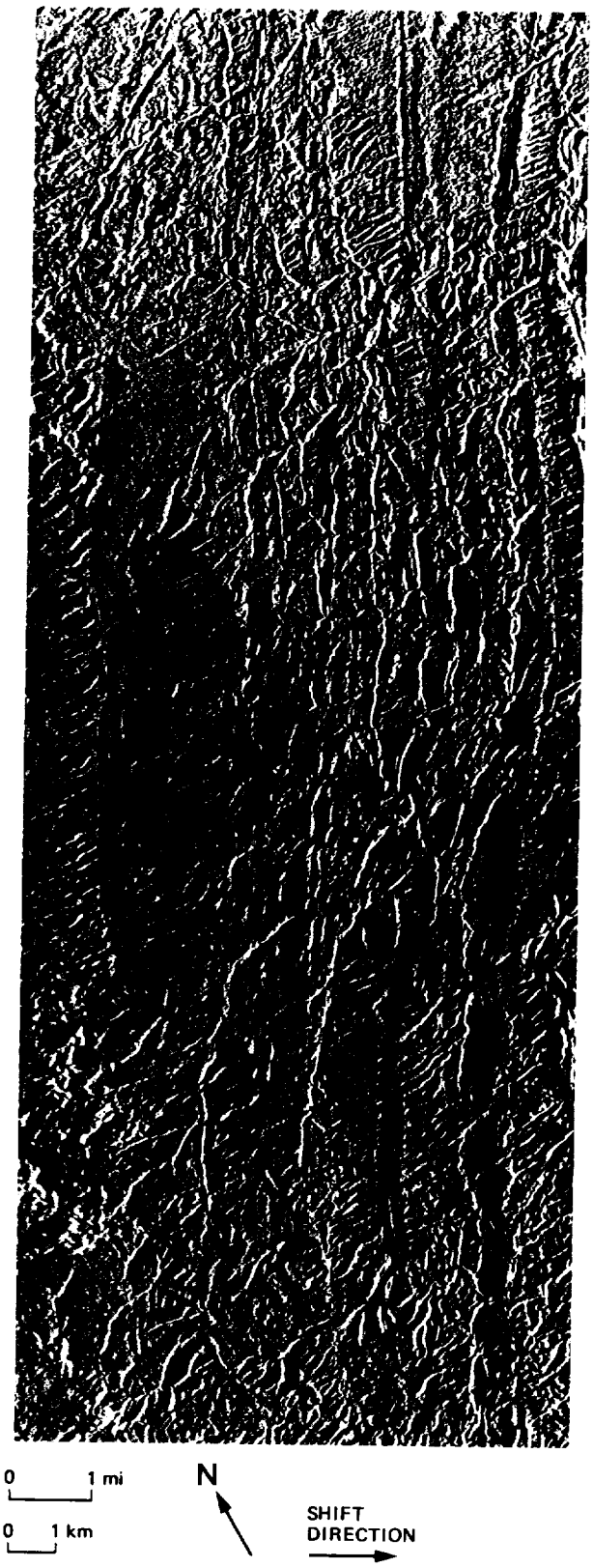

Figure 12-51. NS-001 band 4 shift image: shift direction 0 lines, 5 samples

Figure 12-52. NS-001 band 4 shift image: shift direction 5 lines, 0 samples

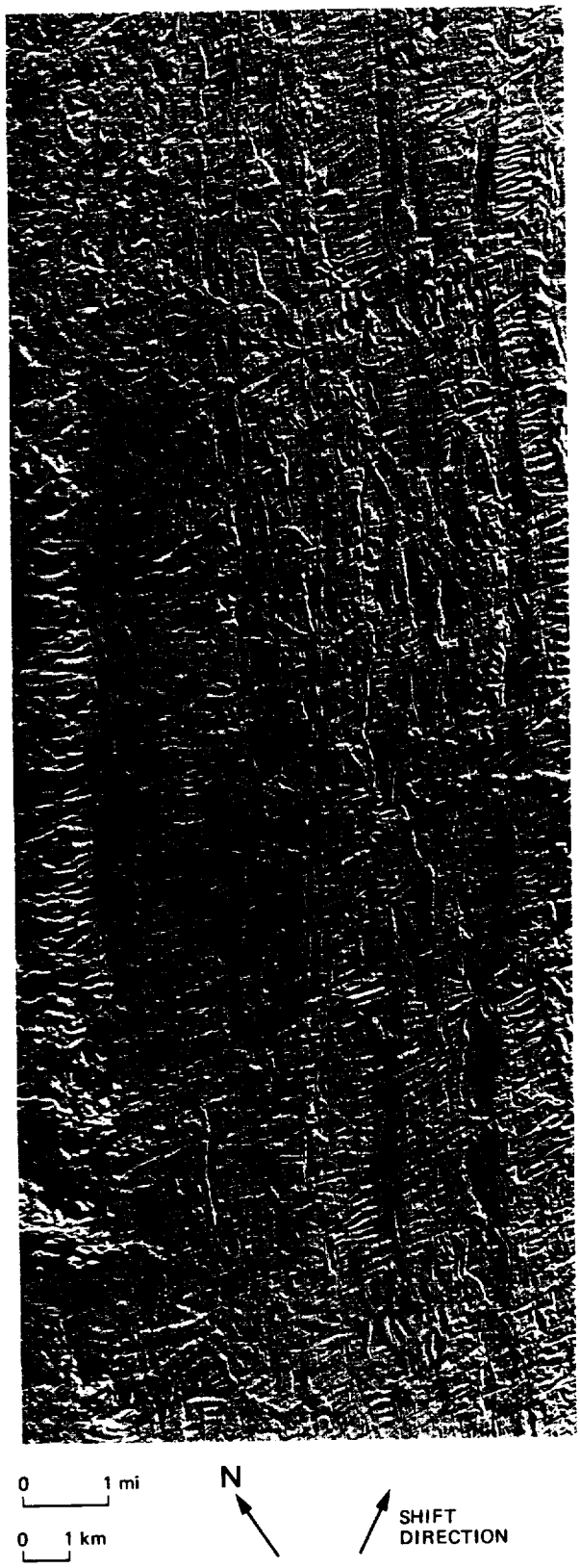

Figure 12-53. NS-001 band 4 shift image: shift direction 4 lines, 2 samples

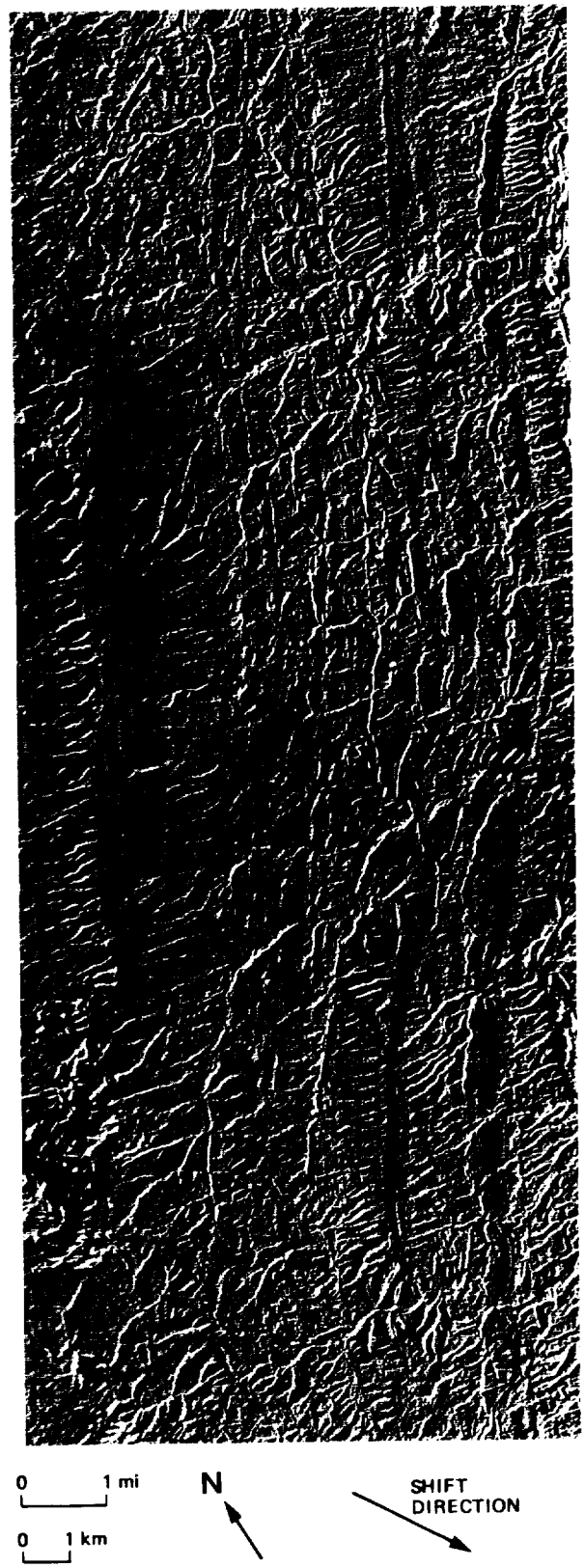

Figure 12-54. NS-001 band 4 shift image: shift direction 2 lines, 4 samples

Table 12-27. Summary of shift image geometry for lineament analysis (October 21, 1980, NS-001 band 4, high-pass images)

Figure Number	Shift[a]		Shift Direction (lineaments subdued)	Shift Direction Perpendicular (lineaments enhanced)
	Lines	Samples		
12-49	2	4	N 85° W	N 5° E
12-50	4	2	N 5° E	N 85° W
12-51	0	5	N 58° W	N 32° E
12-52	5	0	N 32° E	N 58° W
12-53	4	2	N 58° E	N 32° W
12-54	2	4	N 32° W	N 58° E

[a]Average pixel ~ 15 m; flight (line) direction N 32° E.

The procedure used for Landsat MSS lineament density determinations was also used to obtain lineament density values for the composite NS-001 interpretation. In this case, however, a 2.4- by 2.4-km sampling area centered on 1.2-km grid intersections was used. Assuming that the plane-view area of lineament density domains approximates the cross-section-view area of such features, this sampling area was chosen to target producing horizons of less than 2.4-km depth.

The procedure resulted in a 9 by 24 array of 216 lineament density values. The values ranged from 3 to 56 lineaments per 6.4×10^6 m^2. Figure 12-56 is a lineament density isopleth map produced from these data. Areas of high and low lineament density, and trends in lineament density variation are apparent. High lineament density values are confined to the N 30° E trending central portion of the map. Three subareas of high lineament density values (>50) occur in this region. Two in the south–central area form a N 35° E trend. The third area of high lineament density is located on a high N 13° E trend. These two trends of high lineament density are separated by a N 44° W trend of low lineament density values. The lack of geometric fidelity in the unregistered NS-001 data limits the precision of these directional measurements to approximately ±5°.

Figure 12-57 compares these three NS-001 trends in lineament density variation to those recognized in Landsat MSS lineament data and to trends in fracture density documented by Wheeler (1979 and 1980). It is apparent that the Appalachian structural strike and the trend of Wheeler's (1979) Parsons CSD are revealed in both the Landsat MSS and NS-001 lineament density analyses. The Petersburg CSD, only weakly expressed in a Landsat MSS lineament density trend, is not apparent in the NS-001 lineament density data. A previously unrecognized N 2° E to N 17° E trend is apparent in both Landsat MSS and NS-001 lineament density data.

1. NS-001 lineament density trend surface. To further evaluate the lineament density pattern for the Lost River test site, the composite NS-001 lineament density array was used as input for trend surface analysis. The trend surface approach was selected in order to:

(1) Evaluate the regional lineament density pattern in a manner amenable to statistical tests.

(2) Identify areas of statistically significant variation from the regional pattern.

(3) Compare the results of items (1) and (2) to subsurface data available in the Lost River gas field.

Two data sets were used for trend surface analysis. Initially, the entire 9- by 24-point grid array of NS-001 lineament density values was used as input data for Davis' (1973, Program 6.3, p. 332) trend surface analysis program. These data extended to the perimeter of the NS-001 image. A perceptual bias, which may be called the "edge effect," occurs in lineament identification. Because the area of lineament perception must terminate at the edge of an image, the interpreter tends to identify fewer lineaments on the image perimeter. This generally results in higher lineament density values in the center of an image and lower values along the perimeter. Trend surface analysis using the entire array obtained from Figure 12-55 is therefore biased by the lower perimeter values. Because of this perimeter bias and mathematical constraints inherent in trend surface analysis (see Davis, 1973, p. 335–337), simple dome-like surfaces (Figure 12-58) resulted when the entire lineament density value array was used. The second- through sixth-degree equations were unable to accommodate subtle variances in the lineament density array. The best mathematical model among these five trend surfaces appears to be the sixth. This surface explains 82 percent of the variance due to the regression, with a 91 percent correlation between the regression and the data (Appendix C, Table

0 1 mi
0 1 km
N

Figure 12-55. Composite band 4 NS-001 lineament interpretation plotted on a band 8 high-pass filter image base

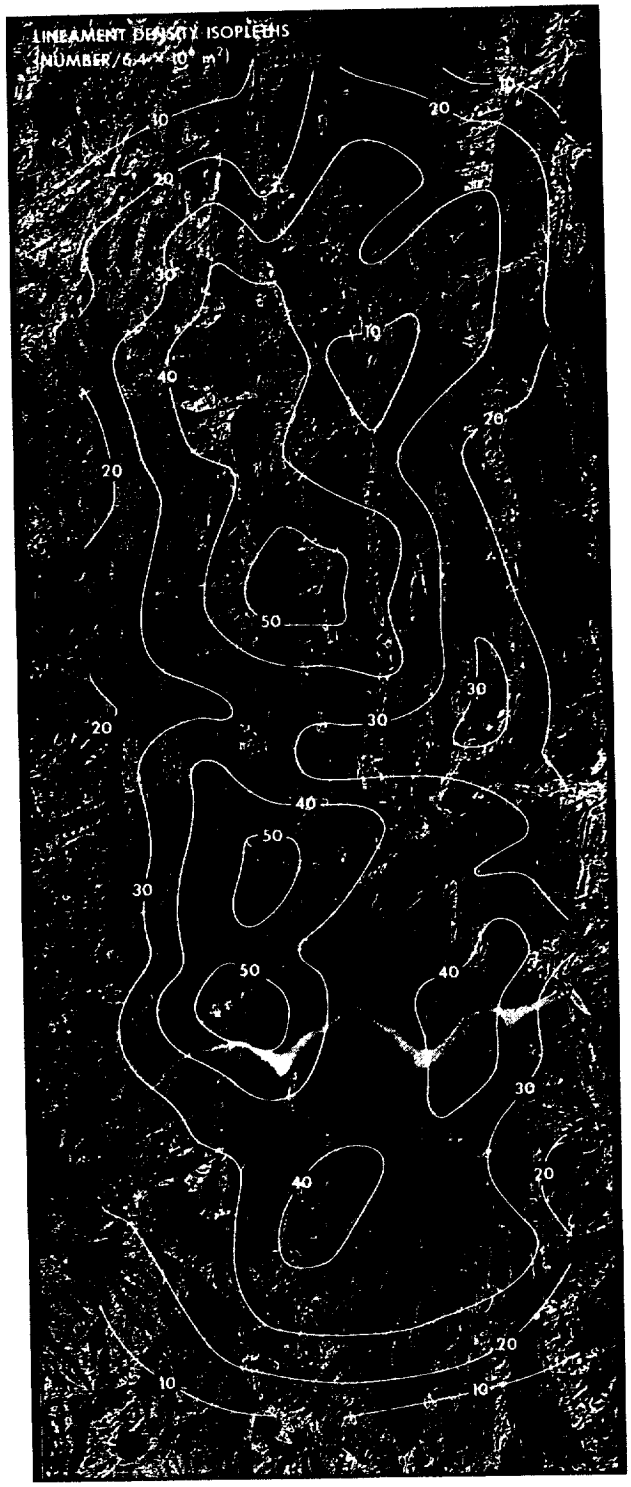

0 1 mi
0 1 km
N

Figure 12-56. Composite NS-001 lineament density isopleth map from an analysis of Figure 12-55. Lineament density is expressed in number of lineaments/6.4 x 10^6 m^2.

C-1). Based on confidence level, however, the sixth-degree surface is inferior to the fourth-degree surface.

A second set of data was analyzed to diminish the impact of the biased low-perimeter lineament density values. A 7- by 22-point array, which excluded all perimeter values, was used as input data for trend surface analysis. Consecutive trend surfaces for degrees two through five each explained more of the surface configuration (Table C-2). The sixth degree failed to add a higher degree of fit. The best trend surface model equation for the NS-001 lineament density value array contains second- through fifth-degree terms. This fifth-degree surface explains 80 percent of the variance due to the regression, with 90 percent correlation between the original data and the regression surface. Figure 12-59 shows the second- and fifth-degree trend surfaces for this second set of NS-001 lineament density data.

2. Geologic model. Figure 12-60 illustrates the fifth-degree lineament density trend surface, with perimeter values excluded, plotted on an NS-001 image base. The surface defines two areas of maximum lineament density located on a N 35° E trending domain of high lineament density.

A comparison of the lineament density pattern portrayed by Figures 12-56 and 12-60 to the subsurface structure of the Lost River gas field portrayed by Plate 12-2 and Figure 12-4 reveals obvious similarities in form. The lineament density pattern mimics the subsurface structure.

In a discussion of the relationship of faults to folds, Hills (1963, p. 266) wrote: "Where faults are geometrically related to individual folds the *prima facie* hypothesis that they are genetically related must be entertained." On the basis of a similar geometric correlation between lineament density trends and subsurface folding, lineaments at Lost River are considered a manifestation of subsurface structure; fracture density, expressed by lineament density, increases in the crestal region of the Whip Cove Anticline East.

The well-documented subsurface structure of the Kettleman Hills Dome, illustrated in Figure 12-61, is considered

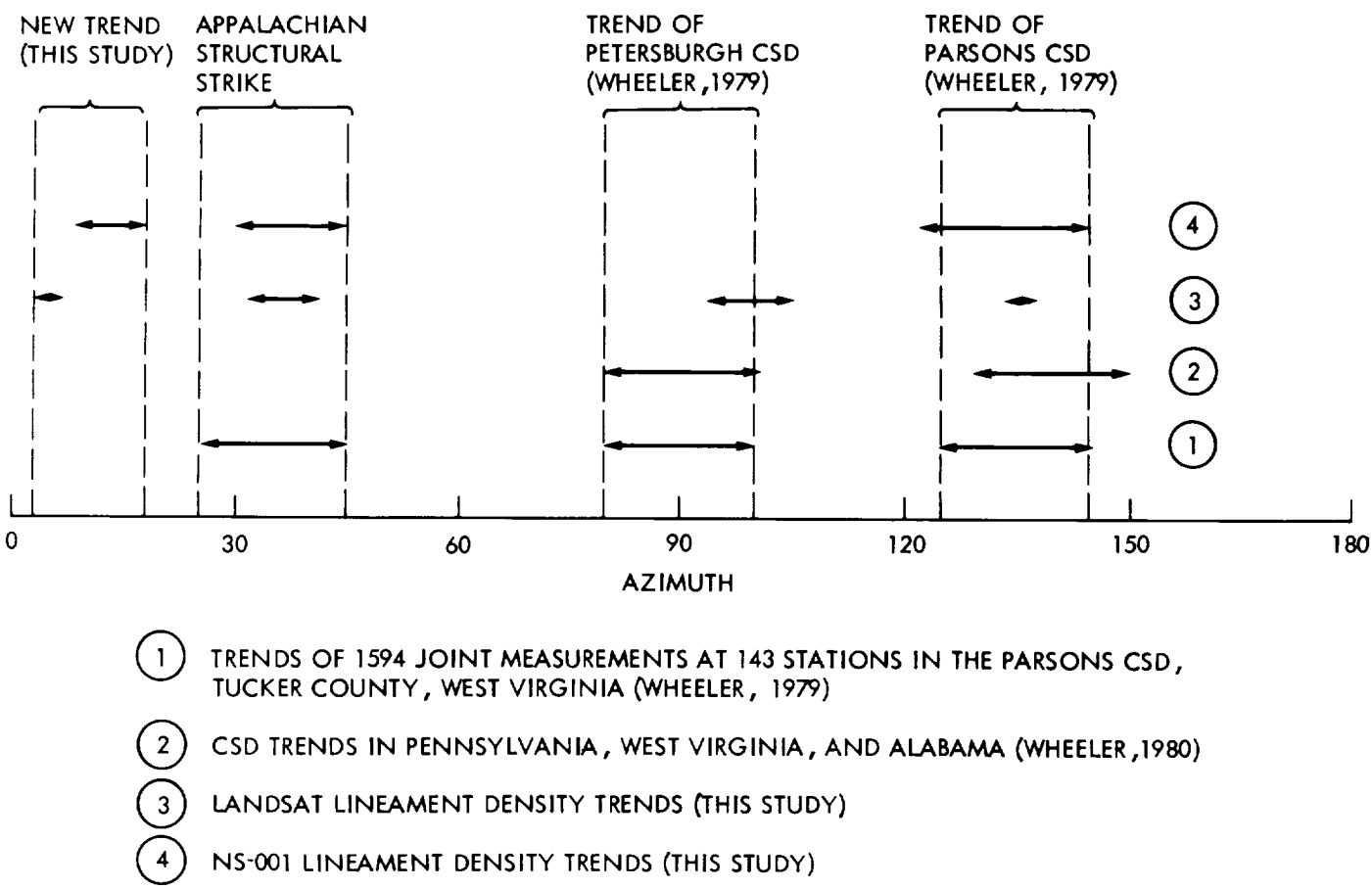

Figure 12-57. Comparison of lineament density trends from the Lost River test site analysis to joint and CSD trends recognized by Wheeler (1979, 1980)

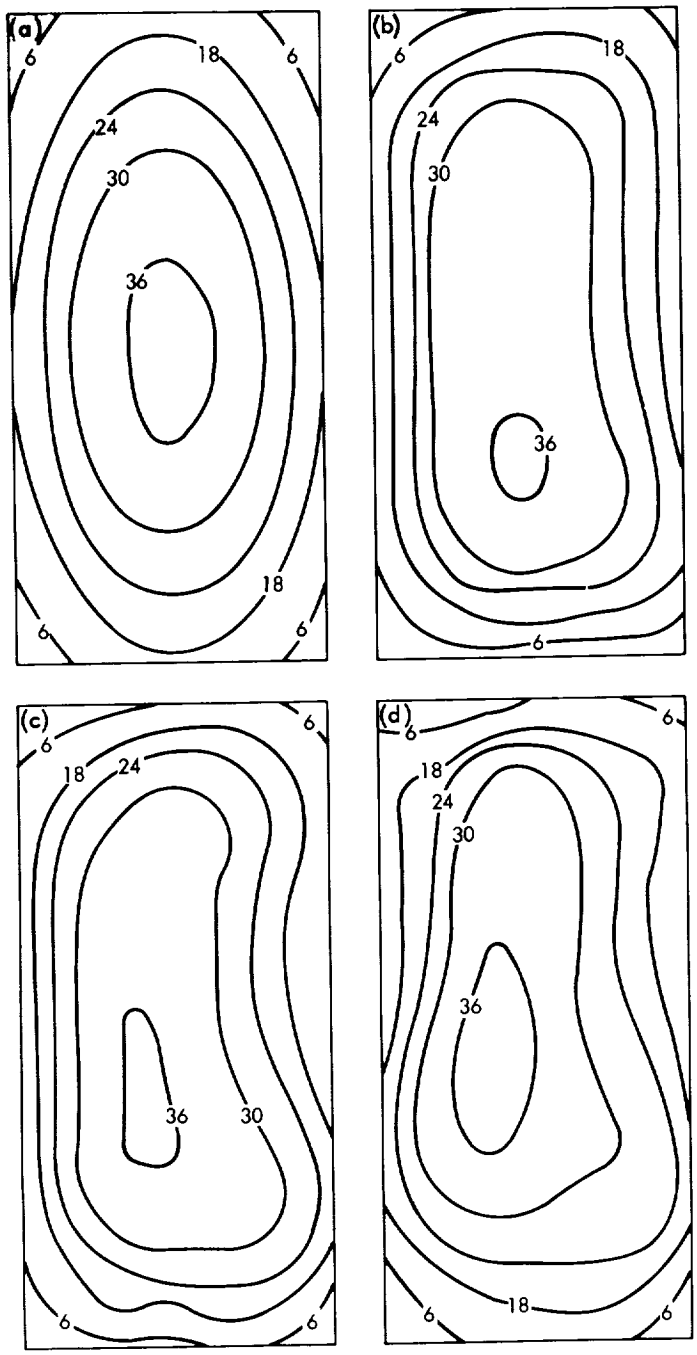

Figure 12-58. Results of trend surface analysis of NS-001 lineament density data using the entire grid array: (a) second degree; (b) fourth degree; (c) fifth degree; (d) sixth degree. The third-degree surface is not included because of its similarity to the second-degree surface.

an analogue to the Lost River structure. Examination of this figure reveals the correspondence between maximum fault density and the crestal trace of the structure. Saunders (1968, p. 109–117) confirmed that fault density maps of the Kettleman Hills Dome reveal the crestal trace. He also applied lineament density mapping procedures, similar to those used in the present investigation, to delineate the subsurface structure of the Nesson Anticline in North Dakota. These observations provide a geologic explanation for the apparent correlation of subsurface structural contour maps and lineament density isopleth maps of the Lost River test site.

XI. Radar Analysis

A. Introduction

The available radar coverage for the Lost River test site consists of Seasat Synthetic Aperture Radar (SAR) images at 23.5-cm wavelength (L-band) and airborne SAR images at 2.8-cm wavelength (X-band). The identification number, date of acquisition, polarization, direction of scene illumination, nominal ground resolution, and correlation mode of the images are given in Table 12-28. All of the available images were enlarged photographically to a scale of 1:48,000 for analysis.

B. Seasat SAR Images

The Seasat SAR coverage of the test site was acquired from two swaths with different illumination directions that are dependent on spacecraft flight-direction bearing at the instant of image acquisition. The data are parallel polarized (HH). In both cases the coverage is situated in the far range of the image swath (Figure 12-62). During image

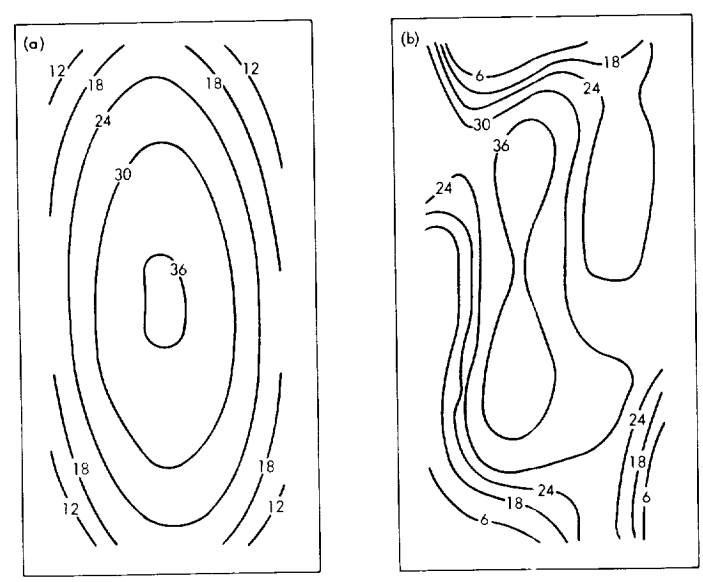

Figure 12-59. Results of trend surface analysis of NS-001 lineament density data excluding biased perimeter values: (a) second degree; (b) fifth degree

Figure 12-60. Fifth-degree lineament density trend surface plotted on an NS-001 band 8 high-pass filter image base. Lineament density is expressed in number of lineaments/6.4 x 10^6 m^2; contour interval is 3.

acquisition, the far range of the swath coincided in position with the distal margin of the main antenna lobe. This condition yields a low signal-to-noise ratio and produces images of marginal clarity, with fine topographic and cultural details being largely obliterated. Thus, in this instance, the ground resolution of the available Seasat SAR images appears to be degraded by a factor of about four from the nominal resolution of 25 m (Ford et al., 1980). Two images provided from these data are shown in Figure 12-63.

The structural strike and the dominant Ridge and Valley topography in the area are oriented about N 35° E. The directions of illumination of the Seasat SAR images are about normal to the structural strike (N 67° W; Rev. 759), and about 30° across the structural strike (N 67° E; Rev. 335). The tone and texture of the radar images are dominated by the interaction of terrain slope and terrain orientation relative to the radar imaging geometry. Most of the terrain is sloping about 10° to 30°, there is very little level ground in the area, and the inclination of the SAR imaging beam was centered about 20° from vertical. Under these conditions, the foreslopes that face the radar beam are strongly compressed or laid over on the images and they appear very bright. Backslopes that face away from the radar beam are extended and appear dark on the images. Thus, the radar backscatter is dominated by slope effects and the images have high tonal contrast and medium to coarse texture. These effects enhance the linear to curvilinear Ridge and Valley topography and highlight major cross-structural topographic features. They also produce strong relief displacement (i.e., distortion) and mask or distort surface details.

Mapping of major linear topographic features along strike and across strike from the Seasat SAR images for the test site compares favorably with similar mapping done from the higher-resolution airborne SAR images and from the multispectral scanner images of the area at a scale of about 1:200,000. The scale is too small for detailed study of the test site, although it is appropriate for reconnaissance studies of larger areas.

Attempts were made to register digitized Seasat SAR images to multispectral images in order to compare surface details in the two data sets. Common tie points were selected, and interpolation between the tie points was done by computer using a polynomial algorithm. The relief displacement and surface distortion on the SAR images create extreme difficulty in locating a sufficient number of common tie points; consequently, a satisfactory registration was not achieved.

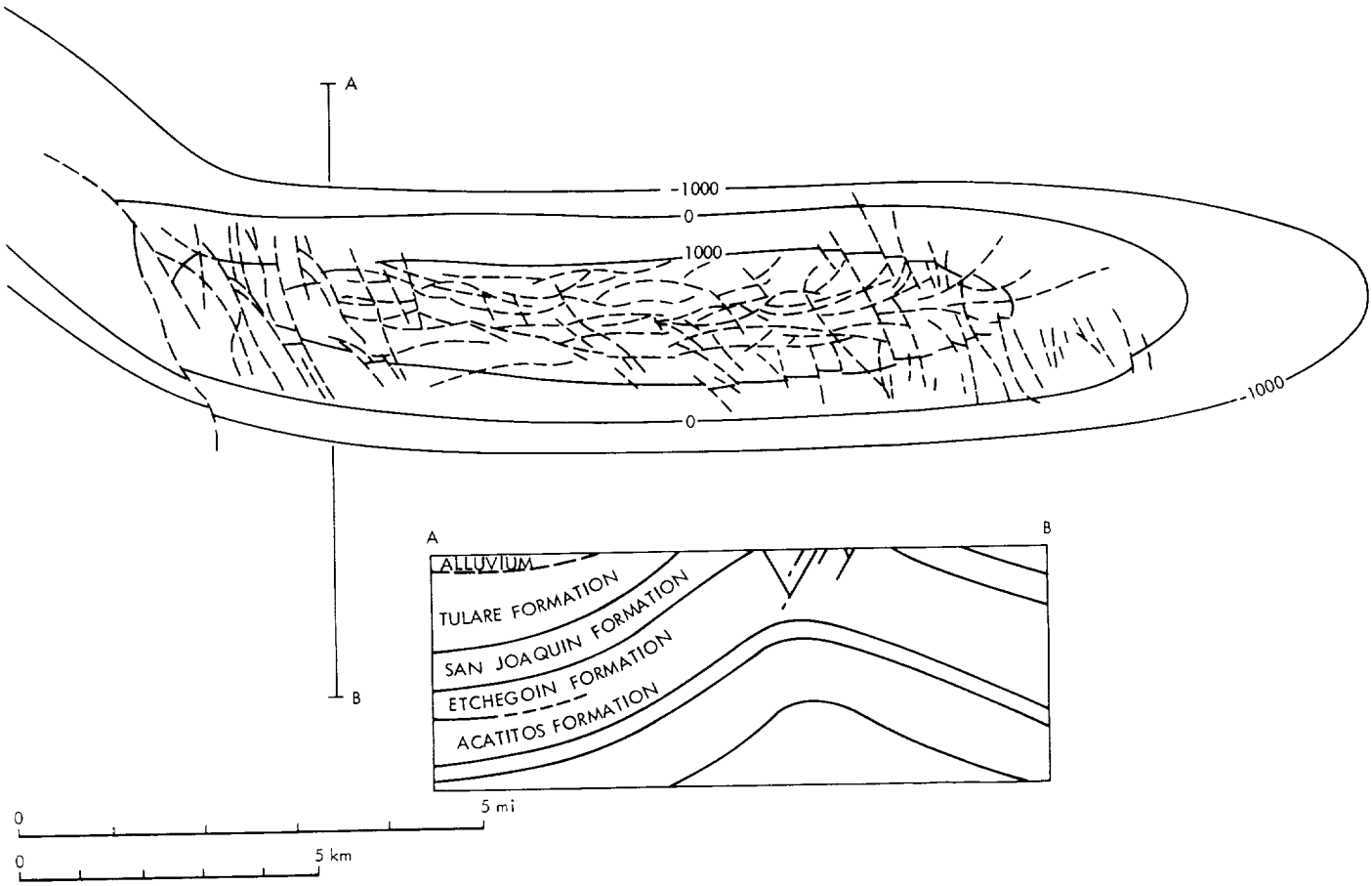

Figure 12-61. Typical domal structure exhibiting crestal fracturing, north dome of Kettleman Hills oil field, California. Note the increased density of longitudinal and transverse normal faults in the crestal region (from Hills, 1963, Figure IX-16, p. 267).

Table 12-28. Characteristics of available SAR image coverage of the Lost River test site

Identification	Date Acquired	Wavelength, cm/band	Polarization[a]	Illumination Direction	Nominal Ground Resolution, m	Correlation Mode
			Seasat (Spaceborne)			
Rev. 759	August 19, 1978	23.5/L	HH	N 67° W	25	Optical
Rev. 335	July 20, 1978	23.5/L	HH	N 67° E	25	Optical
			RB-57 (Airborne)			
Project 0653R1 (JSC)	June 27, 1979	2.8/X	HH & HV	S 55° E (125°) S 35° W (215°)	15	Optical
Project 0653R1 (JSC)	January 26, 1981	2.8/X	HH & HV	N 66.5° W N 66.5° E	15	Optical

[a] HH – parallel polarized
HV – cross polarized

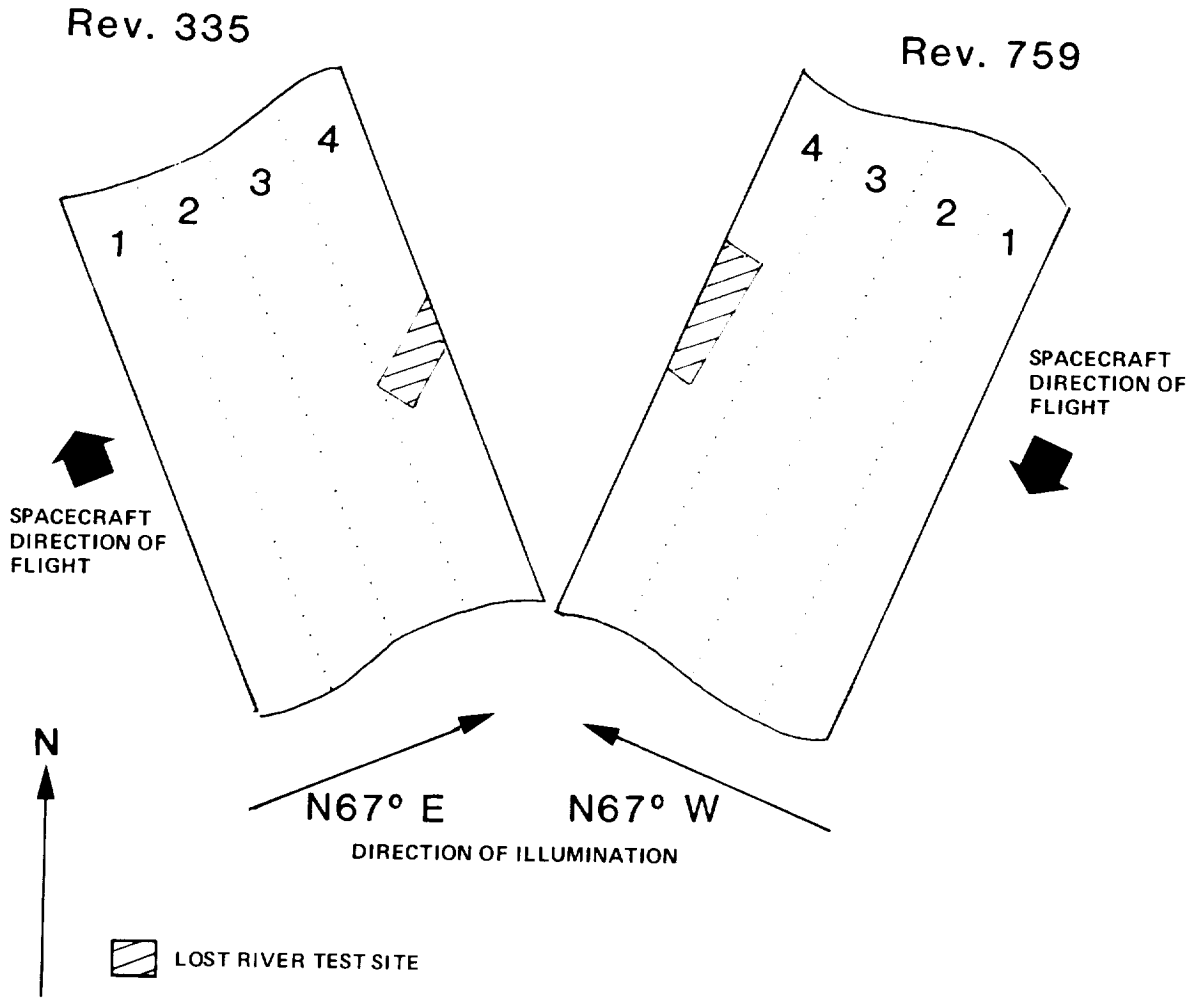

Figure 12-62. Diagram showing the geometry of Seasat SAR coverage. The Lost River test site area is in the far range of swath 4 of optically correlated Rev. 335 and Rev. 759.

C. Airborne SAR Images

The airborne SAR coverage of the test site was acquired in the summer of 1979 (at approximately the same season of the year as the Seasat SAR coverage) and again in the winter of 1981. The airborne SAR data are parallel polarized (HH) and cross polarized (HV). The airborne SAR images taken in summer are illuminated across strike, looking S 35° W (215° azimuth), and along strike, looking S 55° E (125° azimuth). These images have a ground resolution of about 15 m, which conforms with the nominal resolution. The airborne SAR images taken in winter are illuminated in approximately the same directions as the Seasat SAR images (N 66.5° W and N 66.5° E). The resolution of these images is degraded in the range direction by a factor of about four relative to the nominal ground resolution. In both data sets the inclination of the radar beam is centered about 55° from vertical. Under these conditions, compression of foreslopes and extension of backslopes are significantly reduced, layover is eliminated, and topographic features are enhanced by radar shadowing.

Linear topographic features along strike and across strike are selectively enhanced or suppressed depending on their orientation relative to the direction of scene illumination. This characteristic of the aircraft radar data is illustrated in Figures 12-64 and 12-65.

D. Recommendations

Constraints in time and resources precluded the analysis of radar data in as much detail as the multispectral data. The optically correlated aircraft SAR images have been digitized for subsequent computer manipulation. This is preparatory to registration of the SAR images with recti-

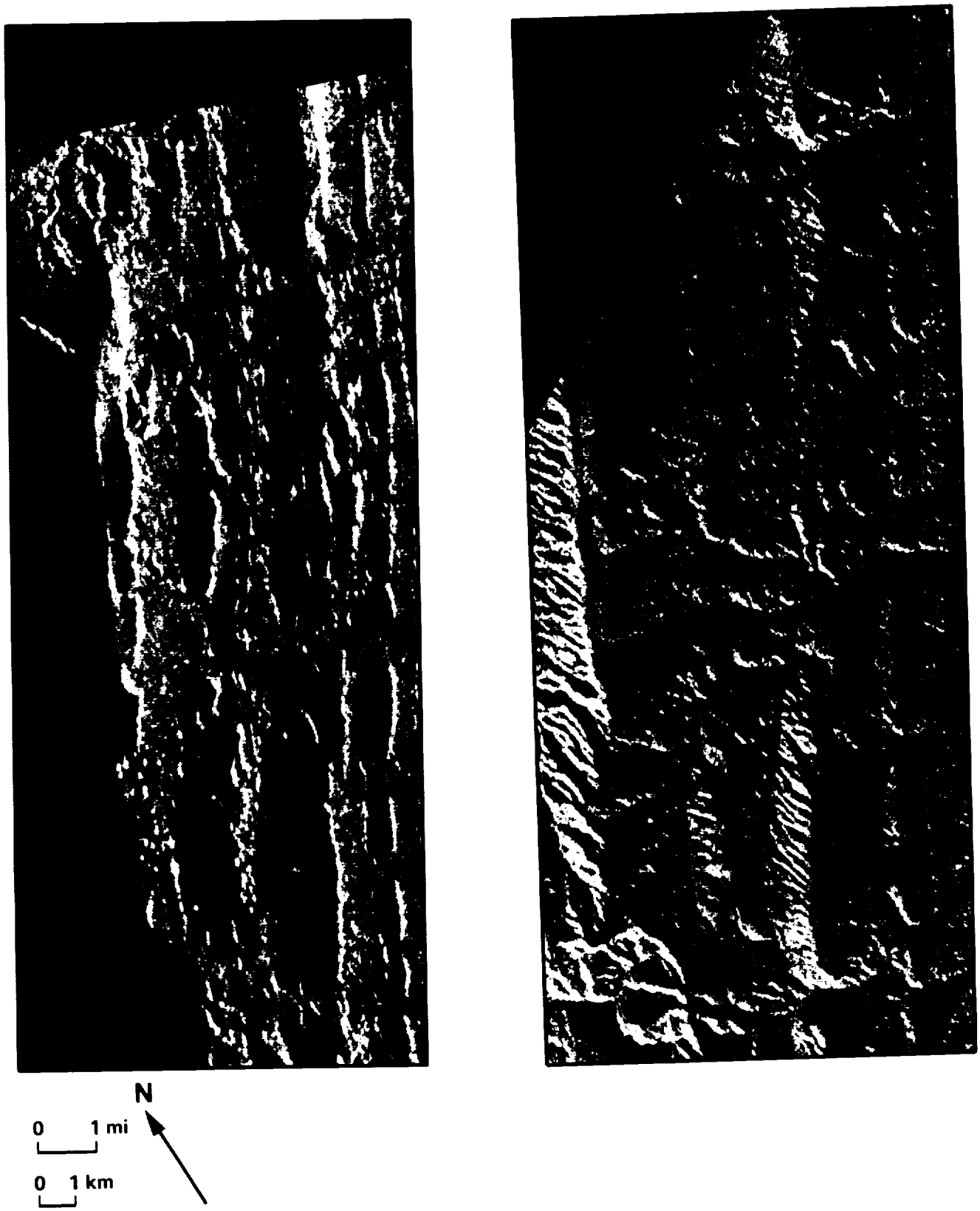

Figure 12-63. Comparison of Seasat SAR optically correlated images showing effects of illumination direction: (a) Rev. 335; (b) Rev. 759. The line border corresponds to the area covered by aircraft, line 1, multispectral data.

fied multispectral images. The radar data can then be compared with multispectral data for discriminability of vegetation and structural analysis, and the synergistic value of the two types of data can be evaluated. Future analysis of radar data acquired at the Lost River test site should also cover the following topics:

(1) Optimum imaging geometry relative to terrain slope and terrain orientation

(2) Preferred scale of terrain analysis relative to the ground resolution of images

(3) Topographic interpretability

(4) Polarization effects

XII. Conclusions and Recommendations

A. Spectral Analysis in Vegetated Terrain

The analysis of NS-001 multispectral data acquired over the Lost River test site provides insight into the utility of these data in densely vegetated terrain in a semihumid, temperate climate. Evaluation of interband correlation matrices, principal components analyses, and stepwise discriminant analyses for supervised classifications reveals that, in order of decreasing utility for vegetation discrimination, the four most important NS-001 VNIR bands are 6, 3, 5, and 4. The somewhat surprising absence of bands 1 and 2 is attributed to their high positive correlation with band 3; the high ranking of band 5 is significant. NS-001 bands 2, 3, and 4 are of considerable value in the process of vegetation discrimination and mapping since they can be used to produce images that mimic aerial CIR photography, an image format with which field botanists are most familiar. On the basis of these observations, band 1 should be excluded and band 5 included in design considerations for future multispectral satellite systems optimized for vegetation discrimination.

B. Vegetation Classification Images

The techniques employed in this study for vegetation mapping have been successful, resulting in two accurate vegetation classification images. Such vegetation classifications have broad applications in energy and mineral exploration, forestry, ecology, and wildlife management.

C. Lineament Density Analysis

Mapping lineament density patterns, rather than considering lineaments as individual entities, provides a potential tool for structural analysis that diminishes the effects of operator bias in lineament interpretation. The lineament density approach to lineament analysis also results in data that are in a form amenable to computer manipulation and statistical analyses.

D. Exploration Strategy

The results of the Lost River test site investigation suggest a strategy for locating favorable exploration targets in vegetated fold mountain belts. A regional lineament density analysis of Landsat MSS or similar data (at a scale of 1:500,000 or 1:200,000) can be used to identify moderate-sized targets. Lineament density analysis of aircraft remote sensing data or Landsat 4 TM data (at a scale of 1:48,000) can then be used to further refine locations of areas with potential enhanced fracture porosity. These small targets can then be evaluated using geobotanical, geochemical, and geophysical techniques.

E. Direct Detection of Hydrocarbons

Addressing the problem of "direct" detection of hydrocarbons by remotely sensing surface alteration associated with microseepage involves three questions:

(1) Does the reservoir leak?

(2) Do leaking hydrocarbons alter surface material?

(3) Can this alteration be detected by remote sensing methods?

A reconnaissance soil manganese survey revealed anomalous manganese concentrations over the Lost River gas field that are consistent with the type of alteration expected over a leaking reservoir. However, a reconnaissance soil microbe survey of Lost River yielded results that did not demonstrate hydrocarbon seepage. Vegetation analysis revealed subtle vegetation distributional anomalies over the field in the form of concentrations of weed trees (maples) at sites where the more typical oak–hickory climax vegetation is expected. This anomalous distribution may relate to anaerobic soil conditions which, in turn, are consistent with gas leakage from the reservoir. These anomalous maple concentrations are shown on supervised vegetation classification maps produced from NS-001 data.

F. Mycorrhizal Fungi

Preliminary experimental data suggest that methane may influence tree species distribution through direct or indirect influence on the host tree's mycorrhizal fungi. Since the state of health of mycorrhizae is likely to be a major factor affecting forest tree distribution at the Lost River test site, detailed field and laboratory studies of the host/fungus relationship, in response to methane, should be conducted.

Figure 12-64. Aircraft X-band SAR image; look-direction (S 63° E) is approximately perpendicular to the Ridge and Valley trend. Compare to Figure 12-65.

Figure 12-65. Aircraft X-band SAR image; look-direction (S 28° W) is approximately parallel to the Ridge and Valley trend. Compare to Figure 12-64.

Acknowledgments

Lost River test site fieldwork, image analysis, interpretation, and reporting were done as a team effort by 16 individuals. Their time, financial support, and laboratory work were provided by seven organizations representing government, industry, and academia. The authors express sincere appreciation to the individuals listed below and to the organizations which they represent. Their participation in discussion, fieldwork, and laboratory analyses contributed substantially to the successful completion of the project.

Participant	Affiliation (during test site study)
Robert Borger	Mobil Research and Development
Matt D. Matthews	Gulf Science and Technology
David McClean	Gulf Mineral Resources
Gordon L. Owens	Columbia Gas Systems
Jay Parrish	Geospectra Corporation

References

Ahmadjian, V. (1967). *The lichen symbiosis.* Waltham, Massachusetts: Blaisdell Publishing.

Canney, F. C., H. L. Cannon, J. B. Cathrall, and K. Robinson (1979). Autumn colors, insects, plant disease, and prospecting. *Econ. Geol., 74,* 1673–1692.

Cardwell, D. H. (1971). Future petroleum potential of West Virginia, Virginia, and Maryland. In I. H. Cram (Ed.), Future petroleum provinces of the United States—Their geology and potential, *AAPG Mem. 15*(2), 1248–1253.

Cardwell, D. H. (1974). Oriskany and Huntersville gas fields of West Virginia. *West Virginia geological and economic survey.* (Mineral Resources Series No. 5)

Carpenter, R. H., and W. B. Hays (1978). Precipitation of iron, manganese, zinc, and copper on clean ceramic surfaces in a stream draining on polymetallic sulfide deposit. *J. Geochem. E., 9,* 31–37.

Chen, P. F. (1980). Oil and gas exploration and potential in the northwestern part of Ridge and Valley Province in West Virginia (Berkeley, Morgan, Hampshire, Hardy, Mineral, Grant and Pendleton Counties). *W. Va. Geol. Econ. Surv. Prel. Open File Rept.*

Conel, J. E., M. J. Abrams, and A. F. H. Goetz (1978). *A study of alteration associated with uranium occurrences in sandstone and its detection by remote sensing methods* (JPL Publication 78-66). Pasadena, California: Jet Propulsion Laboratory.

Cook, F. A., D. S. Albaugh, L. D. Brower, J. E. Kaufman, J. E. Sidney, J. E. Olines, and R. D. Hatcher, Jr. (1979). Thin-skinned tectonics in crystalline southern Appalachians: COCORP seismic profiling of the Blue Ridge and Piedmont. *Geology, 7,* 563–567.

Core, E. L. (1966). *Vegetation of West Virginia.* Parsons, West Virginia: McClain Printing Co.

Core, E. L., and R. L. Guthrie (1977). *Forest trees of West Virginia.* Charleston, West Virginia: West Virginia Department of Natural Resources.

Crow, P. (1981). Gas strikes spark play in Eastern Overthrust. *Oil Gas J., 79*(17), 109–113.

Dalziel, M. C., and T. J. Donovan (1980). Biogeochemical evidence for subsurface hydrocarbon occurrence, Recluse oil field, Wyoming: Preliminary results. *U.S. Geol. Surv. Circ. 837.*

Davis, J. B. (1967). *Petroleum microbiology.* New York: American Elsevier Scientific Publishing Co.

Davis, J. C. (1973). *Statistics and data analysis in geology.* New York: John Wiley & Sons.

Dominik, T. (1959). Synopsis of a new classification of the ectotrophic mycorrhizae established on morphological and anatomical characteristics. *Mycopath. et. Mycol. Appl., 11,* 359–367.

Dubey, A. K. (1980). Model experiments showing simultaneous development of folds and transcurrent faults. *Tectonophysics, 65,* 69–84.

Fenneman, N. M. (1938). *Physiography of eastern North America.* New York: McGraw–Hill.

Flower, F. B., E. F. Gilman, and I. A. Leone (1981). Landfill gas, what it does to trees and how its injurious effects may be prevented. *J. Arboric., 7*(2), 43–51.

Ford, J. P., R. G. Blom, M. L. Bryan, M. I. Daily, T. H. Dixon, C. Elachi, and E. C. Xenos (1980). *Seasat views North America, the Caribbean, and Western Europe with imaging radar* (JPL Publication 80-67). Pasadena, California: Jet Propulsion Laboratory.

Gilman, E. F., I. A. Leone, and F. B. Flower (1981). The adaptability of 19 woody species in vegetating a former sanitary landfill. *Forest Sci., 21*(1), 13–18.

Gwinn, V. E. (1964). Thin-skinned tectonics in the Plateau and northwestern Valley and Ridge Provinces of the central Appalachians. *Geol. Soc. Am. Bull., 75,* 863–900.

Hacskaylo, E. (1972). Mycorrhizae, the ultimate in reciprocal parasitism. *Bioscience, 22,* 577–582.

Hale, M. E. (1974). *The biology of lichens.* New York: American Elsevier Scientific Publishing Co.

Henderson, M. E. K., and R. B. Duff (1963). The release of metallic and silicate ions from minerals, rocks and soils by fungal activity. *J. Soil Sci., 14*(2), 236–246.

Hills, E. S. (1963). *Elements of structural geology.* New York: John Wiley & Sons.

Hovis, W., J. Nichols, A. Potter, and F. Thomson (1975). *Landsat-D Thematic Mapper technical working group final report* (JSC-09797). Houston: Lyndon B. Johnson Space Center, Appendixes A–H.

James, F. C., and H. H. Shugart, Jr. (1970). A quantitative method of habitat description. *Audubon Field Notes, 24*(6), 727–736.

Kay, L. B. (1975). *Anatomy and morphology of ectotrophic mycorrhizae of* Pinus resinosa Ait. *growing on stripmine spoils in Clarion County, Pennsylvania.* Unpublished master's thesis, Clarion State College, Pennsylvania.

King, P. B. (1959). *The evolution of North America.* Princeton, New Jersey: Princeton University Press.

Kulander, B. R., and S. L. Dean (1978). Gravity, magnetics, and structure Allegheny Plateau/Western Valley and Ridge in West Virginia and adjacent states. *West Virginia geological and economic survey* (RI-27).

Kulow, D. L. (1965). Elementary point-sampling. *W. Va. Univ. Ag. Exp. Sta. Circ. 116,* Morgantown, West Virginia.

Kummel, B. (1961). *History of the Earth.* San Francisco: W. H. Freeman.

Leone, I. A., F. B. Flower, J. J. Arthur, and E. F. Gilman (1977). Damage to woody species by anaerobic landfill gases. *J. Arboric., 3*(12), 221–225.

Leone, I. A., F. B. Flower, E. F. Gilman, and J. J. Arthur (1979). Adapting woody species and planting techniques to landfill conditions. *Field and laboratory investigations* (U.S. EPA Report 600/2-79-128), U.S. Environmental Agency.

Lindsey, A. A., J. D. Barton, and S. R. Miles (1958). Field efficiencies of forest sampling methods. *Ecology, 39,* 428–444.

Ludlum, J. C. (1952). The geology of Lost River State Park, West Virginia. *W. Va. Geol. Econ. Surv. Bull. 3.*

Marks, G. C., and R. C. Foster (1967). Succession of mycorrhizal associations on roots of radiata pine. *Aust. For., 31*(3) 193–201.

McCaslin, J. C. (1981). Virginia hosts rare deep exploratory hole. *Oil Gas J., 79*(31), 191–192.

Medve, R. J. (1971). Anatomical study of the endotrophic mycorrhizae of *Acer rubrum. Bull. Torrey Bot. Club, 98*(1), 41–45.

Mikola, P. (1970). Mycorrhizal inoculation in afforestation. *Int. Rev. For. Res., 3,* 123–185.

Patchen, M. A. (1969). Oriskany sandstone–Huntersville chert gas production in the eastern half of West Virginia. *W. Va. Geol. Econ. Surv. Circ. Ser. 9.*

Prouty, W. F. (1926). *Map IV, Hardy County, showing general and economic geology.* West Virginia Geological Survey.

Raven, P., R. Evert, and H. Curtis (1976). *Biology of plants* (2nd ed.). New York: Worth Publishing.

Robinson, R. K. (1971). Changes in mycorrhizal flora on roots of *Pinus patula* in Swaziland. *S. Afr. For. J., 78,* 14–15.

Salomonson, V. V., P. L. Smith, Jr., A. B. Park, W. C. Webb, and T. J. Lynch (1980). An overview of progress in the design and implementation of Landsat-D systems. *IEEE Trans. Geosci. Rem. Sens., GE-18*(2), 137–145.

Sargent, C. S. (1965). *Manual of the trees of North America.* New York: Dover Publications.

Saunders, D. F. (1968). Airborne sensing as an oil reconnaissance tool. In W. B. Heroy (Ed.), *Symposium on unconventional methods in exploration for petroleum and natural gas.* Dallas: Southern Methodist University Press, 105–126.

Siegal, B. S. (1977). Significance of operator variation and the angle of illumination in lineament analysis on synoptic images. *Mod. Geol., 6,* 75–85.

Sites, R. S. (1978). *Structural analysis of the Petersburg lineament, central Appalachians.* Unpublished doctoral dissertation, West Virginia University.

Soil Conservation Service (1979). *Soils map and interpretative guide to soils of Hardy County.* Morgantown, West Virginia: U. S. Department of Agriculture.

Strausbaugh, P. D., and E. L. Core (1978). *Flora of West Virginia.* Grantsville, West Virginia: Seneca Books.

Sturm, R. L. (1977). *Comparison of forest cover types in seven environmentally diverse areas in West Virginia.* Unpublished master's thesis, West Virginia University.

Thornbury, W. D. (1965). *Principles of geomorphology.* New York: John Wiley & Sons.

Trappe, J. M., and R. S. Quinard (1966). *Cenococcum graniforme* in Mexico. *Mycologia, 58,* 647–648.

Weller, R. N. (1970). Photo enhancement by film sandwiches. *Photogramm. Eng., 36,* 468–474.

Werner, E. (1976). *Remote sensing studies in the Appalachian Plateau for application to fossil fuel extraction: Final report.* Morgantown, West Virginia: Energy Research and Development Administration, C-2/1–C-2/10. (Contract E-(40-1)-8040)

Wheeler, R. L. (1979). *Draft report on the applicability of cross-strike structural discontinuities as an exploration rationale.* Morgantown, West Virginia: DOE, Morgantown Energy Technology Center, Eastern Gas Shales Project, Task 17. (Contract DE-AT21-78MC08216)

Wheeler, R. L. (1980). Cross-strike structural discontinuities: Possible exploration tool for natural gas in Appalachian Overthrust Belt. *AAPG Bull., 64,* 2169–2178.

Wiersma, D. J., and D. A. Landgrebe (1980). Analytical design of multispectral sensors. *IEEE Trans. Geosci. Rem. Sens., GE-18*(12) 137–145.

Wyllie, P. J. (1971). *The dynamic Earth: Textbook in geosciences.* New York: John Wiley & Sons.

Zoback, M. L., and M. Zoback (1980). State of stress in the conterminous United States. *J. Geophys. Res., 85*(B11), 6113–6156.

Appendix A
Lost River Rock and Soil Analyses

PRECEDING PAGE BLANK NOT FILMED

INTENTIONALLY BLANK

Table A-1. Lost River Chemung rock bulk chemistry

Station	Element, ppm																
	Fe	Al	Mg	Na	K	Ca	Ti	Mn	Cu	Ni	Pb	Zn	V	Co	Cr	Rb	Sr
55-11a[a]	5.6	10.8	0.49	0.21	3.3	0.065	0.52	71	150	55	33	90	160	23	120	330	28
55-11b[a]	5.5	10.4	0.47	0.21	3.4	0.130	0.53	96	130	50	35	100	160	20	140	350	28
55-10[a]	4.4	7.5	0.63	0.63	1.9	0.070	0.50	68	99	39	39	87	120	19	72	170	24
55-7	6.1	11.6	0.90	0.24	3.9	0.094	0.53	210	99	60	47	120	170	25	130	380	32
4	4.2	10.0	1.00	0.53	3.1	0.110	0.51	100	99	50	30	100	150	20	120	290	28
8[a]	4.5	9.3	0.79	0.52	2.8	0.040	0.49	130	99	44	40	100	130	22	100	270	20
12	1.4	2.2	0.06	0.02	0.6	0.009	0.18	<10	90	10	35	15	25	<10	33	33	<10
A-3[a]	3.7	8.0	0.84	0.71	2.2	0.100	0.50	160	140	44	99	99	110	20	94	210	25
A-6a[a]	0.6	1.0	0.03	0.02	1.6	0.005	0.04	61	95	<10	40	50	10	<10	10	<10	<10
A-6b[a]	0.9	1.3	0.04	0.05	2.1	0.052	0.05	73	90	10	60	68	20	<10	15	15	<10
A-9[a]	3.0	8.4	0.60	0.29	2.3	0.038	0.50	120	170	45	48	100	110	25	93	210	17
A-10[a]	4.5	5.4	0.76	0.83	2.1	0.053	0.59	150	120	34	42	86	120	20	88	200	25
A-15[a]	2.3	4.6	0.41	0.30	1.3	0.022	0.41	59	80	25	46	60	93	10	70	110	18
A-16[a]	2.2	4.5	0.32	0.41	1.2	0.016	0.28	74	99	20	47	60	60	15	40	94	15
A-18[a]	1.5	4.3	0.35	0.25	1.3	0.009	0.26	58	95	29	46	58	51	15	37	93	17
A-19a[a]	5.0	9.8	0.65	0.16	3.2	0.032	0.52	280	170	50	57	140	140	32	110	310	20
A-19b[a]	4.8	8.5	0.60	0.15	3.2	0.048	0.48	250	290	50	50	210	140	30	110	290	20
A-21	4.2	5.3	0.60	0.63	1.4	0.054	0.39	130	120	29	38	79	91	14	72	110	22
B-1-Sd	0.8	1.9	0.08	0.25	0.3	0.029	0.05	40	800	10	50	150	10	10	10		
B-1-Sh	3.9	8.1	0.70	0.56	2.8	0.093	0.43	110	85	5	40	110	120	20	80		
B-2	2.0	6.9	0.43	0.11	2.0	0.013	0.39	64	230	35	99	87	87	20	57		
B-3	4.5	7.9	0.77	0.29	2.5	0.020	0.40	120	200	57	50	120	120	20	80		
B-4	4.0	6.1	0.64	0.75	1.7	0.093	0.45	100	220	35	55	85	92	15	72		
B-5	4.5	5.9	0.60	0.99	1.7	0.099	0.40	120	430	42	55	97	100	15	55		
B-6	4.4	5.1	0.46	0.56	2.2	0.041	0.24	180	340	30	69	72	72	15	32		
B-7	4.5	9.8	0.82	0.39	3.5	0.068	0.47	140	170	52	52	120	150	20	99		
B-8-Sd	3.8	6.6	0.72	0.68	1.9	0.090	0.47	97	160	42	50	74	94	15	67		
B-8-Sh	4.6	10.0	1.00	0.54	3.5	0.270	0.50	220	150	45	65	82	150	25	100		
B-9	4.3	7.5	0.90	0.76	2.4	0.150	0.45	400	200	50	47	100	120	25	82		
B-10	2.7	5.0	0.37	0.55	1.8	0.030	0.24	50	160	25	50	72	50	15	35		

[a]Samples obtained from Chemung outcrops overlying the Lost River gas field.

Table A-2. Lost River Chemung rock <2-μm fraction trace metal chemistry

Station	Element, ppm					
	Mn	Cu	Ni	Pb	Zn	V
55-11	37	150	110	78	140	200
55-10	98	61	110	160	200	210
55-7	74	120	74	89	130	200
4	89	210	130	99	150	220
8	84	15	44	25	84	120
12	12	610	470	98	98	150
A-3	150	36	85	210	200	210
A-6	35	52	52	660	120	170
A-9	96	300	230	110	200	190
A-10	120	50	74	74	150	220
A-15	120	210	96	280	280	260
A-16	73	73	180	85	160	200
A-18	110	90	110	220	200	250
A-19	51	76	76	230	230	250
A-21	120	56	56	90	150	240

Table A-3. Lost River Chemung rock reducing, acid-leachate chemistry

Station	Element, ppm[a]							
	Fe	Al	Ca	Mg	Co	Cu	Mn	Zn
55-11	5.3	11	26	4.5	<0.5	0.9	0.6	<0.5
55-10	15	18	24	5.9	<0.5	0.6	<0.5	<0.5
55-7	290	66	29	8.5	100	3.9	2.9	<0.5
4	25	20	23	11.0	<0.5	0.9	<0.5	<0.5
8	45	33	20	13.0	<0.5	0.8	1.1	<0.5
12	150	26	22	3.5	65	2.0	<0.5	0.5
A-3	29	23	27	8.5	<0.5	1.2	1.1	<0.5
A-6	300	53	18	3.0	140	6.4	0.8	<0.5
A-9	290	60	20	5.7	11	5.2	1.1	<0.5
A-10	55	31	21	9.1	1.9	1.1	1.0	<0.5
A-15	16	16	17	5.3	<0.5	0.6	<0.5	<0.5
A-16	15	9	21	4.6	1.6	0.7	0.5	<0.5
A-18	670	100	21	4.4	250	3.2	<0.5	<0.5
A-19	18	22	19	5.3	<0.5	1.2	3.6	<0.5
A-21	41	22	22	7.9	<0.5	0.9	1.2	<0.5
B-1-Sd	7.1	4.5	23	4.8	<0.5	6.2	<0.5	1.1
B-1-Sh	21	12	27	7.7	0.5	0.7	0.5	<0.5
B-2	4.4	9.8	23	4.3	<0.5	0.8	<0.5	<0.5
B-3	19	16	26	7.7	<0.5	1.7	0.5	<0.5
B-4	200	39	54	8.1	81	5.4	<0.5	<0.5
B-5	110	22	27	6.6	41	2.5	<0.5	<0.5
B-6	390	55	28	6.0	160	2.4	1.3	0.6
B-7	14	12	25	9.3	<0.5	1.1	1.0	<0.5
B-8-Sd	28	11	29	7.5	<0.5	1.3	<0.5	<0.5
B-8-Sh	48	20	43	15.0	1.3	0.8	1.6	<0.5
B-9	36	19	31	11.0	<0.5	1.5	3.4	<0.5
B-10	4.4	8.5	24	5.3	<0.5	1.4	<0.5	<0.5
Blank	<0.5	<0.5	21	3.7	<0.5	<0.5	<0.5	<0.5

[a] Values reported as ppm in solution (0.2 gm soil → 25 ml solution); multiply by 125 to obtain ppm in soil.

Table A-4. Lost River soils reducing, acid-leachate chemistry

Station	Element, ppm[a]								
	Fe	Al	Ca	Mg	Na	K	Co	Cu	Zn
M1	8.2	50	36	62	5.9	9	<0.5	<0.5	5.3
M2	11	12	28	53	5.9	19	<0.5	<0.5	4.8
M3-1	1300	180	26	50	5.2	17	600	12	0.5
M3-2	440	540	27	48	3.8	17	220	3.4	0.7
M4	10	100	30	55	3.5	17	0.8	<0.5	6.0
M5	27	17	26	56	3.4	18	0.5	<0.5	40.0
M6-1	11	13	33	52	4.3	17	<0.5	<0.5	10.0
M6-2	8.9	33	30	48	5.8	15	<0.5	<0.5	6.7
M7	140	38	39	58	4.5	17	70	<0.5	8.9
M8-1	19	28	31	69	3.4	18	0.5	<0.5	13.0
M8-2	19	10	31	69	3.4	19	<0.5	<0.5	17.0
M9	7.3	8	22	44	3.2	15	<0.5	<0.5	1.3
M10	9.9	6.6	27	45	3.2	16	1.0	<0.5	2.6
M11	320	34	26	50	2.7	17	140	2.9	1.4
M12	1800	270	23	46	3.5	17	870	26	1.1
M13	17	19	23	49	3.3	16	0.6	<0.5	12.0
M14	6.8	14	23	44	4.0	16	0.3	<0.5	2.2
M15-1	7.8	6.8	26	47	3.8	17	<0.5	<0.5	<0.5
M15-2	7.8	13	26	50	4.3	18	<0.5	<0.5	0.6
M16	100	74	27	47	6.3	17	–	8.9	<0.5
Blank	0.5	2.0	22	40	4.2	15	<0.5	<0.5	<0.5

[a]Values reported as ppm in solution (0.2 gm soil → 25 ml solution); multiply by 125 to obtain ppm in soil.

Table A-5. Lost River soils oxidizing leachate chemistry

Station	Element, ppm[a]								
	Fe	Al	Ca	Mg	Na	K	Co	Cu	Zn
M1	4.4	2.7	24	37	3.7	13	<0.5	<0.5	1.0
M2	2.4	2.8	25	36	4.7	16	<0.5	<0.5	0.7
M3-1	1.6	2.2	20	33	4.1	14	2.8	9.4	<0.5
M3-2	1.8	3.4	22	38	5.3	15	0.7	1.7	<0.5
M4	2.0	2.4	25	34	3.5	13	<0.5	<0.5	0.7
M5	2.9	3.9	26	39	4.4	14	<0.5	<0.5	0.6
M6-1	3.9	8.4	20	33	4.0	14	<0.5	<0.5	<0.5
M6-2	13.0	8.3	20	35	3.7	14	<0.5	<0.5	<0.5
M7	4.1	23.0	19	30	3.8	13	<0.5	<0.5	<0.5
M8-1	5.3	6.5	21	39	3.7	15	<0.5	<0.5	<0.5
M8-2	5.9	6.3	23	38	4.0	15	<0.5	<0.5	0.5
M9	2.1	3.3	29	39	4.1	15	<0.5	<0.5	0.5
M10	2.5	3.5	29	40	4.1	17	<0.5	<0.5	0.9
M11	3.7	3.7	21	31	4.8	14	<0.5	<0.5	<0.5
M12	2.2	1.7	23	40	5.2	16	2.0	11.0	<0.5
M13	4.8	19.0	26	38	6.3	13	<0.5	<0.5	0.9
M14	2.1	5.0	25	37	4.8	13	<0.5	<0.5	0.5
M15-1	3.0	15.0	25	37	4.4	14	<0.5	<0.5	0.6
M15-2	2.1	58.0	19	29	31.0	10	<0.5	<0.5	1.0
M16	1.9	3.0	24	33	4.3	15	<0.5	0.8	0.6
Blank	1.1	0.9	16	27	3.4	11	<0.5	<0.5	<0.5

[a]Values reported as ppm in solution (0.2 gm soil → 25 ml solution); multiply by 125 to obtain ppm in soil.

Table A-6. Lost River soils reducing, acid-leachate manganese concentration

Site	Mn, %	Site	Mn, %
M1	0.066	M32	0.006
M2	0.060	M33	0.018
M3-1	0.006	M34-W	0.050
M3-2	0.009	M35	0.008
M4	0.075	M36	0.004
M5	0.500	M37	0.006
M6-1	0.125	M38	0.040
M6-2	0.084	M39	0.076
M7	0.111	M40	0.053
M8-1	0.162	M41	0.027
M8-2	0.212	M42	0.035
M9	0.016	M43	0.065
M10	0.032	M44	0.037
M11	0.018	M45	0.058
M12	0.014	M46	0.055
M13	0.150	M47-W	<0.002
M14	0.028	M48	0.039
M15-1	<0.006	M49	0.071
M15-2	0.008	M50	0.007
M16	<0.006	M51	0.031
M17	0.058	M52	0.103
M18	0.005	C1	0.012
M19	0.042	C2	0.039
M20	0.054	C3	0.084
M21	0.002	C4	0.081
M22	0.305	C5-1	0.105
M23	0.012	C5-2	0.101
M24	0.083	C6	0.045
M25	0.084	C7-A	0.066
M26	0.003	C7-B	0.044
M27	0.002	J-1	<0.006
M28	0.009	J-2	<0.006
M29-P	0.082	J-3	<0.006
M30	<0.002	J-4	<0.006
M31	<0.002	J-5	<0.095

Appendix B
Ground Vegetation Analysis Methods

PRECEDING PAGE BLANK NOT FILMED

I. Modified 0.1-acre Circular Plot Method of Vegetation Analysis

In this method, a 10-factor (BAF 10) wedge prism was used to determine a 37-ft horizontal distance (the radius of a 0.1-acre circle) by viewing a target (clipboard) with markers of known dimension (two strips of white tape whose outer boundaries were 13 in. apart). When the target markers were properly displaced, as viewed through the prism, the distance between the prism and the target was 37 ft. The prism was kept at the center of the circle, and a second person carried the target around the boundary of the plot. All trees (any woody specimen possessing a single trunk at least 5 ft in height) within the circle plot were tallied, and a species count and total number of trees count were recorded. Each species was recorded by size class (diameter at breast height or dbh 0 to 4 in., 5 to 8 in., 9 to 12 in., 13 to 16 in., and over 16 in.) as determined by a Biltmore reach stick.

Shrub (woody specimens that branch at the ground level, usually under 5 ft in height) composition was estimated, and percent ground cover and percent canopy cover were determined by means of an ocular tube 2 in. in diameter (when held vertically overhead, 10 points along a diameter transect were recorded; "plus" if canopy cover was seen through the tube, "minus" if no canopy was seen). In a similar manner, 10 points along a similar diameter transect were recorded for ground cover, sighting through the ocular tube held at arm's length at a 45° angle ("plus" if green ground cover was seen, "minus" if none was seen). Canopy height was determined by using a simple triangulation technique.

Dominance (basal area) for woody species per sample plot was determined by means of the wedge prism. All trees not completely offset (displaced) as viewed through the prism were tallied. This number multiplied by 10 gives the basal area of woody trees per acre in square feet (i.e., if seven trees are counted, as determined by sighting through the prism around a sample point, the basal area per acre for that site is 70 ft^2). Borderline trees were not tallied. All trees not offset were counted regardless of size; thus, figures for some sites, especially those occupied by large numbers of small trees close to the sample point, will seem high to the forester (foresters commonly ignore trees with trunks less than 4 in. dbh when making basal area determinations).

The term "tree" follows standard botanical usage (as opposed to that of foresters) and refers to any woody specimen branching at some distance above the ground. A "shrub" would thus be a woody species that branches at the ground level. Young trees less than shoulder height (5 ft) were not tallied, whereas shrubs of any size were considered in estimating the percent of shrubs at a sample site.

II. Field Photographic Methods

Two 35-mm SLR cameras were mounted on a single tripod so that each photographed the same field of view. Each camera was fitted with a 150-mm telephoto lens. One camera was loaded with Ektachrome 200 transparency film (true color), while the other was loaded with Ektachrome Infrared Aero film, type 8443 (false-color infrared). The camera loaded with the infrared film was fitted with a Wratten 12 filter (minus blue) and simultaneous photographs were taken, using the f-stop and shutter speed determined by the true-color camera light meter.

Appendix C
Lost River Statistics for Trend Surface Analysis of NS-001 Lineament Density Values

Table C-1. Statistics for trend surface analysis of NS-001 lineament density values using an entire 9- by 24-point value array

Degree M ⓐ	$\frac{SS}{T_{ss}}R$ γ_r^2	Correlation Coefficient $\sqrt{r^2}$	N	Degrees of Freedom: Regression R	Degrees of Freedom: Deviation D	F-Tests for Significantly Better Fit of Data: $\left(\frac{SS_R}{SS_D} - 1\right)\left(\frac{DF_D}{DF_R}\right)$ ⓑ	F-Tests for Significantly Better Fit of Data: $\frac{SS_{R(M-1)}}{SS_{R(M)}} - 1$	F-Tests for Significantly Better Fit of Data: $\frac{DF_{D(M-1)}}{DF_{R(M-1)}}$ ⓒ	Confidence Level, %
2	65	0.8084	216	5	210	79.20	22.27	2 vs raw data	>99.95
3	68	0.8256	216	9	206	49.00	2.26	3 vs 2	70
4	79	0.8913	216	14	201	55.43	4.81 6.65	4 vs 3 4 vs 2	95 99.5
5	80	0.8961	216	20	195	39.73	<1.00 3.16	5 vs 4 5 vs 3	NS 95
6	82	0.9076	216	27	188	32.52	<1.0	6 vs 5	NS

ⓐ Goodness of fit shown as percent of data explained by regression of degree M.
ⓑ F-test for significance of $[MS_R/MS_D]$ of the Mth degree trend regression surface.
ⓒ F-test for significance of degree $M - 1$ versus M for better explanation of the data.

Table C-2. Statistics for trend surface analysis of NS-001 lineament density values using a 7- by 22-point value array, which excludes biased perimeter values

Degree M ⓐ	$\frac{SS}{T_{ss}}R$ γ_r^2	Correlation Coefficient $\sqrt{r^2}$	N	Degrees of Freedom: Regression R	Degrees of Freedom: Deviation D	F-Tests for Significantly Better Fit of Data: $\left(\frac{SS_R}{SS_D} - 1\right)\left(\frac{DF_D}{DF_R}\right)$ ⓑ	F-Tests for Significantly Better Fit of Data: $\frac{SS_{R(M-1)}}{SS_{R(M)}} - 1$	F-Tests for Significantly Better Fit of Data: $\frac{DF_{D(M-1)}}{DF}$ ⓒ	Confidence Level, %
2	41	0.6415	154	5	148	20.70	21.39	2 vs raw data	>99.95
3	51	0.7127	154	9	144	16.51	8.43	3 vs 2	95
4	59	0.7672	154	14	139	14.20	4.41	4 vs 3	99
5	80	0.8952	154	20	133	26.83	8.02	5 vs 4	99.95
6	65	0.8040	154	27	126	8.53	<1.0 <1.0 1.91	6 vs 5 6 vs 4 6 vs 3	NS NS 90

ⓐ Goodness of fit shown as percent of data explained by regression of degree M.
ⓑ F-test for significance of $[MS_R/MS_D]$ of the Mth degree trend regression surface.
ⓒ F-test for significance of degree $M - 1$ versus M for better explanation of the data.

Section 13

Coyanosa, Texas, Petroleum Test Site Report

Authors/Editors

Harold R. Lang
Jet Propulsion Laboratory

Steve M. Nicolais
Superior Oil Co.
Denver, Colorado

H. Robert Hopkins
EXXON Production and Research Co.
Houston, Texas

Contributors

Ronald E. Alley
Harry E. Stewart
Jet Propulsion Laboratory

Gary I. Ballew
Kevin R. Sundberg
Phillips Petroleum Co.
Bartlesville, Oklahoma

Aderbal C. Correa
CONOCO Exploration Research Div.
Ponca City, Oklahoma

James A. Drahovzal
Gulf Science and Technology Co.
Pittsburgh, Pennsylvania

Paul G. Harrison
Cities Service Co.
Tulsa, Oklahoma

Pamela H. Muller
Edward M. Wingo
University of Texas, Permian Basin
Odessa, Texas

Section 13

Coyanosa, Texas, Petroleum Test Site Report

Contents

I. Introduction 13-1
- A. Site Selection and Objectives 13-1
- B. Test Site Operations 13-1

II. Geographic Setting 13-2
- A. Location and Access 13-2
- B. Climate 13-3
- C. Physiography 13-3
  - 1. Topography 13-3
  - 2. Landforms 13-3

III. Geologic Evolution 13-4
- A. Introduction 13-4
- B. Pre-Ordovician 13-4
- C. Lower and Middle Ordovician 13-4
- D. Upper Ordovician, Silurian, and Devonian 13-4
- E. Late Devonian–Mississippian 13-4
- F. Tectonism 13-8
- G. Pennsylvanian 13-8
- H. Permian 13-9
- I. Triassic 13-9
- J. Cretaceous 13-9
- K. Tertiary–Quaternary 13-9

IV. Subsurface Geology and Producing Reservoirs 13-10
- A. Introduction 13-10
- B. Exploration History 13-13
- C. Reservoir Structure and Stratigraphy 13-13
- D. Production and Reserves 13-13

PRECEDING PAGE BLANK NOT FILMED

PAGE 12 INTENTIONALLY BLANK

V. Vegetation 13-13
A. Introduction 13-13
B. Results 13-17
C. Conclusions 13-19

VI. Soils 13-19
A. Soils of Floodplains, Terraces, and Lower Uplands 13-20
B. Soils of Uplands and Outwash Plains 13-21
C. Soils of Hills and Ridges 13-22
D. Factors of Soil Formation 13-23
1. Parent material 13-23
2. Climate 13-23
3. Living organisms 13-23
4. Topography 13-23
5. Time 13-23
E. Summary 13-24

VII. Soil Geochemistry 13-24
A. Introduction 13-24
B. Results 13-24
1. On-field/off-field analysis 13-24
2. Carbon isotope analysis 13-24
C. Conclusions 13-24

VIII. Remote Sensing Data 13-25
A. Introduction 13-25
B. Preliminary Processing 13-25
C. Analysis and Interpretation 13-26

IX. Spectral Characteristics of Cover Types 13-26
A. Introduction 13-26
B. Spectral Characteristics of Vegetation 13-27
1. Equivalent NS-001 band reflectance values for vegetation 13-27
2. Vegetation shadow 13-28
3. Equivalent NS-001 band-ratio values for vegetation 13-29
C. Spectral Characteristics of Soil/Rock 13-29
1. Mineralogy 13-29
2. Soil/rock texture (grain size) 13-30
3. Equivalent NS-001 band reflectance values obtained from PFRS soil/rock spectra 13-31
4. Equivalent NS-001 band-ratio values for soil/rock 13-32
D. Combined Soil/Rock and Vegetation NS-001 Band-Ratio Values 13-34

X. Sensor Spectral Data 13-35
A. Introduction 13-35
B. NS-001 Data, Mission 403, Line 3 13-35
C. Landsat MSS Data, October 4, 1975 13-36

XI. Geological Interpretation of Landsat MSS and NS-001 Multispectral Data 13-38
A. Image Interpretation 13-38
1. Introduction 13-38
2. Methods of investigation 13-38
B. Structural Interpretation 13-38
1. Introduction 13-38
2. Scientific rationale 13-38
3. Results of structural interpretation 13-39
C. Spectral Interpretation 13-47
1. Introduction 13-47
2. Method of investigation 13-47
3. Results of the spectral interpretation 13-47
4. Other spectral features—Utility of NS-001 scanner 13-55

XII. Conclusions 13-57

Acknowledgments 13-58

References 13-59

Appendixes
A. Remote Sensing Data Acquired for Exxon 13-63
B. Geochemical Survey Laboratory Procedures/ Analytical Results 13-65

Figures

13-1. Location map showing the Coyanosa, Texas, test site 13-2
13-2. Geologic map of the Coyanosa test site 13-6
13-3. Map showing the major tectonic elements of the southern mid-continent of North America 13-7
13-4. Regional cross section of the Delaware Basin 13-7
13-5. Map showing the major pre-Ordovician tectonic elements of the southern mid-continent of North America 13-8
13-6. Isopach map showing the thickness of Cenozoic fill 13-10
13-7. Near-surface cross section 13-11
13-8. Map showing oil and gas fields of the Coyanosa test site area 13-11
13-9. Subsurface structure on top of the Rustler Formation (Ochoan) 13-14
13-10. Subsurface structure on top of the Lamar shale (Guadalupean) 13-14
13-11. Cross section showing Lamar and Delaware productive intervals in fractured reservoirs of the Coyanosa field 13-15
13-12. Subsurface structure on top of the Ellenburger Formation (Ordovician) 13-15
13-13. Cross section showing deep gas production in the horst-block structure of the Coyanosa field 13-16
13-14. Map showing major subsurface faults and fault zones 13-16
13-15. Map showing 19 vegetation study sites 13-17

13-16. South-facing photograph showing creosote (*Larrea tridentata*) as the dominant shrub at vegetation study site V021 (September 1981) 13-18
13-17. South-facing photograph showing mesquite (*Prosopis glandulosa*) as the dominant shrub at vegetation study site V002 (September 1981) 13-18
13-18. North-facing photograph across the Pecos River showing salt cedar (*Tamarix pentandra*) as the dominant shrub at vegetation study site V005 (May 1981) 13-18
13-19. Southeast-facing photograph showing side oats grama (*Bouteloua curtipendula*) as the dominant grass at vegetation study site V016 (September 1981) 13-19
13-20. West-facing photograph across Hackberry Draw showing spring grass and mesquite at vegetation study site V006 (May 1981) 13-19
13-21. West-facing photograph across Hackberry Draw showing spring wildflowers (cowpen daisy, *Verbesina* sp.) at vegetation study site V006, an old grave location (May 1981) 13-19
13-22. North-facing photograph showing broomweed (*Xanthocephalum* sp.), a late summer wildflower, at vegetation study site V009 (September 1981) 13-20
13-23. South-facing photograph showing Russian thistle (tumbleweed, *Salsola* sp.) in a former trail at vegetation study site V022 (September 1981) 13-20
13-24. South-facing photograph showing late summer wildflowers at vegetation study site V012 (September 1981) . . 13-21
13-25. Soil map 13-21
13-26. Map showing 121 of the soil geochemistry sample sites 13-25
13-27. Histogram summarizing the results of carbon isotope analysis of 138 soil/rock samples 13-25
13-28. Map showing flight-line locations and areal coverage for M^2S, NS-001, and color photographic aircraft data acquired at the Coyanosa test site 13-26
13-29. Map showing field and laboratory spectral sample sites 13-27
13-30. Comparison of the field spectrum of a typical Coyanosa soil to typical vegetation field spectra 13-28
13-31. Composite diagrammatic laboratory spectrum illustrating major mineral absorption bands affecting NS-001 data for the Coyanosa test site 13-30
13-32. Three laboratory spectra illustrating the loss of the calcite absorption band near 2.3 μm when grain size is decreased to <74 μm (fine silt and clay) 13-31
13-33. PFRS soil/rock field spectra exhibiting maximum, minimum, and mean equivalent NS-001 band reflectance 13-32
13-34. PFRS soil/rock field spectra exhibiting the maximum equivalent NS-001 VNIR band-ratio values 13-34
13-35. PFRS soil/rock field spectra exhibiting the minimum equivalent NS-001 VNIR band-ratio values 13-35
13-36. PC spectra for NS-001, Mission 403, line 3, June 18, 1979 13-37
13-37. PC spectra for Landsat MSS data, October 4, 1975 13-37

13-38. Full-scene Landsat MSS high-contrast color infrared composite image, October 4, 1975 13-40
13-39. Landsat MSS standard color infrared composite subscene, February 1, 1977 13-41
13-40. Generalized regional interpretation of Figure 13-38 showing major tectonic/physiographic elements of the test site vicinity 13-43
13-41. Regional composite Landsat MSS structural interpretation 13-44
13-42. NS-001, Mission 403, June 18, 1979, color ratio composite mosaic of lines 1, 2, 3 13-46
13-43. Landsat MSS color ratio composite subscene, February 1, 1977 13-49
13-44. Landsat MSS color ratio composite subscene, February 25, 1976 13-50
13-45. Landsat MSS PC subscene, February 25, 1976 13-51
13-46. NS-001, Mission 390, October 12, 1978, color ratio composite subscene from line 3 13-52
13-47. NS-001, Mission 403, June 18, 1979, color composite mosaic of lines 1, 2, 3 13-53
13-48. Full-scene Landsat MSS PGSTR color infrared composite image, February 25, 1976 13-56
B-1. Sample handling procedure for 1979 Coyanosa test site samples 13-66
B-2. Sample handling procedure for 1980 Coyanosa test site samples 13-66

Tables

13-1. Mean air temperature and normal precipitation for the Coyanosa test site 13-3
13-2. Summary of subsurface stratigraphy and producing horizons for major oil and gas pools of the Coyanosa test site area 13-5
13-3. Cumulative oil and gas production for selected Coyanosa test site fields/pools through December 31, 1979 13-12
13-4. Shrubs and succulents characteristic of the Coyanosa test site 13-18
13-5. Grasses characteristic of Hackberry Draw near Coyanosa, Pecos County 13-19
13-6. A partial list of common wildflowers and broadleaf herbs characteristic of the Coyanosa test site 13-20
13-7. Percent ground cover on September 6, 1981, determined at 13 sites in the Coyanosa test site 13-20
13-8. Monthly rainfall for Pecos, Texas, for 1975–1977 and 1980–1981 13-20
13-9. Characteristics of soil units occurring in the Coyanosa test site as mapped in Figure 13-25 13-22
13-10. Discriminant analysis scores for classifying Coyanosa test site soil samples according to location inside or outside local oil field productive areas 13-24

13-11. Comparison of least squares analyses of Coyanosa test site soil samples using a linear model based on the important geochemical variables identified using discriminant analysis and a linear model based on soil type . . 13-25

13-12. Summary of aircraft-acquired multispectral data, Coyanosa test site 13-26

13-13. Summary of Landsat MSS data acquired, Coyanosa test site 13-26

13-14. A comparison of the seven bands of the Landsat 4 TM and the eight bands of the NS-001 aircraft scanner designed to simulate the TM 13-27

13-15. Summary of equivalent NS-001 band reflectance values determined from PFRS field vegetation spectra 13-29

13-16. Summary of equivalent NS-001 band-ratio values calculated from PFRS field vegetation spectra 13-29

13-17. Mineralogy of Coyanosa soil/rock determined by XRD analysis of 45 representative surface samples 13-29

13-18. Summary of equivalent NS-001 band reflectance values determined from 52 soil/rock PFRS field spectra measured at 19 sites, Coyanosa test site 13-32

13-19. Summary of equivalent NS-001 band-ratio values calculated from 52 soil/rock PFRS field spectra measured at 19 sites, Coyanosa test site 13-33

13-20. Summary of equivalent NS-001 band-ratio values including both soil/rock (Table 13-19) and vegetation (Table 13-16) PFRS field spectra 13-36

13-21. Correlation matrix for the six NS-001 VNIR band data (band 5 inoperative) acquired on Mission 403, line 3, June 18, 1979, Coyanosa test site 13-36

13-22. NS-001 Mission 403, line 3, June 18, 1979, PC analysis: Eigenvectors of six VNIR bands (band 5 inoperative) for first three PCs 13-36

13-23. Correlation matrix for Landsat MSS data acquired October 4, 1975, Coyanosa test site 13-37

13-24. Landsat MSS principal components analysis for data acquired October 4, 1975 13-37

13-25. Images used for spectral interpretation 13-48

13-26. Ratio response and class identification determined in the spectral interpretation of NS-001 2/3 (green), 2/4 (blue), 6/7 (red) color ratio composite image 13-54

A-1 Remote sensing data acquired for Exxon during a 1966 study of the Coyanosa area and made available for the joint NASA/Geosat test site investigation 13-64

B-1. Elements determined and analytical procedures used for measurements by Phillips 13-67
B-2. Phillips geochemical data 13-68
B-3. Barringer Lasertrace® geochemical data 13-72
B-4. Classification of Coyanosa test site samples with respect to location relative to local oil/gas production 13-81

Plate[1]

13-1. Coyanosa, Texas: Composite image interpretation

[1] The plate is contained in Part 3 (envelope) of *The Joint NASA/Geosat Test Case Project.*

Section 13

Coyanosa, Texas, Petroleum Test Site Report

I. Introduction

A. Site Selection and Objectives

Coyanosa, Texas, was selected as a test site to evaluate the utility of remote sensing for detecting relatively deep, complex Paleozoic oil and gas traps in a semiarid, relatively flat, sparsely vegetated terrain characterized by meager bedrock exposures. The site is in the prolific Permian Basin of West Texas and is geologically and ecologically typical of many productive Paleozoic basins in the American Southwest and in similar climatic zones on other continents. Production of oil and gas in the test site area is relatively well established, the major exploration effort having been completed during the early 1960s. Thus, site access and ancillary data necessary for evaluating interpretations of remote sensing data were available.

Additionally, earlier studies had suggested that remote sensing data might be useful for exploration in this region, both for the "direct" detection of surface alteration effects associated with potential hydrocarbon seepage and for the detection of subsurface structures based on their surface geomorphic expression:

(1) In 1966, Exxon (Esso) Production Research Company carried out a remote sensing study of the area with the Science Service Division of Texas Instruments, Inc. (Texas Instruments, Inc., 1966). Selected portions of this unpublished study were made available to test site participants by Exxon. In the 1966 study, multispectral aerial photography and aircraft-acquired radar and daytime/nighttime thermal data were interpreted (Appendix A). Results suggested that surface geomorphic features in the Coyanosa area correlate with subsurface structure. Field spectral measurements in the 0.4- to 0.9-μm range were also acquired at 26 sites. Eight of these spectra, which were acquired at sites over known oil and gas production, were interpreted as "anomalous." The criteria used for identifying anomalous spectra were not defined.

(2) Trollinger's (1968) interpretation of Gemini photographs of West Texas showed that previously unrecognized geomorphic features could be used to delineate some of the major subsurface structures of the Permian Basin.

(3) A 1973 study by Saunders (discussed by Halbouty, 1976, p. 779) noted linear and curvilinear tonal features on early Landsat satellite images that coincided in location with some of the major subsurface structures of the Coyanosa test site area.

B. Test Site Operations

This section describes the various investigations conducted during the Coyanosa test site study. The study began with a review of available published and unpublished information and a reconnaissance field examination of the test site area. This information was used to plan vegetation, soil/rock geochemistry, and field reflectance surveys of the area.

Initially available remote sensing data consisted of the data acquired for the 1966 Exxon study and Landsat multispectral data. Subsequently, NASA–Johnson Space Center acquired aircraft multispectral and radar data. The multispectral data were digitally processed by JPL and distributed to participants for further processing and interpretation. Seasat radar data were also acquired. Image

interpretations defined features that were subsequently checked in the field and compared to available published and unpublished information.

To evaluate the possibility of the alteration of soil/rocks due to potential hydrocarbon microseepage, a major effort was made to acquire samples for geochemical analysis. These samples were analyzed in laboratories of Geosat member companies, principally Phillips Petroleum.

II. Geographic Setting

A. Location and Access

The Coyanosa test site is a rectangularly shaped region trending northwest–southeast and covering a 1400-km^2 area in the Trans-Pecos Region of West Texas (Figure 13-1). The site is in northeastern Reeves County and northwestern Pecos County. The northern boundary of the test site

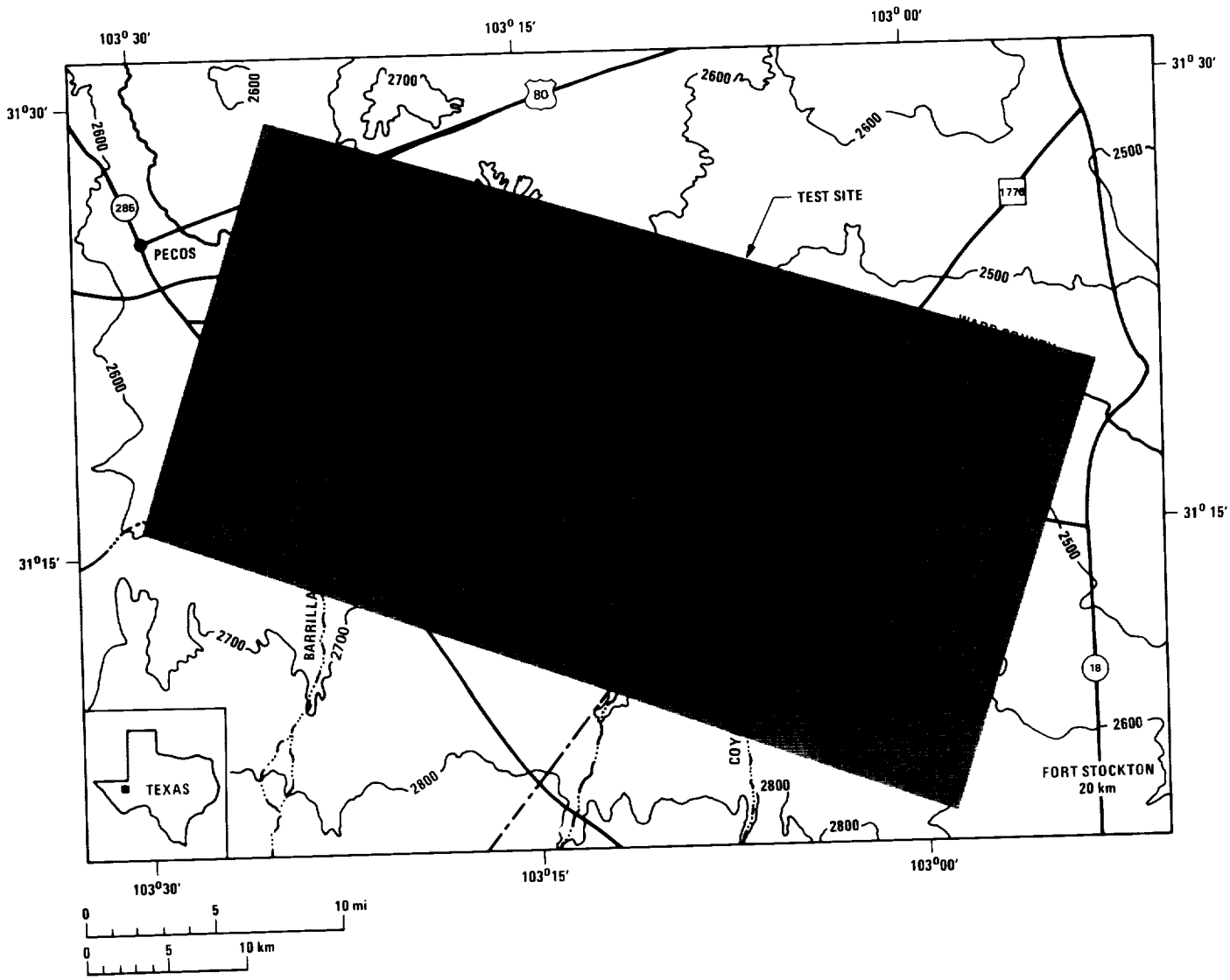

Figure 13-1. Location map showing the Coyanosa, Texas, test site (topographic contour interval 100 ft, datum sea level). Key physiographic and cultural features useful for geographic reference are shown. The circular feature in the west–central test site is a tire testing track, which is also shown in many subsequent figures.

corresponds approximately with the Pecos River. The locations of the corner points are, clockwise from the northeast corner, lat. 31°20′ N, long. 102°57′ W; lat. 31°06′ N, long. 102°59′ W; lat. 31°16′ N, long. 103°30′ W; and lat. 31°30′ N, long. 103°25′ W.

The city of Pecos is about 5 km (3 mi) west of the western edge of the site, and the city of Fort Stockton is about 26 km (16 mi) southeast of the eastern edge of the site. Regional access to the test site is by automobile along U.S. Highway 80 and Interstate Highway 20 through Pecos. Specific access to the test site is from U.S. Highway 285 and Ranch to Market Roads 1450 and 1776; both are good all-weather roads. Additional access is available along unnumbered public paved and dirt roads. Access to field sampling locations and areas for field checking of remote sensing data is along ranch and oil field roads where permission for access had been granted by the landowner.

B. Climate

The test site is characterized by a hot, dry, subtropical desert to steppe climate. Monthly mean air temperatures and normal precipitation are given in Table 13-1.

C. Physiography

1. Topography. The test site is located on a gentle plain, tilted slightly to the north, with a slope of about 12 ft/mi from the southern boundary to the Pecos River Valley. North of the river, the land slopes to the south about 50 ft/mi. The Pecos River crosses the site from west to east near the northern boundary. Numerous tributaries, all intermittent streams, flow south to north across the plain. Some of the larger tributaries have formed broad U-shaped valleys with maximum local relief of 30 m (100 ft). The Pecos River is interpreted to have slowly migrated northward down a gentle slip-off slope, while the north side of the river is a receding undercut slope.

Higher relief ridges were formed by outcrops of Cretaceous rocks along Barrilla Draw, or by what appears from aerial photographs to be areas of Cretaceous subcrops along Hackberry Draw. On the plain of the central test site area, there are a number of shallow depressions. Some of these features may be sinkholes formed by differential solution of the underlying Cretaceous carbonate bedrock, but most appear to be shallow areas of internal drainage caused by incipient sinkholes in a caliche soil horizon.

2. Landforms. The most prominent regional landforms are the relatively high relief valley walls along Barrilla Draw and Hackberry Draw and the northern terminus of alluvial fans originating in the Barrilla and Davis Mountains, approximately 65 km (40 mi) southwest of the test site area.

The relatively high relief valley walls occur on the east and west sides of a stable block of Mesozoic bedrock in the west-central part of the test site. According to Maley and Huffington (1953), evaporites of the Permian Salado and Castile Formations have been differentially removed by solution, and the overlying strata have collapsed, forming depressions now filled with Cenozoic sediment. The valleys of Toyah Creek, Barrilla Draw, and Hackberry Draw

Table 13-1. Mean air temperature and normal precipitation for the Coyanosa test site[a]

Month	Mean Air Temperature, °C	Normal Precipitation, mm		
		Pecos County, Ft. Stockton	Reeves County, Balmorhea	Ward County, Monahans
January	7.5	16	16	20
February	10	14	12	10
March	12.5	11	11	8
April	17.7	20	15	19
May	22.5	40	38	41
June	25	37	37	30
July	27.5	35	40	44
August	27.5	32	35	36
September	22.5	35	42	35
October	17.5	33	32	38
November	10	15	13	9
December	7.5	12	12	14
Annual	17.5	301	305	306

[a]From *Texas Almanac* (1978).

are areas of relatively thick Cenozoic fill probably overlying such areas of salt solution. The intervening blocks have little or no Cenozoic fill and are interpreted to be essentially unaffected by the salt solution.

The alluvial fans occur in the southernmost part of the site. They are the northern terminus of large dissected fans, which are made up of volcanic and carbonate rock fragments derived from the Barrilla and Davis Mountains.

Chemical processes, including solution of Cretaceous carbonate bedrock and subsequent deposition of caliche, comprise the main form of weathering in the test site area. The alluvial fan material is superimposed on the underlying chemical weathering regime. One other local geomorphic process is noteworthy. Evaporite deposits, mainly gypsum, form in Toyah Lake (a playa lake) and are transported eastward by the prevailing wind. Gypsum dunes are present east of the lake along the western edge of the test site. Windblown gypsum and quartz sands are also present at the surface for a distance of 6 km (4 mi) east of the lake.

III. Geologic Evolution

A. Introduction

The Coyanosa test site lies within the Delaware Subbasin of the Permian Basin of western Texas and southeastern New Mexico, a major petroleum-producing province approximately 300 km (200 mi) long and 150 km (100 mi) wide. Major subsurface stratigraphic units recognized in the area are summarized in Table 13-2. The surface geology of the test site is shown in Figure 13-2. Major regional geologic features of this part of the mid-continent of North America are shown in Figure 13-3; Figure 13-4 is a regional cross section of the Delaware Basin. The following is a description of the stratigraphic and tectonic evolution of the area based, except where otherwise noted, on the description by Adams (1965).

B. Pre-Ordovician

During the Precambrian, the test site area, together with the rest of North America, was a part of a Precambrian super continent. During the late Precambrian or early Paleozoic time, continental rifting took place roughly parallel to the present-day Gulf of Mexico. A proto-Atlantic Ocean probably extended into the area of the Gulf (Keller and Cebull, 1973). Initial rifting in the vicinity of Texas may have been punctuated by two triple junctions, the failed arms of which developed into the early Paleozoic Tobosa and Oklahoma Basins (Burke and Dewey, 1973; Nicholas and Rozendal, 1975; Figure 13-5). During the early Paleozoic, the test site lay in the Tobosa Basin—a broad, gentle N–S-oriented downwarp situated between the Concho and Diablo Arches.

The Upper Cambrian Wilberns Sandstone is known in the Val Verde Basin and is thought to be present in the Delaware Basin (Hills, 1968), but knowledge of its extent there is limited by few exploratory drilling penetrations of the basal part of the sedimentary section. It is probable that the Wilberns was deposited over much of the Delaware Basin as a basal transgressive sandstone, but parts or all of it may have been removed by subsequent erosion.

C. Lower and Middle Ordovician

The early passive Atlantic-type margin was followed in the Late Ordovician by the initiation of subduction and subsequent volcanism. In the Tobosa Basin, a flat, broad coastal plain was developed across which the northwest-transgressing Early Ordovician Ellenburger Sea spread a sedimentary wedge of near-shore clastics and shelf carbonates. Due to restricted circulation, evaporites and dolomite were locally deposited. About 700 m (2000 ft) of Ellenburger dolomite underlies the test site (Adams, 1965). During the Middle Ordovician, the Simpson Group, consisting of sandstone, shale, and limestone, was deposited in the basin in the vicinity of the test site. Clastic sediments were derived from highlands adjacent to the basin in the north, east, and northwest. Presently, 350 to 700 m (1000 to 2000 ft) of Simpson strata are in the subsurface of the test site.

D. Upper Ordovician, Silurian, and Devonian

From Late Ordovician through Devonian, there was relatively rapid subsidence of the Tobosa Basin. The supply of clastic detritus was insufficient for sedimentation to keep pace with subsidence. Much of the basin was starved, resulting in the deposition of a dark deep-water dolomite and siliceous limestone facies surrounded by a shelf facies of light-colored chert and dolomite.

The Upper Ordovician Montoya Formation consists of chert and dolomite and is 80 to 160 m (250 to 500 ft) thick in the subsurface of the test site (Vertress et al., 1959). The Hunton Group of Silurian and Devonian age consists of limestone, dolomite, and chert, and attains a thickness of about 500 m (1500 ft) in the area.

E. Late Devonian–Mississippian

During Late Devonian and Early Mississippian time, uplifts in local areas resulted in the erosional truncation of Upper Ordovician through Devonian strata. Terrestrial clastics were deposited in a transgressing sea. Horack (1974)

Table 13-2. Summary of subsurface stratigraphy and producing horizons for major oil and gas pools of the Coyanosa test site area

System	Series	Group	Formation	Member/Informal Subsurface Unit	Major Field-Producing Interval, depth in ft		
					Worsham–Bayer	Waha	Coyanosa
Quaternary							
Cretaceous	Comanche	Fredricksburg					
		Trinity					
Triassic		Dockum	Santa Rosa				
			Tecovas				
Permian	Ochoa		Dewey Lake				
			Rustler				
			Salado				
			Castile				
	Guadalupe	Delaware Mountain	Bell Canyon	Lamar shale	• 2,800		
				Local limestone			• 4,700
				Delaware sand	○• 4,900	○• 4,800	○• 5,000
			Cherry Canyon		○• 7,500	• 7,500	• 5,900
			Brushy Canyon				
	Leonard	Bone Spring					
	Wolfcamp			Wolfcamp limestone			• 8,700
				Wolfcamp shale	• 11,000		
				Coyanosa conglomerate			○• 9,700
				Wolfcamp conglomerate			
Pennsylvanian	Strawn		Black Shale				
	Atoka			Lower Pennsylvanian	○• 12,800		
	Morrow				○		• 10,000
Mississippian	Chester			Barnett			
				Mississippian limestone		○	○• 10,300
	Kinderhock		Woodford				
Siluro–Devonian		Hunton		Devonian	○	○	○ 13,800
				Silurian shale			
				Fusselman	○		
Ordovician	Upper		Montoya				
	Middle		Simpson			○	
	Lower		Ellenburger				
Precambrian					○ 16,000	○ 16,500	○• 14,200

• Oil-producing interval.
○ Gas-producing interval.

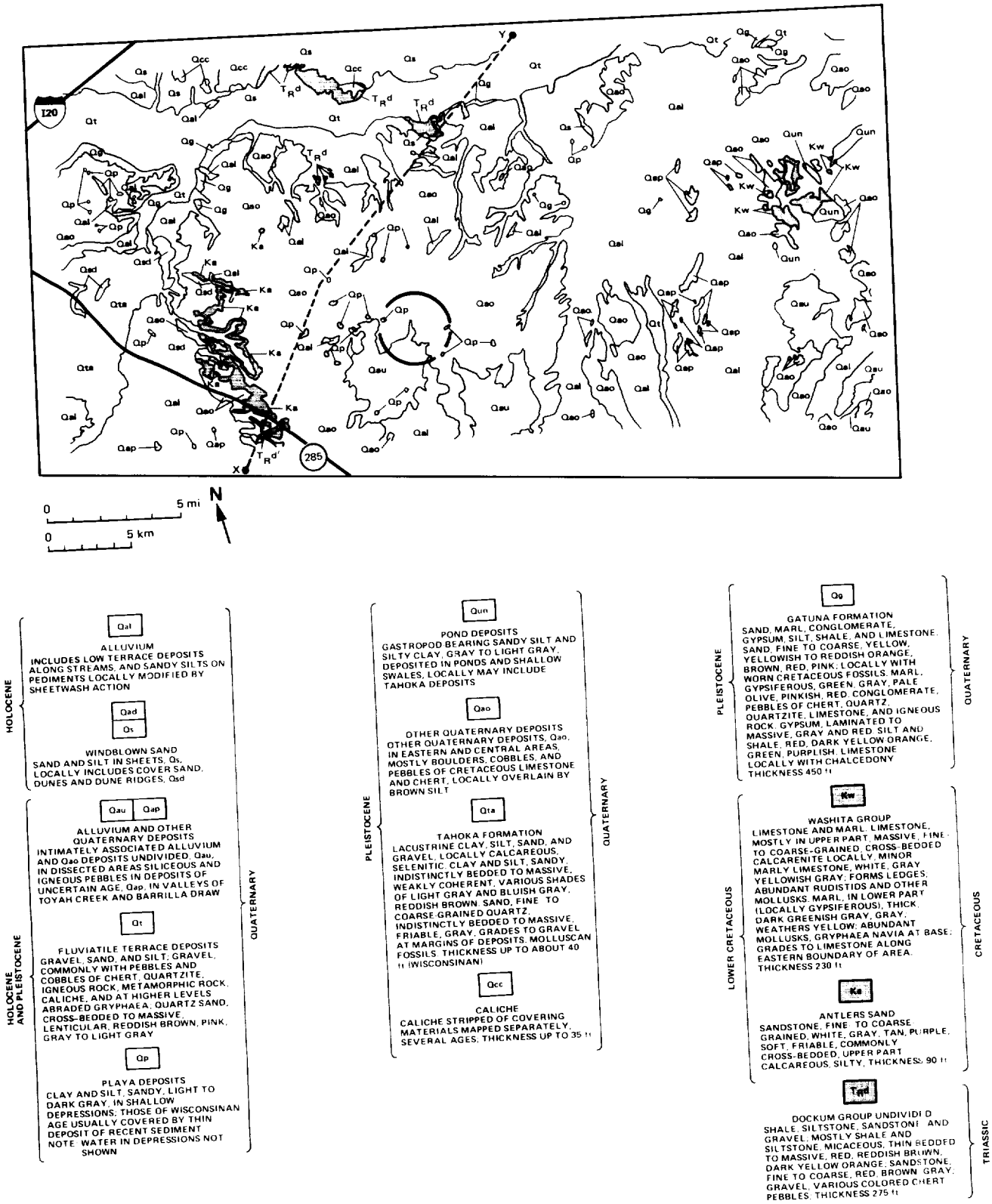

Figure 13-2. Geologic map of the Coyanosa test site, showing paucity of outcrops (dark areas) and lack of surface faulting in this interpretation (compiled from Barnes, 1976, and from unpublished data from Texas Instruments, Inc., 1966). The circular tire testing track is also shown because this feature is a useful geographic reference for comparing this map to subsequent images.

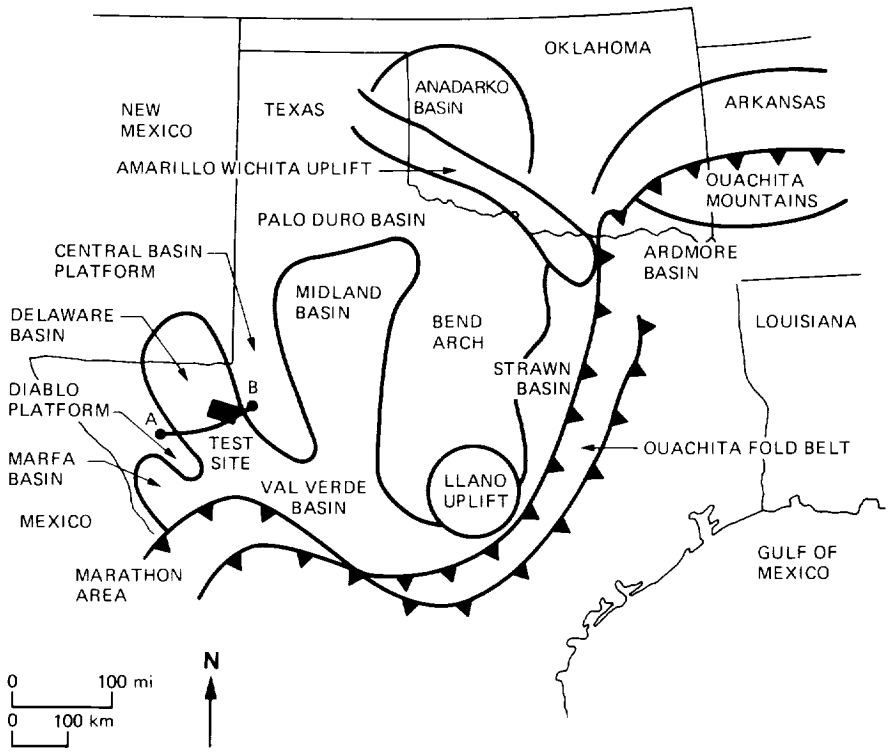

Figure 13-3. Map showing the major tectonic elements of the southern mid-continent of North America. A-B is the location of the regional cross section shown in Figure 13-4 (from Nicholas and Rozendal, 1975, Figure 6, p. 198)

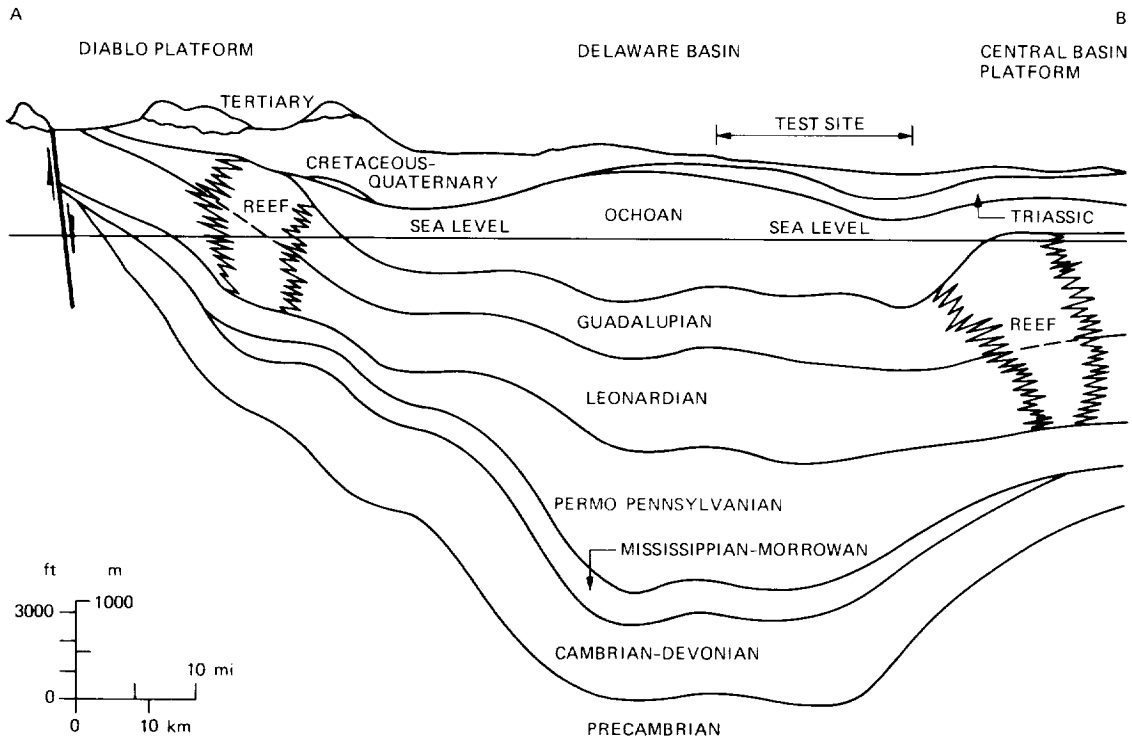

Figure 13-4. Regional cross section of the Delaware Basin (Holmquist, 1965, Figure 3). Refer to Figure 13-3 for location.

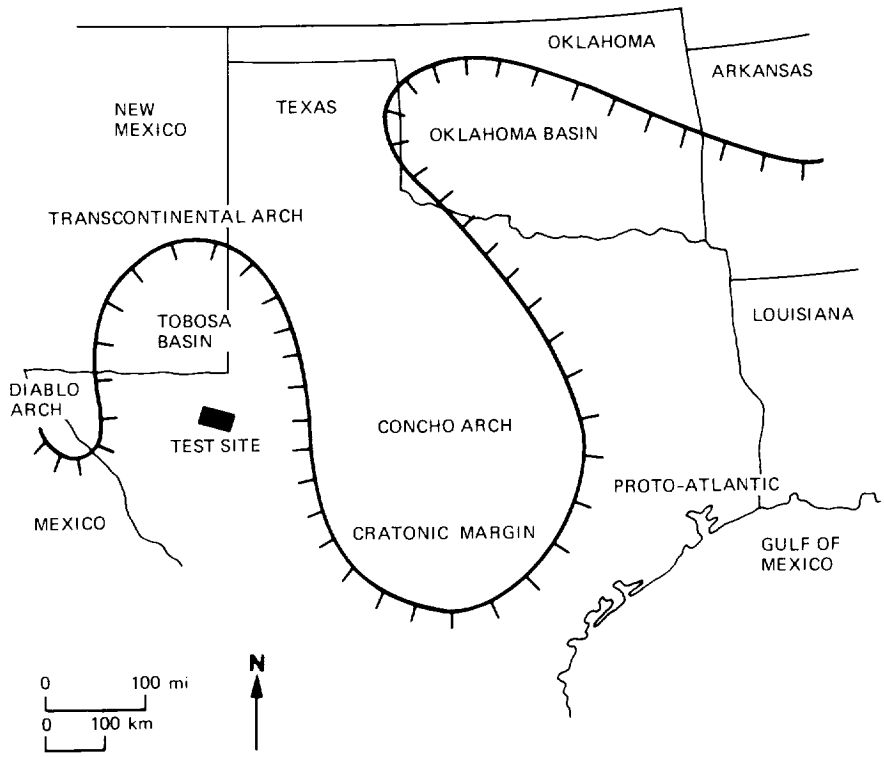

Figure 13-5. Map showing the major pre-Ordovician tectonic elements of the southern mid-continent of North America (modified from Adams, 1965; Nicholas and Rozendal, 1975)

has proposed extensive Antler-related uplift during this period and has suggested early subdivision of the Tobosa Basin by the Central Basin Platform. Most authors (Adams, 1965; McGlasson, 1969; Nicholas and Rozendal, 1975; Vertress et al., 1959) believe that major uplift and subdivision of the basin occurred later and that the slight uplift during Late Devonian was related to Ouachita stresses. The terrestrial clastics deposited in the vicinity of the test site consisted of dark-brown to black sapropelic, highly radioactive, organic-rich shales and minor cherts of the Woodford shale (McGlasson, 1969). About 130 m (400 ft) of the Woodford is present in the subsurface of the test site. In the area, the Late Mississippian was characterized by the deposition of dark-gray and brown clay shales in the starved Devonian depressions. Landward, the thick basinal shales grade into shelf limestones.

F. Tectonism

During post-Mississippian time, the Central Basin Platform divided the Tobosa Basin into the Delaware and Midland Basins (Figure 13-3). The Val Verde Basin developed at the southern termination of the platform. Deformation associated with this subdivision was the result of continental margin tectonism that led to the Ouachita orogeny. The type of plate boundary activity that produced the orogeny is poorly understood. Keller and Cebull (1973) suggested a model modified from Dewey and Bird (1970) that included an Early Ordovician north-facing subduction zone, followed by the formation of an orogenic welt in Mississippian and Pennsylvanian times, and an orogenic culmination in Early Permian with the northward movement of thrust sheets off the flank of the mobile core. Others (Briggs and Roeder, 1975; Graham et al., 1975; Wickham et al., 1976) have suggested that the subduction zone was south dipping and resulted in an arc-continent or continent-continent collision beginning in Early Pennsylvanian and terminating in Early Permian.

G. Pennsylvanian

During Early Pennsylvanian, there was rapid subsidence in the Delaware Basin, and starved shale-basin conditions prevailed throughout the Pennsylvanian. Earliest deposition was restricted to the area north of the test site. Later, sediments reaching the deep basin came from the uplifted area to the east and consisted of a thick wedge of chert conglomerate and shale. Some slightly younger limestone and dolomite units were deposited on shallow shelves. The total preserved thickness of Pennsylvanian rocks in the

subsurface of the test site ranges from about 350 to 700 m (1000 to 2000 ft).

H. Permian

Continuing orogenic movement to the south of the Delaware Basin during Early Permian resulted in several thousand feet of uplift in the Central Basin Platform area and the formation and filling of deep flanking troughs with clastics (arkosic boulder conglomerates, sandstones, shales, and detrital limestones), cherts, and authigenic limestones. The clastics were apparently derived from rising mountains to the northwest, west, and southwest and were distributed by turbidity flows. Areas in the northern, northwestern, and northeastern parts of the Delaware Basin were essentially clastic free; shelf-edge reefs developed on limestone platforms. A total of 875 to 1750 m (2500 to 5000 ft) of Wolfcampian rocks are preserved in the subsurface of the test site.

During Leonardian time, subsidence in the Delaware Basin slowed. Erosion of the highs to the west and northwest resulted in a decrease in the amount and grain size of the clastic detritus. Sedimentation was dominated by dark limestone, shale, and fine-grained sandstone, but also included diatomite and chert. Most of the clastics were distributed by turbidity flows. The Central Basin Platform continued to rise slowly and was capped by shelf limestones. Limestone shelves bordered by reefs also developed along the southern and western margins of the basin. About 525 m (1500 ft) of Leonardian strata are present in the subsurface of the test site (Hills, 1968).

The Guadalupean Epoch was characterized by reef growth. Tectonic activity was reduced and structures were formed primarily by draping over older tectonic features. Reef formation in a time of slowly rising sea level contributed to reduced circulation and the precipitation of evaporites overlain by continental and lagoonal sands and clays. The basin margins consisted of reef-bordered limestone shelves. The Capitan Reef complex developed along the eastern edge of the test site.

Deposits in the deep Central Basin consisted mainly of sandstone and siltstone with some shale, bentonite, and limestone. Some terrestrial clastics flowed through surge channels in the reefs and were deposited as steep cones on talus slopes in front of the reefs until they became oversteepened; clastics were then spread as turbidity flows westward across the basin floor. Carbonate-shelf sands were similarly distributed. With the restriction of the basin by reef growth to the south in early Ochoan time, the entire basin became a deep evaporitic lagoon. During mid-Ochoan time, the basin sagged and the lagoon expanded eastward and northward. The Permian closed with the deposition of marine limestone and dolomite and fine red clastics.

I. Triassic

During Early and Middle Triassic time, epeirogenic uplift exposed the area to erosion (Hills, 1968); but by Late Triassic, subsidence along the eastern edge of the Delaware Basin occurred again, resulting in the deposition of continental clastics. Rocks of this age represent the oldest units exposed at the surface in the area of the test site (Figure 13-2). The Dockum Group is represented by about 90 m (275 ft) of red to dark yellowish-orange shale, siltstone, sandstone, and gravel conglomerate in a few scattered outcrops in the western half of the test site.

J. Cretaceous

The area remained emergent through Jurassic time, but during Early Cretaceous, the sea advanced from the southeast across the test site area. Outcrops of sandstones and limestones of the Comanchean Series in the test site area are representative of this marine incursion.

K. Tertiary–Quaternary

During the early Tertiary, the Davis Mountains southwest of the test site were uplifted and faulted; lava flows then buried exposed Cretaceous rocks. Uplift of the northern Trans-Pecos and adjacent areas in New Mexico in mid-Tertiary times tilted the west flank of the Delaware Basin (Hills, 1968). During the post-Permian to Holocene, differential solution of Permian salt controlled the thickness of Late Tertiary and Quaternary Basin fill derived from the Davis Mountains and the mountains of central New Mexico. Maley and Huffington (1953) have shown a close relationship between areas of thin Permian salt and those of thick basin fill. The marked thickening of basin fill near the eastern edge of the test site (Figure 13-6) is thought to be related to selective solution of Permian salt beds over the older Capitan Reef front, which caused warping, fracturing, water percolation, and solution of superjacent strata (Adams, 1944).

An extensive region, including much of the study area, has existed as a complex of pediment surfaces since at least mid-Tertiary time, and the through-flowing Pecos River, near its present position, has controlled sedimentation in the region (Leonard and Frye, 1962). The sediments consist of coarse colluvium interspersed with strips of alluvium along the tributary streams of the Pecos River drainage. In addition to pediment gravels and clay-textured alluvium, the present surface is also characterized

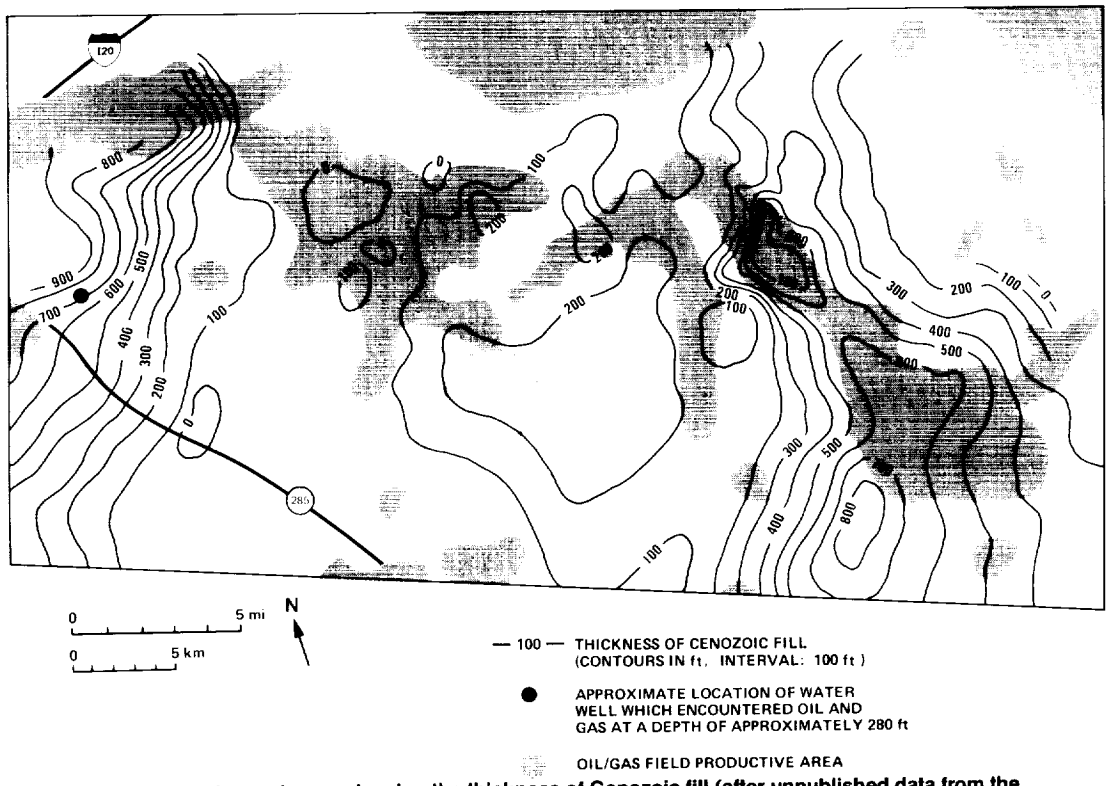

Figure 13-6. Isopach map showing the thickness of Cenozoic fill (after unpublished data from the Geo-Search Corporation, Midland, Texas)

by less extensive lake and terrace deposits. Some dune sand, especially east of Toyah Lake, is also present (Figure 13-2).

The paucity of bedrock exposures and the masking effect of the thick alluvial, eolian, and residual soil cover make it difficult to detect structural features in the test site area. According to Ogilbee and others (1962, p. 21):

> Although the Cretaceous and older rocks in Reeves County are cut by many faults, the trace of most of them is obscured by the mantling Cenozoic alluvium. The bedrock surface in areas where no alluvium is present is characterized by the traces of many faults....

Available geologic maps (Figure 13-2) and near-surface cross sections (Figure 13-7) therefore portray only the broadest aspects of surface geology and show little structure.

IV. Subsurface Geology and Producing Reservoirs

A. Introduction

The Coyanosa test site lies in the prolific West Texas region, an area which accounted for 22 percent of the total U.S. oil production in 1967 (Galley, 1971). Located in the Delaware Subbasin of the Permian Basin, the test site area encompasses three major oil and gas fields (Worsham–Bayer, Waha, and Coyanosa; Figure 13-8) and over 55 minor fields and pools. Available field/pool names, discovery dates, producing depths, and cumulative production for fields in the test site area are summarized in Table 13-3. Production in the area is from Paleozoic reservoirs of Permian to Ordovician age (Table 13-2). Producing horizons range from depths of approximately 1000 m (2800 ft) to over 5500 m (16,500 ft). In general, oil is present in shallower reservoirs and gas in deeper reservoirs. Most deep traps are on faulted anticlines. Shallower reservoirs are incipient drape features controlled by these deeper anticlines or are stratigraphic traps created by facies changes associated with paleotopographic highs controlled by the deep-seated structure. Therefore, shallower traps tend to be stratigraphic with primary porosity and deeper traps structural with fracture porosity. A review of the geographic, structural, and stratigraphic distribution of reservoirs in the test site area leaves the impression that commercial hydrocarbon reserves occur anywhere there is porous rock with closure. Apparently, the Mississippian, Pennsylvanian, and basinal Permian shales are such prolific source rocks (Holmquist, 1965, p. 263) that all potential reservoirs are hydrocarbon-bearing.

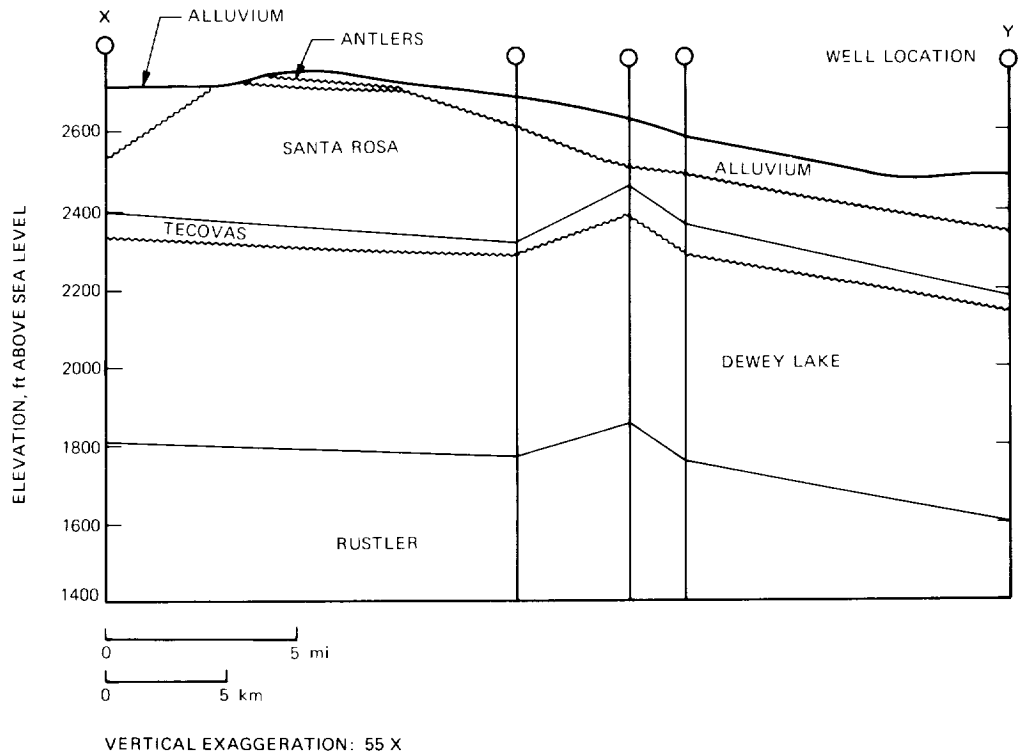

Figure 13-7. Near-surface cross section (refer to Figure 13-2 for location). This interpretation, which relied on straight-line correlation of mechanical log picks from five wells, shows no near-surface faulting (Ogilbee et al., 1962, Plate 6).

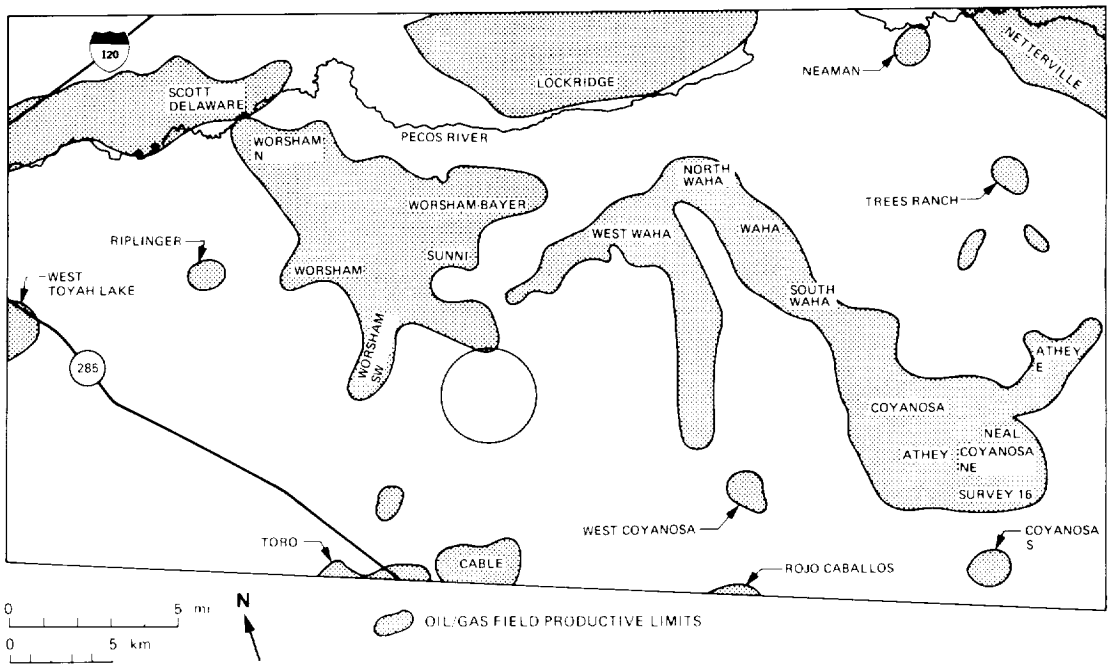

Figure 13-8. Map showing oil and gas fields of the Coyanosa test site area (field names and productive limits are inferred from unpublished data from the Geo-Search Corporation, Midland, Texas)

Table 13-3. Cumulative oil and gas production for selected Coyanosa test site fields/pools through December 31, 1979[a]

Field Name	Discovery		Cumulative Production	
	Date	Depth, ft	Gas, MCF[b]	Oil, kbbl[c]
Athey/Bone Springs	1966	9,100		159
Athey/Wolfcamp	1967	11,200	39,552	1,280
Athey/Wolfcamp	1966	11,600	107,447	1,146
Athey/Penn	1969	11,280		1
Athey, E/Wolfcamp	1967	11,500		549
Cable/Delaware	1978	5,200		12
Cable/Wolfcamp	1953	10,800		5
Coyanosa/Cherry Canyon	1965	5,900		90
Coyanosa/Delaware	1959	4,790		873
Coyanosa/Lamar	1959	4,780		80
Coyanosa/Wolfcamp	1970	11,600	18,174,870	3,671
Coyanosa/Devonian			25,562,398	
Coyanosa/Ellenburger			12,966,398	
Coyanosa/Mississippian		10,500	2,840,903	
Coyanosa, N/Bone Springs	1963	8,700		8
Coyanosa, N/Delaware	1966	4,800		816
Coyanosa, NE/Delaware			14,572	
Coyanosa, S/Mississippian	1977	11,400	46,628	9
Coyanosa, S/Cherry Canyon	1965	6,000		9
Coyanosa, W/Delaware	1962	5,300		160
Riplinger/Devonian			97,755	
Scott/Cherry Canyon	1978	6,100	1,039,861	43
Scott/Delaware	1946	4,200	41,923	949
Sunni/Cherry Canyon		5,900		
Survey 16		10,300	1,316,770	
Waha/Delaware	1960	4,800	2,428,926	920
Waha/Devonian			5,474,207	
Waha/Ellenburger			7,929,590	
Waha/Mississippian			8,854,452	
Waha/Montoya			1,280,185	
Waha, N/Delaware	1960	4,900	58,679	4,925
Waha, S/Delaware	1963	3,450		6
Waha, W/Delaware-cons.	1974	6,500	6,197	900
Waha, W/Delaware	1961	5,000		1,928
Waha, W/Delaware-5500	1963	5,500		189
Waha, W/Delaware-5800	1963	5,800		187
Waha, W/Delaware-6050	1962	5,700		373
Waha, W/Delaware-6250	1972	6,200		2
Waha, W/Delaware-6450	1962	6,450		730
Waha, W/Ellenburger			6,943,861	
Worsham/Castile	1960	2,800		16
Worsham/Cherry Canyon	1967	6,280	2,605,320	30
Worsham/Delaware	1960	4,900	1,489,485	935
Worsham, E/Cherry Canyon			1,491,649	
Worsham, N/Devonian			337,966	
Worsham, N/Ellenburger			89,762	
Worsham, N/Fusselman			1,412,970	
Worsham, S/Castile	1962	3,660		0.4
Worsham, S/Delaware-lower	1962	6,500		1
Worsham, S/Delaware	1961	5,050		338
Worsham, SW/Delaware	1963	1,500		239
Worsham-Bayer/Pennsylvania	1967	12,800	1,281,362	159
Worsham-Bayer/Wolfcamp	1964	11,000		0.5
Worsham-Bayer/Atoka			175,958	
Worsham-Bayer/Devonian			3,117,636	
Worsham-Bayer/Ellenburger			10,138,407	
Worsham-Bayer/Fusselman			37,247	
Total			117,402,936	21,739

[a]Texas Railroad Commission, Oil and Gas Division (1980).
[b]MCF—thousands of cubic feet.
[c]kbbl—thousands of 42-gallon barrels.

B. Exploration History

Prior to organized petroleum exploration, both Native Americans and pioneer settlers were aware of oil seeps in the vicinity of the test site (Warner, 1939, p. 313). The first indication of deep hydrocarbon reservoirs was provided by two water wells drilled in the area in 1901 (Warner, 1939, p. 314):

(1) Near Toyah Lake, on the western margin of the test site (Figure 13-6), a well encountered oil and gas in Cenozoic alluvium at depths of 50 to 90 m (155 to 280 ft).

(2) Approximately 13 km (8 mi) east–northeast of the southeast corner of the test site, a well encountered oil at a depth of 20 m (60 ft).

The major exploration effort in the area occurred between 1959 and 1966. Since that time, development and step-out drilling have added additional reserves. In the last few years, there has been renewed drilling activity in areas adjacent to established production. Discoveries were the result of seismic and subsurface geologic investigations from which the present understanding of the complex subsurface geology of the test site area gradually emerged.

C. Reservoir Structure and Stratigraphy

An angular unconformity at the base of the Permian separates Guadalupe and Castile Reef traps from underlying structural/stratigraphic traps (Hills, 1970, p. 1818–1819; King, 1959, p. 39). Post-Atokan/pre-Strawn tectonic activity created folds and the high-angle reverse and normal faults that provide structural closure in pre-Permian rocks (Holmquist, 1965, p. 263). Throughout the history of the basin, incipient structurally positive areas were formed on basin-margin faults, hinge lines, and horst blocks. These incipient features produced topographic highs which, at times, acted as the source terrain for detritus that shed into the Central Basin. Great clastic wedges, such as the Permian Coyanosa conglomerate, create excellent stratigraphic traps (Holmquist, 1963, p. 264). These wedges were often modified by large-scale submarine slides that further complicate the subsurface structure (Guinan, 1971).

The complex subsurface picture has largely been masked by Triassic through Quaternary strata exposed at the surface. The attitude of these younger units is primarily a response to solution of the lower Ochoa evaporite sequence, not to the pre-Ochoan structure (Ogilbee et al., 1962, p. 20). A series of subsurface structural contour maps and cross sections (Figures 13-9 through 13-13) are provided to illustrate this complexity.

Figure 13-14 shows major subsurface faults reported in the literature. An examination of this figure reveals a lack of subsurface faulting in the western half of the test site area. This absence is considered a product of the inadequacy of available information, rather than an accurate portrayal of the subsurface picture. The absence of any faults in subsurface maps (Figures 13-6, 13-9, and 13-10) is similarly a result of a lack of fault interpretation in contouring, rather than a real lack of faulting in the horizons contoured.

D. Production and Reserves

Figures for the estimated reserves of oil and gas for individual producing fields within the test site area are not available. Proved reserve figures are available for District 8 of the Oil and Gas Division of the Texas Railroad Commission (1980). District 8 covers 20 West Texas counties including the portions of Pecos, Reeves, and Ward Counties within the test site. For this district, proved reserves of oil, as of December 31, 1979, are 2,272,404,000 barrels. The estimated ultimate recovery of natural gas, as of December 31, 1979, is 38,593,978 thousand cubic feet (MCF). General field data and cumulative production statistics for the fields within the test site are shown in Table 13-3.

The potential for future discoveries within the test site area is limited. Precambrian basement has been drilled in several fields; present production is from the deepest known producing horizons, which are at depths exceeding 7000 m (20,000 ft) in some fields. Small field/pool discoveries in shallower horizons may provide additional reserves, but it is doubtful that new reserves similar to those discovered in the 1960s exist in the test site area. There is, however, the potential for establishing significant reserves elsewhere in the Delaware Basin, particularly in areas to the west and south of already established production in the test site.

V. Vegetation

A. Introduction

A field vegetation study was conducted in the test site area to provide information on plant cover that could be used in the evaluation of remote sensing data. Nineteen sampling sites were established in relatively undisturbed areas of homogeneous and typical vegetation cover (Figure 13-15). These sites were visited bimonthly between June 1980 and September 1981 to detect any seasonal variation. On September 6, 1981, percent ground cover was determined at 13 sites along two 33-m (100-ft) transects run at right angles to one another at each site.

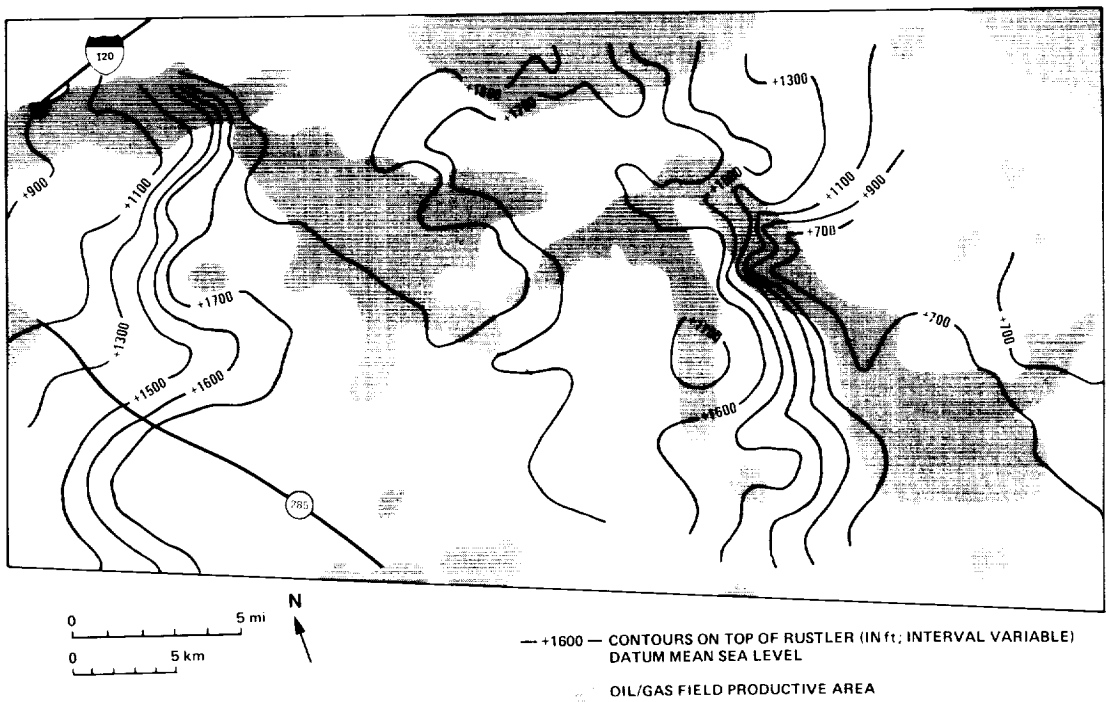

Figure 13-9. Subsurface structure on top of the Rustler Formation (Ochoan) (after unpublished data from the Geo-Search Corporation, Midland, Texas)

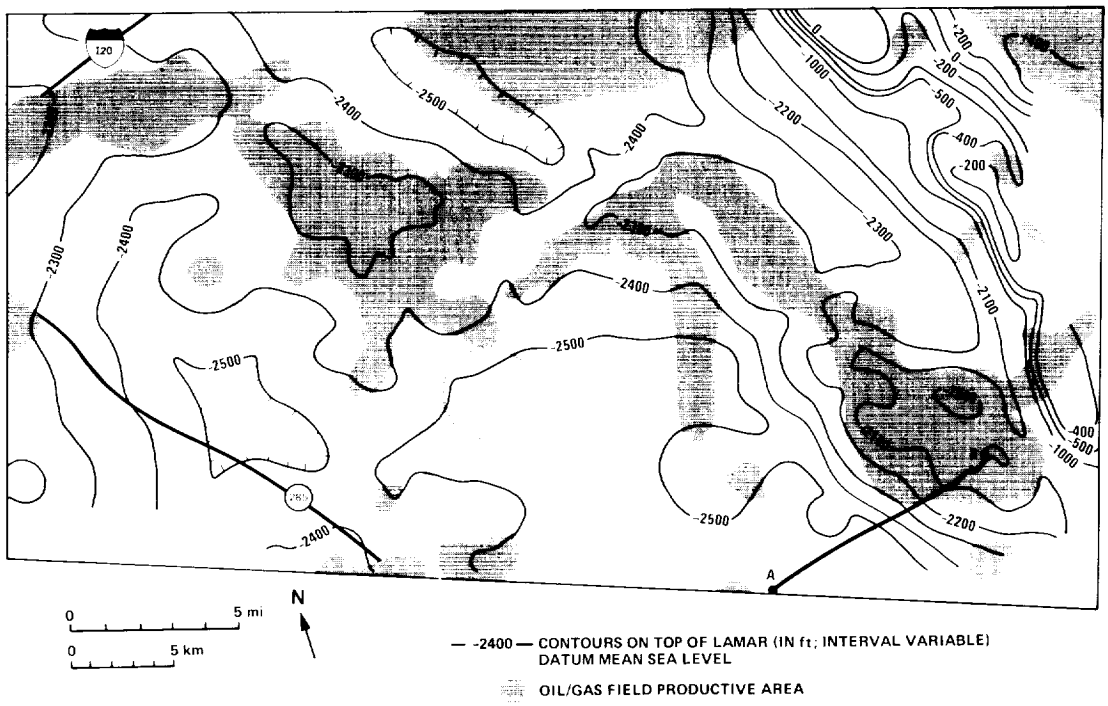

Figure 13-10. Subsurface structure on top of the Lamar shale (Guadalupean) (after unpublished data from the Geo-Search Corporation, Midland, Texas). Cross section A-B is shown in Figure 13-11.

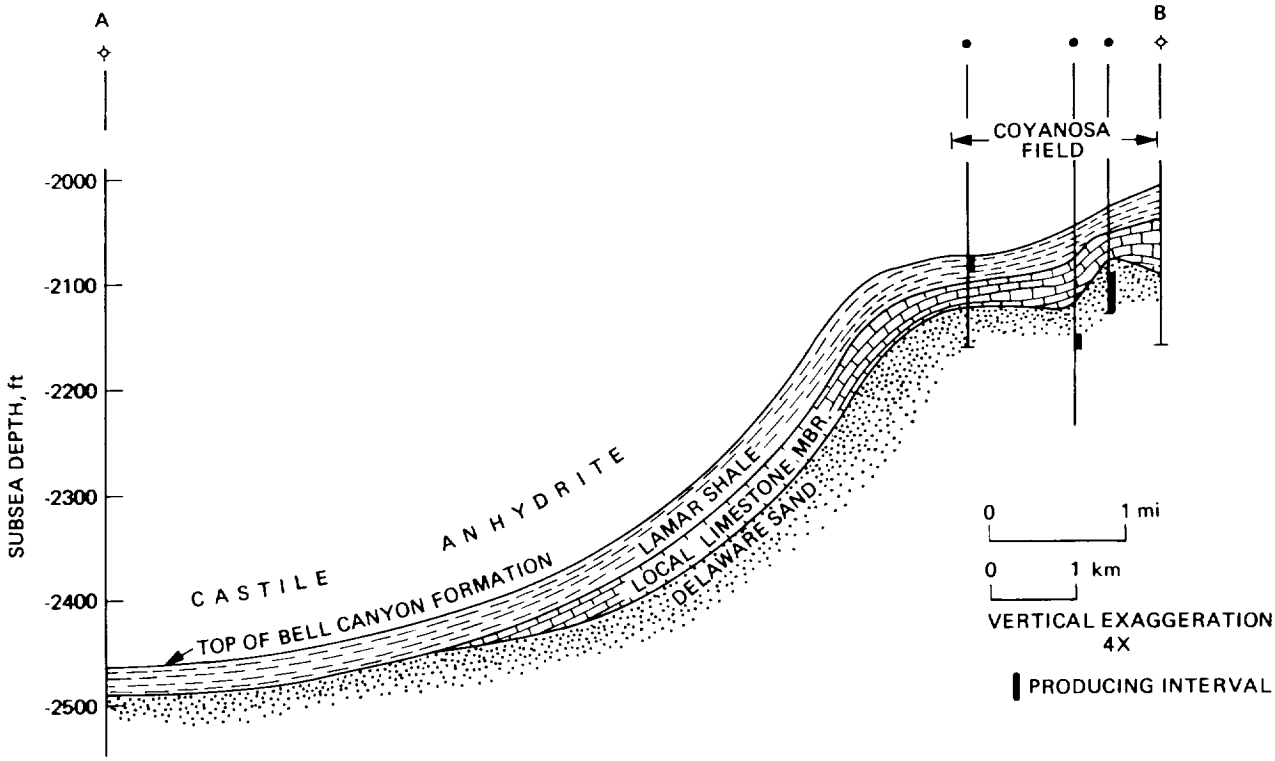

Figure 13-11. Cross section showing Lamar and Delaware productive intervals in fractured reservoirs of the Coyanosa field (Wilson, 1969, p. 68). See Figure 13-10 for location.

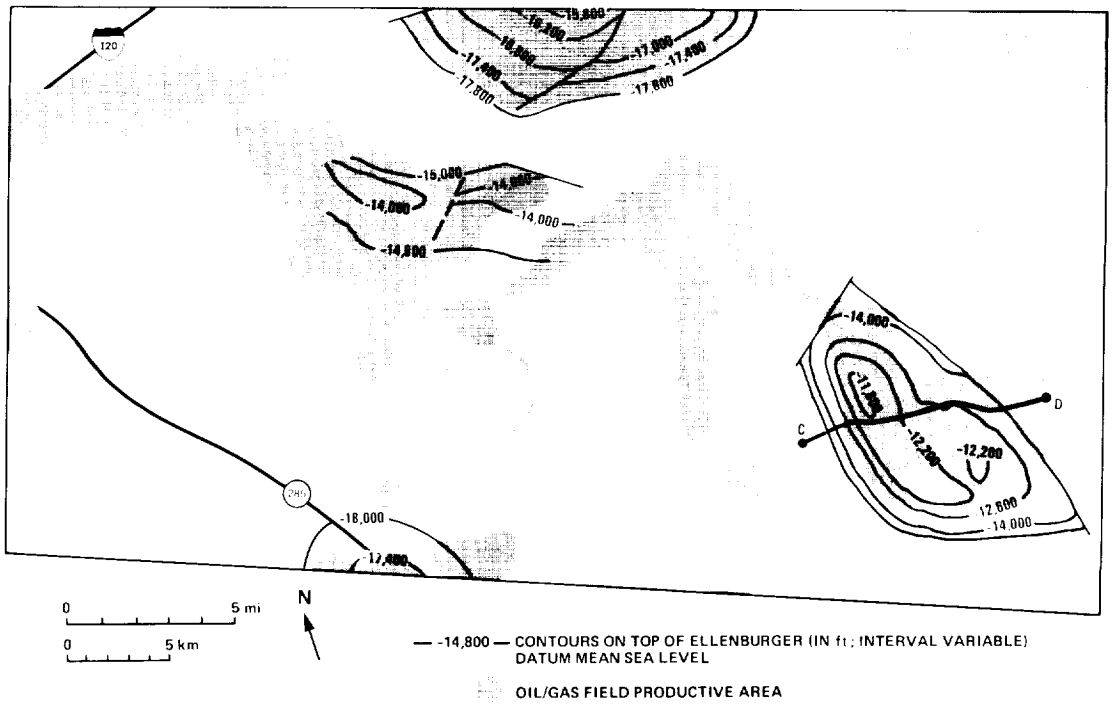

Figure 13-12. Subsurface structure on top of the Ellenburger Formation (Ordovician) (after unpublished data from the Geo-Search Corporation, Midland, Texas). Lack of deep well data results in subsurface information restricted to the four contoured areas shown. Cross section C-D is shown in Figure 13-13.

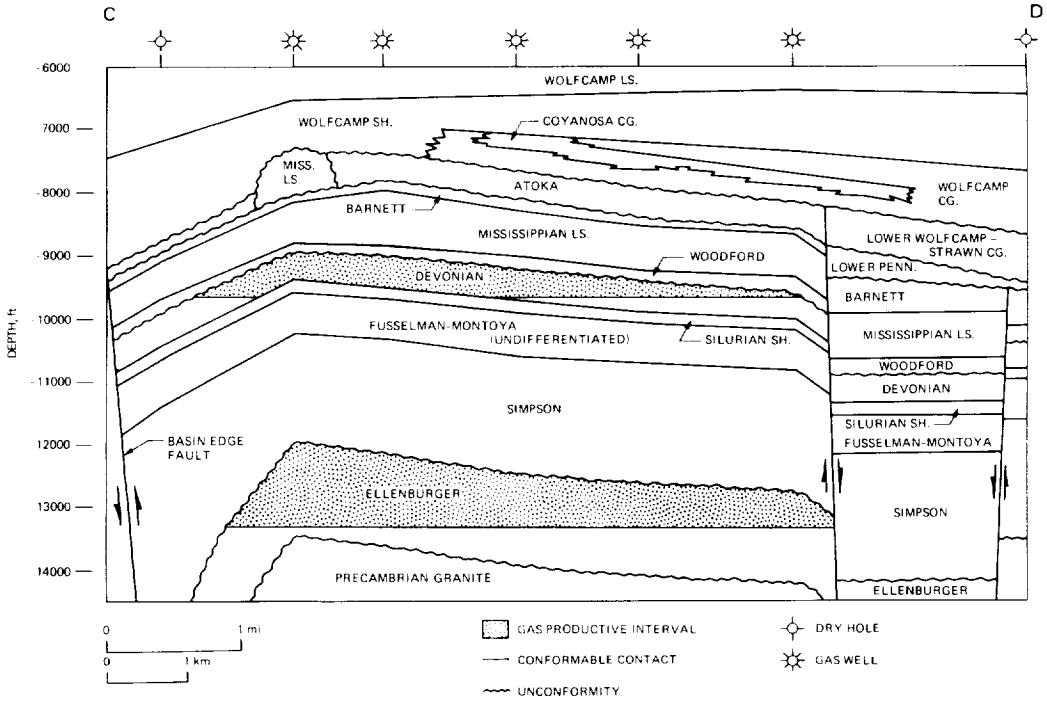

Figure 13-13. Cross section showing deep gas production in the horst-block structure of the Coyanosa field (Guinan, 1971, p. 126). Oil and gas production is also obtained from stratigraphic reservoirs in Mississippian reefal limestones (MISS. LS.) and Coyanosa and Wolfcamp conglomerates. Refer to Figure 13-12 for location.

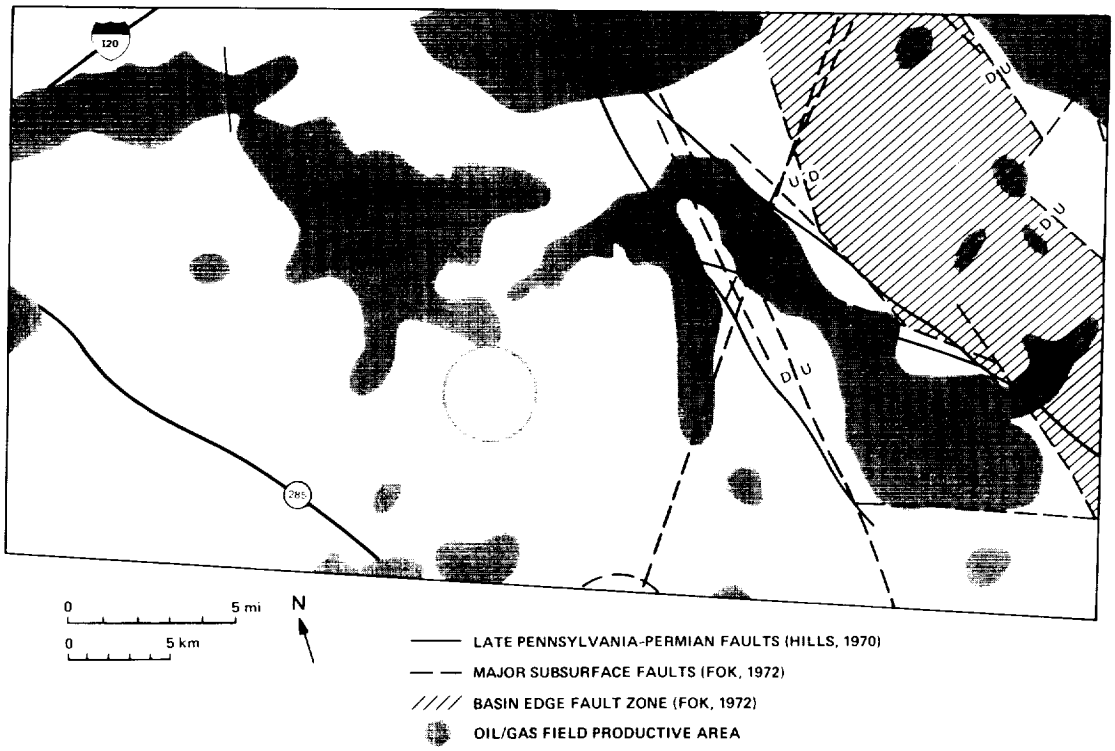

Figure 13-14. Map showing major subsurface faults and fault zones. The absence of major subsurface faulting in the western test site area reflects the lack of available information (Fok, 1972; Hills, 1970).

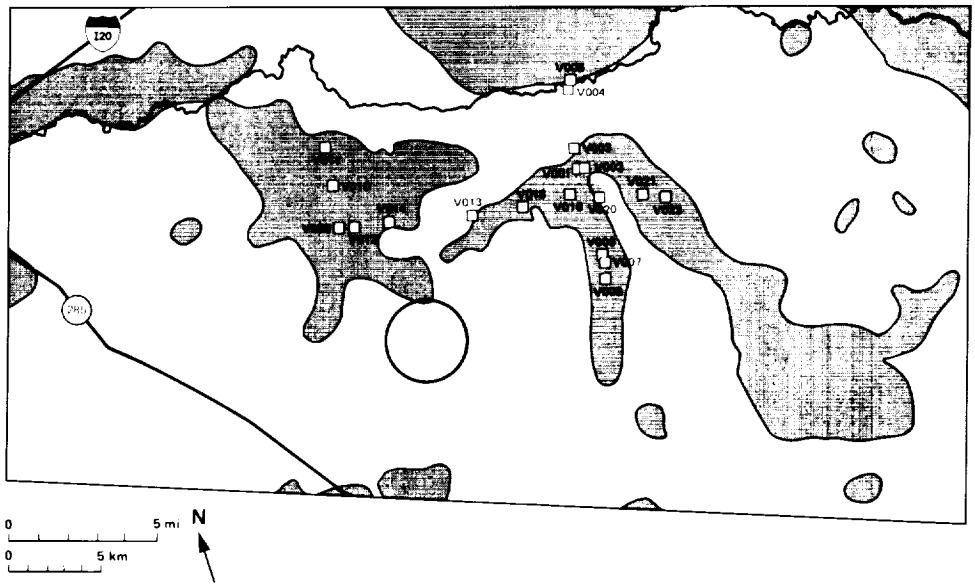

Figure 13-15. Map showing 19 vegetation study sites. Percent ground cover was determined on September 6, 1981 at 13 sites listed in Table 13-7.

In addition, reconnaissance of the vegetation in the entire test site was conducted to determine if any areas of anomalous or stressed vegetation existed. Ground observations were supplemented by visual observation and photographs from an altitude of about 200 m above ground from a small aircraft.

B. Results

The predominant vegetation at the Coyanosa test site is desert shrub, primarily creosote (*Larrea tridentata*, Figure 13-16) and mesquite (*Prosopis glandulosa*, Figure 13-17). On well-drained topographic highs, creosote dominates the sparse vegetation. Mesquite increases in abundance and size toward drainages; 2- to 4-m mesquite trees are common in Hackberry Draw. Along the Pecos River and Toyah Lake, where moisture is more dependable although often saline, salt cedar (*Tamarix pentandra*, Figure 13-18) is common. Shrubs and succulents characteristic of the test site are listed in Table 13-4.

Side oats grama (*Bouteloua curtipendula*, Figure 13-19) is the dominant grass. The grasses listed in Table 13-5 are characteristic of Hackberry Draw near Coyanosa (Rives et al., 1980). Figure 13-20 shows spring grasses in Hackberry Draw.

Broadleaf herbs and some grasses flower and substantially increase ground cover when sufficient moisture is available, especially in draws and drainages (Figure 13-21). The cowpen daisy (*Verbesina* sp.) is the dominant spring wildflower; its yellow flowers can be seen throughout the test site when sufficient winter and spring moisture is available. When late summer rains provide sufficient moisture, broadleaf herbs such as broomweed (*Xanthocephalum* sp., Figure 13-22) substantially increase ground cover. In disturbed soils, Russian thistle or tumbleweed (*Salsola* sp., Figure 13-23) and purple nightshade (*Solanum elaeagnifolium*) dominate. Table 13-6 is a partial list of flowering plants common in the site.

At several of the sampling sites, crusts of blue-green algae (cyanobacteria) and lichen are common. These primitive plants are typically black and, especially during moist weather, might increase spectral absorption in barren areas.

The ground cover survey data are presented in Table 13-7. Kruskal–Wallis' one-way analysis of variance by ranks (Siegel, 1956) revealed no significant differences ($H = 1.49$, $df = 11$) in the physical structure of the community between sites because bare ground was the dominant feature at all the sites. Among the sites, bare ground ranged from 34 percent in Hackberry Draw to 82 percent at site V009, a caliche ridge. Composition of vegetation differed substantially from place to place. Mesquite cover ranged from nearly absent in some gravelly soils to as much as 63 percent in Hackberry Draw. Creosote, which occurs in the drier, rockier areas, ranged from absent to about 20 percent of the cover. The other shrubs accounted for an average of 3.5 percent of the total cover, although tarbush (*Flourensia* sp.) and

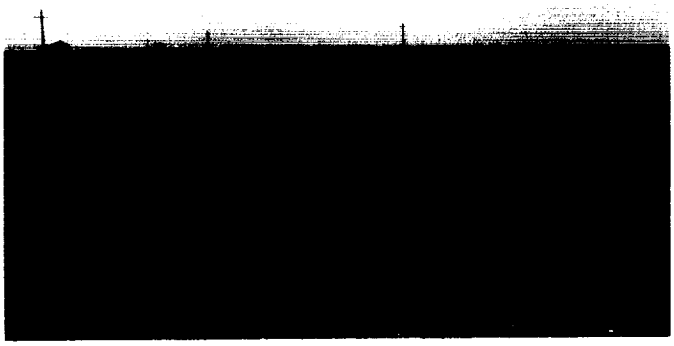

Figure 13-16. South-facing photograph showing creosote (*Larrea tridentata*) as the dominant shrub at vegetation study site V021 (September 1981)

four-wing saltbush (*Atriplex canescens*) were locally common. At the time of the survey, broadleaf herbs and grasses each accounted for about 6 percent of the ground cover. However, evidence of dead or dormant broadleaf herbs in bare areas indicated that these plants can increase cover substantially.

During a year when moisture is relatively abundant, as in 1981 (Table 13-8), the test site appears to be well covered by vegetation. However, as the data in Table 13-7 show, ground cover averages about 38 percent (Figure 13-16). When the survey was conducted, late summer wildflowers

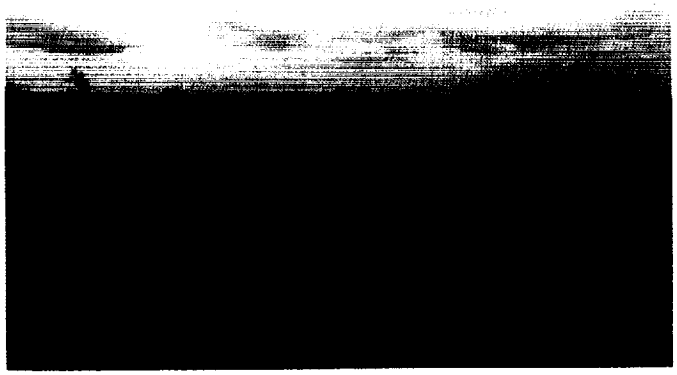

Figure 13-17. South-facing photograph showing mesquite (*Prosopis glandulosa*) as the dominant shrub at vegetation study site V002 (September 1981)

Figure 13-18. North-facing photograph across the Pecos River showing salt cedar (*Tamarix pentandra*) as the dominant shrub at vegetation study site V005 (May 1981)

were abundant (Figure 13-24). During dry periods when only shrubs would provide cover and wildflowers and grasses would be dormant, cover could average as low as 24 percent. At sites such as V009, V014, and V021, cover during very hot summers or dry winters could be 10 percent or less.

Observations from a low-altitude aircraft provided an excellent overview of the test site and revealed no apparent anomalous vegetation features. Likewise, ground-level reconnaissance revealed only vegetation disturbances that were related to agriculture or oil and gas production activities.

Table 13-4. Shrubs and succulents characteristic of the Coyanosa test site

Scientific Name	Common Name
Acacia sp.	Catclaw
Acacia constricta	Whitethorn
Artemesia sp.	Sagebrush
Atriplex canescens	Four-wing saltbush
Chilopsis linearis	Desert willow
Echinocactus horizonthalonius	Devil's head cactus
Ephedra trifurca	Mormon tea
Flourensia sp.	Tarbush
Fouquieria splendens	Ocotillo
Koeberlinia spinosa	Allthorn
Larrea tridentata	Creosote
Lycium berlanderi	Squawberry
Opuntia engelmanni	Prickly pear cactus
O. imbricata	Cane cholla
O. leptocaulis	Pencil cholla
Prosopis glandulosa	Mesquite
Tamarix pentandra	Salt cedar
Yucca elata	Narrow-leaf yucca
Y. torreyi	Broadleaf yucca

Figure 13-19. Southeast-facing photograph showing side oats grama (*Bouteloua curtipendula*) as the dominant grass at vegetation study site V016 (September 1981)

Figure 13-20. West-facing photograph across Hackberry Draw showing spring grass and mesquite at vegetation study site V006 (May 1981)

C. Conclusions

The Coyanosa test site is sparsely vegetated, with an average vegetation cover of approximately 37 percent, but the total cover can vary greatly throughout the year and from year to year depending upon rainfall and the time of year when precipitation occurs. Creosote is the dominant shrub where soils are thin and well drained. Mesquite becomes more abundant and larger as soils become better developed and moisture is less ephemeral. Salt cedar (*Tamarix*) is abundant where water is semipermanent to permanent, especially along the Pecos River and Toyah Lake. Wildflowers and grasses respond to seasonal and year-to-year variations in precipitation and can vary from essentially absent to abundant, especially along drainages.

Table 13-5. Grasses characteristic of Hackberry Draw near Coyanosa, Pecos County[a]

Scientific Name	Common Name
Aristida sp.	Three-awns
Bouteloua breviseta	Gyp grama
B. curtipendula	Side oats grama
B. eriopida	Black grama
B. gracilis	Blue grama
Buchloe dactyloides	Buffalo grass
Digitaria californica	Arizona cottontop
Eragrostis intermedia	Plains love grass
Hilaria belangeri	Common curly mesquite
H. mutica	Tobosa
Leptochloa dubia	Green sprangletop
Muhlenbergia arenicola	Sand muhly
M. porteri	Bush muhly
Panicum obtusum	Vine mesquite
Scleropogon brevifolius	Burro grass
Setaria leucopila	Plains bristle grass
Sporobolus airoides	Alkali sacaton
S. cryptandrus	Sand dropseed
S. flexuosus	Mesa dropseed
Stipa leucotricha	Texas winter grass

[a]Rives et al., 1980.

VI. Soils

Soil information for the test site area (Figure 13-25 and Table 13-9) was compiled from U.S. Department of Agriculture soil survey reports for the counties of Reeves (Jaco

Figure 13-21. West-facing photograph across Hackberry Draw showing spring wildflowers (cowpen daisy, *Verbesina* sp.) at vegetation study site V006, an old grave location (May 1981)

Figure 13-22. North-facing photograph showing broomweed (*Xanthocephalum* sp.), a late summer wildflower, at vegetation study site V009 (September 1981)

Figure 13-23. South-facing photograph showing Russian thistle (tumbleweed, *Salsola* sp.) in a former trail at vegetation study site V022 (September 1981)

Table 13-6. A partial list of common wildflowers and broadleaf herbs characteristic of the Coyanosa test site

Scientific Name	Common Name
Abronia sp.	Sand verbena
Fallugia paradoxa	Apache plume
Nerisyrenia sp.	Mesa greggii
Phlox sp.	Desert phlox
Salsola sp.	Russian thistle (tumbleweed)
Solanum elaeagnifolium	Purple nightshade
Sphaeralcea sp.	Globe mallow
Verbesina sp.	Cowpen daisy
Xanthocephalum sp.	Broomweed

Table 13-7. Percent ground cover on September 6, 1981, determined at 13 sites in the Coyanosa test site

Site	Ground Cover, %					
	Bare	Grass	Broadleaf Herbs	Mesquite	Creosote	Other Shrubs
V001	39	25	0	35	0	1.5
V002	34	1	2	63	0	0
V009	81.5	0	6.5	3	9	0
V010	52.5	0.5	11.5	16	3	16.5
V011	71.5	0	7.5	11.5	9	0.5
V012	65	0	12.5	5.5	17	0
V013	68.5	0	8.5	5	16.5	1.5
V014	75.5	0	10.5	0	12.5	1.5
V015	64.5	0	13.5	0.5	18	3.5
V016	53.3	22	0.3	0.7	13.3	10.3
V020	63	0	4.5	32.5	0	0
V021	55	31	0	0	13	1
V022	76.5	1	0	5.5	14	3
Mean	62.3	7.0	5.9	11.3	9.0	3.5
Standard Deviation	16.3	13.6	6.6	16.3	9.1	6.4

Table 13-8. Monthly rainfall for Pecos, Texas, for 1975–1977 and 1980–1981[a]

Month	Rainfall, mm				
	1975	1976	1977	1980	1981
January	19	2	9	15	29
February	20	1	3	8	21[b]
March	6	1	10	0	34
April	0	2	5	13	92
May	22	21	32	51	34
June	2	16	12	92	13
July	102	13	12	1	39
August	32	24	5	133	46
September	43	75	6	24	**
October	4	31	23	16	**
November	3	17	4	40	**
December	15	4	4	7	**

[a] Adapted from National Oceanic and Atmospheric Administration Climatological Data (1975–1977, 1980–1981).
[b] Pecos data unavailable for Monahans, Texas.
** Data unavailable.

et al., 1980), Pecos (Rives et al., 1980), and Ward (Dittemore and Blum, 1975), in conjunction with geologic data from Ogilbee et al. (1962) and Barnes (1976). Eleven major soil mapping units (Figure 13-25) occur on three principal landforms in the test site area.

A. Soils of Floodplains, Terraces, and Lower Uplands

Loamy to clayey soils, occurring in level areas, comprise about 10 percent of the study area. These young soils exhibit poorly developed profiles.

ORIGINAL PAGE
COLOR PHOTOGRAPH

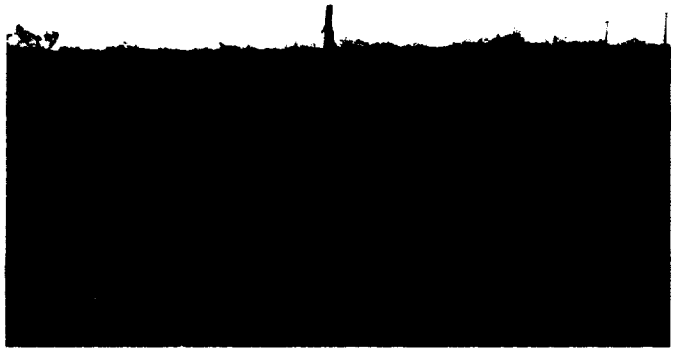

Figure 13-24. South-facing photograph showing late summer wildflowers at vegetation study site V012 (September 1981)

Soils on the floodplain of the Pecos River are moderately to extremely saline, while soils along the Toyah Lake Playa are extremely saline. These soils are well drained to somewhat poorly drained and are used for either rangeland or irrigated cropland. The 12 soil mapping units occurring in these environments may be grouped as follows:

(1) Loamy and clayey soils on Pecos River floodplain formed from Holocene alluvium of lower lying floodplains (Arno, Gila, Patrole, Pecos, Harkey, and Toyah soils).

(2) Loamy soils on Pecos River terraces—formed from Holocene alluvium of Pecos River terraces (Monahans, Pajarito, and Ima soils).

(3) Loamy soils on floodplains—formed from Holocene alluvium of former spring-fed marshes (Balmorhea soils); and saline loamy soils of lower uplands—formed from Holocene alluvium derived from Pleistocene Tahoka Formation (Orla and Saragosa soils).

B. Soils of Uplands and Outwash Plains

These soils comprise about 50 percent of the study area and occur in nearly level to gently undulating areas. Most are deep loamy or clayey soils, some of which contain layers of gypsum and are moderately mature as indicated by their well-developed soil profiles. The soils of uplands and outwash plains are mostly well drained to moderately well drained, are moderately permeable, and are used for rangeland or irrigated cropland. The eight soil mapping units occurring in these environments are combined into the following three categories:

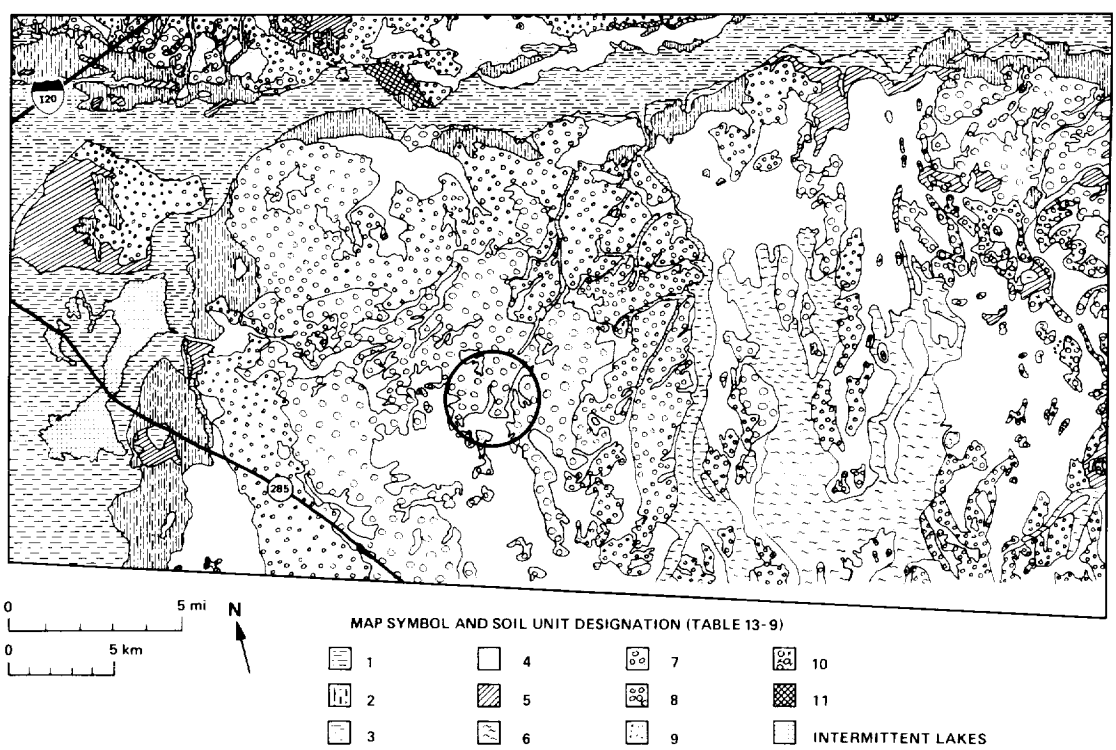

Figure 13-25. Soil map (compiled from Barnes, 1976; Dittemore and Blum, 1975; Jaco et al., 1980; Ogilbee et al., 1962; Rives et al., 1980)

C-4

Table 13-9. Characteristics of soil units occurring in the Coyanosa test site as mapped in Figure 13-25

Soil Designation (Plate 13-1)	Mapping Units Included	Color	Texture	Parent Material
1	Gila, Patrole, Arno, Pecos, Harkey, Toyah	Pale brown to reddish brown and dark grayish brown	Clay to fine sandy loam	Recent alluvium
2	Monahans, Pajarito, Ima	Light yellowish brown to brown	Loam to fine sandy loam	Calcareous/gypsiferous alluvium of stream terraces
3	Balmorhea	Gray to grayish brown	Silty loam	Alluvium of spring-fed marshes
3	Orla, Saragosa	Pale brown to brown	Clay loam	Limestone and gypsum lacustrine deposits
4	Reagan, Hodgins Reakor	Light brownish gray to brown	Silty clay loam to loam	Calcareous loamy alluvium
5	Holloman, Reeves, Hoban, McCarran	Pale brown to brown	Clay loam to silty clay loam	Gypsiferous alluvial beds
6	Dalby	Pinkish gray	Clay	Calcareous valley-fill alluvium
7	Upton, Delnorte	Pale brown to yellowish brown	Gravelly clay loam to very gravelly loam	Limestone and caliche beds
8	Canutio, Delnorte, Nickel	Pale brown to brown	Very gravelly sandy loam	Calcareous gravelly alluvium
9	Pyote, Sharvana, Wickett	Yellowish red to brown	Loamy fine sand	Sandy eolian mantle on caliche beds
10	Lozier	Light brownish gray	Very gravelly loam	Limestone beds
11	Los Tanos, Courthouse, Sandstone outcrops	Red	Fine sandy loam to coarse-grained sandstone	Triassic Santa Rosa sandstone beds

(4) Loamy soils of upland outwash plains and basins—formed from Holocene and Pleistocene alluvium (Reagan, Reakor, and Hodgins soils).

(5) Loamy soils on uplands—formed from younger Pleistocene alluvium of soils derived from gypsum and limestone (Holloman, Reeves, Hoban, and McCarran soils).

(6) Clayey soils of upland outwash plains and valley fills—formed from younger Pleistocene alluvium (Dalby soils).

C. Soils of Hills and Ridges

This group of soils comprises approximately 40 percent of the study area, with most of the soils having a gravelly or rocky surface layer underlain by thick layers of caliche that probably required millions of years to form. The other soils of this group are shallow, young soils that have been recently eroded and are underlain by limestone or sandstone bedrock. All of the soils of this group are well drained, most are moderately alkaline, and almost all are used for rangeland. The 10 soil mapping units occurring in these environments may be grouped into the following five categories:

(7) Gravelly loam of upland plains and foot-slope terraces—formed from older Pleistocene alluvium derived from limestone hills (Upton and some Delnorte soils).

(8) Very gravelly loam of uplands—formed from older Pleistocene alluvium derived from limestone and igneous hills (Delnorte, Nickel, and Canutio soils).

(9) Sandy and loamy soils of uplands—formed from older Pleistocene eolian or alluvial sediments (Pyote, Sharvana, and Wickett soils).

(10) Very gravelly loam on limestone hills—formed from Lower Cretaceous Washita Group limestones (Lozier soils).

(11) Fine, sandy loam and sandstone outcrops—formed from Triassic Santa Rosa Sandstone of the Dockum Group (Los Tanos and Courthouse soils).

D. Factors of Soil Formation

Soil forms as a result of the interaction of five major factors: (1) physical and mineralogical characteristics of the parent material, (2) climate under which the soil formed, (3) living organisms on and in the soil, (4) topographic relief, and (5) length of time that these factors have acted on the soil.

1. Parent material. The unconsolidated mass from which a soil forms limits the physical and chemical characteristics of a soil. The parent materials of the study area are Triassic sandstone, Cretaceous limestone, and Tertiary through Holocene alluvium. Rock fragments in the alluvium include a wide variety of igneous, metamorphic, and sedimentary rocks, many of which have been transported from mountains to the south of the study area. Other parent materials include Pleistocene and Holocene eolian sands, caliche, calcareous and gypsiferous earth, and Holocene lake, marsh, river terrace, and floodplain sediments.

2. Climate. The semiarid climate is uniform over the entire study area and is characterized by hot summers and moderate winters. Major precipitation occurs from May through October in the form of high-intensity thundershowers that frequently cause soil erosion. During the driest part of the year, high winds often erode the soil. The low humidity of the region also produces a high rate of evaporation that limits the growth of plants and the accumulation of organic matter in the soils.

Because the limited rainfall does not provide sufficient moisture to leach the alkaline minerals from most of the soils, calcium carbonate (caliche) accumulates near the surface. Most of the area's soils, especially the deep soils, are seldom moist below the root zone. The dry climate also limits the translocation of clay and the reduction and transfer of iron in the soils.

3. Living organisms. Microorganisms, plants, and animals on or in the soil contribute to the process of soil formation. Gains and losses of organic matter, nitrogen, and other plant nutrients and changes in soil structure and porosity are caused by these living organisms. Plants, especially grasses, are important for soil development since their root systems contribute large amounts of organic matter. The roots of both shrubs and grasses decay to form pores that serve as passageways for water.

Small animals and insects that work and mix the soils hasten the decay of organic matter by microorganisms and improve soil structure and fertility. The activities of man also influence soil development, especially the fencing of rangeland that sometimes allows overgrazing by cattle. Overgrazed grasses return less organic matter to the soil than properly grazed grasses do and retard soil profile development. Irrigation with saline water and the construction of roads and buildings also alter soils in some areas of the test site.

4. Topography. Topography influences soil development through its effect on drainage, erosion rate, plant cover, and soil temperature. The topography of the study area ranges from nearly level on floodplains, to rolling on uplands, and to steep at upland edges. The steep areas have shallow soils, which indicate that the rate of soil development has not been able to keep pace with the rate of erosion.

The degree of soil profile development depends to a large extent on the amount and depth of moisture penetration. Nearly level transported soils of floodplains (Arno, Pecos, Patrole, Toyah, Gila, and Balmorhea soils) have the least developed profiles and are usually the deepest because they are actively forming by the accumulation of sediments derived from surrounding areas.

The nearly level soils on uplands that receive runoff from higher lying areas have weak to moderately good soil profile development (Dalby, Hoban, Hodgins, Reagan, Reakor, and Reeves soils). The upland soils that do not receive additional runoff, however, are shallow to very shallow and have a poorly developed soil profile which typically includes layers of caliche and often contains rock fragments (Delnorte, Upton, Nickel, and Wickett soils). Steep soils that are shallow to very shallow (Courthouse, Los Tanos, and Lozier soils) have a poorly developed profile because of rapid runoff and erosion.

5. Time. The degree of soil profile development is the primary method used to determine the age of a soil. The youngest soils show little profile development, as exemplified by the soils on the Pecos River floodplain. Slightly older soils, many of which contain accumulations of calcium carbonate, formed in topographically higher, older alluvium and have well-developed soil profiles (Hodgins, Ima, and McCarran soils). Further aging results in the leaching of calcium carbonate downward to lower horizons to form soft masses or concretions of caliche, as in the case with the Hoban, Reagan, and Reakor soils. In the oldest soils (Del-

norte, Upton, Sharvana, and Wickett), calcium carbonate accumulations are cemented or indurated and form thick layers of caliche that suggest a long time of formation, probably millions of years (Jaco et al., 1980).

E. Summary

The soils most similar in composition to the underlying geologic units are the shallow soils of hills, ridges, and steeply sloping upland edges. The semiarid climate has permitted the accumulation of calcium carbonate (in the form of caliche) and calcium sulfate (in the form of gypsum) in many of the soils of the study area. The dry climate has also restricted the movement of clay and the reduction and transfer of iron within the soils, while the low density of plant and animal life has resulted in the low organic content of most soils. Topography has influenced soil profile development; the constantly reworked soils of the Pecos River floodplain and the well-drained soils of uplands have the poorest profile development, and the less well-drained soils of uplands exhibit the best profile development. The upland soils, with their thick accumulations of caliche which probably required millions of years to form, suggest that large portions of the uplands have been elevated since at least Pleistocene time.

VII. Soil Geochemistry

A. Introduction

Donovan and others (Dalziel and Donovan, 1980; Donovan, 1974; Donovan et al., 1975) have recognized cases of anomalous concentration, alteration, and distribution of certain elements and isotopes in soils, bedrock, and vegetation over and adjacent to some oil and gas fields. These geochemical anomalies have been attributed to the effect of hydrocarbon microseepage from oil/gas reservoirs. A geochemical survey was conducted as part of the Coyanosa test site study to determine if potential hydrocarbon seepage in the area, suggested by historical water well data (Paragraph IV.B), has resulted in detectable soil geochemical anomalies.

Surface soil samples were collected in 1979 and 1980 at 138 sites in the test site area (Figure 13-26). These samples were analyzed for elemental/isotopic geochemistry by laboratories of Phillips and Barringer, using procedures outlined in Appendix B, Figures B-1 and B-2 and Table B-1. The analytical results are summarized in Tables B-2 (Phillips) and B-3 (Barringer). The Table B-2 data were evaluated to determine any possible indications of microseepage-induced surface alteration.

B. Results

1. On-field/off-field analysis. Each sample was classified as being from inside or outside local oil/gas field productive limits (Table B-4) using the productive limits shown in Figure 13-26. Stepwise discriminant analysis (STEPDISC in the Statistical Analysis System programs) of the Table B-2 data by Phillips identified the variables log Ni, log Ca, log Cd, log Si, log Co, log V, log K, and $\delta^{13}C$ as being the most important in classifying the soil samples with respect to local production.

A discriminant analysis using these eight variables yielded scores summarized in Table 13-10. Although these scores are not random, they may not be meaningful. On the basis of the discriminant analysis of the 69 samples collected from inside the productive limits of known oil and gas fields, 63 were correctly classified. Least squares analysis, however, shows that as much of the variance in on-field versus off-field samples is explained by soil type as is explained by the geochemical variables (Table 13-11). Local petroleum production is associated with structures that may be surficially expressed. Since surface structure will directly affect surface lithology, soil type, and soil geochemistry, the Table 13-10 results probably reflect the structural geology of the area and not microseepage-induced alteration.

2. Carbon isotope analysis. Figure 13-27 summarizes carbon isotope values determined by Phillips (Table B-2). These data support a nonpetroleum source for soil carbonate in the test site area. These results lend further credence to the interpretation that variation in soil geochemistry at the Coyanosa test site is the result of normal surface processes and is not due to microseepage-induced alteration.

C. Conclusions

The results of a limited soil elemental/carbon isotope geochemical survey of the Coyanosa test site revealed no geochemical anomalies attributable to hydrocarbon microseepage.

Table 13-10. Discriminant analysis scores for classifying Coyanosa test site soil samples according to location inside or outside local oil field productive areas

Sample Classified	Sample Collected					
	Outside		Inside		Total	
	No.	%	No.	%	No.	%
Outside	26	43.3	6	8.7	32	24.8
Inside	34	56.7	63	91.3	97	75.2
Total	60	100.0	69	100.0	129[a]	100.0

[a]Some samples were deleted due to missing data.

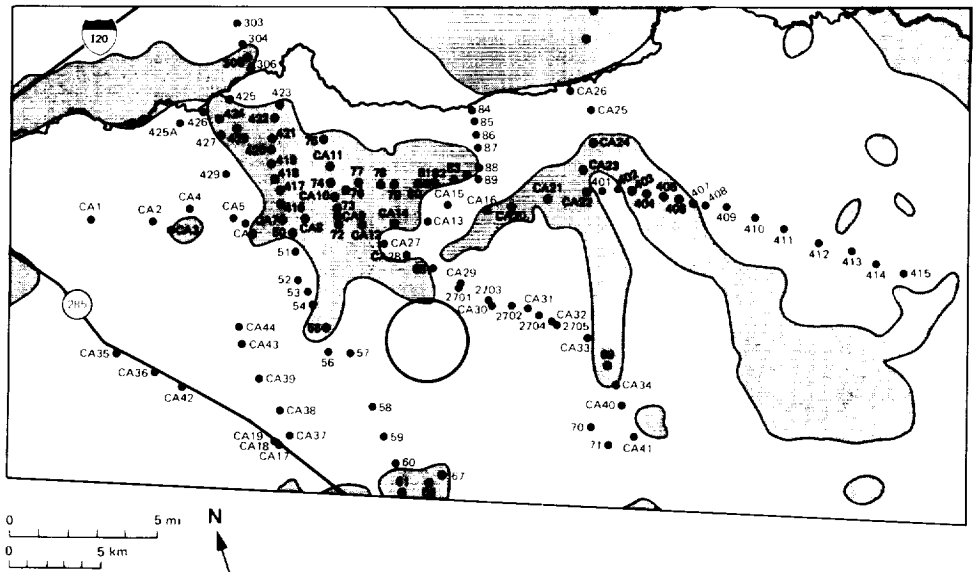

Figure 13-26. Map showing 121 of the soil geochemistry sample sites. Additional samples were obtained from 17 sites north of the area shown.

Table 13-11. Comparison of least squares analyses of Coyanosa test site soil samples using a linear model based on the important geochemical variables identified using discriminant analysis and a linear model based on soil type

Model	R^2	Prob F[a]
Geochemistry	0.184	0.002
Soil type	0.188	0.002

[a]Significance of model after adjusting for the mean.

VIII. Remote Sensing Data

A. Introduction

New aircraft remote sensing data acquired during the test site investigation included multispectral visible and near infrared (Table 13-12 and Figure 13-28), daytime/nighttime thermal infrared (Mission 383, Table 13-12), X- and L-band synthetic aperture radar (SAR), and passive microwave. Additionally, color photography was acquired during all multispectral scanner overflights. All new aircraft data were acquired by Johnson Space Center. Aircraft remote sensing data acquired for Exxon during a 1966 study of the Coyanosa area were also made available for use in the test site investigation (Appendix A). Satellite-acquired remote sensing data included Landsat Multispectral Scanner (MSS) (Table 13-13) and Seasat L-band SAR (Rev. 738, October 10, 1979). For a discussion of the characteristics of all sensors used in the test site study, refer to the Technical Appendix, Section 14.

B. Preliminary Processing

Preliminary processing of all aircraft-acquired multispectral data was carried out by JPL's Image Processing Laboratory (IPL). A list and description of IPL programs used in processing these data are included in the Technical Appendix, Section 14.

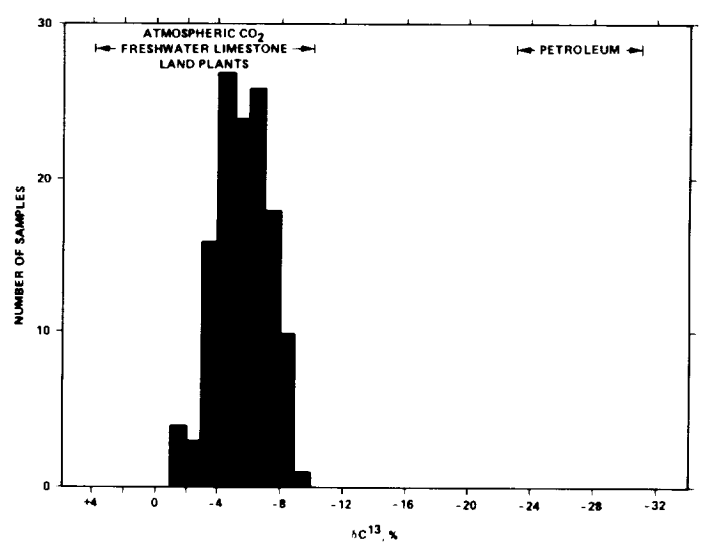

Figure 13-27. Histogram summarizing the results of carbon isotope analysis of 138 soil/rock samples. Results are consistent with a nonpetroleum carbon source. (Ranges of values for atmospheric, freshwater limestone, land plants, and petroleum sources are after Fairbridge, 1972, Figure 1, p. 134.)

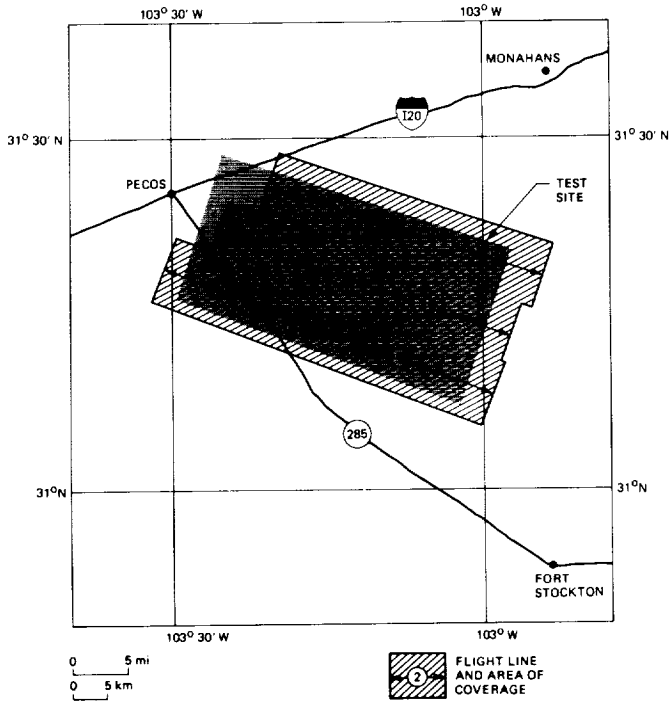

Figure 13-28. Map showing flight-line locations and areal coverage for M²S, NS-001, and color photographic aircraft data acquired at the Coyanosa test site

Table 13-12. Summary of aircraft-acquired multispectral data, Coyanosa test site

Date	Mission	Photography	Multispectral Scanner[a]
July 13, 1978	383	Color infrared	M²S[b]
October 12, 1978	390	Color infrared	NS-001[c]
June 18, 1979	403	Color infrared	NS-001

[a]Ground resolution for all data ~ 15 m; refer to the Technical Appendix, Section 14, for sensor characteristics.
[b]Modular Multispectral Scanner.
[c]NS-001 Thematic Mapper Simulator.

During the investigation, JPL retained master sets of both digital and film format data. JPL distributed copies of these data to two participating companies for distribution, on a request basis, to other participating companies. Digital data were sent to Conoco and negatives of selected IPL-produced images were sent to Phillips.

C. Analysis and Interpretation

Analysis and interpretation of the data were performed by all test site team members in common sessions or independently. Because of constraints of personnel, time, and image-processing facilities, all remote sensing data sets were not equally evaluated. Data that after initial examination demonstrated the greatest potential utility were given the greatest analytical attention. Multispectral data—Landsat MSS (Table 13-13) and NS-001 Thematic Mapper Simulator from Mission 403 (Table 13-12)—provided the most information and were therefore analyzed in the greatest detail. Landsat MSS data were commonly interpreted at a scale of 1:500,000 to 1:200,000 and NS-001 data at a scale of 1:48,000.

Table 13-13. Summary of Landsat MSS data acquired, Coyanosa test site

Date	Scene Identification	Processed By
July 30, 1972	10007-16584	JPL
October 24, 1973	14570-16565	Exxon
October 4, 1975	20255-16461	JPL
February 25, 1976	20399-16440	JPL
February 1, 1977	2741-16332	Superior & EROS

The principal purpose of multispectral image analysis was to evaluate the utility of these data in hydrocarbon exploration in a semiarid environment characterized by sparse vegetation, relatively thick soil and alluvial cover, and poorly exposed bedrock. Specifically, these data were evaluated for their utility in lithologic discrimination, geomorphic analysis, structural mapping, and surface alteration detection. The approach used in the analysis of the multispectral data is reflected in the following discussions, which include spectral characteristics of cover types, structural interpretation of images, and spectral interpretation of images.

IX. Spectral Characteristics of Cover Types

A. Introduction

Hunt and others (Hunt and Salisbury, 1970a, 1970b, 1976; Hunt et al., 1971a–1973) reported the visible and near-infrared (VNIR) laboratory spectral characteristics of most rocks and minerals. Their work demonstrated the potential utility of VNIR multispectral remote sensing methods for the discrimination and identification of geologic materials. To apply these laboratory results to the specific problems of VNIR multispectral image enhancement and interpretation at Coyanosa, a program of field and laboratory spectral measurements and mineralogical analysis was conducted in the test site area. This program emphasized the part of the VNIR spectrum sampled by the NS-001 aircraft scanner in order to evaluate the potential utility of the Landsat 4 Thematic Mapper (TM) satellite sensor, which it was designed to simulate (Table 13-14).

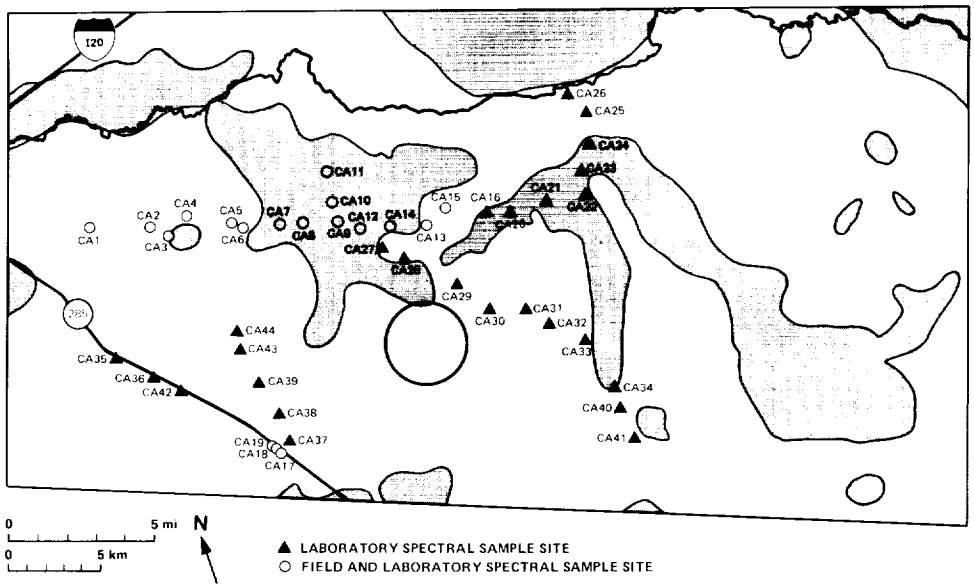

Figure 13-29. Map showing field and laboratory spectral sample sites

A total of 75 Beckman DK2A spectrophotometer laboratory spectral measurements were made for samples obtained from 45 sites; 52 field reflectance measurements were also made at 19 sites with JPL's Portable Field Reflectance Spectrometer (PFRS) (Goetz et al., 1975). Additionally, laboratory X-ray diffraction (XRD) mineralogical analyses were performed on 45 samples selected from the field and laboratory spectral sample suite. Figure 13-29 shows the locations of field and laboratory spectral and mineralogical sample sites. The site locations and materials sampled at each site were selected to include the major surface cover types of the test site area. A synthesis of the results of this investigation is presented below; only those spectra considered illustrative of significant relationships are included.

Table 13-14. A comparison of the seven bands of the Landsat 4 TM and the eight bands of the NS-001 aircraft scanner designed to simulate the TM. An equivalent to band 5 of the NS-001 is not included in the TM. NS-001 multispectral data acquired at Coyanosa had a spatial resolution of approximately 15 m. The TM has 30-m resolution.

Equivalent NS-001 Band	Wavelength, μm	Equivalent Landsat 4 TM Band
1	0.45 0.52	1
2	0.52 0.60	2
3	0.63 0.69	3
4	0.76 0.90	4
5	1.00 1.30	
6	1.55 1.75	5
7	2.08 2.35	7
8	10.4 12.5	6

B. Spectral Characteristics of Vegetation

Vegetation locally constitutes 18 to 66 percent of the ground cover at the Coyanosa test site (Table 13-7). Data acquired by multispectral scanners are significantly affected by this vegetation. An understanding of the spectral characteristics of vegetation is therefore essential for the enhancement and interpretation of the multispectral images for the test site area.

Figure 13-30 includes typical PFRS spectra for vegetation (S1, green sage; S2, brown sage) and shows the locations of the seven NS-001 VNIR bands. Five of these band locations (1, 2, 3, 4, and 6) were selected specifically for the identification of vegetation species, vigor, and density (Hovis et al., 1975, p. G-7). The significant spectral features of vegetation which occur in the seven VNIR bands of the NS-001 are discussed in detail in the Lost River, West Virginia, Petroleum Test Site Report, Section 12.

1. Equivalent NS-001 band reflectance values for vegetation. Table 13-15 shows equivalent NS-001 band reflectance values that were determined from the vegetation spectra shown in Figure 13-30. These data serve as a guide for understanding NS-001 response to vegetation.

Highest reflectance values occur in bands 4 and 5. Vigorous vegetation (S1) has significantly higher reflectance than less vigorous vegetation (S2) in bands 1 through 5. In bands 6 and 7, vigorous vegetation may exhibit lower reflectance values than less vigorous vegetation.

The highest range of reflectance values for vegetation occurs in bands 4 and 5 and the lowest range of values in bands 6 and 7.

In vegetation, reflectance values for bands 1 and 3 exhibit low correlation with bands 2 and 4; bands 6 and 7 also exhibit low correlation with bands 2 and 4. Band 1 exhibits low correlation with band 2 and high correlation with band 3. Band 2 exhibits high correlation with band 4; bands 6 and 7 are also highly correlated in vegetation. The correlation of other bands to band 5 is variable.

The comparison of the vegetation and soil spectra illustrated in Figure 13-30 demonstrates that the reflectance values in all bands (albedo) are typically higher in soil than in vegetation. Spectra for vegetation and soil exhibit the greatest disparity in bands 6 and 7 and the least disparity in bands 4 and 5. Maximum reflectance values typically occur in bands 4 and 5 for vegetation and in bands 6 or 7 for soils, although the reflectance of specific plants in bands 4 and 5 may exceed those of some soils.

2. Vegetation shadow. Shrubs (creosote and mesquite) are the dominant vegetation type at Coyanosa. A shadow is associated with each shrub, except when the shrub cover is 100 percent or when the solar elevation is vertical. The spectral effect of this vegetation-shadow component is to decrease the albedo. The significance of this effect is illustrated by the observation that a surface with 80 percent shrub cover and a 60° solar elevation (typical for the time of NS-001 acquisition at Coyanosa) will be seen by an aircraft or satellite sensor as 100 percent shrub and shrub-shadow cover.

The relative spectral contribution of plant material and plant shadow is dependent on both plant density (percent cover) and plant geometry. In the case of Coyanosa vegetation, there are two distinct plants in terms of geometry—shrubs and grasses. Because of the broader leaf area of shrubs compared to grasses (as viewed from above by a sensor), dense shrubby vegetation should have a smaller relative shadow component compared to *dense* grass cover. This should result in less distinct carotinoid, chlorophyll,

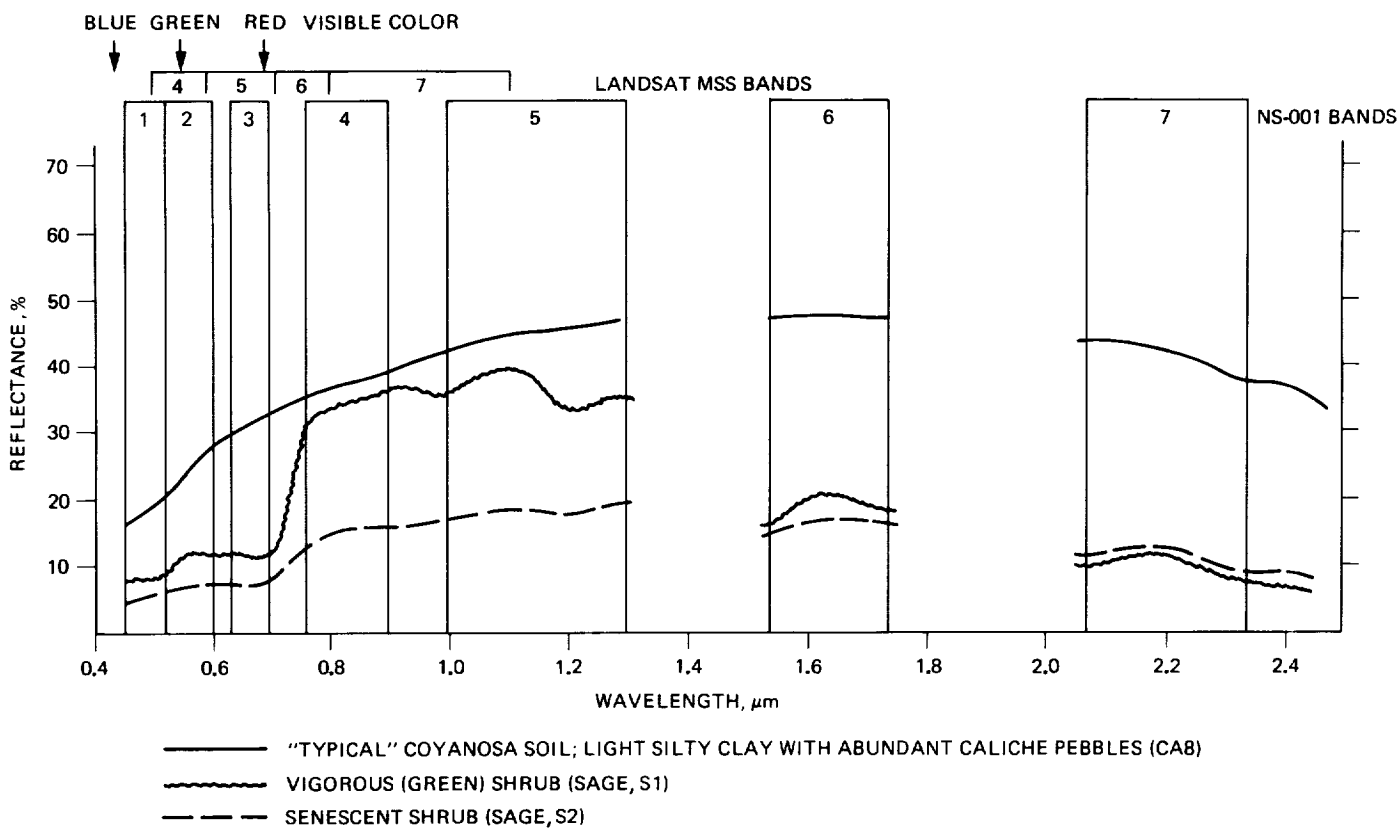

Figure 13-30. Comparison of the field spectrum of a typical Coyanosa soil to typical vegetation field spectra

Table 13-15. Summary of equivalent NS-001 band reflectance values determined from PFRS field vegetation spectra

Equivalent NS-001 Band	Reflectance Value, %, From PFRS Spectra (Sample)			
	Maximum	Minimum	Range	Mean
1	9.4 (S1)	6.6 (S2)	2.8	8.0
2	12.0 (S1)	7.0 (S2)	5.0	9.5
3	11.6 (S1)	7.8 (S2)	3.8	9.7
4	34.2 (S1)	15.4 (S2)	18.8	24.8
5	34.8 (S1)	18.2 (S2)	16.6	26.5
6	19.6 (S1)	17.4 (S2)	2.2	18.5
7	11.8 (S2)	10.8 (S1)	1.0	11.3

and leaf-water spectral features for *dense* grass cover compared to dense shrub cover.

3. Equivalent NS-001 band-ratio values for vegetation. Band-ratio images are used extensively in the evaluation of multispectral remote sensing data (Goetz and Rowan, 1981). The band reflectance values of Table 13-15 may be used to calculate equivalent NS-001 band-ratio values for vegetation. Table 13-16 summarizes the 21 equivalent NS-001 ratio values calculated for the two vegetation spectra shown in Figure 13-30. These data give insight into the response of vegetation in NS-001 VNIR band-ratio images.

Table 13-16. Summary of equivalent NS-001 band-ratio values calculated from PFRS field vegetation spectra

Equivalent NS-001 Ratio	Calculated Ratio Value From PFRS Spectra (Sample)			
	Maximum	Minimum	Range	Mean
2/1	1.3 (S1)	1.1 (S2)	0.2	1.2
3/1	1.2 (S1)	1.1 (S2)	0.1	1.2
4/1	3.6 (S1)	2.3 (S2)	1.3	3.0
5/1	3.7 (S1)	2.8 (S2)	0.9	3.3
6/1	2.6 (S2)	2.1 (S1)	0.5	2.4
7/1	1.8 (S2)	1.2 (S1)	0.6	1.5
3/2	1.1 (S2)	1.0 (S1)	0.1	1.1
4/2	2.9 (S1)	2.2 (S2)	0.7	2.6
5/2	2.9 (S1)	2.6 (S2)	0.3	2.8
6/2	2.5 (S2)	1.6 (S1)	0.9	2.1
7/2	1.7 (S2)	0.9 (S1)	0.8	1.3
4/3	3.0 (S1)	2.0 (S2)	1.0	2.5
5/3	3.0 (S1)	2.3 (S2)	0.7	2.7
6/3	2.2 (S2)	1.7 (S1)	0.5	2.0
7/3	1.5 (S2)	0.9 (S1)	0.6	1.2
5/4	1.2 (S2)	1.0 (S1)	0.2	1.1
6/4	1.1 (S2)	0.6 (S1)	0.5	0.9
7/4	0.8 (S2)	0.3 (S1)	0.5	0.6
6/5	1.0 (S2)	0.6 (S1)	0.4	0.8
7/5	0.7 (S2)	0.3 (S1)	0.4	0.5
7/6	0.7 (S2)	0.6 (S1)	0.1	0.7

Maximum band-ratio values occur in vigorous vegetation (S1) for ratios 4/1 and 5/1. Minimum values are also associated with vigorous vegetation in ratios 7/4 and 7/5. The maximum range of values occurs in ratios 4/1, 4/3, 5/1, and 6/2; the minimum range in ratios 3/1, 3/2, and 7/6.

C. Spectral Characteristics of Soil/Rock

1. Mineralogy. The laboratory spectral measurements of Hunt and others discussed above demonstrated that many minerals have diagnostic spectral absorption bands in the VNIR. These bands are caused by electronic and vibrational processes within the crystal lattice and are related to composition.

Table 13-17 lists the minerals identified in XRD analyses of 45 selected surface samples from the Coyanosa test site. This suite of 16 minerals represents the major mineral constituents of the soils and rocks exposed in the test site area. Thirteen of the minerals listed in Table 13-17 are characterized by absorption bands in the portion of the VNIR spectrum sensed by the NS-001 scanner. Figure 13-31 is a composite diagrammatic laboratory spectrum showing the locations and relative depths of absorption bands identified in 75 DK2A laboratory spectra. The locations of the seven NS-001 VNIR bands are also shown as a guide for the prediction of the response of this sensor to the minerals listed in Table 13-17.

For the samples analyzed at Coyanosa, there are only five ions, radicals, and molecules that cause the absorption features shown in Figure 13-31: Fe^{+2}, Fe^{+3}, HOH, OH, and CO_3^{-2}. A review of the chemical formulas of minerals

Table 13-17. Mineralogy of Coyanosa soil/rock determined by XRD analysis of 45 representative surface samples

Mineral	Formula
Biotite	$K(MgFe)_3(AlSi_3O_{10})(OH)_2$
Calcite	$CaCO_3$
Clinoptilolite (?)	$(Na, K, Ca)_{2-3}Al_3(Al, Si)_2Si_{13}O_{36} \cdot 12H_2O$
Goethite	$FeO(OH)$
Gypsum	$Ca(SO_4) \cdot 2H_2O$
Hematite	Fe_2O_3
Hornblende	$Ca_4Na_2(MgFe)_8(AlFe)_2(Al_4Si_{12}O_{44})(OH,F)_4$
Illite	$K(Al_4Fe_4Mg_4Mg_6)(AlSi_7O_{20})(OH)_4$
Kaolinite	$Al_2(Si_2O_5)(OH)_4$
Microcline[a]	$K(AlSi_3O_8)$
Magnetite (?)	$FeFe_2O_4$
Montmorillonite	$X(AlMg)_2(AlSi)_4O_{10}(OH)_2$
Muscovite	$KAl_2(AlSi_3O_{10})(OH)_2$
Plagioclase[a]	$(CaNa)(AlSi)_4O_8$
Talc (?)	$Mg_3(Si_4O_{10})(OH)_2$
Quartz[a]	SiO_2

[a]Mineral without absorption features in TM/NS-001 bands.

listed in Table 13-17 and consideration of the multimineralic nature of Coyanosa soil and rock demonstrate that unique mineral identification is impossible using spectral reflectance data from the seven NS-001 VNIR channels *alone*. Furthermore, a comparison of the depths and locations of absorption bands shown in Figure 13-31 to the absorption features associated with vegetation shown in Figure 13-30 demonstrates the significant potential for confusion in the analysis of the spectra of mineral and vegetation mixtures. This observation is consistent with the conclusion of Siegal and Goetz (1977, p. 195) in their modeling of the spectral response of soil/vegetation mixtures: "Naturally occurring vegetation significantly masks and alters the spectral response of earth materials. The significance of vegetative cover depends primarily on the amount and type of vegetation and the spectral reflectance of the ground."

2. Soil/rock texture (grain size). Variations in soil or rock texture (grain size) may induce significant variations in the spectral response of soils and rocks. Grain-size-induced variations in visible spectral response have long been recognized by the hand-specimen mineralogist. Finely powdered, nonopaque material tends to be lighter colored (has higher albedo in the visible spectrum) than coarse material. This visible albedo effect has long been utilized in the so-called "streak test" used in hand-specimen mineralogy. This albedo increase with decreasing particle size was reported by Adams and Filice (1967). They noted that there are also wavelength-dependent spectral changes associated with the decrease in particle size below 0.5 mm (medium sand). They attribute such wavelength-dependent, grain-size-induced changes to the relative contribution of the diffuse and specular component of reflected energy.

Fine particulate materials (<20 μm in diameter, i.e., fine silt and clay) form reflecting surfaces with a larger specular component when compared to coarser materials. Apparently the Rayleigh criterion for a smooth surface approaches satisfaction with such particle diameters in the higher wavelengths of the VNIR (Beckman and Spizzichino, 1963, p. 9). This results in less diffuse energy (the absorbed component) being available for interaction within the reflecting material. The result is a decrease in the net amount of

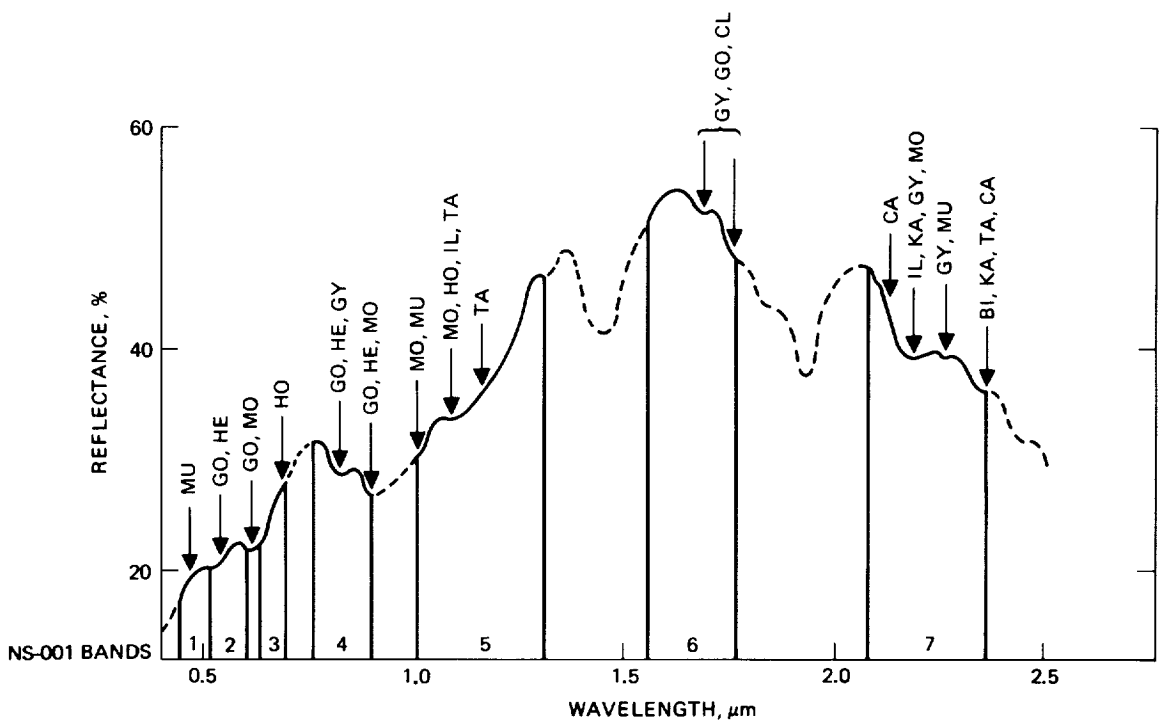

MU	MUSCOVITE	HO	HORNBLENDE	CL	CLAY
GO	GOETHITE	GY	GYPSUM	CA	CALCITE
HE	HEMATITE	IL	ILLITE	KA	KAOLINITE
MO	MONTMORILLONITE	TA	TALC	BI	BIOTITE

Figure 13-31. Composite diagrammatic laboratory spectrum illustrating major mineral absorption bands affecting NS-001 data for the Coyanosa test site. Absorption feature identifications are after Hunt and Salisbury (1970a, 1970b, 1976) and Hunt et al. (1971a–1973).

incident energy available for absorption and a decrease in the depth of absorption bands characteristic of the material.

The practical significance of these relationships is illustrated in Figure 13-32. Sample CA13, a light-tan, silty clay soil from the central portion of the test site area, was found to be primarily calcite, based on XRD and acid digestion analyses. The laboratory and field spectra for this sample lacked the characteristic CO_3^{-2} absorption band near 2.3 μm. Sieve grain-size analysis revealed that this sample was composed of particles <74 μm in diameter (fine silt and clay). Also shown in Figure 13-32 are the spectra of a calcite crystal and a <74-μm powder obtained from grinding the crystal. Comparison of these curves reveals a loss of the diagnostic absorption band, which is attributed to the decrease in grain size. According to Hunt and Salisbury (1970b, p. 26), this grain-size-dependent variation in absorption band depth is most significant in materials, such as calcite, which have high refractive indices.

3. Equivalent NS-001 band reflectance values obtained from PFRS soil/rock spectra. To evaluate the response of the NS-001 scanner to soil and rocks exposed at the Coyanosa test site, PFRS field spectral data were used to determine equivalent NS-001 band reflectance values. This information, in conjunction with laboratory spectral data and mineralogical data, may be used as a guide for the design and interpretation of NS-001 images.

Equivalent NS-001 band reflectance values were determined from each of the 52 PFRS spectra. This was accomplished by visually estimating the average interval reflectance for each of the seven NS-001 VNIR bands in each of the 52 PFRS spectra. These data were tabulated and used to determine band reflectance maxima and minima, band-ratio maxima and minima, ranges, means, and standard deviations. Table 13-18 and Figure 13-33 summarize the raw band equivalent PFRS reflectance values from all field spectra.

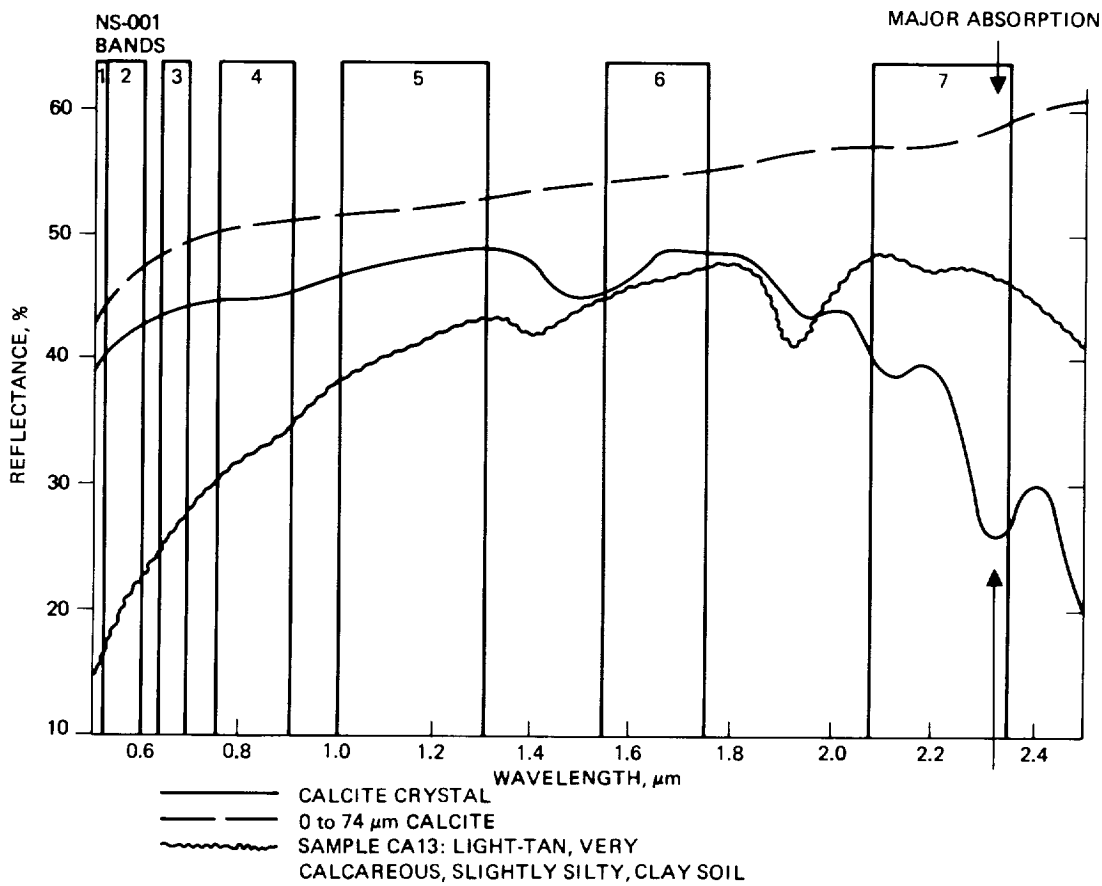

Figure 13-32. Three laboratory spectra illustrating the loss of the calcite absorption band near 2.3 μm when grain size is decreased to <74 μm (fine silt and clay)

Table 13-18. Summary of equivalent NS-001 band reflectance values determined from 52 soil/rock PFRS field spectra measured at 19 sites, Coyanosa test site

Equivalent NS-001 Band	Reflectance Value, %, From PFRS Spectra (Sample)				
	Maximum	Minimum	Range	Mean	Standard Deviation
1	29.8 (CA2)	9.4 (CA19)	20.4	17.7	4.0
2	36.0 (CA2)	13.0 (CA19)	23.0	23.9	4.6
3	43.4 (CA2)	16.2 (CA19)	27.2	30.4	5.5
4	51.4 (CA2)	21.6 (CA19)	29.8	36.6	5.6
5	59.8 (CA2)	30.0 (CA19)	29.8	44.7	5.5
6	60.0 (CA18)	37.0 (CA19)	23.0	47.5	4.8
7	49.4 (CA2)	30.2 (CA19)	19.2	40.3	4.1

Maximum reflectance values in bands 1, 2, 3, 4, 5, and 7 occur in the spectrum of sample CA2, a light-tan, gypsiferous, calcareous, and kaolinitic soil located on a playa. Maximum reflectance for band 6 occurs in the spectrum of sample CA18, a goethitic, kaolinitic limestone. A comparison of these maximum reflectance values to those of vegetation (Table 13-15) demonstrates consistently higher values for soil/rock.

Minimum reflectance values in all bands occur in the spectrum of sample CA19, a gray, sandy, kaolinitic and slightly goethitic limestone. A comparison of these minimum reflectance values to those for vegetation (Table 13-15) demonstrates consistently higher values for soil/rock. In fact, in bands 1, 2, 3, 6, and 7, the minimum reflectance for soil/rock exceeds the maximum reflectance for vegetation.

4. Equivalent NS-001 band-ratio values for soil/rock. The same procedure used to determine equivalent NS-001 band-ratio values for vegetation was used to establish equivalent band-ratio values for soil/rock.

Table 13-19 summarizes the 21 equivalent NS-001 ratio values determined from the 52 soil/rock PFRS spectral measurements at Coyanosa. Figures 13-34 and 13-35 show those PFRS spectra that exhibit maximum and minimum ratio values. This information, in conjunction with field descriptions and laboratory spectral and mineralogical data, may be used as a guide for the optimal enhancement and interpretation of NS-001 ratio images for soil/rock discrimination in the Coyanosa test site.

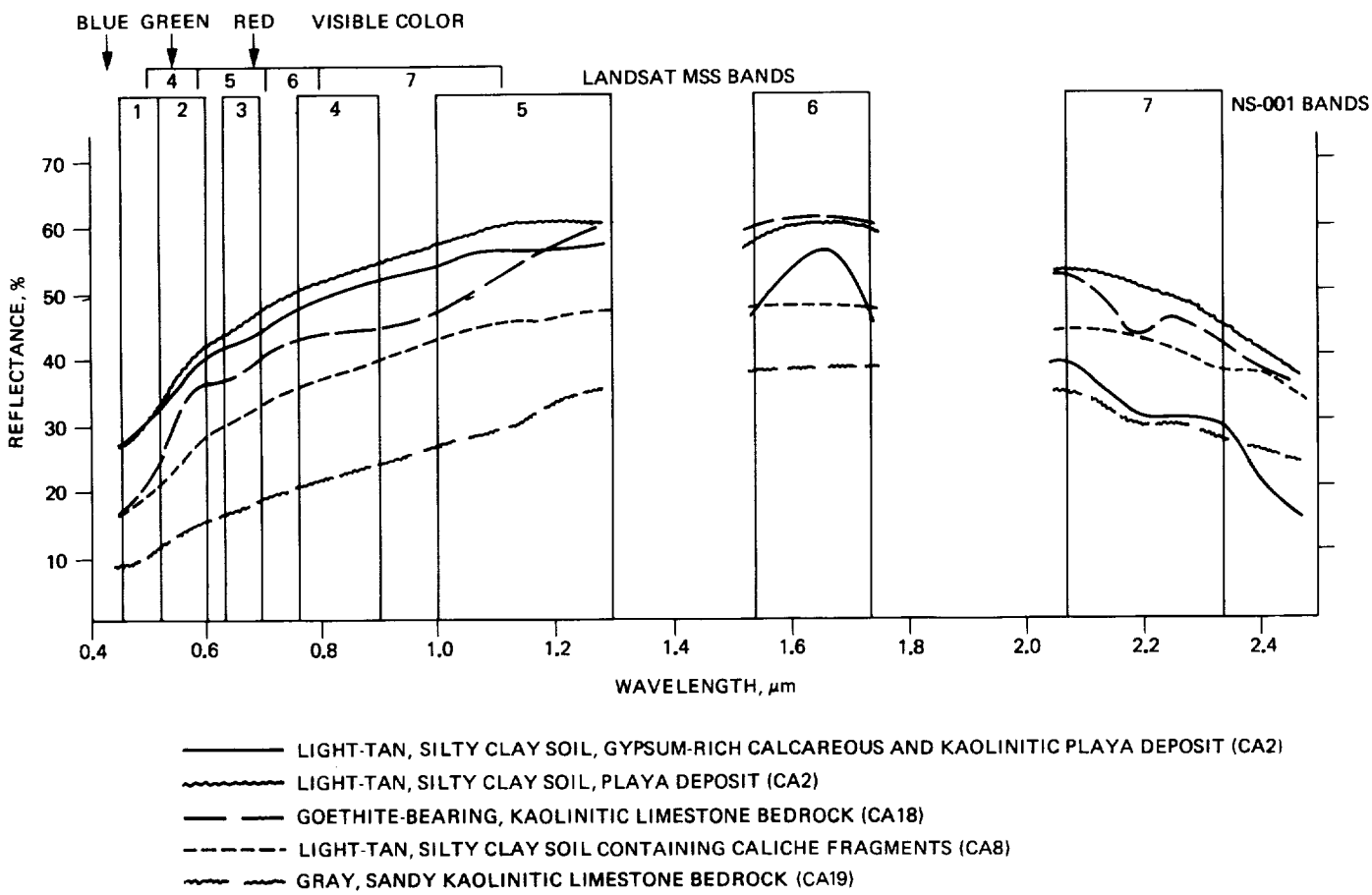

Figure 13-33. PFRS soil/rock field spectra exhibiting maximum, minimum, and mean equivalent NS-001 band reflectance (see Table 13-18)

Table 13-19. Summary of equivalent NS-001 band-ratio values calculated from 52 soil/rock PFRS field spectra measured at 19 sites, Coyanosa test site

Equivalent NS-001 Ratio	Calculated Ratio Value From PFRS Spectra (Sample)				
	Maximum	Minimum	Range	Mean	Standard Deviation
2/1	1.7 (CA18)	1.2 (CA2)	0.5	1.4	0.1
3/1	2.3 (CA11)	1.4 (CA2)	0.9	1.7	0.2
4/1	2.8 (CA11)	1.7 (CA2)	1.1	2.1	0.2
5/1	3.6 (CA18)	1.9 (CA2)	1.7	2.6	0.4
6/1	4.1 (CA18)	1.8 (CA2)	2.3	2.8	0.5
7/1	3.5 (CA11)	1.0 (CA2)	2.5	2.4	0.4
3/2[a]	1.5 (CA11)	1.2 (CA2)	0.3	1.3	0.1
4/2	1.9 (CA11)	1.3 (CA6)	0.6	1.5	0.1
5/2	2.3 (CA11, CA19)	1.5 (CA2)	0.8	1.9	0.2
6/2	2.9 (CA19)	1.5 (CA2)	1.4	2.0	0.3
7/2	2.4 (CA19)	0.8 (CA2)	1.6	1.7	0.3
4/3[a]	1.5 (CA7)	1.1 (CA6)	0.4	1.2	0.1
5/3	1.9 (CA7, CA19)	1.3 (CA4)	0.6	1.5	0.1
6/3	2.3 (CA19)	1.3 (CA2)	1.0	1.6	0.2
7/3	1.9 (CA19)	0.7 (CA2)	1.2	1.4	0.2
5/4[a]	1.5 (CA18)	1.1 (CA2)	0.4	1.2	0.1
6/4[a]	1.9 (CA18)	1.1 (CA2)	0.8	1.3	0.2
7/4	1.4 (CA19)	0.6 (CA2)	0.8	1.1	0.1
6/5[a]	1.3 (CA18)	1.0 (CA2)	0.3	1.1	0.1
7/5[a]	1.0 (CA19)	0.6 (CA2)	0.4	0.9	0.1
7/6[a]	0.9 (CA11)	0.6 (CA2)	0.3	0.9	0.1

[a] Not considered "significant"; range of values not more than one standard deviation above and below the mean.

A maximum ratio value of 4.1 was obtained for band-ratio 6/1 in sample CA18 (goethitic, kaolinitic limestone); a minimum ratio value of 0.6 was obtained for 7/4, 7/5, and 7/6 in sample CA2 (light-tan, kaolinitic, calcareous, silty, gypsiferous clay soil). A maximum range of ratio values occurs in 7/1; a minimum range of ratio values occurs in 6/5 and 7/6. Of the 52 soil/rock PFRS spectra measured at 19 sites, only four exhibit all the maximum ratio values, and three exhibit all the minimum values.

Table 13-19 shows that both the maximum and minimum values for several ratios are represented by the same sample pair, e.g., samples CA18 and CA2 for ratios 2/1, 5/1, 6/1, 5/4, 6/4, and 6/5. Such ratios are considered redundant. For ratios showing the same sample pair for maximum–minimum values, that ratio exhibiting the largest range of values is considered significant for soil/rock-type discrimination, and only those ratios with maximum or minimum values that differ from the mean by more than one standard deviation are considered most significant. On the basis of these two measures of significance and an evaluation of field descriptions and XRD mineralogical analyses of PFRS samples, the following observations specific to the Coyanosa test site have been made:

(1) Band-ratios 3/2, 4/3, 5/4, 6/4, 6/5, 7/5, and 7/6 are not considered significant for soil/rock-type discrimination.

(2) Band-ratios 2/1, 5/1, and 6/1 are equivalent; 5/1 values are most significant because of the larger range of values. High values occur in goethitic, kaolinitic limestone (CA18); low values in quartz-poor, gypsiferous clay (CA2).

(3) Band-ratios 3/1, 4/1, and 7/1 are equivalent; 7/1 values are most significant because of the larger range of values. High values occur in light reddish-brown, gravelly, calcareous, quartz sands (CA11); low values in quartz-poor, gypsiferous clay (CA2).

(4) Band-ratios 6/2, 7/2, 6/3, 7/3, and 7/4 are equivalent; 7/2 values are most significant because of the larger range of values. High values occur in light-tan/gray, silty, calcareous, kaolinitic, quartz sands that are slightly goethitic (CA19); low values in quartz-poor, gypsiferous clay (CA2).

(5) Band-ratio 4/2 is maximum in light reddish-brown, gravelly, calcareous, quartz sand (CA11); minimum in light-tan, sandy, calcareous, silty clay (CA6).

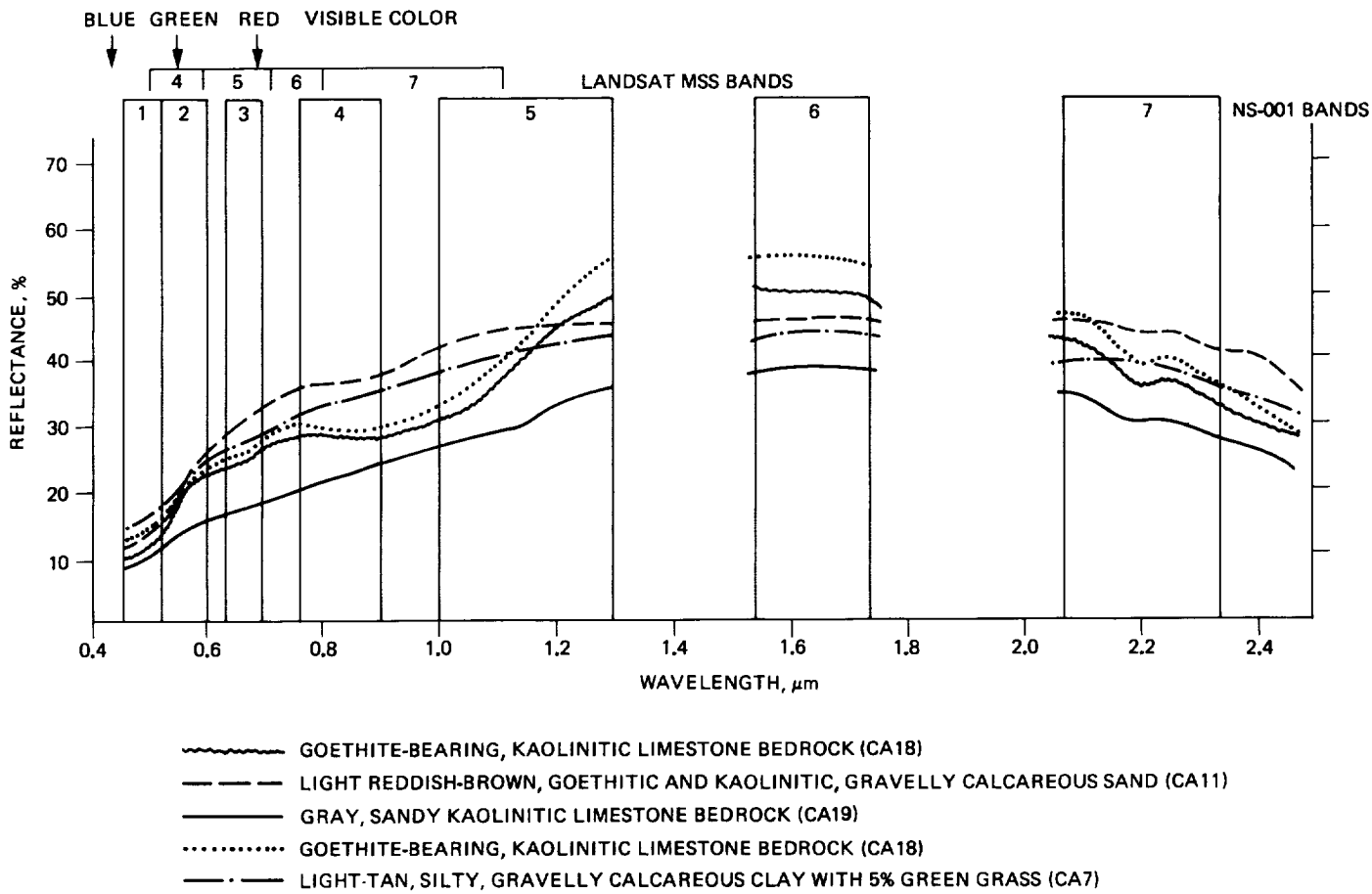

Figure 13-34. PFRS soil/rock field spectra exhibiting the maximum equivalent NS-001 VNIR band-ratio values (see Table 13-19)

(6) Band-ratio 5/2 is maximum in light-tan to light reddish-brown, gravelly, calcareous, silty quartz sands that are slightly goethitic (CA11, CA19); minimum in quartz-poor, gypsiferous clay (CA2).

(7) Band-ratio 5/3 is maximum in light-tan/gray, silty, calcareous, kaolinitic, quartz sands that are slightly goethitic (CA19, CA7); minimum in light-gray, calcareous, gravelly quartz sand (CA4).

D. Combined Soil/Rock and Vegetation NS-001 Band-Ratio Values

Because vegetation cover in the Coyanosa test site averages approximately 30 percent, the spectral characteristics of individual pixel areas sensed by the NS-001 are the result of a mixture of both soil/rock and vegetation spectral components. To enhance and evaluate NS-001 ratio images, the effects of this spectral mixing must be considered. Insight into this mixing problem may be gained by comparing the range of equivalent PFRS ratio values for the two end-member spectral phases.

Table 13-20 summarizes the combined results of the soil/rock and vegetation field spectra ratio analyses. An evaluation of these data gives insight into potential effects of this mixing on NS-001 data acquired at Coyanosa:

(1) Maximum vegetation ratio values are higher than soil/rock maxima for 4/1, 5/1/ 4/2, 5/2, 4/3, and 5/3. An increase in vegetation cover should therefore result in an increase in these ratio values

(2) Minimum vegetation ratio values are lower than soil/rock minima for 2/1, 3/1, 3/2, 5/4, 6/4, 7/4, 6/5, 7/5, and 7/6. An increase in vegetation cover should therefore result in a decrease in these ratio values.

(3) Ratios for which both maximum and minimum values occur in soil/rock spectra (i.e., the range of vegetation values is intermediate) are 6/1, 7/1, 6/2, 7/2, 6/3, and 7/3. Based on the evaluation of soil/rock ratio redundance of these six ratios, only three are considered nonredundant: 6/1, 7/1, and 7/2.

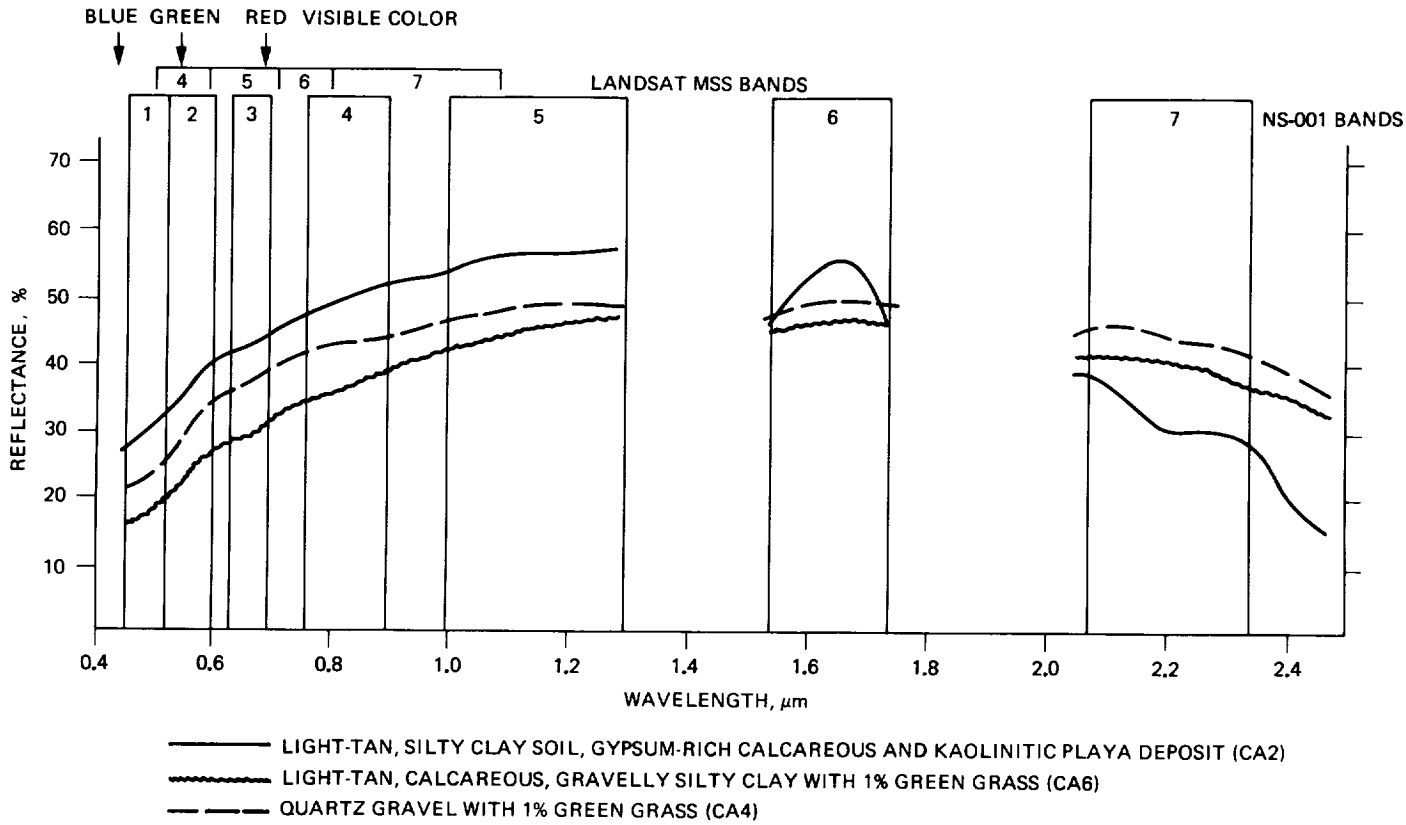

Figure 13-35. PFRS soil/rock field spectra exhibiting the minimum equivalent NS-001 VNIR band-ratio values (see Table 13-19)

(4) No ratios have both maximum and minimum values in vegetation spectra.

X. Sensor Spectral Data

A. Introduction

The analysis of the spectral characteristics of Coyanosa cover types was based on 127 field and laboratory spectral measurements at over 60 sites. NS-001 multispectral data acquired in each of two overflights include spectral measurements at over 13,500,000 sites (15-m picture elements, or pixels). Landsat MSS data acquired in each of five scenes used in the test site study include spectral measurements at over 1,000,000 sites (80-m pixels). Clearly, any analysis of the spectral characteristics of the Coyanosa test site should include an evaluation of the image data themselves. The following discussion of multispectral data from one NS-001 test site overflight and one Landsat MSS scene illustrates an approach to evaluating the spectral information contained in these scanner data.

B. NS-001 Data, Mission 403, Line 3

Table 13-21 shows the interband correlation for the six operative NS-001 VNIR bands for data acquired on Mission 403, line 3. This matrix results from the analysis of over 4,500,000 pixels. NS-001 interband correlation is extremely high for the Coyanosa test site area; the test site is spectrally homogeneous in the bands sampled by the scanner. By inference, the spatial variability of Coyanosa cover is very low. The lowest interband correlation is between bands 3 and 4, indicating that the most significant contribution to the variance of these NS-001 data is due to vegetation.

Further insight into the nature of these data is provided by principal components analysis. For a complete discussion of this multivariate statistical technique, refer to Davis (1973).

Table 13-22 summarizes the six operative NS-001 VNIR band eigenvectors for the first three principal components (PCs). These eigenvectors are rather low, reflecting the high

Table 13-20. Summary of equivalent NS-001 band-ratio values including both soil/rock (Table 13-19) and vegetation (Table 13-16) PFRS field spectra

Equivalent NS-001 Ratio	Calculated Ratio Value From PFRS Spectra (Sample)		
	Maximum[a]	Minimum[a]	Range
2/1	1.7 (CA18)	1.1 (S1)	0.6
3/1	2.3 (CA11)	1.1 (S)	1.2
4/1	3.6 (S1)	1.7 (CA2)	1.9
5/1	3.7 (S1)	1.9 (CA2)	1.8
6/1	4.1 (CA18)	1.8 (CA2)	2.3
7/1	3.5 (CA11)	1.0 (CA2)	2.5
3/2	1.5 (CA11)	1.0 (S1)	0.5
4/2	2.9 (S)	1.3 (CA6)	1.6
5/2	2.9 (S)	1.5 (CA2)	1.4
6/2	2.9 (CA19)	1.5 (CA2)	1.4
7/2	2.4 (CA19)	0.8 (CA2)	1.6
4/3	3.0 (S)	1.1 (CA6)	1.9
5/3	3.0 (S)	1.3 (CA4)	1.7
6/3	2.3 (CA19)	1.3 (CA2)	1.0
7/3	1.9 (CA19)	0.7 (CA2)	1.2
5/4	1.5 (CA18)	1.0 (S1)	0.5
6/4	1.9 (CA18)	0.6 (S)	1.3
7/4	1.4 (CA19)	0.3 (S1)	1.1
6/5	1.3 (CA18)	0.6 (S)	0.7
7/5	1.0 (CA19)	0.3 (S1)	0.7
7/6	0.9 (CA11)	0.6 (CA2, S1)	0.3

[a] "S" designation indicates that both S1 and S2 are higher or lower than soil/rock maximum or minimum.

Table 13-21. Correlation matrix for the six NS-001 VNIR band data (band 5 inoperative) acquired on Mission 403, line 3, June 18, 1979, Coyanosa test site

NS-001 Band	1	2	3	4	6	7
1	1.000					
2	0.995	1.000				
3	0.980	0.992	1.000			
4	0.983	0.986	0.977	1.000		
6	0.987	0.989	0.987	0.983	1.000	
7	0.980	0.985	0.988	0.978	0.997	1.000

Table 13-22. NS-001 Mission 403, line 3, June 18, 1979, PC analysis: Eigenvectors of six VNIR bands (band 5 inoperative) for first three PCs

PC	NS-001 Band					
	1	2	3	4	6	7
V1	0.2840	0.4114	0.5111	0.3970	0.3815	0.4309
V2	0.0601	0.1507	0.0174	0.7331	−0.3981	−0.5266
V3	−0.5125	−0.5328	−0.1403	0.5189	0.2188	0.3413

interband correlation already noted. Understanding the physical meaning of these PCs is aided by interpreting the "spectra" shown in Figure 13-36.

The first PC is approximately equally and positively weighted for all bands. It may be considered an approximation of the "mean" radiance in all six bands or a measure of albedo variance of the Coyanosa scene. Ninety-nine percent of the variance of the NS-001 data is explained by this first PC. Apparently, most of the spectral variability of Coyanosa cover may be attributed solely to variation in albedo. This observation is consistent with the high interband correlation shown in Table 13-21. The greatest variation in albedo for surface materials at Coyanosa is associated with differences in the relative cover of soil/rock (high albedo) and vegetation (low albedo). An increase in the first PC is therefore largely a measure of an increase in the contribution of the soil/rock spectral component or a decrease in the vegetation spectral component.

The second PC is most positively weighted on band 4. Low weights are associated with bands 1, 2, and 3 and negative weights with bands 6 and 7. This PC will vary in a manner similar to band ratios having band 4 in the numerator and bands 1, 2, 3, 6, or 7 in the denominator. These relationships and the overall form of the V2 spectrum (compare to S1, Figure 13-30) demonstrate that this component is a measure of the albedo (V1) independent contribution of vegetation spectral variability to the variance of these scanner data.

The third PC is positively weighted on bands 4, 6, and 7 and negatively weighted on bands 1, 2, and 3. This PC will vary in a manner similar to ratios having bands 4, 6, and 7 in the numerator and bands 1, 2, and 3 in the denominator. These relationships and the overall form of the V3 spectrum (compare to Figure 13-31) support the interpretation that this component is a measure of the contribution of iron-oxide-bearing soil/rocks to Coyanosa NS-001 data variance.

C. Landsat MSS Data, October 4, 1975

Tables 13-23 and 13-24 and Figure 13-37 illustrate the results of a similar analysis of Landsat MSS data. Interband correlation is high, although somewhat lower than the NS-001 data. This lower interband correlation may be considered an indication of more information (variance) in these Landsat MSS data. Alternately, correlation differences may only reflect the difference in acquisition dates (June 18, 1979 for the NS-001 data and October 4, 1975 for the Landsat MSS data). As with the NS-001 data, Landsat MSS PC 1 is interpreted as a measure of albedo; PC 2, vegetation; and PC 3, iron-oxide-bearing soil/rock.

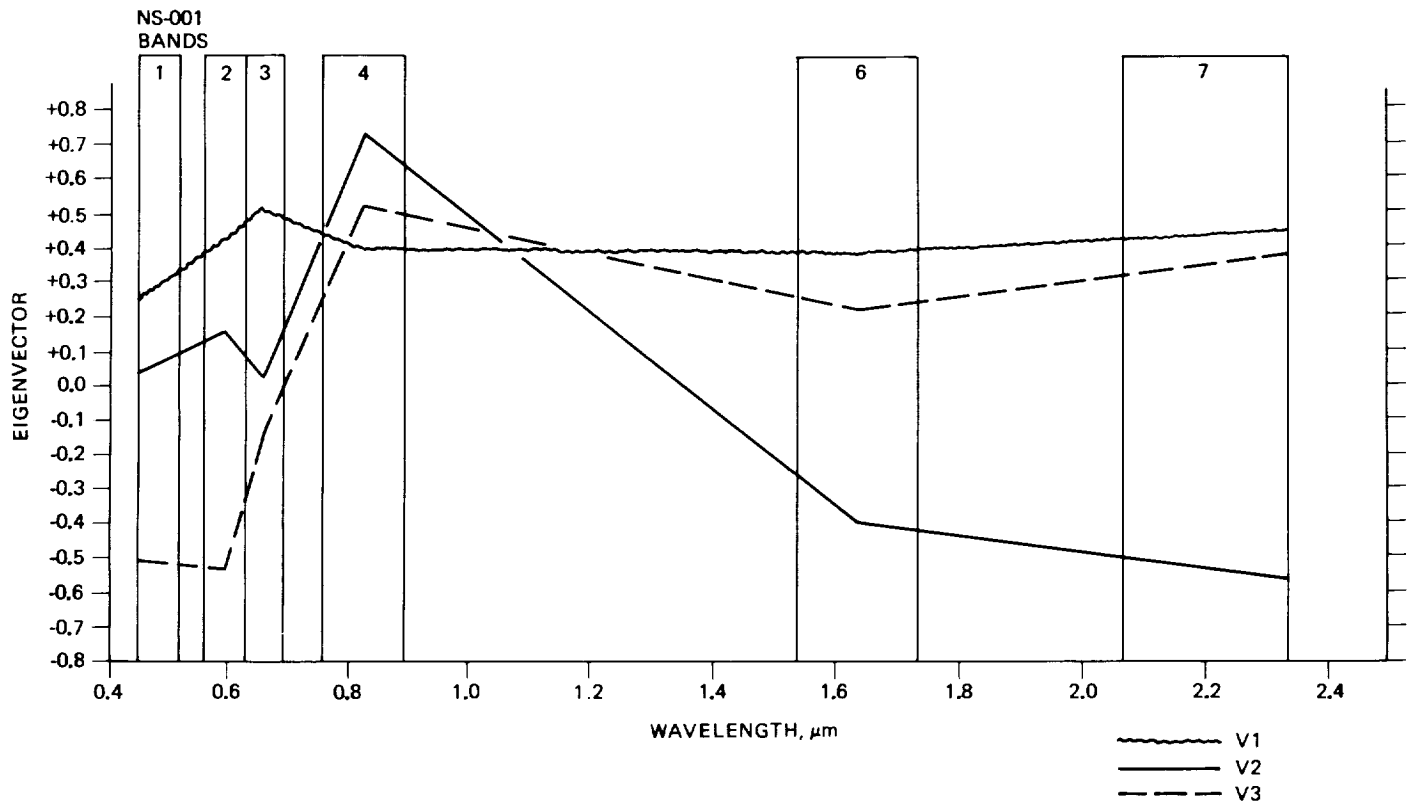

Figure 13-36. PC spectra for NS-001, Mission 403, line 3, June 18, 1979. Spectra were constructed by connecting eigenvector values for each PC (Table 13-22) plotted at band centers.

Table 13-23. Correlation matrix for Landsat MSS data acquired October 4, 1975, Coyanosa test site

MSS Band	4	5	6	7
4	1.000			
5	0.946	1.000		
6	0.826	0.861	1.000	
7	0.718	0.738	0.948	1.000

Table 13-24. Landsat MSS principal components analysis for data acquired October 4, 1975[a]

Variance Explained, %	PC	MSS Band			
		4	5	6	7
89	V1	0.343	0.588	0.579	0.449
9	V2	-0.366	-0.604	0.357	0.611
1	V3	0.799	-0.365	-0.352	0.323

[a] Eigenvectors for the four bands are shown for the first three PCs. The fourth PC explains much less than 1 percent of the variance.

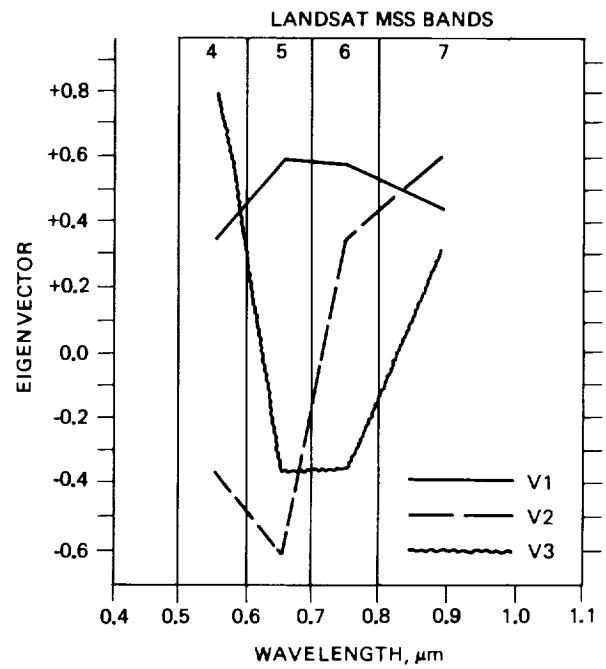

Figure 13-37. PC spectra for Landsat MSS data, October 4, 1975. Spectra were constructed by connecting eigenvector values for each PC (Table 13-24) plotted at band centers.

XI. Geological Interpretation of Landsat MSS and NS-001 Multispectral Data

A. Image Interpretation

1. Introduction. The purpose of image analysis in the test site investigation was (1) to evaluate the geological significance of image features in relation to our current understanding of the surface and subsurface geology, and (2) to establish whether any relatively unique and mappable image features or combination of features occurring at the test site can be used as exploration leads or clues to subsurface accumulations of oil and gas. An understanding of the subsurface structural and stratigraphic controls of an accumulation as well as knowledge of surface geology, soils, vegetation, spectral characteristics of cover materials, and geomorphic processes active in a region are vital to the evaluation of features mapped on images. Wherever possible, these ancillary data were considered in image interpretation.

There were two primary objectives in image analysis:

(1) Initial interpretation of images for any unusual structural, geomorphic, and/or spectral conditions that may coincide geographically with known subsurface hydrocarbon occurrences.

(2) Evaluation of any potentially anomalous structural and/or spectral features from all available surface and subsurface geological and spectral data. Those features that could not be readily explained were selected for more detailed investigation.

2. Methods of investigation. Standard photogeologic techniques were used in the image interpretation and analysis. Typically, higher altitude or smaller scale image data were interpreted first. This approach allowed the interpreter to place the test site in a regional geologic and spectral framework. The regional perspective permits the rapid assessment of the structural and spectral norm against which unusual conditions may be recognized. Because the structural and spectral interpretations were done separately, the results of each will also be discussed separately.

B. Structural Interpretation

1. Introduction. The primary objective of the image structural interpretation was to identify surface geologic structures and/or geomorphic conditions that could be indicative of favorable subsurface structures which are necessary for the entrapment and accumulation of oil and gas. These subsurface structures include folds, horst blocks, and zones of increased porosity and permeability due to fracturing and faulting.

2. Scientific rationale. The principles of geomorphology apply to all scales of image data the way the photogeologic principles of opposing dips, rule of "Vs," stratigraphic offsets, etc., apply to the interpretation of surface structures (folds, dip direction, faults, etc.) on all image scales. The primary effect of changes in scale of image data is a change in the scale of the structure or implied structure recognized. Analysis of small-scale images such as Landsat should reveal the surface effects of large deep-seated structures, whereas analysis of large-scale images tends to reveal smaller and shallower structures, and possibly only a portion of larger deep-seated structures.

Due to the scarcity and erratic distribution of outcrops in the test site area, the utility of standard photogeologic interpretation of structure was very limited. Most structural information was therefore obtained from a geomorphic interpretation of images. Careful analysis of drainage, textural, and erosional patterns can lead to an understanding of the important structural elements in the test site. Geomorphic analysis is especially effective in an area such as the Coyanosa test site, where subcrop dips are gentle and subsurface geology is masked by soil, colluvium, and pediment gravel cover. The main premise in this approach to image interpretation is that the subsurface structure, although covered, is reflected at the surface in drainage, soil, and vegetation patterns by the mechanisms of:

(1) Differential compaction of strata

(2) Draping of strata

(3) Differential erosion of soil units

(4) Minor near-surface readjustments on preexisting faults or uplifts

(5) Faults and fracture zones affecting permeability in near-surface units which in turn affect local soil moisture conditions and vegetation distribution

Surface indications (geomorphic evidence) of possible subsurface structure were mapped as follows:

(1) Indications of fractures (faults, fault zones, and joint systems):

  (a) Anomalously straight stream courses and segments

  (b) Parallel and *en echelon* drainage patterns

  (c) Angular drainage patterns, right-angle bends, and barbed tributaries (linear tributaries entering the main stream against regional slope)

  (d) Alignment of linear tributary segments across streams or ridges

(e) Linear topographic scarps

(f) Tonal or vegetation alignments

(g) Alignment of drainage disruptions, i.e., right-angle bends in tributaries or main streams across several stream courses

(2) Indications of anticlinal or domal uplifts:

(a) Arcuate drainage patterns suggestive of folds

(b) Double drainage deflections (opposing arcuate patterns) by two streams, suggestive of structural highs

3. Results of structural interpretation

a. Structural interpretation – regional. Color infrared Landsat images, 20255-16461 (October 1975, 1:500,000) processed by JPL (Figure 13-38) and 2741-16332 (February 1977, 1:300,000) processed by Superior Oil Company (Figure 13-39), were interpreted for both regional and local structure. Plate 13-1 includes a composite interpretation of both of these images. An EROS-processed EDIES Landsat image (February 1977) was also interpreted but added very little additional information. The JPL and Superior Oil images provided 99 percent of the regional structural information.

The generalized regional structural interpretation (Figure 13-40) illustrates the relationship of the test site to the major structural elements of the area. The region north and east of the Pecos River appears relatively undisturbed structurally. The east edge of the Central Basin Platform and the west margin of the Midland Basin are expressed by a broad tonal change (darker tones in Midland Basin) and a subtle topographic scarp along which light-toned sand dune fields are aligned. A major change in surface units, and possibly structure across the Pecos River to the west and south, is indicated by dramatic texture, tone, and drainage pattern differences on either side of the river.

The regional structural interpretation (Figure 13-41 and Plate 13-1) shows two well-developed NNW lineament systems south of the test site. The easternmost system is expressed as long parallel to subparallel anomalously straight drainage segments (Coyanosa Draw) entering the test site in the vicinity of the Coyanosa field. It continues northward and merges with a NW-trending (Hackberry Draw) lineament system. The western lineament system is less well defined to the south of the test site, but becomes well defined by the long straight segment of Barrilla Draw, where it traverses the southern border of the test site. The region around the test site is also characterized by several locally well-developed NE lineament trends composed of a fairly well-defined parallel set southwest of the test site and by an *en echelon* pattern expressed in the southern extension of Hackberry Draw and its tributaries.

The parallel relationship of the NNW and NW lineaments to the trend of the Central Basin Platform suggests that these lineaments are the surface expression of deep-seated faults and zones of weakness associated with basin tectonics and the development of the Central Basin Platform. The northwest Hackberry Draw *en echelon* system parallels one of the major structural features of the region as mapped in the subsurface by Fok (1972), Figure 13-14.

Regionally, the area south and west of the Pecos River contains an unusually large number of curvilinear drainages, drainage deflections, arcuate scarps, and oval to circular tonal and outcrop patterns. Comparison of these features with producing areas (Figure 13-41b) shows a fair correlation of these features with some structurally controlled oil and gas fields. Only those fields that correlate with a geomorphic feature are shown in Figure 13-41. If all of the oil and gas fields in this prolific region were plotted, they would obliterate the structural information. The fair correlation of geomorphic features with producing areas suggests that many structural closures are expressed at the surface and, therefore, have influenced drainage and erosional patterns in overlying units. But it is important to note that the majority of the oil and gas fields do not appear to be expressed in the geomorphology; therefore, the correlations recognized may partially be a function of the large number of fields in the region. An evaluation of these spatial correlations requires an in-depth study of the structural controls of *all* fields in the region. Nevertheless, the correlations exist as shown and should not be ignored. It would be unreasonable to expect all fields to be equally well expressed on the regional Landsat MSS interpretation. The Worsham field, however, is in part a WNW- to E–W-trending anticline in the subsurface (Figures 13-8, 13-9, 13-10, and 13-12) and is expressed on the Landsat MSS images by opposing arcuate scarps along the east side of Toyah Creek and along the west side of Hackberry Draw. The Worsham field area is bounded on the east and west by regional NNW-trending lineaments.

b. Structural interpretation – Coyanosa test site. Following the regional examination of the area, a detailed Landsat MSS interpretation of the Coyanosa test site was undertaken and the results were transferred to the 1:48,000 base map (Plate 13-1) for comparison with the NS-001 interpretation.

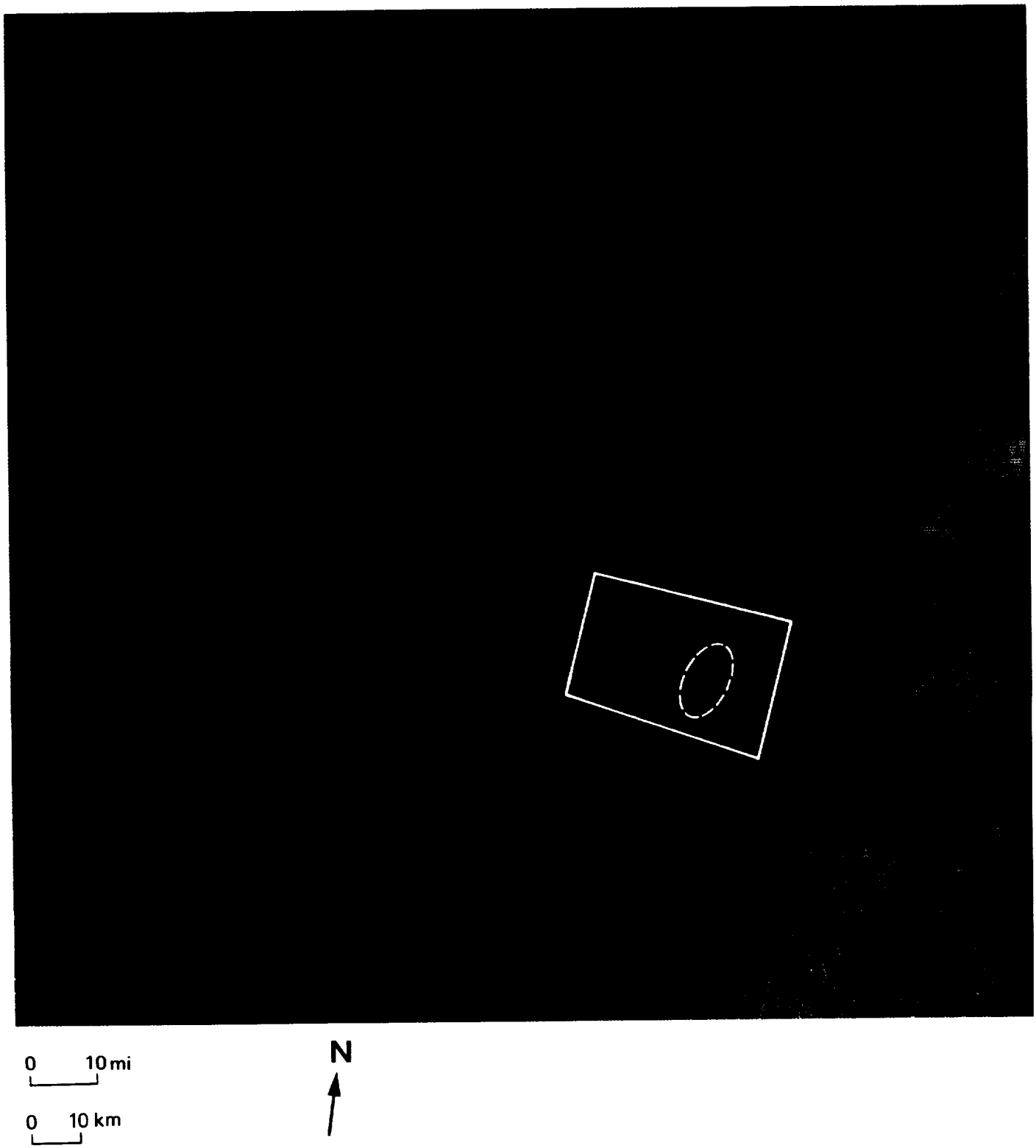

Figure 13-38. Full-scene Landsat MSS high-contrast color infrared composite image, October 4, 1975. This image was produced using a PC stretch (VICAR, PGSTR): band 4 (0.55 μm), blue; band 5 (0.65 μm), green; band 7 (0.86 μm), red. The test site is outlined; dashed line outlines a light tonal feature.

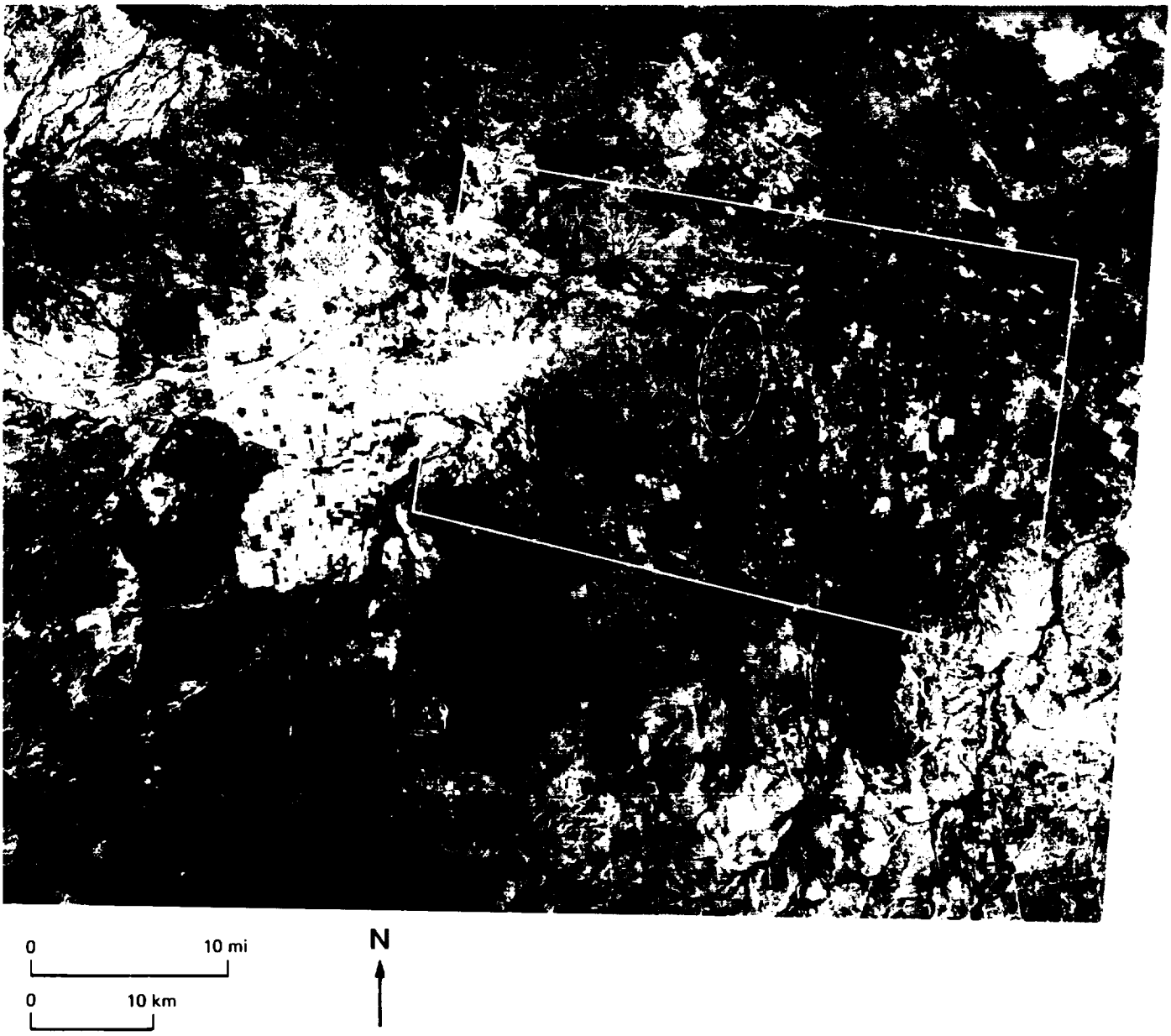

Figure 13-39. Landsat MSS standard color infrared composite subscene, February 1, 1977: bands 4 (blue), 5 (green), 7 (red). The test site is outlined; dashed line outlines a light tonal feature.

The most pronounced structural features in the Coyanosa test site are the NNW-trending lineaments bounding the east and west sides of the Worsham anticline. In addition to these lineaments, the Worsham field is bounded on the northwest by several arcuate topographic scarps along the east side of Toyah Creek. A broad, curved drainage that joins the northwest and northeast linear portions of Hackberry Draw and cuts through the center of Waha field approximately bounds the Worsham field producing area to the east. When this curved drainage is viewed in relation to the curved scarp to the west, it suggests an uplift or closure beneath the Worsham field and along the western half of Waha field. Erosional rounding of a fault intersection, however, may be responsible for the broad curve along Hackberry Draw. The north end of Hackberry Draw enters the Pecos River Valley against the regional slope (i.e., it is a barbed tributary to the Pecos River), indicating probable fault control. The *en echelon* arrangement of the other linear drainages paralleling the south end of Hackberry Draw, coupled with the very angular fracture- or fault-controlled tributaries on its west side, provides additional support for probable fault control of this segment of Hackberry Draw. These structures plus the relatively well-developed double drainage deflection centered over Worsham field are the primary image clues to possible subsurface structural closure or uplift in the Worsham field area.

A compilation of subsurface structures (Figure 13-14) reported by various workers in this area and the structure maps on top of the Lamar shale and the Ellenburger Formation (Figures 13-10 and 13-12) lend very strong supportive evidence that deep structures are expressed in the surface drainage patterns. The following correlations between the Landsat MSS interpretation (Plate 13-1) and subsurface structure are apparent:

(1) The location and trend of the north and south sections of Hackberry Draw closely match regional fault systems (Figure 13-14).

(2) The NNW-trending Coyanosa Draw lineament closely parallels the regional fault trend as well as individual faults mapped in Ordovician (Ellenburger), Mississippian, and Pennsylvanian subsurface horizons. This lineament also coincides with the west-bounding fault of the basement horst block upon which the Coyanosa Anticline developed (Figure 13-14, Basin Edge fault zone).

(3) Although the NW-trending lineament formed by the north end of Hackberry Draw cuts across the Waha field outline, the lineament closely parallels the Waha anticlinal axes and bounds the west side of the Lamar level of structural closure in the field.

(4) The arcuate scarps on either side of the Worsham–Waha fields roughly mark the limits of structural closure at the Lamar level for both fields.

(5) A small double-drainage deflection near the west end of the Worsham field correlates well with a small satellite closure at the Lamar level. This area coincides with the Riplinger field (Figure 13-8).

(6) Although the concentric double-drainage deflections located in the north–central portion of the Worsham field are much smaller than the overall subsurface structural closure, it is important to note that they are located over the crestal or highest structural position of the Lamar shale and the Ellenburger Formation within the field.

Deep Ellenburger production throughout the Delaware and Val Verde Basins is commonly controlled by fold culminations over basement horst blocks. This relationship, coupled with the apparent surface expression of these features on Landsat MSS images, indicates that lineament mapping and drainage analysis are equally important in providing potential structural information that can be used in identifying exploration targets in this region.

An NS-001 color ratio composite image (Figure 13-42) was also interpreted for surface features which might reflect subsurface structure. The results of this interpretation are included in Plate 13-1 for comparison with the composite Landsat MSS interpretation. Such a comparison gives insight into the effects of increased spatial resolution in structural applications:

(1) Most lineaments and arcuate drainage deflections, scarps, and topographic boundaries recognized in the Landsat MSS data were also identified in the independent NS-001 interpretation. Minor spatial offsets of some of these features in the two interpretations may be the result of inaccuracies in image/map registration due to differences in spatial resolution or may be the result of subjective location differences due to operator bias (for example, the Barrilla Draw lineament).

(2) Some of the features shown as lineaments (i.e., interpreted as "straight" on the Landsat MSS interpretation) are identified as arcuate geomorphic features on the NS-001 interpretation (for example, the Coyanosa Draw Landsat MSS lineament). This is probably a result of the "straightening" of slightly curved features with a decrease in image scale and decrease in spatial resolution (1:48,000/15 m for NS-001 structural interpretation and 1:200,000–500,000/80 m for the Landsat MSS composite interpretation).

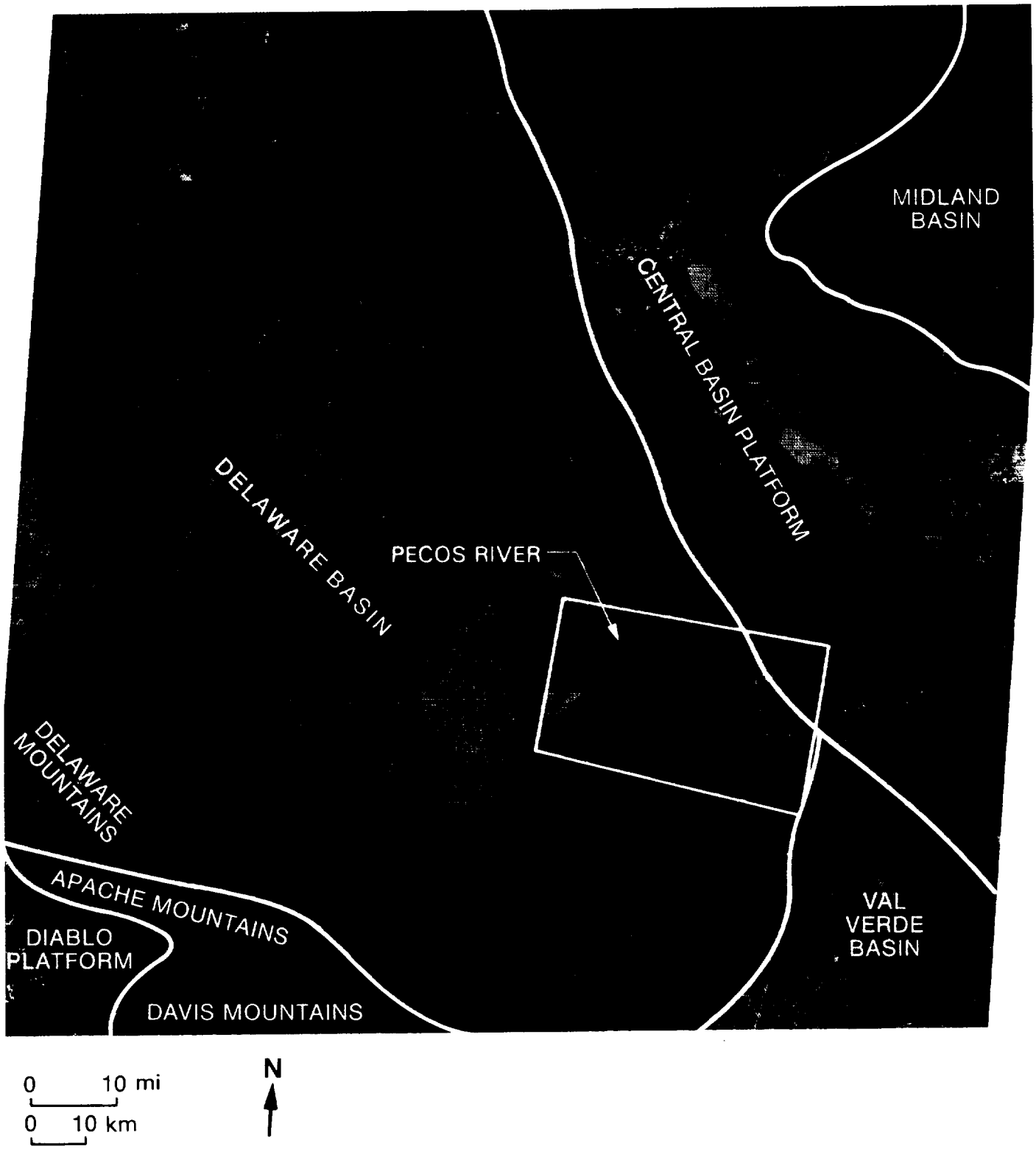

Figure 13-40. Generalized regional interpretation of Figure 13-38 showing major tectonic/physiographic elements of the test site vicinity. The Coyanosa test site is outlined.

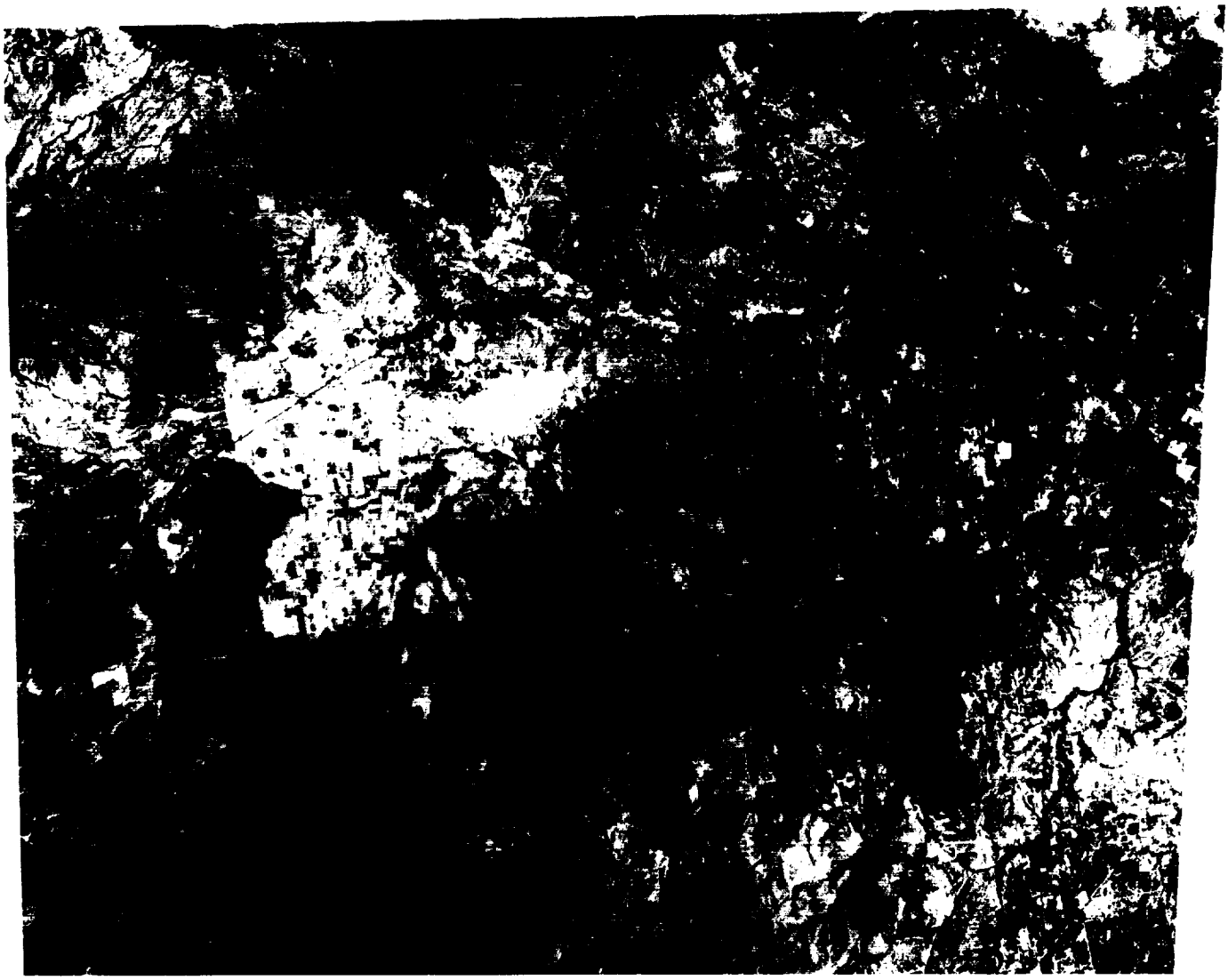

Figure 13-41. Regional composite Landsat MSS structural interpretation: (a) the color infrared Landsat subscene shown in Figure 13-39; (b) regional Landsat structural interpretation showing test site outline and selected oil/gas fields

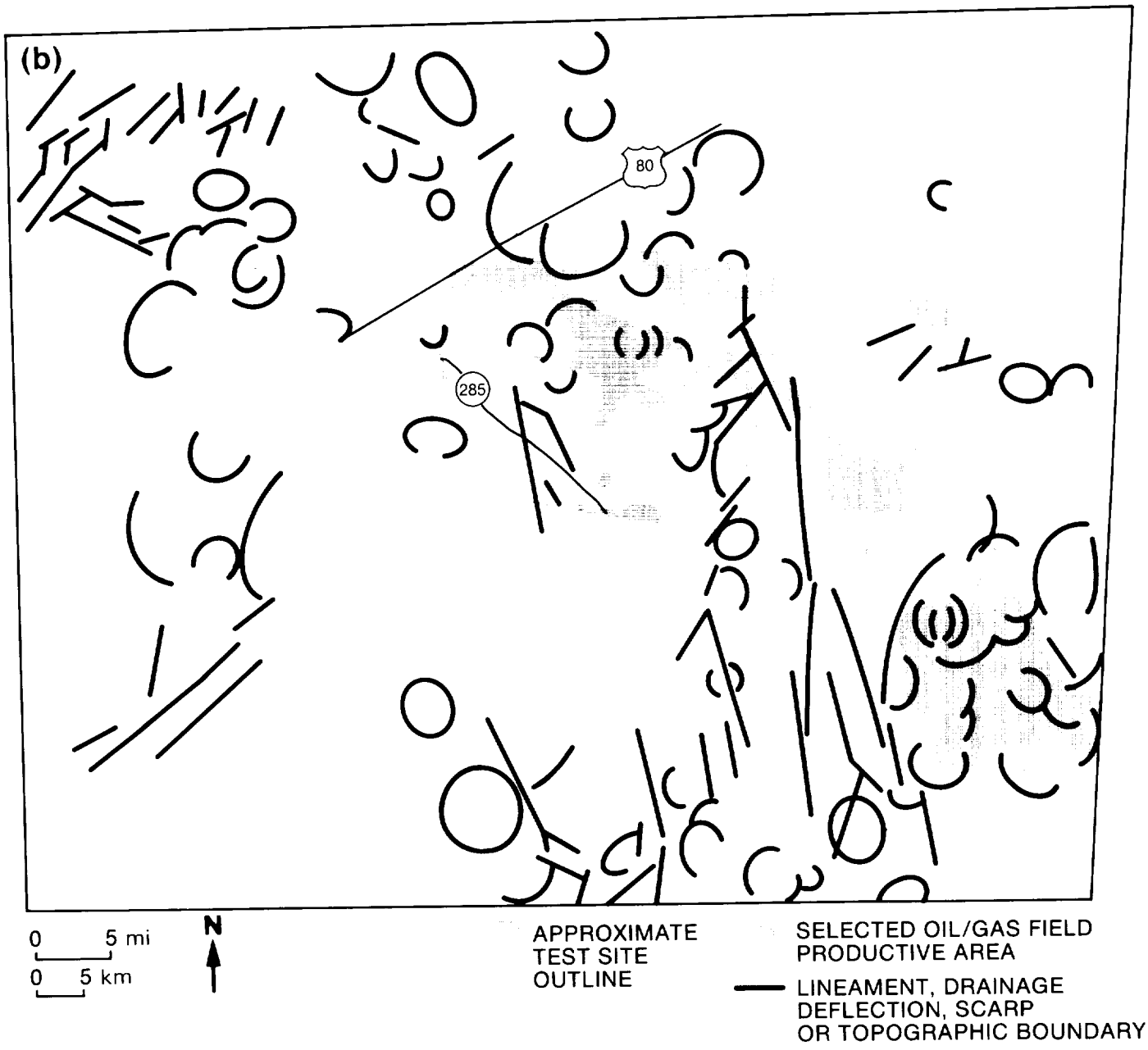
(b)
80
285
0 5 mi
0 5 km
N
APPROXIMATE TEST SITE OUTLINE
SELECTED OIL/GAS FIELD PRODUCTIVE AREA
LINEAMENT, DRAINAGE DEFLECTION, SCARP OR TOPOGRAPHIC BOUNDARY

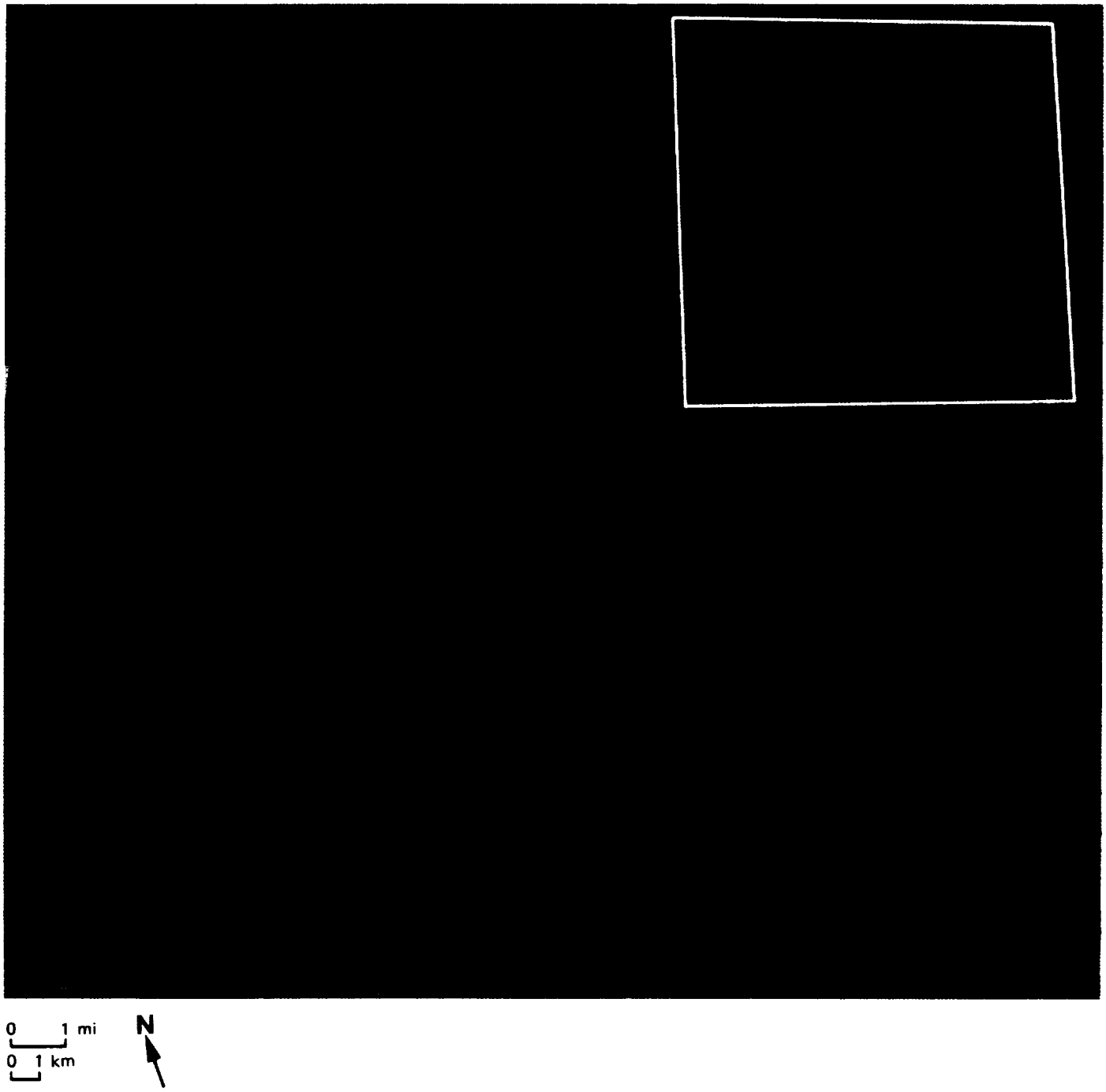

Figure 13-42. NS-001, Mission 403, June 18, 1979, color ratio composite mosaic of lines 1, 2, 3: ratios 2/3 (green), 2/4 (blue), 6/7 (red). This image was printed at 1:48,000 for detailed interpretation shown in Plate 13-1.

(3) In many cases, single Landsat MSS lineaments are portrayed as discontinuous lineament segments (Barrilla Draw) or as a conjugate set of short *en echelon* lineaments (southern Coyanosa Draw) in the NS-001 interpretation. These finer-scale NS-001 features are probably substructures of the larger deep-seated features shown in the Landsat MSS interpretation. This variation also reflects the averaging effect of scale/resolution changes in comparing NS-001 to Landsat MSS images.

(4) Lineaments and arcuate drainage deflections, scarps, and topographic boundaries recognized in the NS-001 image that have no Landsat MSS equivalents are interpreted to be the surface expression of subtler, smaller, and shallower subsurface structures than those expressed by the smaller-scale Landsat MSS data.

C. Spectral Interpretation

1. Introduction. The phenomenon of seepage of hydrocarbons from petroleum reservoirs is known to exist and has been used with varying amounts of success in exploration by geochemists in soil gas surveys both on- and offshore. Surface alteration consisting of chemical and mineralogical changes in soils and rocks overlying leaking hydrocarbon traps has been investigated and documented by Donovan and others (Dalziel and Donovan, 1980; Donovan, 1974; Donovan et al., 1975). An example of this type of surface alteration occurs at the Cement Creek Anticline in the Anadarko Basin of Oklahoma where visible leaching of iron oxides occurs directly over the reservoir, with apparent re-precipitation of this iron around the periphery of the anticline. Additionally, an increase in calcium carbonate cement also occurs in bleached, light-toned rocks in the crestal portion of the anticline.

The objective of spectral interpretation of images is to investigate the Coyanosa test site for the presence of spectral or tonal manifestations of possible alteration of soil/rock or vegetation that is potentially related to the microseepage of hydrocarbons. Although the phenomena sought in the spectral interpretation of images are assumed to be similar to those associated with the Cement Creek Anticline, the basic interpretation model (types of surface anomalies thought to be important) is open ended. This is because the Cement Creek Anticline, while fairly well understood, is probably an end-member example of the effects of alteration. The interpretation of Coyanosa image data was therefore based primarily on the Cement Creek model, but also allowed for the presence of other unexpected surface spectral features potentially related to the seepage of hydrocarbons.

The following spectral classes were important during spectral interpretation and analysis of the image data:

(1) Ferric oxides

(2) Light-toned or bleached zones with possible increase of calcium carbonate

(3) Hydroxyl-bearing minerals (clays, gypsum, etc.)

(4) Anomalous vegetation patterns or spectra

(5) Any other unexplained changes of surface materials and/or their spectra

2. Method of investigation. Once initial mapping was completed, the next step in image interpretation was to thoroughly investigate each spectral feature or class with respect to field and laboratory spectral and mineralogical data, soil maps, geology, and field vegetation information to determine if any anomalous condition existed over oil/gas fields.

To evaluate seasonal spectral variations in the data as well as the difference in response of surface material to a variety of enhancement techniques, five Landsat MSS scenes acquired on three different dates were selected for initial processing and interpretation. Three scenes were processed to produce the six images (Table 13-25) used in the detailed spectral interpretation. NS-001 data were processed to a color infrared composite and color ratio composites for detailed interpretation.

3. Results of the spectral interpretation. All Landsat MSS and NS-001 images were interpreted for tonal and/or spectral features or classes (areas having similar spectral response, color, or tone). The spectral classes or color groups for each image were mapped independently of the other images. The interpretations were then compiled at the same scale for class identification, evaluation, and comparison. Spectral class interpretation involved the identification and assignment of each spectral feature mapped to a composition or cover type assemblage. Identification of the composition of a spectral class was based on its spectral characteristics or ratio response as determined in a field/laboratory spectral analysis of cover types (discussed in Paragraph VIII). Class identification on the PC image was done by comparing the mapped classes to the response of known materials delineated on the ratio image of the same Landsat MSS scene. Evaluation of these results with respect to available soil, geologic, and vegetation information should reveal any potentially anomalous spectral features or classes requiring further analysis.

Table 13-25. Images used for spectral interpretation

Sensor	Processing	Image/Mission Number	Date	Scale
Landsat MSS	JPL: PGSTR	20255-16461	10-4-75	1:500,000
	SUPERIOR: CIR	2741-16332	2-1-77	1:300,000
	SUPERIOR: 4/5,4/6,6/7	2741-16332	2-1-77	1:300,000
	JPL: PGSTR	20399-16440	2-25-76	1:500,000
	JPL: 4/5,4/6,6/7	20399-16440	2-25-76	1:500,000
	JPL: PC	20399-16440	2-25-76	1:500,000
NS-001	JPL: 2,3,4	403	6-18-79	1:48,000
	JPL: 2/3,2/4,6/7	403	6-18-79	1:48,000
	JPL: 6/7,6/1,3/2	390	10-12-78	1:96,000

Analysis of the spectral characteristics of surface materials in the test site made possible the identification of several distinctive spectral/compositional classes. Those most easily identified included vigorous vegetation, barren ground, ferric oxide concentrations in soils and rocks, and mixtures of these. The spectral classes interpreted from selected images and their distribution are shown in Figures 13-43, 13-44, and 13-45 and Plate 13-1.

Comparison of these interpretations illustrates the fairly good correlation and coincidence in the location and distribution of the areas occupied by a number of spectral classes on all images. This agreement among multitemporal images was achieved in spite of the independent interpretation of each image and the subjective nature of this type of visual grouping of classes. Most or possibly all of the location and composition variations among the classes mapped on different images can be explained by the subjectivity in mapping class boundaries and by seasonal and annual differences in the type, density, and vigor of vegetation.

Although several potentially anomalous spectral features were mapped within the test site, their anomalous character was negated when they were evaluated in the context of the surrounding region or compared to the ancillary data. Each of these potentially anomalous spectral classes or surface conditions is discussed below.

a. Ferric oxides. Ferric oxides, occurring in red beds and iron-rich soils, were identified in each of the images studied and comprised the most consistently mapped spectral class. The variation in the size and distribution of this class is primarily a function of the type of image interpreted. Landsat MSS images (Figures 13-43 and 13-44) using the 4/5, 4/6, and 6/7 ratios and the NS-001 ratio image (Figure 13-42 and Plate 13-1) are superior to both the color infrared images (Figures 13-38 and 13-39) and the PC image (Figure 13-45) for enhancing and mapping the distribution of iron oxides. The distribution of ferric oxides ringing the Worsham–Waha field area (Figures 13-43, 13-44, and 13-45 and Plate 13-1) at first appears suspicious until the full geologic and geomorphic setting of the test site is appreciated. The Worsham–Waha fields are located on a relatively flat, locally incised, erosion surface covered in part by pediment gravels and protected from erosion by a well-developed caliche horizon. The regional dip of the underlying units appears to be fairly gentle in a northerly or northeasterly direction. Local downcutting by the Pecos River, to the north, and Barrilla Draw and its tributaries, to the west, have exhumed the underlying Triassic Dockum red beds (Figure 13-2).

The elongate iron-rich zone and associated patches in the north–central portion of the test site belong to the Pyote, Wickett, and Sharvana soils (unit 9, Figure 13-25 and Table 13-9). These soils consist of yellowish-red to reddish-brown loamy fine sands of eolian or alluvial origin. Examination of the Landsat MSS ratio images (Figures 13-43 and 13-44) indicates that these patches are on the southernmost fringe of a regionally widespread soil type that occurs throughout much of the Delaware Basin, primarily in the area north and east of the Pecos River. The other areas of interpreted ferric oxides are primarily iron-rich soils derived locally from near-surface Dockum red beds in the semiarid environment of the test site.

A combination of topography, erosional patterns, and distribution of locally derived, reddish iron-rich soils can create some interesting and potentially "anomalous" patterns, especially if the local geology and geomorphology are ignored. An example is shown in Figure 13-46, an NS-001 color ratio composite image of a small mesa-like feature located just south of the Pecos River in the eastern part of the test site. Preliminary interpretation of this image suggested the presence of an iron-oxide halo or surface alteration effect potentially related to hydrocarbon microseepage. The ring of iron oxides in this ratio image is more

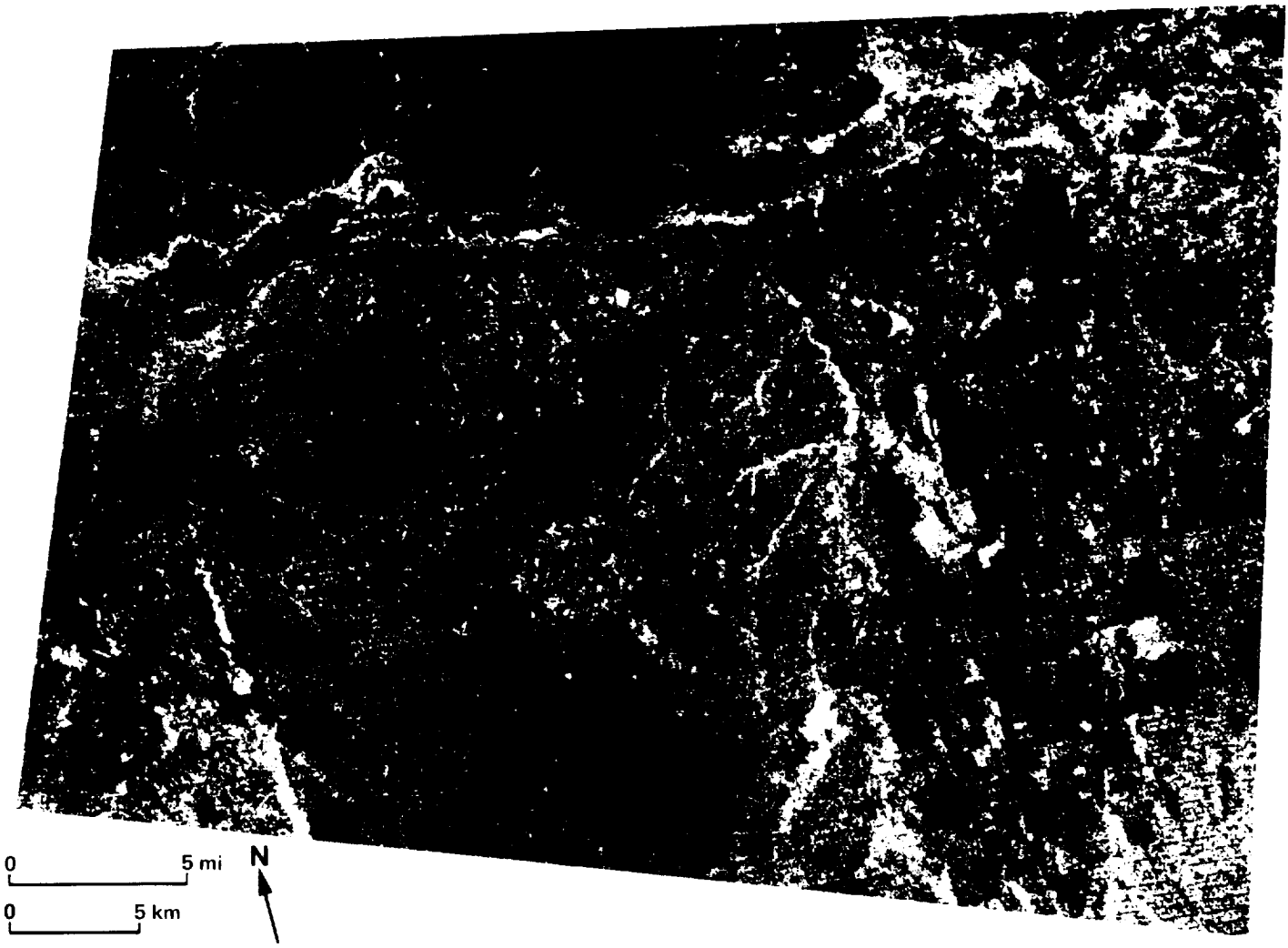

Figure 13-43. Landsat MSS color ratio composite subscene, February 1, 1977: ratios 4/5 (blue), 4/6 (green), 6/7 (red). Spectral classes outlined: F, ferric oxides; V, vigorous vegetation; V and SF, vigorous vegetation with scattered ferric oxides; C, Y-G, and Y-G-C, bare ground and/or dormant vegetation; T, Toyah Lake. U.S. Highways 80 and 285 and circular tire testing track are also shown to aid in location (see Figure 13-1).

likely formed by reddish soils derived from shallow, subcropping Dockum red beds beneath and flanking a flat-topped, NE-dipping erosional remnant of a caliche horizon. A cross section (Figure 13-46) illustrates the configuration of this mesa-like feature. Since ratioing tends to reduce topographic effects, the geomorphic character of this feature is not very evident on the NS-001 ratio images (Figures 13-42 and 13-46). Color infrared photography and the color infrared NS-001 image (Figure 13-47), however, clearly reveal the mesa-like form of this feature. The lack of a striking iron-oxide ring in the NS-001 ratio image (Figure 13-42) used for this study is primarily due to the more vigorous vegetation flanking the mesa on June 18,1979 (date of Mission 403). The mixture of the healthy vegetation spectra with the iron-oxide spectra of these iron-rich soils (Table 13-26) has resulted in a broad, subtle yellow–brown smear in the vicinity of the mesa on Figure 13-42. The NS-001 image (Figure 13-46) was acquired on October 12, 1978, when the vegetation in this area was dormant or very sparse, thereby allowing the iron-oxide spectra of the soil to dominate the ratio image.

No anomalous or unexplained concentration of iron oxides was found in either the outcrops or soils of the Coyanosa test site.

b. Light-toned spectral features. Of all the potentially anomalous features mapped on the Landsat MSS and NS-001 images, the most persistent spectral feature is a N–S-trending, light-toned area which was first recognized on the Landsat MSS February 1, 1977 color infrared (Figure 13-39) and the October 4, 1975 PGSTR color infrared

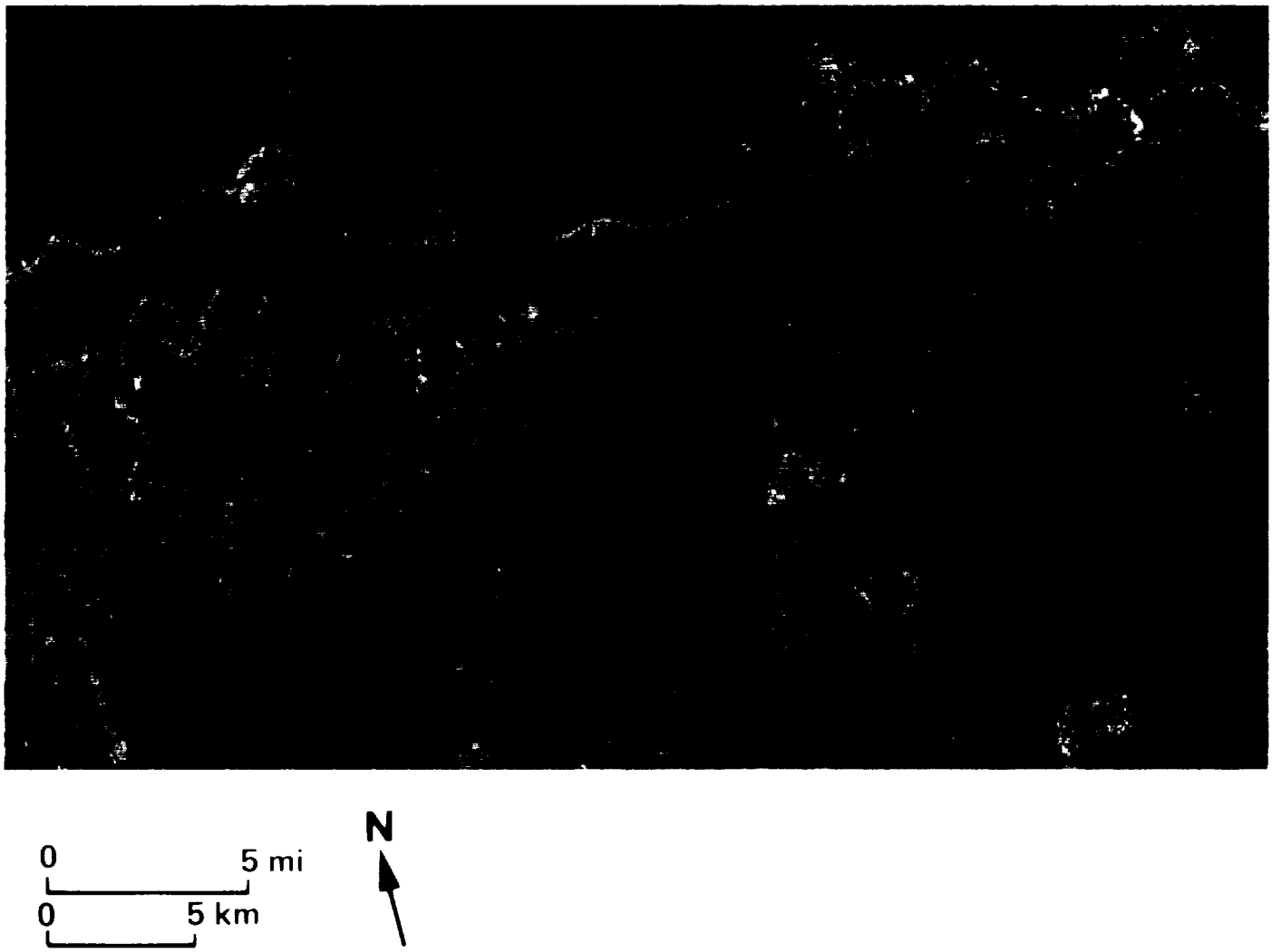

Figure 13-44. Landsat MSS color ratio composite subscene, February 25, 1976: ratios 4/5 (blue), 4/6 (green), 6/7 (red). Spectral classes outlined: F, ferric oxides; V, vigorous vegetation; SF, bare ground with scattered ferric oxides; SV, bare ground with scattered vigorous vegetation; V and SF, vigorous vegetation with scattered ferric oxides; C, L-C, and LTA, bare ground and/or dormant vegetation; T, Toyah Lake.

(Figure 13-38) images. The light-toned area consists of a smooth rounded ridge or broad nose along the west side of Hackberry Draw. The northern third of this spectral feature overlies the western half of the Waha field in the most intensely fractured and faulted portion of the test site. This spatial correlation suggested a possible anomalous situation requiring further investigation.

The tonal feature is much more subtle on the color infrared NS-001 image (Figure 13-47) and is not unusually different from the shallow caliche soils developed over much of the area to the west. It does appear more vegetated over its northern half and along its eastern side. The smooth, light bluish-gray tone and texture of the feature's relatively barren southern end are almost identical to the tone and texture of the very sparsely vegetated areas of caliche soils overlying Dockum red beds along the linear tributary of Barrilla Draw. A comparison of this feature with the soil map (Figure 13-25) shows an excellent correlation with the pale-brown gravelly loam of the Delnorte soils (unit 8, Figure 13-25) that also occur along the eastern side of Barrilla Draw.

The spectral class interpretation of the Landsat MSS and NS-001 ratio images (Figures 13-43 and 13-44 and Plate 13-1) indicates that the Hackberry Draw feature is an area of scattered ferric oxides and relatively sparse but vigorous vegetation as compared with the areas directly over and to the south of Worsham field. Comparison of these spectral classes with the tonal features interpreted originally on the color infrared images, and the distribution of caliche soils, indicates that this light-toned feature correlates well with a

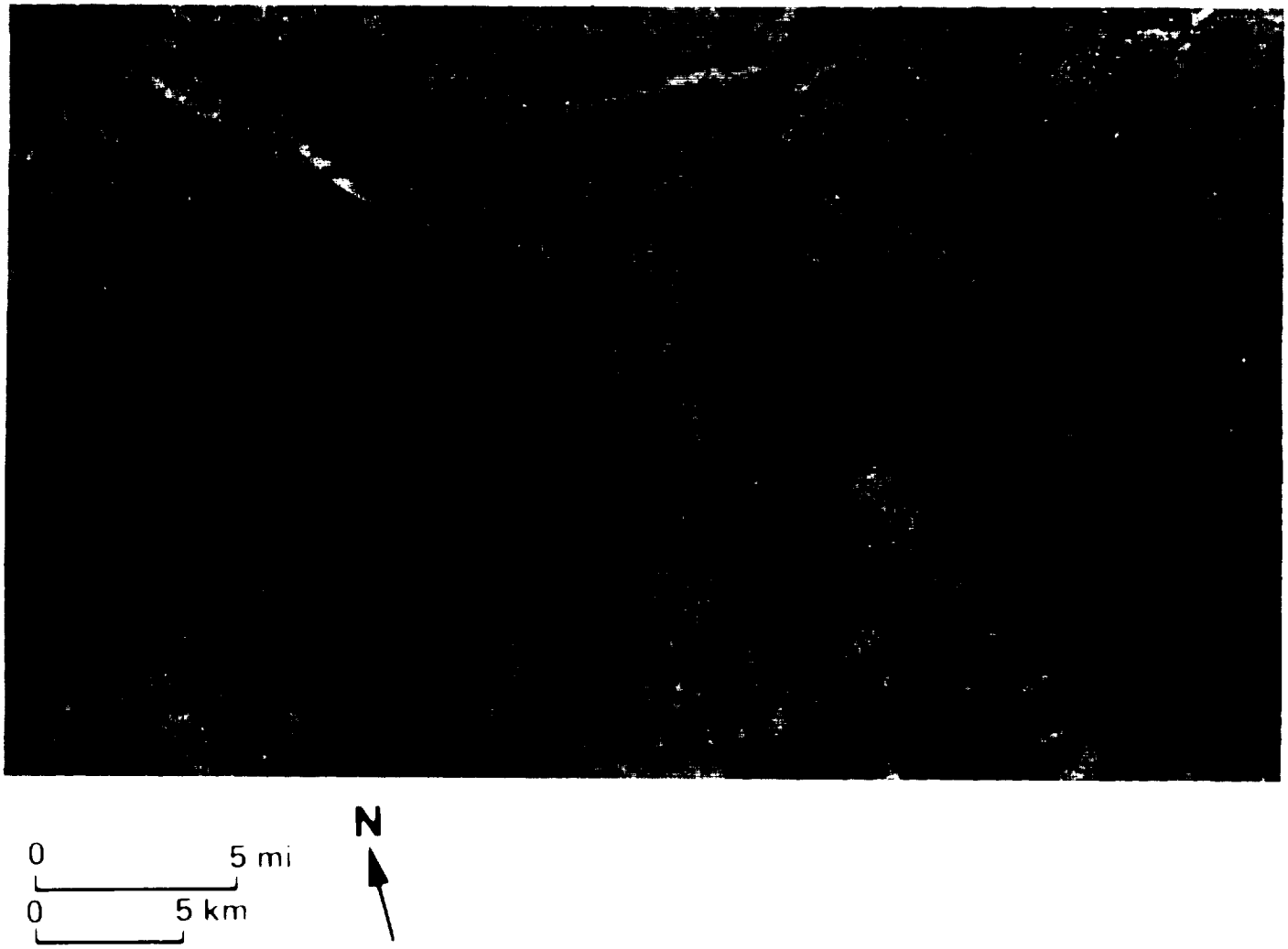

Figure 13-45. Landsat MSS PC subscene, February 25, 1976: bands V1 (blue), V2 (green), V3 (red). Spectral classes outlined: P, L-P, L-Y, Y-P, Y-O, R, and O-P, ferric oxides; L-C, Y-G, and Dark Mix, bare ground and/or dormant vegetation; B-M-C, vigorous vegetation with scattered ferric oxides; Y-G-B, bare ground with scattered vigrous vegetation; T, Toyah Lake.

caliche-rich soil that occurs in an area of dramatic seasonal vegetation change. The geochemical analyses of soil samples from the area do not show any anomalously high or low elemental concentrations. This light-toned area, therefore, is not considered to be anomalous and is interpreted to be unrelated to the subsurface accumulations of oil and gas. No other light-toned features interpreted from images were evaluated since none were as persistent as the Hackberry Draw feature. The Hackberry Draw feature is interpreted to be the result of normal seasonal variation in vegetation density and vigor.

c. Hydroxyl and/or carbonate concentration. Because Landsat MSS data do not have near-infrared 1.6- and 2.2-μm bands sensitive to the minerals containing hydroxyl or carbonate ions, this discussion is limited to the NS-001 ratio image (Figure 13-42) and its interpretation (Plate 13-1). The NS-001 2/3, 2/4, and 6/7 ratio image was interpreted using a ratio response color chart (Figure 12-32, Lost River, West Virginia, Petroleum Test Site Report) to evaluate the color contributions of the various cover types in the test site. Table 13-26 was then prepared to aid in the identification of cover types based on their image color. Vigorous vegetation is yellow, iron oxides are dark brown to black, and soils or rocks containing high concentrations of hydroxyl- or carbonate-bearing minerals are a shade of magenta.

Of the various spectral classes recognized on the NS-001 ratio image, the only potentially anomalous feature is the broad east–west-trending pink to pale-magenta area in the northwest–central part of the test site. This area overlies

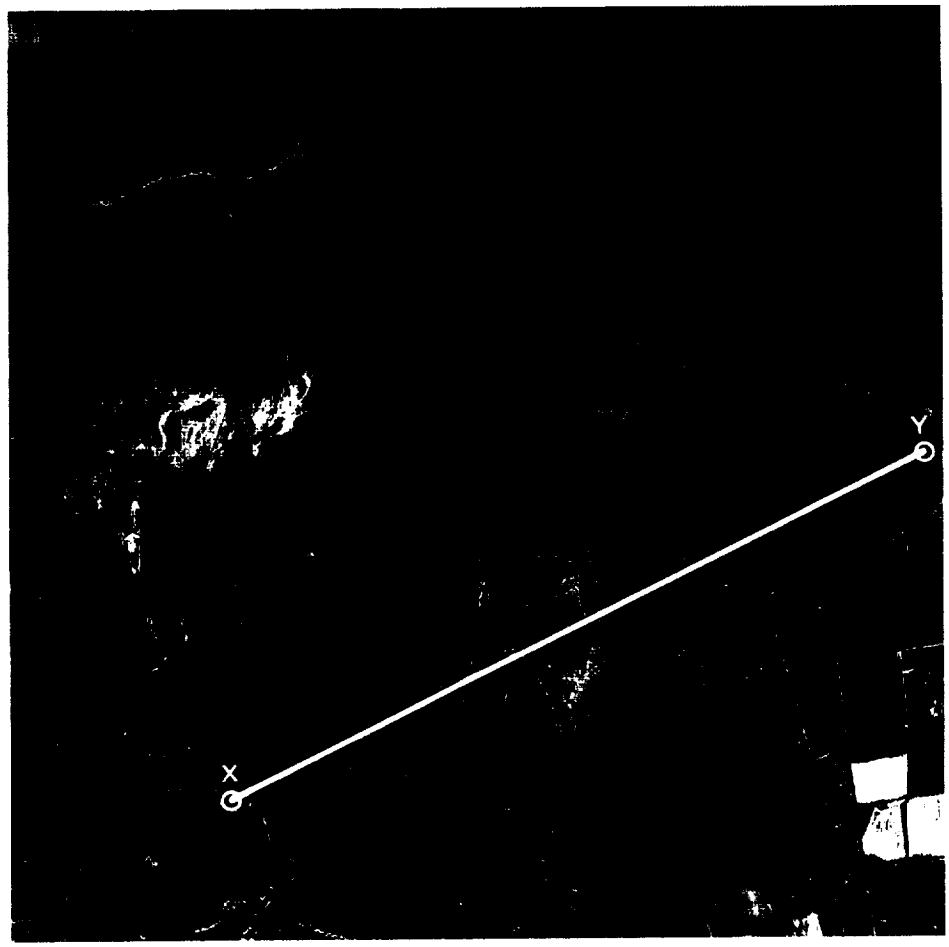

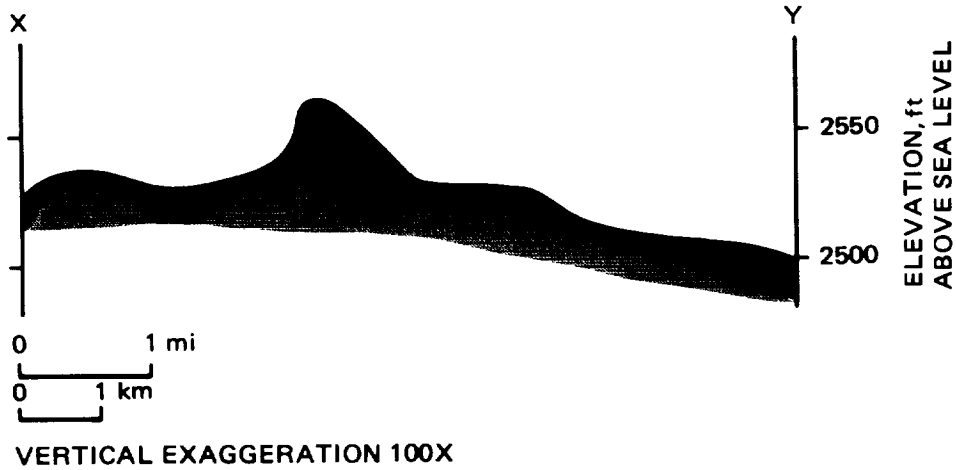

Figure 13-46. NS-001, Mission 390, October 12, 1978, color ratio composite subscene from line 3: ratios 6/7 (blue), 6/1 (green), 3/2 (red). For location of this subscene, refer to Figures 13-42 and 13-47. The cross section clarifies the cause of the yellow iron-oxide "anomaly": The yellow image/cross section unit represents iron-oxide-bearing Dockum-derived soil. The lined yellow cross-section unit represents a caliche interval capping the yellow unit (note pink unit on Figure 13-42). Sparsely vegetated, thin super-caliche soils are shown in brown; more heavily vegetated, thicker alluvium of drainages is shown in blue. Thus, the yellow "anomaly" is a typical outcrop expression of a mesa.

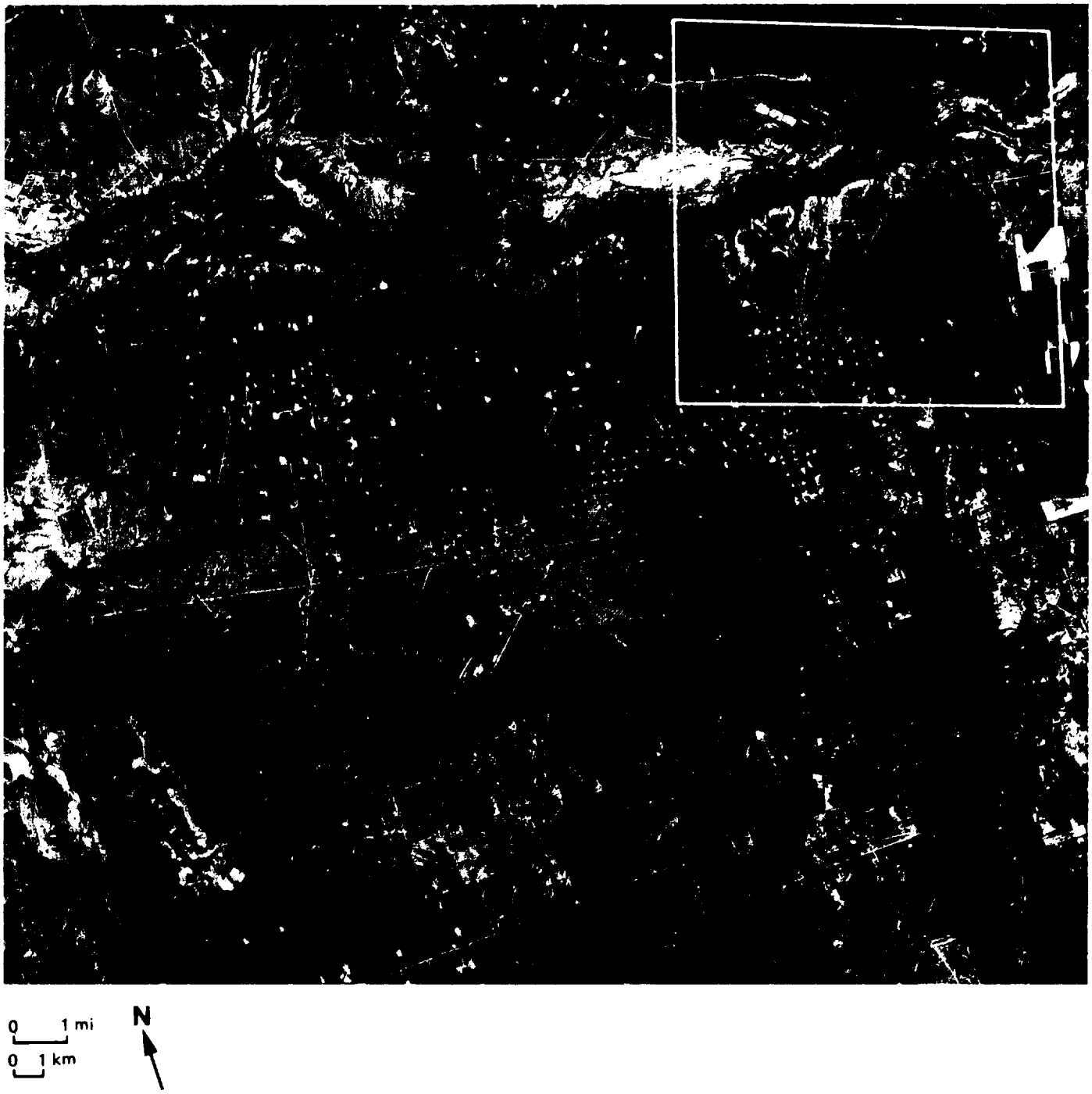

Figure 13-47. NS-001, Mission 403, June 18, 1979, color composite mosaic of lines 1, 2, 3: bands 2 (blue), 3 (green), 4 (red). This band combination was selected to produce an image simulation of color infrared photography. Area outlined is shown in Figure 13-46.

Table 13-26. Ratio response and class identification determined in the spectral interpretation of NS-001 2/3 (green), 2/4 (blue), 6/7 (red) color ratio composite image (Figure 13-42 and Plate 13-1)

Image Color	DN Values[a]			Class Identification[b]
	2/3 (Green)	2/4 (Blue)	6/7 (Red)	
Yellow	200–255	0–100	200–255	Vegetation
Brown–black	0–40	0–40	0–75	Iron oxides
Light brown	88	40	105	Iron oxides
Pink–Pale magenta	150	180	225	OH- and CO_3-bearing minerals
Magenta	115	145	235	OH- and CO_3-bearing minerals
Blue	0–20	145–255	0–20	Bare soil, alluvium, dormant vegetation
Orange	125	75	220	Vegetation with iron oxides

[a] Based on visual comparison of image color to digital number (DN) color chart (Figure 12-32, Lost River, West Virginia, Petroleum Test Site Report, Section 12).
[b] Based on comparison with NS-001 color infrared image (Figure 13-47), field and laboratory spectra acquired at the test site, published spectra, and field observations.

the northern two-thirds of the Worsham field. Its color can be attributed to high 6/7 ratio values, high to moderate 2/4 ratio values, and moderate to low 2/3 ratio values. These ratio values indicate that the area contains sparse to dormant vegetation, low to moderate amounts of iron oxides, and significant amounts of hydroxyl- or carbonate-bearing minerals such as clays, gypsum, or calcite. Several other pink areas on the ratio composite were also mapped; however, these do not overlie any known production (Toyah Lake and farmland northeast of Waha and Coyanosa). The pink image color in the Toyah Lake area results from high soil concentrations of clay and gypsum. This interpretation is also supported by the soil map (Figure 13-25), which shows the Toyah Lake area as a region characterized by a distinctive gypsiferous soil (units 3 and 5).

The broad east–west pink to magenta feature correlates with the northern portion of the horseshoe-shaped distribution of the Delnorte–Nickel soils (unit 8, Figure 13-25). Field examination of the area indicated that the pink feature on the ratio image is best developed north of an east–west-trending erosional scarp marked by numerous outcrops of a caliche soil horizon. These caliche outcrops are clearly mappable units on the ratio image (Figure 13-42, narrow bands of a fairly intense orange–pink color). Several additional pink bands are located along the dissected erosional scarps of the Pecos River. On the north side of the river, the outcrop pattern of Dockum red beds (brown to black on the image) are also overlain by pink beds, suggesting that a clay- or carbonate-rich horizon is currently being exhumed by the on-going dissection of this topographic scarp. This interpretation, which is supported by field observations, indicates that the pink area over the Worsham field is a similar, but possibly thicker, spectrally unique soil horizon exposed on the dissected north slope of the broad topographic high located just south of the Worsham field. The intense orange–pink image response of outcrops on the scarp and the lack of gypsum in soil samples obtained from this area indicate that the 1.6/2.2 μm ratio response is primarily due to the high calcium-carbonate content of an exposed and eroded caliche soil horizon. The caliche zone is widespread over much of the western half of the test site as indicated by caliche outcrops (image pink) above Dockum red beds along Barrilla Draw. This caliche zone is interpreted to extend across the area between Barrilla Draw and Hackberry Draw because of the numerous irregular to circular shallow depressions which pockmark the area. These depressions are interpreted to be solution features (incipient karsting) of the near-surface caliche horizon. The caliche horizon, although widespread, is not as well expressed everywhere on the ratio image. It is generally covered by a thin veneer of light brownish-gray loam of the Upton soils and the light brownish-gray gravelly loams of the Delnorte soils (unit 7, Figure 13-25).

The spectral and compositional characteristics of the broad, pink anomaly on the NS-001 ratio image are not interpreted to be unusual or anomalous and are not interpreted to be related to any surface alteration effects associated with the microseepage of hydrocarbons from the Worsham field. The location and distribution of this feature may, however, be related to subsurface structural closure, which in turn may have influenced the surface erosional patterns. More detailed structural information for shallow subsurface units such as the Dockum red beds would be required to confirm this inferred structural correlation.

d. Vegetation. No microseepage-induced vegetation anomalies were detected in either the Landsat MSS or NS-001 data. Extreme seasonal variations in vegetation, however, are evidenced by the spectral interpretation of multiyear and multiseasonal images. Seasonal or ephemeral variation of vegetation is exemplified by the light-toned image feature mapped along Hackberry Draw. On the February 1, 1977 Landsat MSS image (Figure 13-39), this light-toned feature is barren of vigorous vegetation; however, on the October 4, 1975 MSS image (Figure 13-38), this area is flanked by a vibrant pink tone, indicating vigorous, sparse vegetation. The February 25, 1976 Landsat MSS color infrared image (Figure 13-48) and the June 1979 NS-001 color infrared (Figure 13-47) and ratio (Figure 13-42) images indicate sparse but vigorous vegetation over this area. The Mission 390 NS-001 image data (Figure 13-46) were apparently acquired during a period of very sparse or dormant vegetation as indicated by the appearance of the mesa-like feature discussed in the previous paragraph.

These vegetation differences are interpreted to be a function of both the amount of available moisture and the season. For instance, in the three months prior to the time of acquisition of the October 4, 1975 image data (Figure 13-38), the region had received 177 mm or almost two-thirds of the rainfall for the entire year (Table 13-8). During the three months prior to the time of acquisition of the February 1, 1977 image (Figure 13-39), only 30 mm of rain had fallen. Low rainfall and the mid-winter acquisition date are the probable causes for the dormant vegetation on this image. The sparse but vigorous vegetation in the Hackberry Draw area in the February 25, 1976 image (Figure 13-48) follows only 20 mm of rainfall in the preceding months; however, the date of acquisition corresponds with the beginning of spring in West Texas. Vegetation variations in the Coyanosa test site are therefore ephemeral, depending on both rainfall and season. The field vegetation study of the test site area indicated significant and rapid local variation in plant species, distribution, and density as a function of soil type, topography, and water availability. Any soil/rock spectral variation that could overpower vegetation effects would probably be visible in the field. No such variation was recognized during field examinations of the area by the test site team.

The rapid lateral and temporal variations in vegetation in the Coyanosa test site area, related to factors discussed and illustrated above, preclude any meaningful attempts to decipher or identify anomalous conditions or distributions in the vegetation with the available remote sensing data. Variation in vegetation also hampers the ability to isolate any anomalous spectral soil or rock condition resulting from alteration associated with any potential hydrocarbon microseepage in the test site area.

4. Other spectral features – Utility of NS-001 scanner. Although no unexpected spectral or tonal features were found in image analysis, several observations regarding the utility of the NS-001 Thematic Mapper Simulator data for structural and lithologic mapping were made.

The NS-001 scanner data, with a 15-m resolution and seven VNIR spectral channels, provided a significant increase in the spatial and spectral detail as compared with Landsat MSS data. The additional 1.6- and 2.2-μm bands allowed for the discrimination and identification of a wide range of earth materials.

A significant problem in interpreting the NS-001 images used in this study resulted from extreme spectral changes encountered in photographic image mosaics from one strip (flight line) to the next. Broad east–west color banding (Figure 13-42) along strip boundaries is due primarily to solar gradient effects (brightness differences) introduced by scanning parallel to the solar azimuth (east–west flight lines with southern solar illumination). Although the color infrared image for the same scanner data (Figure 13-47) is relatively unaffected, ratioing, which enhances subtle spectral differences, dramatically enhances gradient effects. These artifacts are difficult and time consuming to remove. Interpretation of spectral classes on NS-001 ratio image mosaics was hampered by these gradient-induced color changes. Image colors for spectral classes recognized on the southern flight line are very different from colors seen in the two northern lines. For example, the iron-oxide area along Barrilla Draw in the middle section of the mosaic (Figure 13-42) is dark brown, while the same unit in the southern section is various shades of orange and red. The spectral class interpretation (Plate 13-1) attempted to correct for these flight-line differences. Much uncertainty exists as to whether subtle but real spectral changes were lost in the process.

Although gradient problems cannot be entirely eliminated, their effects can be minimized by:

(1) Acquiring higher altitude, smaller scale images, produced from data involving fewer flight lines.

(2) Acquiring data along north–south flight lines at times of southern solar azimuth (solar noon).

(3) Developing efficient approaches for making digital rather than photographic mosaics of aircraft-acquired, low-altitude multispectral data.

0 10 mi

0 10 km

N

Figure 13-48. Full-scene Landsat MSS PGSTR color infrared composite image, February 25, 1976: bands 4 (blue), 5 (green), 7 (red)

XII. Conclusions

No evidence of surface alteration attributable to the seepage of hydrocarbons was recognized in the Coyanosa test site.

The presence of oil and gas in a water well in the test site area reported by Warner (1939, p. 314) suggests that hydrocarbon seepage may occur. Vegetation, geochemical, and field/laboratory spectral surveys of the test site revealed no indications of surface material alterations attributable to seeping hydrocarbons. Additionally, no spectral anomalies attributable to seeping hydrocarbons were recognized in the analysis of both Landsat MSS and NS-001 Landsat 4 Thematic Mapper Simulator images.

Structural/spectral interpretations of Landsat MSS and NS-001 images provide geologic information that would have been useful in identifying the Coyanosa test site as a target of exploration interest if these data had been available prior to oil/gas discovery in the area. Landsat MSS images are most useful at a scale of 1:200,000–500,000 and may be interpreted to delineate major deep-seated structures of the West Texas region. NS-001 Landsat 4 Thematic Mapper Simulator images are most useful at a scale of 1:48,000 and may be interpreted to delineate subtler features associated with the deep-seated structures recognized in Landsat MSS images. Additionally, local structures not recognized in Landsat MSS images are revealed in NS-001 data.

Spectral class maps produced from NS-001 images provide information about the distribution of surface materials that compare favorably in quality and detail to available soil, vegetation, and geologic maps of the test site area. With the aid of ancillary data, the contribution of vegetation and OH^{-}-, CO_3^{2-}-, Fe^{+2}-, and Fe^{+3}-bearing soils and rock outcrops may be determined for the mapped spectral classes.

One of the criteria for selecting Coyanosa as a test site was the area's "sparse vegetation cover." It was assumed that vegetation "problems" in geologic image interpretation would be minimal. The test site investigation proved this was not the case. The semiarid climate and sporadic nature of rainfall in the Coyanosa region result in extreme variability in the vegetation cover. "Spring" is an ephemeral event both spatially and temporally. Recognizing the significant influence of vegetation on multispectral scanner response was only possible by an evaluation of multitemporal image data aided by field vegetation study and review of precipitation records.

One of the primary goals of multispectral remote sensing is to use knowledge regarding the spectral characteristics of materials for the purpose of identifying surface materials with scanner data. Analysis of laboratory, field, and image spectral data for the Coyanosa test site demonstrates that in mixed soil/rock/vegetation terrain this goal is not easily accomplished with available multispectral scanner data. Mixing several spectral components in the scanner-acquired radiance data for a single pixel typically precludes unique identifications of surface materials using scanner data alone.

Acknowledgments

Coyanosa test site fieldwork, image analysis, evaluation, and reporting were done as a team effort. Financial and laboratory support were provided by eight organizations representing government, industry, and academia.

The authors express their sincere thanks to the organizations with which they were affiliated during the study and to the numerous individuals who assisted in the effort. Subsurface and remote sensing data supplied by Geo-Search Corporation, Midland, Texas, and Trollinger Geological Associates, Denver, Colorado, contributed significantly to the project.

References

Adams, J. B., and A. L. Filice (1967). Spectral reflectance 0.4 to 2.0 microns of silicate rock powders. *J. Geophys. Res., 72,* 5705–5728.

Adams, J. E. (1944). Upper Permian Ochoa series of the Delaware Basin, West Texas and southeastern New Mexico. *AAPG Bull., 28,* 1576–1625.

Adams, J. E. (1965). Stratigraphic and tectonic development of the Delaware Basin. *AAPG Bull., 49,* 2140–2148.

Barnes, V. E. (1976). *Geologic atlas of Texas—Pecos sheet.* Austin: University of Texas, Bureau of Economic Geology.

Beckman, P., and A. Spizzichino (1963). *The scattering of electromagnetic waves from rough surfaces.* New York: Macmillan.

Briggs, G., and D. Roeder (1975). Sedimentation and plate tectonics, Ouachita Mountains and Arkoma Basin. In G. Briggs, E. F. McBride, and R. J. Moiola (Eds.), *Sedimentology of Paleozoic flysch and associated deposits, Ouachita Mountains–Arkoma Basin, Oklahoma.* Dallas Geological Society, 1–22.

Burke, K., and J. F. Dewey (1973). Plume-generated triple junctions: Key indicators in applying plate tectonics to old rocks. *J. Geol., 81,* 406–433.

Dalziel, M. C., and T. J. Donovan (1980). Biogeochemical evidence for subsurface hydrocarbon occurrence, Recluse oil field, Wyoming: Preliminary results. *U.S. Geol. Surv. Circ. 837.*

Davis, J. C. (1973). *Statistics and data analysis in geology.* New York: John Wiley & Sons.

Dewey, J. F., and J. M. Bird (1970). Mountain belts and the new global tectonics. *J. Geophys. Res., 75,* 2625–2647.

Dittemore, W. H., Jr., and E. L. Blum (1975). *Soil survey of Ward County, Texas City.* USDA Soil Conservation Service in cooperation with Texas Agricultural Experiment Station.

Donovan, T. J. (1974). Petroleum microseepage at Cement, Oklahoma—Evidence and mechanism. *AAPG Bull., 58,* 51–64.

Donovan, T. J., A. R. Barringer, R. S. Foote, and R. D. Watson (1975). Low-altitude remote sensing experiments at Cement and Davenport oil fields, Oklahoma. *Proceedings of the Annual SEG Meeting.* Denver, Colorado.

Fairbridge, R. W. (Ed.) (1972). *The encyclopedia of geochemistry and environmental sciences—Encyclopedia of earth sciences series* (IVA). Stroudsburg, Pennsylvania: Dowden, Hutchinson and Ross.

Fok, H. W. (1972). Deep subsurface structure of the western part of Pecos County, Texas. Unpublished master's thesis, University of Texas, Austin.

Galley, J. E. (1971). Summary of petroleum resources in Paleozoic rocks of region 5—north, central, and west Texas and eastern New Mexico. In I. H. Cram (Ed.), Future petroleum provinces of the United States, *AAPG Mem. 15*, 726–737.

Goetz, A. F. H., F. C. Billingsley, A. R. Gillespie, M. J. Abrams, E. M. Squires, E. M. Shoemaker, I. Lucchitta, and D. P. Elston (1975). *Applications of ERTS images and image processing to regional geologic problems and geologic mapping in northern Arizona* (JPL Technical Report 32–1597). Pasadena, California: Jet Propulsion Laboratory.

Goetz, A. F. H., and L. C. Rowan (1981). Geologic remote sensing. *Science, 211*, 781–791.

Graham, S. A., W. R. Dickinson, and R. V. Ingersoll (1975). Himalayan–Bengal model for flysch dispersal in the Appalachian–Ouachita system. *Geol. Soc. Am. Bull., 86*, 273–286.

Guinan, M. A. (1971). More evidence of the slide-block event will follow Delaware Basin drilling. *Oil Gas J., 69*, 120–127.

Halbouty, M. T. (1976). Application of Landsat imagery to petroleum and mineral exploration. *AAPG Bull., 60*, 745–793.

Hills, J. M. (1968). Gas in Delaware and Val Verde Basins, West Texas and southeastern New Mexico. In Natural gases of North America, Part 3, Natural gases in rocks of Paleozoic age, *AAPG Mem. 9, 2*, 1394–1432.

Hills, J. M. (1970). Late Paleozoic structural directions in southern Permian Basin, West Texas and southeastern New Mexico. *AAPG Bull., 54*, 1809–1827.

Holmquist, H. J. (1965). Deep pays in Delaware and Val Verde Basins. In Fluids in subsurface environments—A symposium, *AAPG Mem. 4*, 257–279.

Horack, R. L. (1974). How Permian Basin, Great Basin relate. *Oil Gas J., 72*, 136–141.

Hovis, W., J. Nichols, A. Potter, and F. Thompson (1975). *Landsat-D Thematic Mapper technical working group final report* (JSC-09797). Houston: Lyndon B. Johnson Space Center.

Hunt, G. R., and J. W. Salisbury (1970a). Visible and near-infrared spectra of minerals and rocks: I. Silicate minerals. *Mod. Geol., 1*, 283–300.

Hunt, G. R., and J. W. Salisbury (1970b). Visible and near-infrared spectra of minerals and rocks: II. Carbonates. *Mod. Geol., 2*, 23–30.

Hunt, G. R., and J. W. Salisbury (1976). Visible and near-infrared spectra of minerals and rocks: XI. Sedimentary rocks. *Mod. Geol., 5*, 211–217.

Hunt, G. R., J. W. Salisbury, and C. J. Lenhoff (1971a). Visible and near-infrared spectra of minerals and rocks: III. Oxides and hydroxides. *Mod. Geol., 2*, 195–205.

Hunt, G. R., J. W. Salisbury, and C. J. Lenhoff (1971b). Visible and near-infrared spectra of minerals and rocks: IV. Sulphides and sulphates. *Mod. Geol., 3*, 1–14.

Hunt, G. R., J. W. Salisbury, and C. J. Lenhoff (1972). Visible and near-infrared spectra of minerals and rocks: V. Halides, phosphates, arsenates, vanadates and borates. *Mod. Geol.*, *3*, 121–132.

Hunt, G. R., J. W. Salisbury, and C. J. Lenhoff (1973). Visible and near-infrared spectra of minerals and rocks: VI. Additional silicates. *Mod. Geol.*, *4*, 85–106.

Jaco, H. B., W. L. Miller, J. L. Rives, W. Dittmore, A. Turner, and A. Kosse (1980). *Soil survey of Reeves County, Texas City.* USDA Soil Conservation Service in cooperation with Texas Agricultural Experiment Station.

Keller, G. R., and S. E. Cebull (1973). Plate tectonics and the Ouachita System in Texas, Oklahoma and Arkansas. *Geol. Soc. Am. Bull.*, *83*, 1659–1666.

King, P. B. (1959). *The evolution of North America.* Princeton, New Jersey: Princeton University Press.

Leonard, A. B., and J. C. Frye (1962). Pleistocene Molluscan faunas and physiographic history of Pecos Valley in Texas. *Texas Bureau Econ. Geol., Rept. Invest.*, No. 45.

Maley, V. C., and R. M. Huffington (1953). Cenozoic fill and evaporate solution in the Delaware Basin, Texas and New Mexico. *Geol. Soc. Am. Bull.*, *66*, 539–546.

McGlasson, E. H. (1969). The Silurian-Devonian of West Texas and Southeast New Mexico. In *West Texas Geol. Soc. Guidebook, Delaware Basin exploration*, No. 68-55a, 35–44.

National Oceanic and Atmospheric Administration (1975–1977, 1980–1981). *Climatological data.* Ashville, North Carolina: Texas Environmental Data and Information Service, National Climatic Center.

Nicolas, R. L., and R. A. Rozendal (1975). Subsurface positive elements within Ouachita Foldbelt in Texas and their relation to Paleozoic cratonic margin. *AAPG Bull.*, *59*, 193–216.

Ogilbee, W., J. B. Weselman, and B. Irelan (1962). Geology and groundwater resources of Reeves County, Texas. *Texas Water Commission Bull. 6214, 1.*

Rives, J. L., P. H. Flores, and E. Blum (1980). *Soil survey of Pecos County, Texas.* USDA Soil Conservation Service in cooperation with Texas Agricultural Experiment Station.

Siegal, B. S., and A. F. H. Goetz (1977). Effects of vegetation on rocks and soil type discrimination. *Photogr. E. R.*, *43*, 191–196.

Siegel, S. (1956). *Nonparametric statistics.* Tokyo, Japan: McGraw–Hill Kogakusha.

Texas Almanac (1978). Galveston, Texas: A. H. Belo Corporation.

Texas Instruments, Inc. (1966). *A geologic evaluation of selected airborne remote sensing techniques, Coyanosa, Texas.* Dallas: Science Service Division, Sec. II–V.

Texas Railroad Commission (1980). *Production statistics and reserves for District 8, 1979.* Austin, Texas: Oil and Gas Division.

Trollinger, W. V. (1968). Surface evidence of deep structure in the Delaware Basin. In *Delaware Basin exploration guidebook* (Publication 68-55). Midland, Texas: West Texas Geological Society, 87–104.

Vertress, C., C. H. Atchison, and G. L. Evans (1959). Paleozoic geology of the Val Verde Basin. In *Geology of the Val Verde Basin and field trip guidebook*. Midland, Texas: West Texas Geological Society, 64–73.

Warner, C. A. (1939). *Texas oil and gas since 1543*. Houston: Gulf Publishing Company.

Wickham, J., D. Roeder, and G. Briggs (1976). Plate tectonics models for the Ouachita Foldbelt. *Geology, 4,* 173–176.

Wilson, H. T. (1969). Coyanosa field. In *Oil and gas fields in West Texas*. Symposium presented at the meeting of the West Texas Geological Society, Midland, Texas, 66–70.

Appendix A
Remote Sensing Data Acquired for Exxon

Table A-1. Remote sensing data acquired for Exxon during a 1966 study[a] of the Coyanosa area and made available for the joint NASA/Geosat test site investigation

Sensor Designation in Report	Sensor	Wavelengths (microns)	Film	Filter(s)	Altitude (ft)	Time	Date (1966)	Approximate Scale	Remarks and Purposes for Film/Filter Selections
EK/3 & 4 Color	Aerial Camera	0.38 - 0.72	Ektachrome Aero 8442	HF-3 & 4 Antivignette	10,000	1038-1307 1024-1124 1004-1557 0950-1446	7 & 16 May 23 Sept	1:68,600	Evaluate quality and quantity of provided data against other film/filter combinations
ICF/16 CD	Aerial Camera	0.54 - 0.90	Ektachrome IR Aero 8443	Tiffen 16 Antivignette	10,000	1038-1307 1024-1124 1004-1557 0950-1446	7 & 16 May 23 Sept	1:68,600	Evaluate quality and quantity of provided data against other film/filter combinations
IR/88A	Aerial Camera	0.72 - 0.90	IR Aerographic 5424	Wratten 88A Antivignette	10,000	1038-1307 1024-1124 1004-1557 0950-1446	7 & 16 May 23 Sept	1:68,600	Record near-infrared wavelengths only for maximum haze penetration and land-water contrast
X/12	Aerial Camera	0.50 - 0.72	Panchromatic Plus-X Aerocon 8401	Wratten 12 Antivignette	10,000	1038-1647 1024-1124 1004-1557 0950-1446	7 & 16 May 23 Sept	1:68,600	Film currently in general use for aerial photography and for use as the standard for comparison on this project
X/167	Aerial Camera	0.63 - 0.69	Panchromatic Plus-X Aerocon 8401	OCLI - 167 Corning 2-59 Antivignette	10,000	1040-1437 1027-1047	8 & 14 May	1:68,600	Enhance contrast of vegetation and drainage vs soil
X/13	Aerial Camera	0.49 - 0.57	Panchromatic Plus-X Aerocon 8401	Tiffin 13 Antivignette	10,000	1040-1437 1027-1047	8 & 14 May	1:68,600	Enhance contrast of Triassic vs Cretaceous sediments (Trinity and Fredericksburg Groups). Enhance contrast between stations 41 and 14 vs "norm"
IR/87C	Aerial Camera	0.83 - 0.90	IR Aerographic 5424	Wratten 87C Antivignette	10,000	1040-1437 1027-1047	8 & 14 May	1:68,600	Enhance contrast of dunes and surrounding caliche surface. Possibly differentiate Trinity and Fredericksburg Groups vs caliche
X/5-59	Aerial Camera	0.37 - 0.48	Panchromatic Plus-X Aerocon 8401	Corning 5-59 Antivignette	10,000	1040-1437 1027-1047	8 & 14 May	1:68,600	Enhance contrast of calcareous deposits vs other soil and bare rock
IR_1-Night 10,000 ft	RS-7 infrared scanner	2-14 (approximately)	RAR 5498	None	10,000	0240 0522	7 May	—	Far-infrared imagery. Record surficial geologic data through variations in radiometric temperatures and compare to photographic data
IR_1-Day	RS-7 infrared scanner	8-14	RAR 5498	3-5 microns filtered out	10,000	1038-1647	7 May	—	
IR_1-Day 2000 ft	RS-7 infrared scanner	8-14	RAR 5498	3-5 microns filtered out	2,000	0858-1152 1040-1438	9 & 12 May	—	
Radar	TAR-1 side-looking scanner	8600 (0.86 cm)	Photoflure Blue	—	2,000	0858-1152 0635-0816	9 & 12 May	1:250,000	Evaluate quality and quantity of provided data against other sensor systems

[a]Texas Instruments, Inc. (1966).

Appendix B
Geochemical Survey Laboratory Procedures/Analytical Results

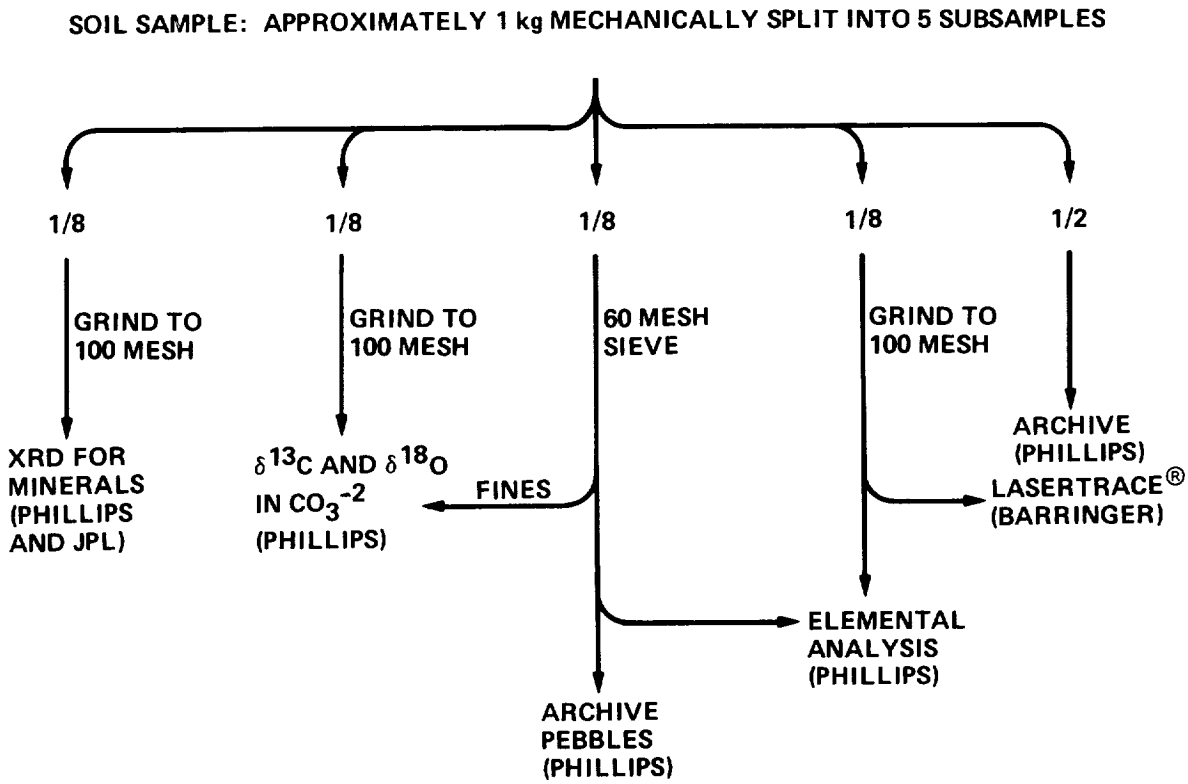

Figure B-1. Sample handling procedure for 1979 Coyanosa test site samples

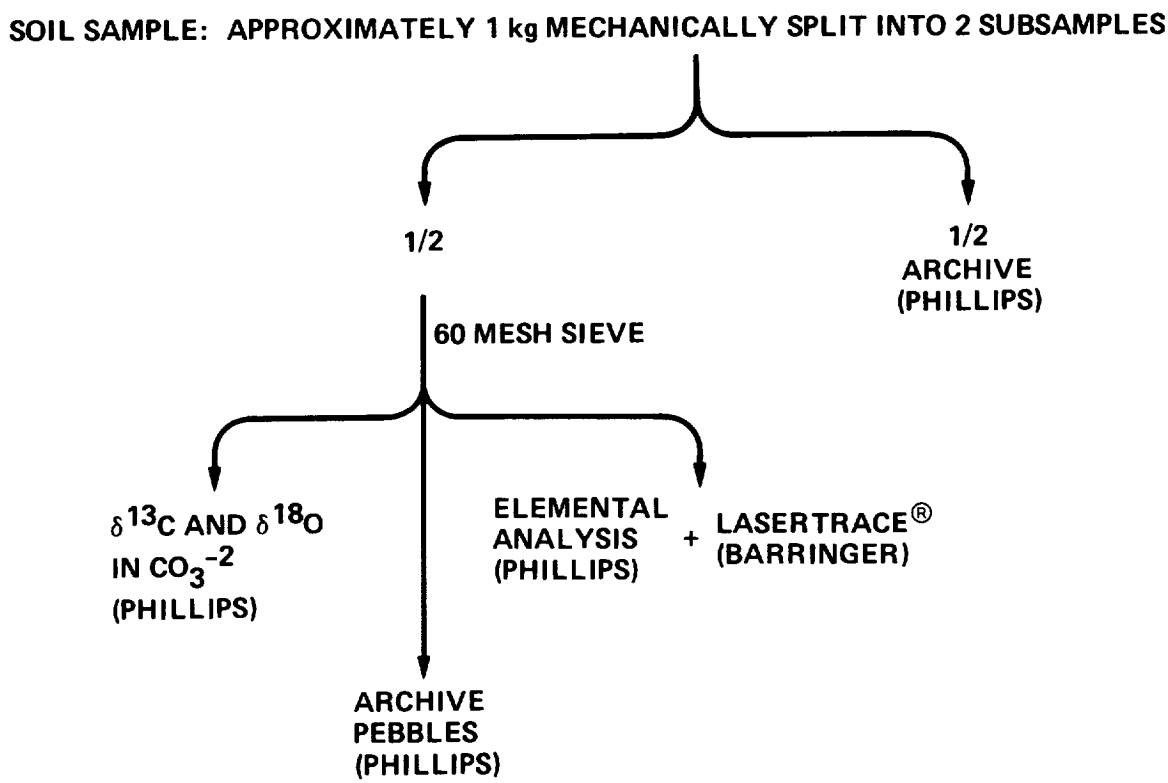

Figure B-2. Sample handling procedure for 1980 Coyanosa test site samples

Table B-1. Elements determined and analytical procedures used for measurements by Phillips

Element	Analysis	Unit
Be	ICP–AES	ppm
Na	ICP–AES	ppm
Mg	ICP–AES	ppm
K	ICP–AES	ppm
Cu	ICP–AES	ppm
Sr	ICP–AES	ppm
Ti	ICP–AES	ppm
V	ICP–AES	ppm
Cr	ICP–AES	ppm
Mu	ICP–AES	ppm
Fe	ICP–AES	ppm
Co	ICP–AES	ppm
Ni	ICP–AES	ppm
Cu	ICP–AES	ppm
Zn	ICP–AES	ppm
Mo	ICP–AES	ppm
Ag	ICP–AES	ppm
Cd	ICP–AES	ppm
P	ICP–AES	ppm
Al	NAA	wt %
Si	NAA	wt %
O	NAA	wt %
As	HGAA	ppm
S	LECO®	wt %
C_{org}	C–GC	wt %
C_{tot}	C–GC	wt %
$\delta^{13}C$		o/oo PDB
$\delta^{18}O$		o/oo PDB

ICP–AES	Inductively coupled plasma atomic emission spectroscopy
NAA	Neutron activation analysis
HGAA	Hydride generation atomic absorption spectroscopy
C–GC	Phillips combustion gas chromatography
ppm	Parts per million
wt %	Weight percent
o/oo	Parts per thousand relative to PDB
LECO®	Induction furnace combustion

Table B-2. Phillips geochemical data[a]

OBS	CODE	NA	MG	K	CA	SR	TI	V	CR	MN	FE	CO	NI	CU
1	CA001	9790	7100	17400	48100	282.0	3300	48.0	25.6	267	19300	6.1	4.0	28.3
2	CA002	2610	15200	6480	161000	1510.0	1110	20.0	13.7	172	8710	6.0	4.0	28.2
3	CA003	5480	10500	10300	108600	1020.0	1600	24.6	14.2	175	10300	6.1	4.1	28.5
4	CA004	9140	8100	18200	55800	301.0	2820	39.6	32.2	281	19700	5.8	4.9	27.2
5	CA005	9520	5120	16800	62000	197.0	2580	31.3	19.0	185	15300	5.3	3.9	24.5
6	CA006	11600	4130	19600	38100	147.0	3400	36.4	19.1	206	18400	5.7	3.8	26.7
7	CA007	11000	4700	20000	43600	153.0	3060	35.6	8.3	215	18600	6.2	4.2	29.1
8	CA008	10800	4210	19200	38000	148.0	3570	43.3	22.3	232	20200	5.9	3.9	27.5
9	CA009	10300	5120	19300	62300	194.0	2590	38.2	20.3	208	16100	6.3	7.2	29.5
10	CA010	9270	4010	16700	51200	157.0	3480	40.5	20.3	220	19700	5.7	3.8	26.6
11	CA011	7450	2660	18900	43300	121.0	2890	46.8	13.5	198	21500	6.3	4.2	29.5
12	CA012	10300	4520	19900	40400	134.0	3090	37.6	21.3	223	19200	5.6	3.7	26.1
13	CA013	10400	3570	19000	20900	101.0	3030	36.1	21.3	196	18600	5.1	3.4	23.6
14	CA014	9450	4030	18200	25800	106.0	3070	36.2	21.4	204	18400	5.1	3.4	23.7
15	CA015	8560	4870	17300	22500	135.0	3640	42.5	13.5	232	19800	10.0	17.7	46.5
16	CA016	5190	8910	20600	53900	151.0	2800	50.7	34.6	347	25100	5.9	10.5	28.3
17	CA016A	5350	9940	21400	57900	175.0	2980	50.6	36.7	373	27200	5.7	3.8	26.4
18	CA017-01	2250	2840	9240	149000	136.0	1600	40.2	13.7	117	12200	5.6	8.4	26.2
19	CA017-02	4070	2160	9230	110800	111.0	1680	30.5	9.9	116	10200	9.2	21.1	27.6
20	CA018	674	1810	20200	20900	105.0	1540	164.0	21.7	2	46100	5.9	3.9	27.5
21	CA019	650	1890	14000	164700	109.0	834	69.8	93.7	1990	24600	10.2	38.0	26.2
22	CA020	9290	3580	17300	26000	102.0	3250	38.1	20.7	214	19100	5.4	3.6	25.0
23	CA021	9080	5130	17700	36800	121.0	3660	46.4	23.4	255	21200	7.0	4.0	28.1
24	CA022	7290	6030	18300	50200	165	2540	42.5	24.9	251	19300	7.8	4.6	25.4
25	CA023	8210	7960	21400	43800	227.	3140	48.2	26.1	397	23600	6.0	3.9	27.2
26	CA024	9880	6340	21200	36300	138.0	2880	40.9	23.3	342	20300	6.1	4.0	28.3
27	CA025	8780	6780	21600	32900	130.0	2600	37.7	33.4	299	20800	5.7	4.9	26.7
28	CA026	8870	6210	19100	53900	373.0	2460	38.4	23.7	228	16900	5.7	3.8	26.6
29	CA027	9450	7180	23200	44800	148.0	3190	45.9	31.5	341	22100	5.4	3.6	25.1
30	CA028	11200	4180	20500	21300	114.0	3790	43.8	25.6	245	22800	5.6	3.8	26.3
31	CA029	8210	5110	17500	32700	104.0	3190	38.8	27.9	256	21000	5.3	3.5	24.5
32	CA030	8290	7200	20000	18300	97.2	3280	45.8	37.6	336	25500	5.6	5.1	26.0
33	CA031	9710	5100	19200	25100	106.0	3900	48.3	35.4	294	24500	5.8	3.9	27.0
34	CA032	8500	3410	15400	55900	109.0	3530	42.7	31.5	212	20600	6.4	7.0	26.4
35	CA033	9310	2850	16400	20400	79.3	3020	36.7	27.6	192	18400	9.6	12.6	24.3
36	CA034	9610	6280	20200	45500	125.0	3080	45.0	32.1	351	22800	11.7	17.2	27.2
37	CA035	9490	9210	17500	54300	519.0	2730	39.4	34.2	438	18200	11.8	15.7	26.1
38	CA036	9410	9770	21100	46600	290.0	3010	48.9	39.9	621	23600	12.5	14.4	25.7
39	CA037	9980	4050	22100	7040	91.8	3020	45.0	27.8	257	23000	6.7	3.6	25.5
40	CA038	14300	2840	25900	6760	91.3	2670	33.9	24.4	198	19600	5.5	3.6	25.5
41	CA039	12800	3980	24200	9260	111.0	4110	46.6	26.0	267	25000	5.7	3.8	26.6
42	CA040	15500	6430	28400	14300	88.3	5350	65.5	61.7	340	39200	5.9	3.9	27.5
43	CA041	13000	7350	25900	28600	139.0	4030	49.1	31.3	506	28400	5.7	3.5	24.6
44	CA042	10600	7510	2300	38700	175.0	3360	46.5	33.1	610	24100	9.5	3.7	26.2
45	CA043	10600	5380	22800	12300	117.0	3700	49.0	31.2	297	25300	5.8	3.9	27.1
46	CA044	11300	3270	21400	10100	101.0	3720	44.4	23.7	236	22800	5.5	3.7	25.6
47	301	4650	3700	12200	59600	169.0	1940	36.1	16.6	149.0	14400	6.50	4.4	30.5
48	302	5540	3290	14200	55200	155.0	1930	29.7	16.6	134.0	13700	7.00	4.6	32.5
49	303	5330	3430	13900	24500	109.0	2580	45.4	20.7	195.0	21500	6.50	4.3	30.4
50	304	6360	3070	14200	15700	90.6	2540	39.9	21.0	164.0	19000	6.50	4.1	30.1
51	305	6610	4260	14800	29700	114.0	2740	44.4	22.5	201.0	21100	6.00	4.0	27.9
52	306	7210	3040	14200	7310	84.0	2460	33.7	18.8	185.0	16900	6.60	4.4	30.7
53	307	5340	3830	12300	20600	85.2	1590	23.9	15.4	110.0	11500	6.70	4.5	31.3
54	308	5780	4090	15700	39400	131.0	2440	41.6	23.3	168.0	19100	6.60	4.4	30.9
55	309	5580	11100	14200	92300	1600.0	1790	36.3	30.1	223.0	14600	6.60	4.4	30.7
56	310	4740	8250	11100	77400	1380.0	1520	24.0	17.7	160.0	11300	6.40	4.3	29.8
57	310B	7320	7380	15700	28500	374.0	1930	34.5	24.9	215.0	14900	6.20	4.1	29.0
58	311	4220	2040	10800	6940	102.0	827	11.8	9.3	63.6	6860	6.10	4.1	28.5
59	312	8540	8020	17900	26500	228.0	2010	31.7	23.5	206.0	16300	6.60	4.4	30.7
60	313	8720	10300	18100	26100	264.0	2030	31.9	22.9	277.0	16300	6.80	4.5	31.8
61	314	7990	4220	17100	14700	169.0	1770	27.3	22.6	185.0	15700	6.70	4.5	31.3
62	315	5450	2120	12600	2330	60.5	1250	18.2	14.6	117.0	11900	6.50	4.3	30.4
63	316	4140	4190	9040	61400	142.0	2080	42.4	18.2	162.0	19200	6.50	4.3	30.3
64	317	8450	3380	13300	38900	149.0	1340	19.4	14.1	202.0	11100	6.40	4.3	30.0
65	401	11600	6300	18900	66900	639.0	2430	35.4	15.8	230.0	19900	7.20	4.5	30.2
66	402	12300	7520	24800	37300	180.0	2890	43.3	30.1	437.0	27300	12.30	4.0	28.3
67	403	10000	8020	23100	53700	181.0	2830	54.7	28.8	370.0	29500	15.00	3.7	25.6
68	404	10200	9190	22900	42800	173.0	2890	49.2	32.1	511.0	32000	18.70	4.0	28.3
69	405	12900	7900	24000	34300	162.0	3150	47.4	31.5	472.0	30900	16.40	4.4	30.6
70	406	8780	11000	25100	50800	186.0	3140	55.5	36.2	540	36500	15.60	4.5	31.6
71	407	12500	7760	26400	27400	144.0	3030	46.8	30.2	388	31300	12.10	4.6	31.9
72	408	9380	10900	25000	56400	208.0	3460	55.2	32.4	554	34000	13.90	4.5	31.3
73	409	13400	4700	25000	20400	99.2	3010	33.3	23.3	238	24000	6.50	4.3	30.3
74	410	11800	6080	24400	22300	113.0	3590	42.1	29.8	282	26200	8.80	4.3	30.4
75	411	11400	8220	27800	55600	223.0	3430	44.6	24.5	337	28200	7.10	4.7	33.1
76	412	14500	2980	24800	33800	112.0	2610	26.4	13.7	198	18600	6.10	4.1	28.7
77	413	10400	4280	19500	70700	196.0	3310	34.3	20.0	219	21200	6.40	4.2	29.7
78	414	8940	5900	19400	68800	278.0	2570	40.7	24.1	240	19500	6.50	4.3	30.2
79	415	9750	5430	18500	41700	159.0	3190	35.2	20.6	241	22000	6.40	4.2	29.7
80	416	11400	4900	20400	33400	150.0	3230	34.7	20.1	254	20700	15.50	3.9	27.6
81	417	10300	5290	19500	50900	155.0	2690	32.2	19.6	246	19300	13.80	4.3	30.2
82	418	10500	4530	19900	45500	148.0	2770	31.0	22.0	211	18000	13.00	4.1	28.5
83	419	9810	6320	20800	28700	136.0	2380	33.1	24.4	375	19500	18.50	3.9	27.3
84	420	9940	5540	18900	52400	162.0	2510	34.0	21.6	247	18000	16.40	4.4	30.5
85	421	12200	4310	21100	42400	147.0	2860	33.0	20.4	210	18400	5.90	4.0	27.8
86	422	10700	3880	19000	36700	123.0	2840	31.6	19.6	196	18000	5.80	3.9	27.2
87	423	7700	10800	21400	66500	281.0	2580	45.4	31.1	434	24800	6.50	3.9	27.3
88	424	8480	20500	14500	69600	1170.0	1710	30.8	18.0	232	12900	5.60	3.8	26.3
89	425	9040	12900	19100	56300	266.0	2280	45.3	30.4	334	20100	5.50	3.7	25.9
90	425A	11700	22900	21200	55200	326.0	2790	70.4	43.7	441	30600	9.20	3.7	26.0
91	426	7510	17700	21700	58400	299.0	2870	58.5	41.6	470	28200	7.30	3.6	25.0
92	427	12600	5430	22600	53400	198.0	27000	32.2	16.2	252	18400	5.40	3.6	25.2
93	428	11600	5250	21700	53600	164.0	2940	34.0	17.6	241	20100	5.10	3.4	23.9
94	429	11600	5400	22900	57600	192.0	2290	28.1	14.4	235	17000	5.90	3.9	27.4

[a]Soil from Coyanosa test site samples collected in 1979 and 1980; the 1979 samples begin with "CA."

Table B-2 (Continued)

OBS	CODE	NA	MG	K	CA	SR	TI	V	CR	MN	FE	CO	NI	CU
95	50	12400	4940	22600	35100	158.0	3980	45.4	36.6	249	24800	6.33	4.2	29.2
96	51	13200	4640	23900	20600	133.0	3520	43.6	36.8	269	24000	7.00	4.7	32.7
97	52	11900	5810	23400	29500	147.0	3730	47.8	40.1	288	25700	7.80	4.3	30.3
98	53	12200	6310	24500	27900	149.0	3280	43.0	41.0	318	24700	6.20	4.1	28.8
99	54	14400	3700	25000	11900	109.0	3530	38.5	34.1	246	23300	6.30	4.2	29.3
100	55	14100	2950	23900	14400	103.0	3450	37.8	30.4	234	22200	6.70	4.4	31.1
101	56	14100	2900	24400	8050	94.9	3610	41.7	33.5	227	24500	6.60	4.4	30.7
102	57	13700	3270	23900	16100	107.0	3890	45.3	40.2	238	25900	6.90	4.6	32.4
103	58	10700	6660	25700	19200	134.0	3110	48.7	43.5	303	27300	7.60	4.2	29.2
104	59	11600	5990	25200	25200	132.0	3180	44.8	44.9	318	2440	6.70	4.5	31.4
105	60	11000	6320	25900	9390	97.8	3410	49.2	44.1	313	29500	7.20	4.0	28.2
106	61	12300	5070	24300	20300	118.0	3210	43.2	39.2	290	25300	6.80	4.5	31.5
107	62	12200	4850	24000	17200	111.0	3330	44.1	39.2	286	25300	6.00	4.0	27.9
108	63	12600	3660	22800	16900	97.7	3400	41.1	35.2	232	24200	6.40	4.2	29.2
109	64	14600	3050	23900	26200	126.0	3620	38.3	32.7	230	22900	6.80	4.5	31.8
110	65	12600	6520	26300	46000	163.0	3490	45.3	41.7	300	26700	8.10	4.5	31.3
111	66	12900	2590	22700	11900	80.1	2510	30.6	15.1	197	19600	6.50	4.3	30.4
112	67	12900	2670	22900	7050	82.1	3700	35.5	15.2	222	23100	6.60	4.4	30.6
113	68	9670	8530	24500	28500	160.0	3130	49.1	32.5	432	27400	9.10	4.4	30.6
114	69	10700	8210	23100	66200	205.0	3530	54.0	25.1	347	28500	8.90	4.1	28.4
115	70	10200	8820	25700	38800	166.0	3680	58.7	31.4	712	35300	12.40	4.6	32.1
116	71	11500	8250	23100	42600	190	3310	49.4	25.0	513	29000	12.1	4.7	33.1
117	72	12000	6080	23400	26900	155	3640	45.0	26.4	308	25000	7.2	4.4	31.1
118	73	12900	3960	22400	42900	179	2190	24.8	16.2	176	15100	6.7	4.5	31.3
119	74	10800	4480	18400	48600	153	3570	38.5	20.8	239	21400	6.7	4.5	31.3
120	75	11400	3180	19700	31100	129	1990	25.7	13.2	149	14200	6.4	4.2	29.7
121	76	10500	4670	17200	87200	359	1730	28.0	15.9	158	13500	6.5	4.3	30.4
122	77	11100	3560	19100	40600	166	3110	37.5	17.3	216	19500	6.4	4.2	29.7
123	78	11000	5080	20000	43100	165	3460	42.6	24.4	232	22200	6.6	4.1	28.4
124	79	9440	5920	20700	38700	151	2340	35.0	21.1	282	21000	7.5	4.0	28.2
125	80	11700	4100	20500	26000	147	4170	45.6	23.1	251	24400	7.2	4.2	29.1
126	81	11800	3860	20100	21300	141	2400	30.2	16.9	194	17900	7.6	4.5	31.5
127	82	11000	5480	20700	36500	180	2740	37.5	46.2	259	20700	7.3	4.5	31.6
128	83	10400	6600	22900	37900	176	2840	44.4	28.7	294	22900	6.8	4.5	31.8
129	84	7550	7240	12800	94400	1070	2000	36.5	16.1	155	14100	6.4	4.3	29.8
130	85F	10000	6810	21800	27000	153	3000	42.9	22.7	305	22700	7.1	4.8	33.3
131	86E	9210	4280	19400	24000	125	2900	31.2	16.5	206	18800	6.7	4.5	31.2
132	87D	10400	3860	20300	23300	120	3250	34.4	16.9	209	20300	6.7	4.5	31.2
133	88C	10400	5880	22600	16500	140	2950	37.6	23.8	289	22300	6.6	4.4	31.0
134	89G	10700	5820	23200	27800	138	2890	35.7	19.9	277	21600	5.9	4.0	27.7
135	90H	11100	5310	22000	19100	151	2880	35.8	22.3	235	18700	6.0	4.0	27.9
136	91A	10300	5130	20200	30900	146	3830	40.0	23.7	250	22400	6.1	4.0	28.2
137	92H	10200	4270	19000	40300	134	3640	44.0	23.5	252	23400	6.1	4.1	28.6
138	93I	10600	3840	19400	25100	114	2890	33.4	18.7	207	20400	6.3	4.2	29.2

Table B-2 (Continued)

OBS	ZN	MO	AG	CD	P	AL	SI	O	AS	S	CORG	CTOT	C13	O18
1	61.9	8.1	28.9	6.3	249.0	3.90	32.40	50.7	7.55	0.23	0.736	1.822	-8.237	-4.673
2	45.9	8.1	20.1	2.0	149.0	1.53	8.86	51.7	5.30	11.34	0.466	1.055	-2.489	-3.128
3	43.8	8.1	20.4	2.8	128.0	2.80	16.90	.	3.96	7.98	0.688	1.671	-6.100	-3.210
4	72.5	7.8	19.4	3.4	247.0	5.03	28.30	48.3	5.52	0.17	0.485	2.235	-8.858	-4.451
5	66.4	7.0	17.5	3.1	170.0	3.94	29.70	49.4	3.58	0.05	0.510	2.696	-5.726	-3.683
6	46.7	7.6	19.1	2.4	191.0	4.06	33.30	49.3	2.95	0.05	0.373	1.484	-5.949	-4.746
7	47.8	8.3	20.8	2.8	196.0	4.27	31.50	48.4	2.71	0.05	0.598	1.795	-7.906	-4.400
8	62.9	7.9	19.7	2.9	186.0	4.04	31.80	49.3	3.98	0.05	0.431	1.498	-7.978	-5.247
9	69.4	8.4	21.0	3.2	257.0	4.10	29.60	49.8	4.12	0.05	0.584	2.644	-6.114	-4.621
10	47.1	7.6	19.0	6.2	110.0	3.50	30.70	46.8	2.72	0.05	0.303	1.832	-7.022	-5.189
11	39.8	8.4	21.1	4.2	108.0	3.31	33.40	47.8	4.21	0.05	0.290	1.624	-6.391	-5.449
12	51.8	7.9	18.7	3.4	228.0	4.38	31.70	48.2	5.88	0.05	0.531	1.551	-6.468	-4.891
13	58.2	11.3	16.9	3.4	166.0	4.30	33.90	47.4	2.88	0.05	0.514	1.004	-6.843	-4.704
14	75.6	10.8	16.9	3.3	230.0	4.83	33.30	.	4.17	0.05	0.636	1.428	-6.535	-4.765
15	109.0	13.4	33.2	5.0	263.0	5.32	34.90	52.6	4.76	0.05	0.590	1.329	-5.582	-5.267
16	86.4	22.5	19.8	4.8	646.0	6.30	26.30	51.3	5.86	0.05	0.894	2.479	.	.
17	81.8	7.6	18.9	3.5	640.0	6.31	24.10	49.9	6.31	0.05	1.110	2.890	.	.
18	34.7	7.5	18.7	2.6	28.0	2.74	17.40	47.3	9.10	0.05	0.349	6.379	-7.069	-5.083
19	33.6	23.1	24.9	3.9	107.0	2.82	19.30	48.5	5.65	0.05	0.560	5.848	.	.
20	26.9	7.9	19.7	5.2	133.0	3.98	34.10	48.7	15.90	0.05	0.509	0.973	.	.
21	65.0	17.5	18.7	1.9	427.0	3.27	17.60	48.8	13.80	0.05	.	.	.	.
22	48.1	7.1	17.8	3.5	229.0	4.15	34.50	48.7	3.19	0.05	0.381	1.165	-6.018	-5.143
23	54.8	8.0	20.1	4.4	357.0	4.34	33.10	50.4	3.08	0.05	0.394	1.385	-5.702	-4.788
24	57.5	7.3	18.1	4.2	353.0	4.64	30.3	49.1	5.13	0.05	0.601	2.226	-5.093	-4.388
25	59.8	7.8	19.5	4.3	504.0	4.87	30.1	51.0	3.47	0.05	0.640	1.771	-5.449	-5.767
26	52.7	8.1	20.2	3.1	338.0	5.01	30.6	48.7	4.54	0.05	0.514	1.497	-2.087	-4.207
27	71.2	7.6	19.1	3.7	440.0	5.43	30.6	48.5	5.49	0.05	0.526	1.405	-4.207	-3.719
28	61.9	7.6	19.0	3.7	327.0	4.26	30.4	48.7	3.42	0.05	0.644	2.308	-7.325	-4.707
29	67.9	7.2	17.9	3.8	656.0	5.23	29.3	48.6	4.60	0.05	0.833	2.005	-3.221	-3.704
30	59.0	7.5	18.8	1.9	241.0	4.45	34.8	48.6	3.52	0.05	0.382	0.885	-7.000	-4.783
31	55.0	7.0	17.5	3.6	292.0	4.80	32.4	49.0	3.44	0.05	0.602	1.494	-6.876	-4.753
32	69.3	7.4	18.6	2.7	385.0	5.46	32.6	51.5	3.97	0.05	0.527	0.922	-4.030	-2.860
33	63.3	7.7	19.3	3.1	337.0	4.80	33.1	46.1	4.31	0.05	0.467	1.010	-5.462	-4.107
34	64.3	7.5	18.9	3.1	218.0	3.68	31.7	49.4	3.55	0.05	0.365	2.126	-4.600	-4.970
35	46.4	16.7	17.7	4.3	252.0	4.05	35.5	48.7	3.04	0.05	0.269	0.760	-5.536	-5.158
36	110.0	23.7	21.3	5.8	573.0	5.69	29.2	48.8	3.91	0.05	0.695	1.987	-3.745	-4.233
37	60.9	16.1	18.6	3.8	572.0	4.62	28.8	49.1	2.87	0.46	0.724	2.188	-4.045	-4.024
38	77.1	17.4	18.4	4.3	846.0	5.74	28.8	48.9	5.37	0.05	0.645	1.855	-3.257	-5.614
39	60.2	7.3	18.2	4.9	201.0	4.70	35.2	48.8	2.87	0.05	0.497	0.601	-8.662	-6.154
40	58.1	7.3	18.2	2.5	216.0	4.68	36.3	47.7	1.71	0.17	0.466	0.601	-7.068	-7.391
41	60.3	7.6	19.0	1.9	259.0	4.55	35.4	49.6	3.76	0.05	0.350	0.530	-6.782	-6.062
42	107.0	7.9	19.7	4.2	216.0	5.51	32.3	48.4	4.58	0.32	0.524	0.840	-4.447	-8.954
43	148.0	7.0	17.6	2.6	655.0	6.24	29.5	48.6	5.20	0.05	0.635	1.326	-1.659	-6.725
44	113.0	7.5	18.7	3.7	648.0	5.68	30.3	49.7	2.79	0.05	0.642	1.645	-5.826	-4.739
45	64.4	7.7	19.4	2.2	435.0	4.54	34.2	49.3	3.93	0.05	0.512	0.720	-5.257	-4.866
46	53.0	7.3	18.3	2.8	224.0	3.98	36.5	49.5	3.48	0.05	0.449	0.668	-7.378	-5.754
47	32.4	8.7	21.8	2.2	84.8	2.46	33.7	50.2	7.48	.	0.354	2.207	-6.09	-5.87
48	28.7	9.3	23.2	2.3	121.0	2.74	33.3	49.7	2.32	.	0.687	2.212	-6.97	-5.92
49	35.0	8.7	21.7	2.2	132.0	2.81	37.2	48.3	1.44	.	0.379	1.022	-7.22	-5.67
50	37.4	8.6	21.5	2.2	129.0	2.82	37.8	49.0	5.05	.	0.401	0.777	-6.06	-6.02
51	40.8	8.0	19.9	2.0	133.0	3.29	35.1	49.3	3.93	.	0.482	1.341	-6.36	-5.71
52	33.5	8.8	22.0	2.2	132.0	2.86	38.4	49.2	3.34	.	0.341	0.479	-6.57	-6.16
53	26.0	8.9	22.4	2.2	137.0	2.69	36.5	50.2	1.83	.	0.279	1.319	-5.77	-5.69
54	37.7	8.8	22.1	2.2	178.0	3.26	34.7	49.8	3.08	.	0.851	1.789	-8.42	-4.98
55	59.0	8.8	21.9	2.2	205.0	3.23	23.4	49.5	4.95	.	1.247	3.099	-5.63	-4.34
56	31.0	8.5	21.3	2.1	151.0	3.00	26.2	50.1	2.34	.	0.777	1.904	-8.59	-4.09
57	44.7	8.3	20.7	3.5	294.0	3.18	35.7	49.6	2.34	.	0.651	1.241	-8.14	-4.93
58	16.0	8.1	20.3	2.0	56.9	1.85	40.8	49.5	2.64	.	0.328	0.383	.	.
59	45.1	8.0	22.0	2.2	271.0	3.90	35.6	50.0	1.54	.	0.779	1.310	-8.16	-4.46
60	57.8	9.1	22.7	2.3	369.0	3.66	34.5	50.8	5.59	.	0.931	1.713	-4.55	-4.55
61	48.4	8.9	22.3	2.2	217.0	3.48	36.1	49.8	4.05	.	0.212	1.394	-6.18	-6.32
62	27.8	8.7	21.7	2.1	129.0	2.56	40.8	51.1	3.05	.	0.392	0.375	.	.
63	30.1	8.7	21.7	2.2	107.0	1.61	34.8	48.9	6.31	.	0.269	2.344	-5.98	-4.80
64	28.7	8.6	21.4	2.1	197.0	2.46	37.1	48.7	6.51	.	0.311	1.413	-4.13	-5.37
65	49.1	8.6	21.6	2.2	234.0	2.62	23.3	38.0	7.80	.	0.035	2.647	-6.56	-4.33
66	83.7	8.1	20.2	2.0	543.0	5.13	30.6	49.2	3.05	.	0.583	1.601	-3.60	-3.61
67	75.5	7.3	18.3	1.8	462.0	5.41	27.7	48.3	4.76	.	0.061	2.292	-1.41	-4.41
68	92.3	10.4	20.2	2.0	648.0	4.15	21.0	38.4	6.13	.	0.684	3.016	-3.24	-4.80
69	83.6	8.7	21.8	2.2	561.0	5.54	30.8	49.3	7.72	.	0.686	1.569	-3.79	-4.67
70	108.0	9.0	22.6	2.3	786.0	6.12	26.9	49.4	7.13	.	1.074	2.406	-2.36	-4.64
71	86.9	9.1	22.8	2.3	466.0	5.51	32.0	48.6	8.48	.	0.597	1.314	-3.04	-5.03
72	88.1	9.0	22.4	2.2	512.0	5.60	28.3	48.5	7.17	.	0.448	1.983	-1.66	-5.22
73	60.3	8.7	21.7	2.2	117.0	4.54	34.8	49.8	6.21	.	0.403	0.811	-6.78	-5.05
74	58.7	8.7	21.7	2.2	124.0	4.75	34.3	49.0	6.59	.	0.607	1.024	-9.71	-5.07
75	76.8	9.5	23.6	2.4	278.0	5.13	29.5	48.7	8.93	.	0.890	2.260	-3.56	-4.49
76	48.9	8.2	20.5	2.0	30.7	3.88	33.8	49.0	7.85	.	0.261	1.125	-4.78	-4.47
77	51.1	8.5	21.2	2.1	93.0	3.58	30.1	48.9	4.43	.	0.633	2.822	-7.13	-4.45
78	53.4	8.6	21.6	2.2	228.0	3.98	29.8	49.3	5.96	.	0.384	2.580	-5.72	-3.17
79	53.6	8.5	21.2	2.1	251.0	3.89	32.9	48.2	4.20	.	0.729	2.029	-7.13	-4.84
80	49.8	15.1	19.7	2.0	237.0	4.42	32.2	48.2	4.94	.	0.468	1.439	-7.64	-4.47
81	56.2	11.0	21.6	2.2	243.0	4.42	31.2	48.7	2.44	.	0.450	2.081	-6.42	-4.36
82	42.9	14.0	20.4	2.0	203.0	4.27	31.4	47.3	4.55	.	0.424	1.837	-7.64	-4.46
83	55.3	21.6	19.5	1.9	533.0	5.23	31.2	48.3	2.93	.	0.875	1.766	-5.46	-4.72
84	46.7	16.3	21.8	2.2	330.0	4.52	29.7	49.3	6.45	.	0.565	2.475	-4.13	-3.95
85	44.1	7.9	19.8	2.0	211.0	4.01	32.5	48.9	3.68	.	0.368	1.591	-7.75	-5.06
86	38.4	8.7	19.4	1.9	134.0	3.78	33.5	48.1	7.33	.	0.345	1.486	-8.04	-4.75
87	61.8	10.8	19.5	2.0	418.0	4.72	26.5	48.9	4.20	.	1.012	3.624	-3.98	-3.77
88	11.3	7.5	18.8	1.9	395.0	3.14	25.7	50.8	3.82	.	0.692	1.477	-4.79	-5.73
89	65.2	8.1	18.5	2.0	332.0	5.01	34.2	55.1	3.19	.	0.726	2.502	-3.67	-6.77
90	78.9	12.1	18.6	3.1	432.0	5.45	26.0	47.5	5.73	.	0.559	2.210	-3.83	-6.84
91	83.3	13.5	17.9	3.1	653.0	5.41	25.6	48.7	3.52	.	1.180	3.075	-3.41	-6.14
92	65.4	13.4	18.0	2.3	183.0	4.21	31.2	48.9	2.50	.	0.396	2.111	-5.72	-5.13
93	27.8	11.7	17.1	1.8	166.0	4.15	31.0	48.2	3.46	.	0.386	1.962	-6.89	-3.82
94	58.3	11.3	19.5	2.1	212.0	4.35	31.2	49.1	3.79	.	0.702	2.184	-5.17	-4.88
95	57.2	13.4	20.9	2.4	840.0	4.37	32.9	50.1	3.31	.	0.513	1.352	-5.60	-3.31
96	51.3	15.6	23.4	2.8	833.0	4.48	33.6	48.4	2.66	.	.	.	-7.93	-4.87

Table B-2 (Continued)

OBS	ZN	MO	AG	CD	P	AL	SI	O	AS	S	CORG	CTOT	C13	O18
97	71.0	18.1	21.7	2.9	940.0	4.73	32.1	47.6	4.94	.	0.547	1.214	-8.25	-6.09
98	61.4	17.7	20.6	2.8	1000.0	4.87	31.7	49.3	2.95	.	0.926	1.392	-8.41	-7.40
99	57.4	16.1	21.0	2.5	843.0	4.37	35.3	48.9	2.95	.	0.657	0.724	-7.21	-7.01
100	57.8	14.0	22.2	2.3	798.0	3.90	36.7	49.0	1.83	.	0.486	0.845	-7.96	-6.33
101	56.7	14.3	22.0	2.3	785.0	4.08	36.4	50.0	2.64	.	0.293	0.435	-6.32	-6.87
102	56.5	12.1	23.1	2.4	792.0	4.08	34.5	48.1	3.21	.	0.375	0.717	-6.95	-6.55
103	71.8	22.0	20.9	3.1	1020.0	5.31	31.9	48.0	7.72	.	1.193	1.546	-4.76	-6.57
104	62.6	19.6	22.4	2.4	1080.0	4.90	32.3	48.7	5.05	.	1.017	1.545	-3.87	-6.58
105	69.0	23.0	20.1	3.0	819.0	5.22	34.2	49.5	0.01	.	0.715	0.757	.	.
106	63.3	15.6	22.5	2.7	925.0	4.40	33.8	47.7	4.80	.	0.690	1.014	-6.43	-5.64
107	87.3	19.5	19.9	4.1	806.0	4.41	33.9	48.5	3.11	.	0.579	0.879	-5.65	-5.65
108	58.1	15.7	20.9	2.1	781.0	4.02	35.8	50.7	2.20	.	0.489	0.662	-5.47	-4.83
109	54.1	13.5	22.7	2.3	853.0	3.90	34.3	48.2	1.88	.	0.261	0.883	-6.38	-5.01
110	63.6	20.1	22.4	2.2	1020.0	5.05	29.6	49.3	7.36	.	0.758	1.788	-6.13	-4.04
111	46.3	12.9	21.7	2.2	179.0	.	36.2	49.3	3.71	.	0.424	0.601	-3.95	-4.75
112	58.3	8.7	21.9	2.2	54.0	3.94	36.5	49.2	3.74	.	0.346	0.286	.	.
113	87.9	8.7	21.8	2.2	674.0	5.37	30.1	49.3	5.19	.	2.145	2.659	-4.37	-4.99
114	74.5	8.1	20.3	2.0	376.0	5.09	25.6	47.4	4.27	.	0.632	2.757	-1.21	-4.32
115	103.0	9.2	22.9	2.3	702.0	6.16	26.7	49.8	4.50	.	0.716	1.749	-2.96	-4.18
116	78.8	9.5	23.7	2.4	443.0	5.20	27.7	47.7	1.26	.	0.732	1.886	-1.69	-4.10
117	65.3	8.9	22.2	2.2	307.0	4.62	32.4	47.9	3.13	.	0.654	1.246	-6.47	-5.01
118	42.6	8.9	22.3	2.2	144.0	3.77	33.0	46.9	1.18	.	0.496	1.566	-6.27	-4.91
119	54.7	8.9	22.3	2.2	165.0	3.55	32.7	49.1	1.15	.	0.501	2.002	-5.63	-4.95
120	32.5	8.5	21.2	2.1	121.0	3.66	35.5	49.6	1.64	.	0.367	1.159	-7.15	-5.97
121	35.9	8.7	21.7	2.2	119.0	3.47	27.4	47.9	2.25	.	0.519	3.613	-7.57	-4.95
122	44.1	8.5	21.2	2.1	127.0	3.40	33.3	47.1	5.28	.	0.404	1.436	-8.24	-4.93
123	56.6	8.1	20.3	2.0	215.0	3.48	33.4	48.5	1.88	.	0.551	1.750	-6.65	-4.35
124	50.7	8.1	20.1	2.0	370.0	4.38	31.9	49.0	1.78	.	0.429	1.475	-5.76	-5.78
125	55.7	8.3	20.8	2.1	162.0	3.88	36.3	51.2	1.10	.	0.375	1.053	-5.69	-5.17
126	48.3	9.0	22.5	2.3	166.0	3.96	35.2	49.0	2.66	.	0.472	1.135	-6.75	-5.88
127	99.2	9.0	22.6	2.3	264.0	4.41	33.0	50.3	3.47	.	.	.	-6.08	-4.66
128	67.3	9.1	22.7	2.3	503.0	4.84	31.2	49.2	2.03	.	1.084	2.057	-5.09	-5.62
129	26.3	8.5	21.3	2.1	47.1	2.53	28.1	49.0	2.43	.	0.328	3.472	-7.78	-4.51
130	52.1	9.5	23.8	2.4	198.0	4.31	34.3	50.4	4.19	.	0.512	1.108	-7.27	-4.07
131	50.5	8.9	22.3	2.2	33.5	3.88	34.9	50.8	2.79	.	0.538	1.089	-7.41	-5.80
132	48.4	8.9	22.3	2.2	33.4	3.82	34.9	48.2	3.50	.	0.310	0.865	-6.44	-6.44
133	62.3	8.9	22.1	2.2	148.0	4.81	34.7	48.9	3.07	.	0.709	1.024	-6.57	-6.93
134	54.3	7.9	19.8	2.0	270.0	4.65	33.6	51.5	4.46	.	0.558	1.175	-6.67	-6.06
135	54.6	8.0	19.9	2.0	223.0	4.52	34.6	50.0	4.03	.	0.653	1.049	-7.35	-6.16
136	53.0	8.1	20.2	2.0	181.0	4.03	33.8	48.6	2.57	.	0.506	1.133	-7.71	-6.41
137	58.4	8.2	20.4	2.0	110.0	3.78	33.4	48.7	4.01	.	0.105	1.605	-8.16	-5.64
138	46.0	8.3	20.9	2.1	157.0	3.97	35.7	50.4	3.80	.	0.529	1.123	-7.91	-5.67

Table B-3. Barringer Lasertrace® geochemical data[a]

SAMPLE ID	C PPM	AL PPM	CA PPM	CU PPM	CR PPM	CO PPM	FE PPM	PB PPM	MG PPM
CA001	1490	79300	123000	53.4	67.6	4.3	28600	112	22300
CA002	855	69500	235000	43.1	43.1	5.36	20700	91.7	22100
CA003	868	85900	202000	59.2	48.1	3.91	23200	87.9	18400
CA004	1160	105000	97000	53.2	83.8	10.8	31200	87.6	13300
CA005	1520	79500	132000	49.5	62.3	9.81	22700	75.9	9770
CA006	1640	73400	166000	50.8	55.4	10.8	26400	80.1	10900
CA007	1850	99600	167000	60.9	88.2	11.9	29800	91.0	11200
CA008	1770	79200	185000	64.1	66.1	9.31	24800	85.1	10900
CA009	1530	91900	134000	55.5	60.6	7.78	27600	83.3	9650
CA010	1760	75900	172000	52.4	51.5	6.46	24400	78.2	10200
CA011	1550	87700	162000	48.8	56.3	4.92	28300	85.8	9460
CA012	1350	96300	111000	57.4	59.1	9.47	27400	82.6	8190
CA013	1600	80100	152000	51.7	49.9	9.52	24000	80.2	9120
CA014	1470	66900	132000	42.5	49.9	4.26	19200	73.0	7300
CA015	1580	75700	134000	140	49.5	6.08	23200	72.2	8070
CA016	1540	114000	77800	76.2	57.0	10.5	31300	80.0	8020
CA016A	1450	112000	63700	96.8	56.9	9.65	30200	78.8	7460
CA017-01	1300	101000	112000	115	50.6	9.35	33800	81.9	7680
CA017-02	3150	53700	356000	98.3	44.8	11.7	21500	103	8520
CA018	1110	97800	64800	111	94.0	8.87	98600	84.9	4680
CA019	1260	53900	95300	99.0	53.9	1.77	32300	66.6	3040
CA020	1010	47800	61500	73.1	41.3	1.10	22700	48.8	3600
CA021	1180	94000	110000	66.4	95.2	17.8	34200	94.4	11700
CA022	1260	80200	69400	57.3	68.6	9.72	29000	73.3	7180
CA023	1400	102000	90800	79.4	72.1	10.1	38500	88.7	11600
CA024	1050	80500	51900	71.5	54.3	4.74	25500	69.3	7570
CA025	1110	114000	61000	59.6	63.3	9.29	37200	83.9	9700
CA026	1290	103000	78000	50.8	57.2	7.63	33200	84.3	9670
CA027	1240	108000	65700	55.1	60.0	9.35	31600	81.6	9710
CA028	1440	96300	126000	57.5	81.3	25.3	26700	81.0	7880
CA029	1230	97100	109000	57.0	76.8	20.7	26500	79.6	7230
CA030	1200	112000	68400	62.2	75.6	18.1	31100	80.1	8080
CA031	1130	105000	101000	59.7	64.0	11.4	34400	87.5	9960
CA032	1560	59700	192000	41.7	42.4	5.56	20300	76.2	8330
CA033	1300	76300	133000	47.5	53.2	8.74	26900	81.1	7760
CA034	1090	97300	84200	54.0	52.5	9.83	28100	76.0	7420
CA035	1030	91100	84500	46.8	47.7	6.70	25800	74.0	8840
CA036	1040	90700	65200	45.3	49.2	6.49	28400	76.6	9530
CA037	792	103000	55300	52.1	57.4	6.84	34400	84.0	10000
CA038	851	93300	47000	41.5	55.5	4.00	33600	78.7	8640
CA039	973	92100	74600	45.8	58.0	8.08	31400	79.6	8260
CA040	781	95100	39400	43.7	56.7	4.26	33100	71.1	7080
CA041	860	104000	40400	48.4	59.4	8.18	36300	84.1	9200
CA042	1000	99700	48000	47.0	58.4	8.10	34500	84.4	10100
CA043	936	107000	57100	53.1	57.8	4.99	37100	85.6	9420
CA044	1050	81200	93100	40.3	49.6	3.47	28100	75.4	9020

[a]Soil from Coyanosa test site samples collected in 1979 and 1980; the 1979 samples begin with "CA."

Table B-3 (Continued)

SAMPLE ID	MN PPM	MO PPM	NI PPM	AG PPM	BE PPM	SR PPM	BA PPM	ZN PPM
CA001	610	1.4	39.8	4.3	3.2	1590	1310	154
CA002	515	1.8	24.7	4.5	3.4	3480	394	91.8
CA003	551	1.8	28.1	4.6	3.2	3320	504	98.6
CA004	717	1.6	43.6	4.7	3.3	1300	1250	113
CA005	526	1.6	31.9	3.9	3.0	823	784	80.7
CA006	494	1.4	28.5	4.1	3.3	711	721	99.9
CA007	566	2.0	55.2	4.5	3.3	749	697	106
CA008	515	2.0	37.4	4.4	3.1	726	1060	104
CA009	617	1.6	31.7	4.5	3.0	629	849	103
CA010	518	1.6	27.9	4.6	3.0	634	996	89.8
CA011	520	1.8	27.1	4.1	3.0	527	878	98.6
CA012	615	1.5	28.0	3.3	2.7	473	764	97.6
CA013	527	1.6	27.1	3.9	2.9	543	784	101
CA014	390	1.1	23.1	3.2	2.5	396	696	68.7
CA015	462	1.5	25.7	3.1	2.7	522	702	110
CA016	612	1.5	28.2	3.1	2.7	399	669	102
CA016A	632	1.3	25.1	2.6	2.7	332	615	103
CA017-01	411	1.3	27.1	2.6	2.6	323	934	107
CA017-02	330	3.1	41.4	7.0	3.7	524	2400	106
CA018	226	2.3	27.1	2.8	3.5	276	1560	127
CA019	1010	1.0	20.1	2.2	1.7	162	840	80.1
CA020	310	.9	15.2	1.9	1.7	198	648	58.0
CA021	639	1.3	54.9	3.2	2.8	370	1380	115
CA022	482	1.0	30.9	2.2	2.3	324	1090	80.9
CA023	688	1.4	32.1	2.9	2.9	560	1420	124
CA024	513	.9	20.8	2.2	2.3	304	1130	90.3
CA025	734	1.4	29.6	3.0	2.9	349	734	121
CA026	717	1.2	27.3	2.8	2.9	683	628	113
CA027	760	1.1	29.1	2.2	2.9	417	569	102
CA028	603	1.7	46.1	3.3	2.8	479	592	106
CA029	652	1.6	41.5	2.9	2.8	374	582	95.0
CA030	685	1.4	41.2	2.6	2.7	295	580	107
CA031	736	1.4	34.5	2.9	3.0	326	648	121
CA032	547	1.4	23.8	6.4	2.8	356	538	75.7
CA033	640	1.1	24.0	3.3	3.1	350	637	107
CA034	735	1.3	24.3	2.7	3.1	309	556	102
CA035	854	1.3	23.6	2.6	3.0	1130	562	113
CA036	979	1.1	23.2	2.4	3.1	739	539	116
CA037	903	1.1	27.8	2.2	3.1	464	608	142
CA038	815	1.0	24.4	2.0	2.9	294	568	133
CA039	701	.9	28.4	2.1	2.8	323	574	122
CA040	627	1.1	25.7	2.0	2.9	206	448	126
CA041	806	.9	28.7	2.1	3.4	228	501	153
CA042	1140	1.3	28.0	2.1	3.4	286	594	135
CA043	863	1.0	25.6	2.3	2.9	290	664	134
CA044	737	.9	22.2	2.4	2.9	298	547	96.3

Table B-3 (Continued)

SAMPLE ID	CD PPM	NA PPM	SI PPM	P PPM	TH PPM	TI PPM	V PPM	K PPM
CA001	.1	3350	242000	1000	25.6	1680	56.8	15400
CA002	.1	1760	185000	773	43.0	1280	49.6	12900
CA003	.1	2070	190000	808	38.0	1490	58.0	17300
CA004	.1	3540	237000	894	24.7	2030	71.3	23300
CA005	.1	5200	245000	716	27.4	1440	45.4	22800
CA006	.1	4900	226000	850	31.2	1430	58.6	21500
CA007	.1	5110	195000	1040	40.6	1790	55.6	27800
CA008	.1	4710	208000	989	35.1	1590	56.2	23900
CA009	.1	4530	227000	1030	29.3	1810	64.5	27400
CA010	.1	4220	222000	899	33.7	1490	53.8	22400
CA011	.1	4090	215000	911	32.2	1420	63.9	23300
CA012	.1	3860	241000	1000	25.1	1760	61.0	25800
CA013	.1	4920	231000	900	28.7	1610	52.0	23400
CA014	.1	7740	258000	731	25.7	1500	40.9	24500
CA015	.1	5490	248000	992	26.9	1540	50.6	23100
CA016	.1	4000	243000	1100	21.0	2100	65.4	28700
CA016A	.1	3450	256000	1130	17.1	2160	66.0	27100
CA017-01	.1	1590	238000	774	20.9	1740	118	17500
CA017-02	.1	848	133000	815	59.0	869	63.4	9910
CA018	.1	1120	231000	887	15.6	1260	333	19100
CA019	.1	781	296000	639	14.2	603	102	20000
CA020	.1	5590	328000	540	11.0	1200	62.0	17200
CA021	.1	3800	237000	1260	24.3	1920	85.0	23300
CA022	.1	6120	281000	821	14.7	1750	75.0	25100
CA023	.1	5440	235000	1160	20.4	2080	87.7	29600
CA024	.1	7420	293000	774	12.4	1740	62.9	26500
CA025	.1	4270	248000	1120	15.3	2250	76.0	29800
CA026	.1	4050	250000	1090	18.7	2090	74.5	29200
CA027	.1	3320	255000	1190	15.4	2190	74.5	28100
CA028	.1	4920	230000	1040	29.5	1900	59.5	27900
CA029	.1	5230	241000	944	26.9	1920	54.9	27900
CA030	.1	4700	251000	935	18.9	2170	61.9	27700
CA031	.1	5420	232000	984	20.7	2190	64.1	27400
CA032	.1	3870	231000	754	32.1	1330	43.6	17100
CA033	.1	8610	242000	916	27.4	1770	52.2	26900
CA034	.1	6950	253000	1010	21.3	2010	60.2	30900
CA035	.1	7550	258000	983	19.5	1940	54.0	29900
CA036	.1	6320	272000	1060	15.9	2030	54.9	27000
CA037	.1	6510	262000	988	13.7	2250	68.8	29100
CA038	.1	8030	276000	936	10.0	2010	59.6	30500
CA039	.1	6570	263000	979	15.2	2020	56.3	28000
CA040	.1	7370	283000	780	12.0	1910	60.0	28900
CA041	.1	7530	268000	1020	13.3	2290	72.0	31700
CA042	.1	6520	268000	1100	13.2	2240	70.8	30500
CA043	.1	5840	255000	1150	10.0	2310	70.8	29900
CA044	.1	5230	265000	920	17.4	1900	54.5	24300

Table B-3 (Continued)

SAMPLE ID	C PPM	AL PPM	CA PPM	CU PPM	CR PPM	CO PPM	FE PPM	PB PPM	MG PPM
50	7080	111000	63000	146	73.4	2.5	38200	146	15300
51	4790	109000	42600	131	72.2	.5	38900	125	11300
52	4870	109000	41700	156	70.1	<.0	38900	120	10200
53	4620	107000	36500	118	78.2	2.1	40300	147	10600
54	4170	105000	28600	113	76.6	2.8	40400	145	13100
55	5470	105000	48200	185	75.0	2.0	41400	139	12700
56	4130	105000	27000	47.4	74.9	2.9	41900	117	14100
57	5040	114000	50600	97.7	68.7	1.9	39300	152	11700
58	4790	112000	21600	167	80.4	2.5	41900	130	10900
59	4630	110000	39400	71.3	78.3	2.5	41300	104	10300
60	3390	108000	10900	109	78.8	2.3	44000	117	10100
61	3680	104000	23300	60.9	73.1	2.3	42400	120	9640
62	4330	107000	20800	159	79.5	2.7	42700	133	10300
63	4400	110000	31500	61.6	72.4	2.7	40300	149	11300
64	5470	101000	72800	54.5	67.3	3.3	36100	125	12400
65	5880	112000	63000	60.5	64.3	2.4	36700	66.6	11000
66	4860	114000	48100	44.4	72.8	3.6	39200	102	11600
67	4470	113000	19500	52.9	76.5	3.2	44500	133	11600
68	5580	114000	31700	43.7	70.5	3.1	39100	105	11600
69	6420	90100	96000	49.7	60.7	3.6	35400	125	11600
70	6290	99400	37700	32.8	68.6	.7	40700	93.0	11500
71	5600	99500	65200	36.8	63.5	.5	37200	136	10900
72	5060	109000	39600	47.5	75.1	.6	40500	159	12600
73	6730	101000	87000	47.4	73.7	1.0	35300	302	15700
74	5830	105000	81400	42.9	71.0	.6	35400	197	14100
75	6780	105000	99400	37.4	74.3	1.0	33600	275	14900
76	9340	91800	119000	59.4	75.1	.0	34900	298	17500
77	8780	102000	109000	45.4	72.7	1.0	34300	348	15100
78	6590	108000	68300	40.4	76.4	.0	36700	301	16000
79	7060	115000	55100	45.4	72.8	.7	37500	116	13300
80	7020	114000	50200	43.6	80.3	1.0	37500	209	16100
81	7040	116000	46400	52.4	84.4	.8	40300	235	14200
82	7790	111000	49700	59.2	87.2	.9	40400	273	14500
83	7630	115000	48000	41.8	78.7	.0	39300	169	14600
84	9610	76200	142000	46.8	73.3	1.1	27500	176	23700
85F	6530	114000	39100	44.6	83.2	2.7	39300	274	16600
86E	5900	117000	44500	43.6	73.8	.0	39600	161	13100
87D	5510	113000	50700	43.2	75.3	.0	38200	185	14200
88C	6280	102000	18500	58.0	83.6	1.4	41300	232	18500
89G	5300	115000	44500	58.2	74.2	.0	38800	168	12800
90B	5390	109000	36800	497	78.3	7.4	40100	253	13900
91A	5760	104000	59100	45.7	72.7	.7	37200	216	13900
92H	5950	111000	61000	41.9	76.1	.7	38800	124	13600
931	6820	107000	56400	44.8	77.1	.6	39400	167	15000
301	8620	96000	123000	48.3	71.3	1.2	32900	182	13900
302	9430	104000	99500	41.3	71.9	1.4	33800	380	14600
303	5700	106000	59300	39.3	75.9	.6	38100	192	14600
304	6660	112000	28900	54.4	84.8	.7	42600	226	14100
305	7140	116000	44400	44.9	82.6	.7	42100	184	15400
306	6450	114000	30800	48.6	83.5	.8	41900	195	15500
307	10800	109000	42000	54.3	93.3	1.3	40800	273	16700
308	8910	106000	85700	45.0	75.5	.8	35800	155	14400
309	8410	89900	126000	47.7	88.8	.8	29700	206	21000
310	5840	88800	114000	41.8	72.5	.9	29200	118	21100
310B	5500	103000	48700	40.3	77.3	.6	36800	150	17800
311	8010	95600	68900	51.8	96.7	1.3	36500	368	24100
312	7890	103000	41100	38.0	89.3	.7	39500	226	23000
313	9900	93800	32700	42.9	86.3	.9	37300	161	28000
314	8450	119000	33600	44.8	84.8	2.1	42400	106	15100
315	6430	128000	9680	46.9	86.9	.6	48100	166	12300
316	11000	84500	169000	41.2	74.3	<.0	32300	63.2	19600
317	8820	98200	158000	32.2	68.0	.8	34000	108	18900
401	11200	92100	123000	31.6	63.9	<.0	33700	69.4	17800
402	7320	112000	59500	33.0	70.4	.6	39800	97.8	14700
403	6560	104000	90300	29.4	64.6	.7	37400	98.3	12400

Table B-3 (Continued)

SAMPLE ID	C PPM	AL PPM	CA PPM	CU PPM	CR PPM	CO PPM	FE PPM	PB PPM	MG PPM
404	7760	112000	48200	26.6	70.5	.7	39500	58.3	12900
405	6340	114000	46400	27.0	69.9	<.0	39700	102	12700
406	8040	114000	40200	22.5	72.2	.9	39700	79.6	15100
407	6980	118000	35300	31.4	76.6	.7	43000	139	15600
408	6500	108000	62700	26.1	67.7	.6	40700	115	13400
409	6680	119000	44000	37.3	77.1	.5	42500	88.0	14200
410	6430	121000	26900	36.0	80.1	.7	42700	107	17300
411	8650	116000	70600	31.8	69.4	.6	39400	113	14900
412	8050	104000	117000	38.1	68.0	.7	35200	84.8	15300
413	9700	108000	109000	37.0	71.1	.7	36400	94.1	15000
414	9280	103000	121000	37.8	69.4	<.0	32600	67.3	13700
415	8150	110000	75200	35.4	74.6	.9	38300	133	16700
416	8660	115000	76000	37.3	74.2	<.0	37900	99.8	17000
417	7410	107000	96600	33.0	73.0	.8	36000	72.4	17500
418	7520	113000	87600	34.1	72.4	.6	37100	97.4	17000
419	8020	114000	45400	35.8	78.8	.5	41700	113	16400
420	8200	110000	98600	34.0	69.9	.6	36100	97.1	15800
421	7360	114000	98700	39.0	72.1	.5	38400	108	14500
422	7430	110000	111000	36.7	69.8	.9	36100	103	14900
423	9340	109000	80400	30.4	77.6	.6	39200	162	17500
424	6320	81800	125000	34.6	97.8	1.2	29000	<.0	49500
425	10100	108000	72700	41.0	98.6	.8	44300	69.9	22700
425A	7600	103000	56800	39.0	98.8	.6	45800	76.3	27100
426	8430	109000	60300	53.3	90.4	.5	41700	123	21800
427	8140	104000	109000	34.0	74.2	.6	36500	121	16500
428	7050	110000	112000	36.9	68.5	.8	35000	136	14800
429	8310	105000	98000	35.5	71.4	.6	36300	95.0	16700

Table B-3 (Continued)

SAMPLE ID	MN PPM	MO PPM	NI PPM	AG PPM	BE PPM	SR PPM	BA PPM	ZN PPM	CD PPM
50	729	1.2	38.2	.4	3.1	436	521	166	.1
51	851	1.3	33.3	.2	2.8	347	521	172	.1
52	806	1.2	28.2	<.0	2.6	318	524	171	.1
53	854	1.3	38.5	.3	2.9	257	519	164	.1
54	871	1.2	33.6	.3	3.0	219	462	178	.1
55	764	1.2	32.2	.3	2.9	298	506	186	.1
56	881	1.2	35.7	.5	3.2	221	474	158	.1
57	733	1.3	30.2	.3	3.3	291	553	158	.1
58	756	1.2	36.9	.7	3.4	189	405	204	.1
59	806	1.3	33.9	.5	3.1	226	483	148	.1
60	771	1.3	35.2	.4	3.3	126	432	166	.1
61	851	1.3	33.9	.3	3.0	176	573	157	.1
62	840	1.4	34.6	.3	3.1	178	664	243	.1
63	688	1.3	30.5	.4	3.2	200	631	146	.1
64	677	1.2	31.7	.5	2.8	405	674	137	.1
65	631	1.2	32.7	.5	3.1	364	496	118	.1
66	741	1.3	33.4	.4	3.4	282	536	122	.1
67	839	1.4	36.2	.5	3.8	178	487	135	.1
68	833	1.2	34.4	.4	3.2	227	467	132	.1
69	599	1.3	30.7	.6	3.4	429	438	114	.1
70	809	1.5	30.4	1.5	4.5	220	379	119	.1
71	711	1.4	36.1	1.2	3.8	381	468	120	.1
72	946	1.4	42.3	1.1	3.4	299	621	164	.1
73	793	1.4	43.9	1.9	3.1	519	759	158	.1
74	730	1.4	43.1	1.4	3.1	425	880	151	.1
75	691	1.5	50.7	2.2	3.4	408	630	135	.1
76	685	1.7	57.0	2.9	3.5	1160	976	156	.1
77	650	1.5	48.5	2.3	3.1	646	653	137	.1
78	725	1.6	46.4	2.0	3.5	358	683	132	.1
79	605	1.4	45.7	1.3	3.5	345	483	128	.1
80	677	1.6	45.7	2.0	3.5	374	599	140	.1
81	968	1.6	53.3	1.7	3.8	312	1410	164	.1
82	900	1.5	49.6	1.7	3.5	340	2810	170	.1
83	792	1.5	45.3	2.0	3.7	314	623	151	.1
84	881	1.5	51.3	2.5	2.6	2900	553	115	.1
85F	869	1.5	44.8	2.0	3.7	326	502	137	.1
86E	797	1.4	42.8	1.3	3.4	321	568	140	.1
87D	705	1.4	39.0	1.5	3.5	301	534	140	.1
88C	939	1.7	49.4	2.3	3.6	187	521	187	.1
89G	807	1.3	41.3	1.2	3.5	247	521	157	.1
90B	941	1.4	45.6	1.6	3.4	274	563	191	.1
91A	790	1.4	47.3	1.4	3.2	357	598	146	.1
92H	803	1.6	48.9	1.6	3.5	308	680	149	.1
93I	779	1.4	45.7	1.4	3.4	297	634	151	.1
301	674	1.6	49.7	2.3	3.0	663	869	123	.1
302	716	1.6	54.5	2.7	3.2	441	823	159	.1
303	727	1.3	45.3	1.4	3.1	351	606	146	.1
304	923	1.5	53.3	1.8	3.6	230	647	187	.1
305	803	1.4	48.9	1.7	3.5	284	729	160	.1
306	1010	1.5	49.6	1.7	3.5	250	845	184	.1
307	802	1.7	67.0	2.6	3.6	263	690	170	.1
308	615	1.3	50.9	1.7	3.1	339	611	132	.1
309	640	1.4	53.9	2.0	2.6	3760	7600	140	.1
310	689	1.4	38.8	2.1	2.6	3440	634	140	.1
310B	838	1.3	44.3	1.4	3.1	1260	532	165	.1
311	783	2.4	85.1	7.2	3.5	1090	494	230	.1
312	913	1.7	57.3	2.9	3.4	558	523	195	.1
313	1050	.8	33.5	.2	3.1	558	460	172	.1
314	921	1.0	36.7	.2	3.6	578	2320	185	.1
315	973	1.0	36.3	.5	4.0	206	619	196	.1
316	517	.7	41.4	.3	2.5	751	1500	145	.1
317	947	.9	33.1	.2	2.8	637	744	156	.1
401	638	.8	34.1	.2	3.7	1980	634	117	.1
402	922	.9	33.8	.2	4.3	347	443	128	.1
403	619	.9	32.2	.2	4.1	378	434	135	.1

Table B-3 (Continued)

SAMPLE ID	MN PPM	MO PPM	NI PPM	AG PPM	BE PPM	SR PPM	BA PPM	ZN PPM	CD PPM
404	935	.9	28.6	.2	4.8	289	459	128	.1
405	776	.8	27.7	<.0	4.1	268	455	126	.1
406	655	.8	33.9	<.0	4.5	240	403	150	.1
407	673	.9	30.3	.2	4.4	231	436	150	.1
408	744	1.0	27.4	.2	4.4	356	468	140	.1
409	725	1.0	34.0	.1	4.0	214	488	140	.1
410	753	.8	38.8	.5	4.0	188	480	133	.1
411	700	1.0	32.5	.1	4.3	438	364	122	.1
412	732	.8	33.7	.2	3.7	420	481	131	.1
413	624	.9	38.5	.2	3.2	439	451	120	.1
414	590	.8	38.6	.2	3.1	631	614	128	.1
415	704	.8	36.3	.2	3.3	449	445	154	.1
416	726	.9	38.1	.2	3.5	473	506	131	.1
417	736	.8	33.2	<.0	3.6	361	466	136	.1
418	702	.8	37.2	.2	3.5	377	464	119	.1
419	1130	1.0	32.7	.1	3.8	267	464	148	.1
420	716	.9	37.1	.2	3.5	394	506	127	.1
421	690	.9	34.2	.1	3.4	442	563	141	.1
422	667	.8	38.5	.2	3.2	452	880	139	.1
423	994	.9	37.0	.2	3.5	496	492	123	.1
424	735	.6	41.7	.3	2.4	6140	385	183	.1
425	862	.9	48.1	.2	3.2	704	484	143	.1
425A	794	1.1	37.4	.2	3.2	519	343	141	.1
426	886	.9	35.5	.1	3.3	543	428	146	.1
427	801	.8	36.4	.1	3.4	544	714	137	.1
428	617	.9	37.8	.6	3.3	406	535	123	.1
429	855	.9	32.8	.2	3.5	429	537	141	.1

Table B-3 (Continued)

SAMPLE ID	NA PPM	SI PPM	P PPM	B PPM	TI PPM	V PPM	K PPM
50	2790	249000	1410	47.2	2250	81.5	22200
51	3000	265000	1340	45.0	2340	79.8	24500
52	3380	265000	1380	44.7	2290	78.2	26200
53	3140	270000	1340	46.5	2370	83.9	25400
54	2920	276000	1370	48.1	2360	79.6	23800
55	2880	263000	1580	48.6	2240	86.3	23500
56	2840	275000	1150	48.8	2540	82.4	23700
57	2860	255000	1200	45.6	2430	75.5	24200
58	2670	273000	1470	49.8	2420	84.5	27300
59	2730	264000	1310	47.1	2320	84.8	27200
60	2760	282000	1020	50.1	2560	86.2	28000
61	3360	279000	1150	48.2	2500	83.8	26800
62	3340	278000	1240	47.9	2510	84.1	26200
63	3150	271000	1010	44.6	2420	81.0	24300
64	2840	255000	1260	44.1	2100	80.8	23200
65	2470	251000	1180	44.4	2290	76.5	26700
66	2500	256000	1180	45.2	2340	85.0	25300
67	2670	272000	1020	50.5	2490	92.1	26300
68	2810	266000	1430	47.1	2450	80.4	26900
69	4100	250000	1010	41.8	2010	83.4	23500
70	5090	274000	1240	47.1	2370	90.2	25300
71	4660	260000	1090	43.7	2210	83.2	24200
72	3470	264000	1390	49.1	2480	90.2	25600
73	3050	243000	1370	47.6	2160	91.7	23500
74	3100	245000	1220	45.2	2140	83.1	22100
75	2620	234000	1260	45.6	2050	96.2	21600
76	3420	230000	1270	49.4	1910	120	19900
77	3170	229000	1420	48.1	2060	96.3	21900
78	3520	248000	1280	48.9	2250	97.9	22300
79	3320	249000	1400	45.8	2200	88.1	27300
80	3630	253000	1300	48.8	2250	96.4	23700
81	3100	253000	1340	50.4	2410	95.6	23700
82	3380	254000	1320	52.5	2300	103	24500
83	2860	252000	1670	52.2	2370	97.5	26200
84	3020	231000	1000	41.8	1590	107	17000
85F	2770	259000	1250	50.4	2370	99.2	23900
86E	3080	255000	1230	48.1	2440	86.8	24700
87D	3150	255000	1280	47.3	2420	88.9	23400
88C	3320	280000	1400	54.7	2500	99.5	23400
89G	2930	257000	1450	47.3	2470	87.6	25300
90B	3240	266000	1440	49.9	2530	93.5	24000
91A	3170	258000	1320	47.0	2220	86.7	23200
92H	3230	250000	1160	48.6	2320	95.8	23500
93I	2900	255000	1410	47.7	2330	88.8	22000
301	2180	229000	1160	46.2	1840	116	19900
302	2910	236000	1350	48.2	1960	103	19800
303	2570	256000	1240	48.7	2300	89.4	22300
304	3070	266000	1320	55.4	2610	101	24800
305	2900	253000	1200	53.3	2530	99.2	23500
306	3130	262000	1450	56.3	2490	101	25200
307	3290	259000	1540	60.3	2430	113	24200
308	2450	241000	1330	49.6	2250	90.1	22700
309	3060	223000	1130	48.5	1750	93.7	20600
310	2670	237000	983	41.5	1740	89.3	19200
310B	2940	263000	1440	47.3	2170	92.9	22400
311	4180	251000	1640	55.1	2120	133	23100
312	3480	262000	1560	53.2	2240	111	24000
313	2390	275000	1630	47.9	2080	72.7	20400
314	2250	256000	1460	53.4	2600	78.3	23300
315	2280	263000	1340	55.9	2980	87.4	24300
316	1880	208000	1060	42.7	1830	66.7	14800
317	1980	202000	1500	42.2	1950	69.6	20500
401	2340	229000	1200	40.4	1920	81.0	19100
402	2910	249000	1450	45.2	2390	69.6	23600
403	2370	241000	1150	40.3	2230	75.6	21200

Table B-3 (Continued)

SAMPLE ID	NA PPM	SI PPM	P PPM	B PPM	TI PPM	V PPM	K PPM
404	3050	258000	1270	44.2	2350	68.8	23000
405	3170	257000	1210	44.1	2420	66.6	23100
406	3660	259000	1330	44.0	2360	68.2	22200
407	2960	257000	1230	47.3	2460	74.8	23100
408	3470	251000	1160	44.3	2310	70.8	22000
409	1950	253000	1110	46.9	2480	73.1	22600
410	2000	261000	1030	47.5	2540	71.4	21100
411	2540	239000	1160	44.9	2290	71.0	23300
412	1980	223000	1220	41.9	2080	70.7	20100
413	1810	225000	1150	45.0	2180	76.7	20100
414	2150	224000	1260	39.3	2040	87.1	21000
415	2060	242000	1360	45.8	2240	65.3	21200
416	1960	236000	1330	44.5	2260	77.1	21900
417	1770	232000	1270	43.2	2170	65.7	20200
418	1990	232000	1230	43.4	2180	63.9	21100
419	2270	252000	1730	50.9	2480	75.0	25700
420	2040	228000	1380	43.3	2180	73.7	22200
421	1970	224000	1450	45.5	2320	73.1	20900
422	1770	222000	1310	42.2	2250	66.7	19800
423	2540	237000	1200	46.4	2250	78.3	22400
424	1500	217000	1630	91.5	1730	71.3	13500
425	2000	235000	1390	60.3	2360	104	22400
425A	8680	243000	1210	65.0	2440	111	20900
426	2190	244000	1580	57.4	2370	88.6	22200
427	2220	226000	1390	44.3	2170	74.8	20000
428	2090	222000	1260	41.6	2190	70.1	20400
429	2250	232000	1520	44.7	2180	70.8	21400

Table B-4. Classification of Coyanosa test site samples with respect to location relative to local oil/gas production

OBS	CODE	PROD[a]
1	CA001	0
2	CA002	0
3	CA003	1
4	CA004	0
5	CA005	0
6	CA006	1
7	CA007	1
8	CA008	1
9	CA009	1
10	CA010	1
11	CA011	1
12	CA012	1
13	CA013	0
14	CA014	0
15	CA015	0
16	CA016	1
17	CA016A	1
18	CA017-01	0
19	CA017-02	0
20	CA018	0
21	CA019	0
22	CA020	1
23	CA021	1
24	CA022	1
25	CA023	1
26	CA024	1
27	CA025	0
28	CA026	0
29	CA027	0
30	CA028	1
31	CA029	0
32	CA030	0
33	CA031	0
34	CA032	0
35	CA033	0
36	CA034	0
37	CA035	0
38	CA036	0
39	CA037	0
40	CA038	0
41	CA039	0
42	CA040	0
43	CA041	0
44	CA042	0
45	CA043	0
46	CA044	0
47	301	0
48	302	0
49	303	0
50	304	0
51	305	1
52	306	1
53	307	1
54	308	0
55	309	1
56	310	1
57	310B	1
58	311	1
59	312	0
60	313	0
61	314	0
62	315	0
63	316	0
64	317	1
65	401	0
66	402	0
67	403	1
68	404	1
69	405	1
70	406	1
71	407	1
72	408	1
73	409	0
74	410	0
75	411	0
76	412	0
77	413	0
78	414	0
79	415	0
80	416	1
81	417	1
82	418	1
83	419	1
84	420	1
85	421	1
86	422	1
87	423	1
88	424	1
89	425	1
90	425A	1
91	426	1
92	427	1
93	428	1
94	429	1
95	50	1
96	51	0
97	52	0
98	53	1
99	54	1
100	55	0
101	56	0
102	57	0
103	58	0
104	59	0
105	60	0
106	61	1
107	62	1
108	63	1
109	64	1
110	65	0
111	66	1
112	67	1
113	68	1
114	69	0
115	70	0
116	71	0
117	72	1
118	73	1
119	74	1
120	75	1
121	76	1
122	77	1
123	78	1
124	79	1
125	80	1
126	81	1
127	82	1
128	83	1
129	84	0
130	85E	0
131	86E	0
132	87D	0
133	88C	1
134	89G	1
135	90B	1
136	91A	1
137	92H	1
138	93I	1

[a]0 = Outside 1 = Inside

Section 14

Technical Appendix

Ronald E. Alley
James M. Soha
Michael J. Abrams
James E. Conel
Harold R. Lang
Jet Propulsion Laboratory

Section 14
Technical Appendix

Contents

I. Sensor Characteristics 14-1
A. NASA Remote Sensing Data 14-1
1. Satellite data 14-1
2. Aircraft instruments 14-2
3. Portable Field Reflectance Spectrometer 14-5
B. Non-NASA Remote Sensing Data 14-8
1. Fraunhofer Line Discriminator 14-8
2. Aerial radiometers 14-11
3. Aerial magnetics 14-11
4. Airtrace® 14-11
5. Surtrace® 14-12

II. Ground Truth Data by Laboratory Techniques 14-13
A. NASA Data 14-13
1. Beckman DK2A Spectrophotometer 14-13
2. X-ray diffraction unit 14-14
B. Non-NASA Data: Lasertrace® 14-14

III. Image Processing Laboratory Facilities 14-15

IV. Computer Processing 14-15
A. General Processing 14-15
1. Data preparation 14-15
2. Analysis and display 14-16
B. Program Descriptions 14-18
1. ASTRTCH2 14-18
2. BAYES 14-18
3. BOXFLT2 14-19
4. C130RECX 14-19
5. DS4 14-19
6. DSTRETCH 14-20
7. EIGEN 14-20
8. F2 14-20
9. FASTCLAS 14-21
10. FFT1 14-21

PRECEDING PAGE BLANK NOT FILMED

11. FFT1PIX 14-21
12. FFT22 14-22
13. FFTFIT 14-22
14. FFTPIC 14-23
15. FILTER 14-24
16. FLOT 14-24
17. FORGRE 14-24
18. GEOM and LGEOM 14-25
19. GEOMA 14-25
20. GRADREM 14-27
21. IDISPLAY 14-27
22. LAVE 14-28
23. LIBEXEC 14-28
24. LIST 14-28
25. LOOKUP 14-28
26. MASK76 14-29
27. MGEOM 14-29
28. MSS 14-30
29. PICREG 14-30
30. PSAR 14-30
31. RATIO 14-31
32. SIMPLIFY 14-31
33. SIZE 14-31
34. STATPLT 14-31
35. STATS 14-32
36. STRETCH 14-32
37. TEXTAD 14-32
38. TFILT 14-32
39. TIECONM 14-32
40. USTATS 14-33
41. VDIGIT 14-33
42. VERTSLOG 14-34
43. VLOGTOP 14-35
44. XFORM 14-35

References 14-36

Figures

14-1. Exploded view of PFRS optical head 14-6
14-2. Composite circular variable filter wheel with indicated positions of the 4 Landsat and 12 Skylab S-192 MSS bands .. 14-6
14-3. Functional block diagram of the PFRS 14-7
14-4. Fraunhofer line profile 14-9
14-5. Airtrace® airborne unit 14-12
14-6. Lasertrace® laboratory-playback unit 14-12
14-7. FORGRE output in two basic formats 14-25
14-8. Transformation of line–sample coordinates 14-26
14-9. Sample quadrilateral tiepoint array 14-26
14-10. Sample triangular tiepoint array 14-27
14-11. Structure of the table record 14-29
14-12. Reformatting procedure 14-35
14-13. Descriptive label 14-35

Tables

14-1. Landsat 1, 2, and 3 MSS characteristics 14-1
14-2. Seasat SAR characteristics 14-1
14-3. NS-001 specifications 14-2
14-4. NS-001 spectral band characteristics 14-2
14-5. M^2S instrument characteristics 14-2
14-6. M^2S spectral characteristics 14-2
14-7. Bendix 24-channel scanner 14-3
14-8. Bendix 24-channel scanner calibration accuracy specification 14-3
14-9. Characteristics of MFMR 14-4
14-10. LIBEXEC commands 14-28
14-11. Conditions for shortening the intermediate file 14-30
14-12. Point-surface generation techniques 14-33

Section 14
Technical Appendix

I. Sensor Characteristics

A. NASA Remote Sensing Data

1. Satellite data

a. Landsat. Landsat 1, 2, and 3 provided systematic, repetitive coverage of the Earth. Each satellite was in a circular, sun-synchronous orbit at an altitude of approximately 920 km. The satellites circled the Earth every 103 minutes, viewing the entire Earth every 18 days. Two instruments carried by Landsat provided image data of the Earth's surface: the Return Beam Vidicon (RBV) and the Multispectral Scanner (MSS). Data used in this study were limited to the MSS data, so only these data are described (*Landsat Data User's Handbook*, 1979).

The MSS is an electromechanical line scanner, obtaining data in four spectral bands in the visible- and infrared-wavelength region for Landsat 1 and 2, and in five spectral bands for Landsat 3. The characteristics of this scanner are given in Table 14-1.

Table 14-1. Landsat 1, 2, and 3 MSS characteristics

Parameter	Value
Altitude, km	920
Swath width, km	185
Instantaneous field of view, m	79
Field of view, deg	11.56
Spectral bands, μm:	
Landsat 1 and 2	4: 0.5 to 0.6, 5: 0.6 to 0.7, 6: 0.7 to 0.8, 7: 0.8 to 1.1
Landsat 3	Same as above, plus 10.4 to 12.6
Orbit	Sun-synchronous, repetitive every 18 days
Coverage, deg	81° N to 81° S

MSS data were obtained in digital form on computer-compatible magnetic tapes (CCTs). Each nominal scene covered an area of 185 by 185 km, imaged at about 9:30 A.M. local solar time.

b. Seasat L-band Synthetic Aperture Radar. On June 29, 1978, NASA launched Seasat, a satellite dedicated to establishing the utility of microwave sensors for remote sensing of the Earth's oceans. On October 10, 1978, a massive short circuit on board the satellite ended the operation. One of the five instruments on board was an L-band (1.3-GHz frequency and 23.5-cm wavelength) Synthetic Aperture Radar (SAR) system. During its 3⅓ months of operation, this system provided data about 100 million square kilometers, 65 million of which covered land. Characteristics of the Seasat SAR system are summarized in Table 14-2.

Table 14-2. Seasat SAR characteristics[a]

Parameter	Value
Satellite altitude, km	800
Radar frequency, GHz	1.275
Radar wavelength, cm	23.5
System bandwidth, MHz	19
Theoretical resolution on the surface, m	25 by 25
Number of looks	4
Swath width, km	100
Antenna dimensions, m	10.74 by 2.16
Antenna look angle, deg	20 from vertical
Incidence angle on the surface	23 ±3 across the swath
Polarization	HH
Transmit pulse length, μs	33.4
Pulse repetition rate, pps	1463 to 1640
Transmitted peak power, W	1000
Time-bandwidth product	634
Data recorder bit rate (on the ground), Mbits/s	110 (5 bits per word)

[a]From Ford et al., 1980.

At the ground processing facility, the radar-signal data were correlated to generate radar images. This can be done either optically or digitally. Details of processing are described by Jordan (1980) and Wu (1980).

2. Aircraft instruments

a. NS-001 multispectral scanner. The NS-001 Thematic Mapper Simulator is a multispectral scanner developed at NASA's Johnson Space Center (JSC) to provide spectral bands similar to those of the Thematic Mapper (TM) scanner flown on the Landsat 4 satellite (Johnson Space Center, 1977). The NS-001 scanner was flown aboard a C-130 aircraft based at JSC.

The NS-001 scanner is a modification and an upgrading of a single-channel scanner built at JSC and flight tested in November 1976. Ground terrain is scanned by a mirror, and the energy from the ground scenes is collimated by a telescope. A dichroic mirror separates the short-wavelength (0.45- to 2.35-μm) and long-wavelength (10.4- to 12.5-μm) radiation. The short-wavelength radiation is dispersed into seven short-wavelength bands by a spectrometer. Calibration of the system is maintained by blackbodies and tungsten calibration sources that are scanned after each line. The video signal from each detector is amplified, digitized, and recorded on tape. Table 14-3 summarizes specifications for the NS-001 scanner. Characteristics of the eight spectral bands are given in Table 14-4.

Table 14-3. NS-001 specifications

Parameter	Value
IFOV, mrad	2.5
Scan angle, deg	100
VH rad/s	0.025 to 0.25
Scan speed, rpm	600 to 6000
Roll compensation, deg	±15
Detector cooling	Thermoelectric and liquid N_2
Gain and level control	Manual
Calibration sources	Blackbodies and tungsten lamp
System aperture, in.	4

Table 14-4. NS-001 spectral band characteristics

Channel	Bandwidth, μm	NER, $Wcm^{-2}SR^{-1}$	NE $\Delta\rho$, %
1	0.45 to 0.52	8.7 by 10^{-6}	0.5
2	0.52 to 0.60	6.8 by 10^{-6}	0.5
3	0.63 to 0.69	5.0 by 10^{-6}	0.5
4	0.76 to 0.90	4.4 by 10^{-6}	0.5
5	1.00 to 1.30	6.0 by 10^{-6}	1.0
6	1.55 to 1.75	6.2 by 10^{-6}	1.0
7	2.08 to 2.35	4.7 by 10^{-5}	<2.0
8	10.4 to 12.5	N/A	NE ΔT = 0.25 K

b. Modular Multispectral Scanner. The Bendix Modular Multispectral Scanner (M^2S) was an 11-channel electro-optical scanner that recorded in the 0.33- to 1.065-μm and 8.0- to 13.5-μm wavelength regions. Ten channels were in the shorter-wavelength region, one in the thermal region. Characteristics are shown in Tables 14-5 and 14-6.

The instrument was flown aboard NASA's C-130 aircraft based at JSC. The 100° scan angle, 2.5-mrad instantaneous field of view (IFOV), and 803 elements per line provided a resolution of 12 m at an elevation of 5000 m. Data were recorded on high-density digital tape (HDDT) and then were converted to CCTs in Universal Format, prior to distribution.

c. Bendix 24-channel scanner. The Multispectral Scanner and Data System (Zeitzeff et al., 1970) was a 24-channel scanner system that JSC (formerly the NASA Manned Spacecraft Center) designed for geological research in 1968. (The system was installed and flown in the C-130 aircraft between 1970 and 1976.) From a remote sensing point of view, the scanner had three uses: (1) collection of data, over large areas of terrain, in a form suitable for analyses on a digital computer, (2) collection of map data outside the spectral range of photographic film and visual observations, and (3) reduction, by an order-of-magnitude, of the problems of film quality control and film scanning.

Table 14-5. M^2S instrument characteristics

Parameter	Value
Number of channels	11
Spectral range, μm	0.33 to 1.065, 8.0 to 13.5
Scan angle, deg	100
IFOV, mrad	2.5
VH range	0.025 to 0.25
Words/scanline	838

Table 14-6. M^2S spectral characteristics

Channel	Bandwidth, μm	Detector
1	0.33 to 0.44	Silicon
2	0.44 to 0.48	Silicon
3	0.49 to 0.54	Silicon
4	0.54 to 0.58	Silicon
5	0.58 to 0.62	Silicon
6	0.62 to 0.66	Silicon
7	0.66 to 0.70	Silicon
8	0.70 to 0.74	Silicon
9	0.76 to 0.86	Silicon
10	0.97 to 1.065	Silicon
11	8.0 to 13.5	Mercury-cadmium-telluride

Table 14-7. Bendix 24-channel scanner

Channel Number	Bandwidth, μm	Detector	Absolute Calibration Source[a]
		Array Number 0	
1	0.34–0.4	Photomultiplier	UV/V/IR
2	0.4–0.44	Photomultiplier	UV/V/IR
3	0.46–0.5	Photomultiplier	UV/V/IR
		Array Number 1	
4	0.53–0.57	Silicon	UV/V/IR
5	0.57–0.63	↕	↕
6	0.64–0.68		
7	0.71–0.75		
8	0.76–0.8		
9	0.82–0.87		
10	0.97–1.05	Silicon	UV/V/IR
		Array Number 2	
11	1.18–1.3	Germanium	UV/V/IR
12	1.52–1.73	Germanium	UV/V/IR
		Array Number 3	
13	2.1–2.36	Indium antimonide	UV/V/IR
14	3.54–4.0	Indium antimonide	Blackbodies
15	4.5–4.75	Indium antimonide	Blackbodies
		Array Number 4	
16	6.0–7.0	Mercury-doped germanium	Blackbodies
17	8.3–8.8	↕	↕
18	8.8–9.3		
19	9.3–9.8		
20	10.1–11.0		
21	11.0–12.0		
22	12.0–13.0	Mercury-doped germanium	Blackbodies
		Array Number 2	
23	1.12–1.16	Germanium	UV/V/IR
		Array Number 1	
24	1.05–1.09	Silicon	UV/V/IR

[a]UV/V/IR: ultraviolet/visible/near infrared.

The spectral region covered by the 24-channel scanner extended from 0.34 to 13.0 μm, encompassing both the reflected solar spectrum and the thermal infrared (Table 14-7). The distribution of channels (1) was limited to atmospheric windows and (2) was governed in detail by the requirements for agricultural, geologic, and oceanographic uses. Channels 23 and 24 were added to measure precipitable water vapor in the observation and illumination paths.

Scan lines were generated by a 45°-scanning, flat rotating mirror with its axis parallel to the flight path, an active scan angle of 80°, and a spatial resolution of 2 mrad.

Calibration accuracy specifications are given in Table 14-8. Two thermoelectrically controlled blackbodies, calibrated to ±0.5 K, were used for the thermal band calibration; these sources were set to the expected high and low extremes of target temperature. The ultraviolet/visible and infrared channels were calibrated by both an internal tungsten–halogen lamp and a skylight reference derived from a diffusing screen on top of the aircraft. The skylight reference was used to infer the terrain illumination level.

Table 14-8. Bendix 24-channel scanner calibration accuracy specification

Spectral Range, μm	Accuracies Required	
	Relative (channel-to-channel)	Absolute
0.34 to 2.36	1%	5%
3.5 to 13.0	0.2 K	0.5 K

Spectral dispersion for the scanner was provided by diffraction gratings. Two spectrometers sharing the same scan mechanism and field-defining aperture were employed, one for the reflected and the other for the thermal channels. The data were recorded digitally with 8-bit digitization, representing a dynamic range of 250:1.

d. X-band side-looking aircraft radar. The Johnson Space Center provided X-band (10.69-GHz frequency and 3-cm wavelength) radar-image data obtained with a Goodyear side-looking aircraft radar (SLAR) system mounted in an RB-57 aircraft. This system recorded one like and one cross-polarized signal (vertical or horizontal, selectable) on an optical recorder. Approximately 20 min of data could be recorded at 740 km/h (400 knots) ground speed. The optical recorder could not be reloaded in flight. Two modes of incidence angles could be selected: one from 14° to 40° and one from 45° to 60°. At 1520 m above terrain, the resulting swath width was approximately 18 km, and the resolution was approximately 20 m.

e. L-band side-looking aircraft radar. NASA's Ames Research Center provided L-band (1.2-GHz frequency and 25-cm wavelength) radar-image data obtained with a system designed by the Jet Propulsion Laboratory (JPL) and mounted in a Convair 990 aircraft. This configuration allowed simultaneous imaging in four polarizations (horizontal, HH; vertical, VV; and two cross polarizations, HV, and VH). The incidence angle was selectable from 0° to 70°. At 1050 m above terrain, the swath width was approximately 15 km, and the resolution was approximately 25 m. The optical recorders had a capacity of 1.5 hours of data and could be changed in flight. A digital recording system was also available and was capable of recording one of the four available channels. The digital data were recorded on tape with a half-hour capacity per tape. The tape could be reloaded in flight.

f. Passive microwave imaging system. The Johnson Space Center provided X-band (10.69-GHz frequency and 3-cm wavelength) passive microwave image data obtained with an Aerojet passive microwave imaging system (PMIS) mounted in a C-130 aircraft. This system digitally recorded the dual-polarized data on a CCT. The phased array antenna system maintained a constant incidence angle of 50°. Along the 70° scan (nadir ±35°), two-dimensional quantitative antenna brightness temperature data were recorded by the low-noise system at 44 beam positions (beam width 1.8° to 2.7°).

g. Multifrequency microwave radiometer. The Johnson Space Center provided four-band passive microwave profile radiometry data obtained with an Aerojet multifrequency microwave radiometer (MFMR) system (modified by JSC) mounted in a C-130 aircraft. This system digitally recorded emitted microwave energy, data which were converted to antenna temperatures on a CCT. Characteristics of the MFMR system are summarized in Table 14-9.

h. Shuttle Multispectral Infrared Radiometer. In 1977, the Shuttle Multispectral Infrared Radiometer (SMIRR) was constructed for the NASA OSTA-1 payload on the second flight of the Shuttle spacecraft. SMIRR was designed to obtain single-point (nonimaging) radiometer data in 10 spectral bands in the 0.5- to 2.4-μm range. The bands were chosen to test the potential of specific wide and narrow spectral bands for future imaging systems for the identification of materials of geological interest (Goetz and Rowan, 1981).

SMIRR consisted of a 19-cm-diameter Cassegrain telescope, behind which were mounted a spinning wheel containing 10 interference filters and a thermoelectrically cooled, short-wavelength-cutoff mercury-cadmium-telluride detector. From a Shuttle altitude of 250 km, the IFOV of the

Table 14-9. Characteristics of MFMR

Parameter	Channel			
	1 (L-band)	2 (Ku-band)	3 (K-band)	4 (Ka-band)
Frequency, GHz	1.42	18.00	22.05	37.00
Wavelength, cm	21	1.65	1.35	0.80
Bandwidth, MHz	27	200	200	500
Polarization	Single (V or H)	Dual (Switched)	Dual (Simultaneous)	Dual (Simultaneous)
Antenna type	71- by 71-cm phased array	Dielectric lens fed by scalar horns	Dielectric lens fed by scalar horns	Dielectric lens fed by scalar horns
Beam width, deg	16	5	5	5
Resolution at 610 m above terrain, m	171	53	53	53

radiometer was approximately 100 m. Two 16-mm framing cameras were bore-sighted with the radiometer telescope. Each camera contained a reseau plate; the position of the radiometer footprint was known with respect to three reseau marks within ± 1 mrad IFOV.

The filters were centered at the following wavelengths: 0.5, 0.6, 1.05, 1.2, 1.6, 2.1, 2.17, 2.20, 2.22, and 2.35 μm. The filters having wavelengths short of 2.17 μm had bandwidths of 0.1 μm. The next three had bandwidths of 0.02 μm, and the 2.35-μm filter had a bandwidth of 0.06 μm. The choice of the filters was based on statistical analyses of thousands of reflectance spectra obtained under field conditions. The filters in the 2.1- to 2.35-μm region were chosen to aid in the identification of alunite, carbonate, and clay minerals.

SMIRR underwent laboratory absolute calibration tests as well as tests using mineral samples of known composition illuminated by the sun. These calibrations formed the basis for interpretation of the radiometric data acquired from Earth orbit. To gain experience with the type of data expected from the Shuttle over natural terrains, SMIRR was installed in the JPL aircraft. Test sites in Utah, Arizona, and Nevada were overflown during 1979 and 1980.

The aircraft was flown approximately 200 m above terrain at an airspeed of 93 m/s (180 knots), resulting in a 1-m IFOV. The small IFOV yielded data showing rapid fluctuations of brightness associated with individual bushes and with shadows cast by small outcrops. Although 128 samples were acquired between sequential photographs, ground location of the IFOV was certain only when camera frames were being exposed. Between camera exposures, the attitude of the aircraft was unknown, and interpolations between centers of individual 16-mm frames only approximately located the ground track.

i. Aerial photography. The Johnson Space Center provided high-quality aerial photography, usually obtained during a multispectral scanner aircraft mission. Two Zeiss systems were available: RMK 30/23 (focal length 30.50 cm and IFOV 47°) and RMK 15/23 (focal length 15.25 cm and IFOV 93°). At approximately 4900 m above terrain, these systems provided continuous coverage, 22.85- by 22.85-cm photographs at a scale of approximately 1:45,000, with ground resolution of approximately 1 m. Film options included aerial color (2443, wavelength 0.42 to 0.7 μm) and Ektachrome infrared (CIR) (SO 193, wavelength 0.52 to 0.9 μm). Either print or positive transparency products could be requested.

3. Portable Field Reflectance Spectrometer. The Portable Field Reflectance Spectrometer (PFRS) is a field-portable instrument designed and built at JPL (Goetz et al., 1975) to meet the following criteria:

(1) Backpack, field-portable

(2) Coverage of the 0.4- to 2.5-μm spectral region with moderate resolution ($\Delta\lambda/\lambda = 0.02$ to 0.04)

(3) Stability over a wide range of temperatures

(4) Digital data recording

The PFRS system consists of a separate optical head and an amplifier-recorder assembly. In the field, the electronics pack is worn by the operator. The optical head, mounted on a tripod, is carried on a pack frame when moving from area to area. A hand-held meter indicates the signal level and is used to set gain levels. All results are reduced to spectral reflectance values for comparison of areas measured under various lighting conditions.

The optical head is illustrated in Figure 14-1. In sequence, the beam enters the instrument at the left and is interrupted by a 280-Hz vibrating reed chopper. A relay lens focuses the incoming light on the slit directly in front of the filter wheel and, by way of a beam splitter, onto a total-field detector. The circular, variable-filter wedge (Figure 14-2) defines the wavelength and, in the three opaque sectors, allows engineering information to be inserted into the data stream. A second lens focuses the beam on a 1- by 6-mm detector.

The PFRS is capable of operating in a 0° to 50° C environment. Both the total-field and the spectral detectors are lead sulfide (PbS), thermoelectrically cooled (or heated) to 15° ± 0.02° C. Stabilizing the temperature of the detectors eliminates a major source of signal drift.

The total-field detector monitors the total irradiance in the field of view as a function of time. Correcting the spectral detector output for irradiance fluctuations over the 30-s scan period permits operation under high cirrus cloud conditions while maintaining reasonable accuracy in reflectance measurement.

Figure 14-3 is a functional block diagram of the recording electronics in the backpack. Both the spectral and total-field detector channels follow parallel-amplification and synchronous-demodulation paths to the multiplexer. Signal measurement and recording occur at 90-ms intervals. Sample-and-hold circuitry is used for integration within the sampling interval. Analog-to-digital converters follow the multiplexer circuit to ensure compatibility of the signals with digital cassette recording.

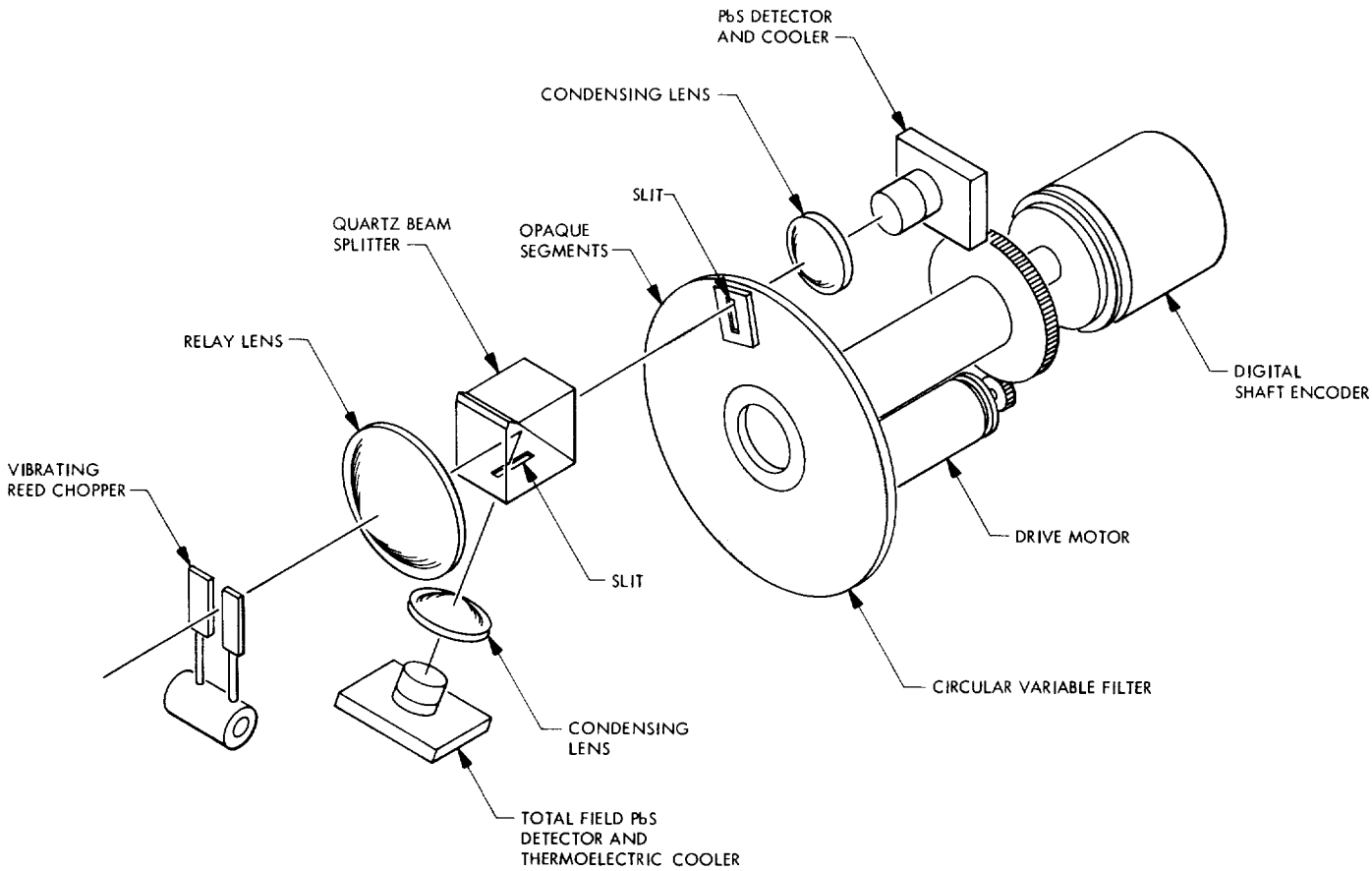

Figure 14-1. Exploded view of PFRS optical head. Infrasil lenses are used.

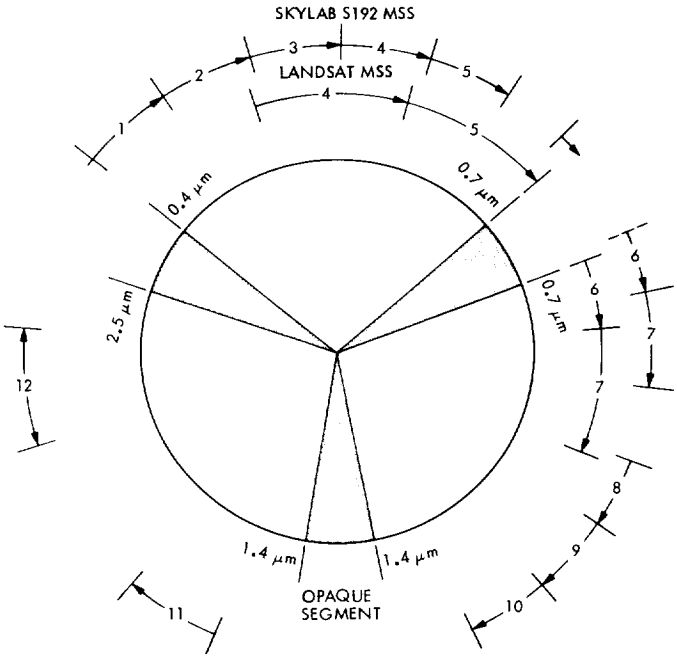

Figure 14-2. Composite circular variable filter wheel with indicated positions of the 4 Landsat and 12 Skylab S192 MSS bands

When spectral measurements are made, four 12-bit words—consisting of the filter-wheel position, total-field detector signal, and spectral-detector signal—are recorded along with file number and gain states in each of the detector channels. When the three opaque segments of the filter wheel (Figure 14-2) are in the field of view, engineering measurements such as battery and power-supply voltages as well as optical-head and backpack temperatures are multiplexed into the signal channels. These diagnostic measurements have proved useful in interpreting anomalies in the field.

Additional digital circuitry formats the signals for recording and controls the filter-wheel rotation. Power is supplied by a 6-V silver–zinc battery with a capacity of 80 A/h. To conserve power, only the detector coolers and the preamplifiers are energized when the unit is in a standby condition. When a run is initiated, the DC-to-DC converters are energized; filter-wheel rotation and digital recording automatically begin after a 2-s warmup. At the end of the rotation, the system automatically returns to the standby condition. A file counter that uses low-power-drain cir-

cuitry remains energized continuously, even after the front-panel power switch is turned off, so that no file-count error is possible.

When in the field, the optical head is mounted on a tripod about 1.3 m above the surface, with the long axis of the slit oriented along the solar azimuth. The surface area covered from this height is approximately 200 cm^2.

Gain settings for both signal channels are made by manually setting the filter to approximately the 0.7-μm position, the point of maximum signal observed on the hand-held meter. The response of the PbS detector is sufficiently flat that only one gain setting is required for the 0.4- to 1.4-μm range. An automatic divide-by-2 gain change is made for the last segment of the filter wheel. A spectrum of the surface is taken, followed immediately by a measure against a standard in the same orientation. Fiberfrax®, a ceramic wool insulation used as the standard, has a surface that is renewable by peeling the upper layer and pressing the surface flat. This is important since contamination is inevitable under field conditions.

It is possible to record 100 spectra on the two sides of one digital cassette. With battery power sufficient to record about 700 spectra, operation is possible for about 2 or 3 days between charges.

A set of interface electronics known as a "playback box" (capable of displaying the file number and accessing the beginning of any desired file) operates the tape recorder within the backpack unit at a field headquarters. A digital-to-analog converter is included for playback on a strip-chart recorder. This unit acts as a tape controller and an interface to the computer for analysis. The spectra are reduced and analyzed with the aid of a Digital Equipment Corporation (DEC) PDP computer and plotter.

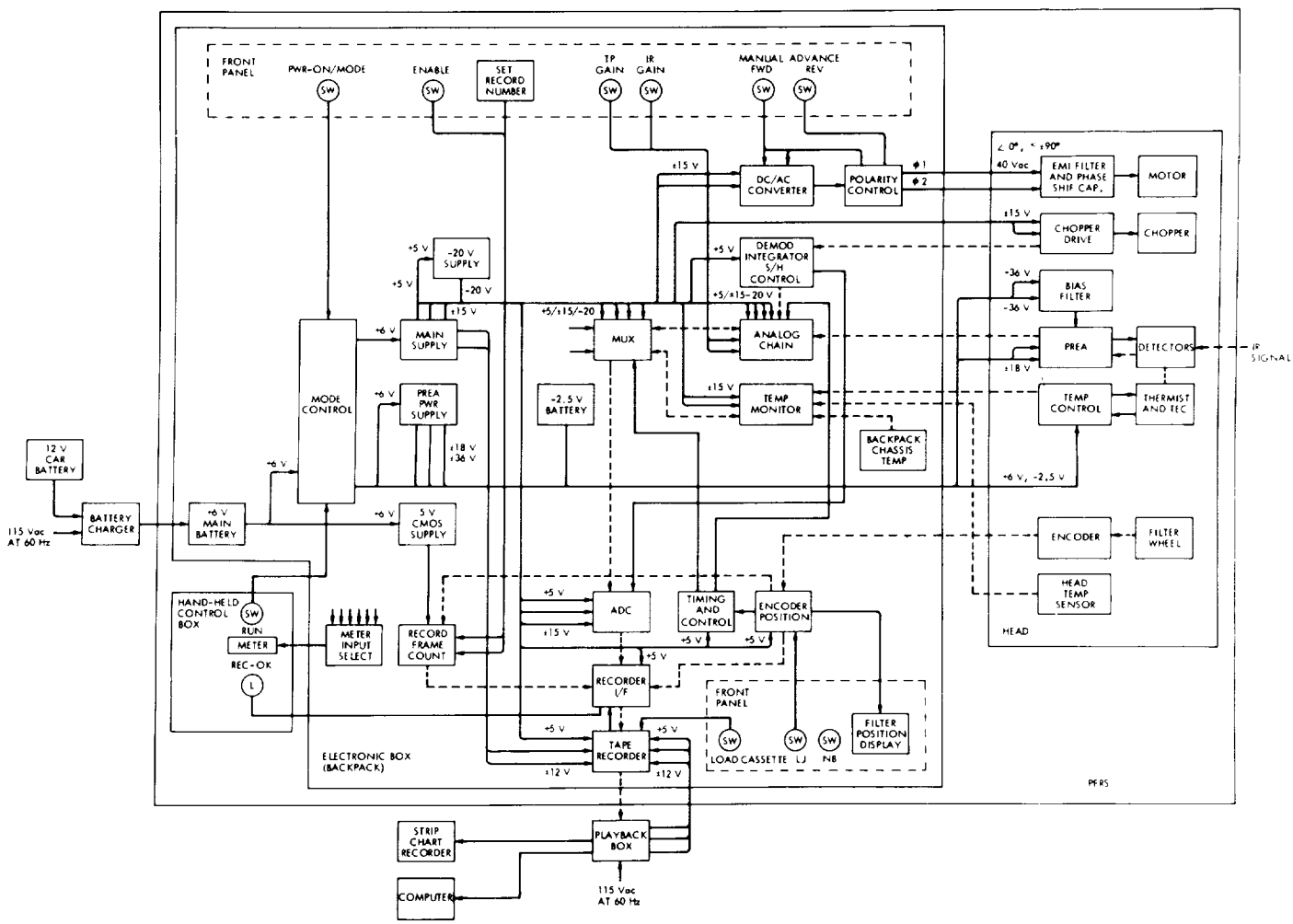

Figure 14-3. Functional block diagram of the PFRS

B. Non-NASA Remote Sensing Data

1. Fraunhofer Line Discriminator. The Fraunhofer Line Discriminator (FLD) is an airborne electro-optical device designed and developed by the U.S. Geological Survey under NASA sponsorship (Watson and Hemphill, 1976). Instruments have been developed that operate as both imaging and nonimaging radiometers. Here we discuss only the imaging system used in observations over test sites at Lisbon Valley (uranium), Copper Mountain (uranium), and Patrick Draw (oil and gas). These instruments permit detection of solar-stimulated luminescence in rock, vegetation, water, and waste targets several orders of magnitude below the intensity detected by the human eye. The FLD method has been used for (1) studies of luminescence in vegetation stressed from copper, zinc, and molybdenum, (2) detection of oil spills and sulfide effluents from paper mills, and uranium, vanadium, and copper mineralization in sedimentary rocks, and (3) exploration for phosphate rocks and gypsum.

The FLD method operates on the Fraunhofer line depth principle first described by Link in 1951 (see Grainger and Ring, 1962). Fraunhofer lines are dark absorption lines 0.1 to 1.0 Å in width; they originate in the solar atmosphere. Such lines are sharpest, strongest, and most numerous in the ultraviolet, visible, and near infrared. Lines commonly used in these studies are located at 3968, 4861, 5184, 5890, and 6563 Å. For any given target, a selection is made from this collection; the selection is based on laboratory analysis of samples of the most active regions. An advanced FLD system used in the reported observation at Lisbon Valley (Theisen et al., 1979) employed the three lines at 4861, 5890, and 6563 Å.

The Fraunhofer line depth method of measuring luminescence involves observing a selected Fraunhofer line in the solar spectrum and measuring the ratio of the central intensity of the line to a convenient point on the continuum a few tenths of a nanometer distant; this ratio is compared to a similar ratio of a conjugate spectrum reflected from a material that is suspected to luminesce. Normally, both ratios are identical; luminescence is indicated when the reflected ratio *exceeds* the solar ratio. Reflectivity differences between the central intensity of the Fraunhofer line and the adjacent continuum can generally be ignored because the variation of reflectivity with wavelengths is negligible for most materials over spectral ranges of only a few tenths of a nanometer.

Figure 14-4(a) shows an idealized Fraunhofer line observed in the solar spectrum directly, which may be expressed as the ratio R:

$$R = \frac{b}{a} \tag{14-1}$$

where
b = central intensity
a = adjacent continuum

The same Fraunhofer line is given in Figure 14-4(b) in a spectrum reflected from a nonluminescing material. The ratio of the line depth in the spectrum reflected by the material is

$$R_m = \frac{\rho b}{\rho} = R_s \tag{14-2}$$

where ρ = reflectance.

Figure 14-4(c) illustrates the luminescence component, L. Because many materials exhibit broadband luminescence (commonly half-widths of several nanometers), the luminescence contribution, L, shown in Figure 14-4(c), may be assumed to be constant across the width of one Fraunhofer line.

Figure 14-4(d) shows the line profile of a material containing both reflected and luminescing components. Since the luminescence component is assumed to contribute equally to both the central intensity and the adjacent continuum,

$$d = \rho a + L \tag{14-3}$$

$$c = \rho b + L \tag{14-4}$$

$$R_m = \frac{\rho b + L}{\rho a + L} = \frac{c}{d}, \qquad R_m > R_s \tag{14-5}$$

The difference between R_m and R_s is a measure of the amount of luminescence. The luminescence component may be measured in terms of the continuum component level, and expressed as a luminescence coefficient by

$$\xi = \frac{L}{a} \tag{14-6}$$

leading to

$$L = \xi a \tag{14-7}$$

where

ξ = luminescence coefficient
L = luminescence
a = continuum component level

Substituting Eq. (14-7) into Eqs. (14-3) and (14-4) yields

$$d = \rho a + \xi a \tag{14-8}$$

$$c = \rho b + \xi a \tag{14-9}$$

These two equations can be solved to determine the two unknowns ρ and ξ. Multiplying Eq. (14-8) by b, and Eq. (14-9) by a, yields

$$bd = \rho ab + \xi ab \tag{14-10}$$

$$ac = \rho ab + \xi a^2 \tag{14-11}$$

Subtracting Eq. (14-10) from Eq. (14-11) yields

$$ac - bd = \xi a(a - b) \tag{14-12}$$

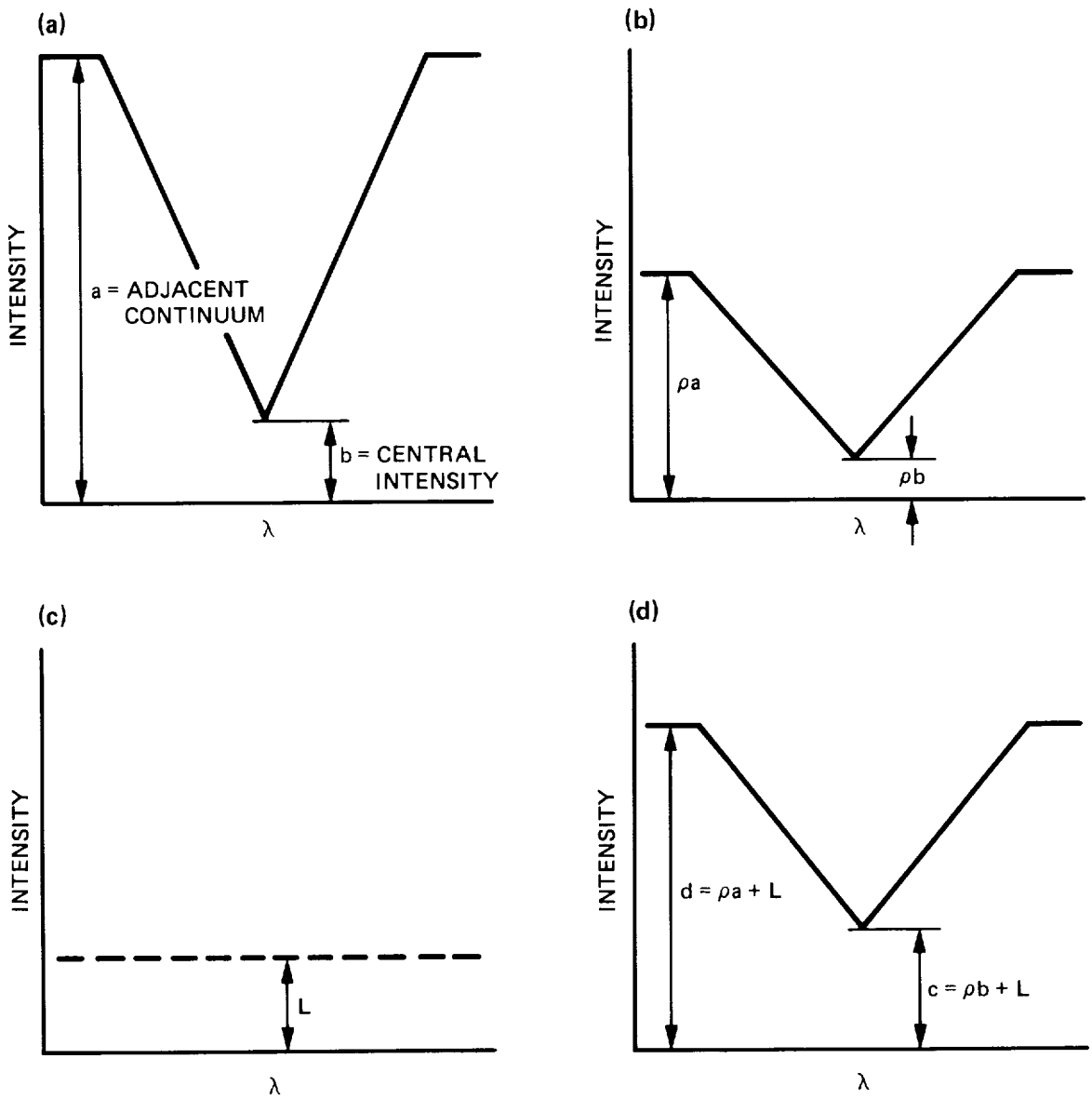

Figure 14-4. Fraunhofer line profile: (a) in the solar spectrum observed directly; (b) in the solar spectrum reflected from nonluminescing materials; (c) of luminescence contribution as a nonvariable with wavelength; (d) of material containing both reflected and luminescent components

Solving for ξ yields

$$\xi = \frac{ac - bd}{a(a - b)} \tag{14-13}$$

$$\xi = \frac{1}{a - b}\left(c - \frac{bd}{a}\right) \tag{14-14}$$

Equation (14-14) is useful because ρ and L are eliminated, and the expression of ξ is independent of incident solar flux.

The engineering model FLD, built by the Perkin Elmer Corporation and delivered to the U.S. Geological Survey in 1974, was designed using the Fraunhofer line depth principle and initally operated as an airborne radiometer. The FLD performed satisfactorily from a helicopter when operating with an instrument bandwidth greater than 0.078 Hz.

In addition to the FLD operating as a radiometer, a system was designed in 1977 to permit operation in an imaging mode. The FLD imaging system is based on a simple optomechanical arrangement which uses a pair of front surface mirrors, one of which is fixed at 45° with respect to the FLD earth telescope and the other oscillated ±9.25° with respect to a position parallel with the 45° mirror. The linearity and total angle of oscillation are controlled by a precision cam, based on an Archimedes spiral design. The rate of oscillation is determined by an electronically controlled precision DC motor with tachometer feedback. The feedback signal is monitored for accurate speed control of one complete sweep (37°) per second. A timing disk is mounted on the motor shaft to provide a beginning-of-sweep trigger, generated by an electro-optical coupler. Ground resolution is determined by the instantaneous 1°-field of view of the FLD. Maximum ground coverage (without overlap) is obtained when the aircraft speed matches the ground resolution of the FLD. For example, with the present system, an aircraft speed of 45m/s (148 ft/s) at 2382 m (7815 ft) above terrain is required for ground area coverage of 80 percent (without overlaps) at a ground resolution of 45 m (148 ft). A bore-sighted television system permits identification of surface features and correlation of these features with measured luminescence and reflectance.

FLD data, recorded on digital tape, are transferred to computer memory where either luminescence or reflectance data for each resolution element can be analyzed and assigned a character representing either a specific value or a range of values. These characters are then reproduced by a printer with a capability of producing 94 distinct characters plus a blank. The computer is programmed to produce gray-scale slicing with a preselected window for luminescence or reflectance.

When a part of the data has been selected for further processing, a histogram is printed. The data are transferred to a DEC PDP 11/45 mainframe computer and compressed to an 8-bit format similar to Landsat TM data. The full range of processing, correction, and enhancement programs used on Landsat data can be applied to the FLD data, and the finished product presented in color form.

In order to assess the sensitivity required to detect luminescing materials, a laboratory fluorescence spectrometer is used to quantify the luminescence intensity of materials at Fraunhofer lines (396.8, 486.1, 518.4, 589.0, and 656.3 nm) in terms of equivalent luminescence of specific concentrations of rhodamine dye. The spectrometer was operated so as to produce excitation spectra; that is, the excitation monochromator was scanned while the emission monochromator was stationary at the wavelength of a specific Fraunhofer line. This arrangement provided a system in the laboratory analogous to an FLD in the field, where the broadband excitation of the sun produces an emission in a luminescent material, the intensity of which is monitored at one or more Fraunhofer lines. The spectrometer—equipped with a corrected spectra attachment—automatically adjusted for the wavelength dependence of the source and detector and produced a corrected distribution of excitation intensity.

In the front-surface mode, solid samples (or liquid or powdered samples in a centimeter quartz cell) were so positioned in the sample compartment that both excitation and emission went through the front surface of the sample. Light from the excitation monochromator illuminated the sample surface at an angle of approximately 30° to the normal, and luminescence from the sample surface was directed in a narrow solid angle (centered at 90° from the incident beam) into the emission monochromator and onto the detector. In the right-angle mode, light from the excitation monochromator passed through the sample cell, with resulting luminescence measured at right angles to the incident beam.

To relate all luminescence spectra to one set of conditions, rhodamine WT was used as the reference "standard" prior to each measurement. When the area under the curve of the excitation spectra of the sample was compared to the area under the curve for rhodamine WT dye (at a specific dye concentration), a relative, equivalent rhodamine WT concentration was obtained. For example, a sample having an integrated excitation intensity of 50 was compared to a rhodamine WT concentration of 10 ppb, which

also has an integrated excitation intensity of 50; the sample is said to have had an equivalent luminescence of 10 ppb rhodamine WT. This standardization makes it possible to correct for instrument response variations during measurement and to assess results achieved in the laboratory in terms of whether the same material in the field would be within the sensitivity range of an airborne FLD.

2. Aerial radiometers. Aerial spectral gamma (γ) radiometric measurements were performed over the Copper Mountain uranium site in 1977 by GeoMetrics, Inc., under subcontract to the Bendix Field Engineering Corporation as part of the NURE program. The technical details below were taken from Bramlett et al. (1979).

a. The measurements. The γ-spectral measurements were made along east–west flight lines spaced at 1.6 km in an outer block and at 0.5 km over a detailed inner grid covering the zone of major mineralization. North–south tie lines were spaced 6.4 km apart in this inner block. A detector utilizing 2048 cm^3 of sodium-iodide crystal was used on board a helicopter. Multispectral data were reduced to potassium (as ^{40}K), uranium (as ^{214}Bi), and thorium (as ^{208}Th) concentrations and to the gross gamma signal for each 1.0-s digital record. The interference between peaks was removed before potassium, e uranium, e thorium, and gross gamma signals were reported. It was assumed that ^{214}Bi and ^{208}Th were in secular equilibrium with uranium and thorium. The data were reduced, and all fiducial and navigational corrections, as well as cosmic ray and airborne ^{214}Bi backgrounds, were accounted for before the survey data were recorded on magnetic tape and were placed on disk file for review and interpretation by Bendix.

b. Four-channel gamma-ray spectrometry. A 4-channel, analog gamma-ray spectrometer, Model DGRS-1002, manufactured by Exploranium/GeoMetrics, was used for this survey. The detector was a sodium-iodide crystal with a volume of 1953.33 cm^3 (113.09 $in.^3$). The spectrometer was used in the differential mode providing a measurement of potassium (as ^{40}K), uranium (as ^{214}Bi), thorium (as ^{208}Th) and the total count from 0.4 to 3.0 MeV. The output of the channels was recorded on an 8-channel recorder.

The aircraft and system radiometric background was measured at the start and end of each workday by overflying a reservoir located near the survey area. Surveys were not conducted during periods of temperature inversions or during or immediately following periods of precipitation. The sampling period was nominally 1 s. The digitized values were acquired in hundredths of inches and were converted to counts per second after the correction for variations in full-scale deflection and variations in the zero level.

Compton Scatter corrections, which include corrections for background, were applied to the converted data, and the striping coefficients were determined from the calibration data obtained over the Walker Field Calibration Pads (Bramlett et al., 1979). Backgrounds used for the corrections were determined from the analog records, and each flight was processed separately. Occasionally, Th_{Corr}, U_{Corr}, K_{Corr}, and Tc_{Corr} were negative, indicating that the backgrounds may have changed locally and/or the aircraft terrain clearance changed. To avoid plotting negative values, the results were adjusted. The adjustments were applied on a flight-by-flight basis.

3. Aerial magnetics. Aerial magnetic data have been compared with images depicting the state of oxidation of granite rocks at Copper Mountain. The magnetic surveys were conducted by the Bendix Field Engineering Corporation as part of the NURE program. The discussion below is taken from Bramlett et al. (1979).

Magnetic data were collected in conjunction with the aerial radiometric survey using a high-sensitivity (0.25-gamma) proton magnetometer. The magnetic data were corrected for diurnal variations, tying to a common magnetic datum and "detrending" by subtracting the regional magnetic field as defined by international convention in 1975. The diurnal magnetic field was monitored by a ground-based magnetometer that sampled every 4 s. These data were recorded on magnetic tape along with the time for synchronization with the airborne data.

These corrected magnetic data were then processed by a tying program that compared the magnetic differences at the intersection of flight lines and tie lines. The 1975 IGRF (updated to the survey date) was subtracted from the corrected, tied magnetic data, thus yielding the reported residual magnetic field.

4. Airtrace®. (The discussion below is largely extracted from Abercrombie et al., 1978, except as otherwise indicated.) The Airtrace® method, developed by Barringer Research Limited, is an airborne geochemical system that samples and measures the elemental composition of particulate material from the lower atmosphere. The system relies upon the phenomenon of atmospheric dispersion of inorganic particulates from surface soils and vegetation.

The system consists of an airborne unit (including an air-collection device, a particulate-sizing module, and a sample impingement-collection deck) and a laboratory-playback unit. The laboratory-playback unit is used with the Lasertrace® analysis system to determine the elemental composition of samples (refer to Paragraph II.B).

The airborne unit for the Airtrace® system is shown in Figure 14-5. The collection mechanism consists of two aerodyne collectors capable of receiving 34 m^3 of air per minute. The system is usually mounted on a helicopter, but it may be used with any suitable aircraft. These collectors are designed to reject particles smaller than 10 μm in diameter and to retain particles greater than 50 μm in diameter. The larger particles have relatively high settling velocities in the atmosphere, with mean dwell time of a few tenths of a second; on the other hand, finer particles have a mean dwell time of hours and in extreme cases, weeks. Under typical conditions, the transport distance of the larger particles is estimated to be in the tens to hundreds of meters. In this manner, only the larger particles of local derivation are retained.

Particles thus sampled are transferred into a small volume of air and then are accelerated to minimize the risk of particle hang-up in the system. The particles are counted, and a switching mechanism is employed to divide the sample into two streams. Both streams are vacuum impacted onto high-purity mylar adhesive tape to form sample "spots" of particulate material covering an area 3 mm in diameter on the sample tape. One stream consists of material characterized by very high flux rates, indicative of rising bodies of air containing particulates of local derivation. This forms the Airtrace® sample. The other stream is characterized by material with more uniform flux rates associated with stagnant or falling air containing exotic particulate material. To improve the precision of the system, material is impacted onto the tape until a fixed number of counts are accumulated on the particle counter monitoring the Airtrace® sample. The sample tape is then automatically advanced and protected with a Teflon cover tape to prevent contamination. The sample spacing along the tape is irregular. Sample location marks are automatically registered on the cover tape. Sampling rates average 400 sample pairs per hour.

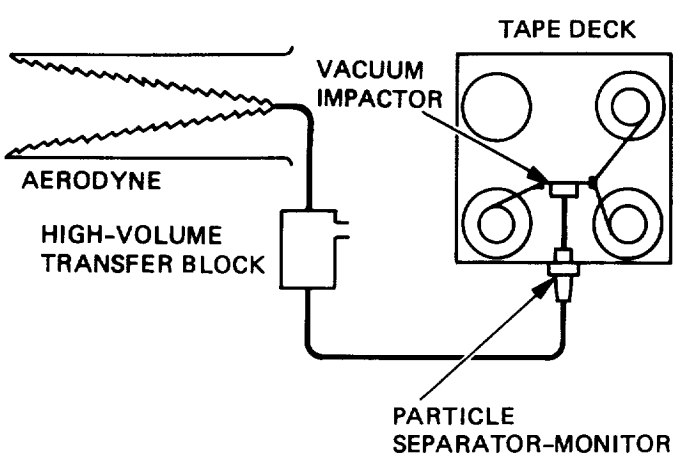

Figure 14-5. Airtrace® airborne unit (from Abercrombie et al., 1978)

Sampling lines are typically flown at 500-m spacings. In normal operation, the average speed of the survey helicopter is 145 km/h at approximately 6 m above the highest object.

Sample tapes are taken to the laboratory where they are played back for analysis using the Lasertrace® analytical system. Figure 14-6 shows the automated playback system.

5. Surtrace®. (The discussion below is largely extracted from Bramlett et al., 1979, except as otherwise indicated.) The Surtrace® method, developed by Barringer Research Limited, is an airborne geochemical system that samples and measures the elemental composition of the interface between the Earth and its atmosphere. The Earth's surface is covered with a layer of particulate materials in contact with the atmosphere. This surface microlayer of residual soils reflects the geochemistry of the underlying parent material. The coarse particulate material occurring on the

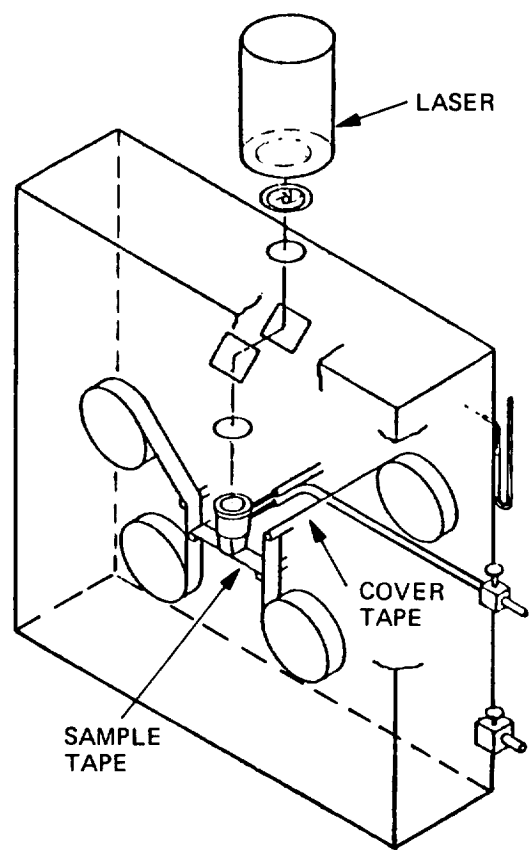

Figure 14-6. Lasertrace® laboratory-playback unit (from Abercrombie et al., 1978)

surface of vegetation and having wholly biological origin also exhibits a chemical composition that closely reflects the geochemistry of the underlying soils.

The Surtrace® system consists of an airborne unit (including a sampling-probe device, a particulate-sizing module, and a sample impingement-collection deck) and a laboratory-playback unit. All subsystems are the same as those used in the Airtrace® system (refer to Paragraph I.B.4) except for the sampling probe.

The sampling probe, located beneath the helicopter, is a lightweight, flexible device carrying a sensor that allows the pilot to keep the probe in contact with the ground. Vacuum equipment removes the surface microlayer of particulate material in a semicontinuous sampling operation, and the sample is size-sorted, concentrated, and impacted onto the collection tape. After a sample is impacted, the sample tube is automatically back-flushed. This flushing period can be varied according to surveying conditions and requirements.

Sampling lines are typically flown at 250-m spacings. In normal operation, the average speed of the survey helicopter is 48 km/h. Samples are usually taken every 5 s, resulting in a sample spacing of approximately 75 m.

A portable backpack and a vehicle-mounted version of the Surtrace® sampling system are also available (Barringer et al., 1978).

II. Ground Truth Data by Laboratory Techniques

A. NASA Data

1. Beckman DK2A Spectrophotometer. The Beckman Model DK2A ratio-recording spectrophotometer is a laboratory instrument designed for the analysis of gases, liquids, and solids in the spectral region of 0.16 to 3.5 μm. The laboratory spectra reported here, however, cover only the region of 0.4 to 2.5 μm, corresponding to the spectral region covered by the PFRS and to the atmospheric window short of the major water-absorption bands near 3 μm. The DK2A is routinely operated in the reflectance mode with a barium-sulfate-coated integrating sphere and special attachments to allow hemispherical measurements on horizontal, uncovered, granulated, and solid samples (Conel and Nash, 1970). All measurements are made with respect to magnesium oxide and can be converted to "absolute" reflectance if the current reflecting properties of this standard are known. A method of averaging reduces the spectra to a standard relative scale $[R_r(\lambda)]$ by dividing the measured reflectance at each wavelength by the average standard reflectance. In this form, the relation between the relative reflectance $[R_r(\lambda)]$ and the sample reflectance $[R_t(\lambda)]$ is given by

$$R_r(\lambda) = \frac{R_t(\lambda)}{R_{MgO}(\lambda)}$$

where R_{MgO} is the hemispherical reflectance of MgO. The signal-to-noise ratio of this instrument is estimated to be approximately 500 throughout the visible and infrared region.

It is important to realize the inherent difference between field and laboratory spectral reflectance measurements under the system in use. The laboratory instrument permits hemispherical reflectance measurements on circular flat samples 1.2 cm in diameter. On the other hand, the PFRS allows areal average spectra of undisturbed ground over a 2° by 11° (0.035 by 0.192 rad) area. These latter measurements are bidirectional in character with the optical path of the spectrometer head lying in the plane of incidence of sunlight with the surface. The field spectra are normalized against Fiberfrax®.

The relationship between the photometric character of these two types of spectral data can be obtained from the theory of the integrating sphere (Edwards et al., 1961; Wendtland and Hecht, 1966), by defining the bidirectional half-space reflectance as $f(\theta, \phi; \theta', \phi')$ for reflectance direction (θ', ϕ') and incidence direction (θ, ϕ) in polar coordinates. The reflectance $\rho(\theta, \phi)$ for monochromatic light is then defined in terms of illumination as

$$\rho(\theta, \phi) = \int_0^{2\pi} \int_0^{\pi/2} f(\theta, \phi; \theta', \phi') \sin\theta' \cos\theta' \, d\theta' \, d\phi' \tag{14-15}$$

Thus, for real diffusely scattering surfaces in most cases, $\rho(\theta, \phi) \geq f(\theta, \phi; \theta', \phi')$, and the two are related by Eq. (14-15). The theory of the integrating sphere (Wendlandt and Hecht, 1966) shows that in error-free measurement, the measured hemispherical reflectance is

$$\rho_m = \frac{\rho_s(\theta, \phi)}{\rho_{st}(\theta, \phi)}$$

where ρ_s is a sample reflectance for incidence directions (θ, ϕ) and ρ_{st} is standard reflectance for these same angles.

From the nature of the procedure, the PFRS measures $f(\theta, 0; 0, 0)$. To go from one set of measurements to another

via Eq. (14-15), some measure of the full functional form of $f(\theta, \phi; \theta', \phi')$ is required. Such measurements are ordinarily not required because the laboratory spectra are generally used only as interpretational guides for features in the field data. An exception to the foregoing occurs of course if the surface is scattering strongly (i.e., is specular) in the direction of observation.

While the values of reflectance obtained by these two methods are only suggestively comparable in magnitude, the wavelength positions of important absorption features remain unaffected for the observation of similar materials.

2. X-ray diffraction unit. An early-model Phillips Norelco diffractometer was updated by replacing the electronics and detection systems while retaining the line voltage regulator, two goniometers, X-ray tube housing, and generator. This updated model is cooled automatically by a circulating chilled-water supply. The X-rays are derived from a CuKa tube. Solid-state electronics include the following units by Mechtronics:

(1) One high-voltage power supply for the detector

(2) One scaler-timer unit

(3) Two amplifier-scanner units with pulse-height discrimination

(4) Two rate meters with standard-error and percent-offset pots and a scaler-multiplier unit

The detector units for the two goniometers include a large d-spacing curved graphite focusing crystal grown by the Union Carbide Company in a Phillips Electronics Company monochrometer, which passes monochromatic radiation pulses to the transistorized scintillation detector. A pulse-height analyzer allows a baseline and window voltage to be set; signals above or below this window are rejected. The data are recorded on two Hewlett-Packard recorders. Two-theta discrimination is at 0.05°. The goniometer scanning range used is from 5° to 65° 2θ.

B. Non-NASA Data: Lasertrace®

Samples collected by the Airtrace® or Surtrace® systems or finely ground ($\sim 10\ \mu$m) samples manually mounted on mylar tape can be analyzed for up to 24 elements with the Lasertrace® system developed by Barringer Research Limited. This system uses a direct-reading Model QA 137 multielement, radio frequency, argon plasma emission spectrometer calibrated to measure concentrations (in ppm) of the following elements: carbon, aluminum, calcium, copper, chromium, cobalt, iron, lead, magnesium, manganese, molybdenum, nickel, silver, beryllium, strontium, barium, zinc, sodium, silicon, phosphorus, thorium, titanium, vanadium, and potassium.

According to Bramlett et al. (1979),

> Survey tapes containing particulates of the appropriate size are analyzed for elemental composition by solid sample transport into the plasma, followed by excitation and light emission at specific wavelengths characteristic of the elements listed above.

According to Abercrombie et al. (1978, p. 39.2),

> The tapes are played back through a lab system which removes the 10 to 500 μg of sample from the adhesive tape surface and transports the resulting aerosol to a multi-element instrument without contamination or matrix interferences.
>
> The tape is placed on a deck and the air purged to establish an argon atmosphere. The optical marks on the tape are used to position the dust spots under a laser beam, and control the logic which removed the cover tape and sequentially advanced the tape drive after each laser-firing-measurement cycle. A pulsed 17 megawatt CO_2 TEA laser releases the airborne particulates from the sample tape. The 10.6 μ laser radiation is transmitted by the tape but strongly absorbed by the particulate matter. The ejected particulates (as formed) are entrained in the flowing argon stream passing through a specially designed glass cell. The ejecta is swept into a radio frequency argon induction coupled plasma for optical emission analysis. Almost 80–85% of the ejected sample is carried to the plasma. The cell design prevents cross contamination between adjacent sample pairs and allows continuous running of the plasma even when the playback assembly is opened to change tapes.
>
> During automated operation, the logic controller advances the sample tape into the laser target zone and fires the laser. After 10 seconds, a front surface mirror in the laser path rotates slightly to reflect the laser beam onto the second sample spot of the pair (generally coarse and fine size) and the laser again fires. After 10 seconds, the mirror rotates to its original position and the sample tape advances to a fresh pair of spots, beginning the cycle again. The plasma spectrometer integration commences coincident with the laser pulse and continues for 3 seconds. During that time interval approximately 80% of the transported material is swept into the plasma. The analytical rate is limited to a 10 second interval by the operating speed of the calculator attached to the polycromator.

The analytical system uses an inductively coupled RF plasma (ICP), which features good sensitivity, wide dynamic range and automated multi-element analysis. The spectrometer is an Applied Research Laboratory QA 137 direct reading spectrometer with 25 element slit array. The output from the ARL digital voltmeter is interfaced through a Hewlett-Packard 9821 programmable calculator to provide magnetic tape cassette storage and thermal printer hard copy record. The QA 137 operates at 1.6 Kwatts full work power at an observation height of 16 mm above the load coil. Coolant plasma and aerosol gas flow rates were approximately 10 and 1 litres/minute respectively.

A detailed discussion of the procedure for converting the millivolt readings from the QA 137 to parts per million and a comparison of these readings to results obtained by atomic adsorption and conventional plasma spectroscopy are also presented in Abercrombie et al., 1978.

III. Image Processing Laboratory Facilities

The Image Processing Laboratory (IPL) is equipped with an IBM 370/158 CPU with 3 megabytes (Mbytes) of main memory and 2800 Mbytes of on-line disk storage. A Floating Point Systems AP-120B array processor, attached to the IBM 370 through a DEC PDP 11/34 minicomputer, provides additional specialized computation capability. Interactive display is provided by three digital refresh image display systems interfaced to the CPU: a Ramtek GX-100B 480-by-640 monochrome system, a Comtal Model 1024 system, and a Comtal 8000 512-by-512 color system. Film recorders include a custom built single laser color device, a Dicomed D47 CRT system, and an Optronics P1500. A Polarization Diversity S-band (PDS) scanning microdensitometer and a Bendix coordinate digitizer allow data entry from film and maps, respectively.

IPL software is structured about the VICAR executive, featuring a high level processing language that controls invocation of any combination of the over 200 applications programs. An interactive version of the control language, LIBEXEC, brings the capabilities of VICAR to the interactive display systems. Image Based Information System (IBIS) software, developed at JPL, is available through VICAR. The Informatics Mark IV information system is also available for data management and cataloging.

IV. Computer Processing

A. General Processing

Computer processing applied to test site image data falls into two categories: (1) data preparation, including reformatting and various necessary corrections, and (2) analysis and display.

1. Data preparation. The preparation of Landsat MSS data used in the study consisted of reformatting the pixel interleaved data received from the Goddard Space Flight Center, applying a set of standard geometric corrections, and removing the striping. All of the geometric corrections were performed in a single resampling operation using bilinear interpolation. Among the distortions removed by resampling were those due to Earth rotation, panorama, roll, aspect ratio, and nonuniformity in mirror-scan velocity. After the aspect-ratio correction, each image pixel represented a resolution element of 80 m $\times$ 80 m. The final step of data preparation removed the characteristic Landsat MSS six-line striping pattern. This was done by matching the average values of full scan lines for each of the six sensors over local areas of any of the spectral components.

Similar types of data preparation were applied to aircraft image data. The first step was to separate the spectral channels by reformatting the band interleaved data supplied by JSC. The next step was to remove systematic geometric distortions. The first distortion, termed "panorama distortion," results from the constant angular sampling of the scanner, causing pixels at the edges of the image to represent much larger footprints on the ground than those pixels in the center, which are sampled directly below the aircraft. Since the angular field of view of the aircraft scanners is large (100° for NS-001), this distortion was considerably more pronounced in the aircraft data than in Landsat MSS data. This distortion was removed by a one-dimensional resampling procedure operating in the cross-track direction (along scan lines). Again, linear interpolation was used. Extra samples were inserted to preserve resolution at the nadir. The second distortion, nonunity aspect ratio, occurred because the instrument scan rate was not synchronized perfectly with aircraft speed so that the spacing of pixel footprint centers at the nadir was different along track than across track. Furthermore, the aspect ratio of the acquired data was unpredictable, varying from flight to flight.

Because the data were invariably oversampled along track, it was possible to remove both aspect-ratio and panorama distortion in a single one-dimensional geometric transformation according to the following procedure. First, the panorama distortion was removed from a single spectral channel. Then the actual aspect ratio was measured by making along-track and across-track distance measurements in the image and comparing these with actual distances measured from a map or aerial photograph. Finally, a panorama correction was made on all channels of data

by decreasing the resampling interval (i.e., more pixels in output image) to the proper proportion so that the resulting aspect ratio was unity. The resulting images contain many more samples across track (at most by a factor of 2 to 3) than the original data. The increase in processing time for future steps was accepted to fully preserve the best resolution segments of the original data. No attempt was made to correct for aircraft roll, pitch, yaw, speed variations, or wobbles in the flight path, except for isolated cases where rectification to a map base was performed.

After the geometric distortions were removed, image segments were concatenated into complete flight lines. Finally, where necessary, systematic across-track intensity gradients were removed. The source of these gradients is uncertain. They were removed by forcing the average intensity along horizontal lines to be constant in a specified (ideally uniform) subsection of the image (i.e., perpendicular to the flight direction).

2. Analysis and display. Many different univariate and multivariate techniques were used in analyzing and displaying the test site image data. These included contrast stretching, color enhancement, ratioing, principal component and other multispectral transformations, multiple-image geometric registration, multivariate statistical analysis, and classification procedures. Existing interactive facilities were used to optimize final displays.

While occasionally performed on the original data, contrast enhancement generally was applied as a final step after the completion of other processing steps. Without effective contrast enhancement, the separation of the materials derived from more complex analysis might not have been fully apparent. Regularly employed contrast-stretching procedures included either manually or automatically selected linear stretches, piecewise linear stretches ("table" stretches), or histogram-normalization procedures, in which nonlinear transformations produced an output image having a histogram that approximated either a Gaussian or a uniform distribution. Pseudocolor transformations of individual raw or derived images (e.g., ratios or classified images) were also employed. Interactive display was often used to select appropriate contrast enhancement, particularly in applying pseudocolor.

A color-enhancement procedure that removes correlation between components was applied to the Landsat MSS data to produce color composites of bands 4, 5, and 7. Normally, high correlations among these bands prevent contrast enhancement of separate channels from achieving full use of the available color display range. The first step in solving this problem was to perform a principal component rotational transformation (rotational in a multispectral rather than geometric sense) to produce a new set of component images that were linear combinations of the original and that were correlated. Next, the images were contrast enhanced to equalize their variances, normally by using a Gaussian stretch. Next it was possible to apply a return multispectral rotation without reintroducing correlation. The resulting images thus show considerably enhanced color differentiation while not evidencing the substantial and unpredictable alteration of colors that occurs in a simple principal component display. To save processing time, the procedure was implemented with three-dimensional lookup tables computed from a subset of the image data, thus avoiding the two rotational transformations.

Another standard procedure used extensively in the analysis of image data was band ratioing and the production of color ratio composites. Band ratioing tends to remove intensity-related correlation and to emphasize spectral differences. Production of ratio images, in which the value of each output sample is proportional to the ratio of two original channels, is straightforward. The only significant procedural consideration is the selection of the proper gain and offset to scale the output into the available dynamic range. This scaling was usually performed automatically by software that accumulates a detailed histogram of ratio values for a subset of the image, that selects gain and offset values appropriately (to saturate some small, specified percentage of the output histogram at 0 and 255), and that then produces the full ratio image. For analysis, pseudocolor density slicing was occasionally performed on individual ratio images, although, more frequently, three selected ratio images were composited to produce a color display. Further contrast enhancement of individual ratio components was generally necessary to produce more easily interpretable color composites. The selection of appropriate ratios to composite was based upon *a priori* knowledge of the spectral characteristics of materials of interest. Band ratioing has the advantage of being an unsupervised analysis technique; that is, examples of materials of interest in the scene need not be identified to control the process. The production of color ratio composites is also a dimensional reduction technique, reducing up to six original spectral components into one color display.

Another dimensional reduction technique used extensively in the analysis of test site data was the principal component transformation. This rotational transformation produces new, artificial component images that are linear combinations of the original spectral channels. The resulting principal component images are uncorrelated (hence, do not contain "duplicate" information) and can be ranked in order of their variance. Since the total variance in the

multi-image set is preserved by the transformation, selecting the three highest-variance principal components for color composite display retains most of the information in the original multispectral data set. In a typical principal component transformation applied to the seven visible and near-infrared components of an NS-001 image flight line, 95 percent of the original information measured as variance was retained in the first three transformed components. Often, the first component, which generally represents image intensity, was omitted from the color display and was replaced by the fourth component.

A principal component transformation is begun by estimating a covariance matrix for the multispectral image. Then a rotation matrix, consisting of the eigenvectors of the covariance matrix, is found and applied to produce the output components. Output image variances are given by the rotated covariance matrix diagonal entries and are, in fact, the eigenvalues of the original matrix. The principal component transformation is an unsupervised technique. While information compaction does occur, there is no guarantee that the most significant information, namely that which discriminates material of interest, will be emphasized in the output components. Occasionally, to add an element of supervision to the process, estimation of the covariance matrix was confined to regions of the image containing a greater concentration of materials of interest to achieve greater separating power in the output components.

In a related procedure, often termed "canonical analysis," training was used to establish new linear combinations of the original spectral channels that have the improved ability to differentiate among predefined groups. Training areas representing the groups of interest are first identified in the scene, generally through the use of an interactive display terminal. Next, between groups and within groups, covariance matrices are estimated using the training samples. Finally, canonical variable coefficients are determined from the eigenvectors of a combined version of the within- and between-groups matrices. Those canonical variables associated with the greatest eigenvalues show the greatest degree of separation-of-class means relative to their variance and hence are color composited for display. Experience has shown that careful, interactive contrast enhancement is often necessary to achieve the full separating potential of a canonical variable composite. This procedure was applied to test site images in selected cases. The BMDO7M program of the UCLA biomedical statistical software package was employed to calculate the canonical variable coefficients.

A variation of the canonical analysis was also used. This variation controls the transformation by using selected PFRS data to provide training. To compute training values, weighted averages of PFRS reflectance values were computed over the bandpasses of the aircraft scanner to simulate the response of the aircraft sensor. Next, a rough attempt was made to calibrate the aircraft data to convert the data into reflectance units compatible with PFRS data. This was done by identifying a light unit and a dark unit in the scene for which PFRS spectra were available, permitting the calculation and application of a linear-transform function for each channel. This procedure enabled the application of a supervised technique without requiring the identification of training samples in the scene.

Although feature-selection and enhancement procedures, which preserve information quite well, were preferred, automated classification was used occasionally in the analysis of test site data. The classification technique most commonly used was a hybrid of a simple parallelepiped technique and a Bayesian algorithm designed to save processing time. The first step in the procedure is to identify training areas and accumulate statistics for each group (normal distributions are assumed for the Bayes algorithm). Then, the hybrid algorithm defines parallelepipeds about each class mean whose dimensions are a specified multiple of the standard deviation of that class. If a multispectral-image pixel falls within a parallelepiped, it is a candidate for that class. The Bayes algorithm is used to decide among the candidate classes. Using the parallelepiped algorithm to eliminate some potential classes is the time-saving feature of the approach. The result of the program is an output image whose numerical value at each pixel indicates the class decision made for that element. Pseudocolor enhancement was used to produce classification map displays.

Geometric transformations were also employed at times in the image analysis phase. The usual objective was spatial registration, either to another image for combined analysis or to a map base. A geometric transformation requires the precise specification of the distortion relationship between the input and output image. Usually for convenience in resampling, this distortion is specified in terms of the output image. The geometric-transformation software used in the test site work controls the applied distortion by specifying the desired translation for a regular, sparse array of points in the output image. The translation for all intermediate points is interpolated using surrounding elements in the control grid. Unfortunately, in the case of image registration (particularly for aircraft-scanner data where precise analytic description of image geometry has been impractical), the desired geomet-

ric relationship is specified by control points or tiepoints, well-defined observable features whose locations are found in both the input image and the target image or map. These points were found by interactive analysis and are almost invariably scattered irregularly throughout the image.

Two different approaches were used to determine the desired displacement at the regular control grid based upon the measured displacement at the irregular tiepoints. One method fits a polynomial surface to the tiepoints and then evaluates the surface at the control grid points. This approach has the advantage of helping to identify incorrectly located tiepoints. The surface is simply evaluated at the tiepoints; those with high residuals were probably positioned incorrectly. The second method determines the displacements of the control grid by triangulation using surrounding tiepoints. This approach has the advantage of being better able to track irregular distortions.

B. Program Descriptions

1. ASTRTCH2. ASTRTCH2 performs an automatic linear-contrast stretch on an input picture or generates a table stretch to produce a picture with a "nearly" uniform histogram or a "nearly" Gaussian histogram. An optional linear poststretch can be performed following the automatic linear contrast stretch. The user specifies an area of the picture to use in generating the histogram. Certain combinations of the following outputs are available: a stretched output picture, a stretched masked picture suitable for film recorder playback, a stretched Polaroid, a printer listing of the histogram, and a printer listing of the cumulative distribution function. The automatic-stretch computation may be specified to saturate a percent of the input picture at the low DN range (0 DN) and the high DN range (255 DN). Alternatively, it may be specified as a number of different stretches about either the peak or mean DN of the input picture. The user may optionally subsample the input picture when generating the initial histogram.

The program ASTRTCH2 generates a frequency distribution (histogram) of the portion of the input picture specified by the size field or the keyword AREA. A modified frequency distribution is then constructed by setting the frequencies of all excluded DN values to zero. These excluded DN values are specified in the parameter field or implied by keyword default. The modified frequency distribution is then analyzed to generate stretch parameters using the criteria specified in the parameter field. Following this procedure, one of the VICAR programs STRETCH or FOTO is invoked by a "fetch" call, and the stretch is performed. The final stretch is a composite of the automatic stretch and the poststretch. The EXCLUDE specifications, except the default, are printed. The mean and standard deviations of the input picture (before exclusion) are printed. The mean and standard deviations of the modified frequency distribution (after exclusion) are printed. The automatic stretch generated by the program is printed. Both the stretched picture and the stretched masked picture contain a label annotation indicating the stretch performed. Also, options exist to print a histogram (DN frequency distribution) and/or cumulative distribution function for the input picture.

The program also accepts an alternate input data set, the histogram of the input picture. This option permits the program to omit the reading of the input picture to accumulate a histogram. Thus, only one pass through the picture is required, the pass which actually generates the stretched output picture. The histogram data set is a standard VICAR labeled data set consisting of one data record of 1024 bytes (byte data) or 2048 bytes (halfword data).

2. BAYES. BAYES is a multispectral classifier that uses the Bayesian maximum-likelihood algorithm. The algorithm implementation is identical to that used in Purdue University's LARSYS classifier, while the program structure is rewritten to run under VICAR. Input is multispectral image data and training statistics from the VICAR program STATS. Output is a classification map and, optionally, a confidence map.

The input data can be in either separate VICAR data sets or in MSS format (all multispectral data interleaved into one VICAR data set). The statistics data set from the VICAR program STATS is also necessary.

The program assumes there are N spectral bands, and considers a pixel as an N-dimensional sample vector $\mathbf{X}$. K_i is the covariance matrix computed for training class i and $\boldsymbol{\mu}_i$, the mean of class i. The multivariate probability P_i that $\mathbf{X}$ is a member of class i is given by

$$P_i = \frac{1}{(2\pi)^{N/2}|K_i|^{1/2}} \exp\left[-\frac{1}{2}(\mathbf{X}-\boldsymbol{\mu}_i)^T K_i^{-1}(\mathbf{X}-\boldsymbol{\mu}_i)\right]$$

where

$$|K_i| = \det(K_i)$$

Since we are interested in only the maximum P over all classes, it is convenient to compute

$$Q_i = \log_e(P_i) = C_i - \frac{1}{2}(\mathbf{X}-\boldsymbol{\mu}_i)^T K_i^{-1}(\mathbf{X}-\boldsymbol{\mu}_i)$$

where

$$C_i = -\frac{1}{2}[N \cdot \log_e(2\pi) + \log_e|K_i|]$$

X is then assigned to the class j, for which Q is a maximum. Furthermore,

$$d^2 = (\mathbf{X} - \boldsymbol{\mu}_j)^T K_j^{-1} (\mathbf{X} - \boldsymbol{\mu}_j)$$

Thus, d is simply the number of standard deviations **X** lies from $\boldsymbol{\mu}_j$ in a multivariate sense.

To have high confidence represented by a high DN, we define the confidence that **X** is correctly classified, h_x, by

$$h_x = 255 - Zd$$

where Z is a scaling factor dependent on the parameter ZERO. Thus, for each pixel in the scene we assign a class number corresponding to the class to which the pixel most likely belongs and a confidence value which represents the likelihood of a correct classification. These output data sets are referred to as the classification map and the confidence map.

3. BOXFLT2. BOXFLT2 is a VICAR applications program that produces a low-pass filtered output image from an input image (two-dimensional filter of all weights = unity). The basic program is essentially the same as VICAR program BOXFLT, but BOXFLT2 has a faster execution time and the expanded capabilities of optional high-pass output and user-controlled image-boundary management.

BOXFLT2 performs a low-pass filter operation by taking the local mean of all pixels contained within a prescribed window of NLW-by-NSW dimensions (the number of lines in the weight matrix by the number of samples in the weight matrix) centered at each pixel of the input image. This mean then replaces the input value. If the high-pass operation is specified, then the difference between the input and the local mean plus a constant replaces the input value. The low-pass output is equivalent to that given by the VICAR program BOXFLT, and the high-pass output is equivalent to that given by the VICAR program FASTFIL2.

The advantages of using BOXFLT2 over either BOXFLT or FASTFIL2 are that the size of the filter window or image size (as in the case of BOXFLT) is not restricted and that no intermediate data sets are required (as in the case of FASTFIL2). Also, the execution of BOXFLT2 is quicker than for either BOXFLT or FASTFIL2. The main advantage of FASTFIL2 is its ingenious no-ring algorithm and its ability to produce "scene-dependent" results based on the local mean.

4. C130RECX. The program C130RECX removes the panorama distortion from images acquired by scanners that employ constant angular sampling. C130RECX can compensate for a field of view not centered at nadir and can adjust the aspect ratio.

5. DS4. The program DS4 attempts to remove six-line striping from Landsat MSS images by performing localized histogram matching of the six sensors.

The input picture is considered to be subdivided into contiguous sets of six lines each. The starting line of a given set is determined by the reference sensor number such that the reference sensor becomes the third line within the set. For example, if the reference sensor were chosen to be 5, then the starting line of the first set would be 3 and that of the second set would be 9, and so on. Note that the line numbers above refer to the image given by the VICAR size field. That is, if a subarea is specified, then line 5 above refers to the fifth line of the subarea.

To initiate the matching process, the cumulative distribution functions (CDFs) for each sensor are compiled using the first group of sets (i.e., the first N2 sets). The reference CDF is that of the specified reference sensor. If the parameter AVERAGE is specified, the reference CDF is taken to be the average of all 6 sensor CDFs. If the parameters FILTER,F1,...,FN are specified, then the reference CDF is low-pass filtered using the integer weights F1,...,FN. The CDF of each sensor is matched to that of the reference CDF, and corresponding transfer tables are generated. The first [(N2 − 1)/2] + 1 sets plus any lines skipped over at the beginning (see the preceding paragraph) are then transformed using the generated transfer table.

Subsequent sets are transformed in the following manner:

(1) The CDFs of the sensors of the first set in the group are subtracted out of the group sensor CDFs.

(2) The CDFs of the sensors in the first set following the group are added to the group sensor CDFs.

(3) The transfer tables are generated as before.

(4) The middle set of the updated group is transformed.

This process continues until the last set of the image has been included in a group. Then the middle set of the group, all sets following it, and any lines after the last set are transformed.

The parameters AVERAGE and RSEN (reference sensor) are not mutually exclusive. While the parameter AVERAGE will override RSEN in terms of how the reference CDF is generated (i.e., from one sensor or from an average of all six sensors), the parameter RSEN can be used to define which lines compose the first set of lines and hence all subsequent sets of lines.

6. DSTRETCH. DSTRETCH forces more color into a multispectral scene by removing interband correlation. Both linear- and Gaussian-variance equalization are available.

Correlation between bands is what makes color enhancement difficult. Individual enhancement of the components does not reduce the correlation. The principal component rotation (as implemented in EIGEN,XFORM) does produce a set of uncorrelated components that can be contrast enhanced separately to produce a full range of color. However, when color composited, a principal component scene will bear no color relationship to the original.

This problem is solved in DSTRETCH by performing an inverse rotation after contrast enhancement of the principal components. If the variances of the principal components are equalized, any further rotation can be performed without reintroducing correlation. Using the inverse principle component rotation restores original color relationships.

To apply this procedure to a general n-dimensional problem, EIGEN,XFORM and ASTRTCH2 can be used, with a minimum of two passes required. DSTRETCH offers a three-dimensional implementation that saves considerable time by not actually performing the rotations. Three, three-dimensional, 5-bit lookup tables are calculated and then are used to enhance the full scene. An automatic prestretch of the inputs and a "city block" interpolation algorithm on the low-order bits combine to preserve reasonable intensity resolution.

7. EIGEN. The program EIGEN will compute the principal component transformation matrix for up to 12 input channels. The covariance matrix, the transformation matrix of eigenvectors, and the eigenvalues are printed. EIGEN will fetch XFORM to perform the transformation. EIGEN will also compute the eigenvectors for multivariate data input via the parameters.

The measure of interdimensional correlation in a multivariate system is usually defined by the covariance matrix of the multivariate data. The linear transformation that diagonalizes the covariance matrix can also be applied to the original data to produce a multivariate system with an interdimensional correlation of zero, i.e., completely uncorrelated multivariate data. The linear transformation that accomplishes this is the matrix of eigenvectors or characteristic vectors.

A common application of this transformation is to reduce the dimensionability of a multivariate system. The objective is to summarize most of the variance, or information content, in a system with fewer "artificial" variates, i.e., principal components. Effectively, uncorrelating the system compresses most of the information into a system with lower dimensionality.

Assuming an n-variate system (n channels of data), the program lets K represent the n-by-n covariance matrix of these data, and lets A represent the matrix of eigenvectors of K. Associated with each eigenvector $\mathbf{A}_j$, there is an eigenvalue or characteristic root, e_j. If $\mathbf{A}_j^T = (a_{1j}, a_{2j}, \ldots, a_{nj})$ is the eigenvector corresponding to the jth largest eigenvalue and if $\mathbf{X} = (x_1, x_2, \ldots, x_n)$ is the n-variate observation (n-dimensional pixel), then the jth principal component of the observation is

$$v_j = \mathbf{A}_j^T \cdot \mathbf{X} = \sum_{i=1}^{n} a_{ij} x_i$$

NOTE: The jth eigenvalue is actually the variance in the jth principal component dimension. Therefore the eigenvalues are useful as a measure of the information that can be expected in the output pictures.

8. F2. The program F2 allows general arithmetic operations to be performed on one or two input images in either byte, halfword, or (mixed) byte-halfword input/output. The arithmetic operation is specified by a FORTRAN-like expression, which can include the following operators:

+ - * / ** unary-
SQRT ALOG ALOG10 ABS AINT (INT)
SIN COS TAN ASIN ACOS ATAN ATAN2
AMAX1 (MAX) AMIN1 (MIN) AMOD (MOD)
.AND. .OR. .XOR. .NOT.
.LT. .LE. .EQ. .NE. .GT. .GE.

Operands to F2 can be integers, floating-point numbers, IN1, IN2, LINE, and SAMP. F2 can operate on zero inputs to generate an output using the operands LINE and SAMP.

F2 performs arithmetic operations on image files. The program uses two library routines, KNUTH and XKNUTH, to compile and interpret FORTRAN-like expressions entered by the parameters in a FORTRAN expression such as the following:

```
((IN1 + IN2)*AINT(ALOG10(IN1*IN2**2))
  +3.14 + IN1/22) + 4*(LINE.EQ.SAMP)
```

IN1 is an element from the first file, and IN2 is the corresponding element from the second file. KNUTH compiles the expression into machine instructions. The expression is applied to the input from each file in XKNUTH to produce the output picture.

When performing arithmetic, F2 converts all integer operands to reals and executes single-precision floating computation. The exceptions are .AND., .OR., .XOR., and .NOT., which operate on the binary equivalent of the truncated floating number. The result is converted back to integer by truncation. When produced, the logical values "true" and "false" are interpreted as 1 and 0, respectively.

To conserve time, repetitive executions of F2 with the same variable are stored as a lookup table. When both input and output are byte data, the table is constructed as a straight lookup table, initialized with every possible combination of IN1 and IN2 from 1 to 256. The table is referenced by indexing the array using the concatenation of IN1 and IN2 to create an index number to the vector table. The table is dimensioned 65,536 to accommodate any possible combination of 256 by 256.

When either the input or output is halfword data, a hashing table is constructed. The equation is then executed each time it encounters a unique combination of IN1 and IN2. A key points to the storage location of the results of XKNUTH. The key is then determined from the remainder obtained by concatenating the two variables and dividing by 10,921. In each case, the key must be checked for a match of the concatenation of IN1 and IN2 that was stored. If no key is found, a solution is calculated and a result of XKNUTH and concatenation of IN1 and IN2 are stored. When the key points to an erroneous combination of IN1 and IN2, the new values and the new key are stored. If the operands LINE or SAMP are used, no table is used; the formula is evaluated at every pixel.

9. FASTCLAS. FASTCLAS is a multispectral classifier using an algorithm that combines the parallelepiped and Bayesian techniques. Inputs are registered multispectral data and training statistics from the VICAR program STATS. The input multispectral data can be either in separate VICAR data sets or in MSS format.

FASTCLAS uses a combination of the parallelepiped algorithm and the Bayesian maximum likelihood algorithm for classifying multispectral data. It assumes that N spectral bands are available and that training statistics from the VICAR program STATS have been computed. FASTCLAS reads the statistics data set and generates a lookup table to hold the boundaries in the N-dimensional decision space for each class. For each dimension (band) the decision boundary is $\mu \pm R\sigma$ where μ is the mean for the class, σ the standard deviation, and R the number of standard deviations to be used. This is the parallelepiped algorithm.

To be assigned to class J (DN_{out} = J), the spectral signature of a pixel must fall within the N-dimensional decision boundary for class J. If the spectral signature falls outside the decision boundary for all classes, the pixel is assigned to the unknown class (DN_{out} = 0). A pixel whose spectral signature falls within the decision boundary for more than one class is considered ambiguous. The user has the option of resolving the ambiguity by using the Bayesian maximum likelihood algorithm or leaving the pixel ambiguous (DN_{out} = 255).

If the keyword CHECK is given, the Bayesian confidence value is computed for each pixel after it is classified. If the spectral signature of the pixel is outside the multivariate confidence interval, the pixel is reclassified as unknown.

The order in which the spectral bands are input to FASTCLAS is important. Since the lookup table uses a process of elimination, bands that give the best spectral separation between classes should be given first. If the spectral data are in MSS format, the order is controlled by the parameter USE.

10. FFT1. FFT1 is a VICAR applications program that computes the forward and inverse complex Fourier transform on a line-by-line basis. Used in conjunction with FFT1PIX, FFT1 provides a versatile one-dimensional filtering technique.

In the forward mode, FFT1 computes the Fourier transform of the input picture, line by line, using the fast Fourier transform subroutine FFT. The transform, which is complex, is written on the output data set (8 bytes/sample). The number of input samples should be an integral power of 2. If not, FFT1 will fill with zeros to make the input the next higher integral power of 2.

In the inverse mode, FFT1 computes the inverse Fourier transform of the input data set, which will now be complex*8, and outputs a byte data set.

11. FFT1PIX. FFT1PIX is a VICAR applications program that works in conjunction with FFT1 to allow the user to display and/or modify the Fourier transform using

existing VICAR programs. The procedure is similar to that used in FFT2, FFTPIC, and TPIKMASK but does not require that the terms of the transform be either set to zero or left unchanged. In the forward mode, the input to FFT1PIX is the complex Fourier transform from FFT1. The output can be an amplitude picture and/or a phase picture of the transform. Those can then be modified to the user's needs and reinput to FFT1PIX in the reverse mode. The Fourier transform is then modified in accordance to the changes made to the amplitude and/or phase pictures.

If $z_k = a_k + ib_k$ is the kth term of the Fourier series of a given line, the amplitude of this term is $|Z|$ and the phase angle $\Theta_k = \tan^{-1}(b_k/a_k)$. Then the DN of the kth sample in the amplitude picture equals $P \cdot |Z|$ where P is a scaling factor. If the LOG option is used, DN $= P \cdot \log_e(|Z|)$. P is determined by the normalization options used.

Similarly the DN of the phase picture equals $q \cdot \Theta_k + s$ where q and s are scaling factors. If NO SIGN is requested, DN $= q \cdot |\Theta_k| + s$. If both are requested, then the amplitude and phase pictures are written out on the primary and secondary output data sets. If requested, amplitudes are plotted. This provides a means of accurately locating noise spikes in the transform. The user may then modify the amplitude or phase picture using existing VICAR programs. Noise spikes may be QSARed out of the amplitude picture, for example.

The modified amplitude and phase pictures are then reinput to FFT1PIX in the reverse mode. The complex*8 transform data set remains as the primary input, the modified amplitude picture as the secondary input, and the modified phase picture as the third input. If the amplitude or phase picture is not modified, then it need not be reinput to FFT1PIX. Each term of the original transform is compared to its appropriate term of the modified amplitude and phase pictures. If the amplitude differs, the term is recomputed to match that of the amplitude picture with phase angle preserved. If the phase angle differs from the phase picture, the term is recomputed to match the new phase angle, amplitude preserved. Thus, the user has control over each term of the transform.

If CONJ is not specified in the reverse mode, the complex conjugate of a term is automatically modified in the identical manner to its conjugate term. The output is complex data in an 8-byte format containing the Fourier transform after modifications have been made to it. If requested, a plot is made of the transform after modification. The modified transform is then ready to be input to FFT1 in inverse mode to produce the image.

12. FFT22. FFT22 performs a two-dimensional Fourier transform on a VICAR-format data set residing on disk. FFT22 has a maximum transform size of 2048 by 2048 and the ability to process input and output as byte, halfword, fullword (floating or integer), or complex-floating data.

The program makes one of the two following computations:

The forward transform,

$$Z_{kl} = \sum_{m=0}^{M-1} \sum_{n=0}^{N-1} Z_{mn} \exp -2\pi i \left(\frac{km}{M} + \frac{ln}{N} \right)$$

for $k = 0,1,\ldots, M-1$ and $l = 0,1,\ldots, M-1$; or the inverse transform,

$$Z_{mn} = \frac{1}{MN} \sum_{k=0}^{M-1} \sum_{l=0}^{N-1} Z_{kl} \exp 2\pi i \left(\frac{km}{M} + \frac{ln}{N} \right)$$

for $m = 0,1,\ldots, M-1$ and $n = 0,1,\ldots, N-1$ where M is the smallest power of 2 greater than the number of lines and N is the smallest power of 2 greater than the number of samples.

In the case of the forward transform, Z_{mn} represents the input data value at line $m + 1$, sample $n + 1$. (The VICAR convention is to count lines from the top down starting with 1 and to count samples from left to right starting with 1.) In this case also, the forward transform represents the output Fourier transform value stored at line $l + 1$, sample $k + 1$. The inverse transform represents the input data value at line $l + 1$, sample $k + 1$, and Z_{mn} represents the output Fourier transform value stored at line $m + 1$, sample $n + 1$.

Thus, the output of the program is stored in transposed format, in the matrix sense. Storing the program output in transposed format is responsible for faster program execution. When a forward and inverse transform are performed in sequence, the two transpositions cancel out and have no net effect. However, the user must be aware of the transposition when working directly with transformed data. For example, when filtering by multiplication with a transfer function, the user must first transpose the transfer function (unless it is transpose-invariant).

13. FFTFIT. FFTFIT is a VICAR applications program that modifies a complex Fourier transform created by the VICAR program FFT22. There are two modifications:

(1) The complex Fourier transform is multiplied by an input picture.

(2) The amplitude of the complex Fourier transform is made proportional to an input picture. The phase is not altered.

FFTFIT can be used to force pictures to have identical power spectra and can provide for the execution of detailed filters.

FFTFIT allows two modes: The first mode forces the amplitude of the Fourier Transform (FT) to be a scaled replica of a picture (PIX):

$$|\mathrm{FT}_{\mathrm{out}}|_{ij} \propto \mathrm{DN}_{ij}$$

$$\mathrm{FT}_{\mathrm{out}_{ij}} = \mathrm{FT}_{ij} \cdot R1 \cdot \frac{\mathrm{DN}_{ij}}{|\mathrm{FT}|_{ij}} = \mathrm{FT}_{ij} \frac{\mathrm{DN}_{ij}}{\mathrm{DN}_{\mathrm{ref}}} \frac{\mathrm{A}_{\mathrm{ref}}}{|\mathrm{FT}|_{ij}}$$

where $R1$ is the scaling factor $\mathrm{A}_{\mathrm{ref}}/\mathrm{DN}_{\mathrm{ref}}$ and $|\mathrm{FT}|$ represents amplitude

$$\sqrt{a^2 + b^2} = |a + ib|$$

where $\mathrm{A}_{\mathrm{ref}}$ and $\mathrm{DN}_{\mathrm{ref}}$ are a reference amplitude for the FT, and a reference DN (brightness) for the picture, respectively. These values are generally estimates of the mean amplitude and brightness. The second mode multiplies the FT by PIX:

$$\mathrm{FT}_{\mathrm{out}_{ij}} = \mathrm{FT}_{ij} \cdot R1 \cdot \mathrm{DN}_{ij} = \mathrm{FT}_{ij} \cdot \frac{\mathrm{DN}_{ij}}{\mathrm{DN}_{\mathrm{ref}}}$$

In both cases the DC term of FT is set apart from the transformation and is never altered. Whatever the result, the mean of the inverse transform of $\mathrm{FT}_{\mathrm{out}}$ is always the same as that of the original picture whose transform is FT.

The keywords LINE and SAMPLE are significant. These values point to the pixel in PIX that will be centered on the DC term (1,1) in the FT picture. In the majority of cases PIX will be a symmetrical function, such as a Gaussian. LINE and SAMPLE will usually refer to the center of symmetry of this function. When this is the case, FFTFIT will be able to divide PIX into symmetrical quadrants and match them to the complex format of FT (with DC in the corners). If the keywords LINE,SAMPLE do not refer to a symmetry point, $\mathrm{FT}_{\mathrm{out}}$ will be asymmetrical, and the inverse transform will produce the real part of a complex picture (if PIX is asymmetrical) or a displaced image (if PIX is symmetrical but just off center).

FT can be created with either FFT2 or FFT22. DC remains the same for both complex formats, but the latter has been transposed relative to the former (rows become columns). FFTFIT assumes the user has organized PIX such that it is compatible with the appropriate FT formats. Symmetrical cases are invariant. One can convert PIX from one format to the other with two executions of FLOT.

When the inverse transform is made (particularly in the amplitude matching mode), the output picture should be halfword. Most operations will cause some DNs to lie outside the byte range, but halfword formatting allows access to these pixels.

14. FFTPIC. The VICAR applications program FFTPIC processes input VICAR-formatted complex Fourier transforms or complex pictures, extracting, reorganizing, and automatically scaling various functions of the complex data for image display. Available functions of the complex input include amplitude, intensity (squared amplitude), phase (with or without sign), real part, and imaginary part. Linear or logarithmical scaling prior to output exists for all functions except phase.

NOTE: The input transform format is assumed to be the equivalent of that produced by the two-dimensional fast Fourier transform program, FFT2.

The input data set is assumed to be a VICAR-formatted complex*8 matrix with a system label specifying the number of bytes per record (8 times the number of complex samples) and the number of records in the matrix.

In the transform-display mode, the number of complex samples and the number of lines must be a power of two, and the data (spatial frequency components) must be organized as required in FFT2. The picture size to be processed is derived from the system label, so the size field is ignored. The output system label is automatically updated based on the operating mode and input size.

Depending on the mode specified, the complex input data are then processed into one (complex picture-display mode) or two (transform-display mode) intermediate data sets. During this processing, the specific display function of the complex input is generated, scaled, and stored as real*4 data. In the complex-picture mode, the entire input is processed uniformly into one intermediate data set. Hence, only one secondary input is required. On the other hand, in the transform-display mode, the input conjugate symmetry is used to divide the display into halves which may have display types specified independently. Hence, two secondary inputs are required. In the transform mode only the-left-half-plus-one samples are processed.

In order to efficiently scale and pack the resulting data into byte format, a logarithmic histogram is accumulated for the entire input. Then the histogram is analyzed to determine a linear transformation on the intermediate data for packing into the output. For phase-information displays, the packing transformation is predefined between − pi and + pi or 0 and + pi, depending on whether SIGN has or has not been specified, respectively.

If the two halves of the transform display are in the same mode, the output display exhibits conjugate central symmetry with spatial frequency. DC (i.e., (0,0) spatial frequency) is located at line (NY/2 + 1) and sample (NX/2 + 2). Positive and negative horizontal spatial frequency components are positioned to the right and left of this point, respectively, along a horizontal axis. Similarly, positive and negative vertical frequency components are located above and below this point along a vertical axis.

If the two halves are in different modes, the display is organized by the spatial frequency component symmetrically about the vertical line with sample coordinate (NX/2 + 1.5). Therefore, DC for the right half is at line (NY/2 + 1) and sample (NX/2 + 2), while DC for the left half is at line (NY/2 + 1) and sample (NX/2 + 1). Positive and negative vertical spatial frequencies are located above and below these DC points, respectively, for each half of the display along vertical axes. Positive horizontal spatial frequency increases to the right for the right-hand display and to the left for the left-hand display along a horizontal axis through these points. Negative horizontal spatial frequency components are not explicitly displayed in this case. The scaling applied to both halves is the same (determined from the composite histogram) except if one half is phase and the other is amplitude (or another nonphase display). In this case, the predefined phase scaling is used on the appropriate half and that derived from the histogram on the other.

15. FILTER. FILTER is a VICAR applications program that performs two-dimensional convolution filtering. For each output sample, the program computes a weighted average of a rectangular set of input pixels followed by a linear transformation. FILTER may be used to perform high-pass (correction for blurring) or low-pass (removal of glare) filtering.

Before FILTER can be used, a proper set of weights must be generated for the sensor system that acquired the image. These weights are usually generated by the filter weight generator program (VICAR program WTGEN).

FILTER accepts as input a rectangular set of weights and calculates each output point FP(L, S) as follows:

$$FP(L, S) = A + \frac{B \bullet TP(L, S)}{D}$$

where

$$TP(L, S) = \sum_{i=1}^{NLW} \sum_{j=1}^{NSW} P\left(L - \frac{NLW+1}{2} + i,\ S - \frac{NSW+1}{2} + j\right) \times W(i,j)$$

and where

P = input data set
W = weight matrix
NLW = number of lines in the weight matrix
NSW = number of samples in the weight matrix
A, B = two scale inputs
D = parameter for scaling

16. FLOT. FLOT is a VICAR applications program for rotating a picture 90° (clockwise or counterclockwise) and for flipping a picture either along its horizontal or vertical axis.

If CLOCKWISE is specified, the input picture is rotated 90° clockwise. If COUNTERCLOCKWISE is specified, the input picture is rotated 90° counterclockwise. If HORIZONTAL is specified, the input picture is reflected through its vertical axis. If VERTICAL is specified, the picture is reflected through its horizontal axis. HALF is specified if the input data set is in halfword format.

17. FORGRE. FORGRE is a VICAR applications program written for the Viking Lander 1976 project. The purpose of FORGRE is to reformat VICAR-formatted images for playback on the Viking Ground Reconstruction Equipment (GRE) playback device. Playback may be performed in either color or black-and-white mode. The use of FORGRE is not restricted to Viking Lander images.

The GRE utilizes extremely accurate machinery, and playback is performed with laser light. The software interface for the GRE accepts 8-bit data with a maximum number of 4800 pixels per line (3250 for color) and a maximum number of 9600 lines per picture at 1-mil spacing. The 2-mil, 4-mil, and 8-mil spacings are also available with proportionately smaller maximum line and sample sizes. If the line count is greater than these values, the hardware

truncates the bottom of the picture. The output of FORGRE may be in two basic formats as shown in Figure 14-7.

18. GEOM and LGEOM. GEOM and LGEOM are VICAR applications programs that make geometric changes in pictures. They can be used for correcting geometric distortion, increasing picture size, and reducing picture size. GEOM should be used when each output line is computed from a small number of input lines; LGEOM should be used when each output line is computed from a large number of input lines since LGEOM is a two-pass GEOM that does not require rereading individual lines. LGEOM requires an intermediate data set, which should be on a different disk than either the input or output. The input data set for GEOM should always be on disk.

In both programs, the user specifies the desired changes by defining rectangles in the corrected output picture and the displacements in lines and samples from equivalent rectangles in the input picture.

19. GEOMA. GEOMA performs geometric transformations on images according to parameters supplied by the user. Its function is similar to GEOM and LGEOM. (GEOM and LGEOM are functionally identical, differing only in algorithm and speed.) In each of the three programs, the picture to be geometrically transformed is subdivided into a number of quadrilaterals. The user must specify the exact mapping from input picture to transformed picture for each corner point of each quadrilateral. Within the quadrilaterals, the programs use a bilinear interpolation to map the interior points from input picture to transformed picture. The GEOM and LGEOM programs restrict the specification of the mapping of the quadrilateral corners (control points) such that, in the transformed (output) picture, they form rectangles whose sides are parallel to the picture edges and have integral line and sample coordinates. The GEOMA program does not impose this restriction and allows more arbitrary specification of the control point mapping. In fact, two of the four control points forming the corners of any given quadrilateral may coincide, causing the quadrilateral to degenerate into a triangle (a quadrilateral having one side of zero length).

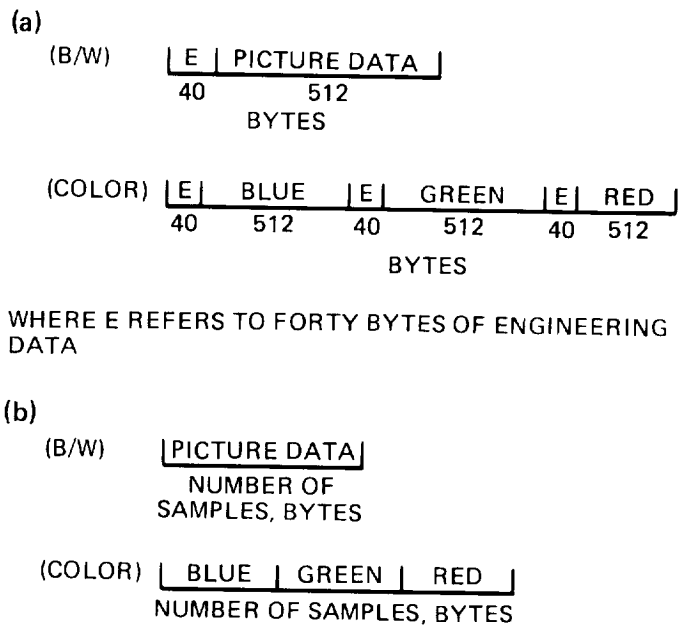

Figure 14-7. FORGRE output in two basic formats: (a) old format (6-bit data); (b) default format (8-bit data)

An additional difference from the GEOM/LGEOM programs is the way the parameters in GEOMA are used to specify the mapping of the control points: The user specifies the line–sample coordinates of the control points in the input and output pictures. In GEOM and LGEOM, the user specifies the line–sample coordinates in the output picture and the *differences* between corresponding input and output picture control point coordinates. GEOMA eliminates the computing of the differences when the actual coordinates are known.

Except for the differences discussed above, the internal algorithm of GEOMA is very similar to that of GEOM. In particular, GEOMA will be very slow under the same circumstances that GEOM would be slow.

As with GEOM and LGEOM, GEOMA will accept its control parameters on a data set instead of or in addition to the conventional VICAR parameters.

The size of the output picture is specified by the VICAR size field or, by default, is the size of the input picture. GEOMA computes the DN value of each pixel in the output picture as follows. First, the program determines within which quadrilateral area in the output picture the pixel lies. The coordinates of the four control points defining that quadrilateral in the output picture are called $x(j)$, $y(j)$, where $j = 1,2,3,4$. In the input picture, they are called $x'(j)$, $y'(j)$, where $j = 1,2,3,4$ (x may be considered the line coordinate and y the sample, although they could as well be reversed for this discussion). The values of all 16 of these numbers are part of the control parameters for GEOMA. A transformation is defined by

$$\begin{aligned} x' &= ax + by + cxy + d \\ y' &= ex + fy + gxy + h \end{aligned} \qquad (14\text{-}16)$$

where the values of the coefficients $a,b, \ldots, h$ are determined by requiring that

$$x'(j) = ax(j) + by(j) + cx(j)y(j) + d$$
$$y'(j) = ex(j) + fy(j) + gx(j)y(j) + h \qquad (14\text{-}17)$$

for $j = 1,2,3,4$. This is the condition that the defined transformation exactly maps the control point coordinates as specified by the parameters.

The transformation is used to transform the line–sample coordinates of the output picture pixel being processed into its corresponding coordinates in the input picture. In general, although the output coordinates are always integers, the input coordinates are not, so the input coordinates do not correspond to any one pixel but, instead, fall between the input pixels as shown in Figure 14-8. If intensity interpolation is not to be performed, as specified by the appropriate keyword parameter, then the DN value assigned to the output pixel is that of the pixel in the input picture nearest the transformed coordinates. The use of this mode considerably reduces the CPU time required by GEOMA. The quality of the result is in general degraded but may be quite acceptable, depending on the nature of the transformation.

Assuming interpolation *is* to be performed to compute the DN value of the output picture, the four pixels nearest the transformed coordinates in the input picture are selected. The interpolation formula is

$$\mathrm{DN} = px' + qy' + rx'y' + s \qquad (14\text{-}18)$$

where x' and y' are the transformed coordinates of the output picture pixel, DN is the data number to be assigned to the output pixel, and p, q, r, and s are constants chosen such that

$$\mathrm{DN}(k) = px'(k) + qy'(k) + rx'(k)y'(k) + s \qquad (14\text{-}19)$$

for $k = 1,2,3,4$, where $x'(k)$, $y'(k)$, and DN (k), $k = 1,2,3,4$, are the coordinates and DN values of the four selected input pixels nearest the transformed coordinates.

For GEOMA to work properly, the tiepoint coordinates in the output picture must satisfy certain constraints. They must be organizable into a rectangular matrix of points. That is, each tiepoint must belong to one row and one column of points; each row must have the same number of points as every other row; and each column must have the same number as every other column. It should be possible

Figure 14-8. Transformation of line–sample coordinates

to number the rows sequentially from top to bottom and the columns from left to right. Quadrilaterals used by the program for performing the geometric transformation are formed by connecting each tiepoint to the adjacent tiepoints in the same column and in the same row. None of these quadrilaterals should be concave (no interior angle of any quadrilateral should be greater than 180°). In addition, each tiepoint should be below any tiepoint in its column and in any preceding row, and above any tiepoint in its column in any subsequent row. Similarly, each tiepoint should be to the right of any tiepoint in its row and in a preceding column, and to the left of any tiepoint in its row and in a subsequent column. The number of vertical areas is the number of *rows* of tiepoints less 1, and the number of horizontal areas is the number of *columns* of tiepoints less 1. Figure 14-9 shows a valid array of tiepoints and the quadrilaterals that they define. The numbering of the tiepoints shows the order in which they would be specified following the TIEPOINTS parameter.

The following caution is issued to potential users of GEOMA. Although the transformation in Eq. (14-16) is very well behaved within the quadrilateral in which it applies, there is no assurance that it is continuous across the boundary between adjacent quadrilaterals, unless the boundary is precisely vertical or horizontal. The degree of discontinuity depends on the details of the tiepoint specifications. In some cases, the discontinuity may be so small that the transformed picture has no visible defect, but in others it may be quite visible.

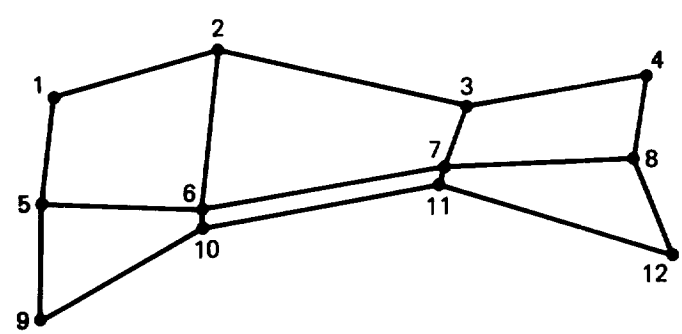

Figure 14-9. Sample quadrilateral tiepoint array (3 horizontal areas, 2 vertical areas)

The user has two choices to minimize the discontinuity: to carefully choose the transformation to minimize the discontinuities, or to specify the tiepoints in such a way that the quadrilaterals degenerate into triangles. A quadrilateral degenerates into a triangle if two adjacent tiepoints defining it have the same coordinates; the user can specify the coordinates in such a way that all quadrilaterals degenerate into triangles. Figure 14-10 shows a sample array of tiepoints satisfying this condition. When an area is a triangle, the cross terms in Eq. (14-16) are eliminated and the transformation becomes

$$\begin{aligned} x' &= ax + by + d \\ y' &= ex + fy + h \end{aligned} \qquad (14\text{-}20)$$

where the values of the coefficients are determined by requiring that

$$\begin{aligned} x'(j) &= ax(j) + by(j) + d \\ y'(j) &= ex(j) + fy(j) + h \end{aligned} \qquad (14\text{-}21)$$

for $j = 1,2,3$. The values of j designate the three distinct tiepoints defining the triangle. Because Eq. (14-20) is linear, the transformation is guaranteed to be continuous at the triangle boundaries; discontinuities in the output picture cannot occur.

There is a question about how to transform picture samples that fall outside all the quadrilaterals defined by parameters. One answer is to avoid this situation by specifying the control point locations so that every sample in the output picture falls within some quadrilateral. This requires some control points to fall exactly on or outside the border of the output picture. The program is not affected in any way by using control points outside the picture.

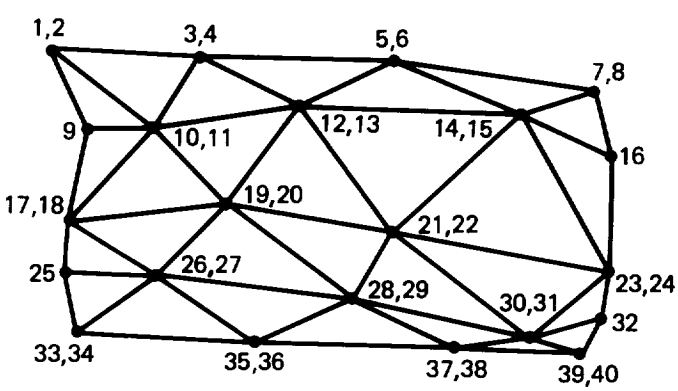

Figure 14-10. Sample triangular tiepoint array (7 horizontal areas, 4 vertical areas)

If some picture samples do fall outside the defined quadrilaterals, the program will process each such sample by assigning it to a nearby quadrilateral. This is done by "extending" the boundaries of all "edge" quadrilaterals to the picture borders. The user should understand that the algorithm can lead to discontinuities in the processed picture in the regions outside the defined quadrilaterals, even when the control areas are triangles.

20. GRADREM. Wide-angle aircraft scanners often exhibit large, systematic and nonlinear artificial brightness gradients along scan lines. GRADREM seeks to remove these gradients by finding the ratio of the input picture to an estimate of the gradient upon a flat field.

The user selects a region of the picture where differences in brightness are believed to be predominantly artificial. The lines in this region are averaged to produce a "standard" DN level at each sample. If requested, a box filter is used to smooth the standard DN function. Each pixel is then divided by its appropriate standard DN, and the specified gains and offsets applied. Floating-point arithmetic is used throughout.

21. IDISPLAY. IDISPLAY is a general purpose interactive display program that allows the black-and-white, color, and pseudocolor display of VICAR data sets. In addition, some basic graphics operations are available. Quick contrast stretching is performed in IDISPLAY by computing a transfer-function table and loading it into the video-hardware lookup table. The internal transfer function may be output to a disk data set and used later in batch operations. Input data sets to IDISPLAY may be in byte, halfword, fullword, integer, or real format.

The basic philosophy behind IDISPLAY is that it is user oriented but, at the same time, general purpose and device independent. Satisfying these criteria is difficult unless some assumptions are made. For color work, IDISPLAY assumes that for the video and graphics device, the IDs are ordered RED, GREEN, BLUE. It is the user's responsibility to ensure this either at logon or through the use of the SET command within IDISPLAY. Thereafter, the user can refer to color planes by name—RED, GREEN, and BLUE.

IDISPLAY contains a separate transfer-function table for each of the color planes. In addition, a pseudocolor table is available. Pseudocolor is produced by assigning a color to each shade of gray. In the pseudocolor mode, the hardware lookup table is loaded with the composite of the transfer-function table and the pseudocolor table.

A histogram is acquired for an area whenever it is displayed. An ACQUIRE command allows the user to acquire a histogram independent of the display. In the color mode, three histograms are acquired, one for each video plane.

IDISPLAY simplifies color work by assuming that, in the color or pseudocolor mode, all requested operations are to be performed on all three color planes at once. The user can suppress this feature by qualifying the command with the explicit statement of the name of the plane to be operated upon.

IDISPLAY can be executed in batch. If parameters are provided in the parameter field of the EXEC statement, IDISPLAY assumes it is operating in the batch mode.

22. LAVE. LAVE calculates averages of an array in either the horizontal or vertical direction. LAVE can be used to obtain quantitative values for horizontal or vertical periodic noises. An example would be the measure of horizontal noise introduced through video scanning. The output of LAVE can be plotted using the VICAR program QPLOT.

23. LIBEXEC. LIBEXEC is an interactive executive program designed to facilitate the task of digital image processing. Under LIBEXEC, the user at an interactive terminal may enter commands to perform three basic tasks:

(1) Locating image or nonimage data sets on disk or tape.

(2) Executing a VICAR program; with disk or tape, data inputs and parameters are set that direct the program's execution.

(3) Saving on disk or tape the output data sets of the VICAR program execution.

LIBEXEC is independent of installation-specific hardware devices. The interface between LIBEXEC and such devices is performed by special-purpose VICAR programs.

LIBEXEC operates as a command processor under TSO (Table 14-10).

24. LIST. LIST is a VICAR applications program that gives a decimal printout of a picture or portions of a picture and produces histograms of the printed areas. Either the printout or histogram may be suppressed. Picture data may be 6-bit, 8-bit, or halfword. Line and sample increments may be other than one.

25. LOOKUP. LOOKUP reassigns the DNs in a VICAR data set based upon the contents of a multichannel lookup table. This table will typically have been created by another VICAR program, IDISPLAY for example, but may be created or modified at the time LOOKUP is executed. The table is passed to LOOKUP via an input data set. Each table may hold up to four independent channels. i.e., four transfer functions.

LOOKUP is useful for creating, in batch VICAR, the same operations that were performed in an IDISPLAY

Table 14-10. LIBEXEC commands

Command	Function
Information	
FILE	Presents file, data set name, volume, and status of one or all allocated files.
LOCATE	Locates a data set name in the OS catalog and prints device and volume.
LOG	Makes a data set entry into the local library support file.
PROCLIB	Establishes a new default for the procedure library name.
PROJECT	Establishes a new default project code.
Data Set	
ALLOC	Allocates a new disk data set.
DELETE	Deletes a permanent or temporary disk data set.
FIND	Allocates an already existing disk data set.
PARAMS	Allocates a parameter data set.
SAVE	Changes the status of a data set from temporary to permanent and permits renaming.
TAPE	Asks for a tape volume to be mounted on an available device.
Execution	
EXEC	Executes a VICAR program.
EXIT	Terminates a LIBEXEC session.
CALL	Invokes a procedure of LIBEXEC commands.
TESTEXEC	Allows use of the TEST command in debugging a VICAR program.
Procedure	
EDIT	Allows creation of a new procedure of LIBEXEC commands in the user's personal procedure library or allows the modification of an existing procedure.
PROMPT	Allows prompting for procedure parameters while the procedure is executing. A command that can be included only in a procedure.
PDELETE	Deletes a procedure from the procedure library.
TTM	Denotes the appearance of a TTM string (here, TTM is not a keyword). A standard TTM string that may be included only within a procedure. TTM is macro language.
TSO	
*	Allows invocation of any TSO command, except TEST, from LIBEXEC.

session. LOOKUP also simplifies the production of pseudocolor pictures in batch.

A lookup table is made up of four independent channels. Each channel defines a mapping or discrete transfer function to be applied to an input picture. One or more of these channels may be undefined, depending upon the application. For example, IDISPLAY loads only the first channel when in the black-and-white mode and the first three channels when in color or pseudocolor mode. The lookup table is limited to four channels because VICAR allows a maximum of four output data sets.

The channels that are to be used by LOOKUP can be controlled with the USE parameters. The default is to use the first channel to map the first input data set to the first output data set, the second channel to map the second input to the second output, etc. If there are more outputs than inputs, the last input is mapped through the remaining channels to create the appropriate number of outputs. Thus, one input picture could be mapped through three independent transfer functions to three outputs. This feature allows simple production of pseudocolor pictures.

An input table may be modified before use with the CHANGE and LTABLE parameters. This modified table may then be saved by specifying the parameter TBLSAVE.

The format of the table data set is as follows: A table data set is made up of one or more tables stored in a VICAR data set. The data set contains a VICAR label followed by one or more records, each record containing a table.

The data-format code in the VICAR label defines the word structure of the table. Each table entry is stored as a "word," i.e., byte, halfword, fullword, integer, or real, depending on the format code. The number of table entries per channel, M, is computed by $M = NS/(4*k)$, where NS is the number of samples (bytes) per record and k is the number of bytes per pixel as specified in the format code of the VICAR label. Therefore, a byte table would have $NS = 1024$ and $M = 256$. The structure of the table record is shown in Figure 14-11.

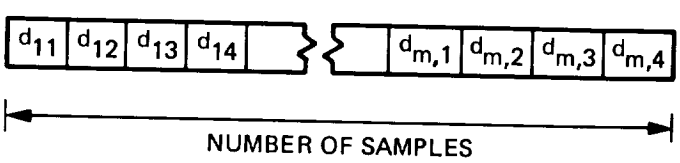

Figure 14-11. Structure of the table record. $d_{i,j}$ is the output DN for the jth channel that corresponds to an input DN = i.

26. MASK76. MASK76 is intended to replace the wide variety of MASK-type programs that have been written at IPL to satisfy various special needs. It combines features of MASKMVM and MASKDISK. It also has some entirely new features, including no maximum picture size; no limit on the number of labels that can be displayed; the display of picture-processing time, user initials (from subfield 1 of the HASP accounting field on the job card), and job name at the bottom of the picture; the ability to log the photo product into the Library Support File (IPLLSF); the capability of mixing labels and histograms at the bottom of the picture (labels at the left, histograms at the right); and the "squeezing" and "crunching" of labels.

27. MGEOM. MGEOM is used to make geometric changes in pictures, for example, to correct for a geometric distortion. MGEOM can also be used to increase picture size, reduce picture size, or rotate a picture. Maximum rotation is limited to 85° in either direction. MGEOM uses new methods for its internal operations but was written to act like the older routines GEOM and LGEOM for user convenience. New features include the following:

(1) Speed as fast or faster than GEOM, LGEOM, or GEOMA

(2) Better accuracy than GEOM, LGEOM, or GEOMA

(3) Preparation of "sharp" edges for mosaicking

(4) Allowance for halfword case

(5) No limits on size of input or output picture

(6) No limits on size of interpolation grid

(7) No "bad cases" involving excessive rereading of disk data sets

In most cases MGEOM should be used with input, intermediate, and output disk files on three different disk drives, or can be output to a tape unit. The intermediate disk file has the same dimensions as the *output* file except twice as many lines. Under certain circumstances, the intermediate file can have fewer lines, or the intermediate file can be omitted and the input file can be from tape. Also, an MGEOM interface to TIECONM has been developed.

MGEOM uses STACKA to obtain all available main-memory space for its operation. Then, based on the amount of space available, it scans the rectangles of the distortion grid to determine the maximum width, W, of output that can be calculated from a corresponding area of input that can be held in main memory. If W exceeds the output image size, then MGEOM operates in a one-pass mode (like GEOMA); otherwise it operates in a two-pass mode (like

LGEOM), using an intermediate data set. MGEOM executes pass 1 by calculating vertical strips in the output of W from curvy strips in the input. These lines are packed into the intermediate file. Pass 2 (if needed) efficiently reassembles the strips into the final output.

MGEOM substitutes double-precision, fixed-point arithmetic for single-precision floating arithmetic (currently used by GEOM, LGEOM, and GEOMA) for the representation of picture element location information and gray-scale bilinear interpolation.

The consequences of MGEOM operation are as follows: If MGEOM is in the two-pass mode, the input file is reread and an intermediate file is needed; these two files should be on disk. If MGEOM is in the one-pass mode, the input is read once and hence can be a tape file; the intermediate file need not be declared. The intermediate file needs twice as many lines as the output file in case of poor packing behavior when two widths are performed but output size is not divisible by two. Under some conditions the intermediate file can be shortened (Table 14-11).

MGEOM will obviously run faster if more region is allocated. To help users optimize region and speed, statistics are printed on phase 1 and phase 2. The phase 1 printout shows the width W; hence, the output line length in bytes divided by W indicates the number of times the input is reread. If the STACKA allocation (region: 60K) is doubled, then W will increase by $\sqrt{2}$. This information can be used to determine how much region is needed to get MGEOM into the single-pass mode. The second width W printed is the actual W chosen to optimize packing of the intermediate file. The printout for phase 2 is usually not significant, but if the number of buffers is *less than* the number of widths, then a severe inefficiency will occur in phase 2. If the keyword HVAR is specified, then the user is responsible for verifying that no more than 50 horizontal grid areas are processed in a single width W. The program will ABEND if more than 50 are attempted.

28. MSS. MSS converts unleaved multispectral data to multispectral scanner format (MSS format). "Unleaved multispectral data" refers to data in which each channel is a separate VICAR data set. MSS combines these data sets into one VICAR data set. This format will save I/O time in programs that require several spectral bands concurrently. All spectral information about a line can be read into core with one read operation.

Table 14-11. Conditions for shortening the intermediate file

Condition: Output Pixels	Intermediate File, NL factor
Odd	2.0
Divisible by 2	1.5
Divisible by 6	1.334
Divisible by 12	1.25
Divisible by 60	1.1667

29. PICREG. PICREG is an interactive program to obtain control points for registering two images. It displays both images in a split-screen fashion and collects tiepoints as they are cursored by the user. The tiepoints can then be formatted for use with TIECONM, GEOMA, LGEOM, or MGEOM.

PICREG will display both images in a split-screen manner, the first input on the left and the second input on the right. The user positions the trackball cursor(s) over identical features in each image and enters these tiepoints by hitting the carriage return. Tiepoint positions can be obtained directly from the trackball, as is, or can be optimized from this initial position using the extreme positions of histograms computed from the sums of rows and of columns of pixels (AREA keyword), or from cross correlation (CORR or POW keywords). In the latter case the expression is

$$CC = FT^{-1}[FT(P1)^* \times FT(P2)]$$

where CC is the correlation map, FT is Fourier transform, $P1$ and $P2$ are the IN and REF picture areas, and * is complex conjugate.

PICREG writes the locations of these raw tiepoints to the first output data set, updating the data set for every new point. PICREG will draw a cross (in the graphic plane) at each tiepoint location visible in the displayed image and label the cross with the corresponding tiepoint number. The raw tiepoints may be edited using the DELETE or REDO keywords. The FIT keyword allows the user to fit various surfaces to the raw tiepoints, and the FORMAT keyword will reformat the points and write them to the second output data set. PICREG will print the message *PICREG READY* whenever it is ready to accept new keywords or a new tiepoint location.

30. PSAR. The polygonal segment adjustment routine (PSAR) will adjust up to 100 polygonal areas (specified by the vertices) and rectangles (specified in the usual manner) by user-specified amounts. PSAR can be used to remove undesirable segments of pictures before mosaicking and can be used to separate desired portions of a picture for individual processing. In addition, PSAR can generate a byte or halfword picture of constant value and can saturate the output picture at user-specified levels.

PSAR adds user-specified values to the DN of each pixel in the polygon and/or rectangle determined by the parameters. The maximum and minimum DNs in the output picture are determined by HSAT and LSAT, respectively. The VICAR program QSAR (which is faster) should be used instead when only rectangular areas are being adjusted.

31. RATIO. RATIO operates on two input pictures to generate a third (comparison) picture. There are four modes of operation:

(1) RATIO OUT = GAIN*(IN1/IN2) + OFFSET

(2) LOG RATIO OUT = GAIN*LN(IN1/IN2) + OFFSET

(3) DIFFERENCE OUT = GAIN*(IN1-IN2) + OFFSET

(4) LOG DIFFERENCE OUT = GAIN*LN(IN1-IN2 + 256) + OFFSET

The GAIN and OFFSET values are calculated by RATIO so that the mean DN of the output picture will be 128 and saturation will be at a user-specified level. RATIO fetches the program F to form the output picture.

The region between the two EXCLUDE values is divided into 500 equal parts. These become the permissible histogram values. The input pictures are sampled according to the parameters AREA, PERCENT, and INCR to form the histogram. Values beyond the EXCLUDE parameters are ignored.

The histogram is filtered; then levels populated below THRESHOLD are set to zero. The mean of this histogram is calculated. Gain and offset values are chosen so that the mean is transformed to 128, and the higher of the dark and bright saturation levels is equal to the requested level of saturation.

The histogram is displayed, the VICAR label modified, and the gain and offset passed to the program F, which generates the output picture.

32. SIMPLIFY. The operation of SIMPLIFY is similar to the operation of any boxfiltering routine except that surface smoothing *does not* take place. In a pictorial sense, a 3-by-3 or a 5-by-5 window is passed over each pixel in the input image. For each pixel and its surrounding neighborhood, defined by the size of the window, a histogram is accumulated to identify the most frequently occurring DN value. If that DN value has occurred more than T times (the THRESHOLD value) and has also occurred more times than the DN value of the central pixel of the window, the DN value of the central pixel will be replaced with that value in the output image. Parameters used to specify special pixel replacement conditions have been added. A specific thematic class value may be simplified individually. Unclassified pixels may be removed where possible.

To accommodate the edges of the image that normally could not be simplified due to edge overlap of the window, the edges are mirrored over. This eliminates the need for special edge-processing procedures. If two DN values have the same frequency of occurrence and are the most frequently appearing DN values, the lower DN value will be used in replacement. The following window operations will demonstrate the operation of SIMPLIFY:

Example 1: Specifying SMALL and THRESHOLD = 4:

INPUT:	OUTPUT:
5 5 5	5 5 5
3 2 5	3 5 5
4 3 3	4 3 3

Example 2: Specifying SMALL and THRESHOLD = 4:

INPUT:	OUTPUT:
5 5 5	No change
3 2 2	
2 2 2	

Example 3: Specifying SMALL, THRESHOLD = 4, and REPLACE:

INPUT:	OUTPUT:
0 0 0	0 0 0
0 0 0	0 2 0
2 2 1	2 2 1

33. SIZE. SIZE is a VICAR applications program that may be used to expand or reduce a picture and/or to change the aspect ratio. The program SIZE duplicates many of the functions of the VICAR programs MAG, EXPAND, and PIXPIK but, for certain operations, is more convenient to use. When used to compress an image, SIZE determines the output DN value from the corresponding pixels in the input picture; it does not use the average of the area being compressed.

34. STATPLT. The program STATPLT generates a CalComp plot tape that contains a graph of the classes in a classification statistics data set. The user may specify which two spectral bands are to be used for the x and y axes.

For each class in a classification statistics data set (or for those specified by the size field), STATPLT does the following:

(1) Marks the position of the centroid of the class.

(2) Labels the centroid with its corresponding class number.

(3) Draws the ellipse that bounds the range of the class. The parameter SIGMA specifies the number of standard deviations within this boundary.

If the centroid of a class lies outside the range of the x or y axis, that class is ignored. Cut lines are drawn before and after the plot. The plotter pen should be positioned at the left edge of the paper before plotting.

35. STATS. STATS computes the statistics of specified training areas on multispectral data. The output consists of printer output, a statistics data set compatible with multispectral classifiers BAYES and FASTCLAS, and (optionally) a picture containing the scribed training areas. Input multispectral data may be in separate VICAR data sets or in MSS format.

If the SCRIBE option is requested, STATS begins by copying the specified input picture to the secondary output data set. The first training area parameters are then processed, and the training area is read from all input bands. Statistics on this area are compiled, and the area is scribed on the output picture. When the statistics for all training fields for a given class have been compiled, the statistics are written on the output STATS data set. The record number on which they are written is the class number of that class. The record will contain the mean, number of pixels, and covariance matrix for that class. The record length is a function of the number of spectral bands used. The maximum record length is 372 bytes, which corresponds to 12 spectral bands. The maximum number of records is 50 since class numbers must range from 1 to 50.

If desired, histograms of each training class in each band are printed. Spectral plots of the spectral signatures can also be printed. The option EXCLUDE allows the user to specify certain DNs for which statistics are ignored. This is useful, for instance, if the training area lies at the edge of a skewed picture. To prevent statistics from including pixels in the background skew, EXCLUDE,0 could be specified.

The printer output includes the training areas for the class, means and standard deviations for each band, and covariance matrix. The covariance matrix is simply the covariance taken between all combinations of spectral band pairs. The keyword NOPRINT suppresses the printer output.

36. STRETCH. STRETCH is a VICAR applications program that changes the point-by-point intensity of a picture by generating a transfer function on the domain of intensity values. The user may choose from among seven types of functions and, in many cases, may limit the domain of the function to a specified range of values. In addition, the user may complement pixel intensities, either before or after applying the transfer function to them. Input data may be in either byte or halfword form.

37. TEXTAD. TEXTAD is an application program with which a user may add notes directly on a picture and may scribe rectangles around areas on a picture.

38. TFILT. TFILT is a VICAR applications program that performs various BOXFILTER-type convolutional filters. TFILT is able to ignore DNs below a threshold when computing the low-pass average and is thus free of ringing in certain images. Scaling allows the dynamic range of high-pass filters to be improved before integer truncation.

At each pixel TFILT computes the average of all DNs greater than THRESH within an area of dimensions NLW by NSW centered on that pixel and performs the filter using this value. If the local average is $\overline{DN}$, if the pixel at the center of the averaged area is DN, and if the output pixel is OUT, then the four TFILT filters are as follows:

$$\text{HIGH} \quad \text{OUT} = (\text{DN}-\overline{\text{DN}})*\text{SCALE}+\text{DCTRAN}*\text{DN}+\text{OFFSET}$$

$$\text{SCENE} \quad \text{OUT} = [(\text{DN}-\overline{\text{DN}})/\overline{\text{DN}}]*\text{SCALE}\ \text{DCTRAN}*\text{DN}+\text{OFFSET}$$

$$\text{LOW} \quad \text{OUT} = \overline{\text{DN}}*\text{SCALE}+\text{OFFSET}$$

$$\text{DIVIDE} \quad \text{OUT} = (\text{DN}/\overline{\text{DN}})*\text{SCALE}+\text{DCTRAN}*\text{DN}+\text{OFFSET}$$

If $\overline{DN}$ should be 0 in the SCENE or DIVIDE filters, it is set to 1.

39. TIECONM. TIECONM prepares a gridded data set for POLYGEOM, GEOMA, LGEOM, MGEOM, or GEOMZ transformations. The input is paired sets of tie-points with no restrictions. It is, in principle, a surface-generation routine but creates the gridded data set so as to best interface with the VICAR routines above. The sequence *GEN, TIECONM, GEOMZ* can be used to generate a surface in image format through an arbitrary set of points. TIECONM uses the finite-element method (triangulation) for surface fitting.

TIECONM operates in two phases. In phase 1, the input points are fully triangulated by the Manacher version of the greedy algorithm. This selects the shortest edges first

and adds them to the triangulation so long as they do not cross previously added (shorter) edges. The algorithm proceeds until all edges are examined. Four extra points are added five diameters away from the convex hull so that the surface will extend smoothly beyond the input tiepoints.

In phase 2, the output grid is formed by evaluating the triangular surface at grid-point locations. That is, a grid point will fall in some triangle, and the GEOM shift will be the linear interpolation of the input shifts at the three corners of the triangle. The user should note that the triangular surface is continuous but not differentiable and that it passes through all of the input points. Point-surface generation techniques can be compared in Table 14-12.

40. USTATS. USTATS is a VICAR applications program that performs an unsupervised, clustering algorithm upon multispectral data. The output is a statistics data set compatible with the programs BAYES and FASTCLAS.

A sampling of pixels is chosen, determined by the keyword parameters INC, LINC, or SINC. The first sampled pixel is set as the first cluster. For each of the remaining pixels to be sampled, the following operations are performed:

(1) The Euclidean distance from the mean of each cluster is computed. The Euclidean distance (ED) is defined as

$$(ED)^2 = \sum_{\substack{\text{All}\\ \text{bands}}} (DN_{Mean} - DN_{Pixel})^2$$

(2) If the Euclidean distance to each of the existing clusters is greater than the value specified by the parameter INITIAL, a new cluster is formed by this pixel. Otherwise, the pixel is added to the nearest cluster, and that cluster's mean for each band is recomputed.

(3) The pixel to the left is then checked to see whether it can be grouped into the same cluster. If its Euclidean distance is not greater than the parameter INITIAL, it too is added to the cluster, and the means recomputed. This process is repeated until a pixel is found that cannot be added to the cluster.

(4) Each pixel to the right is checked in the same manner as in (3), above.

If the parameter NONN has been specified, steps (3) and (4), above, are omitted. If, at some point this process generates more clusters than have been specified in the parameter CLUSTER, the message *SAMPLING INCOMPLETE AT LINE n* will be printed. No more pixels will be sampled, but processing will continue.

When the sampling process is complete, the clusters that have been formed are examined. Clusters containing only one pixel are removed. Standard deviations for each band in each cluster are calculated, and, if the one-standard-deviation regions of two clusters overlap, they are merged into one cluster. The remaining clusters are sorted by population.

The parameters CLASSES and PERCENT determine the number of clusters to be retained as classes for output. If either of these parameters is specified, the default of 10 classes is overridden. If both parameters are specified, the conditions of both parameters must be met for the cluster to be included as an output class.

The output statistics data set is of the same format as the output data set of the program STATS and is suitable for input into BAYES and FASTCLAS. The only difference is that USTATS does not compute the off-diagonal elements of the correlation matrix but sets them to zero.

41. VDIGIT. VDIGIT will create an image containing the points or contours digitized on the Bendix Digitizer. The z coordinates may be entered on the Bendix keyboard and will become the DNs in the output picture. Applications such as creating altitude pictures from topographic maps are possible with VDIGIT.

Table 14-12. Point-surface generation techniques

Method	Properties			
	Continuous	Well-Behaved (No Mesas)	Differentiable	Precise Evaluation at Input Point
Triangulation	Yes	Yes	No	Yes
Interpolation r^{-1}	No	Yes	No	Yes
Interpolation r^{p}	No	No	No	Yes
Polynomial fit	Yes	No	Yes	No
Potential function	Yes	Unknown	Yes	Yes

C-5

VDIGIT should not be considered or confused with a replacement for the existing program DIGA. VDIGIT simply allows alternative utilization and application of the Bendix Digitizer by IPL.

VDIGIT allows for both x,y and x,y,z digitization. With x,y digitization, VDIGIT will generate a picture with the x,y coordinates scribed with a constant DN on a flat-field background. The x,y,z digitization allows the user to specify the z coordinate (via the Bendix keyboard) for a string of x,y coordinates. This z coordinate becomes the DN for the corresponding x,y coordinates (sample–line) in the output picture.

The size of the output picture is controlled with the VICAR size field. During digitization the user should define four approximately rectilinear, corner or limit points. These four points and the size field define the x,y scale of the output picture. To preserve the proper scale in the x and y directions, the user need specify only one, NL or NS. VDIGIT will compute the unspecified size based on the four limits.

The user may define the scaling factors, gain and offset, for converting the z coordinate to DN or may allow VDIGIT to automatically scale the z coordinates. While VDIGIT's scaling algorithm makes byte and halfword data greater than 0, the user may define scaling factors without this restriction on halfword data.

42. VERTSLOG. VERTSLOG replaces VMSS as the logging program for Landsat MSS data. The advantage of VERTSLOG is that it corrects for many of the geometric distortions found in Landsat MSS data. These include skew, aspect ratio, synthetic pixels, mirror-scan velocity profile, panorama effect, and band-for-band misregistration. In addition, the output from VERTSLOG may be full-frame pictures as opposed to the half-frame output of VMSS.

The inputs to VERTSLOG are the four quarter-frame files of the interleaved multispectral data as supplied by NASA's Goddard Space Flight Center. VERTSLOG unleaves the data, geometrically corrects it, and writes each spectral band as a separate VICAR data set.

VERTSLOG begins by reading the first record of each input that is a 40-byte ID record. This contains information such as the Landsat MSS frame number and the tape-sequence number. VERTSLOG checks to see that all input files have the same frame number and that they are in the proper sequence, that is, the first input is tape 1 of 4, the second is 2 of 4, etc. If an error is detected, a message describing the problem is printed, and execution is aborted.

The second record of each input is the annotation record of 624 bytes. From this, VERTSLOG extracts information such as the scene latitude, longitude, and spacecraft heading.

If the user knows that the ID or annotation records from one or more inputs are missing or are unreadable, the user may skip or ignore those records through the use of the parameters.

VERTSLOG is then able to generate a VICAR label for each of the output data sets. Included in the label are the Landsat MSS frame number, band number, title, latitude, longitude, spacecraft heading, sun elevation, azimith, processing code, and picture scale. The processing code describes the geometric corrections applied. The picture scale is in meters per pixel.

From each of the input data sets, VERTSLOG reads a quarter-line segment. A check is made to insure that each segment is synchronized with its corresponding line. If not, an error recovery routine is initiated that attempts to bring the data back into synchronization. If successful, a message is printed giving the line number where the vertical shift error occurred. This line in the output picture will have all zero DNs. If error recovery is unsuccessful, a message is printed, and processing continues with no correction performed.

The multispectral data are unleaved, synthetic pixels are removed, and the data are converted to 8-bit data.

The data for each band are resampled to compensate for distortions such as the mirror-scan velocity profile, panorama, and aspect ratio. A floating-point SKEW and a slight band-for-band registration correction are also then applied. The projection produced may be sinusoidal (equal scale) or space-oblique Mercator.

Resampling is normally done using linear interpolation between neighboring pixels. A cubic spline resampling function that uses four support points may be requested. The SPLINE option increases the execution time of the program by 80 percent.

A line is written for each spectral band, and the process is repeated for each input record. If, for some reason, VERTSLOG finds there are fewer lines than it expected (2340 is the default), a message is printed cautioning the user that the VICAR label contains an erroneous NL in the system label.

The resampling of the picture can be suppressed by specifying a negative aspect ratio. The geometric corrections are not performed in this case.

43. VLOGTOP. VLOGTOP is a VICAR applications program that logs and rectifies National Cartographic Information Center–Defense Mapping Agency (NCIC–DMA) elevation images.

NCIC–DMA tapes are standard label, variable block length, variable record length, 9 track, 1600 BPI. VICAR will not support this data format. JCL may be used to remove the standard label and unblock the tapes. The JCL in-line procedure, given in Figure 14-12, extracts file REC4.A from tape AEC503. It is necessary to know the record DSN. This can be located in the NCIC listings sent with each tape.

VLOGTOP will produce a halfword VICAR labeled data set suitable for use with LANDSAT, MILUS, MMS, or SLR data to provide altitude-control points. Information in the NCIC header is used to produce a descriptive label (Figure 14-13).

VLOGTOP takes out the variable-record-length problem with NCIC data and generates extra points at DN = 0 to produce a rectilinear image. Dimensions of the output data set will vary depending on the amount of rectifying needed. The buffer length is 5000. All size field information is set automatically by VLOGTOP. The number of lines varies, and NL 2500 should be used.

44. XFORM. XFORM performs a linear transformation on the input data. The transformation is specified by a parameter matrix. If desired, XFORM will automatically scale the output to a range of 0 to 255.

The program allows each corresponding pixel from the input data sets to be represented by a vector $\mathbf{X}^T = (\mathbf{X}_1 \mathbf{X}_2 \ldots \mathbf{X}_m)^T$. **A** is the parameter matrix (n by m). Then XFORM computes the product

$$\mathbf{AX} = \mathbf{V}$$

or

$$\begin{pmatrix} a_{11}\, a_{12} \cdots a_{1m} \\ a_{21}\, a_{22} \cdots a_{2m} \\ \cdot \\ \cdot \\ \cdot \\ a_{n1}\, a_{n2} \cdots a_{nm} \end{pmatrix} \begin{pmatrix} x_1 \\ x_2 \\ \cdot \\ \cdot \\ \cdot \\ x_m \end{pmatrix} = \begin{pmatrix} v_1 \\ v_2 \\ \cdot \\ \cdot \\ \cdot \\ v_n \end{pmatrix}$$

A gain and offset is then applied to each component:

$$V'_i = p_i + q_i v_i$$

```
//TOPOLOG JOB
//REFMT PROC
//CPY EXEC PGM=IEBGENER
//SYSPRINT DD SYSOUT=A
//SYSIN DD DUMMY
//SYSUT1 DD UNIT=2400,VOL=SER=&VOLSER,DSN=&DS,
//          DISP=(OLD,PASS),LABEL=&FI
//SYSUT2 DD UNIT=2400,DSN=&DS,DISP=(NEW,PASS),VOL=(,RETAIN,SER=SCRTMP),
//          LABEL=(&FO,BLP),DCB=(RECFM=U,BLKSIZE=32756,DEN=3)
// PEND
//STEP1 EXEC REFMT,FI=1,FO=1,VOLSER=AEC503,DS='REC4.A'
```

Figure 14-12. Reformatting procedure

```
*****DMA-NCIC 1:250000 DIGITAL TERRAIN MAP****U.T.M. PROJECTION**
 SHEET NJ 11-08 W *SERIES  V502 *EDITION ED 5  *ZONE 11*EDU  1=FEET
 PIXEL=.01 INCH*SHEET CORNERS ** GEOGRAPHIC COORDS OF SHEET CORNERS
 NW L(X)=     69 S(Y)=   1798 ** NW LON=-118  0  0  LAT=  38  0  0
 NE L(X)=   1452 S(Y)=   1792 ** NE LON=-117  0  0  LAT=  38  0  0
 SW L(X)=     50 S(Y)=     50 ** SW LON=-118  0  0  LAT=  37  0  0
 SE L(X)=   1452 S(Y)=     44 ** SE LON=-117  0  0  LAT=  37  0  0
 ELEVATION(FEET   ):MIN      1960* MAX     10400*
 NOTE:NORTH IS 90 DEGREES CLOCKWISE FROM UP
```

Figure 14-13. Descriptive label

References

Abercrombie, F. N., A. R. Barringer, J. H. Davies, and R. Dick (1978). *The application of airborne particulate collectors and automated multi-element analysis to studies of air pollution.* Paper presented at the 71st Annual Meeting of the Air Pollution Control Association, Houston, Texas, June 25–30, 1978.

Barringer, A. R., J. H. Davies, and L. Daubner (1978). *Surtrace®, an airborne geochemical system.* Paper presented at the 12th International Remote Sensing Symposium, Manila, Philippines, April 1978.

Bramlett, L., D. Emilia, J. Holden, R. Kerns, S. Moll, and R. Sadowski (1979). *Uranium exploration systems case study, Copper Mountain, Wyoming* (unpublished conference report). Grand Junction, Colorado: Bendix Field Engineering Corporation.

Conel, J. E., and D. B. Nash (1970). Spectral reflectance and albedo of Apollo 11 lunar samples: Effects of irradiation and vitrification and comparison with telescopic observations. *Proceedings of the Apollo 11 Lunar Science Conference, Vol. 3,* 2013–2023.

Edwards, D. K., J. T. Gier, K. E. Nelson, and R. D. Roddick (1961). Integration sphere for imperfectly diffuse samples. *Appl. Optics, 51,* 1279–1288.

Ford, J. P., R. G. Blom, M. L. Bryan, M. I. Daily, T. H. Dixon, C. Elachi, and E. C. Xenos (1980). *Seasat views North America, the Caribbean, and Western Europe with imaging radar* (JPL Publication 80-67). Pasadena, California: Jet Propulsion Laboratory.

Goetz, A. F. H., F. C. Billingsley, A. R. Gillespie, M. J. Abrams, R. L. Squires, E. M. Shoemaker, I. Lucchitta, and D. P. Elston (1975). *Application of ERTS images and image processing to regional geologic problems and geologic mapping in northern Arizona* (JPL Technical Report 32-1597). Pasadena, California: Jet Propulsion Laboratory.

Goetz, A. F. H., and L. C. Rowan (1981). Narrow-band IR radiometery for mineral identification: Shuttle Multispectral Infrared Radiometer (SMIRR) aircraft test results. *Proceedings of the IEEE IGARSS Symposium,* Washington, D.C., June 8–10, 1981. (Summary)

Grainger, J. F., and J. Ring (1962). The luminescence of the lunar surface. In Z. Kopal (Ed.), *Physics and Astronomy of the Moon.* New York: Academic Press, 385–405.

Johnson Space Center (1977). *Operations manual NS-001 Multispectral Scanner* (JSC-12715). Houston, Texas: NASA Johnson Space Center, Sensor Systems Branch, Infrared Section.

Jordan, R. L. (1980). The Seasat-A Synthetic Aperture Radar system. *IEEE J. Ocean Eng. OE-5*(2), 154–164.

Landsat Data User's Handbook (1979). Arlington, Virginia: U.S. Geological Survey.

Theisen, A. F., R. D. Watson, and P. Niesen (1979). Interpretation of luminescence imagery of mineralized areas, Big Indian Valley, Utah. *U.S. Geol. Surv. Open File Rpt. 79-574.*

Watson, R. D., and W. R. Hemphill (1976). Use of an airborne Fraunhofer Line Discriminator for the detection of solar stimulated luminescence. *U.S. Geol. Surv. Open File Rpt. 76-202.*

Wendtland, W. W., and H. G. Hecht (1966). *Reflectance spectroscopy.* New York: Interscience Publisher.

Wu, C. (1980). A digital fast correlation approach to produce Seasat SAR imagery. *Proceedings of the IEEE International Radar Conference,* Arlington, Virginia, 153–160.

Zeitzeff, E. M., C. L. Wilson, and D. H. Ebert (1970). MSDS: An experimental 24-channel multispectral scanner system. *Bendix Tech. J., 3*(2), 20–32.